University of Nevada, Reno

Temporal and Petrological Constraints of Ultrahigh-Pressure Metamorphism And Exhumation of Crustal Material From Mantle Depths To Earth's Surface: Insights From A Large And Small UHP Terrane

A dissertation submitted in partial fulfillment of the
requirements for the degree of Doctor of Philosophy in
Geology

by

Joel W. DesOrmeau

Dr. Stacia M. Gordon/Dissertation Advisor

May, 2016

THE GRADUATE SCHOOL

We recommend that the dissertation
prepared under our supervision by

JOEL WILLIAM DESORMEAU

Entitled

Temporal And Petrological Constraints Of Ultrahigh-Pressure Metamorphism And Exhumation Of Crustal Material From Mantle Depths To Earth's Surface: Insights From A Large And Small Ultrahigh-Pressure Terrane

be accepted in partial fulfillment of the
requirements for the degree of

DOCTOR OF PHILOSOPHY

Dr. Stacia M. Gordon, Advisor

Dr. Gregory B. Arehart, Committee Member

Dr. Christopher D. Henry, Committee Member

Dr. Simon R. Poulson, Committee Member

Dr. Thomas P. Albright, Graduate School Representative

David W. Zeh, Ph. D., Dean, Graduate School

May, 2016

Abstract

Ultrahigh-pressure (UHP) terranes expose continental material that has subducted to mantle depths and then returned to Earth's surface. These terranes typically consist mainly of migmatitic host ortho- and paragneiss, with minor (~5%) layers and lenses of UHP eclogite; at least twenty terranes have been described and identified by the preservation of UHP minerals (i.e., coesite and diamond) mainly within eclogite. These terranes fall into two broad categories: 1) large (30,000 km^2) coherent terranes characterized by slow (>20 Myr) subduction–exhumation histories, and 2) small (~4,000 km^2) terranes that have undergone rapid (<10 Myr) subduction–exhumation histories. To better understand the geodynamic processes involved in deep continental subduction and subsequent exhumation of buoyant crustal material within these two types of UHP terranes, it is important to constrain the timing and conditions of: 1) peak UHP metamorphism recorded in the eclogites; 2) the subsequent eclogite retrograde metamorphism; and 3) the host-rock migmatization which likely occurs during exhumation from the mantle to the upper crust.

This study investigates the Western Gneiss Region (WGR) of Norway, a giant UHP terrane, and the gneiss domes exposed in the D'Entrecasteaux Islands in eastern Papua New Guinea (PNG), a small UHP terrane, in order to understand the similarities and differences among the subduction and exhumation of these end-member terranes. To better understand the maximum pressure and temperature the rocks reached within the mantle, thermobarometry and phase-diagram modeling are applied to the PNG (U)HP eclogites, as previous work suggested a wide range of results, many of which were not at

UHP. In order to understand the timing and rates of subduction and exhumation events, high-precision zircon U-Pb isotope dilution–thermal ionization mass spectrometry geochronology and trace-element analyses (ID-TIMS-TEA) of the (U)HP rocks exposed in the two terranes are used, as these tools can decipher tectonic events that occur on a sub-million year timescale.

In the WGR, UHP rocks are exposed within three domains that have been interpreted to have undergone a similar tectonic history, with a long duration of (U)HP metamorphism from ca. 425–400 Ma associated with the Scandian-phase of the Caledonian orogeny. In order to test if UHP metamorphism was a single ~25 Myr event, eclogite was collected from two of the three UHP domains for high-precision ID-TIMS-TEA analysis. Zircon was extracted from the bulk rock, mounted in an epoxy mount, and screened for Scandian ages using high-spatial resolution laser ablation split-stream inductively coupled plasma mass spectrometry (LASS-ICP-MS). These Scandian-aged zircons were subsequently analyzed by ID-TIMS-TEA. The LASS analyses reveal a spread in results from both samples, with ages between 414 and 397 Ma. In comparison, the ID-TIMS analyses from the exact same zircons analyzed by LASS reveal two age populations of ca. 409 Ma and ca. 402 Ma from a garnet–quartz layer within the Saltaneset eclogite of the southern UHP domain. In comparison, the Ulsteinvik eclogite collected from the central UHP domain also yields two ID-TIMS age populations: ca. 409–407 Ma and ca. 402 Ma. Thus, two eclogites from different regions within the giant WGR UHP terrane reveal the same two age populations. Zircon trace-element data collected via laser-ablation and solution analyses for the two-age populations yield depleted heavy rare earth element (HREE) patterns and flat-to-positive Eu anomalies.

The combined age and trace-element data indicate that the WGR terrane underwent two distinct eclogite-facies zircon (re)crystallization events at ca. 409–407 Ma and ca. 402 Ma at localities ~40 km apart. These results support the interpretation that the UHP terrane was subducted and exhumed as a large (30,000 km^2) coherent slab of crustal material, but that as this terrane was subducted, there were two different events that affected this giant terrane while it was at eclogite-facies conditions.

The Pliocene PNG UHP terrane exposes a series of east–west gneiss domes, Normanby, Oiatabu, Mailolo, and Goodenough that contain eclogites within mainly highly migmatitic quartzofeldspathic gneiss. This UHP terrane is unique in that it is the only one on Earth that is actively exhuming, in this case within the Woodlark Rift. To better understand the pressure-temperature-time-deformation path taken by this young UHP terrane, a suite of fresh to nearly-completely retrogressed eclogites were sampled from Oiatabu, Mailolo, and Goodenough Domes for thermobarometry, pseudosection modeling, and high-precision ID-TIMS-TEA zircon analyses. A kyanite-phengite eclogite from Oiatabu Dome records equilibration at UHP conditions of ~30–31 kbar and ~635–660 °C, whereas a fresh phengite eclogite from the central Mailolo Dome yields peak conditions of ~27–30 kbar and ~510–560 °C. Zircons extracted from the Mailolo Dome eclogite reveal UHP metamorphism occurred from ca. 6.0 to 5.2 Ma, based on zircon that contain inclusions of the peak metamorphic assemblage.

Following UHP recrystallization, the crustal material ascended along a near-isothermal decompression path, accompanied by partial melting and retrogression, to the base of the crust. The host ortho- and paragneiss from the eastern Normanby and Oiatabu Domes record the early stages of this retrogression, with ID-TIMS zircon dates that

document retrogression-related metamorphism in the structurally higher portions of the domes at ca. 5.7–4.5 Ma. Zircons from retrogressed eclogites collected within the Oiatabu and Mailolo Domes, also record initial exhumation at ca. 4.6–4.3 Ma; the zircon from these samples are associated with garnet- and omphacite-breakdown reactions. Continued exhumation and near-complete retrogression in the lower crust occurred at ca. 2.8–2.6 Ma, based on zircons from heavily retrogressed eclogites collected in the westernmost Goodenough Dome. Zircon trace-element data from all the eclogites show depleted HREE and absent negative Eu anomalies suggesting eclogite-facies zircon (re)crystallization, although some grains are clearly in textural equilibrium with lower-pressure phases (i.e., amphibole and plagioclase).

To further track the exhumation history of the PNG UHP terrane, samples representing different melt generations (e.g., strongly-deformed leucosomes versus nondeformed dikes) that formed during exhumation are used to record different parts of the deformation history. The crystallization of strongly-deformed sills and leucosomes likely associated with cooling and amphibolite-facies retrogression suggests the terrane reached neutral buoyancy near the base of the crust first in the east by ca. 4.1 Ma in Normanby Dome, by ca. 3.5–3.0 in the central Mailolo Dome, and by ca. 3.9–2.8 in the far west in Goodenough Dome. Further exhumation and continued amphibolite-facies metamorphism within the mid-crust are marked by weakly deformed dikes recording melt crystallization at ca. 3.0–2.9 Ma in Oiatabu Dome and ca. 2.4–2.3 Ma in Mailolo and Goodenough Domes. Final extension-related exhumation of the entire terrane within the upper crust occurred by ca. 1.8 Ma, as recorded by the crystallization of non-deformed plutons, pegmatites, and dikes.

Taking into account all of the petrologic, structural, geophysical, and geochronologic constraints, a model for the exhumation of the PNG UHP terrane involves (re)crystallization of the previously subducted continental material during a flux of hot asthenospheric fluids related to westward seafloor spreading in the Woodlark Rift from ca. 6.0 to 5.2 Ma. Subsequently, the partially-molten (U)HP rocks rose as diapirs that underwent rapid near-vertical exhumation to the base of the crust, resulting in the generation of abundant partial melting and the initial retrogression of the crustal material. Upon reaching neutral buoyancy at the base of the crust, the (U)HP body laterally flowed, but also cooled, allowing the crystallization of the strongly deformed leucosomes. Further exhumation to the upper crust was assisted by enhanced buoyancy due to later injection of partial melt and concurrent extension within the active Woodlark Rift.

Eclogites from the WGR and eastern PNG were both subjected to upper mantle depths, but they preserve different metamorphic and exhumation histories. The ID-TIMS zircon results from the small PNG UHP terrane document rapid (≥1.5 cm/yr) exhumation from peak metamorphism in the upper mantle at ca. 6.0–5.2 Ma to emplacement within the brittle upper crust in ~3 Myr, some of the fastest rates of UHP exhumation documented on Earth. In comparison, studies based on multiple geochronological techniques have suggested that the WGR likely resided at mantle depths for tens of millions of years, from ca. 425–400 Ma. However, the new results from ID-TIMS U-Pb zircon dates suggest eclogite-facies metamorphism occurred during at least two distinct (re)crystallization events at ca. 409–407 Ma and ca. 402 Ma, at the youngest end of the previously proposed timescale of UHP metamorphism. Thus, these new results suggest that the interpretation that giant UHP terranes undergo a long continuous duration of

UHP metamorphism may need to be reevaluated, as there may be distinct events hidden within this metamorphic window that can only be deciphered via a high-precision geochronometric technique. This is supported by the results from the PNG UHP terrain, where mantle to crustal exhumation occurs in only ~3 Myr. The high-precision results from the two UHP terranes that differ in size, age, and in their exhumation history provide important constraints on the timing and duration of UHP metamorphism and exhumation to the upper crust. Understanding tectonic events on such short timescales has drastic implications for geodynamic models attempting to characterize the switch from subduction to exhumation and the transfer of continental material through the lower crust to Earth's surface via coupled buoyancy-driven and extension-related exhumation processes.

Acknowledgements

As I end this journey, I need to thank those who have been instrumental in my pursuit of rocks. First and foremost, I wish to thank my parents for unending support throughout it all. They raised us boys up right and for that I will always be thankful. I owe everything to my older brothers Todd and Trent. They made sure I grew up knowing how hard it was to be the youngest. Thanks to my sister-in-law Kim, niece Morgan, and nephew Tanner for reminding me there is more to life than school and travel. To all of my non-geology friends, thanks for living pretty boring lives. It makes me feel awesome more often than not.

I would not have finished without the help of all of my friends on the 11th floor at MIT. Seth Burgess took me in as a young pup in the TIMS geochronology world and showed me what not to do to get the best analyses in the lab. Thanks for providing support and guidance at every step of the way and for making the Muddy quite possibly my favorite place on Earth. Jahan Ramezani has been an incredible mentor during my countless/endless visits to MIT and I have him to thank for instilling the ninja in me so that I could take my blanks down to the next level. I have many fond memories of running the sector 54 at 2:00 am while Jahan was working tirelessly at fixing one of the many issues with the other machines. Thanks to my friend Mike Eddy for always getting more excited about my data than me. It wouldn't be a Sunday morning at MIT without Mike sitting at the sector 54 with a coffee and some big tectonic problem on his mind. Thanks to Annie for always being there with a fruit popsicle, a smile, and an empty apartment to crash in after days of "sleeping" in the lab. Special thanks to Mauricio for coming in strong at the end of my time at MIT and carrying on the tradition of double-

batch low blanks followed by a visit to the Muddy. Last but not least, thanks to Sam Bowring for allowing me to pursue high-precision geochronology at MIT. Thanks for pushing me at every turn and allowing me to be a regular in such a special place. I will never forget my time on the 11th floor at MIT.

I've had the incredible opportunity to work alongside Tim Little on the Papua New Guinea project. Tim led us on our treks up river gorges, convinced local tribes to allow us to continue with our research at every turn, and has shared samples from all of his previous field seasons at the drop of a dime. He is the true definition of a collaborator.

I wish to thank my advisor, Stacia Gordon, who provided me the opportunity to perform cutting-edge research and see parts of the world I didn't know existed. Stacia gave me the freedom to work semi-uncontested for years, but was always there to answer an email or question. Her support and mentoring has been instrumental in my development as a scientist. I couldn't have asked for a better mentor and friend over the years. Thanks for taking me in as your first PhD student and showing me the ropes. I look forward to a long career of collaborating with you and the colleagues you have introduced me to. It truly has been an honor.

Thank you to all of those who have listened to me rant about rocks while fishing, hiking, or driving along some lonesome road. My only hope is that one day somebody will remember that time when portions of the Proterozoic Belt Supergroup were thrust eastward over Cretaceous shales and sandstones along the Rocky Mountain front or when the world's youngest eclogites formed in the upper mantle (6.0–5.2 Ma).

TABLE OF CONTENTS

LIST OF TABLES

Chapter 2

Chapter 3

LIST OF FIGURES

Chapter 1

Chapter 2

Chapter 3

Chapter 1: Introduction to the Thesis

Subduction of oceanic lithosphere and incident arc magmatism at active plate margins are an indication of the dynamic evolution of Earth's surface as a result of plate tectonics. Progressive subduction leads to closure of ocean basins and eventual arc-continent and continent-continent collisions (O'Brien, 2001; Ernst 2005; Zheng, 2008). These collisions allow for continental material to reach high-pressure (HP), eclogite-facies conditions, and possibly even greater pressures and temperatures, within the ultrahigh-pressure (UHP) realm, where coesite and diamond are stable. The discoveries of coesite (e.g., Chopin, 1984; Smith, 1984) and micro-diamond (Sobolev and Shatsky, 1990) inclusions in metamorphic minerals of supracrustal rocks provided the mineralogical evidence for this burial of continental material to depths of >120 km.

To date, over twenty UHP terranes have been identified throughout the world; many formed during the Phanerozoic (Fig. 1; Carswell and Compagnoni, 2003; Liou et al., 2009; Zheng, 2012) and are part of major collisional orogens. Most UHP terranes are dominated by (migmatitic) quartzofeldspathic gneiss that host lenses of eclogite that commonly preserve the mineral assemblages diagnostic of high-pressure metamorphism. In numerous UHP terranes, coesite and diamond have also been identified in rigid host minerals (i.e., zircon, omphacite, garnet) within the host gneisses, suggesting that both the host gneiss and eclogite experienced UHP metamorphism.

Characterizing the processes that lead to the formation and preservation of UHP mineral assemblages requires a detailed understanding of how much crustal material was subducted and subsequently exhumed and the rates at which processes occurred that drove this subduction and exhumation. Within UHP terranes, some fresh eclogite commonly exists; however, many UHP rocks are overprinted by thorough to complete

retrograde-mineral reactions during exhumation to the surface. In addition, within UHP terranes, there is significant evidence for decompression-driven *in situ* partial melting that likely accompanies this retrogression.

In this study, I link the evidence for the timing and conditions of peak metamorphism with temporal constraints for eclogite retrogression reactions and migmatization of the host rocks to provide a detailed history of UHP exhumation for two contrasting UHP terranes: the Western Gneiss Region (WGR) of Norway and the D'Entrecasteaux Islands in eastern Papua New Guinea (PNG). The Western Gneiss Region consists of a giant area of high-pressure continental rocks (30,000 km^2), with ~5,000 km^2 of UHP rocks exposed across three domains: the northern, central, and southern domains (Fig. 2; Root et al., 2005, Kylander-Clark et al., 2012). Previous geochronological studies interpret that (U)HP rocks remained at eclogite-facies conditions from ca. 425–400 Ma prior to exhumation from mantle depths. To reside at mantle depths for ~25 Myr requires that the crustal rocks experienced multiple UHP events or that the crust was thick and slowly (>20 Myr) subducted (Root et al., 2005, Hacker, 2007; Kylander-Clark et al., 2009). In contrast, the D'Entrecasteaux Islands of eastern PNG expose ~4,000 km^2 of migmatitic gneisses hosting eclogite within domal structures, including from west to east, the Normanby, Oiatabu, Mailolo, Morima, and Goodenough Domes (Fig. 3; e.g., Davies and Warren, 1988, 1992; Hill and Baldwin, 1993; Baldwin et al., 2008 Little et al., 2011). Studies of this UHP terrane have documented a short-lived (≤6 Myr) subduction–exhumation history (Baldwin et al., 2004; Monteleone et al., 2007, Zirakparvar et al., 2011; Gordon et al., 2012; Baldwin and Das, 2015). The primary goal of this research is to better understand the timing and duration of UHP metamorphism and exhumation

within these two terranes of contrasting size, age, and tectonic evolution in order to place tighter constraints on the geodynamic processes involved with the transfer of buoyant crustal material to and from mantle depths.

Most investigations of UHP terranes have relied upon *in situ* U-Pb zircon high-spatial resolution and garnet–whole rock geochronological techniques to link time to the pressure-temperature path taken by UHP rocks (Gebauer et al., 1997; Hermann et al., 2001; Lapen et al., 2003; Schmidt et al., 2011). However, *in situ* results commonly have large errors (typical uncertainties of 2%), and in some cases, are inaccurate. These issues result from a variety of potential problems, including: the small amount of radiogenic Pb measured, uncertainties in the common-Pb correction, and the standards used for matrix matching and fractionation during analysis do not match with the unknowns. Garnet geochronometers also have limitations, including that garnet dating requires the analysis of multiple garnet fractions that may be mixing zoned garnets (typical fractions are ~200–250 mg). In addition, some datasets are limited to two-point isochrons, and assessing open- versus closed-system behavior (i.e., diffusion of Lu–Hf or Sm–Nd) is difficult for UHP terranes that have experienced high temperatures. In comparison, high-precision ID-TIMS geochronology has the ability to measure fragments of single zircons to a precision better than 0.1% for a $^{206}Pb/^{238}U$ date. This precision results from eliminating issues with Pb-loss by chemically abrading zircons prior to dissolution (Mattinson, 2005), spiking grains with a known tracer solution, separating Pb and U from the remainder of the zircon via column chemistry (Krogh, 1973), and hours of stable ion beam analyses, which have small and predictable mass-dependent fractionation (Schoene et al., 2013).

For this study, I have integrated high-spatial resolution LASS and high-precision ID-TIMS-TEA geochronology on the exact same single zircons, or fragments of zircon, from (U)HP eclogites from the WGR and PNG UHP terranes to document UHP metamorphism on the finest-timescales possible. This resolution is required to decipher multiple metamorphic events (i.e., to determine if multiple UHP events occurred and to separate UHP versus retrogression metamorphism) that occur on geologically short timescales that would otherwise be masked by low-precision techniques. In addition, ID-TIMS zircon dates from host gneiss, retrogressed eclogites, and crystallized melt fractions document the deformation history and exhumation of the PNG terrane at a sub-million year timescale. Previous investigations of PNG (U)HP eclogites poorly constrain the peak metamorphic conditions due to limitations in the techniques available for those studies; therefore, the peak conditions for UHP eclogite-facies metamorphism in the eastern PNG terrane are addressed to better document the depths from which rapid exhumation occurred. Overall, these results provide important P-T-t estimates for ongoing studies investigating the geodynamic processes involved in deep continental subduction, the mantle residence times of crustal material, the preservation of exhumed UHP crustal material, and the exhumation mechanisms and rates of UHP terranes.

The following chapters of this dissertation are written as separate scientific papers. The second chapter, *Insights into (U)HP metamorphism of the Western Gneiss Region, Norway: A high-spatial resolution and high-precision zircon study*, was published in Chemical Geology in 2015 (DesOrmeau et al., 2015). This work details the timing and duration of UHP metamorphism within the giant UHP terrane, the Western Gneiss Region of Norway. Combined measurements of zircon U-Pb and trace-element

compositions by LASS and ID-TIMS-TEA techniques allowed for a better understanding of peak eclogite-facies metamorphism experienced by two widely separated UHP eclogites across the large terrane. Previous work had described a long duration of eclogite-facies metamorphism from ca. 425–400 Ma (Terry et al., 2000; Bingen et al., 2004; Root et al., 2004; Kylander-Clark et al., 2007, 2009; Krogh et al., 2011), whereas the new ID-TIMS-TEA results reveal two separate eclogite-facies events at ca. 409–407 Ma and ca. 402 Ma from both localities. These results further support the idea the giant WGR UHP terrane acted as a large, coherent body during subduction to and exhumation from the upper mantle during the Scandian orogeny.

The third chapter, *Phase-diagram calculations of kyanite- and phengite-bearing eclogites from the D'Entrecasteaux Islands, Papua New Guinea*, focuses on providing better estimates of the peak metamorphic conditions attained by (U)HP eclogites from Oiatabu and Mailolo Domes. Thermobarometry was combined with updated net-transfer reactions and phase-diagram modeling using the thermodynamic modeling program Perple_X (Connolly, 2005) to refine the previously estimated wide range of P–T conditions of ~14–27 kbar and ~530–930 °C, reported for PNG (U)HP eclogites (Davies and Warren, 1992; Hill and Baldwin, 1993; Baldwin et al., 2004, 2008; Monteleone et al., 2007). Phase-diagram modeling uses an effective bulk composition of the rock to calculate predicted mineral-stability fields and mineral compositions and proportions in P–T–X space for a specific rock (Powell and Holland, 2008, 2010). Results from a kyanite-phengite eclogite from Oiatabu Dome record equilibration at UHP conditions within the coesite-stability field at ~30–31 kbar and ~635–660 °C, whereas a kyanite eclogite from Oiatabu Dome records lower P–T conditions within the quartz stability

field at ~22–27 kbar and 560–640 °C. In comparison, a fresh phengite eclogite from Mailolo Dome to the west records UHP conditions of ~27–30 kbar and ~510–560 °C. Thus far, coesite has only been identified within one eclogite in PNG (Baldwin et al., 2008); however, the new results from Oiatabu Dome indicate that the exhumed crustal rocks within this dome were also subjected to UHP conditions. This chapter will be submitted to the Journal of Metamorphic Geology.

The fourth chapter, *Mantle to crustal depths at plate-tectonic rates: High-precision U-Pb and trace-element zircon results from the Pliocene Papua New Guinea (U)HP terrane*, will soon be submitted to Science Advances. This contribution details the timing of peak metamorphism and eclogite retrogression across Oiatabu, Mailolo, and Goodenough Domes of the PNG UHP terrane. In addition, the timing of retrogression-related metamorphism of the host gneiss and melt crystallization within the Oiatabu Dome is also presented. The high-precision ID-TIMS zircon dates reveal discrete tectonic events on a sub-million year timescale, recording the timing of peak metamorphism at 6.0–5.2 Ma, to retrogression during initial exhumation ~1.0–1.5 Myr later, and near-complete retrogression of eclogites ~2.0–1.5 Myr after the initial exhumation. The ID-TIMS results from the host gneiss show coeval retrogression-related metamorphism with the structurally deeper eclogites. Weakly deformed dikes record late melt crystallization and document the final stages of ductile deformation within the Oiatabu Dome. Zircons dated by ID-TIMS in this study contain peak HP mineral inclusions, whereas other zircons are associated with retrogression reactions. These results provide detailed resolution of (U)HP eclogite exhumation from the mantle to lower crust, with the Mailolo

Dome eclogite recording some of the fastest (≥1.5 cm/yr) exhumation rates reported among UHP terranes.

The fifth chapter, *Tracking the Exhumation of a Pliocene (U)HP terrane: U-Pb and Trace-element Constraints from Zircon, D'Entrecasteaux Islands, Papua New Guinea*, was published in Geochemistry, Geophysics, and Geosystems in 2014 (DesOrmeau et al., 2014). This work focuses on the role of partial melting in aiding the exhumation of the PNG (U)HP terrane. Across the PNG (U)HP terrane, the domes expose arguably the greatest amount of crystallized partial melt of any UHP terrane on Earth. Abundant strongly deformed leucosomes, weakly deformed dikes, and nondeformed plutons, pegmatite, and dikes are found and provide temporal estimates on the deformation and exhumation history. Rapid exhumation from mantle depths to the base of the lower crust is recorded by the short timescales (<1 Myr) between the end of UHP metamorphism and the crystallization of strongly deformed sills and layer-parallel leucosomes from Normanby, Mailolo, and Goodneough Domes. The final stages of ductile-deformation are recorded by the crystallization of weakly deformed dikes over a narrow ~0.5 Myr range across all domes. Nondeformed plutons, pegmatite, and dikes record the final emplacement of the UHP terrane in the upper crust ~3 Myr after peak metamorphism. The ID-TIMS results document the near-continuous exhumation of a melt-rich UHP terrane within an active rift environment.

The sixth and final chapter will summarize the utility of combined high-spatial resolution and high-precision zircon geochronology for deciphering UHP metamorphism, the use of phase-diagram modeling of (U)HP eclogites to determine peak P–T conditions,

and using high-precision geochronology to track the exhumation of a small UHP terrane from the upper mantle to Earth's surface.

REFERENCES

Baldwin, S.L., and J.P. Das (2015), Atmospheric Ar and Ne returned from mantle depths to the Earth's surface by forearc recycling, *PNAS*, doi:10.1073/pnas.1424122112.

Baldwin, S.L., B. Monteleone, L.E. Webb, P.G. Fitzgerald, M. Grove, and E.J. Hill (2004), Pliocene eclogite exhumation at plate tectonic rates in eastern Papua New Guinea, *Nature*, **431**, 263–267, doi:10.1038/nature02846.

Baldwin, S.L., L.E. Webb, and B.D. Monteleone (2008), Late Miocene coesite-eclogite exhumed in the Woodlark Rift, *Geology*, **36**, 735–738, doi: 10.1130/G25144A.1.

Bingen, B., Austrheim, H., Whitehouse, M.J., Davis, W.J. (2004), Trace element signature and U–Pb geochronology of eclogite-facies zircon, Bergen Arcs, Caledonides of W Norway. *Contrib. Mineral. Petrol.*, **147**, 671–683, http://dx.doi.org/10.1007/s00410-004-0585-z.

Carswell, D.A., R. Compagnoni, *Eds.* (2003), Ultra-High Pressure Metamorphism. European Mineralogical Union, Notes in Mineralogy, **vol. 5**, 508pp.

Chopin, C., C. Henry, and A. Michard (1991), Geology and petrology of the coesite-bearing terrain, Dora Maira Massif, Western Alps, *Eur. .J. Mineral.* **3**, 263-291, doi:10.1127/ejm/3/2/0263.

Davies, H. L. (1973), The Geology of Fergusson Island, *map with explanatory notes*, Australia Bureau of Mineral Resources.

Davies, H.L., and R.G Warren (1988), Origin of eclogite-bearing, domed, layered metamorphic complexes (core complexes) in the D'Entrecasteaux Islands, Papua New Guinea, *Tectonics,* **7**, 1–21, doi: 10.1029/TC007i001p00001.

Davies, H.L., and R.G. Warren (1992), Eclogites of the D'Entrecasteaux Islands, *Contrib. Mineral. Petrol.*, **112**, 463–474, doi: 10.1007/BF00310778.

DesOrmeau, J. W., S. M. Gordon, T. A. Little, and S. A. Bowring (2014), Tracking the exhumation of a Pliocene (U)HP terrane: U-Pb and trace-element constraints from zircon, D'Entrecasteaux Islands, Papua New Guinea, *Geochem. Geophys. Geosyst.*, **15**, doi:10.1002/2014GC005396.

DesOrmeau, J.W., et al. (2015), Insights into (U)HP metamorphism of the Western Gneiss Region, Norway: A high-spatial resolution and high-precision zircon study, *Chem. Geol.*, **414**, 138–155, http://dx.doi.org/10.1016/j.chemgeo.2015.08.004.

Ernst, W.G. (2005), Alpine and Pacific styles of Phanerozoic mountain building: subduction-zone petrogenesis of continental crust. *Terra Nova* **17**, 165–188.

Gebauer D, H.P. Schertl, M. Brix, and W. Schreyer (1997), 35 Ma old ultrahigh-pressure metamorphism and evidence for very rapid exhumation in the Dora Maira Massif, Western Alps, *Lithos*, **41**, 5-24.

Gilotti, J.A. (2013), The realm of ultrahigh-pressure metamorphism, *Elements*, **vol. 9**, 255–260.

Gordon, S.M., T.A. Little, B.R. Hacker, S.A. Bowring, S.L. Baldwin, and A.R.C. Kylander-Clark, (2012), Multi-stage exhumation of young UHP–HP rocks: timescales of melt crystallization in the D'Entrecasteaux Islands, southeastern Papua New Guinea, *Earth Planet. Sci. Lett.*, **351–352**, 237–246, doi: 10.1016/j.epsl.2012.07.014.

Hacker, B.R. (2007), Ascent of the ultrahigh-pressure Western Gneiss Region, Norway. In: Cloos, M., W.D. Carlson, M.C. Gilbert, J.G. Liou, and S.S. Sorenson (Eds.), Convergent Margin Terranes and Associated Regions, A Tribute to W.G. Ernst, *Geological Society of America Special Paper*, **419,** Geological Society of America, Boulder, CO, 171–184, doi: 10.1130/2006.2419(09).

Hacker, B.R., Andersen, T.B., Johnston, S., Kylander-Clark, A.R.C., Peterman, E.M., Walsh, E.O., Young, D. (2010), High-temperature deformation during continental-margin subduction & exhumation: the ultrahigh-pressure Western Gneiss Region of Norway. *Tectonophysics*, **480(1–4)**, 149–171. doi:http://dx.doi.org/10.1016/j.tecto.2009.08.012.

Hermann, J., D. Rubatto, A. Korsakov, and V.S. Shatsky (2001), Multiple zircon growth during fast exhumation of diamondiferous, deeply subducted continental crust (Kokchetav Massif, Kazakhstan), *Contrib. Mineral. Petrol.*, **141**, 66–82, doi: 10.1007/s004100000218.

Hill, E.J. (1994), Geometry and kinematics of shear zones formed during continental extension in eastern Papua New Guinea, *J. Struct. Geol.*, **16**, 1093–1105, doi: 10.1016/0191-8141(94)90054-X.

Hill, E.J., and Baldwin, S.L. (1993), Exhumation of high-pressure metamorphic rocks during crustal extension in the D'Entrecasteaux region: Papua New Guinea, *J. Metamorph. Geol.*, **11**, 261–277, doi: 10.1111/j.1525-1314.1993.tb00146.x.

Kylander-Clark, A.R.C., Hacker, B.R., Johnson, C.M., Beard, B.L., Mahlen, N.J., Lapen, T.J. (2007), Coupled Lu–Hf and Sm–Nd geochronology constrains prograde and exhumation histories of high- and ultrahigh-pressure eclogites from western Norway. *Chem. Geol.*, **242(1–2)**, 137–154, http://dx.doi.org/10.1016/j.chemgeo.2007.03.006.

Kylander-Clark, A.R.C., Hacker, B.R., Johnson, C.M., Beard, B.L., Mahlen, N.J. (2009), Slow subduction and rapid exhumation of a thick ultrahigh-pressure terrane. *Tectonics*, **28(2)**, TC2003, http://dx.doi.org/10.1029/2007TC002251.

Kylander-Clark, A. R. C., B.R. Hacker, and C.G. Mattinson (2012), Size and exhumation rate of ultrahigh-pressure terranes linked to orogenic stage, *Earth Planet. Sci. Lett.*, **321–322**, 115–120, doi: 10.1016/j.epsl.2011.12.036.

Krogh, T.E. (1973), A low contamination method for hydrothermal decomposition of zircon and extraction of U and Pb for isotopic age determination. *Geochim. Cosmochim. Acta.*, **37**, 485–494.

Krogh, T.E., Kamo, S.L., Robinson, P., Terry, M.P., Kwok, K. (2011), U–Pb zircon geochronology of eclogites from the Scandian Orogen, northern Western Gneiss Region, Norway: 14–20 million years between eclogite crystallization and return to amphibolite-facies conditions. *Can. J. Earth Sciences*, **48(2)**, 441–472, http://dx.doi.org/10.1139/E10-076.

Lapen T.J., C.M. Johnson, L.P. Baumgartner, N.J. Mahlen, B.L. Beard, and J.M. Amato (2003), Burial rates during prograde metamorphism of an ultra-high-pressure terrane: an example from Lago di Cignana, western Alps, Italy, *Earth and Planetary Science Letters*, **215**, 57-72.

Liou, J.G., Ernst, W.G., Zhang, R.Y., Tsujimori, T., Jahn, J.G., (2009), Ultrahigh-pressure minerals and metamorphic terranes—the view from China. *Journal of Asian Earth Sciences*, **35**, 199–231.

Little, T. A., S. L. Baldwin, P. G. Fitzgerald, and B. Monteleone (2007), Continental rifting and metamorphic core complex formation ahead of the Woodlark Spreading Ridge, D'Entrecasteaux Islands, Papua New Guinea, Tectonics, 26, TC1002, doi:10.1029/2005TC001911.

Little, T.A., B.R. Hacker, S.M. Gordon, S.L. Baldwin, P.G. Fitzgerald, S. Ellis, and M. Korchinski (2011), Diapiric exhumation of Earth's youngest (UHP) eclogites in the gneiss domes of the D'Entrecasteaux Islands, Papua New Guinea, *Tectonophysics*, **510**, 39–68, doi: 10.1016/j.tecto.2011.06.006.

Mattinson, J.M. (2005), Zircon U-Pb chemical abrasion ("CA-TIMS") method: combined annealing and multi-step partial dissolution analysis for improved precision and accuracy of zircon ages, *Chem. Geol.*, **220**, 47–66, doi: 10.1016/j.chemgeo.2005.03.011.

Mysen, B.O., Heier, K.S. (1972), Petrogenesis of eclogites in high-grade metamorphic gneisses exemplified by the Hareidland eclogite, west Norway. *Contrib. Mineral. Petrol.*, **36**, 73– 94, http://dx.doi.org/10.1007/BF00372836.

O'Brien, P.J. (2001), Subduction followed by collision: Alpine and Himalayan examples. *Physics of the Earth and Planetary Interiors*, **127**, 277–291.

Powell R., and T.J.B. Holland (2008), On thermobarometry, *Journal of Metamorphic Geology*, **26**, 155-179.

Powell R., and T.J.B. Holland (2010), Using equilibrium thermodynamics to understand metamorphism and metamorphic rocks, *Elements*, **6**, 309-314.

Renedo, R.N., Nachlas, W.O., Whitney, D.L., Teyssier, C., Piazolo, S., Gordon, S.M., Fossen, H. (in press), Fabric development during exhumation from ultrahigh-pressure in an eclogite-bearing shear zone, Western Gneiss Region, Norway. *J. Struct. Geol.*, http://dx.doi.org/-10.1016/j.jsg.2014.09.012.

Root, D.B., Hacker, B.R., Mattinson, J.M., Wooden, J.L. (2004), Zircon geochronology and ca. 400 Ma exhumation of Norwegian ultrahigh-pressure rocks: an ion microprobe and chemical abrasion study. *Earth Planet. Sci. Lett.*, **228**, 325–341, http://dx.doi.org/10.1016/-j.epsl.2004.10.019.

Root, D.B., Hacker, B.R., Gans, P.B., Ducea, M.N., Eide, E.A., Mosenfelder, J.L. (2005), Discrete ultrahigh-pressure domains in the Western Gneiss region, Norway; implications for formation and exhumation. *Journal of Metamorphic Geology*, **23**, 45–61.

Schmidt A., K. Mezger, and P.J. O'Brien (2011), The time of eclogite formation in the ultrahigh pressure rocks of the Sulu terrane: Constraints from Lu–Hf garnet geochronology, *Lithos*, **125**, 743-756.

Schoene, B. (2013), U-Th-Pb Geochronology. In: Rudnick, R. (Eds.), Treatise on Geochemistry 2nd edition, *Elsevier*, **4.10**, 341–378, http://dx.doi.org/10.1016/B978-0-08-095975-7.00310-7.

Smith, D.C. (1984), Coesite in clinopyroxene in the Caledonides and its implications for geodynamics. *Nature*, **310**, 641–644.

Sobolev, N.V., Shatsky, V.S., (1990), Diamond inclusions in garnets from metamorphic rocks; a new environment of diamond formation. *Nature*, **343**, 742–746.

Terry, M.P., Robinson, P., Hamilton, M.A., Jercinovic, M.J. (2000), Monazite geochronology of UHP and HP metamorphism, deformation, and exhumation, Nordøyane, Western Gneiss Region, Norway, *Amer. Mineral.*, **85**, 1651–1664.

Zheng, Y.F. (2008), A perspective view on ultrahigh-pressure metamorphism and continental collision in the Dabie–Sulu orogenic belt. *Chinese Science Bulletin*, **53**, 3081–3104.

Zheng, Y.F. (2012) Metamorphic chemical geodynamics on continental subduction zones. *Chemical Geology*, **328**, 5–48.

Zirakparvar, N.A., S.L. Baldwin, and J.D. Vervoort (2011), Lu–Hf garnet geochronology applied to plate boundary zones: insights from the (U)HP terrane exhumed within the Woodlark Rift, *Earth Planet. Sci. Lett.*, **309**, 56–66, doi: 10.1016/j.epsl.2011.06.016

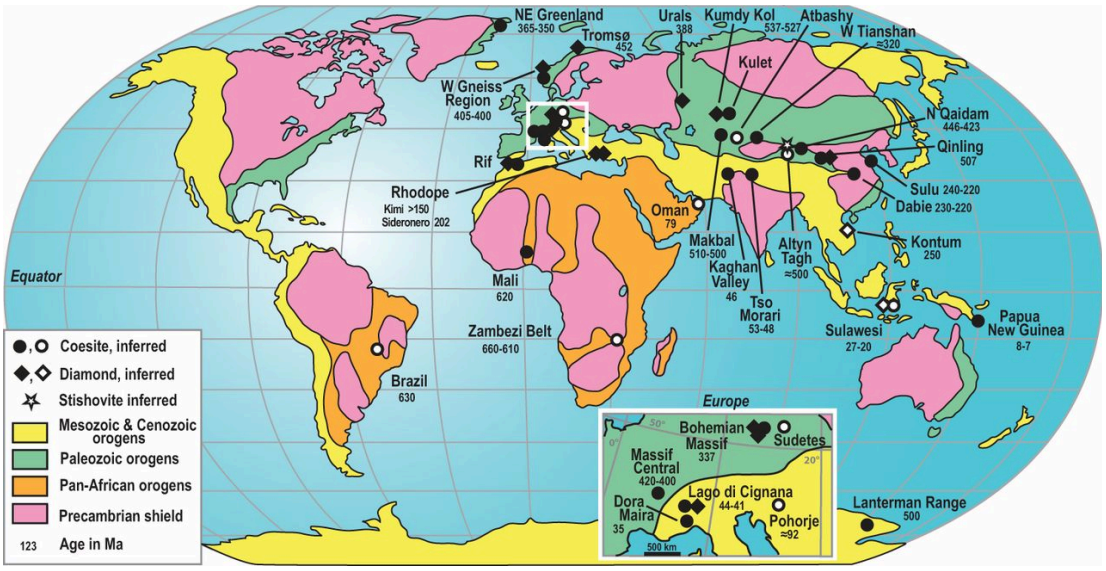

Figure 1.1 Simplified geologic map showing the known ultrahigh-pressure (UHP) terranes on Earth. The giant Western Gneiss Region UHP terrane is due north of the white inset box, and the small eastern Papua New Guines UHP terrane is northeast of Australia. Closed circles and diamonds represent confirmed coesite and diamond, whereas open symbols are inferred. Figure from Gilotti (2013).

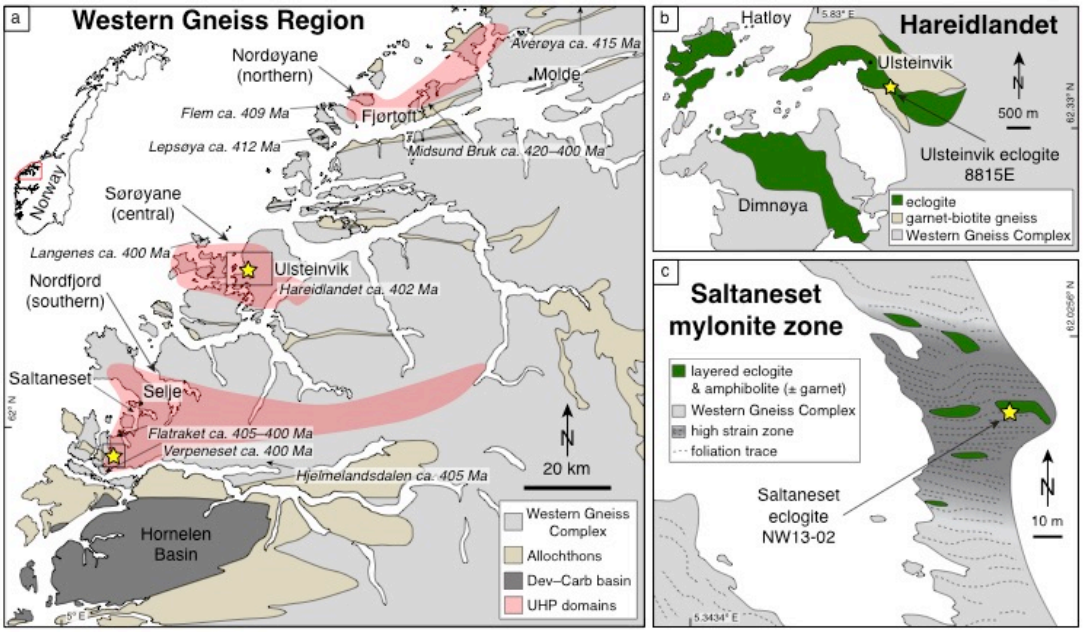

Figure 1.2 (a) Generalized geologic map of the Western Gneiss Region showing the southern, central, and northern UHP domains, after Hacker et al. (2010). Locations of (U)HP eclogites and their respective U-Pb zircon dates are shown. Simplified geologic maps of (b) the Ulsteinvik eclogite on Hareidlandet within the central UHP domain (after Mysen and Heier, 1972) and (c) the SW coast of Saltaneset within the southern UHP domain showing the layered eclogite within the Saltaneset mylonite zone (after Renedo et al., 2014). Stars mark the location in which the two UHP eclogites were collected for this study.

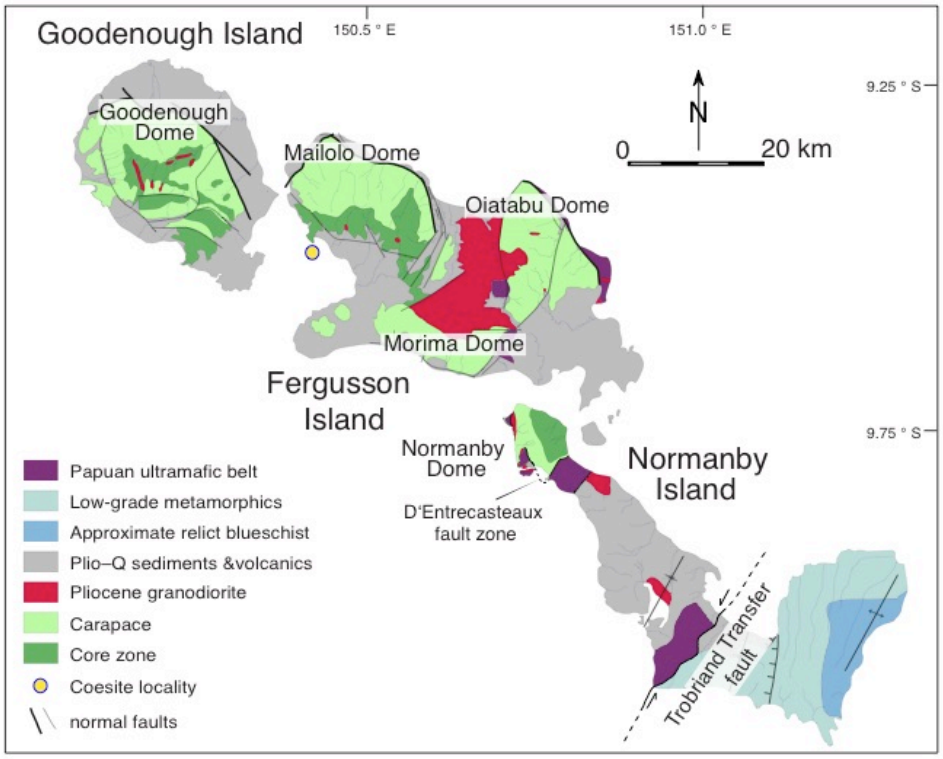

Figure 1.3 Simplified geological map of the D'Entrecasteuax Island gneiss domes showing various lithologies, the core and carapace zones, and the dome-bounding faults, including the D'Entrecasteaux fault zone (after Davies, 1973; Hill, 1994; Little et al., 2007, 2011).

Chapter 2: Insights into (U)HP metamorphism of the Western Gneiss Region, Norway: A high-spatial resolution and high-precision zircon study

Joel W. DesOrmeau[*], Stacia M. Gordon[*], Andrew R.C. Kylander-Clark[**], Bradley R. Hacker[**], Samuel A. Bowring[***], Blair Schoene[****], Kyle M. Samperton[****]

[*]Department of Geological Sciences, University of Nevada Reno, Nevada, USA
[**]Department of Earth Science, University of California, Santa Barbara, California, USA
[***]Department of Earth, Atmospheric, and Planetary Sciences, Massachusetts Institute of Technology, Cambridge, Massachusetts, USA
[****]Department of Geosciences, Princeton University, Princeton, New Jersey, USA

This chapter has already been published and is included as part of this dissertation **with permission from *Chemical Geology*, 414, 138–155, http://dx.doi.org/10.1016/j.chemgeo.2015.08.004, 2015, 0009-2541/**

Abstract

Combining high-spatial resolution and high-precision geochronology and geochemistry of zircon provides constraints on the timing and duration of ultrahigh-pressure (UHP) metamorphism resulting from the collision of Baltica–Avalonia and Laurentia during the Scandian orogeny in the Western Gneiss Region of Norway. Zircons were extracted from a layered eclogite in the Saltaneset region (southern UHP domain) and from an eclogite in the Ulsteinvik region (central UHP domain). Zircons were first analyzed for U-Pb and trace element compositions by laser ablation split-stream (LASS) inductively coupled plasma mass spectrometry (ICP-MS), followed by analysis of those same zircons that yielded Scandian dates by integrated U-Pb isotope dilution–thermal ionization mass spectrometry and trace element analysis (TIMS-TEA). LASS results from a garnet–quartz layer within the Saltaneset eclogite give Scandian dates of ca. 413–397 Ma, with subsequent ID-TIMS analyses ranging from 408.9 ± 0.4 Ma to 401.4 ± 0.2 Ma (2σ). An omphacite-rich layer from the same eclogite yields LASS dates of ca. 414–398 Ma and a single ID-TIMS date of 396.7 ± 1.4 Ma. In comparison, the Ulsteinvik eclogite LASS results give dates spanning ca. 413–397 Ma, whereas ID-TIMS analyses range from 409.6 ± 0.6 Ma to 401.3 ± 0.4 Ma. ID-TIMS zircon data from the eclogites reveals two age populations: 1) ca. 409–407 Ma and 2) ca. 402 Ma. Both *in situ* and solution trace element data show a distinct pattern for Scandian zircons, with strongly-depleted HREE and weakly-negative Eu anomalies (Eu/Eu*), whereas inherited zircon REE patterns are distinguished by steep HREE slopes and marked negative Eu/Eu*. When coupled with partition coefficients calculated for zircon and garnet, these REE patterns indicate that

zircon (re)crystallized during eclogite-facies metamorphism at ca. 409–407 Ma and ca. 402 Ma at two widely separated UHP localities.

Introduction

The Western Gneiss Region (WGR) of western Norway is one of the largest and best-exposed ultrahigh-pressure (UHP) terranes on Earth. Because of this, the WGR has been extensively studied to better understand the geodynamics of subduction and subsequent exhumation of 30,000 km^2 (5,000 km^2 of which are UHP rocks) of continental crust (e.g., Krogh et al., 1974, 2011; Krogh, 1977, 1982; Lappin and Smith, 1978; Griffin and Brueckner, 1980, 1985; Austrheim, 1987; Tucker et al., 1990; Andersen et al., 1991; Wain, 1997; Cuthbert et al., 2000; Wain et al., 2000; Terry et al., 2000a, 2000b; Root et al., 2005; Hacker, 2007; Kylander-Clark et al., 2009; Hacker et al., 2010). Since the initial discovery of a coesite-eclogite province in the southern WGR (Smith, 1984, 1988), thermobarometry and identification of microdiamonds, coesite, and polycrystalline quartz grains within eclogite and quartzofeldspathic gneiss has aided in the recognition of three separate UHP domains (Root et al., 2005): the southern (Nordfjord), central (Sørøyane), and northern (Nordøyane) domains (Fig. 1a) (e.g., Dobrzhinetskaya et al., 1995; Wain, 1997; Cuthbert et al., 2000; Terry et al., 2000a; Wain et al., 2000; Carswell and Cuthbert, 2003; Carswell et al., 2003a; Walsh and Hacker, 2004; Young et al., 2007; Butler et al., 2013; Smith and Goddard, 2013).

A general increase in peak UHP pressure and temperature (*P–T)* to the northwest across the WGR points to the coherent nature of the terrane during subduction and exhumation from mantle depths (e.g., Krogh, 1977; Lappin and Smith, 1978; Griffin et al., 1985; Andersen et al., 1991; Cuthbert et al., 2000; Carswell and Cuthbert, 2003; Carswell et al., 2006; Hacker et al., 2010). Characterizing the processes involved in the deep subduction and exhumation of such a large tract of continental crust requires a

detailed understanding of the timescales of peak UHP metamorphism (e.g., Terry et al., 2000b; Carswell et al., 2003a, 2003b; Root et al., 2004; Kylander-Clark et al., 2007, 2009; Krogh et al., 2011).

Some (U)HP terranes were likely at mantle depths for tens of millions of years prior to exhumation (Kylander-Clark et al., 2012). This was first recognized in the Dabie Shan of China (Hacker et al., 1998), and then in the WGR of Norway (Kylander-Clark et al., 2008), where geochronological data suggests (U)HP metamorphism from ca. 430–400 Ma (Table 1; Section 2.2). Previous efforts to determine the timing of (U)HP metamorphism in the WGR have relied on techniques that analyze minerals that can be directly linked to the metamorphic evolution of eclogites (e.g., garnet and clinopyroxene) as well as more refractory accessory minerals (e.g., zircon and monazite) (Table 1). However, limitations in some previous geochronological studies of the WGR include: (1) data sets consisting of relatively few analyses (e.g., two-point isochrons); (2) dating of zoned garnet, for which isotopic ages may be averaging dates from multiple, distinct growth zones; (3) dating of multi-grain separates by U-Pb ID-TIMS that may result in inaccurate and/or mixed ages; and (4) ambiguities in how the dated minerals relate to the (U)HP metamorphism. This study builds upon these previous efforts by obtaining U-Pb dates from the same zircon domains via both laser ablation–inductively coupled plasma mass spectrometry (LA-ICP-MS) and from single-grain chemical abrasion–isotope dilution–thermal ionization mass spectrometry (ID-TIMS)—combining a high-spatial resolution technique and a high-precision technique on the same zircon.

In order to interpret geochronological data obtained from eclogites, it is crucial to link dates to different parts of the *P–T* path. The trace element composition of zircon can be

used as a tool in age interpretations, particularly when coupled with the trace element composition of coexisting garnet. Zircon that (re)crystallizes at high pressure will likely display a flat normalized heavy rare earth element (HREE) pattern (e.g., Lu/Gd ~ < 3), due to the presence of garnet. Moreover, high-pressure zircon may have a flat-to-positive Eu anomaly (e.g., Eu/Eu* > 0.75), indicating (re)crystallization when plagioclase was unstable (Hinton and Upton, 1991; Schaltegger et al., 1999; Hoskin and Ireland, 2000; Rubatto, 2002; Hoskin and Schaltegger, 2003; Rubatto and Hermann, 2003; Rubatto and Hermann, 2007a). In addition, empirically and experimentally determined REE partition coefficients allow assessment of equilibrium between zircon and garnet (e.g., Hinton and Upton, 1991; van Westrenen et al., 1999; Rubatto, 2002; Whitehouse and Platt, 2003; Kelly and Harley, 2005; Harley and Kelly, 2007; Rubatto and Hermann, 2007b; Taylor et al., 2014), an additional test to determine whether zircon (re)crystallized in the presence of garnet.

This study presents new U-Pb zircon dates from two coesite- and polycrystalline quartz-bearing eclogites to further evaluate the timescales of UHP metamorphism within the southern and central WGR. Trace element analyses of zircon provide insight into the *P–T* conditions under which zircon (re)crystallization occurred. The results reveal two separate populations of zircon that (re)crystallized under eclogite-facies conditions at ca. 409–407 Ma and ca. 402 Ma within the Ulsteinvik eclogite of the central UHP domain and the Saltaneset eclogite of the southern UHP domain. These results suggest a UHP metamorphic history for the Ulsteinvik eclogite older than the previously recognized 401.6 ± 1.6 Ma age (multi-grain zircon; Carswell et al., 2003a; Tucker et al., 2004), and a

UHP history for the Saltaneset eclogite younger than the previously measured 408.3 ± 6.7 Ma age (Sm-Nd isochron; Carswell et al., 2003b).

Geologic Background

Western Gneiss Region

The autochthonous basement of the WGR, the Western Gneiss Complex (WGC) (Fig. 1), is a polymetamorphic terrane composed mainly of granodioritic–tonalitic intrusive rocks predominantly formed between ca. 1690–1620 Ma (Brueckner, 1972; Carswell and Harvey, 1985; Tucker et al., 1990; Skår et al., 1994; Skår, 2000; Austrheim et al., 2003; Corfu et al., 2013) during the Gothian orogeny (Gaál and Gorbatschev, 1987). The WGC was intruded by mafic magmas at ca. 1470–1450 Ma and ca. 1260–1250 Ma (Austrheim et al., 2003; Tucker et al., 2004; Krogh et al., 2011; Corfu et al., 2013; Beckman et al., 2014). Moreover, a ca. 1000–900 Ma granulite-facies overprint related to the Sveconorwegian orogeny accompanied pluton and dike emplacement and migmatization chiefly southwest of Molde (Brueckner, 1972, 1979; Skår et al., 1994; Austrheim, 2003; Skår and Pederson, 2003; Røhr et al., 2004, 2013; Tucker et al., 2004; Root et al., 2005; Glodny et al., 2008; Kylander-Clark et al., 2008; Krogh et al., 2011; Corfu et al., 2013).

This study focuses on metamorphism of the WGR during the Scandian orogeny, the final stage of the early Paleozoic Caledonian orogeny (Roberts and Gee, 1985; Stephens and Gee, 1989; Roberts, 2003; Brueckner and van Roermund, 2004; Hacker and Gans, 2005: Hacker et al., 2010). The Scandian orogeny included a series of tectonic events: (1) closure of the Iapetus Ocean resulted in thrusting of oceanic and continental allochthons east–southeastward over the autochthonous basement of the WGR from ca. 430–415 Ma

(Roberts, 2003; Tucker et al., 2004; Hacker and Gans, 2005); (2) westward continental subduction of the Baltica basement and segments of overlying allochthons beneath Laurentia from ca. 430–400 Ma (Andersen et al., 1991, 1998; Terry et al., 2000a; Bingen et al., 2004; Root et al., 2004, 2005; Kylander-Clark et al., 2007, 2009; Spengler et al., 2009; Krogh et al., 2011); and (3) ca. 400–385 Ma near-isothermal decompression and exhumation of the subducted crust from mantle to shallow crustal depths (Andersen et al., 1998; Tucker et al., 1990, 2004; Terry et al., 2000a; Schärer and Labrousse, 2003; Walsh and Hacker, 2004; Root et al., 2005; Hacker, 2007; Kylander-Clark et al., 2008; Krogh et al., 2011; Gordon et al., 2013; Spencer et al., 2013; Kylander-Clark and Hacker, 2014).

The Scandian collision between Laurentia and Baltica–Avalonia produced an extensive area (30,000 km^2) of (U)HP eclogites that record *P-T* conditions of 1.5–3.9 GPa and 600–820 °C (Krogh, 1977, 1982; Lappin and Smith; 1978; Griffin et al., 1985; Cuthbert and Carswell, 1990; Wain, 1997; Cuthbert et al. 2000; Terry et al., 2000b; Ravna and Terry, 2004; Walsh and Hacker, 2004; Root et al., 2005; Hacker, 2006; Carswell et al., 2006; Young et al., 2007; Butler et al., 2013). Root et al. (2005) used the spatial distribution of eclogites and K-white mica $^{40}Ar/^{39}Ar$ ages to conclude that the UHP rocks crop out in three east–southeast-plunging antiforms: the southern (Nordfjord), central (Sørøyane), and northern (Nordøyane) UHP domains (Fig. 1a).

There is an overall northwestward increasing gradient in the peak *P–T* conditions recorded across the WGR (e.g., Krogh, 1977; Lappin and Smith, 1978; Griffin et al., 1985; Cuthbert et al., 2000; Labrousse et al., 2004; Hacker et al., 2010). The southern UHP domain contains a transition from HP quartz eclogite (2.4 GPa and 600 °C) to UHP coesite and microdiamond eclogite (> 3.5 GPa and 750 °C; Cuthbert et al., 2000; Young

et al., 2007; Smith and Goddard, 2013). The central UHP domain records *P-T* conditions up to 3.2 GPa and 795 °C (Krogh Ravna in Carswell et al., 2003b; Root et al., 2005). Peak *P-T* conditions reached a maximum of 3.8–3.9 GPa and 820–850 °C for eclogites and microdiamond-bearing paragneiss within the northern UHP domain (Terry et al., 2000b; Carswell et al., 2006). Even greater *P–T* estimates have been suggested for peridotite within the host gneiss of the northern WGR (e.g., Vrijmoed et al., 2006, 2008; Scambelluri, et al., 2008; Spengler et al., 2009; van Roermund, 2009).

Geochronological overview of WGR Scandian UHP metamorphism

Over the past ~35 years, many studies of the WGR have focused on the timing of peak UHP metamorphism during the subduction of Baltica–Avalonia beneath Laurentia during the Scandian orogeny. These studies and the techniques used to resolve the timing and duration of the UHP event are summarized below and in Table 1. Reported uncertainties are at the 2-sigma or 95% confidence level unless otherwise stated.

Sm-Nd geochronology

The first Sm-Nd eclogite ages ever obtained were garnet–omphacite isochron dates from the WGR (Griffin and Brueckner, 1980, 1985); they yielded an average age of ca. 425 Ma, discrediting initial suggestions of a Precambrian age for the eclogite-facies metamorphism (e.g., Krogh, 1977). Additional Sm-Nd studies of eclogites throughout the WGR gave younger isochron dates of ca. 412–408 Ma (Mearns, 1986; Mørk and Mearns, 1986; Jamtveit et al., 1991; Carswell et al., 2003b; see section 2.3). Peridotites within the northern UHP domain yielded Sm-Nd garnet–omphacite isochron dates interpreted to

represent prograde subduction at 429.5 ± 3.1 Ma (Spengler et al., 2009) and cooling at 393.4 ± 3.4 Ma and 380.7 ± 5.7 Ma (Vrijmoed et al., 2006). More recent studies that combined the Lu-Hf and Sm-Nd isotopic systems for HP eclogites across the WGR show a ~20 Myr range of prograde garnet growth during eclogite-facies metamorphism from ca. 419–410 Ma (Lu-Hf) and ca. 414–397 Ma (Sm-Nd) (Kylander-Clark et al., 2007, 2009).

Rb-Sr geochronology

Isochron dates using the Rb-Sr system have also been described from southern WGR eclogites. Griffin and Brueckner (1985) reported an Rb-Sr isochron date of 397 ± 8 Ma (2%) (recalculated by Root et al., 2004) using whole-rock and mineral fractions of the Verpeneset eclogite in the southern UHP domain. Three eclogites collected ~65 km south of the southern UHP domain yielded a weighted-mean multi-mineral Rb-Sr isochron date of 404.0 ± 2.1 Ma (Glodny et al., 2008).

U-Th-Pb monazite

Terry et al. (2000b) employed secondary ion mass spectrometry (SIMS) and electron-microprobe (EMP) techniques on a microdiamond-bearing gneiss to constrain UHP metamorphism in the northern UHP domain using U-Th-Pb monazite geochronology. Monazite inclusions within inferred UHP garnet of the microdiamond sample yielded a SIMS weighted-mean $^{206}Pb/^{238}U$ age of 415.0 ± 6.8 Ma. The first LASS study of monazite obtained four weighted-mean $^{206}Pb/^{238}U$ ages of 426.5 ± 5.6 Ma, 408.8 ± 6.3

Ma, 395.0 ± 3.9 Ma, and 390.3 ± 4.9 Ma from a HP garnet–muscovite–kyanite gneiss from Leinøya in the central UHP domain (Kylander-Clark et al., 2013). Based on the variation in MREE–HREE patterns, Sr abundances, and Eu anomalies, Kylander-Clark et al. (2013) interpreted monazite (re)crystallization to have occurred at ca. 427–395 Ma in the presence of garnet, and the breakdown and recrystallization of plagioclase to have occurred between ca. 427 Ma and 390 Ma.

U-Th-Pb zircon

Much effort has focused on U-Pb zircon multi- and (sparse) single-grain ID-TIMS studies of WGR (U)HP eclogite. The northern WGR at Averøya hosts a probable UHP eclogite with the oldest zircon age of 415.2 ± 0.6 Ma (multi-grain weighted-mean $^{206}Pb/^{238}U$ age), whereas younger single zircon grains, interpreted to date an amphibolite-facies overprint, gave $^{206}Pb/^{238}U$ ages of 410.8 ± 1.4 Ma and 409.6 ± 1.5 Ma (Krogh et al., 2011). Furthermore, within the northern UHP domain, multi-grain zircon fractions from the eclogitized margin of the Flem Gabbro yielded a weighted-mean $^{206}Pb/^{238}U$ age of 409 ± 3 Ma, and a probable UHP eclogite from Midsund Bruk yielded a $^{206}Pb/^{238}U$ age of 405 ± 1 Ma (Krogh et al., 2011). Lastly, a HP hornblende eclogite from Lepsøya gave a weighted-mean, multi-grain $^{206}Pb/^{238}U$ age of 412 ± 1 Ma (Krogh et al., 2011).

The same zircon separates from the ca. 405 Ma Midsund Bruk eclogite described above were analyzed by LASS, which produced weighted-mean 207-corrected $^{206}Pb/^{238}U$ ages of 420.6 ± 8.4 Ma and 400.4 ± 8.0 Ma and a range of dates from ca. 409–407 Ma (Kylander-Clark et al., 2013). The three age populations are distinguished by different

REE patterns (e.g., variation in MREE and a lack of a steep, positive HREE pattern and negative Eu anomalies) and are interpreted to record protracted (re)crystallization at eclogite-facies conditions (Kylander-Clark et al., 2013).

An early multi-grain ID-TIMS study of the Ulsteinvik eclogite within the central UHP domain (Fig. 1b) gave an initial age of 401± 20 Ma, marking the first record of a Devonian history for the WGR (Krogh et al., 1974). Subsequent analyses of zircon multi-grain fractions from the Ulsteinvik eclogite provided a more-precise weighted-mean $^{207}Pb/^{206}Pb$ age of 401.6 ± 1.6 Ma (Tucker et al., 2004). Some of these zircons contain omphacite or rutile, and coesite inclusions were discovered in the zircon separates after the TIMS work (Carswell et al., 2003a), leading these authors to interpret the 401.6 ± 1.6 Ma age as the best record of UHP metamorphism within the WGR.

The first study to combine chemical-abrasion ID-TIMS (CA-TIMS, Mattinson, 2005), high-spatial resolution SIMS, and trace-element analysis of zircon washes by solution ICP-MS was completed in the WGR by Root et al. (2004). Multi-grain zircons analyses on the Flatraket eclogite yielded discordant U-Pb dates interpreted to represent zircon (re)crystallization at ca. 405–400 Ma with minor discordance attributed to inherited cores. Eclogite-facies garnet inclusions in the zircons and flat HREE zircon profiles revealed from the TIMS wash solutions are compatible with (re)crystallization at or near peak metamorphism. Zircons from the eclogites at Verpeneset and Langenes also yielded discordant CA-TIMS data compatible with ca. 400 Ma metamorphic zircon and 1.6 Ga igneous zircon (Root et al., 2004). Finally, at Hjelmelandsdalen near the southern UHP domain, two air-abraded single grains from a (U)HP eclogite gave an ID-TIMS weighted-mean $^{206}Pb/^{238}U$ age of 405 ± 2 Ma (Young et al., 2007).

UHP eclogites of the central and southern domains

In this study, two UHP eclogites, Ulsteinvik and Saltaneset, were collected from the central and southern WGR, respectively (Fig. 1a). These sample localities have been extensively studied and are known to preserve or are interpreted to have once contained coesite (Cuthbert et al., 2000; Wain et al., 2000; Carswell et al., 2003a, 2003b). The large Ulsteinvik eclogite of the central UHP domain is exposed on Hareidlandet and extends to the nearby islands of Dimnøya and Hatløy (Fig. 1b). This internally layered eclogite is one of the largest eclogite bodies within the WGR (~6 km long by 0.2–1.5 km wide) and is hosted in predominantly garnet–biotite–kyanite gneiss (Mysen and Heier, 1972). The quartz-bearing eclogite contains accessory rutile and minor kyanite and amphibole. The eclogite is pervasively retrogressed with omphacite replaced by multiple stages of symplectite with progressively less sodic-clinopyroxene and more-calcic plagioclase (Mysen, 1972; Mysen and Heier, 1972). Further evidence of retrogression includes partial replacement of garnet by hornblende and biotite with plagioclase (Carswell et al., 2003a). As described above, zircons with inclusions of omphacite, garnet, rutile, quartz, and coesite have been identified from the Ulsteinvik eclogite (Krogh et al., 1974; Carswell et al., 2003a). ID-TIMS dating provided a weighted-mean $^{207}Pb/^{206}Pb$ age of 401.6 ± 1.6 Ma (n = 4, MSWD = 0.48); scatter in the isotopic dates was inferred to be a result of recent Pb loss (Tucker et al., 2004).

The coesite-bearing Saltaneset eclogite, first reported in detail by Wain et al. (2000), is located ~2 km south of Selje within the southern UHP domain (Fig. 1c). The main Saltaneset eclogite is a tabular, compositionally layered body (20 m long by ~3–5 m

wide), consisting of mostly omphacite-rich layers and fewer garnet-rich, quartz layers that are 3–25 mm thick (Carswell et al., 2003b; Renedo et al., 2014). The eclogite is within a mylonite zone of fine-grained, quartzofeldspathic gneiss (Renedo et al., 2014). Relict coesite and polycrystalline quartz are preserved within garnet from a quartz layer of the Saltaneset eclogite (Cuthbert et al., 2000; Wain et al., 2000). Carswell et al. (2003b) described two generations of garnet within a garnet-rich quartz layer and argued that the layers were originally garnet-bearing coesitites based on the presence of abundant quartz pseudomorphs after coesite within the second generation of garnet. An Sm-Nd isochron age (garnet–omphacite–whole rock) of 408.3 ± 6.7 Ma (MSWD = 0.81) was determined for this Saltaneset eclogite (Carswell et al., 2003b).

Methods

Representative samples of the Ulsteinvik eclogite and the garnet–quartz- and omphacite-rich layers of the Saltaneset eclogite were collected. Zircon was extracted from the whole-rock Ulsteinvik sample, whereas individual garnet–quartz and omphacite-rich layers from the Saltaneset eclogite were separated and then separately crushed to extract zircon from each layer. Polished grain mounts were prepared and imaged by cathodoluminescence (CL) to reveal zoning (Fig. 2). This study utilized two separate geochronologic techniques on the same zircons: 1) high-spatial resolution laser ablation split-stream (LASS)–inductively coupled plasma–mass spectrometry, allowing for the simultaneous collection of U-Th-Pb data and trace element data for individual spot analysis (Kylander-Clark et al., 2013); and 2) high-precision, single-grain U-Pb chemical abrasion ID-TIMS and trace element analysis (TIMS-TEA; Mattinson, 2005; Schoene et

al., 2010). Chemical abrasion removes high-U zones of the zircon susceptible to Pb loss, therefore minimizing or wholly eliminating Pb-loss correction (Mattinson, 2005). TIMS-TEA allows for the same zircon dated by U-Pb ID-TIMS to be analyzed for trace element composition by solution ICP-MS (Root et al., 2004; Schoene et al., 2010).

Transects across different generations of garnet within the Ulsteinvik and Saltaneset eclogites were analyzed by LA-ICP-MS in thin sections of the same rocks that were crushed (Fig. 6). Trace-element data from both zircon and garnet are normalized to the chondrite values of Sun and McDonough (1989).

LASS analyses were first performed to identify Scandian zircon. From there, Scandian whole grains or Scandian subdomains *within* grains were targeted for ID-TIMS analysis. A combination of single grains, fragments of grains, and multiple fragments from the same grain were analyzed by ID-TIMS to try to identify grain-to-grain and intragrain heterogeneity that might cause inaccurate and/or mixed ages (e.g., Mundil et al., 2001; Schoene, 2013). All grains were annealed at 900 °C for 60 hours and chemically abraded at 220 °C for 12 hours (Mattinson et al., 2005). ID-TIMS analyses have typical uncertainties of ~0.05% for Th-corrected $^{206}Pb/^{238}U$ weighted-mean dates and <0.2% for individual Th-corrected $^{206}Pb/^{238}U$ dates that are inversely proportional to the radiogenic/common Pb ratio (Pb*/Pbc; Table 3). Most ID-TIMS analyses do not define a single population and are reported as individual Th-corrected $^{206}Pb/^{238}U$ dates. In comparison, LASS $^{206}Pb/^{238}U$ dates have typical uncertainties of ~1–2% for single spot analyses, including both analytical and propagated uncertainties (Table 2). Reported uncertainties throughout the text, data tables, and figures are at the 2-sigma or 95% confidence level unless otherwise stated.

We first report zircon U-Pb and trace element data from grains that were analyzed by both LASS and TIMS-TEA. These results are then compared to zircons analyzed by LASS only. Finally, zircon-garnet trace element partition coefficients are calculated to link U-Pb dates to the *P-T* history of the samples (Figs. 4a–b, 5, 6, and 7). All LASS and ID-TIMS inherited zircon analyses are presented on concordia diagrams in Fig. S1. The online supporting information provides a more-detailed description of the methodology for U-Pb LASS and TIMS-TEA zircon analyses and data tables for the zircon and garnet trace-element analyses (Tables 4 and 5, respectively).

Results

U-Pb zircon LASS and ID-TIMS geochronology

Zircons extracted from the Ulsteinvik eclogite within the central UHP domain are mostly irregular to sub-rounded, and CL images reveal patchy- and polygonal-sector zoning (Fig. 2). In comparison, zircons from the garnet–quartz and omphacite layers of the Saltaneset eclogite from the southern UHP domain are rounded to sub-rounded and have patchy zoning and homogenous, dark-CL rim overgrowths (Fig. 2). No difference in the CL patterns of the zircons from the two layers was detected. All zircons are interpreted to be metamorphic based on morphology, zoning (e.g., Corfu et al., 2003), and low (< 0.04) Th/U ratios (Fig. S2a; Tables 2 and 3). LASS zircon analyses targeted both the cores and rims of grains (Fig. 2; Table 2).

Ulsteinvik eclogite

Eclogite sample 8815E was collected from the layered body on the island of Hareidlandet, approximately 1 km southeast of Ulsteinvik (Fig. 1b). Analysis of thirteen zircons by LASS yields single-spot $^{206}Pb/^{238}U$ dates ranging from 412.8 ± 5.4 Ma to 400.5 ± 4.7 Ma (n = 24; Figs. 3b and 4a; Table 2). ID-TIMS results from thirteen whole grains or microsampled fragments of the same zircons give Th-corrected $^{206}Pb/^{238}U$ dates from 409.6 ± 0.6 Ma to 401.3 ± 0.4 Ma (n = 15; Figs. 3a and 4a; Table 3). To test for dispersion of ID-TIMS dates within a single grain, a ~200 μm zircon was microsampled, and the three fractions yield indistinguishable $^{206}Pb/^{238}U$ dates of 401.9 ± 0.2 Ma, 401.9 ± 0.4 Ma, and 402.1 ± 0.3 Ma (z1 in Figs. 4a and 2; Table 3). Overall, the ID-TIMS results cluster into two populations, ca. 409–407 Ma and ca. 402 Ma, but only the youngest population yielded a weighted-mean $^{206}Pb/^{238}U$ date with a statistically acceptable MSWD (401.9 ± 0.1 Ma, MSWD = 1.9, n = 5) (Fig. 4a). Ten additional zircons analyzed by LASS alone yielded $^{206}Pb/^{238}U$ dates ranging from 412.0 ± 5.3 Ma to 397.2 ± 5.2 (n = 10; Fig. 4a; Table 2) and older dates of ca. 475–430 Ma (n = 5; Fig. 3b; Table 2).

Saltaneset eclogite: garnet–quartz and omphacite layers

Sample NW13-02 was collected from an eclogite within the 60 m Saltaneset mylonite shear zone (Fig. 1c) (Renedo et al., 2014). Zircon LASS analyses from four zircons extracted from the garnet–quartz layer give $^{206}Pb/^{238}U$ dates of 407.8 ± 5.1 Ma to 398.1 ± 8.7 Ma (n = 4; Figs. 3b and 4b; Table 2). These same zircons yielded ID-TIMS $^{206}Pb/^{238}U$ dates ranging from 409.0 ± 0.4 Ma to 401.4 ± 0.2 Ma (Figs. 3a and 4b; Table 3). These

results reveal two populations with weighted-mean $^{206}Pb/^{238}U$ dates of 408.8 ± 0.2 Ma (n = 2) and 401.4 ± 0.1 Ma (n = 2), respectively (Fig. 4b). Nine additional zircons analyzed by ID-TIMS yield discordant dates, which when combined with the Scandian ID-TIMS dates reveal weak discordia arrays with upper-intercept ages of ca. 1560 Ma and ca. 943 Ma (Fig. S1; Table 3). The remaining zircons analyzed by LASS produced Scandian $^{206}Pb/^{238}U$ dates from 413.4 ± 9.8 Ma to 396.8 ± 8.8 Ma (n= 10; Figs. 3b and 4b; Table 2). Similar to the ID-TIMS results, LASS results also include discordant analyses that define a discordia array with an upper-intercept of ca. 970 Ma (Fig. S1; Table 2); however, LASS analyses do not reproduce the older ca. 1600 Ma discordia array revealed by ID-TIMS analyses.

Only one zircon from the omphacite-rich layer (NW13-02-O) yielded a Scandian age for both techniques. LASS analysis resulted in a $^{206}Pb/^{238}U$ date of 404.1 ± 5.1 Ma, and ID-TIMS analysis yielded a $^{206}Pb/^{238}U$ date of 396.7 ± 1.4 Ma (Figs. 2, 3a, and 4b; Tables 2 and 3, respectively). Other zircons from NW13-02-O yielded older, discordant ID-TIMS dates defining a discordia array, suggesting a protolith age of ca. 936 Ma (Fig. S1; Table 2). Additional zircons dated by LASS yielded $^{206}Pb/^{238}U$ dates ranging from 414.4 ± 5.8 Ma to 398.4 ± 8.1 Ma (n = 5; Figs. 3b and 4b; Table 2), as well as two discordia arrays with upper intercepts of ca. 1599 Ma and 954 Ma (Fig. S1).

Zircon trace-element data

LASS trace element results are shown for the Ulsteinvik eclogite and the Saltaneset garnet–quartz and omphacite layers in Figs. 5a–c. The solution ICP-MS trace element

data obtained from the ID-TIMS washes are in Figs. 5d–e, S2a–b, and Table 4. All Scandian solution ICP-MS analyses for the Saltaneset garnet–quartz and omphacite layers are combined in Fig. 5e as there is only a single Scandian zircon ID-TIMS date from the omphacite layer.

Ulsteinvik eclogite LASS and solution ICP-MS zircon trace element data

The LASS zircon REE patterns from the Ulsteinvik eclogite reveal two distinct patterns. Scandian (ca. 413–397 Ma) zircons analyzed by LASS record a flat HREE slope (Lu_N/Gd_N = 0.62–4.40; n = 34) and mostly flat-to-positive Eu anomalies (Eu/Eu* = $Eu_N/(Sm_N \times Gd_N)^{0.5}$ = 0.75–1.93; n = 29), although slightly negative Eu anomalies were also obtained (Eu/Eu* = 0.56–0.73; n = 5) (Fig. 5a; Table 4). The individual REE patterns of most analyses reveal an overall higher concentration of MREE and HREE for the younger Scandian analyses (ca. 405–397 Ma) compared to the older Scandian analyses (ca. 413–406) (Fig. 5a; Table 4). The second pattern represented by inherited dates (ca. 475–430 Ma; n = 5) is characterized by an increase in the overall REE concentration, steep HREE slopes (Lu_N/Gd_N = 42–128), and prominent-to-flat Eu anomalies (Eu/Eu* = 0.35–0.94) (Fig. 5a; Table 4).

The solution ICP-MS trace element patterns of Scandian (ca. 409–402 Ma) Ulsteinvik zircons are similar to laser ablation analyses of the same zircons: flat HREE slopes (Lu_N/Gd_N = 0.54–5.51, n = 14) and a lack of strongly-negative Eu anomalies (Eu/Eu* = 0.88–1.53, n = 14) (Figs. 5d and S2a). These analyses record an overall greater abundance of MREE–HREE for the younger analyses in comparison to the laser-ablation analyses; however, similar to the LASS analyses, there is a correlation between younger

Scandian dates and higher MREE–HREE abundances (Figs. 5d and S2b; Table 4). Furthermore, the younger Scandian ca. 402 Ma zircons yielded greater Y/Sc and Zr/Hf ratios (Fig. S2b).

Saltaneset garnet–quartz and omphacite layers zircon LASS and solution ICP-MS trace element data

Zircon LASS trace element data from the garnet–quartz layer, NW13-02-G, also reveal two separate REE patterns. The Scandian (ca. 413–397 Ma) zircons are characterized by flat (Lu_N/Gd_N = 1.87–3.93, n = 12) to slightly positive (Lu_N/Gd_N = 5.81–10.38, n = 2) HREE slopes and absent (0.75–1.24, n = 7) to slightly negative Eu anomalies (Eu/Eu* = 0.43–0.64, n = 7) (Fig. 5b; Table 4). In comparison, inherited (ca. 966–528 Ma) zircons show more enriched REE patterns, with steep HREE slopes (Lu_N/Gd_N = 7.95–97.87, n = 39) and prominently negative (Eu/Eu* = 0.19–0.48, n = 35) to slightly negative Eu anomalies (Eu/Eu* = 0.57–0.70, n = 3) (Fig. 5b; Table 4).

The omphacite-rich layer, NW13-02-O, yielded LASS zircon REE patterns similar to the Saltaneset garnet–quartz layer and the Ulsteinvik eclogite. The youngest population of zircons (ca. 414–398 Ma) is represented by flat (Lu_N/Gd_N = 1.95–3.24, n = 3) to slightly-positive HREE slopes (Lu_N/Gd_N = 5.33–8.89, n = 3). These grains lack negative Eu anomalies (Eu/Eu*=0.80–1.47, n = 5), with the exception of a single analysis (Eu/Eu*=0.70) (Fig. 5c, Table 4). In contrast, ca. 1600–433 Ma zircons are distinguished by enrichment in all REE, especially HREE. These inherited grains have steep HREE slopes (Lu_N/Gd_N = 4.34–150.7, n = 39). A variety of Eu anomalies are preserved, from strongly negative to absent (Eu/Eu* = 0.23–0.83, n = 40) (Fig. 5c; Table 4).

Individual Scandian zircon solution ICP-MS REE patterns for the Saltaneset garnet–quartz layer (ca. 409–402 Ma) and a single analysis from the omphacite layer (ca. 397 Ma) have positive Eu anomalies (Eu/Eu* = 0.75–1.05, n = 5) and are depleted in HREE, producing HREE slopes similar to Scandian LASS analyses for both layers. The depleted HREE signatures show flat to slightly positive slopes (Lu_N/Gd_N = 1.72–3.34, n = 5) (Figs. 5e and S2a–b; Table 4). Similar to the Ulsteinvik solution ICP-MS analyses, the ca. 402 Ma grains from the Saltaneset garnet–quartz layer have increased MREE–HREE abundances and greater Y/Sc and Zr/Hf ratios (Fig. S2b). Solution ICP-MS analyses (ca. 1512–425 Ma) for the inherited grains are similar to the LASS REE patterns of inherited zircons from both Saltaneset eclogite layers (Fig. 5e). The individual zircon trace-element profiles show pronounced to slightly-negative Eu anomalies (Eu/Eu* = 0.34–0.72, n = 5) and strong enrichment in HREE with steep slopes (Lu_N/Gd_N = 5.29–46.47, n = 5) (Fig. 5e; Table 4).

Garnet LA-ICP-MS trace element data

Ulsteinvik eclogite garnet LA-ICP-MS trace-element data

Garnet within the Ulsteinvik eclogite consists of large (1–4 mm), fractured porphyroblasts and later polycrystalline garnet in the matrix and rimming some of the early porphyroblasts. Transects across the porphyroblasts and the polycrystalline matrix garnet from the same portion of the eclogite in which zircon was extracted revealed variable trace-element signatures. The porphyroblasts have slight variation in LREE composition and flat MREE–HREE signatures (Lu_N/Gd_N = 0.69–1.43, n = 141) (Fig. 6a; Table 5). In contrast, late polycrystalline garnet in the matrix and rimming early garnet

have lower and more variable LREE, with more consistent MREE and HREE (Lu_N/Gd_N = 0.77–3.74, n = 39) (Fig. 6b; Table 5). Both generations of garnet preserve flat Eu anomalies (Eu/Eu* = 1.10–1.67, n = 198) (Figs. 6a–b; Table 5).

Saltaneset garnet–quartz and omphacite layers garnet LASS trace element data

The Saltaneset eclogite contains garnet within both of its layers. The large (1–3 mm), subhedral garnets located within the quartz vein have similar LREE, whereas core-to-rim variation in MREE and HREE is preserved. The rims show flat patterns (Lu_N/Gd_N = 2.21–4.79, n = 8) that transition to negative HREE slopes for the garnet core (Lu_N/Gd_N = 0.15–0.96, n = 17) (Fig. 6d; Table 5). In comparison, small (0.5–0.8 mm) anhedral garnets from the omphacite-rich layer have homogenous trace element profiles with slightly-positive HREE slopes (Lu_N/Gd_N = 2.25–5.72, n = 11) (Fig. 6c; Table 5). Garnet analyses within both layers of the eclogite have positive Eu anomalies (Eu/Eu* = 0.73–1.20, n = 36) (Figs. 6c–d; Table 5).

Zircon-garnet trace-element partition coefficients

Rare earth element partitioning between zircon and garnet (i.e., D_{REE} (zrn/grt)) was calculated for the Ulsteinvik and Saltaneset eclogite layers to further assess whether zircon (re)crystallized in equilibrium with garnet (Fig. 7). To determine D_{REE} (zrn/grt), average trace element compositions for the two zircon populations (ca. 409–407 Ma and ca. 402 Ma) from each sample were paired with the average composition of different garnet populations (see below). For consistency, both solution ICP-MS (Fig. 7) and laser ablation ICP-MS (Fig. S3) trace-element analyses are used separately in the partition

coefficient calculations. However, the trends in REE (Lu_N/Gd_N and MREE–HREE abundances) versus age from both techniques are similar and thus the calculated distribution coefficients are similar (Figs. 5 and S2a–b). As some LREE were below detection limits for most of the zircon solution ICP-MS analyses, D_{LREE} values were only calculated from a few analyses.

Within the Ulsteinvik eclogite, there are two garnet populations: 1) early garnet porphyroblasts; and 2) late, recrystallized garnet as a matrix phase and as rims on the porphyroblasts. The trace element data for the porphyroblasts show consistent LREE–HREE patterns, whereas the later recrystallized garnet have more variably-depleted LREE (Figs. 6a–b; Table 5). The overlap of some LREE–MREE analyses for the two garnet types may reflect growth of early and late garnet under similar P-T conditions (Fig. 6b). D_{REE} was calculated from pairing the older zircon population with the early garnet porphyroblasts and the younger zircon population with the late-recrystallized garnet (Fig. 7). The young (ca. 402 Ma) zircons/late garnets have D_{REE} near unity for the MREE–HREE (Fig. 7). A similar, flat D_{HREE} partitioning pattern is observed for the old (ca. 409 Ma) zircons/early garnets; however, the values are slightly less than unity (Fig. 7). In addition, the D_{MREE} values decrease with decreasing atomic number for the old zircon/early-garnet pairs (Fig. 7).

For the Saltaneset eclogite, the garnet cores from the quartz layer have greater MREE (Sm–Tb) and less HREE (Tm–Lu) relative to their rims (Fig. 6d; Table 5). D_{REE} for the garnet–quartz layer were calculated by pairing the trace element compositions of the older zircon population with the garnet cores, and the younger zircon population with the garnet rims (Fig. 7). D_{HREE} and D_{MREE} for the young zircon/garnet rim compositions are

consistent and greater than unity, whereas the older zircon/garnet core pairs indicate preferential partitioning of the Lu into zircon ($D_{Lu} = 5.81$), with D_{REE} decreasing to near-unity values at Dy and for the remaining MREE (Fig. 7).

In comparison to the garnet–quartz layer, garnets from the Saltaneset omphacite-rich layer have consistent core-to-rim trace element profiles, with weakly positive HREE slopes (Fig. 6c; Table 5). D_{REE} for the Saltaneset omphacite layer were calculated with the zircon trace element composition of the single ID-TIMS analysis and the LA-ICP-MS average trace element composition of the homogeneous garnet; these results show consistent D_{REE} values slightly above unity from Lu–Sm (Fig. 7).

Discussion

The preservation of (U)HP eclogites and mantle peridotites across 30,000 km^2 of the WGR provides irrefutable evidence for the deep subduction and exhumation of a large body of continental crust during the late stages of the Caledonian orogeny. Previous geochronological investigations have concluded that the rocks remained at eclogite-facies depths from ca. 425–400 Ma. In order for the subducted material to have remained at eclogite-facies conditions for > 20 Myr prior to exhumation, studies have argued that either multiple UHP events occurred at different times across the WGR or that the subducted crust was thick and subduction was slow (Root et al., 2005; Hacker, 2007; Kylander-Clark et al., 2009). Evaluating these endmember models requires constraining the timing and duration of UHP metamorphism at different locations across the WGR.

Zircon: Ulsteinvik and Saltaneset eclogites

LASS and solution ICP-MS analyses from all of the Scandian zircons from both the Ulsteinvik and Saltaneset eclogites show REE patterns consistent with (re)crystallization during eclogite-facies metamorphism, with depleted, flat HREE signatures and weak, negative Eu anomalies (Figs. 5 and S2a). The LASS U-Pb zircon results from the Ulsteinvik eclogite presented in this study reveal protracted Scandian zircon (re)crystallization at eclogite-facies conditions from ca. 413–397 Ma, with single-crystal ID-TIMS analyses suggesting two zircon (re)crystallization events at ca. 409–407 Ma and 401.9 ± 0.1 Ma (Figs. 3a and 4a). Previous studies of the Ulsteinvik eclogite had documented UHP eclogite-facies inclusions within zircon (i.e., omphacite, garnet, rutile, quartz, and coesite) and argued that the 401.6 ± 1.6 Ma zircon age best represents the timing of WGR UHP metamorphism (Krogh et al., 1974; Carswell et al., 2003a). However, this Ulsteinvik zircon age is a multi-grain, weighted-mean $^{207}Pb/^{206}Pb$ age derived from four different U-Pb ratios; thus, this age may incorporate and average multiple generations of zircon (re)crystallization. The younger of the two populations revealed by ID-TIMS is equivalent to the earlier reported value of 401.6 ± 1.6 Ma; however, the older population reveals an earlier eclogite-facies history than previously reported, suggesting that the Ulsteinvik body was at (U)HP conditions by at least ca. 409 Ma.

The layered Saltaneset eclogite previously yielded an Sm-Nd garnet–omphacite–whole rock isochron date of 408.3 ± 6.7 Ma (n = 3, MSWD = 0.81) (Carswell et al., 2003b). In comparison to the Sm-Nd age, U-Pb zircon results from the Saltaneset eclogite garnet–quartz layer suggest a prolonged (U)HP history, with LASS analyses yielding a

range of Scandian dates from ca. 413–397 Ma and ID-TIMS results revealing a bimodal population of 408.8 ± 0.2 Ma and 401.4 ± 0.1 Ma (Figs. 3a and 4b; Tables 2 and 3). As only two zircons make up the ca. 409 Ma ID-TIMS population, it is possible that this population represents mixing of minor inherited zircon domains with the ca. 402 Ma age domains (Fig. S1); however, the calculated discordia arrays show scatter (high MSWDs), the ca. 409 Ma dates overlap concordia within uncertainty (Fig. 3a), and the previously reported Sm-Nd isochron age is in good agreement with this U-Pb age. Furthermore, the solution trace element data shows distinct MREE–HREE abundances and steepness of the HREE patterns for the inherited, ca. 409 Ma, and ca. 402 Ma zircon populations (Figs. 5a–e and S2b). Therefore, the ca. 409 Ma zircons in the Saltaneset garnet-quartz layer likely record an eclogite-facies event that is also evident in the Ulsteinvik eclogite.

Only a single Scandian zircon was dated by both techniques from the omphacite-rich layer, as the majority of the grains were inherited (Figs. 3b and S1; Tables 2 and 3). This Scandian zircon revealed the youngest ID-TIMS date of this study: 396.7 ± 1.4 Ma (Fig. 4b; Table 3). LASS analyses from this layer reveal a range of Scandian dates from ca. 414–398 Ma and a similar inherited zircon population as recorded in the quartz-dominated layer (Figs. 4b and S1; Table 2). Based on these similar zircon inheritance patterns, it is likely that the Saltaneset omphacite and garnet–quartz layers underwent the same P–T history.

Zircon-garnet equilibrium patterns

Multiple studies have used trace element partitioning between zircon and garnet as a means of assessing equilibrium between the two minerals across a range of temperatures

in granulite-facies rocks (e.g., Harley et al., 2001; Rubatto, 2002; Hermann and Rubatto, 2003; Rubatto and Hermann, 2003; Hokada and Harley, 2004, Kelly and Harley, 2005; Buick et al., 2006; Rubatto et al., 2006; Harley and Kelly, 2007) and to a lesser extent in eclogite-facies rocks (Fig. 7; e.g., Rubatto, 2002; Rubatto and Hermann, 2003; Baldwin et al., 2004; Monteleone et al., 2007; Rubatto and Hermann, 2007b).

The calculated zircon–garnet partition coefficients for the Ulsteinvik eclogite and Saltaneset eclogite layers show two different D_{HREE} patterns (Fig. 7). The first is represented by constant D_{REE} values, as observed for the Ulsteinvik eclogite, the Saltaneset garnet–quartz young zircon/rim garnet pairs, and the Saltaneset omphacite-layer (Fig. 7). The second, from the old zircon/garnet core compositions from the Saltaneset garnet–quartz layer, is marked by a decrease in HREE partitioning into zircon from Lu to Dy (Fig. 7).

Both D_{HREE} patterns described above for the Ulsteinvik and Saltaneset eclogites have previously been suggested to be indicative of zircon/garnet equilibrium. The flat pattern with near-unity D_{HREE} values has been observed in natural eclogite- and granulite-facies rocks and in experiments (e.g., Harley et al., 2001; Whitehouse and Platt, 2003; Hokada and Harley, 2004; Kelly and Harley, 2005; Harley and Kelly, 2007; Monteleone et al., 2007; Taylor et al., 2014). The second pattern, marked by a decrease in zircon partitioning from HREE–MREE, has been inferred to represent equilibrium between zircon and garnet in eclogites and experimental studies (e.g., Baldwin et al., 2004; Rubatto, 2002; Rubatto and Hermann, 2003, 2007b). In contrast to the zircon/garnet pairings discussed above, if the different garnet and zircon REE compositions are switched (i.e., young/core and old/rim), similar D_{REE} patterns are obtained. Based on

these results, it is suggested that the different zircon and garnet populations from both eclogites were likely in equilibrium during this prolonged period of eclogite-facies metamorphism; thus, (re)crystallization of zircon under garnet-stable conditions likely occurred from ca. 409–402 Ma.

Older (≥430 Ma) Caledonian Eclogite Ages

In addition to the Scandian dates, zircons from the Ulsteinvik eclogite also reveal a nearly continuous spread of older concordant Caledonian dates that range from ca. 475–430 Ma (Fig. 3b; Table 2). Root et al. (2005) suggested that the Ulsteinvik eclogite is allochthonous based on the similarity of the host rock lithologies, including garnet–biotite–kyanite schist, quartzite, marble (Mysen and Heier, 1972), and coarse augen gneiss, to the allochthonous Blåhø and Risberget Nappes, exposed to the north (Robinson, 1995). Furthermore, the ca. 475–430 Ma zircons overlap with ca. 459 Ma eclogite zircon ages, interpreted to be mainly igneous (Th/U = 0.19–0.72), from the Blåhø Nappe exposed ~150 km to the east and ca. 440 Ma eclogite metamorphic zircon (re)crystallization ages (Th/U = 0.03–0.13) from allochthons exposed ~60 km to the southeast (Walsh et al., 2007). The metamorphic (re)crystallization ages are possibly related to allochthon emplacement (e.g., Hacker and Gans, 2005).

In comparison, the Saltaneset layered eclogite records evidence of the Gothian and Sveconorwegian orogenic events (e.g., Skår, 2000; Austrheim et al., 2003), with upper intercept ages of ca. 1600–1560 Ma and ca. 970–936 Ma from two separate discordia arrays (Fig. S1). These results suggest the metabasite protolith likely intruded the WGC basement rocks and crystallized at ca. 1600 Ma. It was then reworked during the

Sveconorwegian and Caledonian orogenies. Similar eclogite protolith ages have been obtained across the WGR for both events (e.g., Root et al., 2004; Walsh et al., 2007) in addition to the abundant record of these events recorded by felsic basement rocks (e.g., Brueckner, 1972, 1979; Carswell and Harvey, 1985; Tucker et al., 1990, 2004; Skår et al., 1994; Skår, 2000; Austrheim et al., 2003; Skår and Pederson, 2003; Røhr et al., 2004, 2013; Root et al., 2005; Glodny et al., 2008; Kylander-Clark et al., 2008; Krogh et al., 2011; Corfu et al., 2013).

UHP metamorphism in the central and southern UHP domains

New LASS and ID-TIMS results support previous conclusions that UHP metamorphism occurred from ca. 410–400 Ma in the central and southern UHP domains (Krogh et al., 1974; Mearns, 1986; Carswell et al., 2003a, 2003b; Root et al., 2004; Tucker et al., 2004; Young et al., 2007). However, the new high-precision, single-crystal data also indicate that zircon (re)crystallization was locally episodic, at ca. 409–407 Ma and at ca. 402 Ma, rather than continuous. The possibility of prolonged subduction has been inferred on a larger scale from U-Pb zircon, Lu-Hf garnet, and Sm-Nd garnet dates (Kylander-Clark et al., 2007, 2009; Krogh et al., 2011). This is the first study, however, to record multiple discrete ages of (U)HP zircon (re)crystallization events within individual samples from two separate localities, with both events occurring during the end stages of the previously-interpreted eclogite-facies history (425–400 Ma).

The younger zircon population (ca. 402 Ma) may represent (re)crystallization at HP during the early stages of exhumation and retrogression. The use of Eu anomaly to assess zircon (re)crystallization pressure is limited by the maximum pressure stability of

plagioclase at ~ 1.6 GPa (depending on temperature and bulk composition), well below coesite stability (Bohlen and Boettcher, 1982; Bose and Ganguly, 1995). Thus, these results may record HP events rather than parts of the UHP history. A recent study of variably deformed felsic leucosomes and dikes across the WGR revealed an overlap in the youngest eclogite ages and the oldest melt-crystallization ages, suggesting that the younger zircon population detected in this study may be recording (re)crystallization during retrogression (Kylander-Clark and Hacker, 2014). Moreover, the minor population of zircon dates from both localities that cluster between ca. 398–396 Ma (n=7; Tables 2 and 3) may also reflect this subsequent (re)crystallization during exhumation at garnet-stable conditions. Regardless, the results from the southern and central UHP domains provide evidence for at least two eclogite-facies metamorphic events, revealing a shorter timescale of (U)HP metamorphism in comparison to previous studies that suggested a >20 Myr long-term residence at eclogite-facies depths for a large portion of the WGR (Kylander-Clark et al., 2007, 2009).

Conclusions

This study combines high-spatial resolution (LASS) and high-precision (ID-TIMS-TEA) techniques on the same zircon from two UHP eclogites within the Western Gneiss Region of Norway. The results capture metamorphism from 409.6 ± 0.6 Ma to 401.3 ± 0.4 Ma and 409.0 ± 0.4 Ma to 401.4 ± 0.2 Ma, with the data suggesting two (U)HP zircon (re)crystallization events at ca. 409–407 Ma and ca. 402 Ma. Trace-element analyses from both populations of zircon show flat, depleted HREE signatures and weak negative Eu anomalies interpreted to represent metamorphism under eclogite-facies conditions

during these two events. Zircon and garnet trace-element abundances yield distribution coefficients that imply equilibrium between the two minerals. This study highlights the utility of coupled high-precision ID-TIMS and high-spatial resolution LASS zircon studies of eclogites across the WGR to test models for the subduction and exhumation of the WGR during the Scandian orogeny.

Acknowledgements

This work was supported by NSF Grants EAR-1019709, -1062187 (Gordon), and -1219942 (Hacker). High-precision mass spectrometry at MIT is possible because of an Instrumentation and Facilities grant (EAR-0931839 to S.A.B) and the collective sharing of knowledge by the EARTHTIME community. Thanks to Jahan Ramezani for providing assistance in the MIT Isotope Laboratory. Helpful reviews from F. Corfu and H. Brueckner greatly improved the manuscript.

References

Andersen, T.B., Jamtveit, B., Dewey, J.F., Swensson, E. (1991), Subduction and eduction of continental crust: major mechanisms during continent-continent collision and orogenic extensional collapse, a model based on the south Norwegian Caledonides. *Terra Nova*, **3**, 303-310, http://dx.doi.org/10.1111/j.1365-3121.1991.tb00148.x.

Andersen, T.B., Berry, H.B. IV, Lux, D.R., and Andresen, A. (1998), The tectonic significance of pre-Scandian $^{40}Ar/^{39}Ar$ phengite cooling ages in the Caledonides of western Norway. *Geological Society [London] Journal*, **155**, 297–309, http://dx.doi.org/10.1144/-gsjgs.155.2.0297.

Austrheim, H. (1987), Eclogitization of lower crustal granulites by fluid migration through shear zones. *Earth Planet. Sci. Lett.*, **81**, 221–232, http://dx.doi.org/10.1016/0012-821X(87)90158-0.

Austrheim, H. (1998), The influence of fluid and deformation on metamorphism of the deep crust and consequences for the geodynamics of collision zones. In: Hacker, B., Liou, J.G. (Eds.), When Continents Collide: Geodynamics and Geochemistry of Ultrahigh Pressure Rocks, *Chapman & Hall*, 297–323, http://dx.doi.org/10.1007/978-94-015-9050-1_12.

Austrheim, H., Corfu, F., Bryhni, I., Andersen, T.B. (2003), The Proterozoic Hustad igneous complex: a low strain enclave with a key to the history of the Western Gneiss Region of Norway. *Precambrian Res.*, **120**, 149–175, http://dx.doi.org/10.1016/S0301-9268(02)00167-5.

Auzzanneau, E., Vielzeuf, D., Schmidt, M.W. (2006), Experimental evidence of decompression melting during exhumation of subducted continental crust. *Contrib. Mineral. Petrol.*, **152**, 125–148, http://dx.doi.org/10.1007/s00410-006-0104-5.

Baldwin, S.L., Monteleone, B., Webb, L.E., Fitzgerald, P.G., Grove, M., and Hill, E.J. (2004), Pliocene eclogite exhumation at plate tectonic rates in eastern Papua New Guinea, *Nature*, **431**, 263–267, http://dx.doi.org/10.1038/nature02846.

Beckman, V., Möller, C., Söderlund, U., Corfu, F., Pallon, J. & Chamberlain, K. R. (2014), Metamorphic zircon formation at the transition from gabbro to eclogite in Trollheimen–Surnadalen, Norwegian Caledonides. In: Corfu, F., Gasser, D. & Chew, D. M. (Eds.), New Perspectives on the Caledonides of Scandinavia and Related Areas. *Geological Society of London Special Publications*, **390**, 403–424, http://dx.doi.org/10.1144/SP390.26.

Bingen, B., Austrheim, H., Whitehouse, M.J., Davis, W.J. (2004), Trace element signature and U–Pb geochronology of eclogite-facies zircon, Bergen Arcs,

Caledonides of W Norway. *Contrib. Mineral. Petrol.*, **147**, 671–683, http://dx.doi.org/10.1007/s00410-004-0585-z.

Bohlen, S.R., Boettcher, A.L. (1982), The quartz–coesite transformation: a precise determination and the effects of other components, *J. Geophys. Res.*, **87**, 7073–7078, http://dx.doi.org/-10.1029/JB087iB08p07073.

Bose, K., Ganguly, J. (1995), Quartz–coesite transition revisited: reversed experimental determination at 500–1200 °C and retrieved thermochemical properties, *Am. Mineral.*, **80**, 231–238.

Bowring, J.F., McLean, N.M., Bowring, S.A. (2011), Engineering cyber infrastructure for U–Pb geochronology: Tripoli and U–Pb redux. *Geochem., Geophys., Geosyst.*, **12**, Q0AA19, http://dx.doi.org/10.1029/2010GC003479.

Brueckner, H. K. (1972), Interpretation of Rb-Sr Ages from the Precambrian and Paleozoic rocks of southern Norway. *American Journal of Sciences*, **272-4**, 334-358, http://dx.doi/10.2475/ajs.272.4.334.

Brueckner, H. K. (1979), Precambrian ages from the Geiranger-Tafjord-Grotli area of the Basal Gneiss Region, west Norway. *Norsk Geologisk Tidsskrift*, **59**, 141-153, ISSN 0029-196X.

Brueckner, H.K., van Roermund, H.L.M. (2004), Dunk tectonics: a multiple subduction/eduction model for the evolution of the Scandinavian Caledonides. *Tectonics*, **23**, TC2004, http://dx.doi.org/10.1029/2003TC001502.

Buick, I.S., Hermann, J., Williams, I.S., Gibson, R.L., Rubatto, D. (2006), A SHRIMP U-Pb and LASS trace element study of the petrogenesis of garnet-cordierite-orthoamphibole gneisses from the Central Zone of the Limpopo Belt, South Africa. *Lithos*, **88**, 150-172, http://dx.doi.org/10.1016/j.lithos.2005.09.001.

Butler, J.P., Jamieson, R.A., Steenkamp, H.M., Robinson, P. (2013), Discovery of coesite–eclogite from the Nordøyane UHP domain, Western Gneiss Region, Norway: field relations, metamorphic history, and tectonic significance. *J. Metamorph. Geol.*, **31**, 147–163, http://dx.doi.org/10.1111/jmg.12004.

Carswell, D.A., Harvey, M.A. (1985), The intrusive history and tectonometamorphic evolution of the Basal Gneiss Complex in the Moldefjord area, west Norway. In: Gee, D.G, Sturt, B.A, (Eds.), The Caledonide Orogen—Scandinavia and related areas, *Wiley*, Chichester, UK, 843–858.

Carswell, D.A., Tucker, R.D., O'Brien, P.J., Krogh, T.E. (2003a), Coesite inclusions and the U-Pb age of zircons from the Hareidland Eclogite in the Western Gneiss Region of Norway. *Lithos*, **67**, 181–190, http://dx.doi.org/10.1016/S0024-4937(03)00014-8.

Carswell, D.A., Brueckner, H.K., Cuthbert, S.J., Mehta, K., O'Brien, P.J. (2003b), The timing of stabilisation and exhumation rate for ultrahigh-pressure rocks in the Western Gneiss Region of Norway. *J. Metamorph. Geol.*, **21**, 601–612, http://dx.doi.org/10.1046/j.1525-1314.2003.00467.x.

Carswell, D.A., Cuthbert, S.J. (2003), Ultrahigh pressure metamorphism in the Western Gneiss Region of Norway. In: Carswell, D.A., Compagnoni, R. (Eds.), Ultrahigh pressure metamorphism, *EMU Notes in Mineralogy*, **5**, 51–73.

Carswell, D.A., van Roermund, H.L.M., Wiggers de Vries, D.F. (2006), Scandian ultrahigh-pressure metamorphism of Proterozoic basement rocks on Fjørtoft and Otrøy, Western Gneiss Region, Norway. *International Geology Review*, **48**, 957–977, http://dx.doi.org/10.2747/0020-6814.48.11.957.

Corfu F., Hanchar J.M., Hoskin P.W.O., Kinny P. (2003), Atlas of zircon textures. In: Hanchar, J.M. and Hoskin P.W.O. (eds.), Zircon. *Reviews in Mineralogy and Geochemistry*, **53**, 468–500. Washington, DC: Mineralogical Society of America.

Corfu, F., Austrheim, H. Ganzhorn, A.C. (2013), Localized granulite and eclogite facies metamorphism at Flatraket and Kråkeneset, Western Gneiss Region: U-Pb data and tectonic implications. *Geological Society of London Special Publications*, **390**, 425–442, http://dx.doi.org/10.1144/SP390.22.

Cuthbert, S.J., Carswell, D.A. (1990), Formation and exhumation of medium-temperature eclogites in the Scandinavian Caledonides. In: Carswell, D.A. (eds.), Eclogite Facies Rocks, *Chapman and Hall*, New York, 180–203.

Cuthbert, S.J., Carswell, D.A., Krogh-Ravna, E.J., Wain, A. (2000), Eclogites and eclogites in the Western Gneiss Region, Norwegian Caledonides. *Lithos*, **52**, 165–195, http://dx.doi.org/10.1016/S0024-4937(99)00090-0.

Dobrzhinetskaya, L.F., Eide, E.A., Larsen, R.B., Sturt, B.A., Trønnes, R.G., Smith, D.C., Taylor, W.R., Posukhova, T.V. (1995), Microdiamond in high-grade metamorphic rocks of the Western Gneiss region, Norway. *Geology*, **23**, 597–600, http://dx.doi.org/10.1130/0091-7613(1995) 023<0597:MIHGMR> 2.3.CO;2.

Engvik, A.K., Austrheim, H., Andersen, T.B. (2000), Structural, mineralogical and petrophysical effects on deep crustal rocks of fluid-limited polymetamorphism, Western Gneiss Region, Norway. *Geological Society [London] Journal*, **157**, 121–134, http://dx.doi.org/-10.1144/jgs.157.1.121.

Gáal, G., Gorbatschev, R. (1987), An outline of the Precambrian evolution of the Baltic shield. *Precambrian Research*, **35**, 15–52, http://dx.doi.org/10.1016/0301-9268(87)90044-1.

Gebauer, D., Lappin, M.A., Grünenfelder, M., Wyttenbach, A. (1985), The age and origin of some Norwegian eclogites: a U–Pb zircon and REE study. *Chem. Geol.*, **52**, 227–247, http://dx.doi.org/10.1016/0168-9622(85)90020-X.

Glodny, J., Kühn, A., Austrheim, H. (2008), Diffusion v. recrystallization processes in Rb–Sr geochronology: isotopic relicts in eclogite facies rocks, Western Gneiss Region, Norway. *Geochim. et Cosmochim. Acta.*, **72**, 506–525, http://dx.doi.org/10.1016/j.gca.2007.10.021.

Griffin, W.L., H.K. Brueckner (1980), Caledonian Sm-Nd ages and a crustal origin for Norwegian eclogites, *Nature*, **285**, 319–321, http://dx.doi.org/10.1038/285319a0.

Griffin, W.L., Brueckner, H.K. (1985), REE, Rb-Sr and Sm-Nd studies of Norwegian eclogites. *Chem. Geol.*, **52**, 249–271, http://dx.doi.org/10.1016/0168-9622(85)90021-1.

Griffin, W.L., Austrheim, H., Brastad, K., Bryhni, I., Krill, A.G., Krogh, E.J., Mørk, M.B.E., Qvale, H., Tørudbakken, B. (1985), High-pressure metamorphism in the Scandinavian Caledonides. In: Gee, D.G, Sturt, B.A, (Eds.), The Caledonide Orogen—Scandinavia and related areas, *Wiley*, Chichester, UK, 783-801.

Gordon, S. M., Whitney, D. L., Teyssier, C. & Fossen, H. (2013), U–Pb dates and trace-element geochemistry of zircon from migmatite, Western Gneiss Region, Norway: significance for history of partial melting in continental subduction. *Lithos*, **170–171**, 35–53, http://dx.doi.-org/10.1016/j.lithos.2013.02.003.

Hacker, B.R. (2007), Ascent of the ultrahigh-pressure Western Gneiss Region, Norway. In: Cloos, M., W.D. Carlson, M.C. Gilbert, J.G. Liou, and S.S. Sorenson (Eds.), Convergent Margin Terranes and Associated Regions, A Tribute to W.G. Ernst, *Geological Society of America Special Paper*, **419,** 171–184, Geological Society of America, Boulder, CO, http://dx.doi.org/10.1130/2006.2419(09).

Hacker, B.R., Gans, P.B. (2005), Continental collisions and the creation of ultrahigh-pressure terranes: Petrology and thermochronology of nappes in the central Scandinavian Caledonides. *Geological Society of America Bulletin*, **117**, 117–134, http://dx.doi.org/-10.1130/B25549.1.

Hacker, B.R., Andersen, T.B., Johnston, S., Kylander-Clark, A.R.C., Peterman, E.M., Walsh, E.O., Young, D. (2010), High-temperature deformation during continental-margin subduction & exhumation: the ultrahigh-pressure Western Gneiss Region of Norway. *Tectonophysics*, **480(1–4)**, 149–171. doi:http://dx.doi.org/10.1016/j.tecto.2009.08.012.

Harley, S.L., Kinny, P., Snape, I., Black, L.P. (2001), Zircon chemistry and the definition of events in Archean granulite terrains. In: Fourth International Archean Symposium, Extended Abstract Volume, *AGSO Geoscience Australia Record*, 2001/37, 511-513.

Harley, S.L., Kelly, N.M. (2007), The impact of zircon-garnet REE distribution data on the interpretation of zircon U-Pb ages in complex high-grade terrains: An example from the Rauer Islands, East Antarctica. *Chem. Geol.*, **241**, 62-87, http://dx.doi.org/-10.1016/j.chemgeo.2007.02.011.

Hermann, J., Rubatto, D. (2003), Relating zircon and monazite domains to garnet growth zones: Age and duration of granulite facies metamorphism in the Val Malenco lower crust. *J. Metamorph. Geol.*, **21**, 833-852, http://dx.doi.org/10.1046/j.1525-1314.2003.00484.x.

Hinton, R., Upton, B. (1991), The chemistry of zircon: variations within and between large crystals from syenite and alkali basalt xenoliths. *Geochim. et Cosmochim. Acta.*, **55**, 3287–3302, http://dx.doi.org/10.1016/0016-7037(91)90489-R.

Hokada, T., Harley, S.L. (2004), Zircon growth in UHT leucosome: Constraints from zircon-garnet rare earth elements (REE) relations in Napier Complex, East Antarctica. *J. Mineral. Petrol. Sciences*, **99**, 180-190, http://dx.doi.org/10.2465/jmps.99.180.

Hoskin, P.W.O., Ireland, T.R. (2000), Rare earth element chemistry of zircon and its use as a provenance indicator. *Geology*, **28**, 627–630, http://dx.doi.org/10.1130/0091-7613(2000) 28<627:REECOZ> 2.0.CO;2.

Hoskin, P.W.O., Schaltegger, U. (2003), The composition of zircon and igneous and metamorphic petrogenesis. *Rev. Mineral. Geochem.* **53**, 27–62, http://dx.doi.org/-10.2113/0530027.

Jamtveit, B., Carswell, D.A, Mearns, E.W. (1991), Chronology of the high-pressure metamorphism of Norwegian garnet peridotites/pyroxenites, *J. Metamorph. Geol.*, **9**, 125–139, http://dx.doi.org/10.1111/j.1525-1314.1991.tb00509.x.

Kelly, N.M., Harley, S.L. (2005), An integrated microtextural and chemical approach to zircon geochronology: Refining the Archaean history of the Napier Complex, east Antarctica. *Contrib. Mineral. Petrol.*, **149**, 57-84, http://dx.doi.org/10.1007/s00410-004-0635-6.

Krogh, E.J. (1977), Evidence for Precambrian continent-continent collision in western Norway. *Nature*, **267**, 17-19, http://dx.doi.org/10.1038/267017a0.

Krogh, E.J. (1982), Metamorphic evolution of Norwegian country-rock eclogites, as deduced from mineral inclusions and compositional zoning in garnets. *Lithos*, **15**, 305-321, http://dx.doi.org/10.1016/0024-4937(82)90021-4.

Krogh, T.E. (1982), Improved accuracy of U–Pb zircon dating by creation of more concordant systems using air abrasion technique. *Geochim. et Cosmochim. Acta.*, **46**, 637–649, http://dx.doi.org/10.1016/0016-7037(82)90165-X.

Krogh, T.E., Mysen, B.O., Davis, G.L. (1974), A Paleozoic age for the primary minerals of a Norwegian eclogite. Annual Report of the Geophysical Laboratory. *Carnegie Institution*, Washington, **73**, 575–576.

Krogh, T.E., Kamo, S.L., Robinson, P., Terry, M.P., Kwok, K. (2011), U–Pb zircon geochronology of eclogites from the Scandian Orogen, northern Western Gneiss Region, Norway: 14–20 million years between eclogite crystallization and return to amphibolite-facies conditions. *Can. J. Earth Sciences*, **48(2)**, 441–472, http://dx.doi.org/10.1139/E10-076.

Kylander-Clark, A.R.C., Hacker, B.R. (2014), Age and significance of felsic dikes from the UHP western gneiss region. *Tectonics*, **33 (12)**. 2342–2360, http://dx.doi.org/10.1002/2014TC003582.

Kylander-Clark, A.R.C., Hacker, B.R., Johnson, C.M., Beard, B.L., Mahlen, N.J., Lapen, T.J. (2007), Coupled Lu–Hf and Sm–Nd geochronology constrains prograde and exhumation histories of high- and ultrahigh-pressure eclogites from western Norway. *Chem. Geol.*, **242(1–2)**, 137–154, http://dx.doi.org/10.1016/j.chemgeo.2007.03.006.

Kylander-Clark, A.R.C., Hacker, B.R., Mattinson, J.M. (2008), Slow exhumation of UHP terranes: titanite and rutile ages of the Western Gneiss Region, Norway. *Earth Planet. Sci. Lett.*, **272(3-4)**: 531–540, http://dx.doi.org/10.1016/j.epsl.2008.05.019.

Kylander-Clark, A.R.C., Hacker, B.R., Johnson, C.M., Beard, B.L., Mahlen, N.J. (2009), Slow subduction and rapid exhumation of a thick ultrahigh-pressure terrane. *Tectonics*, **28(2)**, TC2003, http://dx.doi.org/10.1029/2007TC002251.

Kylander-Clark, A. R. C., B.R. Hacker, C.G. Mattinson (2012), Size and exhumation rate of ultrahigh-pressure terranes linked to orogenic stage, *Earth Planet. Sci. Lett.*, **321–322**, 115–120, http://dx.doi.org/10.1016/j.epsl.2011.12.036.

Kylander-Clark, A.R.C., Hacker, B.R., Cottle, J.M., (2013), Laser-ablation split-stream ICP petrochronology. *Chem. Geol.*, **345**, 99–112, http://dx.doi.org/10.1016/j.chemgeo.-2013.02.019.

Labrousse, L., Jolivet, L., Andersen, T.B., Agard, P., Hébert, R., Maluski, H., Schärer, U. (2004), Pressure–temperature–time-deformation history of the exhumation of ultrahigh-pressure rocks in the Western Gneiss region, Norway. In: Whitney, D.L., Teyssier, C., Siddoway, C.S. (Eds.), Gneiss Domes in Orogeny, *Geological Society of America Special Paper*, **380**, 155–183, Geological Society of America, Boulder, CO, http://dx.doi.org/10.1130/0-8137-2380-9.155.

Labrousse, L., G. Prouteau, A.C. Ganzhorn (2011), Continental exhumation triggered by partial melting at ultrahigh pressure, *Geology*, **39**, 1171–1174, http://dx.doi.org/10.1130/-G32316.1.

Lappin, M.A., Smith, D.C. (1978), Mantle-equilibrated orthopyroxene eclogite pods from the Basal Gneisses in the Selje District, western Norway. *J. Petrol.*, **19**, 530–584, http://dx.doi.org/10.1093/petrology/19.3.530.

Mattinson, J.M. (2005), Zircon U-Pb chemical abrasion ("CA-TIMS") method: combined annealing and multi-step partial dissolution analysis for improved precision and accuracy of zircon ages, *Chem. Geol.*, **220**, 47–66, http://dx.doi.org/10.1016/j.chemgeo.2005.03.011.

Mattinson, C.G., Wooden, J.L., Liou, J.G., Bird, D.K., Wu, C.L. (2006), Age and duration of eclogite-facies metamorphism, North Qaidam HP/UHP terrane, Western China. *Amer. J. Science*, **306**, 683–711, http://dx.doi.org/10.2475/09.2006.01

McClelland, W.C., Power, S.E., Gilotti, J.A., Mazdab, F.K., and Wopenka, B. (2006), U-Pb SHRIMP geochronology and trace element geochemistry of coesite-bearing zircons, North-East Greenland Caledonides, In: Hacker, B.R., McClelland, B., and Liou, J.G. (Eds.) Ultrahigh-Pressure Metamorphism: Deep Continental Subduction: *Geological Society of America Special Paper*, **403**, 23–43, Geological Society of America, Boulder, CO, http://dx.doi.org/10.1130/2006.2403(02).

McLean, N.M., Bowring, J.F., Bowring, S.A. (2011), An algorithm for U-Pb isotope dilution data reduction and uncertainty propagation, *Geochem. Geophys. Geosyst.*, **12**, Q0AA18, http://dx.doi.org/10.1029/2010GC003478.

Mearns, E. W. (1986), Sm-Nd ages for Norwegian garnet peridotite, *Lithos*, **19**, 269–278, http://dx.doi.org/10.1016/0024-4937(86)90027-7.

Monteleone, B.D., Baldwin, S.L., Webb, L.E., Fitzgerald, P.G., Grove, M., Schmitt, A.K. (2007), Late Miocene–Pliocene eclogite facies metamorphism, D'Entrecasteaux Islands, SE Papua New Guinea, *J. Metamorph. Geol.*, **25**, 245–265, http://dx.doi.org/10.1111/j.1525-1314.2006.00685.x.

Mørk, M.B.E., Mearns, E.W. (1986), Sm-Nd isotopic systematics of a gabbro-eclogite transition, *Lithos*, **19**, 255–267, http://dx.doi.org/10.1016/0024-4937(86)90026-5.

Mundil R., Metcalfe I., Ludwig K.R., Renne P.R., Oberli F., Nicoll, R.S. (2001), Timing of the Permian–Triassic biotic crisis: Implications from new zircon U-Pb age data (and their limitations). *Earth Planet. Sci. Lett.*, **187**, 131–145, http://dx.doi.org/10.1016/S0012-821X(01)00274-6.

Mysen, B.O. (1972), Five Clinopyroxenes in the Hareidland eclogite, Western Norway. *Contrib. Mineral. Petrol.*, **34**, 315–325, http://dx.doi.org/10.1007/BF00373761.

Mysen, B.O., Heier, K.S. (1972), Petrogenesis of eclogites in high-grade metamorphic gneisses exemplified by the Hareidland eclogite, west Norway. *Contrib. Mineral. Petrol.*, **36**, 73– 94, http://dx.doi.org/10.1007/BF00372836.

Peterman, E.M., Hacker, B.R., Baxter, E.F. (2009), Phase transformations of continental crust during subduction and exhumation: Western Gneiss Region, Norway. *Eur. J. Mineral.*, **21**, 1097–1118, http://dx.doi.org/10.1127/0935-1221/2009/0021-1988.

Ravna, E.J.K., Terry, M.P. (2004), Geothermobarometry of UHP and HP eclogites and schists–an evaluation of equilibria among garnet–clinopyroxene–kyanite–phengite–coesite/quartz. *J. Metamorph. Geol.*, **22**, 579–592, http://dx.doi.org/10.1111/j.1525-1314.2004.00534.x.

Renedo, R.N., Nachlas, W.O., Whitney, D.L., Teyssier, C., Piazolo, S., Gordon, S.M., Fossen, H. (in press), Fabric development during exhumation from ultrahigh-pressure in an eclogite-bearing shear zone, Western Gneiss Region, Norway. *J. Struct. Geol.*, http://dx.doi.org/-10.1016/j.jsg.2014.09.012.

Roberts, D. (2003), The Scandinavian Caledonides: Event chronology, palaeogeographic settings and likely modern analogues. *Tectonophysics*, **365**, 283–299, http://dx.doi.org/10.1016/-S0040-1951(03)00026-X.

Roberts, D., Gee, D.G. (1985), An introduction to the structure of the Scandinavian Caledonides. In: Gee, D.G, Sturt, B.A, (Eds.), The Caledonide Orogen—Scandinavia and related areas, *Wiley*, Chichester, UK, 55– 68.

Robinson, P. (1995). Extension of Trollheimen tectono-stratigraphic sequence in deep synclines near Molde and Brattvåg, Western Gneiss Region, southern Norway. *Norsk Geologisk Tidsskrift*, **75**, 181–198.

Røhr, T.S., Corfu, F., Austrheim, H., Andersen, T.B. (2004), Sveconorwegian U–Pb zircon and monazite ages of granulite-facies rocks, Hisarøya Gulen, Western Gneiss Region, Norway. *Norwegian J. Geol.*, **84**, 251–256, ISSN 029-196X.

Røhr, T.S., Bingen, B., Robinson, P., Reddy, S.M. (2013), Geochronology of Paleoproterozoic augen gneisses in the Western Gneiss Region, Norway: evidence for Sveconorwegian zircon neocrystallization and Caledonian zircon deformation. *J. Geol.*, **121**, 105–128, http://-dx.doi.org/10.1086/669229

Root, D.B., Hacker, B.R., Mattinson, J.M., Wooden, J.L. (2004), Zircon geochronology and ca. 400 Ma exhumation of Norwegian ultrahigh-pressure rocks: an ion

microprobe and chemical abrasion study. *Earth Planet. Sci. Lett.*, **228**, 325–341, http://dx.doi.org/10.1016/-j.epsl.2004.10.019.

Root, D.B., Hacker, B.R., Gans, P.B., Ducea, M.N., Eide, E.A., Mosenfelder, J.L. (2005), Discrete ultrahigh-pressure domains in the Western Gneiss Region, Norway: implications for formation and exhumation. *J. Metamorph. Geol.*, **23**, 45–61, http://dx.doi.org/10.1111/-j.1525-1314.2005.00561.x.

Rubatto, D. (2002), Zircon trace element geochemistry: distribution coefficients and the link between U–Pb ages and metamorphism. *Chem. Geol.*, **184**, 123–138, http://dx.doi.org/-10.1016/S0009-2541(01)00355-2.

Rubatto, D., Hermann, J. (2003), Zircon formation during fluid circulation in eclogites (Monviso, Western Alps): implications for Zr and Hf budget in subduction zones. *Geochim. et Cosmochim. Acta.*, **67**, 2173–2187, http://dx.doi.org/10.1016/S0016-7037(02)01321-2.

Rubatto, D., Hermann, J., Buick, I.S. (2006), Temperature and bulk composition control on the growth of monazite and zircon during low-pressure anatexis (Mount Stafford, central Australia). *J. Petrol.*, **47**, 1973–1996, http://dx.doi.org/10.1093/petrology/egl033.

Rubatto, D., Hermann, J. (2007a), Zircon behaviour in deeply subducted rocks, *Elements*, **3**, 31–35, http://dx.doi.org/10.2113/gselements.3.1.31.

Rubatto, D., Hermann, J. (2007b), Experimental zircon/melt and zircon/garnet trace element partitioning and implications for the geochronology of crustal rocks. *Chem. Geol.*, **241**, 38-61, http://dx.doi.org/10.1016/j.chemgeo.2007.01.027.

Scambelluri, M., Pettke, T., van Roermund, H.L.M. (2008), Majoritic garnets monitor deep subduction fluid flow and mantle dynamics. *Geology*, **36**, 59–62. http://dx.doi.org/-10.1130/G24056A.1.

Schärer, U., Labrousse, L. (2003), Dating the exhumation of UHP rocks and associated crustal melting in the Norwegian Caledonides, *Contrib. Mineral. Petrol.*, **144**, 758–770, http://-dx.doi.org/10.1007/s00410-002-0428-8.

Schaltegger, U., Fanning, C.M., Günther, D., Maurin, J.C., Schulmann, K., Gebauer, D. (1999), Growth, annealing and recrystallization of zircon and preservation of monazite in high-grade metamorphism: conventional and in situ U–Pb isotope, cathodoluminescence and microchemical evidence. *Contrib. Mineral. Petrol.*, **134**, 186–201, http://dx.doi.org/10.1007/-s004100050478.

Schoene, B., C. Latkoczy, U. Schaltegegger, and D. Günther (2010), A new method integrating high-precision U–Pb geochronology with zircon trace-element analysis

(U–Pb TIMS-TEA), *Geochim. et Cosmochim. Acta.*, **74**, 7144–7159, http://dx.doi.org/10.1016/j.gca.2010.09.016.

Schoene, B. (2013), U-Th-Pb Geochronology. In: Rudnick, R. (Eds.), Treatise on Geochemistry 2nd edition, *Elsevier*, **4.10**, 341–378, http://dx.doi.org/10.1016/B978-0-08-095975-7.00310-7

Skår, Ø. (2000), Field relations and geochemical evolution of the Gothian rocks in the Kvamsøy area, southern Western Gneiss Complex, Norway. *Nor. Geol. Unders. Bull*. **437**, 5–23.

Skår, Ø., Furnes, H., Claesson, S. (1994), Middle Proterozoic magmatism within the Western Gneiss Region, Sunnfjord, Norway. *Norsk Geol. Tidsskr.*, **74**, 114–126, ISSN 0029-196X.

Skår, Ø., Pedersen, R.B. (2003), Relations between granitoid magmatism and migmatization: U–Pb geochronological evidences from the Western Gneiss Complex, Norway. *Geological Society [London] Journal*, **160**, 935–946, http://dx.doi.org/10.1144/0016-764901-121.

Smith, D.C. (1984), Coesite in clinopyroxene in the Caledonides and its implications for geodynamics. *Nature*, **310**, 641–644, http://dx.doi.org/10.1038/310641a0.

Smith, D.C. (1988), A review of the peculiar mineralogy of the "Norwegian coesite-eclogite province", with crystal-chemical, petrological, geochemical and geodynamical notes and an extensive bibliography. In: Smith, D.C. (Eds.), "Eclogites and eclogite-facies rocks". *Elsevier*, 1-206.

Smith, D.C., Godard, G. (2013), A Raman spectroscopic study of diamond and disordered sp3-carbon in the coesite-bearing Straumen eclogite pod, Norway. *J. Metamorph. Geol.*, **31**, 19–33, http://dx.doi.org/10.1111/jmg.12007.

Spencer, K.J., Hacker, B.R., Kylander-Clark, A.R.C., Andersen, T.B., Cottle, J.M., Stearns, M.A., Poletti, J.E., Seward, G.G.E. (2013), Campaign style titanite U–Pb dating by laser-ablation ICP: implications for crustal flow, phase transformations and titanite closure. *Chem. Geol.*, **341**, 84–101, http://dx.doi.org/10.1016/j.chemgeo.2012.11.012.

Spengler, D., Brueckner, H.K., van Roermund, H.L.M., Drury, M.R., Mason, P.R.D. (2009), Long-lived, cold burial of Baltica towards 200 km depth. *Earth Planet. Sci. Lett.*, **281**, 27–35, http://dx.doi.org/10.1016/j.epsl.2009.02.001.

Stephens, M.B., Gee, D.G. (1989), Terranes and polyphase accretionary history in the Scandinavian Caledonides. *Geol. Soc. Am. Spec.* Paper, **230**, 17– 30, Geological Society of America, Boulder, CO, http://dx.doi.org/10.1130/SPE230-p17.

Straume, A.K., Austrheim, H. (1999), Importance of fracturing during retro-metamorphism of eclogites. *J. Metamorph. Geol.*, **17**, 637–652, http://dx.doi.org/10.1046/j.1525-1314.1999.00218.x.

Sun S.S., McDonough, W.F. (1989), Chemical and isotopic systematics of oceanic basalts: implications for mantle composition and processes, *Geological Society of London Special Publications*, **42**, 313–345, http://dx.doi.org/10.1144/GSL.SP.1989.042.01.19.

Taylor, R.J.M., Harley, S.L., Hinton, R.W., Elphick, S., Clark, C., Kelly, N.M. (2014), Experimental determination of REE partition coefficients between zircon, garnet, and melt: a key to understanding high-temperature crustal processes. *J. Metamorph. Geol.*, http://-dx.doi.org/10.1111/jmg.12118.

Terry, M.P., Robinson, P., Ravna, E.J.K. (2000a), Kyanite eclogite thermobarometry and evidence for thrusting of UHP over HP metamorphic rocks, Nordøyane, Western Gneiss Region, Norway. *Amer. Mineral.*, **85**, 1637–1650.

Terry, M.P., Robinson, P., Hamilton, M.A., Jercinovic, M.J. (2000b), Monazite geochronology of UHP and HP metamorphism, deformation, and exhumation, Nordøyane, Western Gneiss Region, Norway, *Amer. Mineral.*, **85**, 1651–1664.

Tucker, R.D., Robinson, P., Solli, A., Gee, D.G., Thorsnes, T., Krogh, T.E., Nordgulen, Ø., Bickford, M.E. (2004), Thrusting and extension in the Scandian hinterland, Norway: New U–Pb ages and tectonostratigraphic evidence. *Amer. J. Science*, **304(6)**, 477–532, http://-dx.doi.org/10.2475/ajs.304.6.477.

Tucker, R.D., Krogh, T.E., Råheim, A. (1990), Proterozoic evolution and age-province boundaries in the central part of the Western Gneiss Region, Norway. Results of U–Pb dating of accessory minerals from Trondheimsfjord to Geiranger. In Mid-Proterozoic Laurentia–Baltica. Edited by C.F. Gower, A.B. Ryan, and T. Rivers. *Geological Association of Canada, Special Paper*, **38**, 149–173.

Van Roermund, H.L.M. (2009), Recent progress in Scandian UHPM in the northernmost domain of the Western Gneiss Complex, SW Norway: continental subduction down to 180–200 km. *Geological Society [London] Journal*, **166**, 1–13, http://dx.doi.org/10.1144/0016-76492008-020.

Van Westrenen, W., Blundy, J., Wood, B. (1999), Crystal–chemical controls on trace element partitioning between garnet and anhydrous silicate melt. *Amer. Mineral.*, **84**, 838–847.

Vrijmoed, J.C., Van Roermund, H.L.M., Davis, G.R. (2006), Evidence for diamond-grade ultrahigh-pressure metamorphism and fluid interaction in the Svartberget Fe–Ti

garnet peridotite-websterite body, Western Gneiss Region, Norway. *Mineral. Petrol.*, **88**, 381–405. http://dx.doi.org/10.1007/s00710-006-0160-6.

Vrijmoed, J.C., Smith, D.C., Van Roermund, H.L.M. (2008), Raman confirmation of microdiamond in the Svartberget Fe–Ti type garnet peridotite, Western Gneiss Region, Western Norway. *Terra Nova*, **20**, 295–301, http://dx.doi.org/10.1111/j.1365-3121.2008.00820.x.

Wain, A. (1997), New evidence for coesite in eclogite and gneisses: Defining an ultrahigh-pressure province in the Western Gneiss region of Norway. *Geology*, **25**, 927–930, http-://dx.doi.org/0.1130/0091-7613(1997) 025<0927:NEFCIE> 2.3.CO;2.

Wain, A., Waters, D., Jephcoat, A., Olijnyk, H. (2000), The high-pressure to ultrahigh-pressure transition in the Western Gneiss Region, Norway. *Eur. J. Mineral.*, **12**, 667–687, http://-dx.doi.org/10.1127/0935-1221/2000/0012-0667.

Wain, A., Waters, D., Austrheim, H. (2001), Metastability of granulites and processes of eclogitization in the UHP region of western Norway, *J. Metamorph. Geol.*, **19**, 609–625, http://dx.doi.org/10.1046/j.0263-4929.2001.00333.x.

Walsh, E.O., Hacker, B.R. (2004), The fate of subducted continental margins: two-stage exhumation of the high-pressure to ultrahigh-pressure Western Gneiss Region, Norway. *J. Metamorph. Geol.*, **22**, 671–687, http://dx.doi.org/10.1111/j.1525-1314.2004.00541.x.

Whitehouse, M.J., Platt, J.P. (2003), Dating high-grade metamorphism–Constraints from rare-earth elements in zircon and garnet. *Contrib. Mineral. Petrol.*, **145**, 61–74, http://dx.doi.org/-10.1007/s00410-002-0432-z.

Whitney, D.L., Evans, B.W., 2010. Abbreviations for names of rock-forming minerals. Am. Mineral. 95, 185–187.

Young, D.J., Hacker, B.R., Andersen, T.B., Corfu, F. (2007), Prograde amphibolite facies to ultrahigh-pressure transition along Nordfjord, western Norway: implications for exhumation tectonics. *Tectonics*, **26**, TC1007, http://dx.doi.org/10.1029/2004TC001781.

Table 1

Geochronological summary of various Scandian (U)HP eclogites from the Western Gneiss Region

Dating Technique	MSWD, n	location	notes
Sm–Nd isochron age (minerals), sample			
418 ± 11 Ma[1, 2] (grt-cpx), 1428; 418 ± 27 Ma' (grt-cpx)	*, n = 2	Tverrfjell (~15 km NE of Nordøyane)	Sm–Nd grt-cpx mineral-pair isochron ages for eclogites across the WGR. Average of all five mineral
423 ± 30 Ma[1, 2] (grt-cpx), N16; 422 ± 19 Ma' (grt-cpx)	*, n = 2	Ulsteinvik (Sorøyane)	pair dates yields an age of ca. 425 Ma (Griffin and Brueckner, 1980[1], 1985[2]).
423 ± 12 Ma[1, 2] (grt-cpx), 5/79; 423 ± 8 Ma' (grt-cpx)	*, n = 2	Vågsøy (Nordfjord)	All five dates recalculated by Root et al. (2004)'.
407 ± 24 Ma[1, 2] (grt-cpx), K6; 407 ± 17 Ma' (grt-cpx)	*, n = 2	Frei (~45 km NE of Nordøyane)	Two-point Sm–Nd isochron dates and associated uncertainities do not form a single statistical population.
408 ± 8 Ma[3] (w.r.-grt-cpx), 8067; 408 ± 6 Ma' (grt-cpx)	*, n = 3; *, n = 2	Almklovdalen (Nordfjord)	Three-point Sm–Nd isochron date for eclogite (Mearns, 1986)[3]. Recalculated by Root et al. (2004)'.
407 ± 76 Ma' (w.r.-grt-cpx)	MSWD = 3.7, n = 3		
400 ± 16 Ma[4] (w.r.-grt-cpx), EH13	*, n = 3	Flemsøya (Nordøyane)	Three-point Sm–Nd isochron date for eclogite (Mørk and Mearns,1986)[4]. Recalculated by Root et al. (2004)'.
410 ± 16 Ma' (w.r.-grt-cpx)	MSWD = 0.2, n = 3		
412 ± 12 Ma[5] (grt-cpx); 412 ± 4 Ma' (grt-cpx)	*, n = 2	Eiksunddal (Sorøyane)	Two-point Sm–Nd isochron date for eclogite (Jamtveit,1991)[5]. Recalculated by Root et al. (2004)'.
408.3 ± 6.7 Ma[6] (w.r.-grt-cpx), Salt00-48	MSWD = 0.8, n = 3	Salta (Nordfjord)	Three-point Sm–Nd isochron date for UHP eclogite (Carswell et al., 2003b)[6].
402.7 ± 4.6 Ma[7] (w.r.-grt), R3703A2	*, n = 2	Vigra (~20 km SW of Nordøyane)	Three- and two-point Sm–Nd isochron dates for (U)HP eclogites (Kylander-Clark et al., 2007)[7].
398.3 ± 5.5 Ma[7] (w.r.-grt-cpx), 9826J	MSWD = 2.0, n = 3	NW Gurskøy (~5 km S of Sorøyane)	Remøya and Otrøy inferred to be UHP eclogites, whereas Vigra and NW Gurskøy are HP eclogites.
388 ± 10 Ma[7] (w.r.-grt-cpx), 8815B	MSWD = 0.2, n = 3	Otrøy (Nordøyane)	
384 ± 11 Ma[7] (w.r.-grt-cpx), 8906A11	MSWD = 1.4, n = 3	Remøya (Sorøyane)	
397.1 ± 4.8 Ma[8] (w.r.-grt-cpx), P5701A	MSWD = 1.7, n = 4	Sandvik (Sorøyane)	Four-point Sm–Nd isochron dates for HP eclogites (Kylander-Clark et al., 2009)[8].
398.3 ± 8.1 Ma[8] (w.r.-grt-cpx), E1612Q5	MSWD = 1.9, n = 4	Geiranger (southern edge of Nordfjord)	
413.9 ± 3.7 Ma[8] (w.r.-grt-cpx), NOR205	MSWD = 0.5, n = 4	Gossa (Nordøyane)	
393.4 ± 3.4 Ma[9] (grt-cpx), 8	*, n = 2	Svartberget (Nordøyane)	Two-point Sm–Nd isochron dates for a garnet peridotite body (6) and garnet websterite
380.7 ± 5.7 Ma[9] (grt-cpx), 6	*, n = 2		vein (8) (Vrijmoed et al., 2006)[9].
429.5 ± 3.1 Ma[10] (w.r.-grt-cpx), (DS0384, DS0380, Fl99-26)	*, n = 3	Otrøy and Flemsøy (Nordøyane)	Weighted-mean date of one three-point and two two-point Sm–Nd isochron dates for Otrøy and Flemsøy garnet pyroxenites (Spengler et al., 2009)[10].
Lu–Hf isochron age (minerals), sample			
419.5 ± 4.3 Ma[7] (w.r.-grt-cpx), 9901B1	MSWD = 1.8, n = 4	Verpeneset (Nordfjord)	Four- and three-point Lu–Hf isocrhon dates for (U)HP eclogites (Kylander-Clark et al., 2007)[7]. Verpeneset,
416.3 ± 3.7 Ma[7] (grt-cpx, preferred age), R3703A2	*, n = 2	Vigra (~20 km SW of Nordøyane)	Remøya (inferred), and Otrøy (inferred) UHP eclogites, whereas Vigra and NW Gurskøy are HP eclogites.
411.5 ± 4.1 Ma[7] (grt-w.r.), R3703A2	*, n = 2		
412.0 ± 4.7 Ma[7] (w.r.-grt-cpx), 9826J	MSWD = 1.8, n = 4	NW Gurskøy (~5 km S of Sorøyane)	All fractions for Vigra (R3703A2) gave an MSWD=10.7. The garnet-clinopyroxene fractions were
380 ± 14 Ma[7] (w.r.-grt-cpx), 8815B	MSWD = 1.0, n = 3	Otrøy (Nordøyane)	interpreted as the best representation of eclogite-facies metamorphism.
369 ± 11 Ma[7] (w.r.-grt-cpx), 8906A11	MSWD = 0.2, n = 4	Remøya (Sorøyane)	
410.2 ± 3.1 Ma[8] (w.r.-grt-cpx), K5622A2	MSWD = 0.9, n = 3	Vollstein (~60 km S of Nordfjord)	Three-point Lu–Hf isochron dates for HP eclogites (Kylander-Clark et al., 2009)[8].
391 ± 13 Ma[8] (w.r.-grt-cpx), P5701A	MSWD = 1.8, n = 3	Sandvik (Sorøyane)	
415 ± 23 Ma[8] (w.r.-grt-cpx), E1612Q5	MSWD = 2.5, n = 3	Geiranger (SE edge of Nordfjord)	
Rb–Sr isochron age (minerals), sample			
398 ± 1 Ma[2] (w.r.-cpx-zois-phen), NV-52b	*, n = 4	Verpeneset (Nordfjord)	Four-point Rb–Sr isochron dates for a UHP eclogite (Griffin and Brueckner, 1985)[2]. Recalculation of the
397 ± 8 Ma' (w.r.-phen-zois), NV-52b (±2% uncertainty)	MSWD = 0.2, n = 3		results by Root et al. (2004)' has shown that no single isoschron can fit four or more ratios. Three-point
398 ± 51 Ma' (omph-phen-ky), NV-52b (±2% uncertainty)	MSWD = 2.2, n = 3		Rb–Sr isochrons are also shown.
403.9 ± 2.9 Ma[11] (phen-grt-cpx-bt), B11	MSWD = 1.1, n = 6	Bårdsholmen, Dalsfjorden	Glodny et al. (2008)[11] report a weighted mean for the three Rb–Sr isochron dates for HP eclogites at
403.2 ± 3.7 Ma[11] (phen-zoisite), BOR2	MSWD = 0.9, n = 4	(~65 km S of Nordfjord)	404.0 ± 2.1 Ma (no MSWD).
406.1 ± 5.3 Ma[11] (phen-cpx-w.r.), B45	MSWD = 12, n = 6		
U–Th–Pb monazite age (type), sample			

415.0 ± 6.8 Ma[13] (weighted-mean $^{206}Pb/^{238}U$ age), UHP1	*, n = 7	Fjørtoft (Nordøyane)	Secondary ion mass spectrometry (SIMS) weighted-mean $^{206}Pb/^{238}U$ age (ca. 415) and electron microprobe (EMP) mean-chemical $^{206}Pb/^{238}U$ age (ca. 408) for the same monazite inclusions in garnet of UHP microdiamond gneiss. EMP mean-chemical $^{206}Pb/^{238}U$ age (ca. 407) is from additional analyses of microdiamond gneiss and mylonite (Terry et al., 2000b)[13].
408.0 ± 5.6 Ma[13] (mean-chemical $^{206}Pb/^{238}U$ age), UHP1	*, n = 40		
407.0 ± 2.1 Ma[13] (mean-chemical $^{206}Pb/^{238}U$ age), UHP1, 929	*, n = 64		
U–Pb zircon age (type), sample			
415.2 ± 0.6 Ma[14] (weighted-mean $^{206}Pb/^{238}U$ age), TK97-20	*, n = 3	Tevik, Averøya	Zircon (air) multi-grain isotope dilution thermal inoization mass spectrometry (ID-TIMS).
410.8 ± 1.4 Ma and 409.6 ± 1.5 Ma[14] ($^{206}Pb/^{238}U$ age), TK97-20	*, n = 2	(~20 km NE of Nordøyane)	Single-grain ID–TIMS $^{206}Pb/^{238}U$ ages (TK97-20) of zircon tips (Krogh et al., 2011)[14].
409 ± 3 Ma[14] (weighted-mean $^{206}Pb/^{238}U$ age), TK98-23	*, n = 2	Flem gabbro (Nordøyane)	Eclogites from Averøya, Flem gabbro, and Midsund Bruk are inferred to be UHP, whereas Lepsøya sample TK98-26 is a HP-hornblende eclogite.
411 ± 2 Ma[14] (weighted-mean $^{207}Pb/^{206}Pb$ age), TK98-23			
405.0 ± 0.9 Ma[14] (weighted-mean $^{206}Pb/^{238}U$ age), TK98-17	*, n = 1	Midsund Bruk (Nordøyane)	The youngest, most concordant fraction was chosen for the minimum age of metamorphism for the Midsund Bruk eclogite (Krogh et al., 2011)[14].
412 ± 1 Ma[14] (weighted-mean $^{206}Pb/^{238}U$ age), TK98-26	*, n = 2	Lepsøya (~6 km SW of Nordøyane)	
ca. 421–400[15] ($^{206}Pb/^{238}U$ dates), TK98-17	*, n = 37	Midsund Bruk (Nordøyane)	Spit-stream LA–ICP-MS results from Krogh et al., 2011 zircon separates. Interpreted as crystallization of distinct groups based on REE (ca. 421, 409–404 Ma, and 400 Ma) (Kylander-Clark et al., 2013)[15].
401 ± 20 Ma[16] (weighted-mean $^{206}Pb/^{238}U$ age), TK-72-1		Ulsteinvik (Sorøyane)	Zircon multi-grain ID–TIMS weighted-mean $^{206}Pb/^{238}U$ age (Krogh T. et al., 1974)[16].
401.6 ± 1.6 Ma[17] (weighted-mean $^{207}Pb/^{206}Pb$ age), TK-72-1	MSWD = 0.5, n = 4	Ulsteinvik (Sorøyane)	Zircon (air) multi-grain ID–TIMS weighted-mean $^{206}Pb/^{238}U$ age of UHP eclogite (Carswell et al., 2003a)[17].
ca. 407–403 Ma[18] ($^{206}Pb/^{238}U$ ages), Flatraket UHP eclogite		Flatraket (Nordfjord)	Zircon multi-grain ID–TIMS $^{206}Pb/^{238}U$ ages (Root et al., 2004)[18]. Zircon chemically abraded by the CA–TIMS method of Mattinson (2005). High-temperature steps (> 170 ºC) reveal discordant $^{206}Pb/^{238}U$ dates. Authors preferred ages are ca. 405–400 Ma for Flatraket UHP eclogite.
ca. 405–400 Ma[18] ($^{206}Pb/^{238}U$ ages, preferred age)			
ca. 437–395 Ma[18] (207-age corrected $^{206}Pb/^{238}U$ spot dates)	*, n = 21		
ca. 414–408 Ma[18] ($^{206}Pb/^{238}U$ ages), Verpeneset UHP eclogite		Verpeneset (Nordfjord)	
403 ± 21 Ma[18] (207-corr. weighted-mean $^{206}Pb/^{238}U$ date)	MSWD = 0.92, n = 3		SIMS $^{207}Pb/^{238}U$ single spot ages are corrected for common Pb using ^{207}Pb. Uncertainties on single spot dates range from 30–3 Ma (Root et al., 2004)[18].
ca. 424–410 Ma[18] (207-corr. $^{206}Pb/^{238}U$ spot dates)	*, n = 2	Otnheim (Nordfjord)	
ca. 398 Ma[19] ($^{206}Pb/^{238}U$ age), SEL1	*, n = 1	Grytting, Selje (Nordfjord)	Zircon multi-grain ID–TIMS $^{206}Pb/^{238}U$ age of HP eclogite (Gebauer et al., 1985)[19].
405 ± 2 Ma[20] (weighted-mean $^{206}Pb/^{238}U$ age), Y1611N	MSWD = 1.0, n = 2	Nordfjord	Zircon (air) single-grain ID–TIMS weighted-mean $^{206}Pb/^{238}U$ age (U)HP eclogite (Young et al., 2007)[20].
412 ± 25 Ma[21] (concordia age), e9812d2	MSWD = 1.1, n = 5	~20 km E of Sorøyane	SIMS and LA–ICP-MS zircon concordia ages for HP eclogites (Walsh et al., 2007)[21].
396 ± 10 Ma[21] (concordia age), e1612q	MSWD = 0.94, n = 3	Nordfjord	
403 ± 21 Ma[21] (concordia age), e9801e	MSWD = 0.21, n = *	~80 km E of Sorøyane	
423 ± 4 Ma[22] (Tera-Wasserburg intercept age), BH2	MSWD = 1.7, n = 32	Lindås nappe (~ 150km SW of Nordfjord)	SIMS zircon Tera-Wasserburg intercept age for HP eclogite (Bingen et al., 2004)[22].

Reported uncertainties are at the 2-sigma or 95% confidence level unless otherwise stated.

*No MSWD calculated or exact number of analyses reported.

Nordfjord (southern UHP domain), Sorøyane (central UHP domain), Nordøyane (northern UHP domain).

Air: zircons treating with the air abrasion method of Krogh T. (1982).

Table 2

Zircon U–Th–Pb LA–ICP-MS isotopic data from the Western Gneiss Region: Ulsteinvik and Saltaneset eclogites

	Composition			Isotopic Ratios												Dates (Ma)								ID-TIMS Dates (Ma)		
	Approx. U (ppm)	Approx. Th (ppm)	Th/U	$^{207}Pb/^{235}U$	±2σ abs	$^{206}Pb/^{238}U$	±2σ abs	ror Correlati	$^{238}U/^{206}Pb$	±2σ abs	$^{207}Pb/^{206}Pb$	±2σ abs	ror Correlatic	$^{208}Pb/^{232}Th$	±2σ abs	$^{206}Pb/^{238}U$ date (Ma)	±2σ abs	$^{207}Pb/^{235}U$ date (Ma)	±2σ abs	$^{207}Pb/^{206}Pb$ date (Ma)	±2σ abs	Fraction	$^{206}Pb/^{238}U$ date <Th>	±2σ abs
LA–ICP-MS results for Ulsteinvik and Saltaneset eclogite garnet-quartz and omphacite layers dated by ID–TIMS																										
8815E, Ulsteinvik																										
Sample, Laser spot number, ID–TIMS zircon fraction																										
Ulsteinvik_1_z1-1	280	7	0.03	0.480	0.007	0.0641	0.0008	0.64	15.6	0.2	0.0545	0.0007	0.08	0.04	0.02	400.5	4.7	398.5	5.0	392.0	18.7	z1-1	401.9	0.2
Ulsteinvik_2_z1-3	330	10	0.03	0.487	0.008	0.0645	0.0009	0.77	15.5	0.2	0.0549	0.0007	0.02	0.025	0.005	403.0	5.3	402.9	5.7	406.0	17.9	z1-3	401.9	0.4
Ulsteinvik_3_z1-4	416	14	0.03	0.487	0.007	0.0645	0.0008	0.74	15.5	0.2	0.0548	0.0007	0.18	0.024	0.004	403.0	5.2	402.5	5.2	402.0	17.0	z1-4	402.1	0.3
Ulsteinvik_5_z1	263	9	0.03	0.484	0.008	0.0641	0.0009	0.76	15.6	0.2	0.0551	0.0007	-0.13	0.023	0.005	400.6	5.3	400.4	5.7	417.0	19.8			
Ulsteinvik_6_z1	269	10	0.04	0.492	0.007	0.0648	0.0008	0.66	15.4	0.2	0.0551	0.0007	0.11	0.021	0.007	404.8	5.1	406.4	5.4	415.0	19.8			
Ulsteinvik_9_z2	246	7	0.03	0.496	0.008	0.0658	0.0009	0.68	15.2	0.2	0.0545	0.0007	0.12	0.02	0.01	410.7	5.6	408.8	6.0	389.0	21.5	z2	407.9	0.3
Ulsteinvik_12_z3	243	6	0.03	0.499	0.007	0.0659	0.0009	0.79	15.2	0.2	0.0550	0.0007	-0.01	0.026	0.007	411.2	5.3	411.0	5.5	414.0	18.0	z3	405.1	0.2
Ulsteinvik_15_z4	258	7	0.03	0.498	0.007	0.0659	0.0008	0.65	15.2	0.2	0.0548	0.0007	0.08	-0.02	-0.05	411.6	5.0	409.8	5.6	401.0	18.8	z4	408.3	0.2
Ulsteinvik_13_z5	437	8	0.02	0.497	0.007	0.0652	0.0008	0.75	15.3	0.2	0.0551	0.0006	0.17	0.022	0.003	407.2	5.1	409.9	5.3	414.0	16.3	z5	401.9	0.2
Ulsteinvik_14_z5	413	5	0.01	0.490	0.007	0.0651	0.0009	0.80	15.4	0.2	0.0549	0.0006	0.12	0.01	0.01	406.3	5.3	405.2	5.4	408.0	15.3			
Ulsteinvik_27_z8	193	3	0.02	0.488	0.008	0.0643	0.0009	0.64	15.5	0.2	0.0552	0.0008	0.08	-0.01	-0.03	401.8	5.3	403.6	5.8	422.0	21.7	z8	407.9	0.3
Ulsteinvik_7_z10	195	6	0.03	0.495	0.009	0.0647	0.0009	0.74	15.5	0.2	0.0556	0.0008	-0.10	0.02	0.01	403.9	5.5	408.3	6.2	431.0	24.6	z10	409.6	0.3
Ulsteinvik_22_z12	297	9	0.03	0.504	0.008	0.0661	0.0009	0.80	15.1	0.2	0.0550	0.0007	-0.02	0.028	0.006	412.8	5.4	414.2	5.8	410.0	16.2	z12	408.7	0.5
Ulsteinvik_23_z12	391	16	0.04	0.502	0.007	0.0654	0.0008	0.79	15.3	0.2	0.0555	0.0007	0.13	0.021	0.003	408.8	5.3	413.1	5.4	433.0	16.5			
Ulsteinvik_31_z13	239	6	0.03	0.494	0.008	0.0655	0.0009	0.67	15.3	0.2	0.0547	0.0007	0.02	0.030	0.006	409.1	5.4	407.4	5.9	401.0	21.5	z13	409.6	0.6
Ulsteinvik_35_z14	252	8	0.03	0.493	0.008	0.0656	0.0009	0.72	15.2	0.2	0.0549	0.0007	0.04	0.024	0.006	409.6	5.4	406.4	5.8	409.0	18.9	z14	407.3	0.3
Ulsteinvik_16_z15	511	11	0.02	0.484	0.007	0.0643	0.0009	0.84	15.5	0.2	0.0546	0.0006	0.07	0.026	0.004	401.7	5.5	400.6	5.3	393.0	15.2	z15	401.3	0.4
Ulsteinvik_17_z15	523	11	0.02	0.489	0.007	0.0647	0.0009	0.89	15.5	0.2	0.0546	0.0006	0.01	0.028	0.006	404.2	5.5	404.3	5.3	394.9	12.6			
Ulsteinvik_18_z15	373	6	0.02	0.494	0.007	0.0651	0.0009	0.78	15.4	0.2	0.0552	0.0007	0.10	0.04	0.02	406.4	5.4	407.5	5.3	418.0	16.3			
Ulsteinvik_45_z16	413	15	0.04	0.496	0.007	0.0654	0.0009	0.82	15.3	0.2	0.0552	0.0006	-0.05	0.021	0.003	408.2	5.3	409.1	5.4	417.0	15.4	z16	408.6	0.3
Ulsteinvik_46_z16	263	7	0.03	0.498	0.008	0.0653	0.0009	0.70	15.3	0.2	0.0553	0.0007	0.10	0.019	0.009	407.9	5.2	410.4	5.7	423.0	19.9			
Ulsteinvik_47_z16	301	8	0.03	0.499	0.007	0.0657	0.0008	0.69	15.2	0.2	0.0549	0.0007	0.06	0.026	0.006	410.2	5.2	410.8	5.4	407.0	17.1			
Ulsteinvik_48_z16	261	8	0.03	0.504	0.008	0.0658	0.0009	0.73	15.2	0.2	0.0552	0.0007	-0.03	0.017	0.007	410.6	5.5	414.2	6.0	419.0	21.7			
Ulsteinvik_20_z17	159	3	0.02	0.491	0.009	0.0648	0.0009	0.72	15.4	0.2	0.0544	0.0008	0.07	0.015	0.008	405.0	5.8	405.0	6.3	388.0	24.3	z17	407.2	0.7
NW13-02-G, Saltaneset (garnet-quartz layer)																										
NW13_02_grt_3_z1-2	385	9	0.02	0.49	0.01	0.064	0.001	0.90	15.7	0.3	0.0554	0.0006	0.20	0.023	0.002	398.1	8.7	403.8	6.8	425.9	15.7	z1-2	401.5	0.2
NW13_02_grt_6_z3	507	12	0.02	0.49	0.01	0.064	0.001	0.89	15.5	0.3	0.0552	0.0006	0.19	0.022	0.002	402.6	8.8	406.5	6.8	418.7	15.8	z3	401.4	0.2
NW13_02_grt_19_z6	197	4	0.02	0.50	0.01	0.065	0.001	0.77	15.3	0.3	0.0556	0.0007	0.09	0.022	0.008	406.9	9.0	409.6	7.2	439.0	20.0	z6	408.8	0.2
NW13_02_grt_4_z16	582	4	0.01	0.498	0.007	0.0653	0.0008	0.89	15.3	0.2	0.0553	0.0009	-0.04	0.017	0.005	407.8	5.1	410.1	5.1	428.0	21.1	z16	408.9	0.4
NW13-02-O, Saltaneset (omphacite layer)																										
NW13_02_omph_2_z5	429	12	0.03	0.485	0.006	0.0647	0.0008	0.86	15.5	0.2	0.0538	0.0008	0.20	0.021	0.002	404.1	5.1	401.5	4.9	361.7	18.8	z5	396.7	1.4
LA–ICP-MS results for Ulsteinvik and Saltaneset eclogite garnet-quartz and omphacite layers not dated by ID–TIMS																										
8815E, Ulsteinvik																										
Sample, Laser spot number																										
Ulsteinvik_10	266	8	0.03	0.494	0.008	0.0658	0.0009	0.69	15.2	0.2	0.0548	0.0007	0.04	0.024	0.007	410.5	5.3	407.6	5.7	401.0	21.5			
Ulsteinvik_21	247	8	0.03	0.503	0.007	0.0659	0.0008	0.68	15.2	0.2	0.0549	0.0007	0.04	0.021	0.004	411.4	5.1	413.6	5.4	407.0	18.8			
Ulsteinvik_24	281	8	0.03	0.503	0.007	0.0660	0.0009	0.66	15.2	0.2	0.0552	0.0007	0.20	0.028	0.005	412.0	5.3	413.8	5.4	424.0	19.0			
Ulsteinvik_28	310	10	0.03	0.500	0.008	0.0658	0.0009	0.79	15.2	0.2	0.0551	0.0007	-0.03	0.022	0.004	411.0	5.3	411.4	5.6	414.0	17.1			
Ulsteinvik_33''	243	6	0.02	0.496	0.008	0.0654	0.0009	0.65	15.3	0.2	0.0550	0.0008	0.24	0.04	0.02	408.8	5.7	408.8	5.9	412.0	22.6			
Ulsteinvik_34''	263	7	0.03	0.499	0.008	0.0656	0.0009	0.78	15.3	0.2	0.0553	0.0007	0.06	0.01	0.01	409.4	5.3	410.7	5.7	427.0	19.0			
Ulsteinvik_37'''	333	5	0.02	0.485	0.007	0.0642	0.0008	0.72	15.6	0.2	0.0549	0.0007	0.07	0.014	0.007	401	5	401.2	5.5	408.0	18.9			
Ulsteinvik_39'''	537	10	0.02	0.481	0.007	0.0636	0.0008	0.90	15.7	0.2	0.0551	0.0006	-0.19	0.023	0.004	397.2	5.2	398.6	5.3	417.4	12.9			
Ulsteinvik_40'''	377	6	0.02	0.489	0.007	0.0644	0.0008	0.80	15.5	0.2	0.0550	0.0007	-0.01	0.01	0.02	402.4	5.2	403.9	5.4	411.0	17.1			
Ulsteinvik_41	258	7	0.03	0.491	0.008	0.0647	0.0009	0.78	15.5	0.2	0.0552	0.0007	-0.05	0.03	0.01	403.9	5.3	405.6	5.6	421.0	18.1			
Ulsteinvik_25	164	12	0.07	0.532	0.008	0.0690	0.0009	0.63	14.5	0.2	0.0559	0.0008	0.20	0.027	0.004	429.8	5.7	432.8	6.1	447.0	22.8			
Ulsteinvik_29	606	381	0.6	0.599	0.008	0.077	0.001	0.86	13.1	0.2	0.0568	0.0006	0.06	0.024	0.003	475.2	6.1	476.4	5.9	483.8	13.7			
Ulsteinvik_32	328	29	0.09	0.551	0.008	0.0708	0.0009	0.80	14.1	0.2	0.0566	0.0007	0.03	0.026	0.003	441.0	5.6	445.2	5.7	478.0	17.0			
Ulsteinvik_43	377	301	0.8	0.565	0.008	0.0727	0.0009	0.74	13.7	0.2	0.0562	0.0007	0.14	0.024	0.003	452.5	5.7	454.8	5.7	461.0	15.9			
Ulsteinvik_44	276	114	0.4	0.591	0.009	0.076	0.001	0.77	13.2	0.2	0.0567	0.0007	0.06	0.024	0.003	471.0	6.4	471.1	6.4	482.0	18.7			
NW13-02-G, Saltaneset (garnet-quartz layer)																										
NW13_02_grt_15	681	3	0.004	0.50	0.01	0.066	0.002	0.92	15.1	0.4	0.0554	0.0006	0.08	0.02	0.01	413.4	9.8	414.2	7.8	427.0	16.3			
NW13_02_grt_20	768	9	0.01	0.50	0.01	0.066	0.001	0.93	15.2	0.3	0.0550	0.0006	0.09	0.022	0.002	411.5	9.0	411.9	7.1	413.5	15.0			
NW13_02_grt_21	397	4	0.01	0.50	0.01	0.065	0.001	0.85	15.3	0.3	0.0553	0.0006	0.09	0.022	0.004	407.3	8.8	409.3	7.1	424.0	16.8			

NW13_02_grt_22	638	5	0.01	0.50	0.01	0.066	0.001	0.93	15.2	0.3	0.0557	0.0006	-0.07	0.04	0.02	410.0	9.2	414.0	7.3	439.4	16.2
NW13_02_grt_24	747	15	0.02	0.48	0.01	0.063	0.001	0.92	15.8	0.3	0.0550	0.0006	-0.15	0.021	0.002	396.8	8.8	398.5	7.0	411.0	15.9
NW13_02_grt_25	944	20	0.02	0.48	0.01	0.064	0.001	0.94	15.7	0.3	0.0551	0.0006	0.04	0.021	0.002	397.4	8.7	399.6	6.8	418.2	14.8
NW13_02_grt_30	512	8	0.02	0.49	0.01	0.065	0.001	0.93	15.3	0.3	0.0550	0.0006	-0.06	0.024	0.002	407.2	8.9	405.4	7.0	410.3	15.4
NW13_02_grt_34	513	11	0.02	0.50	0.01	0.066	0.001	0.90	15.1	0.3	0.0550	0.0006	0.16	0.021	0.002	412.3	9.2	410.3	7.1	413.0	15.9
NW13_02_grt_7	573	11	0.02	0.490	0.006	0.0652	0.0008	0.85	15.3	0.2	0.0545	0.0008	0.07	0.022	0.002	407.1	4.8	405.1	4.8	389.6	19.6
NW13_02_grt_13	400	12	0.03	0.482	0.006	0.0637	0.0008	0.86	15.7	0.2	0.0543	0.0009	0.07	0.016	0.002	398.0	5.0	399.5	4.9	383.0	20.4
NW13_02_grt_1	616	213	0.3	1.27	0.03	0.131	0.003	0.96	7.6	0.2	0.0696	0.0007	-0.16	0.048	0.004	795.7	17.4	830.5	13.8	916.8	28.0
NW13_02_grt_2	54	86	1.6	1.43	0.04	0.146	0.004	0.84	6.9	0.2	0.0708	0.0010	-0.10	0.050	0.004	875.0	21.2	901.0	16.8	951.0	34.3
NW13_02_grt_4	426	163	0.4	0.96	0.02	0.104	0.002	0.94	9.6	0.2	0.0663	0.0007	-0.14	0.031	0.003	638.3	13.9	681.9	11.3	816.4	25.7
NW13_02_grt_7.1	376	104	0.3	1.45	0.03	0.148	0.003	0.96	6.8	0.2	0.0705	0.0007	-0.01	0.052	0.004	889.8	20.0	908.0	15.3	944.7	29.1
NW13_02_grt_9	141	222	1.6	1.54	0.04	0.157	0.004	0.89	6.4	0.1	0.0710	0.0008	-0.07	0.052	0.004	938.8	20.7	946.5	15.9	959.0	30.8
NW13_02_grt_10	735	167	0.2	1.14	0.03	0.122	0.003	0.96	8.2	0.2	0.0683	0.0007	-0.03	0.043	0.004	739.1	16.8	774.5	13.3	877.1	27.1
NW13_02_grt_11	1103	222	0.2	1.41	0.03	0.146	0.003	0.97	6.9	0.1	0.0699	0.0007	-0.15	0.049	0.004	875.7	18.8	891.7	14.4	926.1	28.2
NW13_02_grt_12	100	147	1.5	1.49	0.03	0.154	0.003	0.85	6.5	0.1	0.0700	0.0008	0.11	0.052	0.004	920.8	20.1	923.8	15.4	928.0	29.9
NW13_02_grt_13.1	710	154	0.2	1.27	0.03	0.134	0.003	0.97	7.5	0.2	0.0689	0.0007	-0.10	0.044	0.004	808.5	17.7	833.7	13.7	895.1	27.3
NW13_02_grt_14	242	324	1.3	1.55	0.03	0.159	0.003	0.91	6.3	0.1	0.0707	0.0008	0.08	0.053	0.004	951.2	20.6	951.5	15.6	949.1	29.6
NW13_02_grt_16	877	258	0.3	1.39	0.03	0.145	0.003	0.97	6.9	0.2	0.0697	0.0007	-0.02	0.047	0.004	871.6	18.9	885.3	14.5	919.1	28.0
NW13_02_grt_17	320	158	0.5	1.41	0.03	0.147	0.003	0.95	6.8	0.2	0.0695	0.0007	0.01	0.049	0.004	881.4	19.4	890.9	14.8	914.3	28.3
NW13_02_grt_23	679	56	0.1	0.94	0.02	0.104	0.002	0.97	9.6	0.2	0.0656	0.0007	-0.41	0.052	0.004	636.0	14.4	672.3	12.2	793.5	25.0
NW13_02_grt_26	652	67	0.1	0.73	0.02	0.086	0.002	0.98	11.7	0.3	0.0620	0.0007	-0.50	0.049	0.004	530.7	12.6	557.5	10.7	671.9	21.6
NW13_02_grt_27	492	34	0.1	0.78	0.02	0.089	0.002	0.89	11.3	0.3	0.0635	0.0008	-0.42	0.055	0.005	548.5	12.5	585.3	11.6	726.0	27.6
NW13_02_grt_28	104	54	0.5	0.85	0.02	0.096	0.002	0.85	10.4	0.2	0.0650	0.0008	-0.01	0.039	0.003	590.1	13.7	625.0	11.7	773.0	28.2
NW13_02_grt_31	616	149	0.2	1.42	0.03	0.145	0.003	0.98	6.9	0.2	0.0710	0.0007	0.01	0.049	0.004	873.4	19.8	895.5	15.1	958.2	29.3
NW13_02_grt_32	697	175	0.3	1.44	0.03	0.149	0.003	0.98	6.7	0.2	0.0701	0.0007	0.01	0.048	0.004	896.5	19.9	903.0	15.0	929.7	28.2
NW13_02_grt_33	282	148	0.5	1.35	0.03	0.140	0.003	0.93	7.1	0.2	0.0701	0.0008	0.24	0.046	0.004	843.9	19.3	868.3	14.6	929.9	29.1
NW13_02_grt_35	598	143	0.2	1.38	0.03	0.145	0.003	0.96	6.9	0.2	0.0698	0.0007	0.09	0.047	0.004	870.2	19.0	881.8	14.4	923.6	28.2
NW13_02_grt_36	479	157	0.3	1.50	0.03	0.155	0.003	0.96	6.4	0.1	0.0701	0.0007	-0.01	0.048	0.004	930.2	19.9	928.7	14.8	930.0	28.3
NW13_02_grt_37	109	83	0.8	1.18	0.03	0.127	0.003	0.90	7.9	0.2	0.0678	0.0008	-0.11	0.047	0.004	771.4	17.2	791.5	13.7	861.0	28.1
NW13_02_grt_38	864	157	0.2	1.32	0.03	0.139	0.003	0.98	7.2	0.2	0.0695	0.0007	-0.22	0.047	0.004	837.9	18.6	855.8	14.4	914.2	27.8
NW13_02_grt_39	112	143	1.3	1.39	0.04	0.146	0.004	0.90	6.9	0.2	0.0696	0.0008	-0.09	0.050	0.004	877.0	21.3	884.7	16.2	917.0	30.9
NW13_02_grt_40	97	121	1.2	1.58	0.04	0.162	0.004	0.87	6.2	0.1	0.0712	0.0008	0.12	0.052	0.004	966.2	21.2	964.0	15.7	963.0	30.9
NW13_02_grt_41	793	192	0.2	1.48	0.03	0.153	0.003	0.97	6.6	0.1	0.0706	0.0007	-0.07	0.050	0.004	914.9	20.1	922.9	15.1	946.8	28.8
NW13_02_grt_44	680	212	0.3	1.46	0.03	0.152	0.003	0.97	6.6	0.1	0.0697	0.0007	0.10	0.049	0.004	909.8	20.1	913.2	15.0	920.2	28.1
NW13_02_grt_45	1026	387	0.4	1.41	0.03	0.147	0.003	0.98	6.8	0.2	0.0697	0.0007	0.09	0.051	0.004	884.3	19.6	893.8	14.7	918.2	27.8
NW13_02_grt_1.1	730	413	0.6	1.26	0.03	0.132	0.003	0.99	7.6	0.2	0.069	0.001	-0.73	0.043	0.004	796.0	15.2	826.0	14.6	903.2	41.2
NW13_02_grt_2.1	264	77	0.3	0.77	0.01	0.089	0.001	0.83	11.2	0.2	0.062	0.001	0.01	0.042	0.004	549.3	7.7	577.7	7.8	690.0	34.1
NW13_02_grt_3	579	79	0.1	1.10	0.03	0.118	0.003	0.99	8.5	0.2	0.067	0.001	-0.74	0.047	0.005	718.0	17.5	750.0	16.8	848.0	40.0
NW13_02_grt_5	84	102	1.2	1.14	0.02	0.123	0.002	0.75	8.1	0.1	0.068	0.001	0.03	0.041	0.004	746.8	9.5	772.1	9.7	856.0	41.0
NW13_02_grt_8	677	252	0.4	1.43	0.02	0.148	0.002	0.95	6.76	0.09	0.070	0.001	0.17	0.047	0.005	889.6	11.0	902.6	10.3	933.0	42.3
NW13_02_grt_9.1	611	135	0.2	1.17	0.02	0.124	0.002	0.95	8.1	0.1	0.068	0.001	0.12	0.045	0.005	754.9	10.4	785.9	9.6	874.0	39.9
NW13_02_grt_10.1	262	217	0.8	1.24	0.02	0.130	0.002	0.97	7.7	0.1	0.069	0.001	-0.13	0.045	0.005	788.0	12.7	816.6	11.9	887.5	40.6
NW13_02_grt_12.1	182	88	0.5	0.89	0.01	0.099	0.001	0.86	10.1	0.1	0.065	0.001	-0.17	0.034	0.003	606.6	7.7	644.5	8.3	767.0	36.5
NW13_02_grt_14.1	403	43	0.1	0.75	0.01	0.088	0.001	0.95	11.4	0.2	0.061	0.001	-0.26	0.047	0.005	542.0	8.8	567.3	8.7	643.3	30.4
NW13-02-O, Saltaneset (omphacite layer)																					
NW13_02_omph_14	597	16	0.03	0.48	0.01	0.064	0.001	0.71	15.7	0.3	0.0548	0.0006	0.12	0.022	0.002	398.4	8.1	400	6	401.4	14.9
NW13_02_omph_10	481	15	0.03	0.495	0.004	0.0651	0.0008	0.73	15.4	0.1	0.0550	0.0006	0.05	0.021	0.002	406.8	3.3	408.3	4.9	413.0	19.4
NW13_02_omph_12	465	11	0.02	0.493	0.004	0.0652	0.0008	0.71	15.3	0.1	0.0548	0.0006	-0.01	0.023	0.002	407.3	3.1	407.1	4.9	404.0	19.9
NW13_02_omph_15	457	13	0.03	0.507	0.004	0.0664	0.0008	0.74	15.1	0.1	0.0552	0.0006	0.13	0.026	0.002	414.2	3.2	416.6	4.8	420.0	18.4
NW13_02_omph_20	374	6	0.02	0.507	0.008	0.0664	0.0009	0.83	15.1	0.2	0.0556	0.0009	-0.02	0.030	0.007	414.4	5.8	416.4	5.8	435.0	24.1
NW13_02_omph_4	288	180	0.6	2.46	0.06	0.192	0.004	0.95	5.2	0.1	0.093	0.001	-0.43	0.066	0.005	1130.3	24.4	1259.1	20.2	1488.9	45.1
NW13_02_omph_5	4495	265	0.1	0.58	0.01	0.074	0.002	0.94	13.6	0.3	0.0570	0.0006	-0.31	0.026	0.002	458.6	9.6	463.9	7.5	492.4	15.8
NW13_02_omph_7	302	206	0.7	2.79	0.06	0.214	0.005	0.96	4.7	0.1	0.095	0.001	-0.48	0.068	0.005	1248.8	26.5	1352.1	21.7	1527.8	46.2
NW13_02_omph_9	1389	281	0.2	1.33	0.03	0.140	0.003	0.97	7.2	0.2	0.0692	0.0007	-0.48	0.046	0.004	842.6	17.8	859.9	13.8	904.4	27.7
NW13_02_omph_10.1	1573	294	0.2	1.15	0.03	0.123	0.003	0.98	8.1	0.2	0.0680	0.0007	-0.59	0.040	0.003	747.1	16.6	777.4	13.5	867.8	26.9
NW13_02_omph_11	1510	325	0.2	0.71	0.01	0.085	0.002	0.94	11.8	0.2	0.0609	0.0006	-0.32	0.027	0.002	525.2	10.7	545.3	8.5	633.9	19.7
NW13_02_omph_12.1	803	192	0.2	0.57	0.01	0.072	0.001	0.85	13.9	0.3	0.0571	0.0006	-0.08	0.024	0.002	448	9	454.9	7.2	495.8	16.5
NW13_02_omph_13	140	70	0.5	0.69	0.01	0.079	0.002	0.70	12.7	0.3	0.0630	0.0007	-0.09	0.025	0.002	488.6	10.1	529.9	8.6	710.0	25.0
NW13_02_omph_15.1	247	178	0.7	1.71	0.04	0.144	0.003	0.89	6.9	0.1	0.0860	0.0009	-0.24	0.045	0.004	867.2	18.0	1011.1	15.9	1339.9	41.0
NW13_02_omph_4.1	133	54	0.4	1.142	0.009	0.106	0.001	0.53	9.44	0.08	0.0782	0.0009	0.28	0.035	0.003	649	5	773.8	8.9	1154.0	42.4
NW13_02_omph_5.1	128	60	0.5	0.591	0.008	0.0707	0.0008	0.48	14.2	0.1	0.0612	0.0009	0.01	0.023	0.002	440.1	3.6	471.3	6.7	648.0	33.0
NW13_02_omph_7.1	1112	275	0.2	0.931	0.008	0.103	0.001	0.91	9.68	0.08	0.0653	0.0007	-0.17	0.033	0.003	633.5	5.3	668.6	7.8	785.0	28.4
NW13_02_omph_9.1	984	192	0.2	1.13	0.01	0.121	0.002	0.95	8.24	0.08	0.0675	0.0007	-0.37	0.038	0.003	738.2	6.8	769.1	9.3	854.0	30.5
NW13_02_omph_13.1	1461	385	0.3	1.28	0.01	0.134	0.002	0.93	7.47	0.07	0.0687	0.0007	-0.24	0.042	0.003	810.2	7.0	834.6	9.8	888.1	31.8
NW13_02_omph_14.1	276	239	0.9	3.84	0.02	0.282	0.003	0.88	3.55	0.03	0.099	0.001	0.08	0.082	0.007	1600.1	11.0	1601.9	16.8	1599.5	56.3

NW13_02_omph_16	144	86	0.6	2.80	0.03	0.215	0.003	0.85	4.65	0.05	0.094	0.001	0.12	0.071	0.006	1255	13	1356	16	1511.0	54.0
NW13_02_omph_17	1019	226	0.2	1.29	0.01	0.137	0.002	0.95	7.32	0.07	0.0684	0.0007	-0.18	0.042	0.003	825.3	7.4	842.2	9.7	881.6	31.3
NW13_02_omph_18	102	116	1.1	0.88	0.01	0.099	0.001	0.68	10.1	0.1	0.0642	0.0009	-0.03	0.032	0.003	609.8	7.1	638.9	9.2	751.0	34.3
NW13_02_omph_19	753	220	0.3	1.53	0.02	0.157	0.002	0.94	6.37	0.07	0.0707	0.0007	-0.05	0.048	0.004	940	9	943.5	11.2	947.8	33.9
NW13_02_omph_20.1	1813	144	0.1	0.621	0.005	0.0768	0.0009	0.92	13.0	0.1	0.0588	0.0006	-0.05	0.025	0.002	477.2	3.9	490.8	5.8	560.2	20.6
NW13_02_omph_21	182	114	0.6	1.06	0.02	0.103	0.002	0.90	9.7	0.1	0.074	0.001	-0.42	0.033	0.003	634.3	8.3	730.8	12.3	1035.0	41.4
NW13_02_omph_1	780	143	0.2	1.43	0.02	0.148	0.002	0.97	6.77	0.09	0.069	0.001	-0.02	0.045	0.005	887.8	11.5	900.5	10.6	905.7	41.1
NW13_02_omph_4.2	1076	231	0.2	1.43	0.02	0.150	0.002	0.96	6.68	0.08	0.069	0.001	0.06	0.045	0.005	899.9	10.8	902	10	890.7	40.4
NW13_02_omph_5.2	861	187	0.2	1.34	0.02	0.142	0.002	0.97	7.0	0.1	0.068	0.001	-0.01	0.044	0.004	855.2	11.4	864.6	10.2	867.0	39.3
NW13_02_omph_8	329	141	0.4	3.40	0.05	0.256	0.004	0.95	3.91	0.05	0.096	0.001	0.03	0.080	0.008	1468	19	1503.7	16.9	1548.8	70.0
NW13_02_omph_9.2	138	63	0.5	2.21	0.04	0.179	0.003	0.95	5.57	0.09	0.089	0.001	-0.11	0.056	0.006	1063	16	1183.6	14.9	1407.8	63.8
NW13_02_omph_10.2	489	16	0.0	0.534	0.008	0.0676	0.0009	0.84	14.8	0.2	0.0572	0.0009	-0.18	0.042	0.005	421.7	5.2	434	6	500.0	26.0
NW13_02_omph_11.1	1184	253	0.2	1.30	0.02	0.136	0.002	0.98	7.3	0.1	0.069	0.001	-0.34	0.046	0.005	823.2	11.5	844.4	10.7	897.7	40.7
NW13_02_omph_14.2	901	158	0.2	1.37	0.02	0.143	0.002	0.95	7.00	0.09	0.070	0.001	0.00	0.046	0.005	861.1	11.0	876.9	10.4	917.1	41.7
NW13_02_omph_15.2	474	68	0.1	1.10	0.02	0.120	0.002	0.97	8.4	0.1	0.067	0.001	-0.30	0.037	0.004	728.3	11.8	755.3	11.1	837.3	38.5
NW13_02_omph_16.1	1096	226	0.2	1.04	0.01	0.113	0.002	0.97	8.8	0.1	0.067	0.001	0.33	0.037	0.004	691.1	9.1	722.5	8.6	823.0	37.3
NW13_02_omph_17.1	352	90	0.3	1.39	0.02	0.123	0.002	0.93	8.1	0.1	0.082	0.001	0.04	0.039	0.004	746.4	9.7	883.6	10.4	1245.8	56.5
NW13_02_omph_19.1	663	204	0.3	1.40	0.03	0.143	0.003	0.94	7.0	0.1	0.071	0.001	-0.27	0.047	0.005	860	15	888.1	13.3	963.0	44.7
NW13_02_omph_21.1	245	154	0.6	2.28	0.03	0.182	0.003	0.95	5.48	0.08	0.091	0.001	0.17	0.065	0.006	1079.9	14.5	1206.1	13.8	1455.4	65.7
NW13_02_omph_22	298	68	0.2	0.75	0.02	0.083	0.002	0.94	12.1	0.2	0.066	0.001	-0.32	0.025	0.003	512.5	9.2	567.9	9.6	814.0	39.2
NW13_02_omph_23	594	113	0.2	3.50	0.05	0.259	0.003	0.98	3.86	0.05	0.098	0.001	0.01	0.075	0.008	1486	19	1527.3	16.8	1595.1	71.9
NW13_02_omph_24	1233	286	0.2	1.43	0.02	0.148	0.002	0.97	6.74	0.09	0.070	0.001	-0.03	0.046	0.005	891.7	12.0	902.5	10.8	942.2	42.7
NW13_02_omph_25	887	179	0.2	1.24	0.02	0.130	0.002	0.95	7.7	0.1	0.070	0.001	-0.26	0.042	0.004	784.6	11.1	819.3	10.5	931.0	42.5
NW13_02_omph_26	557	251	0.5	3.58	0.05	0.264	0.004	0.99	3.79	0.06	0.099	0.001	-0.05	0.077	0.008	1508	21	1544.1	17.8	1597.5	71.9
NW13_02_omph_27	1486	302	0.2	0.91	0.01	0.103	0.001	0.98	9.7	0.1	0.064	0.001	-0.10	0.032	0.003	632.2	8.6	660.0	8.2	756.1	34.4

Table 3

Zircon U–Pb ID–TIMS isotopic data from the Western Gneiss Region: Ulsteinvik and Saltaneset eclogites

				Composition				Isotopic Ratios							Dates (Ma)							Correlation Coefficient
Sample	location[a]	mineral assemblage[b]	Fraction	Pb*/ Pbc [h]	Pb* (pg) [f]	Pbc (pg) [g]	Th/ U [e]	$^{206}Pb/^{204}Pb$ [i]	$^{206}Pb/^{238}U$ <Th> [i,c]	±2σ %	$^{207}Pb/^{235}U$ [j]	±2σ %	$^{207}Pb/^{206}Pb$ <Th> [i,c]	±2σ %	$^{206}Pb/^{238}U$ date <Th> [c]	±2σ abs	$^{207}Pb/^{235}U$ date [d]	±2σ abs	$^{207}Pb/^{206}Pb$ date <Th> [c]	±2σ abs	$^{207}Pb/^{206}Pb$ [d]	±2σ abs	$^{206}Pb/^{238}U$<Th>-$^{207}Pb/^{235}U$ corr. coeff.[j]
8815E-Ulsteinvik	32V 337447 6915556	Omp, Grt, Aug, Pl, Qz, Amp, Bt, Rt, Zrn	z1-1	366	68	0.2	0.03	24984	0.06	0.06	0.5	0.1	0.05	0.09	401.9	0.2	402.1	0.4	402.9	2.1	403.5	2.1	0.77
			z1-3	48	8	0.2	0.03	3271	0.06	0.1	0.5	0.3	0.05	0.3	401.9	0.4	403.2	1.1	410.6	6.8	411.1	6.8	0.48
			z1-4	481	214	0.4	0.03	32805	0.06	0.07	0.5	0.1	0.05	0.05	402.1	0.3	402.9	0.4	408.0	1.4	408.5	1.4	0.85
			z2	73	13	0.2	0.03	5022	0.07	0.08	0.5	0.3	0.05	0.3	407.9	0.3	407.6	0.9	405.9	5.9	406.5	5.9	0.38
			z3	80	14	0.2	0.04	5490	0.06	0.06	0.5	0.3	0.05	0.2	405.1	0.2	404.4	0.8	400.1	5.2	400.7	5.2	0.40
			z4	49	11	0.2	0.03	3390	0.07	0.06	0.5	0.3	0.06	0.3	408.3	0.2	410.6	1.0	423.4	6.6	424.0	6.6	0.28
			z5	110	20	0.2	0.01	7544	0.06	0.05	0.5	0.2	0.05	0.1	401.9	0.2	402.4	0.6	405.1	3.0	405.7	3.0	0.71
			z8	87	14	0.2	0.03	5919	0.07	0.08	0.5	0.2	0.05	0.2	407.9	0.3	408.0	0.7	408.3	3.9	408.8	3.9	0.57
			z10	56	10	0.2	0.03	3878	0.07	0.08	0.5	0.4	0.05	0.3	409.6	0.3	409.1	1.3	406.1	7.3	406.6	7.3	0.80
			z12	25	4	0.2	0.03	1709	0.07	0.1	0.5	0.8	0.05	0.7	408.7	0.5	408.4	2.6	407.0	16.0	407.0	16.0	0.47
			z13	23	5	0.2	0.03	1603	0.07	0.2	0.5	0.6	0.06	0.5	409.6	0.6	410.5	2.0	415.0	12.0	416.0	12.0	0.37
			z14	19	45	2.4	0.03	1329	0.07	0.07	0.5	0.6	0.06	0.6	407.3	0.3	409.5	2.1	422.0	14.0	423.0	14.0	0.27
			z15	11	25	2.4	0.02	739	0.06	0.1	0.5	1.1	0.06	1.1	401.3	0.4	404.7	3.8	424.0	25.0	425.0	25.0	0.20
			z16	53	139	2.6	0.03	3619	0.07	0.06	0.5	0.3	0.06	0.2	408.6	0.3	409.4	0.9	414.1	5.3	414.7	5.3	0.44
			z17	6	14	2.2	0.03	441	0.07	0.2	0.5	1.9	0.06	1.9	407.2	0.7	412.8	6.6	444.0	42.0	445.0	42.0	0.25
NW13-02-G	32V 308668 6882327	Qz, Grt, Rt, Zr	z1-1	394	109	0.3	0.1	25938	0.07	0.05	0.5	0.1	0.06	0.07	425.4	0.2	431.1	0.3	461.9	1.6	462.5	1.6	0.75
Saltaneset garnet–quartz layer			z1-2	682	194	0.3	0.03	46563	0.06	0.05	0.49	0.09	0.05	0.05	401.5	0.2	402.0	0.3	404.8	1.2	405.4	1.2	0.86
			z2-1	573	187	0.3	0.2	36975	0.09	0.06	0.8	0.1	0.06	0.06	555.7	0.3	582.3	0.4	687.4	1.2	687.8	1.2	0.85
			z2-2	315	54	0.2	0.1	21011	0.07	0.05	0.6	0.1	0.06	0.07	449.7	0.2	460.5	0.4	514.9	1.7	515.4	1.7	0.73
			z3	72	21	0.3	0.03	4945	0.06	0.05	0.5	0.2	0.05	0.2	401.4	0.2	401.8	0.7	404.3	4.3	404.9	4.3	0.46
			z5-1	177	23	0.1	0.3	11148	0.14	0.06	1.3	0.1	0.07	0.1	825.6	0.4	844.6	0.8	895.1	2.1	895.3	2.1	0.74
			z6	39	30	0.8	0.02	2671	0.07	0.06	0.5	0.3	0.06	0.3	408.8	0.2	410.0	1.1	416.9	7.0	417.5	7.0	0.34
			z7	26	4	0.2	0.05	1741	0.1	0.2	0.6	0.6	0.06	0.5	476.2	0.8	491.6	2.2	563.8	11.3	564.3	11.3	0.38
			z9	461	90	0.2	0.05	31210	0.07	0.05	0.58	0.09	0.06	0.08	452.8	0.2	464.2	0.3	521.3	1.8	521.8	1.8	0.46
			z11	60	10	0.2	0.2	3885	0.08	0.1	0.7	0.3	0.06	0.2	524.9	0.5	548.6	1.1	648.5	4.8	648.9	4.8	0.51
			z14	4	8	2.3	0.05	268	0.07	0.3	0.6	3.0	0.06	3.0	444.2	1.2	475.3	11.4	628.1	63.7	628.6	63.7	0.24
			z15	3	7	2.5	0.5	175	0.2	0.5	2.9	3.0	0.1	2.9	1260.1	6.0	1387.9	22.5	1590.2	54.0	1590.3	54.0	0.25
			z16	11	24	2.2	0.01	767	0.07	0.1	0.5	1.1	0.06	1.1	408.9	0.4	411.8	3.7	427.9	24.1	428.5	24.1	0.25
NW13-02-O	32V 308668 6882327	Omp, Grt, Qz, Pl, Amp,Rt, Zrn	z1-3	583	98	0.2	1.0	30157	0.26	0.06	3.6	0.1	0.10	0.06	1512.2	0.8	1543.6	0.8	1586.9	1.1	1587.0	1.1	0.85
Saltaneset omphacite layer			z1-4	238	74	0.3	0.8	13026	0.22	0.06	2.8	0.1	0.09	0.08	1279.8	0.8	1349.1	0.9	1460.8	1.5	1460.9	1.5	0.77
			z2	382	116	0.3	0.3	23744	0.14	0.09	1.6	0.1	0.08	0.06	866.9	0.8	955.0	0.7	1163.7	1.3	1164.0	1.3	0.80
			z3-2	97	21	0.2	0.2	6269	0.13	0.06	1.2	0.2	0.07	0.1	770.7	0.4	794.6	0.9	862.3	2.8	862.5	2.8	0.59
			z4-1	137	19	0.1	0.8	7537	0.2	0.2	2.6	0.2	0.09	0.1	1202.2	1.9	1301.3	1.6	1468.7	2.1	1468.8	2.1	0.86
			z4-3	83	15	0.2	0.6	4774	0.2	0.2	2.6	0.3	0.09	0.2	1215.0	2.4	1296.5	2.2	1434.1	4.0	1434.2	4.0	0.74
			z4-4	1066	276	0.3	0.9	56664	0.22	0.05	2.91	0.09	0.09	0.05	1300.1	0.6	1383.5	0.7	1514.7	0.9	1514.8	0.9	0.91
			z5	3	6	2.3	0.04	211	0.06	0.4	0.5	4.2	0.06	4.1	396.7	1.4	407.2	14.1	466.7	91.4	467.2	91.4	0.23
			z6	12	27	2.3	0.05	804	0.07	0.1	0.6	1.0	0.06	1.0	437.2	0.5	447.9	3.7	503.1	22.0	503.7	22.0	0.25
			z9	12	26	2.2	0.2	805	0.1	0.1	1.3	0.9	0.07	0.8	801.7	0.9	830.8	4.8	909.6	17.0	909.9	17.0	0.28
			z10	19	47	2.4	0.2	1266	0.13	0.08	1.2	0.6	0.07	0.5	786.0	0.6	810.5	3.1	878.1	11.2	878.4	11.2	0.32

[a] outcrop locality (UTM)

[b] mineral assemblage: Grt = garnet, Omp = omphacite, Aug = augite, Amp = amphibole, Pl = plagioclase, Qz = quartz, Bt = biotite, Rt = rutile, Zrn = zircon. Abbreviations after Whitney and Evans, 2010

[c] Corrected for initial Th/U disequilibrium using radiogenic 208Pb and Th/U[magma] = 2.8.

[d] Isotopic dates calculated using the decay constants λ238 = 1.55125E-10 and λ235 = 9.8485E-10 (Jaffey et al. 1971).

[e] Th contents calculated from radiogenic 208Pb and the 207Pb/206Pb date of the sample, assuming concordance between U-Th and Pb systems.

[f] Total mass of radiogenic Pb.

[g] Total mass of common Pb.

[h] Ratio of radiogenic Pb (including 208Pb) to common Pb.

[i] Measured ratio corrected for fractionation and spike contribution only.

[j] Measured ratios corrected for fractionation, tracer and blank.

Table 4

Chondrite normalized zircon LASS and solution ICP-MS trace-element data from the Western Gneiss Region: Ulsteinvik and Saltaneset eclogites

Zircons analyzed by ID-TIMS and LASS	La	Ce	Pr	Nd	Pm*	Sm	Eu	Gd	Tb	Dy	Ho	Er	Tm	Yb	Lu
Ulsteinvik-8815E, eclogite															
Ulsteinvik_ z1_1	bdl	3.8	0.03	0.04	0.2	1.6	3.3	7.7	11.8	15.6	18.6	24.6	24.4	27.6	24.8
Ulsteinvik_ z1_2	bdl	4.7	0.04	0.2	0.7	2.9	4.7	11.9	14.7	26.3	29.3	31.8	37.7	37.4	38.0
Ulsteinvik_z1_3	0.003	6.0	0.02	0.2	1.0	3.9	6.3	12.3	26.4	31.3	42.4	45.4	46.8	49.8	54.0
Ulsteinvik_z1_5	0.004	4.2	0.1	0.9	1.7	3.6	6.6	15.9	23.9	33.3	35.5	37.1	42.8	48.0	49.2
Ulsteinvik_z1_6	bdl	3.8	0.1	0.4	1.3	4.6	6.2	15.7	20.2	29.2	34.0	41.1	46.4	46.8	47.6
Ulsteinvik_z2_9	0.02	3.9	0.04	0.4	1.0	2.9	5.2	14.1	14.6	20.0	18.2	18.6	21.6	25.8	26.4
Ulsteinvik_z3_12	0.06	3.3	0.03	0.1	0.2	0.5	2.1	7.0	7.9	10.9	8.4	6.0	5.8	7.0	7.0
Ulsteinvik_z4_15	0.02	3.5	0.1	0.1	0.4	1.6	1.9	6.9	9.4	10.9	10.0	8.1	11.3	12.1	10.2
Ulsteinvik_z5_13	0.03	4.8	0.1	0.4	1.3	4.1	5.3	14.9	18.3	24.5	26.5	23.1	27.2	29.1	29.6
Ulsteinvik_z5_14	0.07	4.3	0.05	0.4	0.9	2.3	2.9	8.5	12.2	16.2	15.8	20.6	20.8	22.5	25.2
Ulsteinvik_z8_27	bdl	2.8	0.1	0.3	0.7	1.4	3.5	8.0	8.3	10.2	12.4	13.1	13.4	14.3	19.2
Ulsteinvik_z10_7	0.02	2.7	0.1	0.2	0.4	0.9	1.7	4.4	5.4	4.1	7.3	6.3	7.2	7.5	7.6
Ulsteinvik_z12_22	0.01	4.9	bdl	0.02	0.2	1.2	3.7	8.6	8.0	9.6	11.5	12.6	9.1	12.7	12.3
Ulsteinvik_z12_23	0.03	6.8	0.003	0.3	1.0	3.6	9.5	16.6	26.4	27.1	24.2	22.9	24.0	24.4	24.0
Ulsteinvik_z13_31	0.01	3.9	bdl	0.2	0.8	3.5	5.7	9.0	16.1	16.3	20.9	17.8	16.4	20.9	22.4
Ulsteinvik_z14_35	0.03	3.6	0.1	0.1	0.5	1.8	7.0	13.4	15.8	17.9	20.0	19.4	15.7	24.2	22.8
Ulsteinvik_z15_16	0.04	5.7	0.1	0.9	2.9	9.8	15.2	25.5	32.8	37.4	35.3	32.2	34.4	37.1	37.6
Ulsteinvik_z15_17	0.01	5.5	0.02	0.9	2.6	7.0	13.9	28.0	30.6	35.5	32.7	34.3	32.0	38.8	45.2
Ulsteinvik_z15_18	0.03	4.1	0.2	0.4	1.3	4.5	5.7	11.0	15.6	19.5	20.5	22.4	19.4	27.5	38.0
Ulsteinvik_z16_45	bdl	7.6	0.1	0.04	0.4	4.5	13.0	19.1	29.7	26.5	25.8	21.4	18.5	22.0	26.8
Ulsteinvik_z16_46	bdl	4.4	bdl	0.2	0.7	3.6	5.0	8.3	10.3	11.4	10.5	9.7	9.6	12.2	10.4
Ulsteinvik_z16_47	bdl	4.6	0.1	0.1	0.6	2.6	3.9	7.7	10.8	10.9	8.6	9.5	9.8	12.2	10.2
Ulsteinvik_z16_48	bdl	4.5	0.1	0.2	1.1	5.0	8.4	11.7	17.7	17.4	16.0	17.4	16.1	16.7	22.6
Ulsteinvik_z17_20	0.02	2.4	0.01	0.1	0.5	1.7	2.2	3.5	7.1	6.8	7.8	6.9	5.2	8.1	7.7
NW13-02-G, Saltaneset eclogite (garnet-quartz layer)															
NW13_02_grt_z1_3	0.03	5.4	bdl	0.04	0.3	1.8	2.3	8.0	11.1	16.1	18.7	23.1	20.6	23.2	23.4
NW13_02_grt_z3_6	0.03	6.6	0.1	0.2	0.7	2.2	5.3	8.3	15.0	18.0	21.1	22.5	25.5	32.0	28.5
NW13_02_grt_z6_19	0.02	4.4	bdl	0.3	0.6	1.6	1.4	7.2	8.1	11.7	12.1	15.3	15.4	15.4	13.4
NW13_02_grt-z16_4	0.0001	3.0	bdl	0.2	0.7	3.0	5.6	13.6	13.1	12.2	10.5	12.3	19.0	37.3	84.1
NW13-02-O, Saltaneset eclogite (omphacite layer)															
NW13_02_omph_z5_2	0.2	9.4	0.7	2.8	3.8	5.1	8.3	15.0	19.4	21.7	23.8	25.4	28.3	34.5	29.3
Zircons analyzed by LASS															
Ulsteinvik-8815E, eclogite															
Ulsteinvik_10	bdl	4.7	bdl	0.4	0.8	1.7	4.0	11.0	9.7	10.5	9.5	7.8	4.6	7.5	6.8
Ulsteinvik_21	bdl	3.7	bdl	0.4	1.2	3.2	3.3	7.9	9.1	11.4	14.7	13.4	14.7	19.6	18.8
Ulsteinvik_24	0.01	4.0	0.1	0.2	0.6	2.0	3.6	8.6	10.0	11.8	13.3	12.2	13.5	13.2	11.4
Ulsteinvik_28	0.02	4.8	bdl	0.3	0.7	1.8	3.9	9.1	10.5	12.1	13.6	14.3	17.6	18.1	18.0
Ulsteinvik_33	0.05	3.6	bdl	bdl	-	0.7	4.6	8.2	8.8	8.4	9.8	9.1	9.0	12.5	17.2
Ulsteinvik_34	0.01	3.8	0.2	0.1	0.4	2.0	4.3	8.1	8.0	11.5	12.5	12.3	9.1	12.1	14.8
Ulsteinvik_37	2.1	3.5	0.2	0.3	0.8	2.2	5.9	6.7	11.6	14.5	16.2	20.9	17.8	20.9	21.7
Ulsteinvik_39	0.06	5.4	0.4	0.5	1.7	6.0	9.5	16.2	25.6	28.4	32.4	34.3	33.6	42.9	44.8
Ulsteinvik_40	bdl	4.3	bdl	0.3	1.3	5.5	5.3	7.9	11.6	15.2	17.5	18.2	22.8	25.6	28.8
Ulsteinvik_41	bdl	3.0	bdl	0.2	0.5	1.5	3.9	6.5	8.0	10.3	10.7	11.2	11.5	13.2	14.8
Ulsteinvik_25	0.001	2.6	bdl	0.4	0.8	1.6	3.1	12.1	17.2	37.0	71.6	164.4	348.4	791.3	1552.0
Ulsteinvik_29	0.01	47.8	1.2	3.9	8.5	18.6	19.6	165.8	323.1	686.2	1403.6	2512.5	3772.0	6074.5	7972.0
Ulsteinvik_32	0.08	7.0	0.2	1.0	2.4	5.5	12.3	31.3	48.1	118.7	238.2	398.1	656.0	1118.0	1844.0
Ulsteinvik_43	bdl	13.2	1.5	2.9	7.5	19.4	16.1	96.5	219.2	400.8	772.7	1275.0	1936.0	2981.4	4084.0
Ulsteinvik_44	bdl	4.7	0.3	1.0	2.6	6.6	9.6	39.8	86.4	168.3	321.8	549.4	844.0	1341.6	2044.0
NW13-02-G, Saltaneset eclogite (garnet-quartz layer)															
NW13_02_grt_15	bdl	3.9	bdl	0.1	0.4	3.5	2.9	8.8	9.3	12.7	13.0	13.0	9.7	18.6	16.7
NW13_02_grt_20	bdl	6.4	bdl	0.4	0.9	2.4	5.2	10.4	13.3	18.1	22.2	20.1	22.7	29.9	40.7

NW13_02_grt_21	0.02	3.7	bdl	0.2	0.6	2.2	3.4	5.1	10.8	13.7	14.7	12.0	19.0	13.2	14.6
NW13_02_grt_22	0.02	3.9	0.1	0.5	0.8	1.4	3.6	6.5	12.9	12.2	11.2	12.6	15.4	17.3	20.3
NW13_02_grt_24	bdl	7.3	bdl	0.4	0.9	2.2	6.0	12.3	18.6	25.7	24.4	31.4	34.8	42.9	43.5
NW13_02_grt_25	bdl	7.4	0.03	0.4	1.5	4.9	5.5	15.0	23.0	27.9	33.5	39.0	49.8	54.0	56.1
NW13_02_grt_30	bdl	5.2	bdl	0.3	0.7	1.9	2.3	7.3	11.4	16.6	16.7	24.6	27.5	39.1	75.6
NW13_02_grt_34	bdl	4.9	0.1	0.2	0.6	1.9	2.6	6.5	13.0	15.2	16.1	20.1	19.6	26.1	24.4
NW13_02_grt_7	0.0002	5.4	bdl	0.2	0.8	3.2	3.5	11.9	13.4	21.7	27.8	26.8	35.6	41.3	41.1
NW13_02_grt_13	0.0001	5.0	0.1	0.2	0.7	2.5	3.3	8.6	14.9	18.5	22.3	19.9	21.9	35.0	29.3
NW13_02_grt_1	bdl	20.6	2.3	2.1	5.1	12.6	6.6	59.8	107.5	201.2	377.3	637.5	979.8	1565.2	1963.4
NW13_02_grt_2	bdl	99.2	*9.9*	19.0	40.1	84.5	54.9	254.3	335.2	516.3	800.4	1118.8	1336.0	1937.9	2020.3
NW13_02_grt_4	bdl	51.4	5.9	7.0	11.6	19.4	12.8	59.8	100.0	182.1	323.6	547.5	821.9	1248.4	1540.7
NW13_02_grt_7.1	bdl	37.5	2.8	8.3	17.4	36.5	14.6	109.0	166.2	284.6	457.9	650.0	882.6	1291.9	1516.3
NW13_02_grt_9	bdl	95.6	6.3	15.4	33.8	74.3	27.4	267.3	423.8	672.0	1078.8	1575.0	1971.7	2658.4	2971.5
NW13_02_grt_10	bdl	17.5	0.1	0.5	1.6	5.9	5.0	30.7	85.6	167.1	329.7	623.8	1016.2	1689.4	2439.0
NW13_02_grt_11	bdl	11.7	0.1	0.6	1.3	3.0	2.2	14.9	31.3	59.3	119.8	206.9	352.2	608.7	849.6
NW13_02_grt_12	bdl	105.7	5.0	12.3	26.3	56.3	25.9	177.9	274.0	443.1	694.1	981.3	1307.7	1826.1	2089.4
NW13_02_grt_13.1	bdl	13.5	0.1	0.5	1.3	3.4	3.0	24.1	63.2	118.7	243.6	455.0	704.5	1267.1	1861.8
NW13_02_grt_14	bdl	101.5	7.5	17.1	38.0	84.5	33.4	277.4	459.8	743.9	1168.5	1662.5	2242.9	3018.6	3191.1
NW13_02_grt_16	bdl	26.1	0.9	1.9	4.1	8.9	5.7	47.2	94.5	189.8	355.3	634.4	1056.7	1801.2	2585.4
NW13_02_grt_17	bdl	71.5	3.4	6.5	14.8	33.8	14.9	96.0	165.1	262.6	452.4	711.3	975.7	1496.9	1780.5
NW13_02_grt_23	bdl	6.1	bdl	0.2	0.6	2.2	2.7	9.9	16.9	29.6	52.0	94.4	159.9	293.8	455.3
NW13_02_grt_26	bdl	14.1	0.2	0.7	2.3	7.8	4.3	30.4	51.5	82.5	148.4	251.3	342.5	515.5	682.9
NW13_02_grt_27	0.02	7.5	0.2	0.2	0.9	3.2	2.2	11.4	19.9	36.2	62.6	121.9	199.2	337.9	500.4
NW13_02_grt_28	bdl	51.1	1.1	3.8	9.7	24.9	16.9	71.9	126.0	209.8	351.6	525.6	631.6	917.4	1166.7
NW13_02_grt_31	bdl	11.7	0.1	0.8	1.8	4.3	3.8	21.9	53.7	104.1	208.8	359.4	591.1	1049.7	1422.8
NW13_02_grt_32	bdl	15.6	0.1	0.6	1.7	4.9	2.2	17.9	42.1	80.9	171.1	311.3	534.4	950.3	1317.1
NW13_02_grt_33	bdl	60.4	2.8	6.5	13.5	28.0	15.6	90.5	149.3	244.3	408.4	619.4	874.5	1329.2	1682.9
NW13_02_grt_35	bdl	16.2	0.2	0.2	0.9	4.1	2.1	17.8	43.5	88.6	174.0	323.8	542.5	1000.0	1500.0
NW13_02_grt_36	bdl	25.1	0.8	1.6	4.5	12.6	6.9	43.2	88.1	163.0	289.4	508.8	761.1	1248.4	1800.8
NW13_02_grt_37	bdl	81.1	2.1	7.3	17.1	40.1	19.2	113.6	185.0	287.8	441.4	632.5	815.8	1136.6	1386.2
NW13_02_grt_38	bdl	10.1	0.2	0.6	1.7	4.5	2.6	13.0	28.3	50.4	103.8	195.0	292.3	534.2	813.0
NW13_02_grt_39	bdl	109.1	10.3	15.8	28.9	53.0	23.4	131.7	233.8	374.0	593.4	847.5	1117.4	1559.0	1955.3
NW13_02_grt_40	bdl	102.6	2.9	5.8	13.9	33.0	16.5	113.1	188.1	291.9	483.5	693.8	906.9	1397.5	1707.3
NW13_02_grt_41	bdl	11.4	0.1	0.7	1.4	2.8	1.9	14.0	27.7	54.5	110.3	208.1	350.6	619.3	951.2
NW13_02_grt_44	bdl	9.3	0.1	0.6	1.6	4.1	3.7	18.6	41.6	75.2	158.4	301.3	465.6	888.2	1390.2
NW13_02_grt_45	bdl	43.9	3.3	4.3	7.7	14.0	7.8	57.8	124.7	228.9	404.8	625.0	1012.1	1540.4	2040.7
NW13_02_grt_1.1	0.1	52.2	1.0	4.6	12.8	35.8	14.2	145.7	285.3	500.0	860.8	1381.3	1983.8	2981.4	3617.9
NW13_02_grt_2.1	0.2	52.7	1.3	4.9	11.4	26.6	12.8	74.9	131.3	194.7	305.9	474.4	599.2	842.9	987.8
NW13_02_grt_3	0.0001	8.5	0.1	0.3	1.0	3.2	3.3	14.4	29.9	72.4	139.2	270.0	538.5	962.7	1406.5
NW13_02_grt_5	0.3	60.4	3.4	9.0	19.8	43.6	23.1	133.2	198.3	311.4	479.9	673.8	902.8	1236.0	1369.9
NW13_02_grt_8	25.3	147.6	84.1	65.0	46.0	32.6	16.9	39.2	69.8	141.5	261.9	426.9	716.6	1115.5	1544.7
NW13_02_grt_9.1	8.9	33.0	11.0	12.5	15.8	20.0	8.5	37.9	72.9	148.0	280.2	510.6	902.8	1441.0	2008.1
NW13_02_grt_10.1	0.3	78.6	3.3	9.8	25.7	66.9	23.6	200.0	332.4	561.0	860.8	1312.5	1854.3	2546.6	2898.4
NW13_02_grt_12.1	0.6	54.6	3.2	6.9	13.0	24.7	15.8	55.0	106.1	182.5	308.1	461.3	728.7	1024.8	1227.6
NW13_02_grt_14.1	0.05	17.8	0.3	1.1	3.0	7.8	5.5	32.5	56.5	110.2	179.5	275.6	398.0	583.9	711.4
NW13-02-omph, Saltaneset eclogite (omphacite layer)															
NW13_02_omph_14	bdl	8.9	3.9	4.4	5.7	7.4	6.6	9.1	14.4	16.3	23.4	33.1	40.5	52.2	80.9
NW13_02_omph_10	bdl	6.2	0.4	1.0	1.8	3.4	4.9	8.8	15.1	15.4	20.7	23.1	29.1	34.2	47.2
NW13_02_omph_12	bdl	5.2	0.2	0.4	1.0	3.1	4.1	8.2	14.7	18.0	17.4	16.0	21.1	22.9	24.0
NW13_02_omph_15	bdl	12.7	5.7	4.8	6.2	7.9	5.9	8.9	13.7	15.0	21.8	21.1	30.4	31.6	28.9
NW13_02_omph_20	0.1	3.9	0.2	0.2	0.4	0.8	3.0	5.1	8.0	11.3	14.5	17.4	18.2	27.9	30.1
NW13_02_omph_4	bdl	24.0	1.7	4.6	10.0	21.6	27.7	79.9	156.0	285.8	520.1	930.6	1327.9	2198.8	3211.4
NW13_02_omph_5	bdl	32.0	18.3	16.0	17.1	18.4	16.0	28.3	52.4	90.2	208.2	419.4	801.6	1614.9	3101.6
NW13_02_omph_7	bdl	15.5	1.9	2.3	5.7	14.1	17.1	47.7	94.2	176.0	313.2	577.5	951.4	1602.5	2369.9
NW13_02_omph_9	bdl	12.7	0.3	0.4	1.6	7.1	8.3	41.2	76.2	158.5	331.1	634.4	1093.1	1658.4	2764.2
NW13_02_omph_10.1	bdl	12.5	0.4	1.0	2.4	5.4	6.6	20.8	49.0	96.7	184.1	351.3	554.7	1045.3	1593.5
NW13_02_omph_11	bdl	12.4	0.6	0.9	2.6	7.6	5.5	28.1	63.4	125.2	243.6	433.8	713.0	1316.8	2126.0
NW13_02_omph_12.1	bdl	11.4	0.6	0.5	1.7	6.0	3.5	20.6	39.6	71.1	142.9	263.1	449.4	838.5	1349.6

NW13_02_omph_13.1	bdl	15.4	0.5	3.0	6.1	12.4	11.7	31.6	57.3	102.0	194.1	368.1	522.3	906.8	1357.7
NW13_02_omph_15.1	bdl	19.6	2.1	3.7	7.0	13.2	13.2	55.3	107.8	215.4	413.9	756.3	1178.1	1987.6	2780.5
NW13_02_omph_4.1	bdl	13.6	0.9	1.6	3.6	8.0	9.2	27.4	63.4	115.0	248.4	455.6	728.7	1211.2	1699.2
NW13_02_omph_5.1	bdl	13.9	1.5	1.4	3.5	9.1	11.0	37.2	71.2	131.7	287.5	493.8	821.9	1260.9	1800.8
NW13_02_omph_7.1	bdl	10.4	0.2	0.5	1.2	2.8	3.4	13.4	34.1	71.1	128.8	241.9	433.2	764.0	1219.5
NW13_02_omph_9.1	bdl	9.1	0.3	0.4	1.6	6.2	3.9	22.5	46.8	93.5	199.1	365.0	627.5	1130.4	1654.5
NW13_02_omph_13.2	bdl	24.7	2.6	2.2	6.0	16.3	8.0	56.3	117.2	204.1	368.1	650.0	1085.0	1813.7	2613.8
NW13_02_omph_14.1	bdl	27.6	6.2	9.0	18.2	36.8	36.9	143.7	282.8	504.5	848.0	1321.3	1878.5	2732.9	3374.0
NW13_02_omph_16	bdl	15.8	2.3	2.8	7.4	19.3	21.0	60.8	121.6	201.2	355.3	556.3	874.5	1273.3	1500.0
NW13_02_omph_17	bdl	10.6	0.3	0.8	2.3	6.8	3.9	20.5	51.2	95.5	184.1	318.8	510.1	937.9	1382.1
NW13_02_omph_18.1	bdl	68.0	3.6	8.3	18.0	38.7	25.0	130.2	200.8	280.1	439.6	557.5	765.2	1136.6	1276.4
NW13_02_omph_19	bdl	14.8	0.3	0.5	1.3	3.6	4.0	21.1	54.8	104.1	192.9	379.4	627.5	1111.8	1715.4
NW13_02_omph_20.1	bdl	11.8	1.4	1.4	1.7	2.0	1.8	11.1	27.4	56.1	116.8	235.0	398.8	751.6	1113.8
NW13_02_omph_21	bdl	18.0	2.2	3.9	8.4	18.1	21.1	58.9	115.8	226.4	382.8	638.1	935.2	1397.5	1857.7
NW13_02_omph_1.1	0.1	8.4	0.1	0.6	1.5	3.7	3.0	19.8	44.6	97.2	184.8	353.1	562.8	1105.6	1540.7
NW13_02_omph_4.2	0.7	10.9	1.4	1.9	3.9	7.9	7.6	32.7	60.1	126.0	238.5	459.4	753.0	1316.8	1886.2
NW13_02_omph_5.2	0.2	9.3	0.3	1.0	2.2	5.2	4.1	23.1	50.7	98.4	190.5	348.1	595.1	1073.9	1569.1
NW13_02_omph_8	0.1	11.6	0.5	1.2	2.4	4.7	8.3	21.5	47.9	100.4	236.3	438.1	777.3	1428.6	2036.6
NW13_02_omph_9.2	0.2	9.2	0.5	0.9	2.0	4.4	4.4	14.6	29.1	57.3	115.2	245.0	404.9	701.2	1056.9
NW13_02_omph_10.2	2.2	10.3	4.7	3.8	4.0	4.3	4.8	8.2	15.0	18.0	22.5	22.4	26.4	40.1	35.8
NW13_02_omph_11.1	0.1	13.2	0.2	0.9	2.1	5.1	4.3	23.3	49.6	102.4	198.9	366.9	607.3	1062.1	1528.5
NW13_02_omph_14.2	9.7	24.8	15.7	12.7	11.1	9.7	3.7	16.3	45.4	87.8	175.8	328.1	562.8	950.3	1443.1
NW13_02_omph_15.2	0.1	5.2	0.2	0.5	0.8	1.4	1.5	8.3	12.7	24.8	48.0	100.0	184.6	349.7	516.3
NW13_02_omph_16.1	32.5	39.2	21.6	16.4	15.6	14.9	7.6	21.5	46.0	88.6	158.6	284.4	468.0	869.6	1130.1
NW13_02_omph_17.1	0.1	13.8	0.8	1.5	3.2	6.7	8.3	16.8	34.3	78.0	205.1	475.0	870.4	1596.3	2536.6
NW13_02_omph_19.1	0.0	11.6	0.2	0.5	1.4	4.3	4.8	23.7	50.1	94.7	185.9	341.3	506.1	968.9	1386.2
NW13_02_omph_21.1	0.1	21.5	1.7	3.9	8.6	19.1	17.8	70.9	143.2	274.8	540.3	900.0	1271.3	1981.4	2223.6
NW13_02_omph_22	0.3	11.1	0.6	1.2	3.0	7.2	7.1	17.9	31.0	73.2	163.0	354.4	655.9	1173.9	1817.1
NW13_02_omph_23	0.1	30.0	0.4	1.3	4.4	14.5	7.1	68.3	162.9	336.6	697.8	1400.0	2425.1	4105.6	6577.2
NW13_02_omph_24	21.9	14.4	4.3	3.9	6.1	9.6	9.6	39.7	77.6	149.6	286.8	510.0	870.4	1453.4	2113.8
NW13_02_omph_25	0.2	10.3	0.7	1.4	2.7	5.5	6.3	22.5	51.8	99.2	192.3	381.3	655.9	1198.8	1731.7
NW13_02_omph_26	0.2	78.6	1.2	4.5	10.3	23.3	19.2	102.5	228.3	521.1	1080.6	1925.0	3052.6	5173.9	7032.5
NW13_02_omph_27	0.1	12.5	0.3	1.3	2.8	6.0	7.1	40.2	70.4	141.9	258.1	496.9	872.9	1449.1	2142.3

Zircons analyzed by ID-TIMS-TEA	La	Ce	Pr	Nd	Pm	Sm	Eu	Gd	Tb	Dy	Ho	Er	Tm	Yb	Lu
Ulsteinvik-8815E, eclogite															
Ulsteinvik z1-1	bdl	10.0	bdl	bdl	-	6.5	11.7	25.2	29.9	36.7	41.9	46.9	44.2	44.9	47.9
Ulsteinvik z1-3	bdl	17.2	bdl	bdl	-	4.5	14.5	23.3	31.7	37.2	42.3	49.7	45.0	50.5	49.4
Ulsteinvik z1-4	bdl	4.5	bdl	bdl	-	5.3	12.0	17.8	24.7	29.6	36.1	40.4	39.6	38.8	45.3
Ulsteinvik z2	1.1	10.8	bdl	bdl	-	6.5	12.0	21.4	22.2	20.1	19.1	20.3	15.9	18.4	20.7
Ulsteinvik z3	bdl	0.3	bdl	bdl	-	3.5	7.9	20.8	20.7	23.6	31.6	44.7	51.3	75.6	114.4
Ulsteinvik z4	bdl	bdl	bdl	bdl	-	2.0	6.6	12.2	15.7	19.0	22.6	21.0	19.6	24.3	27.6
Ulsteinvik z5	bdl	1.9	bdl	bdl	-	6.4	10.5	22.4	22.7	27.2	26.8	32.1	32.2	47.9	76.1
Ulsteinvik z8	bdl	4.7	bdl	bdl	-	2.9	9.2	19.9	20.1	21.3	24.5	27.8	23.9	29.5	38.1
Ulsteinvik z10	bdl	3.1	bdl	bdl	-	3.8	8.6	16.7	17.8	19.3	17.7	21.1	17.6	19.1	20.2
Ulsteinvik z12	bdl	bdl	bdl	bdl	-	bdl	6.5	18.1	19.2	14.3	11.8	12.2	10.9	8.5	9.8
Ulsteinvik z14	bdl	6.2	bdl	bdl	-	4.0	9.6	20.0	20.2	20.4	20.1	20.3	18.2	21.0	23.5
Ulsteinvik z15	bdl	2.0	bdl	bdl	-	6.8	15.4	32.1	29.7	30.3	29.4	32.7	27.8	33.0	39.4
Ulsteinvik z16	bdl	9.1	bdl	bdl	-	5.9	11.9	24.9	22.3	21.2	19.0	19.0	18.0	19.8	22.7
Ulsteinvik z17	bdl	0.5	bdl	bdl	-	0.5	2.7	6.4	11.4	18.7	20.3	17.8	15.6	16.1	18.4
NW13-02-G, Saltaneset eclogite (garnet-quartz layer)															
NW13-02-G z1-1	bdl	30.9	bdl	bdl	-	18.8	17.4	70.3	88.2	116.4	149.1	204.2	233.3	302.7	371.8
NW13-02-G z1-2	1.2	13.5	bdl	bdl	-	7.2	11.9	32.5	38.5	45.6	47.5	52.9	51.3	61.2	70.2
NW13-02-G z2-1	bdl	43.2	bdl	bdl	-	24.6	15.6	82.7	109.1	164.4	243.1	383.1	504.8	736.1	1050.1
NW13-02-G z2-2	bdl	28.0	bdl	bdl	-	14.6	13.0	54.1	71.7	100.2	137.8	201.7	248.5	334.9	448.1
NW13-02-G z3	bdl	1.8	bdl	bdl	-	4.9	14.0	36.2	49.7	52.0	58.5	63.1	62.8	73.6	84.7
NW13-02-G z6	bdl	5.4	bdl	0.4	1.4	4.3	6.8	17.9	25.7	25.8	28.1	29.1	26.6	28.1	30.8
NW13-02-G z16	bdl	bdl	bdl	0.2	0.8	3.9	7.3	19.5	24.2	25.4	25.2	26.7	32.2	40.9	66.9

NW13-02-omph, Saltaneset eclogite (omphacite layer)															
NW13-02-O z1-3	bdl	59.5	8.7	21.4	46.0	98.9	101.8	388.3	586.4	872.4	1413.5	2198.7	2631.4	3534.0	4610.6
NW13-02-O z2	bdl	15.6	0.7	1.7	3.6	7.7	10.7	29.0	50.3	90.9	173.9	334.3	495.4	834.2	1345.2
NW13-02-O z5	bdl	bdl	bdl	0.4	1.4	5.4	8.3	23.0	29.0	31.8	35.6	37.0	37.2	41.2	51.4

Average zircon trace-element compositions by method	La	Ce	Pr	Nd	Pm	Sm	Eu	Gd	Tb	Dy	Ho	Er	Tm	Yb	Lu
Ulsteinvik-8815E, eclogite															
zircon (n = 34) all LA-ICP-MS	0.1	4.3	0.1	0.3	-	3.1	5.6	11.2	14.9	17.7	18.9	19.3	19.7	22.7	24.0
ca.397–405 (n=14) LA-ICP-MS	0.3	4.1	0.1	0.4	-	3.7	6.3	12.2	17.0	21.3	23.7	25.5	26.8	29.9	31.5
ca. 406–413 (n=20) LA-ICP-MS	0.03	4.4	0.1	0.2	-	2.7	5.1	10.5	13.4	15.2	15.5	14.9	14.7	17.6	18.8
zircon (n = 14) all solution ICP-MS	1.1	5.9	bdl	bdl	-	4.5	9.9	20.1	22.0	24.2	25.9	29.0	27.1	32.0	39.5
ca.400–402 (n=5) solution ICP-MS	bdl	7.1	bdl	bdl	-	5.9	12.8	24.2	27.7	32.2	35.3	40.4	37.8	43.0	51.6
ca.405 (n=1) solution ICP-MS	bdl	0.3	bdl	bdl	-	3.5	7.9	20.8	20.7	23.6	31.6	44.7	51.3	75.6	114.4
ca. 407–409 (n=8) solution ICP-MS	1.1	5.7	bdl	bdl	-	3.7	8.4	17.4	18.6	19.3	19.4	19.9	17.5	19.6	22.6
NW13-02-G, Saltaneset eclogite (garnet-quartz layer)															
zircon (n = 14) all LA-ICP-MS	0.02	5.2	0.1	0.2	-	2.5	3.8	9.3	13.4	17.2	18.9	20.9	24.0	30.4	36.6
ca.397–405 (n=5) LA-ICP-MS	0.02	6.3	0.1	0.3	-	2.7	4.5	10.4	16.5	21.2	24.0	27.2	30.5	37.4	36.2
ca. 406–413 (n=9) LA-ICP-MS	0.01	4.5	0.1	0.2	-	2.3	3.4	8.6	11.7	14.9	16.0	17.4	20.4	26.5	36.8
zircon (n=4) all solution ICP-MS	1.2	6.9	bdl	0.3	-	5.1	10.0	26.5	34.5	37.2	39.8	42.9	43.2	50.9	63.2
ca.401 (n=2) solution ICP-MS	1.2	7.7	bdl	bdl	-	6.0	12.9	34.3	44.1	48.8	53.0	58.0	57.0	67.4	77.4
ca. 409 (n=2) solution ICP-MS	bdl	5.4	bdl	0.3	-	4.1	7.0	18.7	25.0	25.6	26.7	27.9	29.4	34.5	48.9
NW13-02-O, Saltaneset eclogite (omphacite layer)															
zircon (n = 5) all LA-ICP-MS	0.2	7.7	1.9	2.2	-	4.6	5.5	9.2	14.2	16.3	20.3	22.7	27.9	33.9	40.0
zircon (n = 1) solution ICP-MS	bdl	bdl	bdl	0.4	-	5.4	8.3	23.0	29.0	31.8	35.6	37.0	37.2	41.2	51.4

Trace-element data normalized to chondrite values of Sun and McDonough (1989)

* Pm = (Sm*Nd)^0.5

Eu/Eu*=Eu/(Sm*Gd)^0.5

Hf	Eu/Eu*	Lu/Gd norm.	Th/U	$^{206}Pb/^{238}U$ date (Ma)	Error
111068	0.9	3.2	0.03	400.5	4.7
116117	0.8	3.2	0.03	403.0	5.3
121553	0.9	4.4	0.03	403.0	5.2
129903	0.9	3.1	0.03	400.6	5.3
114563	0.7	3.0	0.04	404.8	5.1
170874	0.8	1.9	0.03	410.7	5.6
155340	1.2	1.0	0.03	411.2	5.3
118252	0.6	1.5	0.03	411.6	5.0
116796	0.7	2.0	0.02	407.2	5.1
108350	0.7	3.0	0.01	406.3	5.3
113592	1.0	2.4	0.02	401.8	5.3
118058	0.8	1.7	0.03	403.9	5.5
130777	1.1	1.4	0.03	412.8	5.4
150485	1.2	1.4	0.04	408.8	5.3
143689	1.0	2.5	0.03	409.1	5.4
130097	1.4	1.7	0.03	409.6	5.4
111748	1.0	1.5	0.02	401.7	5.5
110777	1.0	1.6	0.02	404.2	5.5
118058	0.8	3.5	0.02	406.4	5.4
134951	1.4	1.4	0.04	408.2	5.3
123010	0.9	1.3	0.03	407.9	5.2
126602	0.9	1.3	0.03	410.2	5.2
128932	1.1	1.9	0.03	410.6	5.5
138058	0.9	2.2	0.02	405.0	5.8
251456	0.6	2.9	0.02	398.1	8.7
235922	1.2	3.4	0.02	402.6	8.8
295146	0.4	1.9	0.02	406.9	9.0
282524	0.9	6.2	0.01	407.8	5.1
254369	1.0	1.9	0.03	404.1	5.1
122816	0.9	0.6	0.03	410.5	5.3
138835	0.7	2.4	0.03	411.4	5.1
157282	0.8	1.3	0.03	412.0	5.3
120388	0.9	2.0	0.03	411.0	5.3
117573	1.9	2.1	0.02	408.8	5.7
119903	1.1	1.8	0.03	409.4	5.3
107767	1.5	3.2	0.02	401	5
110583	1.0	2.8	0.02	397.2	5.2
107767	0.8	3.7	0.02	402.4	5.2
110291	1.2	2.3	0.03	403.9	5.3
130097	0.7	128.2	0.07	429.8	5.7
91359	0.4	48.1	0.63	475.2	6.1
119320	0.9	59.0	0.09	441.0	5.6
96408	0.4	42.3	0.80	452.5	5.7
86214	0.6	51.4	0.41	471.0	6.4
258252	0.5	1.9	0.00	413.4	9.8
286408	1.0	3.9	0.01	411.5	9.0

245631	1.0	2.9	0.01	407.3	8.8
253398	1.2	3.1	0.01	410.0	9.2
281553	1.2	3.5	0.02	396.8	8.8
269903	0.6	3.7	0.02	397.4	8.7
246602	0.6	10.4	0.02	407.2	8.9
292233	0.7	3.7	0.02	412.3	9.2
275728	0.6	3.4	0.02	407.1	4.8
267961	0.7	3.4	0.03	398.0	5.0
277670	0.2	32.8	0.34	795.7	17.4
105825	0.4	7.9	1.58	875.0	21.2
218447	0.4	25.8	0.38	638.3	13.9
192330	0.2	13.9	0.28	889.8	20.0
144660	0.2	11.1	1.57	938.8	20.7
253398	0.4	79.6	0.23	739.1	16.8
187379	0.3	56.9	0.20	875.7	18.8
99029	0.3	11.7	1.48	920.8	20.1
215534	0.3	77.2	0.22	808.5	17.7
165049	0.2	11.5	1.34	951.2	20.6
270874	0.3	54.7	0.29	871.6	18.9
204854	0.3	18.6	0.49	881.4	19.4
231068	0.6	45.8	0.08	636.0	14.4
265049	0.3	22.5	0.10	530.7	12.6
294175	0.4	44.1	0.07	548.5	12.5
159223	0.4	16.2	0.52	590.1	13.7
210680	0.4	64.9	0.24	873.4	19.8
258252	0.2	73.4	0.25	896.5	19.9
215534	0.3	18.6	0.52	843.9	19.3
258252	0.2	84.3	0.24	870.2	19.0
253398	0.3	41.7	0.33	930.2	19.9
141748	0.3	12.2	0.76	771.4	17.2
177670	0.3	62.5	0.18	837.9	18.6
175728	0.3	14.9	1.27	877.0	21.3
204854	0.3	15.1	1.25	966.2	21.2
203883	0.3	68.1	0.24	914.9	20.1
230097	0.4	74.8	0.31	909.8	20.1
212621	0.3	35.3	0.38	884.3	19.6
233010	0.2	24.8	0.57	796.0	15.2
244660	0.3	13.2	0.29	549.3	7.7
268932	0.5	97.9	0.14	718.0	17.5
177670	0.3	10.3	1.22	746.8	9.5
222330	0.5	39.4	0.37	889.6	11.0
278641	0.3	53.0	0.22	754.9	10.4
233010	0.2	14.5	0.83	788.0	12.7
207767	0.4	22.3	0.48	606.6	7.7
264078	0.3	21.9	0.11	542.0	8.8
260194	0.8	8.9	0.03	398.4	8.1
240777	0.9	5.3	0.03	406.8	3.3
227184	0.8	2.9	0.02	407.3	3.1
316505	0.7	3.2	0.03	414.2	3.2
300000	1.5	5.9	0.02	414.4	5.8
88350	0.7	40.2	0.62	1130.3	24.4
221359	0.7	109.6	0.06	458.6	9.6
85146	0.7	49.6	0.68	1248.8	26.5
213592	0.5	67.1	0.20	842.6	17.8
131068	0.6	76.8	0.19	747.1	16.6
154369	0.4	75.5	0.22	525.2	10.7
227184	0.3	65.5	0.24	448	9

76117	0.6	43.0	0.50	488.6	10.1
77961	0.5	50.3	0.72	867.2	18.0
79320	0.6	61.9	0.40	649	5
81942	0.6	48.4	0.47	440.1	3.6
207767	0.6	90.9	0.25	633.5	5.3
93883	0.3	73.5	0.20	738.2	6.8
210680	0.3	46.4	0.26	810.2	7.0
80971	0.5	23.5	0.87	1600.1	11.0
85534	0.6	24.7	0.60	1255	13
102913	0.3	67.4	0.22	825.3	7.4
89515	0.4	9.8	1.13	609.8	7.1
243689	0.5	81.3	0.29	940	9
220388	0.4	100.3	0.08	477.2	3.9
85534	0.6	31.5	0.62	634.3	8.3
181553	0.4	77.8	0.18	887.8	11.5
184466	0.5	57.7	0.21	899.9	10.8
187379	0.4	67.9	0.22	855.2	11.4
105825	0.8	94.7	0.43	1468	19
154369	0.6	72.3	0.46	1063	16
276699	0.8	4.3	0.03	421.7	5.2
192233	0.4	65.6	0.21	823.2	11.5
187379	0.3	88.6	0.18	861.1	11.0
207767	0.4	61.9	0.14	728.3	11.8
187379	0.4	52.5	0.21	691.1	9.1
144660	0.8	150.7	0.25	746.4	9.7
241748	0.5	58.4	0.31	860	15
77961	0.5	31.4	0.63	1079.9	14.5
162136	0.6	101.3	0.23	512.5	9.2
214563	0.2	96.2	0.19	1486	19
177670	0.5	53.2	0.23	891.7	12.0
191262	0.6	76.9	0.20	784.6	11.1
165049	0.4	68.6	0.45	1508	21
175243	0.5	53.3	0.20	632.2	8.6

Lu/Gd norm.	Eu/Eu*	sum MREE–HREE (ppm)	Zr (ppm)	Hf (ppm)	Y (ppm)	Sc (ppm)	Zr/Hf	Y/Sc	Th/U	$^{206}Pb/^{238}U$ <Th> Date (Ma)	±2σ abs
1.9	0.9	35	485406	11766	101	332	41	0.3	0.03	401.9	0.2
2.1	1.4	36	484839	12357	99	307	39	0.3	0.03	401.9	0.4
2.5	1.2	29	478214	12232	1464	5113	39	0.3	0.03	402.1	0.3
1.0	1.0	19	483197	14086	49	292	34	0.2	0.03	407.9	0.3
5.5	0.9	36	483368	13899	75	271	35	0.3	0.04	405.1	0.2
2.3	1.3	18	483238	14054	51	287	34	0.2	0.03	408.3	0.2
3.4	0.9	30	484725	12545	66	283	39	0.2	0.01	401.9	0.2
1.9	1.2	23	483891	13380	59	294	36	0.2	0.03	407.9	0.3
1.2	1.1	18	483494	13788	47	300	35	0.2	0.03	409.6	0.3
0.5	NA	13	483698	13587	33	318	36	0.1	0.03	408.7	0.5
1.2	1.1	19	484199	13043	49	326	37	0.2	0.03	407.3	0.3
1.2	1.0	30	484863	12373	75	309	39	0.2	0.02	401.3	0.4
0.9	1.0	20	483477	13769	47	327	35	0.1	0.03	408.6	0.3
2.9	1.5	14	483245	14002	52	328	35	0.2	0.03	407.2	0.7
5.3	0.5	151	483081	13697	345	350	35	1.0	0.1	425.4	0.2
2.2	0.8	44	483408	13720	114	349	35	0.3	0.03	401.5	0.2
12.7	0.3	294	481435	14971	592	322	32	1.8	0.2	555.7	0.3
8.3	0.5	150	481534	15294	327	322	31	1.0	0.1	449.7	0.2
2.3	1.0	51	483711	13411	140	339	36	0.4	0.03	401.4	0.2
1.7	0.8	23	481238	15998	75	305	30	0.2	0.02	408.8	0.2
3.4	0.8	26	481675	15581	66	292	31	0.2	0.01	408.9	0.4

11.9	0.5	1498	483116	9048	3533	388	53	9.1	1.0	1512.2	0.8
46.5	0.7	274	484808	11738	455	358	41	1.3	0.3	866.9	0.8
2.2	0.7	31	482339	14859	88	311	32	0.3	0.04	396.7	1.4

Table 5

Chondrite normalized garnet LA-ICP-MS trace-element data and calculated zircon-garnet partition coefficients from the Western Gneiss Region: Ulsteinvik and Saltaneset eclogites

***In situ* garnet analyses**	La	Ce	Pr	Nd	Pm*	Sm	Eu	Gd	Tb	Dy	Ho	Er	Tm	Yb	Lu	Eu/Eu*	Lu/Gd norm.
8815E, Ulsteinvik eclogite																	
garnet 1 8815E-low-1	0.07	0.3	1.3	5.5	11.8	25.1	39.2	39.7	43.9	38.4	36.3	40.2	39.8	37.1	39.2	1.2	1
8815E-low-2	0.04	0.4	2.3	7.6	15.9	32.9	48.2	43.5	44.3	39	33	36.2	34.5	34	34.5	1.3	0.8
8815E-low-3	0.02	0.4	2.3	7.5	15.9	33.5	50.4	44.3	44.5	39.2	33.9	38.6	36.3	35.1	34	1.3	0.8
8815E-low-4	0.02	0.4	2.1	7.7	15.7	32.2	48.2	45	44.0	38.7	32.9	35.7	34.4	34.2	33.2	1.3	0.7
8815E-low-5	0.02	0.3	1.9	7.1	15.4	33.6	46.9	43.3	43.9	39.1	33.8	37	35.1	33.7	33.9	1.2	0.8
8815E-low-6	0.02	0.2	1.6	7	14.9	31.5	47.3	41.9	43.6	37.6	32.6	36.6	34.2	31.6	35.1	1.3	0.8
8815E-low-7	0.02	0.4	2.2	8.9	17.7	35.1	47.8	43.5	44.6	38.9	32.9	34.8	35.3	32.2	32	1.2	0.7
8815E-low-8	0.02	0.4	2.4	8.7	17.9	36.6	48	45	45	37.6	31.5	36.2	34.5	33.3	33.4	1.2	0.7
8815E-low-9	0.04	0.5	2.3	9.4	18.4	35.9	49.5	43.6	46.1	37.5	33.7	36.1	34.9	33.3	33.7	1.2	0.8
8815E-low-10	0.03	0.5	2.9	8.8	18	36.8	48.9	44.3	41.5	38.6	33	36.3	33	33.1	34	1.2	0.8
8815E-low-11	0.02	0.4	2.5	9.5	18.4	35.5	49.1	45.5	43.2	37.2	33.6	37	33.8	33.7	33.3	1.2	0.7
8815E-low-12	0.03	0.4	2.5	9.4	18.7	37.4	49.5	46.7	44.5	38.9	33.7	37.3	33.1	32.5	34.6	1.2	0.7
8815E-low-13	0.02	0.5	2.6	9.5	19.2	38.8	50	45.5	45.8	37.8	34.5	36.1	33.7	35.4	35.8	1.2	0.8
8815E-low-14	0.04	0.5	3.1	10.5	20	38.2	50.5	43.4	43.9	40.2	36.9	36	33.9	34.7	34.4	1.2	0.8
8815E-low-15	0.02	0.5	3.2	10.2	19.7	38.1	48.8	43.1	42	36.9	34.9	36.7	34.3	34	35	1.2	0.8
8815E-low-16	0.02	0.5	2.9	10.1	19	35.8	50.3	43	42.6	39.1	35.5	35.3	36	34.2	34.8	1.3	0.8
8815E-low-17	0.03	0.5	3.1	10.5	20.2	38.9	50	44.1	43.7	38	34	36.5	35.4	35.1	35	1.2	0.8
8815E-low-18	0.1	0.8	3.6	12.6	22.5	40.1	50.5	43.8	43.6	39.5	33.5	35.4	33.9	33.6	34.3	1.2	0.8
8815E-low-19	0.02	0.6	3.3	11	20.2	37.1	51.8	45.3	42.8	37.2	33.3	35.4	36.3	35	32.2	1.3	0.7
8815E-low-20	0.03	0.6	3.3	11	20.9	39.6	48.9	42.6	42.8	37.1	33.9	36.1	34.1	35.6	33.6	1.2	0.8
8815E-low-21	0.03	0.6	3.3	11.2	20.4	37.4	49.8	42.7	40.8	38.9	35.6	36.4	35.2	35.5	34.7	1.2	0.8
8815E-low-22	0.06	0.7	3.5	12.1	21.2	37.1	48.9	42.4	42.4	37.2	33.8	35.8	34.2	33.7	33.5	1.2	0.8
8815E-low-23	0.05	0.6	3.5	12.2	21.3	37.1	50.2	42.4	41.7	37.7	33.1	35.2	34.1	35.5	35.4	1.3	0.8
8815E-low-24	0.1	0.8	4.1	13.4	22.4	37.6	48.2	42.4	42	38.1	34.8	35.1	34.9	36.3	33.3	1.2	0.8
8815E-low-25	0.05	0.8	3.8	12.7	21.9	37.7	51.8	46.4	44.8	39	34.1	36.2	34.3	35.7	36.1	1.2	0.8
8815E-low-26	0.05	0.7	3.8	12.4	21.4	37	49.1	43.8	43.8	39.2	34.8	35.7	35	34.9	33.5	1.2	0.8
8815E-low-28	0.06	0.7	3.6	12.5	21.6	37.4	52	41.7	40	39	36	37.3	36.9	35.8	34	1.3	0.8
8815E-low-29	0.04	0.7	3.5	11.7	20.9	37.4	50.9	42.7	40.9	38	34.7	37	34.7	36.7	34.6	1.3	0.8
8815E-low-30	0.03	0.5	2.7	9.6	19.3	38.4	51.8	42.7	40.7	36.4	34.6	34.9	34.3	35.4	33.5	1.3	0.8
8815E-low-31	0.07	0.6	2.6	9.6	18.5	35.8	45.8	41	40.9	37.6	35.4	37.2	38	37.3	35.8	1.2	0.9
8815E-low-32	0.05	0.6	3.2	10.2	19.8	38.4	51.7	44.9	43.1	38.5	34.3	35.6	33.8	33.7	32.8	1.2	0.7
8815E-low-33	0.06	0.6	2.6	9.9	19	36.4	52.8	47.7	42.8	38.9	35.1	34.9	34.8	35.5	36.3	1.3	0.8
8815E-low-34	0.03	0.4	1.8	6.9	14.6	30.7	44.8	45	43.1	39.4	36.4	35.9	33.4	35.5	36.5	1.2	0.8
8815E-low-35	0.02	0.2	1.4	4.6	10.7	25.1	39.5	40.7	40.8	37.5	35.5	36.6	37.2	39.8	38	1.2	0.9
8815E-low-36	0.03	0.3	1.9	7.3	15.6	33.4	48.2	43.8	44.5	39.1	34.7	35.4	33.4	36.0	35	1.3	0.8
8815E-low-37	0.03	0.4	2.5	9.1	18.2	36.6	50	43.5	44.3	38.5	35.3	35.4	31.9	36.0	32.6	1.3	0.7
8815E-low-38	0.2	0.8	3.2	10.3	19.5	37.1	52	43.8	43.5	40.2	35.1	35.4	35.6	35.6	33.4	1.3	0.8
8815E-low-39	0.05	0.6	3	10.5	19.9	37.8	51.4	46.3	43.3	41.6	35.7	36.4	34.5	35.0	35.3	1.2	0.8
8815E-low-40	0.05	0.6	3.1	11	20.9	39.7	50.4	44.9	42.9	38.1	36.3	35.4	34	37.1	33.9	1.2	0.8
8815E-low-41	0.03	0.5	2.9	9.9	18.7	35.4	48	44.9	43.2	40	35.5	37.9	35.6	35.2	33.4	1.2	0.7
8815E-low-42	0.03	0.5	2.9	9.4	18.4	36	46.6	42.3	43.2	40.6	36.9	36.5	36.5	35.8	35.3	1.2	0.8
8815E-low-43	0.02	0.4	2.4	8.8	17.2	34	47	42.7	41.7	40.3	37.7	37.9	36.5	35.8	34.5	1.2	0.8
8815E-low-44	0.03	0.5	3.1	11.1	20.4	37.6	50.4	44.4	46.1	40.1	38.2	36.1	35	37.0	34.3	1.2	0.8
8815E-low-45	0.06	0.6	3.5	11.4	20.9	38.2	50.2	45.5	43.6	39.1	34.8	35.9	34.9	35.4	33.3	1.2	0.7
8815E-low-46	0.05	0.6	3.9	11.3	20.3	36.6	50.2	43.9	43.7	40	36.8	36.9	34.8	36.5	33.7	1.3	0.8
8815E-low-48	0.05	0.8	4	12.1	21.4	37.9	50.9	42.3	42.9	40.7	36.7	36.1	35	35.5	35	1.3	0.8
8815E-low-49	0.06	0.9	4.2	13.1	22.1	37.2	46.4	43.8	43	38.8	36.1	36.8	35.9	36.6	32	1.2	0.7
8815E-low-50	0.05	0.7	4.2	12.4	21.8	38.4	47.5	44.4	42.8	40.6	34.9	36.9	34	36.6	33.3	1.2	0.8
8815E-low-51	0.06	0.8	3.9	11.6	20.7	37	48.8	44.5	43	38.9	35	35.9	33.6	35.3	34.7	1.2	0.8
8815E-low-52	0.04	0.7	3.8	11.9	21.5	38.5	50.2	42.5	42	38.9	35.7	36.3	35.6	36.3	33	1.2	0.8
8815E-low-53	0.05	0.7	3.7	11.9	21.7	39.9	49.5	41.6	41	38	34.6	35.5	33	34.2	32.9	1.2	0.8
8815E-low-54	0.06	0.6	3.8	11.2	20.3	36.7	49.1	45	41.4	38.7	36.2	34.6	35.3	33.8	33.7	1.2	0.7
8815E-low-55	0.06	0.6	3.5	11.8	21.1	37.8	46.8	44.3	39.4	38.9	34.4	36.2	35.7	35.3	33.7	1.1	0.8
8815E-low-56	0.04	0.6	3.3	11	20.4	38	52.5	45.6	41.7	39.6	34.2	35.6	33.4	33.3	33.5	1.3	0.7
8815E-low-57	0.03	0.5	3.4	11.5	20	34.6	50.4	42	42.7	40	35	36.2	34.2	33.9	35.8	1.3	0.9
8815E-low-58	0.04	0.5	2.9	11	19.3	34	49.3	42.9	41.4	39.4	34.3	34.9	35	35.7	35	1.3	0.8
8815E-low-59	0.03	0.5	3.2	10.9	19.8	36	48.6	45.2	41	40.7	34.4	34.1	33.5	33.9	34.8	1.2	0.8
8815E-low-60	0.02	0.5	3.1	10.5	20.1	38.2	48	44.5	42	39.9	34.2	36.4	34.6	32.9	34.6	1.2	0.8

8815E-low-61	0.03	0.4	3	11.1	19.8	35.4	48.4	42.1	40.5	38.9	35.1	36	34.5	34.9	33.7	1.3	0.8
8815E-low-62	0.03	0.4	2.7	10.6	19.6	36.2	48.4	43.2	41.4	37.8	33	34.5	33.6	35.5	36.1	1.2	0.8
8815E-low-63	0.03	0.5	3	11.2	20.4	37.4	51.4	47	41.8	39.8	33.8	36.7	32.8	36.4	34.7	1.2	0.7
8815E-low-64	0.02	0.3	2.8	10.2	19.1	35.7	49.9	43.4	44.2	39.7	34.3	35.8	34.2	34.9	33.9	1.3	0.8
8815E-low-65	0.01	0.3	2.5	10.5	19.7	37.1	48.8	43.6	41.3	38.7	32.6	35.7	34.1	35.5	32.5	1.2	0.7
8815E-low-66	0.01	0.3	2.4	9.1	18.3	36.5	47.2	42.9	40.2	39.3	33.5	34.9	34.4	33.5	35.2	1.2	0.8
8815E-low-67	0.003	0.2	1.9	8.4	16.5	32.4	47.1	42.9	42	39.1	32.5	34.3	33.2	34.3	33.7	1.3	0.8
8815E-low-68	bdl	0.2	2.0	9.5	18.2	34.8	48.6	43.7	42.3	38.5	33.2	35.4	34	34.7	34	1.2	0.8
8815E-low-69	bdl	0.2	1.7	7.9	16.3	33.6	46.1	44.4	42.3	38.1	33.5	34.8	31.3	33.9	32.7	1.2	0.7
8815E-low-70	0.01	0.2	1.7	7.8	16.6	35.1	48.4	45.9	41.8	40	34.8	35.1	32.5	35.4	31.7	1.2	0.7
8815E-low-71	0.02	0.2	1.6	6.9	14.3	29.5	42	41.2	39.8	37.7	34.7	33	32.1	33.7	34.8	1.2	0.8
8815E-low-72	0.001	0.2	1.4	7.1	14.6	30.1	46	42.8	40.3	37.6	33.5	34.4	30.6	33.3	31.7	1.3	0.7
Ulsteinvik eclogite-8815E-garnet 1 recrystallized rim																	
8815E-low-73	bdl	0.09	0.9	4.4	11	27.2	39.9	40.4	40.1	37.5	34.7	34.2	35.5	35	31.4	1.2	0.8
8815E-low-74	bdl	0.03	0.2	0.9	2.9	9	27.9	39.3	49.4	45.3	38.4	35.6	32.8	35	34	1.5	0.9
8815E-low-75	bdl	0.05	0.5	2.8	7.7	21.4	33.6	36.5	37.2	38.5	35.5	35.1	33.5	34.6	34.3	1.2	0.9
8815E-low-76	0.01	0.02	0.03	0.4	1.7	7.1	21.4	32	43.1	40.2	33.1	34.2	33.4	35.1	36.6	1.4	1.1
8815E-low-79	bdl	0.004	bdl	0.1	0.6	2.9	9.7	19	28.3	35.5	39	41.8	44.5	48.5	45.6	1.3	2.4
8815E-low-80	bdl	bdl	0.02	0.1	0.5	2.7	6.6	13.2	25.8	35.7	40.7	44.5	46	52.6	49.5	1.1	3.8
8815E-low-81	bdl	0.02	0.1	0.5	1.7	6.3	19.2	30.9	38.4	38.9	34.5	34.8	34.8	36.7	35.2	1.4	1.1
8815E-low-82	bdl	0.01	0.1	0.3	1.3	5.4	17.6	28	39.6	40.5	35.3	32.9	29.6	33.2	30.1	1.4	1.1
8815E-low-83	bdl	0.01	0.03	0.6	2.1	7.4	21.1	31.8	42.3	37.7	34	35.4	34.4	37	37.4	1.4	1.2
8815E-low-84	bdl	0.003	0.1	0.3	1.1	4.2	13.2	22.7	34.2	38.4	34.1	36.4	36.2	38.8	35.2	1.4	1.5
8815E-low-85	bdl	0.02	0.1	0.4	1.6	6.2	18.9	29	39	36.7	34.7	33.3	34.1	36.6	34.4	1.4	1.2
8815E-low-86	bdl	0.002	0.04	0.3	1.2	4.2	13.5	22	35.6	36.4	36	37	36.5	38	35.3	1.4	1.6
8815E-low-87	bdl	bdl	0.01	0.3	1.1	4.4	11	22.4	33.5	41.3	40.4	43.3	45.6	46.5	43.1	1.1	1.9
8815E-low-88	0.001	bdl	0.05	0.4	1.5	6	16.9	25.5	38	40.1	38.5	37.1	41.3	40.6	39.2	1.4	1.5
8815E-low-89	0.004	0.01	0.05	0.3	1.3	5.1	15.9	25.9	39.9	40.9	38.3	37.3	40.1	44	39.4	1.4	1.5
Ulsteinvik eclogite-8815E-garnet 2																	
8815E g2-1	0.01	0.08	0.9	4.3	10	23.1	34	32.2	39.6	38.1	37.2	39.5	38	39.8	38	1.2	1.2
8815E g2-2	0.01	0.06	0.6	3.0	6.6	14.6	22.8	25.8	40.6	46	44.0	39.8	40.4	37.5	36.8	1.2	1.4
8815E g2-3	0.01	0.3	2.0	7.8	17	37	44.8	42.1	43.7	39.2	36.0	35.5	36.5	36.8	36.6	1.1	0.9
8815E g2-4	0.01	0.1	1.3	6.2	13.2	27.9	37.3	36.6	42.8	41.5	37.2	37.6	38.0	40.5	40	1.2	1.1
8815E g2-5	bdl	0.3	2.3	9.0	18.6	38.3	48	43.7	43.8	39.8	37.3	37.1	34.2	36.2	37.2	1.2	0.9
8815E g2-6	0.01	0.3	2.4	9.0	17.7	35.1	49.8	43.4	44.3	38.2	36.4	37.0	39.4	37.1	36	1.3	0.8
8815E g2-7	0.01	0.3	2.7	10.5	19.8	37.3	47.5	42.1	42.1	40.2	36	34.3	35.6	34.6	36.3	1.2	0.9
8815E g2-8	0.01	0.3	2.6	10.0	19.9	39.5	48	40.5	43.1	38.8	36.9	35.8	36.8	37	39.1	1.2	1.0
8815E g2-9	0.002	0.3	2.8	10.9	20.2	37.7	49	40.9	45.4	40.7	36.1	36.1	37.5	33.5	37.9	1.2	0.9
8815E g2-10	0.01	0.3	2.9	10.0	18.9	35.8	48	40.3	44.1	39.1	35.1	36.9	36.9	34.5	36.4	1.3	0.9
8815E g2-11	0.005	0.3	2.9	10.5	19.7	37.1	47.7	42.9	44.3	38.8	35.3	34.6	34.3	33.5	37.2	1.2	0.9
8815E g2-12	0.03	0.4	2.9	10.5	19.5	36.4	45.5	42.7	43.4	37.7	34.3	34.8	37.7	34.6	35.5	1.2	0.8
8815E g2-13	0.02	0.3	2.8	10.5	20	38	49.3	42.4	43.9	39.2	34.9	35.8	38.1	36.1	36.6	1.2	0.9
8815E g2-14	0.003	0.4	2.8	10.7	19.5	35.8	46.8	39.7	43	36.9	34.5	35.1	36.6	34.2	35.9	1.2	0.9
8815E g2-15	0.01	0.4	2.8	10.5	20.2	38.8	48.1	41.9	43.1	39	34.3	35.5	35.1	34.3	37.4	1.2	0.9
8815E g2-16	0.02	0.4	2.7	10.9	20.2	37.2	47.7	40.5	43.5	37.7	34	35.9	35.5	34.8	35.7	1.2	0.9
8815E g2-17	0.01	0.4	2.8	10.9	20.5	38.6	46.8	42.2	43.9	38.7	31.9	34.4	34	34.3	37	1.2	0.9
8815E g2-18	0.01	0.4	3.0	10.9	19.9	36.4	49.9	39.2	43.4	38.9	33.3	34.9	37.1	34	37.1	1.3	0.9
8815E g2-19	0.001	0.4	2.6	10.3	19.4	36.5	45.5	39.3	43.6	37.7	33.4	34.8	33.9	34.2	35.9	1.2	0.9
8815E g2-20	0.01	0.4	2.9	10.7	19.6	35.9	47	41	43.4	37.8	35.5	34.9	33.8	33.9	38	1.2	0.9
8815E g2-21	0.01	0.3	2.6	10.9	19.9	36.4	46.4	40.4	42.4	38.1	34.2	34.9	36	33.9	34.6	1.2	0.9
8815E g2-22	0.01	0.4	3.2	10.9	20.1	37.0	45.9	40.4	42.6	37.7	34.5	36.1	35.1	34.2	34	1.2	0.8
8815E g2-23	0.01	0.4	3.1	10.9	20.1	37.0	48	42.9	42.8	37.8	35.4	35.1	36.3	34.9	36.8	1.2	0.9
8815E g2-24	0.02	0.5	3.3	11.3	21.3	40	48	41.8	43.8	37.6	35.9	35.8	35.8	36.2	37.6	1.2	0.9
8815E g2-25	0.01	0.4	2.8	10.9	20.3	37.7	47.7	42.2	43.4	39.3	35.3	34.9	34.7	34.3	33.1	1.2	0.8
8815E g2-26	0.004	0.4	3.0	9.9	18.9	35.9	48.0	40.3	40.6	36.8	35.7	34.1	34	33.3	33.6	1.3	0.8
8815E g2-27	0.01	0.5	2.9	10.9	20.6	39.2	47.7	42.3	42.0	36.9	34.4	35.2	35.7	33.8	36.4	1.2	0.9
8815E g2-28	0.02	0.5	3.2	10.6	20.9	40.9	50	43.8	45.1	38.2	36.4	36.3	36.2	33	33.4	1.2	0.8
8815E g2-29	0.01	0.4	2.7	10.3	19.2	35.7	49.1	40	42.9	39.5	35.8	35.1	35.4	35.7	36.7	1.3	0.9
8815E g2-30	0.01	0.4	2.7	10.6	19.2	34.9	47.9	43.5	44.9	38.4	35.5	36.5	37.3	36.2	35.8	1.2	0.8
8815E g2-31	0.01	0.4	2.8	10.9	19.9	36.6	49.3	40.2	42.7	37	34.1	36.4	35	34.7	38	1.3	0.9
8815E g2-32	0.01	0.3	2.9	11.1	19.7	35.2	48.9	43.3	44.8	38.9	34.5	35.8	33.7	34.9	37.4	1.3	0.9
8815E g2-33	0.01	0.4	2.9	10.5	19.8	37.2	47.9	42.2	43.2	37.8	36.2	35.2	34.3	35.3	34.9	1.2	0.8
8815E g2-34	bdl	0.4	2.5	9.7	19.1	37.6	47.7	40.7	41	39.3	34.3	35.1	33.6	35.4	36.1	1.2	0.9

8815E g2-35	0.01	0.3	2.5	9.2	17.8	34.6	45.2	41.3	40.9	37.4	33.2	35.9	35.3	34.7	34.8	1.2	0.8
8815E g2-36	0.01	0.3	2.4	9.4	18.1	34.6	45.4	41.8	44.2	37.2	33.1	34.9	34.6	34.2	36.6	1.2	0.9
8815E g2-37	0.02	0.3	2.3	9.9	18.9	36.1	47.3	40.9	41.5	38.5	33.5	33.6	35.9	35.5	34.9	1.2	0.9
8815E g2-38	0.01	0.3	2.3	9.6	18.9	37.2	45	40.7	43.9	37.8	34	35.6	33.8	34.5	33.3	1.2	0.8
8815E g2-39	bdl	0.3	2.4	9.5	18.4	35.9	46.4	41.1	42.5	36.9	34.5	34.8	34.7	35.1	32.7	1.2	0.8
8815E g2-40	0.01	0.3	2.4	8.9	17.6	34.7	45.9	41.1	40.4	36.7	34.2	33.5	34.8	35.5	34.5	1.2	0.8
8815E g2-41	0.02	0.3	2.2	8.9	17.6	34.9	46.3	41.6	40.8	37.4	35.9	35.4	35.5	35.8	36.2	1.2	0.9
8815E g2-42	0.02	0.3	2.3	9.1	18.1	35.8	44.7	41.1	42.9	37.8	34.9	35.6	34.8	35.1	34.6	1.2	0.8
8815E g2-43	0.01	0.3	2.3	8.8	17.5	35.1	45.2	42.8	42.4	37.2	34.6	32.5	34.6	33.7	34.1	1.2	0.8
8815E g2-44	0.01	0.2	2.3	8.9	18.3	37.2	44.5	39.9	40.4	37.2	34.6	34.6	35.3	34.7	35.2	1.2	0.9
8815E g2-45	0.02	0.4	2.3	9.3	18.6	37.1	45.9	41.9	43.1	37.4	34.8	33.6	33.2	34.6	36.1	1.2	0.9
8815E g2-46	0.01	0.3	2.1	8.8	18.1	37.2	47	42.8	41.8	38.4	35.6	34.6	33.6	35.7	33.9	1.2	0.8
8815E g2-47	0.01	0.3	2.1	8.4	17.8	37.7	46.1	40.6	43.6	38	35.4	35.9	34.2	36.5	32.6	1.2	0.8
8815E g2-48	0.001	0.3	2.1	8.5	17.4	35.5	46.8	42.4	41.4	37.5	34.7	35.1	34.9	34.9	33.6	1.2	0.8
8815E g2-49	0.002	0.3	2.5	10	18.6	34.4	47	41.9	40.3	37.9	33.6	35	34	35.4	32.4	1.2	0.8
8815E g2-50	0.01	0.3	2.2	9.1	17.7	34.3	47.7	42.1	41.1	36.1	33.8	35.8	32.9	34.9	33.7	1.3	0.8
8815E g2-51	0.02	0.3	2.1	9.8	19.1	37.5	47.3	43.3	44.3	37	34.2	34	33.6	35.2	34	1.2	0.8
8815E g2-52	0.03	0.3	2.4	9.7	19.2	38.3	49.6	44.3	46.5	37.8	35.1	34.4	34.1	37.1	33.3	1.2	0.8
8815E g2-53	0.01	0.4	2.6	10.2	19.1	35.8	46.3	43.9	42.4	36.7	33.6	33.9	31.7	33.4	36	1.2	0.8
8815E g2-54	0.02	0.4	2.5	10.5	20.2	38.7	47.9	42.2	43.4	38.5	34.8	36.1	35.8	36.3	35.6	1.2	0.8
8815E g2-55	0.02	0.3	2.4	9.4	18.5	36.4	46.3	44.7	43	38.4	33.3	34.8	34	33.6	34.7	1.1	0.8
8815E g2-56	0.02	0.3	2.0	8.5	17.1	34.3	45.7	41	42.5	37.7	34.1	35.2	32.2	34	32.5	1.2	0.8
8815E g2-57	0.02	0.4	2.6	9.4	18.5	36.4	48.2	42.8	41.6	38.1	35.1	35.1	34.3	35.3	35.8	1.2	0.8
8815E g2-58	0.01	0.3	2.2	9.6	19	37.6	49.3	44.5	42.2	38.6	34.5	34.4	34.6	35.8	33	1.2	0.7
8815E g2-59	0.03	0.3	2.3	8.9	17.7	35.3	48.6	45.2	41.6	37.4	33.9	33.8	33.8	33.2	35.7	1.2	0.8
8815E g2-60	0.02	0.3	2.0	9.4	19	38.3	48	42.5	41.8	39.6	34.2	35.2	35.3	35.5	33.7	1.2	0.8
8815E g2-61	0.03	0.4	2.4	8.8	17.6	35.3	47.9	42.6	44.3	38.6	33.4	35.4	35.1	33.1	34.6	1.2	0.8
8815E g2-62	0.03	0.3	1.9	8.8	17.1	33.2	46.6	40.5	42.2	38.2	33.1	34.1	32.7	34.5	32.6	1.3	0.8
8815E g2-63	0.01	0.3	1.8	7.7	16	33.2	48.6	43.6	44.1	36.9	34.7	35.3	32.6	33.9	33	1.3	0.8
8815E g2-64	0.02	0.3	1.8	7.8	16.1	33.4	45.4	42.7	44.2	37.9	32.2	33.3	32.9	33.3	33.7	1.2	0.8
8815E g2-65	0.02	0.3	1.8	7.7	16	33.4	49.5	42.1	43.2	37.6	34	32.7	32.8	33.7	33.3	1.3	0.8
8815E g2-66	0.01	0.2	1.5	6.6	14.1	30	44.6	44.3	43.3	38.2	35.2	34.8	35.9	36	34.6	1.2	0.8
8815E g2-67	0.01	0.2	1.5	6.9	14.6	30.9	45	45.2	43.1	39.8	35.8	34.3	33.1	35.8	31	1.2	0.7
8815E g2-68	0.01	0.2	1.6	7.1	14.6	30.2	45.6	42.4	42.4	38.5	35.5	34.8	33.7	35.2	32	1.3	0.8
8815E g2-69	0.01	0.3	1.7	8.4	16.7	33	47.3	43.7	41.6	39.2	35.5	34.1	34.2	34.7	33	1.2	0.8
8815E g2-70	0.01	0.2	1.2	6.1	13.4	29	43.9	42.5	43.1	38.6	36.3	35.2	34.8	34.2	33.9	1.3	0.8
8815E g2-71	0.003	0.3	1.6	6.5	14.1	30.5	43.7	41.8	43.9	38	36.7	35.8	35.3	35.7	35	1.2	0.8
Ulsteinvik eclogite-8815E-garnet 3																	
8815E g3-1	0.005	0.01	0.3	1.8	5	14.3	27.3	30.1	37.5	39.6	35	34.7	34.3	34.7	36.5	1.3	1.2
8815E g3-2	0.01	0.06	0.6	3.7	9.2	22.5	36.1	37.4	40.5	38.5	35.1	36.3	33.2	35.3	33.6	1.2	0.9
8815E g3-3	bdl	0.01	0.05	0.1	0.5	2.2	8.1	16	37.5	45.3	44.7	46	45.4	43.5	42.4	1.4	2.6
8815E g3-4	0.0008	0.01	0.1	0.4	1.2	4.1	10.9	19.7	31.9	35.8	35.6	37.8	39	39.6	40.9	1.2	2.1
8815E g3-5	bdl	0.01	0.05	0.2	0.8	3.3	8.1	15.4	28.7	34.3	35.6	36.5	38	36.6	38.3	1.1	2.5
8815E g3-6	0.01	0.09	0.9	4.0	9.7	23.8	37.9	38	42.3	39.1	35.3	36.6	36	37.1	37.8	1.3	1
8815E g3-7	bdl	0.004	0.05	0.2	0.6	2.2	8.4	16.8	36.1	41.8	42.1	44.5	42.3	44	43.6	1.4	2.6
8815E g3-8	0.002	0.01	0.1	0.3	1.4	6.1	20.4	32.4	45.9	43.5	35.8	38.3	37.2	36	37.4	1.4	1.2
8815E g3-11	0.003	0.01	0.1	0.4	1.9	8.6	18.7	29.4	39.6	37.3	31.9	34.7	34.2	34.6	33.2	1.2	1.1
8815E g3-12	bdl	0.01	0.1	0.4	1.7	7.3	17.0	28.6	41.9	38.7	34.2	33.5	31.3	31.1	34	1.2	1.2
8815E g3-13	0.004	0.02	0.1	0.5	1.8	6.8	20.1	30.6	43	37.9	33.8	33.6	31.3	33.9	34.6	1.4	1.1
8815E g3-14	bdl	0.02	0.1	0.4	1.6	5.7	14.8	25	39	39.6	37.7	40	38.2	40.2	41.3	1.2	1.7
8815E g3-15	bdl	0.01	0.1	0.2	1	4.6	14.6	23.9	40.2	38.3	34.4	33.8	33.8	34.1	35.2	1.4	1.5
8815E g3-16	bdl	0.01	0.04	0.1	0.7	4.4	13.5	23.2	38.2	37.9	35.8	36.4	33.8	33.4	34.8	1.3	1.5
8815E g3-17	bdl	0.02	0.1	0.5	1.6	5.8	17.3	25.1	39.6	38.7	35.2	38.4	39.3	39.8	39.7	1.4	1.6
8815E g3-18	0.03	0.4	2.2	7.6	15.5	31.6	48	42.8	42.3	38.5	36.9	36.8	35.6	34.5	34.4	1.3	0.8
8815E g3-19	0.05	0.5	2.5	8.7	16.7	32.3	44.4	43.1	44.2	40	38.1	38.3	35.2	34.7	33.2	1.2	0.8
8815E g3-20	bdl	0.01	0.02	0.04	0.2	1	4.4	13.9	35.4	48	52.9	53.9	51.6	52.5	51.9	1.2	3.7
8815E g3-21	0.003	0.06	0.3	3.2	8.2	21.3	33.7	34	39.9	37.7	34.7	34.9	35.3	37	35.1	1.3	1
8815E g3-22	bdl	0.04	0.4	2.8	7.3	19.4	32.1	36.1	40.3	39.0	35	36.8	35.8	35.7	34.6	1.2	1
8815E g3-24	0.01	bdl	0.01	0.1	0.2	0.7	4.7	11.8	31.4	44.2	46.5	50.6	45.7	46	42.9	1.7	3.6
8815E g3-26	0.004	0.05	0.3	2	5.4	14.3	27	30.7	37.7	39	38.5	41.8	39.7	44.4	41.3	1.3	1.3
8815E g3-27	0.01	0.04	0.5	2.7	6.5	15.9	30.7	32	40.1	39.6	35.5	40.9	39.5	40.9	39.8	1.4	1.2
8815E g3-28	0.02	0.05	0.5	2.8	7.4	19.2	34.1	34.9	38.6	39.6	35.9	39.9	39.4	41.4	39.4	1.3	1.1

NW13-02-G, Saltaneset eclogite (garnet-quartz layer)																	
NW13-02-G-garnet 1																	
Spot 91-rim	0.06	0.08	0.1	0.2	0.6	2.1	4.4	9.8	15.2	20	19.7	23.5	22.4	28	29.6	1	3
Spot 92	0.05	0.07	0.1	0.4	1.3	3.9	5.5	9.8	15.8	18.3	15.6	15.1	12.2	10.5	9.4	0.9	1
Spot 93	0.02	0.04	0.2	0.7	2.3	8	12.1	17.4	22	22.6	15.9	12	9.4	7.3	4.9	1	0.3
Spot 94	0.2	0.3	0.4	0.9	2.5	6.8	12.9	17.2	22.1	20.9	15.3	9.7	6.3	5.2	3.1	1.2	0.2
Spot 95	0.01	0.04	0.1	0.9	2.7	8.2	12.3	17.1	20.7	20.7	15.1	9.3	5.8	4.5	3.0	1	0.2
Spot 96	0.005	0.02	0.1	0.5	1.7	5	7.8	13.4	16.6	16	12.1	8.9	5.3	3.9	2.6	1	0.2
NW13-02-G-garnet 2																	
Spot 97-rim	0.02	0.04	0.1	0.6	1.6	4.3	5.8	9.8	17.3	19.3	19.7	22.5	22.6	24.5	24.5	0.9	2.5
Spot 98-rim	0.005	0.02	0.1	0.4	1.1	2.8	4.7	8.9	13.1	17.2	17.6	18.9	19.6	25.5	26.5	0.9	3
Spot 101-rim	0.01	0.02	0.1	0.3	1	3.5	6	9.8	14.5	21.1	19.7	21.3	23.3	28.4	28.2	1	2.9
Spot 103-rim	0.02	0.03	0.1	0.3	1.2	4.3	5.1	11.3	14.7	19.2	16.7	18.8	22.3	24.5	24.8	0.7	2.2
Spot 104	0.07	0.1	0.2	0.5	1.8	5.7	8.8	13	20.5	21.5	18.4	17	12.1	12.9	11.4	1	0.9
Spot 105	0.03	0.03	0.2	0.5	1.5	4.7	6.7	12.6	21.6	22	19.2	16.6	17.7	13.9	11.5	0.9	0.9
Spot 106	0.004	0.01	0.1	0.7	1.9	5.5	8.6	12.3	20.1	22.4	19.8	17	15.9	13.1	11	1	0.9
Spot 107	0.01	0.02	0.1	0.4	1.3	4.1	7	10.6	14.6	18.5	16	13.6	11	11.3	9.1	1.1	0.9
Spot 108	0.02	0.03	0.1	0.4	1.7	6.7	7.9	13.5	20.5	22.1	19	16.6	16.4	14	11.2	0.8	0.8
Spot 109	0.03	0.03	0.1	0.5	1.6	5.4	8.6	15.7	20.3	22.5	22.7	18.3	14.5	14.2	12.1	0.9	0.8
Spot 110	0.01	0.02	0.1	0.7	1.8	4.7	8.5	12.9	20.2	22.6	20.3	16.2	13.5	12.8	11.6	1.1	0.9
Spot 112	bdl	0.02	0.2	0.4	1.6	5.4	8.3	13.9	20.1	20.3	19.8	16.9	13.4	12.4	10.9	1	0.8
Spot 113	bdl	0.02	0.1	0.5	1.7	5.5	8.4	12.6	19.7	23.6	18.7	18.2	13.3	14.5	9.8	1	0.8
Spot 115-rim	0.004	0.04	0.1	0.2	0.7	2.9	3.9	6.6	10.5	14.8	14.1	17.1	16.7	18.5	19.5	0.9	3
NW13-02-G-garnet 3																	
Spot 121-rim	0.01	0.02	0.05	0.2	0.8	2.6	2.9	4.6	8.5	13.2	13.4	16.4	15.5	21.2	22.2	0.9	4.8
Spot 122	bdl	0.04	0.1	0.9	2.9	8.8	12.3	18.6	20.6	21.5	15.2	11	7.1	4.9	2.9	1	0.2
Spot 123	0.06	0.01	0.1	0.5	1.8	6.1	9.7	13.6	15.8	17.1	13	9.8	6.6	6.6	5.4	1.1	0.4
Spot 124	0.02	0.02	0.1	0.3	1.7	8.4	11	16.7	19.2	19.4	14.3	10.6	8.7	6.2	5.7	0.9	0.3
Spot 126-rim	0.005	0.02	0.1	0.5	1.3	3.8	6.8	9.9	14.3	18.9	21	24.1	23.4	28.3	24.4	1.1	2.5
NW13-02-O, Saltaneset eclogite (omphacite layer)																	
NW13-02-O-garnet 1																	
Spot 69	0.02	0.03	0.2	0.5	1.2	2.7	4.3	7.1	10.8	14.4	17.1	19.3	22.2	28.2	28.8	1	4
Spot 70	0.01	0.04	0.1	0.5	1.4	4.4	5.3	10.6	12.8	17.1	18.3	19.6	20.3	24.1	25.1	0.8	2.4
Spot 71	bdl	0.02	0.1	0.7	1.7	4.3	6.5	9.4	13.4	17.8	21	21.8	23.5	27.5	27.7	1	2.9
Spot 72	0.01	0.04	0.1	0.5	1.5	4.5	5.6	10.8	14.1	19.1	17.9	20.9	21.9	24.5	24.3	0.8	2.2
Spot 73	0.03	0.03	0.2	0.5	1.7	5.5	9.1	11.8	17.1	23.9	25.1	27.9	30.5	33.1	34.6	1.1	2.9
Spot 74	0.02	0.03	0.2	0.6	1.8	5.9	7.9	14.6	19.3	25.4	27.7	31.1	32.9	37.3	35.7	0.8	2.4
NW13-02-O-garnet 2																	
Spot 78	0.01	0.04	0.1	0.4	1.1	3.4	5.9	10.7	13.1	17.8	19.5	21.4	20.8	26.8	25	1	2.4
Spot 79	0.04	0.06	0.2	0.5	1.3	3.3	6.1	10.8	13.2	18.6	21.4	23.2	26.7	27	32.5	1	3
Spot 80	0.02	0.03	0.1	0.5	1.4	4.1	6.0	9.9	14.9	18.7	20	21.4	22.3	27.4	23.9	0.9	2.4
NW13-02-O-garnet 3																	
Spot 85	0.005	0.03	0.2	0.4	1.2	3.6	4.8	8.4	14.8	19.8	25.1	31.3	38.6	43.7	48.3	0.9	5.7
Spot 87	0.01	0.03	0.07	0.4	1.2	3.3	6.3	10.9	15.6	19.6	21.1	23.3	29.4	31.4	31.8	1.1	2.9

Trace-element data normalized to chondrite values of Sun and McDonough (1989)

* Pm = (Sm*Nd)^0.5

Eu/Eu*=Eu/(Sm*Gd)^0.5

Average garnet and zircon trace-element compositions	La	Ce	Pr	Nd	Pm	Sm	Eu	Gd	Tb	Dy	Ho	Er	Tm	Yb	Lu
Ulsteinvik-8815E, eclogite															
8815E-early garnet (1-2) (n = 141)	0.03	0.4	2.7	9.9		36.4	48.6	43.6	43.7	39.4	35.5	36.4	35.5	35.8	35.5
8815E-late garnet (1-rim and 3) (n = 48)	0.02	0.05	0.3	1.2		8.8	18.7	25.8	37.3	39.2	37.3	38.7	38.0	39.7	38.5
zircon (n = 34) all LA-ICP-MS	0.1	4.3	0.1	0.3		3.1	5.6	11.2	14.9	17.7	18.9	19.3	19.7	22.7	24.0
ca.397–405 (n=14) LA-ICP-MS	0.3	4.1	0.1	0.4		3.7	6.3	12.2	17.0	21.3	23.7	25.5	26.8	29.9	31.5
ca. 406–413 (n=20) LA-ICP-MS	0.03	4.4	0.1	0.2		2.7	5.1	10.5	13.4	15.2	15.5	14.9	14.7	17.6	18.8
zircon (n = 14) all solution ICP-MS	1.1	5.9	bdl	bdl		4.5	9.9	20.1	22.0	24.2	25.9	29.0	27.1	32.0	39.5
ca.400–402 (n=5) solution ICP-MS	bdl	7.1	bdl	bdl		5.9	12.8	24.2	27.7	32.2	35.3	40.4	37.8	43.0	51.6
ca.405 (n=1) solution ICP-MS	bdl	0.3	bdl	bdl		3.5	7.9	20.8	20.7	23.6	31.6	44.7	51.3	75.6	114.4
ca. 407–409 (n=8) solution ICP-MS	1.1	5.7	bdl	bdl		3.7	8.4	17.4	18.6	19.3	19.4	19.9	17.5	19.6	22.6

NW13-02-G, Saltaneset eclogite (garnet-quartz layer)														
NW13-02-G-garnet 1, 2, 3 (rims labeled above)														
garnet rims (n = 9)	0.02	0.03	0.1	0.4	3.4	5.3	9.7	14.4	19.0	19.1	21.2	21.4	25.8	25.7
garnet core (n = 20)	0.05	0.1	0.2	0.6	5.9	8.9	13.9	19.5	20.8	17.3	14.3	11.7	10.4	8.4
zircon (n = 14) all LA-ICP-MS	0.02	5.2	0.1	0.2	2.5	3.8	9.3	13.4	17.2	18.9	20.9	24.0	30.4	36.6
ca.397–405 (n=5) LA-ICP-MS	0.02	6.3	0.1	0.3	2.7	4.5	10.4	16.5	21.2	24.0	27.2	30.5	37.4	36.2
ca. 406–413 (n=9) LA-ICP-MS	0.01	4.5	0.1	0.2	2.3	3.4	8.6	11.7	14.9	16.0	17.4	20.4	26.5	36.8
zircon (n=4) all solution ICP-MS	1.2	6.9	bdl	0.3	5.1	10.0	26.5	34.5	37.2	39.8	42.9	43.2	50.9	63.2
ca.401 (n=2) solution ICP-MS	1.2	7.7	bdl	bdl	6.0	12.9	34.3	44.1	48.8	53.0	58.0	57.0	67.4	77.4
ca. 409 (n=2) solution ICP-MS	bdl	5.4	bdl	0.3	4.1	7.0	18.7	25.0	25.6	26.7	27.9	29.4	34.5	48.9
NW13-02-O, Saltaneset eclogite (omphacite layer)														
NW13-02-O-garnet 1, 2, 3 (n = 14)	0.02	0.04	0.1	0.5	4.0	6.2	10.5	14.6	19.7	21.4	23.9	26.7	30.6	31.0
zircon (n = 6) all LA-ICP-MS	0.2	7.7	1.9	2.2	4.6	5.5	9.2	14.2	16.3	20.3	22.7	27.9	33.9	40.0
zircon (n = 1) solution ICP-MS	bdl	bdl	bdl	0.4	5.4	8.3	23.0	29.0	31.8	35.6	37.0	37.2	41.2	51.4

Calculated REE partition coefficients for zircon and garnet using LA-ICP-MS and solution ICP-MS analyses

	La	Ce	Pr	Nd	Pm	Sm	Eu	Gd	Tb	Dy	Ho	Er	Tm	Yb	Lu
Ulsteinvik-8815E, eclogite															
$D_{REE}(zrn_{LA\text{-}ICP\text{-}MS\ (young)}/garnet_{late})$	15.1	88.5	0.4	0.3		0.4	0.3	0.5	0.5	0.5	0.6	0.7	0.7	0.8	0.8
$D_{REE}(zrn_{LA\text{-}ICP\text{-}MS\ (old)}/garnet_{early})$	1.1	10.6	0.03	0.02		0.1	0.1	0.2	0.3	0.4	0.4	0.4	0.4	0.5	0.5
$D_{REE}(zrn_{ID\text{-}TIMS\ (young)}/garnet_{late})$	bdl	152.4	bdl	bdl		0.7	0.7	0.9	0.7	0.8	0.9	1.0	1.0	1.1	1.3
$D_{REE}(zrn_{ID\text{-}TIMS\ (old)}/garnet_{early})$	41.8	13.6	bdl	bdl		0.1	0.2	0.4	0.4	0.5	0.5	0.5	0.5	0.5	0.6
NW13-02-G, Saltaneset eclogite (garnet-quartz layer)															
$D_{REE}(zrn_{LA\text{-}ICP\text{-}MS\ (young)}/garnet_{rim})$	1.0	200.0	0.6	0.7		0.8	0.8	1.1	1.1	1.1	1.3	1.3	1.4	1.5	1.4
$D_{REE}(zrn_{LA\text{-}ICP\text{-}MS\ (old)}/garnet_{core})$	0.3	87.4	0.4	0.4		0.4	0.4	0.6	0.6	0.7	0.9	1.2	1.7	2.5	4.4
$D_{REE}(zrn_{ID\text{-}TIMS\ (young)}/garnet_{rim})$	62.4	242.8	bdl	bdl		1.8	2.4	3.5	3.1	2.6	2.8	2.7	2.7	2.6	3.0
$D_{REE}(zrn_{ID\text{-}TIMS\ (old)}/garnet_{core})$	bdl	104.5	bdl	0.5		0.7	0.8	1.3	1.3	1.2	1.5	2.0	2.5	3.3	5.8
NW13-02-O, Saltaneset eclogite (omphacite layer)															
$D_{REE}(zrn_{avg\ LA\text{-}ICP\text{-}MS}/garnet_{avg})$	7.9	220.2	13.0	4.6		1.2	0.9	0.9	1.0	0.8	0.9	0.9	1.0	1.1	1.3
$D_{REE}(zrn_{avg\ ID\text{-}TIMS}/garnet_{avg})$	bdl	bdl	bdl	0.7		1.3	1.3	2.2	2.0	1.6	1.7	1.5	1.4	1.3	1.7

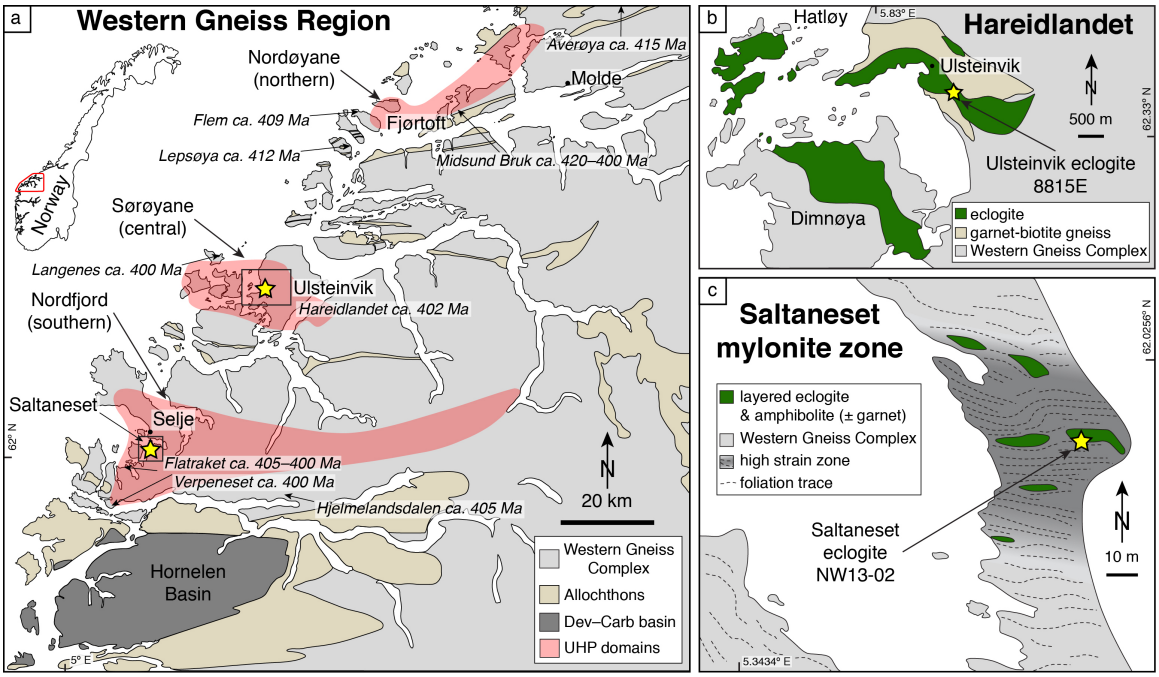

Figure 2.1: (a) Generalized geologic map of the Western Gneiss Region showing the southern, central, and northern UHP domains after Hacker et al. (2010). Locations of (U)HP eclogites and their respective U-Pb zircon dates are shown. Simplified geologic maps of (b) the Ulsteinvik eclogite on Hareidlandet within the central UHP domain (after Mysen and Heier, 1972) and (c) the SW coast of Saltaneset within the southern UHP domain showing the layered eclogite within the Saltaneset mylonite zone (after Renedo et al., 2014). Stars and areas outlined mark sample localities in a, b, and c.

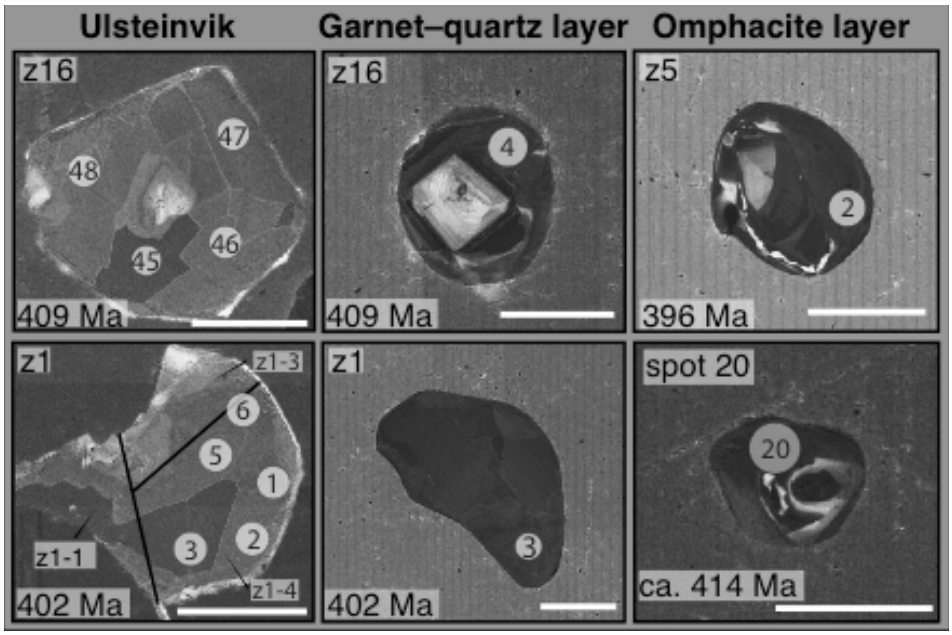

Figure 2.2: Cathodoluminescence images from the Ulsteinvik eclogite and Saltaneset garnet-quartz and omphacite layers displaying patchy- and polygonal-sector zoning, along with some rim overgrowths, preserved within the metamorphic zircon of the two samples. Corresponding ID-TIMS dates are also shown. Black lines denote microsampled fragments of Ulsteinvik z1. Omphacite layer zircon (spot 20) did not yield a Scandian ID-TIMS date; therefore, the LASS date is shown. Scale bar is 100 micrometers.

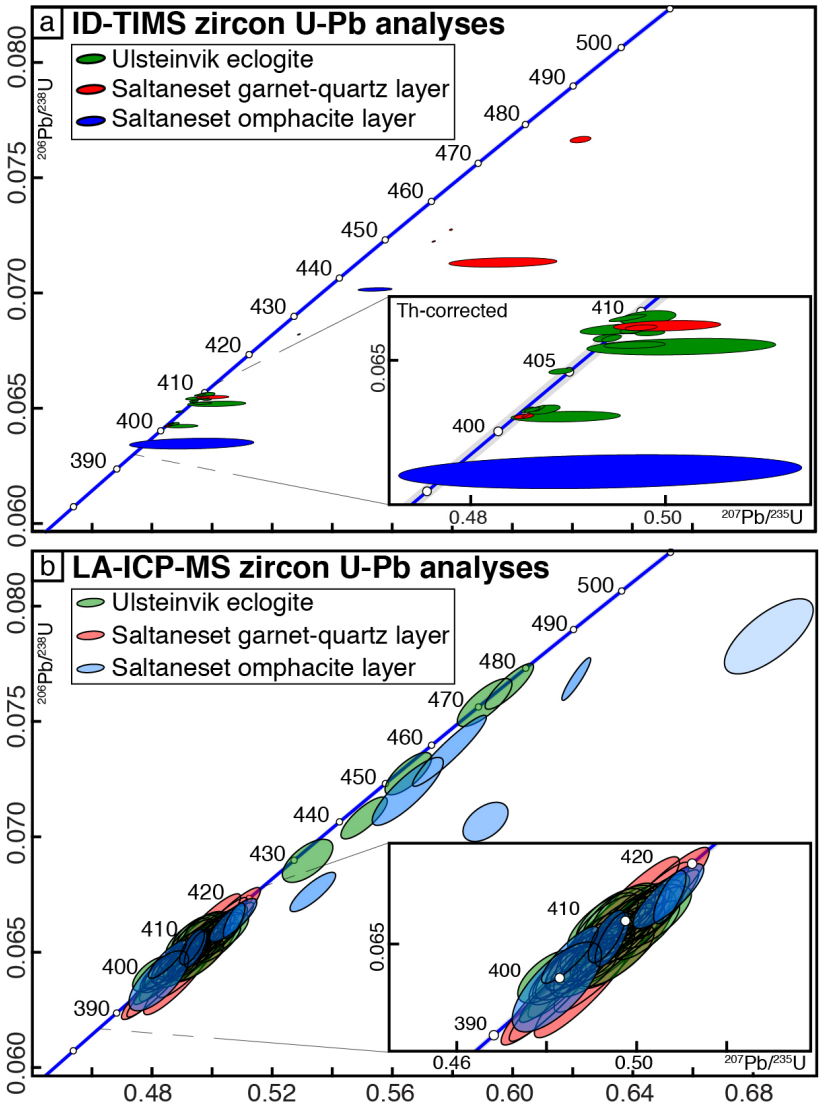

Figure 2.3: Concordia diagrams showing all of the Caledonian U-Pb zircon analyses from both the Ulsteinvik and Saltaneset layered eclogite: (a) individual ID-TIMS analyses; (b) LA-ICP-MS analyses. Insets show Scandian (U)HP dates from both techniques. Dates given in Ma.

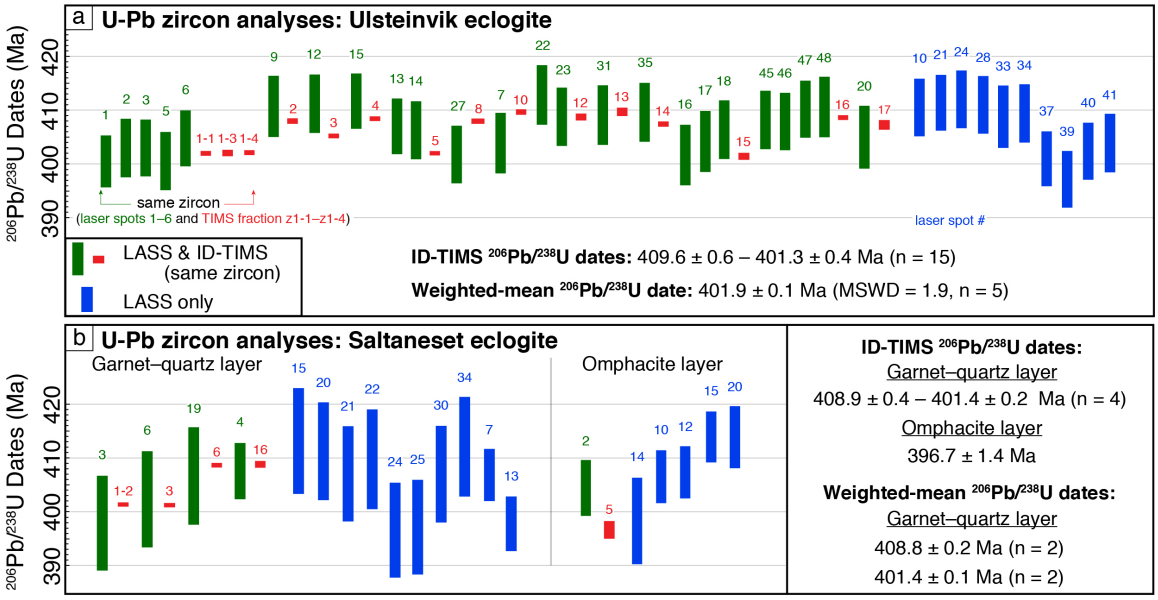

Figure 2.4: U-Pb zircon analyses (LASS (green) and ID-TIMS (red) dates from the exact same zircon) from the two eclogites: (a) Ulsteinvik and (b) Saltaneset (see Table 2), along with additional LASS dates (blue). The numbers correspond to the laser spot (LASS) and zircon grain or fraction (ID-TIMS). The range of single grain or fraction of a grain ID-TIMS analyses are reported as Th-corrected $^{206}Pb/^{238}U$ dates.

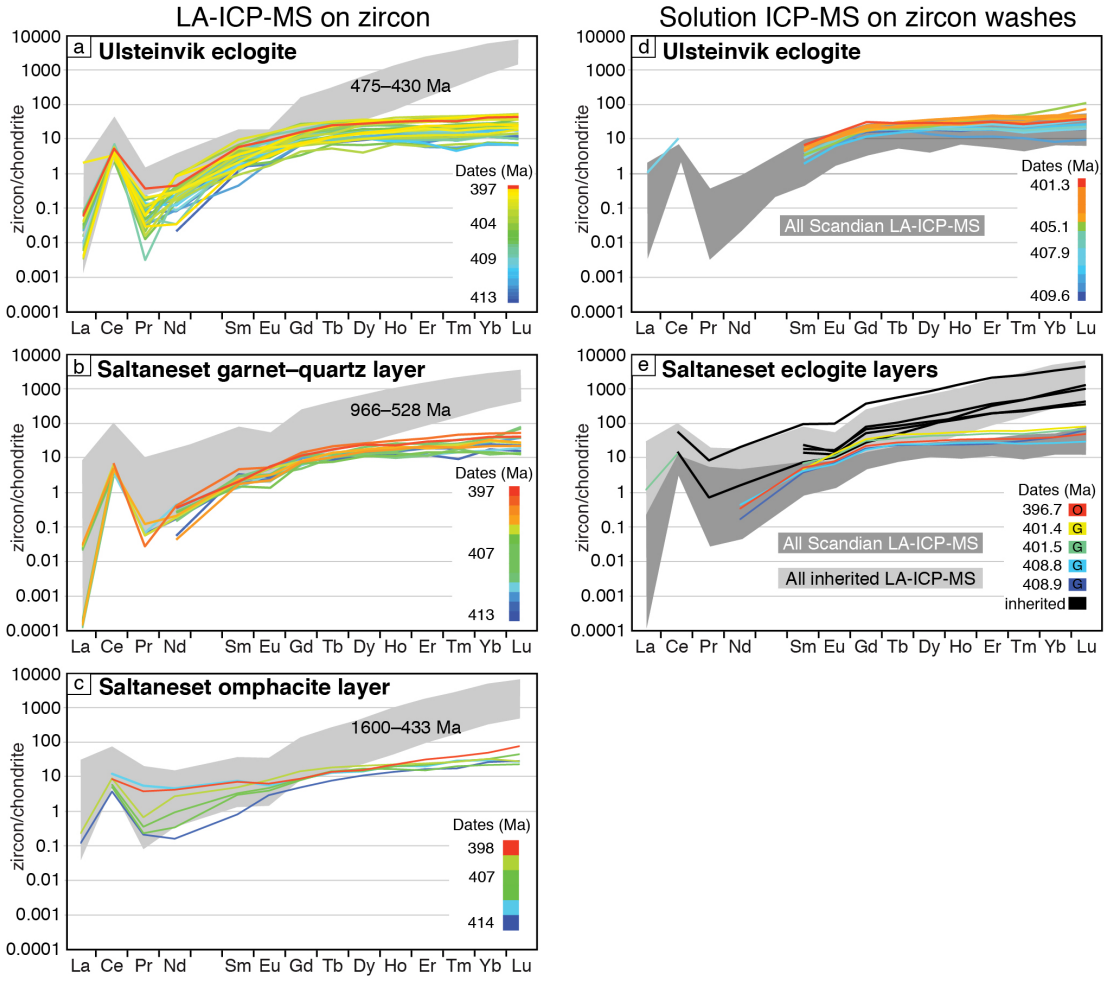

Figure 2.5: Chondrite-normalized zircon trace element data collected by LASS and color-coded by the corresponding LASS dates for (a) the Ulsteinvik eclogite, (b) the garnet–quartz layer of the Saltaneset eclogite, and (c) the omphacite-rich layer of the Saltaneset eclogite. Shaded regions show range of LASS analyses from inherited zircons. Solution ICP-MS analyses (TEA), color-coded by the corresponding ID-TIMS dates, for (d) the Ulsteinvik eclogite and (e) the combined Saltaneset eclogite garnet–quartz (G) and omphacite-rich (O) layers. LASS trace-element results from the same samples (shaded regions) are shown for comparison.

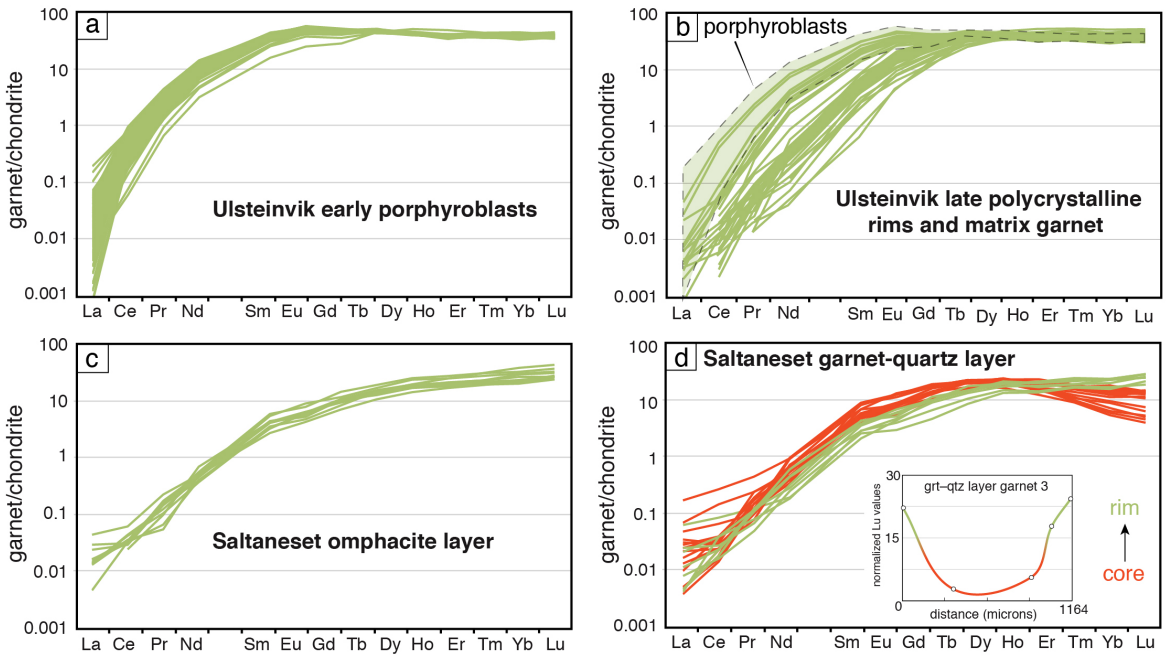

Figure 2.6: Chondrite-normalized garnet trace element data collected by LA-ICP-MS for (a) early-formed garnet porphyroblasts of the Ulsteinvik eclogite, (b) late-recrystallized garnet along some of the early garnet rims and within the matrix of the Ulsteinvik eclogite, (c) the omphacite-rich layer of the Saltaneset eclogite, and (d) garnet–quartz layer of the Saltaneset eclogite with Lu profile across representative zoned garnet 3.

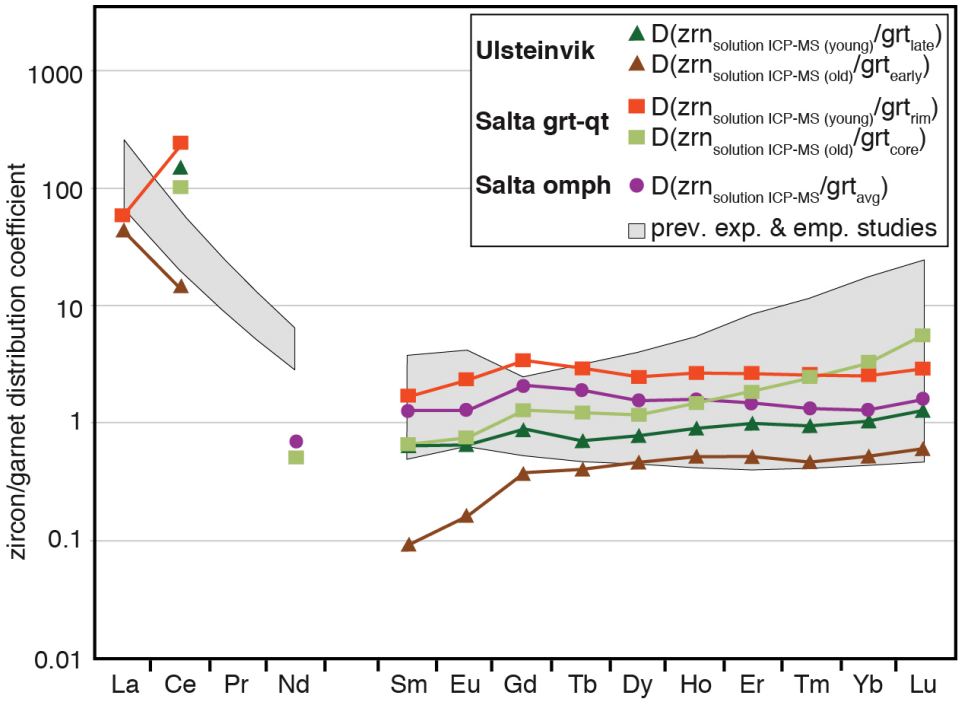

Figure 2.7: Zircon/garnet partition coefficients for the different populations and/or generations of zircon (solution ICP-MS) and garnet analyses (LA-ICP-MS). Averaged zircon trace element compositions of the two age populations are paired with the average of the different garnet trace-element compositions observed in Ulsteinvik and Saltaneset eclogite layers. Also shown is the range in previously calculated experimental and empirical zircon/garnet partition coefficients discussed in the text.

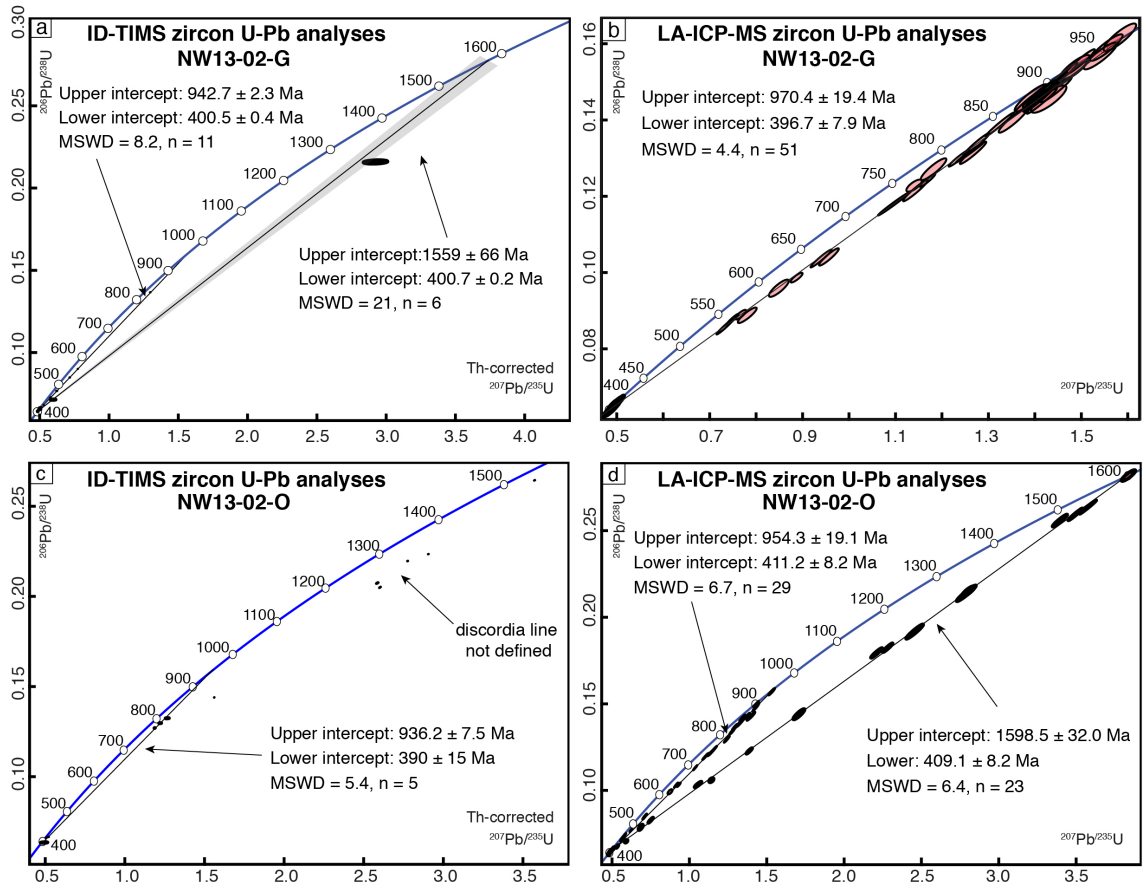

Figure 2.S1: Concordia diagrams showing U-Pb zircon results from the (a and b) Saltaneset garnet–quartz layer (NW13-02-G) and (c and d) the omphacite-rich layer (NW13-02-O) analyzed by ID-TIMS and LASS, respectively. Upper- and lower-intercept ages were calculated using the program U-Pb_Redux (Bowring et al., 2011; McLean et al., 2011). Each ellipse represents a single zircon or spot analysis and the 2-sigma uncertainties. Dates listed on concordia are in Ma.

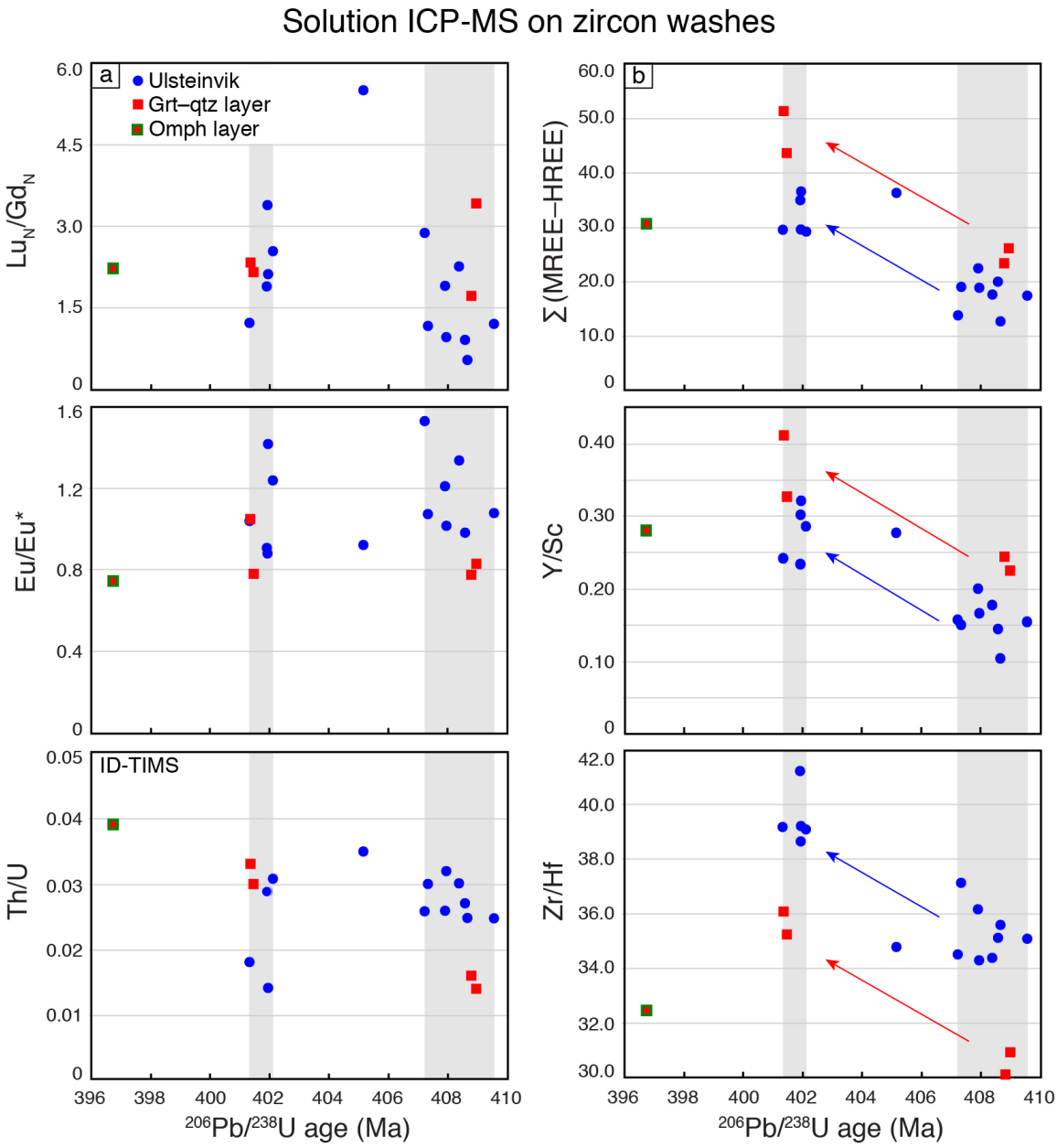

Figure 2.S2: Scandian zircon trace elements as a function of time. Plots are shaded for ca. 409–407 and ca. 402 Ma zircon populations. (a) Lu_N/Gd_N, Eu/Eu*, and Th/U data and (b) sum of absolute concentrations (ppm) of MREE–HREE, Y/Sc, and Zr/Hf data vs. ID-TIMS $^{206}Pb/^{238}U$ (Th-corrected) age for the Ulsteinvik eclogite, the garnet–quartz layer of the Saltaneset eclogite, and the omphacite-rich layer of the Saltaneset eclogite. Lu_N/Gd_N and Eu/Eu* analyses are normalized to chondrite values of Sun and McDonough (1989).

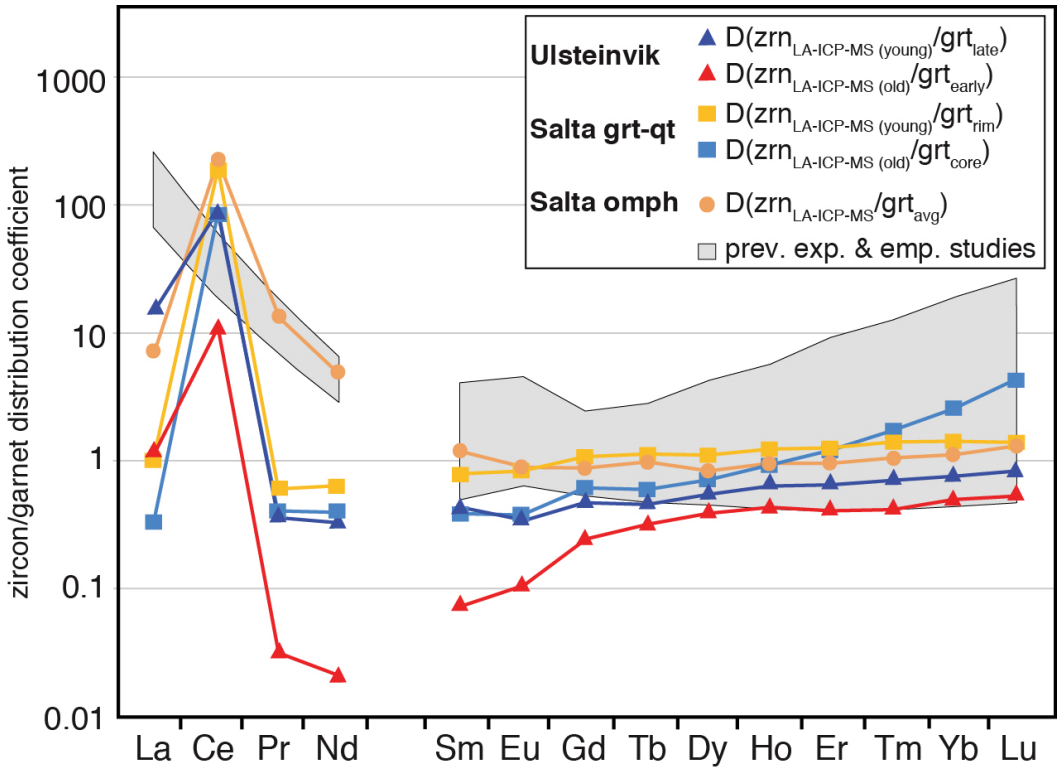

Figure 2.S3: Zircon/garnet partition coefficients for the different populations and/or generations of zircon (LASS) and garnet analyses (LA-ICP-MS). Average zircon trace element compositions of the young (ca. 405–397 Ma) and old (ca. 414–406 Ma) age populations are paired with the average of the different garnet trace-element compositions observed in Ulsteinvik and Saltaneset eclogite layers. Also shown is the range in previously published experimental and empirical zircon/garnet partition coefficients discussed in the text.

Chapter 3: Phase-diagram calculations of kyanite- and phengite-bearing eclogites from the D'Entrecasteaux Islands, Papua New Guinea

Joel W. DesOrmeau[*], Stacia M. Gordon[*], Timothy A. Little [**], Hugh Davies[***], Nilanjan Chatterjee[****]

[*]Department of Geological Sciences, University of Nevada Reno, Nevada, USA
[**] School of Geography, Environment and Earth Sciences, Victoria University of Wellington, Wellington, New Zealand
[***]Earth Sciences, University of Papua New Guinea, University NCD, Papua New Guinea
[****]Department of Earth, Atmospheric, and Planetary Sciences, Massachusetts Institute of Technology, Cambridge, Massachusetts, USA

This chapter will be submitted to the *Journal of Metatmorphic Geology* in the near future.

Abstract

Domal structures exposed across the D'Entrecasteaux Islands of Eastern Papua New Guinea (PNG) consist of migmatitic quartzofeldspathic gneiss that host the world's youngest ultrahigh-pressure (UHP) eclogites. The PNG UHP terrane is unique in that it resides within an active rift and has not been overprinted by later tectonic activity. The only known coesite eclogite occurs in the central Mailolo Dome, and thermobarometry of (U)HP eclogites from the eastern Oiatabu, central Mailolo and western Goodenough Domes reveal a large spread in peak pressure and temperature estimates (~12–24 kbar and ~530–930 °C), none of which suggest UHP conditions. A suite of variably retrogressed eclogites was collected across these domes for thermobarometry and phase-diagram calculation to determine the peak P-T conditions attained and to better understand the exhumation of this young UHP terrane. The results reveal that the Oiatabu Dome kyanite-phengite eclogite equilibrated at UHP conditions of ~30–31 kbar and ~635–660 °C, whereas a kyanite eclogite from nearby shows P-T conditions of ~22–27 kbar and ~560–650 °C. To the west, a Mailolo Dome phengite eclogite records peak metamorphism within the coesite-stability field at ~27–30 kbar and ~510–560 °C. Furthermore, this eclogite contains ca. 6.0–5.2 Ma zircons that have inclusions of the peak assemblage, including omphacite, garnet, rutile, and phengite. The combined thermobarometry and phase-diagram P-T results suggest both domes experienced UHP conditions likely at ca. 6.0 Ma. Initial eclogite retrogression at ca. 4.6–4.3 Ma across the terrane is associated with the breakdown of peak garnet and omphacite to form symplectite of Na-poor clinopyroxene, amphibole, and plagioclase, and in some eclogites, assemblages of zircon, rutile, quartz, and apatite. Furthermore, Oiatabu Dome

eclogites all preserve amphibole porphyroblasts related to fluid infiltration during exhumation. In the west, ca. 2.8–2.6 Ma Goodenough Dome eclogites record the strongest amphibolite-facies overprint of the terrane with abundant amphibole and plagioclase growth. Based on mineralogical and textural evidence and the P-T results, the Mailolo and Oiatabu Dome eclogites were subducted to the greatest depths and were exhumed earlier than the Goodnough Dome to the west. In comparison, the Goodenough Dome was exhumed ~2 Myr later and was likely more affected by the active rift environment.

Introduction

Exposure of high-pressure (HP) and ultrahigh-pressure (UHP) eclogites provide insight into the tectonometamorphic history associated with the deep burial and exhumation of continental crust within continent-continent collisional zones. Knowledge of the pressure and temperature (P-T) conditions at which (U)HP eclogites equilibrate, coupled with the timing and the duration of peak metamorphism, is fundamental for assessing the rates and mechanisms involved in the transfer of crustal material to and from mantle depths (e.g., Hermann et al., 2001; Parrish et al., 2006; Kylander-Clark et al., 2007, 2009; Hacker and Gerya, 2013; Warren, 2013).

Determining peak P-T conditions for eclogites at high temperatures and pressures, where hydrous minerals such as phengite are unstable, is difficult due to the composition of the peak minerals not varying much with changing P-T (Stipska and Powell, 2005). Typically minimum pressure estimates have been constrained by the jadeite component of omphacite within eclogite (Gasparik and Lindsley, 1980; Holland, 1980) and temperatures are calculated using the garnet-clinopyroxene Fe-Mg exchange thermometer, despite the poor estimates on mineral Fe^{3+}/Fe^{2+} (e.g., Proyer et al., 2004). For eclogites that contain phengite, the garnet-clinopyroxene-phengite assemblage is used as a barometer due to its shallow dP/dT slope and overall estimated uncertainty of < 2kbar (Waters and Martin, 1993; Carswell et al., 1997; Wain, 1998; Cuthbert et al., 2000; Nowlan et al., 2001; Schmid, 2001, Wain et al., 2001; Ravna and Terry, 2004). Finally, if the eclogite contains kyanite and an SiO_2 phase, net-transfer reactions (1: pyrope + grossular + celadonite = diopside + muscovite; 2: pyrope + grossular + coesite/quartz = kyanite + diospide) can be used and are advantageous because they use equlibria

involving Mg rather than Fe (e.g., Ravna and Terry, 2004). Thus, these reactions circumvent the issues associated with unknown Fe^{3+} content in clinopyroxene and garnet (e.g., Ravna and Paquin, 2003; Proyer et al., 2004) and reveal the most precise and accurate estimates of peak P-T conditions for eclogites of the available thermobarometry calculations. Using this approach has shown that most UHP terranes record pressures of ~25–40 kbar and temperatures of 600–800 °C.

Phase-diagram modeling (i.e., pseudosections) can also provide constraints on the P-T history of subducted crustal material. Calculated psuedosections have the ability to show the modal and compositional change of minerals (i.e., garnet and phengite) for a specific bulk-rock composition in P-T space (e.g., Powell and Holland, 2008, 2010; Massonne, 2013). Most eclogites have typically been retrogressed during exhumation. Because of this, using the bulk-rock composition collected through standard XRF analyses may not be representative of the rock when it was at peak P-T. Therefore, an "effective" bulk-rock composition is calculated through a weighted calculation involving the peak mineral proportions present in the thin section and their representative compositions (e.g. Carson et al., 1999; Indares et al., 2008), but disregarding the retrograde phases (Palin et al., 2015). The combination of the effective bulk composition with pseudosection modeling is the best method for deciphering the history of a rock that has experienced extreme metamorphic conditions.

The D'Entrecasteaux Islands of eastern Papua New Guinea (PNG) expose Pliocene (U)HP eclogites within five domal structures from east to west: Normanby, Oiatabu, Morima, Mailolo, and Goodenough Domes (Figs. 1 and 2; Davies and Warren, 1988; 1992; Hill et al., 1992; Baldwin et al., 2004, 2008; Little et al., 2011). Previous

investigations of the P-T conditions for eclogite-facies metamorphism based on thermobarometry (garnet-clinopyroxene thermometry and jadeite-content in omphacite barometry) have shown a wide range of pressures, from 12 to 24 kbar, and temperatures, from 530 °C to >900 °C (Davies and Warren, 1992; Hill and Baldwin, 1993; Baldwin et al., 2004). The identification of coesite within an eclogite from Mailolo Dome (Baldwin et al., 2008) indicated that the crustal rocks were subducted to upper-mantle conditions and opens the possibility that the rocks exposed in the other domes may have also been subjected to similar conditions. This study aims to assess the peak conditions attained by kyanite- and phengite-bearing eclogites from Oiatabu and Mailolo Domes through the combined approach of thermobarometry based on the net-transfer reactions in kyanite-phengite eclogites and phase-diagram modeling. The results are used to show that multiple domes record UHP conditions but that the far western dome experienced much more thorough overprinting in comparison to the other domes, suggesting a different exhumation history that was more thoroughly affected by the active rift environment.

Tectonic and metamorphic history of the PNG (U)HP terrane

Woodlark Basin

The convergence between the Pacific and Australian plates at ~10–11 cm/yr has caused the formation and rotation of microplates since the Eocene (Tregoning et al., 1998; Wallace et al., 2004, 2014). The Paleogene collisional event, the Papuan Orogen, resulted from the northeastward subduction of the northern Australian rifted margin beneath an island-arc terrane, causing obduction of the arc basement on the mainland Papuan Peninsula, now called the Papuan Ultramafic Belt (PUB) (Davies and Jacques, 1984;

Cloos et al., 2005; Little et al., 2011). The PUB was obducted above a deformed wedge of Australian plate material (Owen Stanley metamorphics) along the Owen Stanley Fault at 58.3 ± 0.4 Ma ($^{40}Ar/^{39}Ar$ amphibole; Lus et al., 2004). The Owen Stanley metamorphics consist of blueschist, pumpellyite-actinolite, and lower greenschist-facies rocks (Fig. 1) (Davies and Jacques, 1984; Davies and Warren, 1988). Ages of ca. 45 to 22 Ma (K-Ar and $^{40}Ar/^{39}Ar$ amphibole dates) constrain the northward subduction of the Australian plate during the Papuan Orogen, whereas white mica dates of ca. 24–22 Ma (cooling through ~400 °C) (Davies and Williamson, 1988) suggest the collisional event had ended by the early Miocene (Davies and Jacques, 1984; Rogerson et al., 1987; Davies, 1990; Van Ufford and Cloos, 2005, Davies, 2012). The deep subduction of this Australian plate material provided the protolith of the PNG (U)HP terrane located ~20 km offshore of the mainland peninsula in the D'Entrecasteaux Islands (Figs. 1, 2).

Tectonic reorganization within eastern PNG subsequent to the Papuan orogeny occurred due to continued rapid convergence between the Australian and Pacific plates. Slab pull associated with subduction of the Solomon Sea microplate at the New Britain Trench (Weissel et al., 1982; Wallace et al., 2004; Westaway, 2007) has driven northward, counterclockwise, rotation of the Woodlark and Solomon Sea microplates relative to Australia since the late Miocene (Wallace et al., 2004). Since 6 Ma, this rotation has been accommodated through seafloor spreading within the Woodlark Basin (Fig. 1) (Taylor et al, 1999; Kington and Goodliffe, 2008). Across the basin, seafloor spreading and high extension rates in the east (e.g., Taylor et al., 1999; Taylor and Huchon, 2002) transition to lower (<10–20 mm/yr) extension rates in the Woodlark Rift, the western continental portion of the rift-seafloor spreading system (Tregoning et al.,

1998; Wallace et al., 2004). In this portion of the rift, thin crust (~20 km-thick) lies directly beneath the D'Entrecasteaux Islands, which consist of 2–2.5 km high gneiss domes spread across the Islands (Figs. 1, 2; Abers et al., 2002). Active extension within all levels of the lithosphere, from the mantle to the crust is evident from geophysical, geodetic, and structural results (Tregoning, 1998; Taylor et al., 1999; Abers 2001; Abers et al., 2002; Wallace et al., 2004, 2014; Little et al., 2011, 2013; Eilon et al., 2014, 2015).

D'Entrecasteaux Islands

Five domal structures are exposed across the D'Entrecasteaux Islands: Normanby (northwest Normanby Island), Morima (southern Fergusson Island), Oiatabu (eastern Fergusson Island), Mailolo (western Fergusson Island), and Goodenough (Goodenough Island) (Figs. 1 and 2). The domes consist of quartzofeldspathic gneiss, with lesser amounts of mafic rocks (eclogite and amphibolite), and minor marbles, quartzites, and paragneiss (Fig. 2) (Davies and Warren, 1988; Little et al., 2011). The northern flanks of the Goodenough, Mailolo, and Oiatabu domes are cut by normal faults that dip 30–40° to the north and have convex-up scarps that crosscut an older, more gently dipping fault that preserves fragments of the ophiolitic upper plate rocks in its hanging wall (Little et al., 2011). This older structure, the D'Entrescasteaux fault zone (Little et al., 2011), is interpreted to be correlative to the Owen Stanley Fault (Fig. 1), upon which obduction of the PUB occurred during the Paleogene Papuan Orogen. Erosional remnants of the upper plates of the gneiss domes consist of the regionally extensive sheet of PUB and its unmetamorphosed Neogene sedimentary cover, whereas the lower plate of the domes are

characterized by the (U)HP rocks (Fig. 2; Davies and Warren, 1988, 1992; Hill et al., 1992; Baldwin et al., 2004, 2008; Monteleone et al., 2007; Little et al, 2011, 2013).

Hill (1994) structurally divided the lower plates of the domes into an uppermost carapace zone (up to 1.5 km thick) consisting of a strong, planar LS tectonite fabric, and an inner, structurally deeper, core zone with chaotic fabrics (Fig. 2). All structural levels of the domes contain eclogite-facies mafic rocks and layer-parallel leucosomes, dikes, and plutons. However, Gordon et al (2012) report an increase in the amount of leucosome in the carapace to the core from ~15–70 vol. % (Gordon et al., 2012). Melt-present deformation within the cores of the domes is characterized by quartz microstructures, melt-filled strain shadows, and shape-preferred orientations of magmatic feldspar suggest (Little et al., 2011, 2013).

Pressure–Temperature results from PNG (U)HP eclogites

Eclogites from the domes exposed on Goodenough and Fergusson Islands have a wide range of compositional (e.g., omphacite ranging from Jd>20 vs. Jd<20) and textural characteristics (e.g., whether peak omphacite is preserved) (Davies and Warren, 1992), and have thus been described with a range of names, including “true” eclogites (i.e., omphacite-garnet-rutile±kyanite±phengite), retrogressed eclogites (i.e., omphacite partly replaced by less-Na clinopyroxene or amphibole and plagioclase), and Na-poor eclogites containing diopsidic clinopyroxene (Jd<20) rather than omphacite. Geothermobarometry studies focused on these eclogites have shown considerable variability in pressure and temperature (P-T) results from ~14–27 kbar and ~530–930 °C.

Early studies of PNG eclogites report temperature estimates using garnet-clinopyroxene thermometry (Davies and Warren, 1992; Hill and Baldwin, 1993; Baldwin et al., 2004, 2008), whereas more recent studies have also utilized trace-element thermometers, including Zr-in-rutile and Ti-in-zircon (Monteleone et al., 2007, Baldwin et al., 2008; Vry and Gazley, submitted manuscript). For pressure, nearly all estimates have relied on a minimum estimate calculated from the jadeite component in omphacite within eclogite (Gasparik and Lindsley, 1980; Holland, 1980); however, peak pressures are calculated for the coesite-bearing eclogite from Mailolo Dome using the garnet-clinopyroxene-phengite barometer (Ravna and Terry, 2004) and are assumed to be ≥27 kbar at ~700 °C, based on the preservation of coesite. General P-T estimates for each dome are discussed below and in Table 1. All results are from garnet-clinopyroxene thermometry and the jadeite content in omphacite (minimum pressures), unless otherwise noted.

Eclogites from Fergusson Island have received the most attention throughout the D'Entrecasteaux Islands. The carapace of southwestern Oiatabu Dome exposes kyanite- and phengite-bearing eclogites containing omphacite with $Jd_{27–39}$; these samples reveal a P-T range of ~13–16 kbar and ~600–800 °C (Davies and Warren, 1992). An eclogite from the same area of SW Oiatabu Dome contains more Na-rich omphacite (Jd_{60}) and gives higher P-T conditions of ~21 kbar and ~850 °C (Hill and Baldwin, 1993). In comparison, eclogites sampled ~20 km to the west in the carapace of Morima Dome, are characterized by omphacite with $Jd_{43–49}$ and reveal P-T results of ~17 kbar and ~530–700 °C (Davies and Warren, 1992).

To the northwest ~20 km, Mailolo Dome preserves the only known coesite-bearing eclogite; however, most eclogites contain radial fractures around quartz included within garnet that likely developed during the transition of coesite to quartz during decompression (Fig. 4). Finally, these eclogites also contain the most Na-rich omphacite ($Jd_{43–66}$; Table 1). Core-zone eclogites from Mailolo Dome show a P-T range from ~16–18 kbar and 725–850 °C (Davies and Warren, 1992), ~15–21 kbar and 730–870 °C (Hill and Baldwin, 1993), and ~20–24 kbar and 870–930 °C (Baldwin et al., 2004). Prior to the discovery of coesite in an eclogite from Tumagabuna Island (Baldwin et al., 2008), multiple eclogite samples from this locality revealed similar P-T results of ~17–19 kbar and 725–730 °C (Davies and Warren, 1992; Hill and Baldwin, 1993). In comparison, the coesite eclogite gives higher P-T results from ~18–27 kbar and 600–760 °C (garnet-clinopyroxene-phengite thermobarometry; Baldwin et al., 2008), whereas trace-element thermometry yields temperatures of 612–743 °C (Zr-in-rutile, assuming P=28 kbar) and 650–680 °C (Ti-in-zircon) (Monteleone et al., 2007; Baldwin et al., 2008).

Goodenough Dome in the far west contains eclogites that are characterized by Na-poor bulk-rock compositions and diopsidic clinopyroxene ($Jd_{10–16}$; Table 1)(Davies and Warren, 1992). Overall, these eclogites are typically extensively retrogressed compared to other domes. Core-eclogites from the northern and southern flanks of the dome give similar results to the other domes, with a wide range of P-T estimates of ~15–25 kbar and 700–830 °C (Davies and Warren, 1992). An eclogite from the southern flank of the core zone yields a pressure of ~14 kbar and Zr-in-rutile temperatures of 677–817 °C (Monteleone et al., 2007). Monteleone et al. (2007) also studied eclogites from Goodenough Dome that do not contain omphacite; therefore, only temperatures were

determined: Zr-in-rutile and Ti-in-zircon thermometers show considerable scatter from 718–1015 °C and 740–870 °C, respectively.

The large spread in the previous eclogite P-T studies is likely attributed to partial-to-complete overprinting of the peak mineral assemblage and imprecision associated with the garnet-clinopyroxene thermometer due to the unknown amount of Fe^{3+} in garnet and clinopyroxene (e.g., Proyer et al., 2004). Most studies assume that all Fe is Fe^{2+}, which results in a bias towards higher estimated temperatures and associated pressures (Stipska and Powell, 2005). Moreover, the large range in previous geothermobarometry has not been directly correlated with the degree of retrogression within a sample (e.g., Monteleone et al., 2007). A suite of eclogites from Oiatabu, Mailolo, and Goodenough Domes are discussed in detail below in an attempt to better define P-T conditions attained by the eclogites within each dome and to provide a more refined tectonometamorphic history for the entire Pliocene (U)HP terrane.

Petrography and Mineral Chemistry

In this study, we utilize thermobarometry and calculated phase-diagrams, including modeling mineral assemblages and compositional data based on an effective bulk composition, using the software Perple_X (Connolly, 2005) to more systematically characterize the peak conditions that were attained by eclogites within three of the PNG (U)HP domes. The samples include a fresh kyanite-phengite eclogite, two eclogites preserving only kyanite and phengite separately, and four retrogressed eclogites in which omphacite is minor or absent (Figs. 3, 4, and 5). Moreover, zircon has been dated from these eclogites and thus the combined data is used to better understand the timing and

nature of peak conditions at which the crustal material was subducted, and that data is used to better document retrogression during decompression and exhumation of the (U)HP terrane. Mineral compositions were measured by electron-microprobe analysis with a JEOL JXA-733 Superprobe at the Massachusetts Institute of Technology using an accelerating voltage of 15 kV and a beam current of 10 nA. Spot analyses of garnet, clinopyroxene, phengite, amphibole, biotite, plagioclase, and clinozoisite were placed using backscattered electron (BSE) images and EDS compositional maps of select textural areas related to fresh and retrogressed portions of thin sections constructed with a JEOL 7100 scanning electron microscope at the University of Nevada, Reno. Representative analyses of all major minerals are given in Tables 2–5. Mineral chemistry plots of garnet, clinopyroxene, phengite, and amphibole are presented in Figures 6–9. Mineral abbreviations are after Whitney and Evans (2010). Eclogite bulk-rock compositional data are presented in Table 6 and were performed by Activation Laboratories, Canada. For pseudosection modeling (see discussion below), modified effective bulk-rock compositions were determined for each eclogite by combining compositional analyses of homogenous major phases and their volume proportion currently preserved in the rock. Estimates of major phases were aided by EDS area mapping of thin sections and petrography.

Fresh eclogites (Oiatabu and Mailolo Domes)

Oiatabu Dome: Kyanite-phengite eclogite B20 and kyanite eclogite 4329

Kyanite-phengite eclogite B20 and kyanite eclogite 4329 both consist of a fine-grained matrix of garnet and omphacite, with lesser amounts of rutile, and quartz (Figs. 3a, b).

The samples have distinct kyanite poikiloblasts that contain inclusions of garnet, omphacite, and rutile. Euhedral to subhedral kyanite is more abundant in sample 4329. The high-pressure peak assemblages consists of garnet + omphacite ± phengite + kyanite ± clinozoisite + rutile + coesite/quartz, which contain an extensive network of fractures consisting of fine-grained chlorite and/or K-feldspar. These fractures are truncated by late amphibole porphyroblasts (0.25–1.25 cm) that also contain inclusions of matrix garnet, omphacite, and rutile, and in sample 4329, large (up to 0.75 mm across) amorphous quartz adjacent to kyanite margins (Fig. 3b). Minor symplectite growth of less Na-rich clinopyroxene + plagioclase or amphibole + plagioclase occurs along peak garnet and omphacite and later amphibole boundaries. In addition, thin rims of very fine-grained spinel–sapphirine + plagioclase symplectites mantle kyanite poikiloblasts.

Kyanite-phengite eclogite B20 consists of ~28% garnet, ~17% omphacite, ~8% phengite, ~3%, ~30%, ~2% quartz, and ~1% rutile. The eclogite contains matrix garnet and garnet inclusions within kyanite that are euhedral to subhedral, 0.1–0.3 mm across, and show no systematic zoning with a typical composition of $Alm_{33–41}Prp_{42–50}Grs_{12–17}And_{0–4}Sps_{1}$ (Fig 3a; Table 2). Omphacite found within the matrix and as inclusions in kyanite have a composition of $Jd_{28–32}$ and ranges in size from 0.1–0.6 mm across (Fig 3a; Table 3). Matrix phengite is up to 0.2 cm in length. The celadonite component varies over the range in Si from 3.38–3.50 atoms per formula unit (a/fu; Table 4), although phengite margins have been partially replaced by fine-grained biotite and plagioclase. Late porphyroblasts of amphibole (magnesio-hornblende) show little variation in composition with high $Mg\#_{92–94}$ (Table 5). Retrograde plagioclase growth along the margin between kyanite, garnet and omphacite has a composition of $An_{75–78}$, whereas plagioclase

replacing garnet inclusions in kyanite is $An_{51–55}$ (Table 4). The extremely fine-grained biotite and plagioclase after phengite and sapphirine–spinel and plagioclase within symplectites that mantle kyanite could not be analyzed.

In comparison, kyanite eclogite 4329 has mineral phase proportions consisting of ~35% garnet, ~17% omphacite, ~9% kyanite, ~30% amphibole, ~3% quartz, and ~1% rutile. Matrix garnet are euhedral to subhedral and fine-grained, and omphacite grains are typically 0.15 mm across (Fig. 2b). Larger omphacite grains, up to 0.3 mm across, occur as clusters throughout the matrix. The euhedral–subhedral garnets found within the matrix and as inclusions within kyanite show no systematic zoning and range from $Alm_{29–39}Prp_{38–47}Grs_{16–26}And_{0–4}Sps_{1}$ (Table 2). Matrix omphacite and omphacite inclusions within kyanite have a composition of $Jd_{28–32}$ (Table 3). The compositions of late magnesio-hornblende porphyroblasts are similar to that of sample B20 with $Mg\#_{92–95}$. Retrograde plagioclase that rims kyanite, garnet, and omphacite ranges from $An_{54–59}$, whereas plagioclase associated with the breakdown of omphacite included within kyanite ranges from $Ab_{50–59}$ (Table 4). As in B20, extremely fine-grained symplectites of sapphirine–spinel and plagioclase mantling kyanite could not be analyzed.

Mailolo Dome: Phengite-bearing eclogite PNG08-010F

Phengite eclogite (PNG08-010F), collected from the coesite locality, consists mainly of elongate garnet and omphacite that define a weak foliation. The overall mineral phase proportions preserved in PNG08-010f are ~50% omphacite, ~30% garnet ~8% quartz, ~3% phengite, ~2% rutile, and <1% amphibole. Interstitial quartz and minor phengite, with accessory phases apatite, rutile, and zircon, are found among the garnet and

omphacite. Minor symplectite growth of diopsidic clinopyroxene and/or amphibole and plagioclase occurs along rims of garnet, omphacite, and phengite. Retrograde matrix amphibole is rare. The well-preserved high-pressure peak assemblage consists of garnet + omphacite + coesite/quartz + phengite + rutile.

Within this Mailolo eclogite, garnet contain inclusions of phengite and zircon, along with minor amphibole. The subhedral to anhedral garnets are typically 0.1–0.5 mm across and exhibit a very limited range of compositions: $Alm_{58–61}Prp_{22–24}Grs_{16–19}Sps_{1}$ (Table 2). Omphacite is subhedral to anhedral, typically 0.8 mm across, has sodic-rich compositions ($Jd_{63–68}$), and occurs as the main matrix phase. Larger omphacite grains (3.5 mm in length) are also found in the sample (Fig. 4a; Table 3). Phengite occurs as tabular grains that are typically 0.7 mm in length and the rims show minor retrogression to fine-grained biotite and plagioclase. The grains are weak zoned, with a decrease in celadonite component from core to rim. In addition, the phengite give a wide range in Si from 3.33–3.51 a/fu, but typical matrix grains have Si = 3.33–3.43 a/fu (Table 4). Minor amphiboles, both matrix and grains included within garnet, range from taramite to ferro-taramite, with Mg# of 0.43–0.68 (Table 5). Symplectite along the rims of garnet and omphacite contain katophorite ($Mg\#_{0.70–0.71}$) and albite ($Ab_{96–98}$) (Table 4). Quartz occurs within the matrix and as inclusions within garnet that are associated with distinct radial fractures (Fig. 4a).

Zircons extracted from the fresh matrix of this eclogite contain inclusions of the peak assemblage, including omphacite, garnet, rutile, and rare phengite (Fig. 6a, b). The ~5–10 μm inclusions of omphacite and garnet have identical compositions to matrix omphacite (Jd_{66}) and garnet ($Alm_{59}Prp_{23}Grs_{18}Sps_{1}$) (Tables 2 and 3), indicating zircon growth during

peak metamorphic mineral crystallization from ca. 6.0–5.2 Ma (DesOrmeau et al., Chapter 4 in this dissertation).

Variably retrogressed eclogites (Oiatabu, Mailolo, and Goodenough Domes)

Oiatabu Dome: eclogite PNG12-95a

Eclogite PNG12-95a has undergone extensive retrogression, with eclogite-facies phases (anhedral garnet, omphacite, and quartz) only occurring as minor grains in the matrix, which consists mainly of abundant coarse amphibole (Fig. 3c). The coarse amphibole is set in a fine-grained matrix of clinopyroxene, amphibole and plagioclase symplectite with accessory rutile and zircon. The mineral proportions are ~30% amphibole, ~13% garnet, ~13% omphacite, ~30% symplectite, ~5% quartz, and ~5% plagioclase. The high-pressure, plagioclase-free assemblage was garnet + omphacite + quartz + rutile. Breakdown and replacement of high-pressure garnet by amphibole and omphacite by less Na-rich clinopyroxene, amphibole, and minor plagioclase is ubiquitous.

Kelyphitic amphibole rims anhedral garnets that are up to 1.0 cm across. Typical garnet compositions range from $Alm_{36–44}Prp_{36–47}Grs_{14–19}And_{0–2}Sps_{1}$ (Table 2). Garnets are relatively homogenous with respect to the grossular content; however, pyrope shows a rimward decrease (from Prp_{46} to Prp_{41}), whereas almandine increases towards the rim (Alm_{36} to Alm_{40}). Matrix omphacite has a narrow composition of $Jd_{28–30}$ (Table 3). Symplectite along the omphacite rims consist of diopside ($Jd_{4–8}$) and plagioclase ($Ab_{92–96}$). Where omphacite has completely broken down within the matrix, a pseudomorph of symplectite consisting of a range of clinopyroxene ($Jd_{5–11}$), magnesio-ferri-hornblende and actinolite ($Mg\#_{82–87}$), and plagioclase ($Ab_{84–87}$) is found (Tables 3, 4, and 5).

Granoblastic matrix amphiboles, up to 0.5 mm in length, are magnesio-hornblende ($Mg\#_{88–94}$), whereas kelyphitic amphiboles are pargasite ($Mg\#_{61–77}$) (Table 5).

Mailolo Dome: eclogite PNG09-041c

Sample PNG09-041c is a medium- to coarse-grained eclogite, consisting of garnet and omphacite set in a matrix of sodic-calcic amphibole, calcite–dolomite, and coarse symplectite of less Na-rich clinopyroxene, amphibole, and plagioclase. Accessory phases include zircon, rutile, and apatite. The overall mineral phase proportions preserved are ~45% garnet, ~15% amphibole ~10% omphacite, ~10% calcite/dolomite, 5% quartz, 5% symplectite, 3% plagioclase, ~2% zircon, and ~2% rutile. The high-pressure, plagioclase-free assemblage was garnet + omphacite + quartz + rutile. Breakdown of interstitial omphacite is evident through growth of coarse to fine-grained symplectite between abundant garnet grains. A distinct population of ca. 4.6 Ma zircon is associated with calcic-amphibole that rims garnet and is in contact with peak omphacite and symplectite (Fig. 4b). The zircon also occurs as inclusions within interstitial calcite–dolomite and in most of these textural settings is associated with rutile, quartz, and apatite.

Within the Mailolo eclogite, garnets are subhedral to euhedral, typically range from 0.1–0.5 cm across, contain inclusions of amphibole and omphacite, and range in composition from $Alm_{53–61}Prp_{19–26}Grs_{17–20}And_{0–2}Sps_{1–2}$ (Table 1). Portions of matrix omphacite are preserved, with symplectite replacing rims, and in some cases, omphacite cores. Matrix omphacite gives a varied composition $Jd_{43–58}$, that does not correlate with location, whereas an omphacite inclusion in garnet (Jd_{57}) overlaps with the highest matrix

values (Table 3). Breakdown of peak omphacite results in symplectite consisting of less Na-rich omphacite ($Jd_{20–31}$) and a narrow plagioclase composition ($Ab_{88–93}$) (Table 4). Amphiboles occur as inclusions within garnet cores and are pargasite ($Mg\#_{57–66}$). In comparison, amphibole in contact with garnet, apatite, zircon, and calcite–dolomite in the matrix are sodic-calcic ($Mg\#_{54–69}$) (Table 5). Garnet typically contains a kelyphite of pargasite ($Mg\#_{63–71}$) (Table 5).

Goodenough Dome: eclogite PNG10-035a

Eclogite PNG10-035a has mineral phase proportions consisting of ~45% garnet, ~15% amphibole, ~15% clinopyroxene, ~10% plagioclase, ~5% quartz, and ~5 biotite, <1% rutile. Garnet are euhedral to subhedral and are set in a medium- to coarse-grained matrix of clinopyroxene and amphibole, with lesser amounts of plagioclase, quartz, biotite, and accessory rutile and zircon. The inferred peak metamorphic assemblage is garnet + clinopyroxene ± biotite + quartz + rutile. Retrogression has resulted in minor kelyphitic amphibole growth on peak garnet and replacement of peak clinopyroxene by amphibole and plagioclase (Fig. 5a).

Garnet ranges from 0.1–0.4 cm across, with a nearly homogenous composition of $Alm_{34–40}Prp_{42–47}Grs_{15–20}Sps_{1}And_{0–1}$ (Table 2). Matrix clinopyroxene is diopside ($Jd_{14–20}$), and clinopyroxene inclusions within garnet have similar Na-poor compositions ($Jd_{17–20}$) (Fig. 5a; Table 3). Biotite occurs in textural equilibrium with garnet and clinopyroxene and shows a range in TiO_2 (1–5 wt.%, up to 0.3 Ti a/fu) and $Mg\#_{74–84}$ (Tables 4 and 5), with no zoning observed. Matrix amphibole is strictly magnesio-hornblende, with $Mg\#_{79–}$

$_{86}$, whereas a single inclusion in garnet is tschermakite ($Mg\#_{86–87}$) (Table 5). Plagioclase, $Ab_{73–76}$, is typically associated with amphibole and quartz (Table 4).

Goodenough Dome: eclogite PNG12-82a

Eclogite PNG12-82a consists of subhedral to anhedral garnet in a medium-grained matrix of amphibole, plagioclase, and lesser clinopyroxene, biotite, and quartz. Eclogite PNG12-82a consists of ~40% garnet, ~20% amphibole, ~15% plagioclase, ~10% clinopyroxene, ~5% quartz, ~5% biotite, and ~1% rutile and the inferred peak metamorphic assemblage is garnet + clinopyroxene ± biotite + rutile. Retrogression has resulted in symplectite coronae of amphibole and plagioclase around peak garnet, and abundant amphibole and plagioclase growth at the expense of clinopyroxene and garnet (Fig. 5b). Garnets are deformed by brittle fractures that contain K-feldspar and/or chlorite within these zones.

Garnets are subhedral to anhedral, typically range from 0.2 to 0.5 cm across, and have a composition of $Alm_{35–44}Prp_{36–45}Grs_{16–20}And_{0–3}Sps_{1–2}$ (Table 1). In addition, garnets contain inclusions of diopside (Fig. 5b) that have a different composition in comparison to matrix diopside ($Jd_{14–18}$ vs. $Jd_{1–2}$, respectively) (Table 3). Throughout the eclogite, biotite occurs as randomly oriented crystals that are up to 1 mm in length and in contact with garnet, clinopyroxene, amphibole, and plagioclase. Biotite has high TiO_2 (up to 4 wt.%, 0.2 Ti a/fu) and a range in $Mg\#_{0.70–0.79}$ (Table 4). Tschermakite to magnesio-hornblende ($Mg\#_{0.75–0.91}$) amphibole extensively replaces matrix clinopyroxene and garnet, and it occurs with plagioclase within the matrix and as pargasitic ($Mg\#_{0.77–79}$) amphibole in symplectite surrounding garnet (Table 5). Matrix plagioclase is dominantly $Ab_{75–81}$, while plagioclase within symplectite is anorthite ($An_{84–89}$) (Table 4).

P-T estimates

Conventional geothermobarometry

Kyanite- and phengite-bearing eclogites from Mailolo and Oiatabu Domes preserve assemblages best suited for thermobarometry; however, eclogite-facies pressures and temperatures were not calculated for the more retrogressed samples exposed in the other domes. As discussed above, determining peak P-T conditions for eclogites that mainly consist of a bimineralic assemblage of garnet and omphacite is restrictive in that only minimum pressures can be calculated from the jadeite content of clinopyroxene. However, eclogite B20 from Oiatabu Dome contains an assemblage amenable to calculating peak P-T conditions via net-transfer reactions using the internally consistent expressions for Grt-Cpx-Phe and Grt-Cpx-Ky-SiO_2 equilibria, which nearly eliminates the uncertainties of Fe^{2+}/Fe^{3+}, as Mg-end members are the major components of these phases (Ravna and Terry, 2004). Using this equilibria, the Oiatabu Dome kyanite-phengite eclogite B20 yields P-T results that plot just below the coesite-stability field at ~27–28 kbar and ~630–640 °C (Fig. 12d).

In comparison, absolute P-T estimates can be determined for the phengite-bearing eclogite PNG08-010f by Grt-Cpx-Phe geothermobarometry, although uncertainties associated with Grt-Cpx thermometry are higher (±3.2 kbar and ±85 °C vs. ±3.2 kbar and ±65 °C) (Ravna and Terry, 2004). For PNG08-010f, a combination of the Fe–Mg exchange thermometer (Ravna, 2000) and the net-transfer reaction equilibria, 6diopside + 3muscovite = 2grossular + pyrope + 3celadonite were used to estimate peak P-T (Ravna and Terry, 2004). The Fe-Mg exchange thermometer and Grt-Cpx-Phe barometer

intersect at a fairly high angle on the quartz-coesite transition at P-T conditions of ~27.5 kbar and ~550 °C (Fig. 14d) for PNG08-010f.

The maximum pressure conditions for both samples were determined with the following mineral compositions: 1) omphacite with the highest jadeite content; 2) garnet with a maximum grossular $(a_{grs})^2a_{prp}$; and 3) phengite with the highest Si content (c.f., Ravna and Terry, 2004).

Phase-diagram modeling

Phase-diagram models (i.e., pseudosections) represent phase equilibria as a function of pressure and temperature for a specific bulk-rock composition, and within pseudosection models, mineral proportions and compositions (isopleths) can be contoured across P-T space. Important constraints can be taken from the contoured pseudosections: 1) the compositional change in minerals with increasing pressure (e.g., increase of Si content in phengite); 2) the variation in modal proportions of phases (e.g., omphacite, garnet, kyanite, amphibole) with changing P-T conditions; and 3) the appearance or disappearance of minerals at specific pressures (e.g., kyanite, phengite, amphibole).

Phase-diagram pseudosections were calculated with the software Perple_X (Connolly, 2005; version 6.7.0 Jan. 2015) and the Paralyzer tool (Mark Caddick, VT), using the internally consistent thermodynamic dataset of Holland and Powell (1998, hp02ver.dat). The pseudosections were calculated for the system Na_2O-CaO-FeO-MgO-Al_2O_3-SiO_2-H_2O-TiO_2-O_2 (NCFMASHTO), which models the peak metamorphic conditions for Oiatabu and Mailolo kyanite- and phengite-bearing eclogites. Pseudosections were calculated with the following solid-solution models (accessible

through the Perple_X datafile solution_model.dat): garnet (Gt(WPPH): White et al., 2005); clinopyroxene and amphibole (Omph(GHP2), cAmph(DP2): Diener and Powell, 2012); phengite (Pheng(HP)), biotite (TiBio(HP)), talc (T (HP)), chlorite (Chl(HP)), and epidote (Ep(HP)): Holland and Powell, 1998); ilmenite (Ilm(WPH): White et al., 2000); carbonate (odCcMS(EF): Franzolin et al., 2011); and feldspar (Fuhrman and Lindsley, 1988). Mineral isopleths calculated by the Perple_X 6.7.0 subprogram Werami are pyrope = Mg/Mg+Ca+Fe+Mn, grossular = Ca/Mg+Ca+Fe+Mn, almandine = Fe/Mg+Ca+Fe+Mn, omphacite = Na/Na+Ca, phengite = Si content based on 11 oxygens, and amphibole Mg# = $Mg^{2+}/Mg^{2+} + Fe^{2+}$. Representative chemical compositions of major phases are presented in Tables 2–5.

To investigate the P-T-X conditions for kyanite-phengite eclogite B20, compositional analyses of the pyrope content ($Prp_{44–50}$) in matrix garnet and garnet included in kyanite and the maximum Si content in phengite (Si = 3.5 a/fu) are used to determine peak conditions. The effective bulk composition (in mol%) used in the calculation is SiO_2 = 47.90, Al_2O_3 = 10.10, CaO = 9.11, MgO = 16.67, FeO = 6.25, Fe_2O_3 = 0.56, MnO = 0.14, K_2O = 0.53, Na_2O = 1.21, TiO_2 = 1.15, and H_2O = 1.15, and the stable mineral assemblages are calculated over a pressure range of 10–35 kbar and temperatures of 550–800 °C (Fig. 11). The observed assemblage in the rock, garnet-omphacite-kyanite-phengite-quartz/coesite-rutile, is stable across the entire temperature range at pressures above ~20–23 kbar, although the assemblage varies in the proportions of hydrous minerals (Fig. 11). The Si in phengite isopleths for this assemblage are subparallel to the P-axis providing well-constrained pressures. The maximum Si content indicates pressures of ~30–31 kbar, which intersects pyrope isopleths in the observed mineral-assemblage

field at temperatures in the range of ~635–660 °C (Fig. 12a, d). In addition, the estimated mineral proportions of peak phases, including garnet, omphacite, and phengite (Figs. 12b, c), are in agreement with observed amounts that would have been in the rock at peak pressures based on the proportions of the retrograde phases. The first appearance of amphibole occurs at pressures of ~23–18 kbar (Fig. 12d). The hydrous phases talc and lawsonite are predicted in minor proportions (<1%) for the peak P-T conditions, but are not observed in the rock.

Fresh eclogite PNG08-010f is modeled with an effective bulk composition of SiO_2 = 53.96, Al_2O_3 = 10.18, CaO = 9.11, MgO = 8.73, FeO = 9.37, Fe_2O_3 = 1.12, MnO = 0.17, K_2O = 0.20, Na_2O = 4.48, TiO_2 = 2.07, and H_2O = 0.60, and the stable mineral assemblages are calculated over the pressure range of 10–35 kbar and temperatures of 500–750 °C (Fig. 13). The observed peak mineral assemblage of garnet-omphacite-phengite-quartz/coesite-rutile is predicted at high pressures (above ~18 kbar) across the entire temperature range. The measured and calculated Si content in phengite (3.51) intersects the range in pyrope content ($Prp_{22–24}$) at pressures of ~27–30 kbar and temperatures of ~510–560 °C within the coesite-stability field (Fig. 14a, d). At these conditions, the mineral proportions of omphacite, garnet, quartz, and phengite calculated for the fresh eclogite are in very good agreement with the amount of peak phases preserved in the rock (Fig. 10b, c). Along the retrograde path, amphibole becomes stable with decreasing pressure and increasing temperature below ~26 kbar at ~550 °C and ~20 kbar at ~625 °C (Fig 14c). Minor kyanite (~1%) and lawsonite (<1%) are predicted to be stable in the modeled peak assemblage, but are not observed in the rock.

Determining peak P–T conditions by pseudosection modeling for Oiatabu kyanite eclogite 4329 is more limited compared to the other eclogites due to the absence of phengite in the rock. A phase diagram is calculated over a pressure range of 10–30 kbar and 550–900 °C for an effective bulk composition of SiO_2 = 47.73, Al_2O_3 = 14.69, CaO = 10.00, MgO = 15.72, FeO = 8.63, Fe_2O_3 = 0.28, MnO = 0.24, Na_2O = 1.08, TiO_2 = 1.50, and H_2O = 0.13 (Fig. 15a). The calculated and measured average pyrope, grossular, and almandine intersect the average jadeite component within the peak assemblage field observed in the rock over a range of P–T conditions from ~22–27 kbar and 560–650 °C (Fig. 15a). The predicted modal proportions of kyanite are slightly higher (~14%) than the modal percent in the rock (~9%; Fig. 15b). In addition, talc is predicted to be stable in minor amounts, but is not observed. Similar to the phengite-bearing pseudosections, amphibole becomes stable at ~23–18 kbar, and plagioclase is stable below pressures of ~16 kbar (Figs. 15a, b).

Discussion

Although the (U)HP eclogites of the D'Entrecasteaux Islands have been investigated over the last ~25 years, this is the first study to apply conventional thermobarometry using the net-transfer reactions among garnet-clinopyroxene-phengite-kyanite-coesite/quartz reactions and phase-equilibria modeling on the same samples to determine the peak P–T conditions. The combination of the two methods provides the most accurate and precise estimates of peak and retrograde P-T conditions for the PNG eclogites. Thermobarometry using the net-transfer reactions that involve the low-variance assemblage garnet + omphacite ± kyanite ± phengite + quartz reveals peak P-T estimates of ~27–28 kbar and

~630–640 °C for kyanite-phengite eclogite B20 and ~27.5 and ~550 °C for phengite-bearing eclogite PNG08-010f.

Pseudosection models that take into account the bulk-rock compositions provide estimates of the peak conditions, where there is good agreement between the modeled and observed peak mineral assemblages and where the calculated isopleths for garnet and phengite intersect within this mineral-stability field. Isopleths for kyanite-phengite eclogite B20 from Oiatabu Dome intersect at UHP conditions of ~30–31 kbar and ~635–660 °C, and isopleths for phengite eclogite PNG08-010f reveal pressures of ~27–30 kbar and temperatures of ~510–560 °C for the Mailolo eclogite. Lower P–T conditions for kyanite eclogite 4329 are loosely determined by garnet and omphacite isopleth intersections at ~22–27 kbar and 560–650 °C within the quartz-stability field.

The P–T results from thermobarometry and pseudosection modeling overlap within uncertainty (~10% for both techniques, although these may be underestimated, i.e., Baldwin et al., 2007; Palin et al., 2015). The pseudosections yield slightly higher pressures in comparison to the thermobarometry, and this likely results from the chosen activity models for clinopyroxene and garnet. The garnet-clinopyroxene-phengite barometer of Ravna and Terry (2004) uses the clinopyroxene model of Holland and Powell (1990) and garnet model of Ganguly et al. (1996), whereas the pseudosection models were calculated with more recent garnet (White et al., 2005) and clinopyroxene (Diener et al., 2012) models that take Fe^{3+} into account.

Pliocene UHP metamorphism

The Cenozoic Papuan orogen resulted in the northeast subduction of the northern

Australian rifted margin beneath the Papuan Ultramafic Belt (Davies and Jacques, 1984; Cloos et al., 2005; Little et al., 2011). Deeply subducted crustal material associated with this collision is thought to have remained metastable in the paleosubduction channel for >15 Myr, prior to the onset of ca. 6 Ma seafloor spreading within the Woodlark Basin (Little et al., 2011). The circulation of hot asthenospheric fluids ahead of the westward propagating spreading center likely recrystallized the crustal material at UHP (Little et al., 2011). Initial studies of PNG eclogites record pressures up to ~24 kbar and temperatures as high as ~900 °C (e.g., Davies and Warren, 1992; Hill and Baldwin, 1993; Baldwin et al., 2004), and the discovery of coesite within an eclogite from Mailolo Dome (Baldwin et al., 2008) confirmed that at least the core zone rocks of Mailolo Dome achieved depths > 90 km during their subduction–exhumation history (Fig. 16). This is supported by omphacite with the highest Jd content of all eclogites analyzed across the terrane and the common occurrence of radial fractures around quartz inclusions within rigid host minerals (i.e., garnet and omphacite) of the Mailolo Dome eclogites.

The P–T estimates from kyanite-and phengite-bearing eclogites in this study suggest both Mailolo and Oiatabu Dome eclogites equilibrated at UHP conditions (~27–31 kbar and 510–660 °C) prior to exhumation. Moreover, these new results provide the best estimate of the peak temperatures, as the previous estimates relied on thermometry that could be affected by Fe^{3+} (Fig. 16). The well-preserved peak assemblage in the Mailolo Dome eclogite indicates limited fluid infiltration during exhumation. In comparison, Oiatabu Dome eclogites also contain a well-preserved matrix of garnet and omphacite, although phengite is partially replaced by biotite and plagioclase in eclogite B20. The P–T results from both eclogites suggest that the dehydration-melting curve for phengite was

not approached during peak conditions (Fig. 16); therefore, phengite breakdown may have resulted from decompression during exhumation or from fluid infiltration associated with the formation of the late amphibole porphyroblasts. The porphyroblasts occur in both kyanite eclogites from Oiatabu Dome and are predicted from pseudosections to be stable at pressures below ~23–20 kbar. The prediction of initial amphibole as well as clinozoisite growth at ~23–18 kbar is a common feature in lower-temperature UHP eclogites (< 640 °C) (e.g., Tso Morari (Palin et al., 2014); Erzgebirge and Dabie Shan UHP terranes (Massonne, 2012)) and is interpreted to result from the destabilization of hydrous minerals and/or externally-derived fluids during exhumation. The Mailolo Dome eclogite does not contain late amphibole porphyroblasts, which is in agreement with the cooler (~100 °C) temperatures attained by both P-T methods. The previous P-T estimates of Goodenough Dome eclogites suggest they reached higher temperatures (>800 °C; Davies and Warren, 1992; Monteleone et al., 2007) in comparison to the other domes. These eclogites also contain abundant amphibole and plagioclase, which is associated with extensive amphibolite-facies overprinting. This may be related to more influence of the hot, rift environment, rather than a distinct fluid infiltration event that caused the distinctive Oiatabu amphibole porphyroblast growth.

A variety of ID-TIMS zircon dates have been collected from the eclogite across the PNG UHP terrane. The kyanite-phengite eclogites from Oiatabu Dome did not yield any zircon and have thus not been dated; however, DesOrmeau et al., (in prep.) report rapid zircon (re)crystallization at ca. 4.6 Ma in a retrogressed eclogite collected ~10 km to the northwest in Oiatabu. These zircon are interpreted to record fluid infiltration associated with retrogression of the peak eclogite mineral assemblage at ca. 4.6 Ma, as the coarse

zircon are likely associated with matrix and symplectite amphibole growth. This retrogression event may have also affected the kyanite-phengite eclogites studied here. In comparison, Mailolo Dome phengite eclogite was likely within the mantle at ca. 6.0–5.2 Ma (DesOrmeau et al., 2014), based on the zircon containing inclusions of the peak assemblage (omphacite, garnet, rutile, and phengite); omphacite and garnet inclusion compositions match the matrix mineral compositions used to constrain UHP conditions (Fig. 10). The combination of the zircon results that record the timing of the UHP and retrograde metamorphism, with the crystallization of nondeformed melt within the upper crust, suggests rapid UHP exhumation of the eastern PNG terrane at plate-tectonic rates (≥1.5 cm/yr) (DesOrmeau et al., in prep.).

Upon recrystallization under UHP conditions at ca. 6.0–5.2 Ma, the partially molten crustal material rose rapidly as one or more diapirs following a near-isothermal decompression path that was assisted by melting to the base of the crust (Davies and Warren, 1992; Hill and Baldwin, 1993; Baldwin et al., 2004; Ellis et al., 2011; Little et al., 2011; this study). During this ascent, initial retrogression of eclogites likely took place in Mailolo and Oiatabu Domes. Phengite eclogite from Mailolo Dome appears to have escaped fluid interaction during exhumation from UHP conditions, whereas eclogite PNG09-041c records fluid infiltration associated with the growth of the ca. 4.6 Ma zircon, rutile, quartz, and apatite assemblages along the rims of peak garnet and omphacite (DesOrmeau et al., in prep.). This fluid interaction, or lack thereof, could be an indication of the timing of exhumation to a part of the crust where rift-associated fluids were present, such that PNG08-010f escaped fluid interaction during rapid exhumation compared to other PNG eclogites that record fluid interaction at ca. 4.6–4.3 Ma.

Furthermore, Oiatabu Dome eclogites all preserve amphibole porphyroblasts and/or symplectite of amphibole and plagioclase likely associated with fluid interactions during exhumation from peak P-T conditions. Upon reaching the base of the crust, the exhumed UHP material likely slowed, allowing the UHP body to flow laterally and undergo migmatization (Little et al., 2011). This amphibolite-facies overprinting event is characterized by retrogressed ca. 2.8–2.6 Ma eclogites within Goodenough Dome in the west and by the crystallization of strongly deformed sills and layer-parallel leucosomes from Normanby, Mailolo and Goodneough Domes at ca. 4.1–2.8 Ma, followed by weakly deformed dikes recording melt crystallization as young as ca. 2.3 Ma across the domes (Gordon et al., 2012; DesOrmeau et al., 2014). The cooling and crystallization of nondeformed dikes, plutons, and pegmatite record the final emplacement of the domes within the upper crust by 1.8 Ma (Baldwin et al., 1993; DesOrmeau et al., 2014).

Conclusion

Peak pressure and temperature conditions are calculated for kyanite-and phengite-bearing eclogites from Mailolo and Oiatabu Domes by integrating thermobarometry and pseudosection modeling. Oiatabu Dome kyanite-phengite and Mailolo Dome phengite-bearing eclogite both record P–T conditions within the coesite-stability field at ~27–31 kbar and 630–660 °C and ~27–30 kbar and 510–560 °C, respectively. An additional Oiatabu Dome eclogite with kyanite, but no phengite, records a larger P–T range at high-pressure conditions of ~22–27 kbar and ~560–650 °C. These results suggest that eclogites preserved within two different domes, the Mailolo and Oiatabu Domes, were subducted to similar conditions in the upper mantle prior to different exhumation paths.

Subsequently, Oiatabu Dome eclogites underwent a retrogression event that caused the partial breakdown of phengite and the growth of amphibole porphyroblasts that partly replaced the peak assemblage. In comparison, the Mailolo Dome phengite eclogite was well armored within the core of a mafic boudin and was not likely affected by fluids during its ascent form mantle depths. The new P-T results from Oiatabu and Mailolo Dome eclogites indicate UHP recrystallization from ca. 6.0–5.2 Ma and their subsequent exhumation from mantle depths to shallow depths occurred at plate-tectonic rates (≥1.5 cm/yr).

References

Abers, G.A. (2001), Evidence for seismogenic normal faults at shallow depths in continental rifts. In: Wilson, R.C.L., R.B. Whitmarsh, B. Taylor, N. Froitzham, (Eds.), Non-volcanic Rifting of Continental Margins, pp. 305–318, *The Geological Society of London, Special Publications*, **187**, London.

Abers, G.A., A. Ferris, M. Craig, H. Davies, A.L. Lerner-Lam, J.C. Mutter, and B. Taylor (2002), Mantle compensation of active metamorphic core complexes at Woodlark rift in Papua New Guinea, *Nature*, **418**, 862–865, doi:10.1038/nature00990.

Baldwin, S.L., and J.P. Das (2015), Atmospheric Ar and Ne returned from mantle depths to the Earth's surface by forearc recycling, *PNAS*, doi:10.1073/pnas.1424122112.

Baldwin, S.L., G.S. Lister, E.J. Hill, D.A. Foster, and I. McDougall (1993), Thermochronologic constraints on the tectonic evolution of active metamorphic core complexes, D'Entrecasteaux Islands, Papua New Guinea, *Tectonics*, **12**, 611–628, doi: 10.1029/93TC00235.

Baldwin, S.L., B. Monteleone, L.E. Webb, P.G. Fitzgerald, M. Grove, and E.J. Hill (2004), Pliocene eclogite exhumation at plate tectonic rates in eastern Papua New Guinea, *Nature*, **431**, 263–267, doi:10.1038/nature02846.

Baldwin, J. A., Powell, R., Williams, M. L., & Goncalves, P. (2007). Formation of eclogite, and reaction during exhumation to mid-crustal levels, Snowbird tectonic zone, western Canadian Shield. *Journal of Metamorphic Geology*, *25*(9), 953-974.

Baldwin, S.L., L.E. Webb, and B.D. Monteleone (2008), Late Miocene coesite-eclogite exhumed in the Woodlark Rift, *Geology*, **36**, 735–738, doi: 10.1130/G25144A.1.

Carson, C.J., Powell, R., Clarke, G.L., 1999. Calculated mineral equilibria for eclogites in CaO**e**Na2O**e**FeO**e**MgO**e**Al2O3**e**SiO2**e**H2O: application to the Pouébo Terrane, Pam Peninsula, New Caledonia. Journal of Metamorphic Geology 17, 9**e**24. http://dx.doi.org/10.1046/j.1525-1314.1999.00177.x.

Carswell, D. A., O'Brien, P. J., Wilson, R. J. & Zhai, M., 1997. Thermobarometry of phengite-bearing eclogites in the Dabie Mountains of central China. Journal of Metamorphic Geology, 15, 239–252.

Cloos, M., B. Sapiie, Q.A. vanUfford, R.J. Weiland, P.Q. Warren, and T.P. McMahon (2005), Collisional delamination in New Guinea: the geotectonics of slab break-off, *Geological Society of America Special Paper* 400, **51**, doi: 10.1130/2005.2400.

Connolly, J. A. D. (2005). Computation of phase equilibria by linear programming: A tool for geodynamic modeling and its application to subduction zone decarbonation. Earth and Planetary Science Letters 236, 524–541.

Cuthbert, S. J., Carswell, D. A., Ravna, E. J. K. & Wain, A. L., 2000. Eclogites and eclogites in the Western Gneiss Region, Norwegian Caledonides. Lithos, 52, 165–195.

Ganguly, J., Cheng, W. & Tirone, M., 1996. Thermodynamics of aluminosilicate garnet solid solution: new experimental data, an optimized model, and thermometry applications. Contributions to Mineralogy and Petrology, 126, 137–151.

Davies, H. L. (1973), The Geology of Fergusson Island, *map with explanatory notes*, Australia Bureau of Mineral Resources.

Davies, H.L. (1980), Crustal structure and emplacement of ophiolite in southeastern Papua New Guinea, *Colloques Internationaux du C.N.R.S*, **272**, 17–33.

Davies, H.L. (1990), Structure and evolution of the border region of New Guinea. In: Carman, G.J., Z. Carman, (Eds.), Petroleum Exploration in Papua New Guinea: *Proceedings of the First PNG Petroleum Convention, Port Morseby, February 12–14, 1990*, 249–269.

Davies H.L. (2012), The geology of New Guinea: the cordilleran margin of the Australian continent, *Episodes*, **35**, 87–102.

Davies, H.L., and A.L. Jaques (1984), Emplacement of ophiolite in Papua New Guinea, *Geological Society of London Special Publication 13*, 341–350, doi: 10.1144/GSL.SP.1984.013.01.27.

Davies, H.L., and R.G Warren (1988), Origin of eclogite-bearing, domed, layered metamorphic complexes (core complexes) in the D'Entrecasteaux Islands, Papua New Guinea, *Tectonics,* **7**, 1–21, doi: 10.1029/TC007i001p00001.

Davies, H.L., and R.G. Warren (1992), Eclogites of the D'Entrecasteaux Islands, *Contrib. Mineral. Petrol.*, **112**, 463–474, doi: 10.1007/BF00310778.

Davies, H.L., and A.N. Williamson (1998), Buna, Papua New Guinea, 1:250,000 Geological Series, *Geological Survey of Papua New Guinea Explanatory Notes SC/55-3.*, Port Moresby, Papua New Guinea.

DesOrmeau, J. W., S. M. Gordon, T. A. Little, and S. A. Bowring (2014), Tracking the exhumation of a Pliocene (U)HP terrane: U-Pb and trace-element constraints from zircon, D'Entrecasteaux Islands, Papua New Guinea, *Geochem. Geophys. Geosyst.*, **15**, doi:10.1002/2014GC005396.

Diener, J.F.A., Powell, R., 2012. Revised activity**e**composition models for clinopyroxene and amphibole. Journal of Metamorphic Geology 30, 131**e**142.

Eilon, Z., G. A. Abers, G. Jin, and J. B. Gaherty (2014), Anisotropy beneath a highly extended continental rift, *Geochem. Geophys. Geosyst.*, **15**, 545–564, doi:10.1002/2013GC005092.

Eilon, Z., G. A. Abers, J. B. Gaherty, and G. Jin (2015), Imaging continental breakup using teleseismic body waves: The Woodlark Rift, Papua New Guinea, *Geochem. Geophys. Geosyst.*, **16**, doi:10.1002/2015GC005835.

Ellis, S.M., T.A Little, L.M. Wallace, B.R. Backer, and S.J.H Buiter (2011), Feedback between rifting and diapirism can exhume ultrahigh-pressure rocks, *Earth Planet. Sci. Lett.*, **311**, 427–438, doi: 10.1016/j.epsl.2011.09.031.

Fitzgerald, P.G., S.L. Baldwin, S.L. Miller, S.E. Perry, L.E. Webb, and T.A. Little (2008), Low temperature constraints on the evolution of metamorphic core complexes of the Woodlark rift system, *Annual Meeting of the American Geophysical Union. AGU, EOS Transactions*, San Francisco, CA.

Franzolin, E., Schmidt, M.W. & Poli, S. 2011. Ternary Ca–Fe–Mg carbonates: subsolidus phase relations at 3.5 GPa and a thermodynamic solid solution model including order/disorder. Contributions to Mineralogy and Petrology, 161, 213–227, http://dx.doi.org/10.1007/s00410-010-0527-x

Fuhrman, M. L., & Lindsley, D. H. (1988). Ternary-feldspar modeling and thermometry. *American Mineralogist*, *73*(3-4), 201-215.

Ganguly, J., Cheng, W. & Tirone, M., 1996. Thermodynamics of aluminosilicate garnet solid solution: new experimental data, an optimized model, and thermometry applications. Contributions to Mineralogy and Petrology, 126, 137–151.

Gasparik, T. & Lindsley, D. L. in Pyroxenes: Reviews in Mineralogy (ed. Prewitt, C. T.) 309–340 (Mineralogical Society of America, Washington DC, 1980).

Gordon, S.M., T.A. Little, B.R. Hacker, S.A. Bowring, S.L. Baldwin, and A.R.C. Kylander-Clark, (2012), Multi-stage exhumation of young UHP–HP rocks: timescales of melt crystallization in the D'Entrecasteaux Islands, southeastern Papua New Guinea, *Earth Planet. Sci. Lett.*, **351–352**, 237–246, doi: 10.1016/j.epsl.2012.07.014.

Hacker, B.R., 2006. Pressures and temperatures of ultrahigh-pressure metamorphism: implications for UHP tectonics and H2O in subducting slabs. International Geology Review 48, 1053–1066.

Hacker, B. R., & Gerya, T. V. (2013). Paradigms, new and old, for ultrahigh-pressure tectonism. *Tectonophysics*, *603*, 79-88.

Hermann, J., D. Rubatto, A. Korsakov, and V.S. Shatsky (2001), Multiple zircon growth during fast exhumation of diamondiferous, deeply subducted continental crust (Kokchetav Massif, Kazakhstan), *Contrib. Mineral. Petrol.*, **141**, 66–82, doi: 10.1007/s004100000218.

Hill, E.J. (1994), Geometry and kinematics of shear zones formed during continental extension in eastern Papua New Guinea, *J. Struct. Geol.*, **16**, 1093–1105, doi: 10.1016/0191-8141(94)90054-X.

Hill, E.J., S.L. Baldwin, and G.S. Lister (1992), Unroofing of active metamorphic core complexes in the D'Entrecasteaux Islands, Papua New Guinea, Geology, **20**, 907–910, doi: 10.1130/0091-7613(1992) 020<0907:UOAMCC> 2.3.CO;2.

Hill, E.J., and Baldwin, S.L. (1993), Exhumation of high-pressure metamorphic rocks during crustal extension in the D'Entrecasteaux region: Papua New Guinea, *J. Metamorph. Geol.*, **11**, 261–277, doi: 10.1111/j.1525-1314.1993.tb00146.x.

Hill, J., S.L. Baldwin, and G.S Lister (1995), Magmatism as an essential driving force for formation of active metamorphic core complexes in eastern Papua New Guinea, *J. Geophys. Res.*, **100**, 10441–10451, doi: 10.1029/94JB03329.

Holland, T. J. B. The reaction albite . jadeite . quartz determined experimentally in the range 600–1200**8**C. Am. Mineral. 65, 129–134 (1980).

Holland, T. J. B. & Powell, R., 1990. An enlarged and updated internally consistent thermodynamic dataset with uncertainties and correlations: The system K2O–Na2O–CaO–MgO–MnO–FeO–Fe2O3–Al2O3–TiO2–SiO2–C–H2–O2. Journal of Metamorphic Geology, 8, 89–124.

Holland, T.J.B., Powell, R., 1998. An internally-consistent thermodynamic dataset for phases of petrological interest. Journal of Metamorphic Geology 16, 309**e**344. http://dx.doi.org/10.1111/j.1525-1314.1998.00140.x.

Indares, A., White, R.W., Powell, R., 2008. Phase equilibria modelling of kyanitebearing anatectic paragneisses from the central Grenville Province. Journal of Metamorphic Geology 26, 815**e**836. http://dx.doi.org/10.1111/j.1525-

Kington, J. D., and A. M. Goodliffe (2008), Plate motions and continental extension at the rifting to spreading transition in Woodlark Basin, Papua New Guinea: Can oceanic plate kinematics be extended into continental rifts?, Tectonophysics, 458, 82–95.

Korchinski, M., et al. (2014), Timing of UHP exhumation and rock fabric development in gneiss domes containing the world's youngest eclogite-facies rocks, Woodlark Rift, southeastern Papua New Guinea, *J. Metamorph. Geol*., **32**, 1019–1039, http://dx.doi.org/10.1111/jmg.12105.

Kylander-Clark, A.R.C., Hacker, B.R., Johnson, C.M., Beard, B.L., Mahlen, N.J., Lapen, T.J. (2007), Coupled Lu–Hf and Sm–Nd geochronology constrains prograde and exhumation histories of high- and ultrahigh-pressure eclogites from western Norway. *Chem. Geol.*, **242(1–2)**, 137–154, http://dx.doi.org/10.1016/j.chemgeo.2007.03.006.

Kylander-Clark, A.R.C., Hacker, B.R., Johnson, C.M., Beard, B.L., Mahlen, N.J. (2009), Slow subduction and rapid exhumation of a thick ultrahigh-pressure terrane. *Tectonics*, **28(2)**, TC2003, http://dx.doi.org/10.1029/2007TC002251.

Kylander-Clark, A. R. C., B.R. Hacker, C.G. Mattinson (2012), Size and exhumation rate of ultrahigh-pressure terranes linked to orogenic stage, *Earth Planet. Sci. Lett.*, **321–322**, 115–120, http://dx.doi.org/10.1016/j.epsl.2011.12.036.

Little, T. A., S. L. Baldwin, P. G. Fitzgerald, and B. Monteleone (2007), Continental rifting and metamorphic core complex formation ahead of the Woodlark Spreading Ridge, D'Entrecasteaux Islands, Papua New Guinea, Tectonics, 26, TC1002, doi:10.1029/2005TC001911.

Little, T.A., B.R. Hacker, S.M. Gordon, S.L. Baldwin, P.G. Fitzgerald, S. Ellis, and M. Korchinski (2011), Diapiric exhumation of Earth's youngest (UHP) eclogites in the gneiss domes of the D'Entrecasteaux Islands, Papua New Guinea, *Tectonophysics*, **510**, 39–68, doi: 10.1016/j.tecto.2011.06.006.

Little, T.A., B.R. Hacker, S.J. Brownlee, and G. Seward (2013), Microstructures and quartz lattice-preferred orientations in the eclogite-bearing migmatitic gneisses of the D'Entrecasteaux Islands, Papua New Guinea, *Geochem., Geophys., Geosyst.*, ***14*** **(6)**, 2030–2062, doi: 10.1002/ggge.20132.

Lus, W.Y., I. McDougall, and H.L. Davies (2004), Age of metamorphic sole of the Papuan Ultramafic Belt ophiolite, Papua New Guinea, *Tectonophysics, 392*, 85–101, doi: 10.1016/j.tecto.2004.04.009.

Mattinson, J.M. (2005), Zircon U-Pb chemical abrasion ("CA-TIMS") method: combined annealing and multi-step partial dissolution analysis for improved precision and accuracy of zircon ages, *Chem. Geol.*, **220**, 47–66, doi: 10.1016/j.chemgeo.2005.03.011.

Mattinson, C.G., Wooden, J.L., Liou, J.G., Bird, D.K., Wu, C.L. (2006), Age and duration of eclogite-facies metamorphism, North Qaidam HP/UHP terrane, Western China. *Amer. J. Science*, **306**, 683–711, http://dx.doi.org/10.2475/09.2006.01.

Massonne, H. J. (2013). Constructing the pressure–temperature path of ultrahigh-pressure rocks. *Elements*, *9*(4), 267-272.

Monteleone, B.D., S.L. Baldwin, L.E. Webb, P.G. Fitzgerald, M. Grove, and A.K. Schmitt (2007), Late Miocene–Pliocene eclogite facies metamorphism, D'Entrecasteaux Islands, SE Papua New Guinea, *J. Metamorph. Geol.*, **25**, 245–265, doi: 10.1111/j.1525-1314.2006.00685.x.

Nowlan, E. U., Schertl, H.-P. & Schreyer, W., 2000. Garnet–omphacite–phengite thermobarometry of eclogites from the coesite-bearing unit of the southern Dora-Maira Massif, Western Alps. Lithos, 52, 197–2000.

O'Brien, P.J., 2001. Subduction followed by collision: Alpine and Himalayan examples. Physics of the Earth and Planetary Interiors 127, 277–291.

Palin, R.M., St-Onge, M.R., Waters, D.J., Searle, M.P., Dyck, B., 2014. Phase equilibria modelling of retrograde amphibole and clinozoisite in mafic eclogite from the Tso Morari massif, northwest India: constraining the **P-T-M**(H2O) conditions of exhumation. Journal of Metamorphic Geology 32, 675**e**693. http://dx.doi.org/10.1111/jmg.12085.

Palin, R.M., et al., (in press), Quantifying geological uncertainty in metamorphic phase equilibria modelling; a Monte Carlo assessment and implications for tectonic interpretations, Geoscience Frontiers, http://dx.doi.org/10.1016/j.gsf.2015.08.005

Parrish, R.R., Gough, S.J., Searle, M.P., Waters, D.J., 2006. Plate velocity exhumation of ultrahigh-pressure eclogites in the Pakistan Himalaya. Geology 34, 989–992.

Powell, R., Holland, T.J.B., 2008. On thermobarometry. Journal of Metamorphic Geology 26, 155**e**179.

Powell R, Holland T (2010) Using equilibrium thermodynamics to understand metamorphism and metamorphic rocks. Elements 6: 309-314

Proyer, A., Dachs, E. & McCammon, C., 2004. Pitfalls in geothermobarometry of eclogites: Fe3+ and changes in the mineral chemistry of omphacite at ultrahigh pressures. Contributions to Mineralogy and Petrology, 147, 305–318.

Ragozin, A. L., J. G. Liou, V.S. Shatsky, and N.V. Sobolev (2009), The timing of the retrograde partial melting in the Kumdy-Kol region (Kokchetav Massif, Northern Kazakhstan), *Lithos*, **109**, 274–284, doi:10.1016/j.lithos.2008.06.017.

Ravna, E. J. K., 2000. The garnet–clinopyroxene geothermometer–an updated calibration. Journal of Metamorphic Geology, 18, 211–219.

Ravna, E.K., and Terry, M.P., 2004, Geothermometry of UHP and HP eclogites and schists and evaluation of equilibria among garnet-clinopyroxene-kyanite-phengite-coesite/quartz: Journal of Metamorphic Geology, v. 22, p. 579–592, doi:10.1111/j.1525–1314.2004.00534.x.

Ravna, E. J. K. & Paquin, J., 2004. Thermobarometric methodologies applicable to eclogites and garnet ultrabasites. EMU Notes in Mineralogy, vol. 5, Ch. 8, 229–259.

Rogerson, R., D.B. Hilyard, E.J. Finlayson, D.J. Holland, S.T.S. Nion, R.M. Sumarang, J. Dugaman, and C.D.C. Loxton (1987), The geology and mineral resources of the Sepik headwaters region, Papua New Guinea, *Papua New Guinea Geological Surveys Memoir, 12*.

Rubatto, D. (2002), Zircon trace element geochemistry: distribution coefficients and the link between U-Pb ages and metamorphism, *Chem. Geol.*, **184**, 123–138, doi: 10.1016/S0009-2541(01)00355-2.

Rubatto, D., and J. Hermann (2001), Exhumation as fast as subduction?, *Geology*, **29***,* 3–6, doi: 10.1130/0091-7613(2001) 029<0003:EAFAS> 2.0.CO;2.

Rubatto, D., Hermann, J. (2003), Zircon formation during fluid circulation in eclogites (Monviso, Western Alps): implications for Zr and Hf budget in subduction zones. *Geochim. et Cosmochim. Acta.*, **67**, 2173–2187, http://dx.doi.org/10.1016/S0016-7037(02)01321-2.

Rubatto, D., Hermann, J. (2007a), Zircon behaviour in deeply subducted rocks, *Elements*, **3**, 31–35, http://dx.doi.org/10.2113/gselements.3.1.31.

Rubatto, D., Hermann, J. (2007b), Experimental zircon/melt and zircon/garnet trace element partitioning and implications for the geochronology of crustal rocks. *Chem. Geol.*, **241**, 38-61, http://dx.doi.org/10.1016/j.chemgeo.2007.01.027.

Schmid, R., (2001). Geology of Ultra-High-Pressure Rocks from the Dabie Shan, Eastern China. Dissertation am Institut für Geowissenschaften der Universität Potsdam, 141 pp.

Schoene, B., C. Latkoczy, U. Schaltegegger, and D. Günther (2010), A new method integrating high-precision U–Pb geochronology with zircon trace-element analysis (U–Pb TIMS-TEA), *Geochim, et Cosmochim. Acta.*, **74**, 7144–7159, doi: 10.1016/j.gca.2010.09.016.

Sizova, E., Gerya, T., and Brown, M., 2012. Exhumation mechanism of ultrahigh pressure crustal rocks during collision of spontaneously moving plates, J. Metamorph. Geol., 30, 927–955, doi:10.1111/j.1525-1314.2012.01004.x.

Smith, D.C. (1984), Coesite in clinopyroxene in the Caledonides and its implications for geodynamics, *Nature*, **310**, 641–644, doi:10.1038/310641a0.

Sobolev, N.V., and V.S. Shatsky (1990), Diamond inclusions in garnets from metamorphic rocks; a new environment of diamond formation, *Nature*, **343**, 742–746, doi:10.1038/343742a0.

Stípská, P., Powell, R., 2005. Constraining the **PeT** path of a MORB-type eclogite using pseudosections, garnet zoning, and garnet**e**clinopyroxene thermometry: an example from the Bohemian Massif. Journal of Metamorphic Geology 23, 725**e**743. http://dx.doi.org/10.1111/j.1525-1314.2005.00607.x.

Sun S. S., and W.F. McDonough (1989), Chemical and isotopic systematics of oceanic basalts: implications for mantle composition and processes, *Geological Society of London Special Publications*, **42**, 313–345, doi: 10.1144/GSL.SP.1989.042.01.19.

Taylor, B., A.M. Goodliffe, F. Martinez (1999), How Continents break-up: insights from Papua New Guinea, *J. Geophys. Res.*, **104**, 7497–7512, doi: 10.1029/1998JB900115.

Taylor, B., and P. Huchon (2002), Active continental extension in the western Woodlark Basin: a synthesis of Leg 180 results, in Proceedings of the Ocean Drilling Program, Scientific Results [CD ROM], vol. 180, edited by P. Huchon, B. Taylor, and A. Klaus, pp. 1–36, Ocean Drill. Prog., Texas A&M Univ., College Station, Tex.

Tregoning, P., K. Lambeck, A. Stoltz, P. Morgan, S. C. McClusky, P. van der Beek, H. McQueen, R. J. Jackson, R. P. Little, A. Laing, and B. Murphy (1998), Estimation of current plate motions in Papua New Guinea from Global Positioning System observations, *J. Geophys. Res.*, **103**, 12,181– 12,203, doi: 10.1029/97JB03676.

Utsunomiya, S., Valley, J. W., Cavosie, A. J., Wilde, S. A., & Ewing, R. C. (2007). Radiation damage and alteration of zircon from a 3.3 Ga porphyritic granite from the Jack Hills, Western Australia. *Chemical Geology*, *236*(1), 92-111.

Van Ufford, Q.A., and M. Cloos (2005), Cenozoic tectonics of New Guinea, *Am. Assoc. Pet. Geol. Bull.*, **89**, 119–140, doi:10.1306/08300403073.

Vry, J., and M. Gazley (submitted manuscript), Zr-in-rutile: A thermobarometer for eclogites, *J. Metamorph. Geol.* (2015).

Wain, A., 1998. Ultrahigh-pressure metamorphism in the Western Gneiss region of Norway. D. Phil. Thesis, University of Oxford, Oxford.

Wain, A., Waters, D. J. & Austrheim, H., 2001. Metastability of granulites and processes of eclogitisation in the UHP region of western Norway. Journal of Metamorphic Geology, 19, 609–625.

Waters, D. J. & Martin, H. N., 1993. Geobarometry of phengite-bearing eclogites. Terra Abstracts, 5, 410–411.

Waggoner, A., S.L. Baldwin, L.A Webb, T.A. Little, and P.G. Fitzgerald (2008), Temporal constraints on continental rifting and the exhumation of the youngest known HP metamorphic rocks, SE Papua New Guinea, *Eos Trans. AGU, 89(53)*, Fall Meet. Suppl., Abstract T41B-1961.

Wallace, L.M., C. Stevens, E. Silver, R. McCaffrey, W. Loratung, S. Hasiata, R. Stanaway, R. Curley, R. Rosa, and J. Taugaloidi (2004), GPS and seismological constraints on active tectonics and arc-continent collision in Papua New Guinea: implications for mechanics of microplate rotations in a plate boundary zone, *J. Geophys. Res.*, **109**, doi:10.1029/2003JB002481.

Wallace, L. M., S. Ellis, T. Little, P. Tregoning, N. Palmer, R. Rosa, R. Stanaway, J. Oa, E. Nidkombu, and J. Kwazi (2014), Continental breakup and UHP rock exhumation in action: GPS results from the Woodlark Rift, Papua New Guinea, Geochem. Geophys. Geosyst., 15, 4267–4290, doi:10.1002/2014GC005458.

Warren, C., 2013. Exhumation of (ultra-)high-pressure terranes: concepts and mechanisms. Solid Earth 4, 75–92.

Wallis, S., Tsuboi, M., Suzuki, K., Fanning, M., Jiang, L., and Tanaka, T., 2005, Role of partial melting in the evolution of the Sulu (eastern China) ultrahigh-pressure terrane: Geology, v. 33, p. 129–132.

Weissel, J.K., B. Taylor, and G.D Karner (1982), The opening of the Woodlark Basin, subduction of the Woodlark spreading system, and the evolution of northern Melanesia since mid-Pliocene time, *Tectonophysics*, **87**, 253–277, doi: 10.1016/0040-1951(82)90229-3.

Westaway, R. (2007), Correction to "Active low angle normal-faulting in the Woodlark extensional province, Papua New Guinea: a physical model, *Tectonics*, **26**, TC1003.

White, R. W., Pomroy, N. E., & Powell, R. (2005). An in situ metatexite–diatexite transition in upper amphibolite facies rocks from Broken Hill, Australia. *Journal of Metamorphic Geology*, *23*(7), 579-602.

Whitney, D.L. & Evans, B.W., 2010. Abbreviations for names of rock-forming minerals. American Mineralogist, 95, 185–187. doi:10.2138/am.2010.3371

Zirakparvar, N.A., S.L. Baldwin, and J.D. Vervoort (2011), Lu–Hf garnet geochronology applied to plate boundary zones: insights from the (U)HP terrane exhumed within the Woodlark Rift, *Earth Planet. Sci. Lett.*, **309**, 56–66, doi: 10.1016/j.epsl.2011.06.016.

Table 1. Previous thermobarometry studies of D'Entrecsteaux Islands (U)HP eclogites

	Sample	Gneiss Dome locality	Temerature (°C)	Pressure (kbar)	Jd content (highest)	Notes
Davies and Warren, 1992	B20	western Oiatabu	~600	14	27	ky, ph
	4329	western Oiatabu	~800	16	39	ky
			~600	13		
	B57	Morima	~700	17	49	ph
	B60	Morima	-	-	46	ph
	A3	western Morima	-	-	45	
	B130	western Morima	~530	17	43	ph
	A223	Mailolo	~850	18	43	ph
			~725	16		
	A10	coesite locality, Mailolo	~725	17	50	ph
			~530	12		
	4317	western Mailolo	~830	17	41	
	A276a	southeast Goodenough	~830	25	16	
	4309	southern Goodenough	~700	15	10	
	4313	northern Goodenough	~750	16	13	
	4314	Goodenough	~730	17	13	
Hill and Baldwin, 1993	890432	western Oiatabu	~850	21	60	
	890061	coesite locality, Mailolo	~730	19	59	
	870913	Mailolo	~830	17	30	
	870914	Mailolo	~850	15	26	
	870952	Mailolo	~870	21	60	
Baldewin et al., 2004	870921	Mailolo	870–930	24	57	
Monteleone et al., 2007	89321a	coesite locality, Mailolo	650–680*	15	65	coesite, ph
			612–740**	18–26 (grt-cpx-ph)		
	03092a	western Mailolo	633–719**	-	-	no omp
	03118b	southeast Goodenough	677–817**	14	n.r.	
	89302	northern Goodenough	718–958**	-	-	no omp
	89304	northern Goodenough	740–870*	-	-	no omp
			820–1015**			
Baldwin et al., 2008	89321c	coesite locality, Mailolo	600–760	18–27 (grt-cpx-ph)	65	coesite, ph
			695–743**			
This study	PNG08-010f (net)	coesite locality, Mailolo	~550	~27.5 (grt-cpx-ph)	66	ph
	pseudosection		~510–560	~27–30		
	B20 (net)	western Oiatabu	~630–640	~27–28	32	ky, ph
	pseudosection		~635–660	~30–31		
	4329 (pseudosection)	western Oiatabu	~560–650	~22–27	32	ky

Temperatures are calculated with grt-cpx thermometry, except for * Ti-in-zircon temperature, ** Zr-in-rutile temperature estimates, and this study (net-transfer reactions (Ravna and Terry, 2004) and pseudosection results).
All pressures are a minimum, except for grt-cpx-ph barometry (Ravna and Terry, 2004) and this study (net-transfer reactions (Ravna and Terry, 2004) and pseudosection results).
Some samples have multiple estimates, for example Oiatabu Dome 4329.
n.r. - not reported

Table 2. Representative compositions of garnet for D'Entrecasteaux Islands eclogites

Sample	B20	B20	4329	4329	PNG08-010F	PNG08-010F	PNG12-95a	PNG12-95a	PNG09-041c	PNG09-041c	PNG10-035a	PNG12-82a
Mineral	Grt	Grt	Grt	Grt	Grt	Grt	Grt	Grt	Grt	Grt	Grt	Grt
Analysis	1_4	9_1	1_4	2	4_4	zrn_g1	1_1	1_9	10_47	10_19	3_6	1_21
Type	Matrix	Incl	Matrix	Incl	Matrix	Incl	Matrix	Matrix	Matrix	Matrix	Matrix	Matrix
Assoc. min/loc.		Ky		Ky		Zrn	Rim	Core	Rim	Core		
SiO_2	39.54	39.83	39.75	40.88	38.69	39.51	39.50	40.09	39.19	38.91	40.31	39.86
TiO_2	0.02	0.00	0.02	0.00	0.02	0.00	0.23	0.25	0.23	0.18	0.09	0.22
Al_2O_3	22.97	23.18	23.32	23.21	22.84	23.55	22.35	22.47	22.61	22.38	23.37	22.75
Cr_2O_3	0.01	0.06	0.10	0.02	0.00	0.00	0.03	0.02	0.00	0.00	0.00	0.00
Fe_2O_3	1.31	1.20	1.35	0.00	0.00	0.00	1.08	0.13	0.00	0.00	0.31	0.02
FeO	17.47	16.86	16.29	17.20	26.63	26.18	18.77	17.57	25.48	25.29	17.07	18.13
MnO	0.46	0.37	0.51	0.46	0.48	0.44	0.55	0.50	0.54	0.78	0.50	0.62
MgO	11.89	12.72	12.81	12.08	5.97	5.71	11.10	12.12	6.59	6.01	12.49	11.62
CaO	6.34	6.03	5.91	6.97	5.97	6.12	6.50	6.59	6.16	7.18	6.56	6.44
Na_2O	0.01	0.00	0.06	0.01	0.06	0.00	0.00	0.01	0.15	0.04	0.01	0.03
K_2O	0.00	0.00	0.02	0.00	0.00	0.00	0.00	0.00	0.00	0.00	0.00	0.00
Total	100.02	100.25	100.15	100.83	100.66	101.51	100.11	99.74	100.94	100.77	100.70	99.69
Si	2.95	2.95	2.95	3.01	2.98	3.00	2.97	2.99	3.00	2.99	2.97	2.99
Ti	0.00	0.00	0.00	0.00	0.00	0.00	0.01	0.01	0.01	0.01	0.01	0.01
Al	2.02	2.03	2.04	2.01	2.07	2.11	1.98	1.98	2.04	2.03	2.03	2.01
Cr	0.00	0.00	0.01	0.00	0.00	0.00	0.00	0.00	0.00	0.00	0.00	0.00
Fe^{3+}	0.07	0.07	0.08	0.00	0.00	0.00	0.06	0.01	0.00	0.00	0.02	0.00
Fe^{2+}	1.09	1.05	1.01	1.06	1.72	1.66	1.18	1.10	1.63	1.63	1.05	1.14
Mn	0.03	0.02	0.03	0.03	0.03	0.03	0.04	0.03	0.04	0.05	0.03	0.04
Mg	1.32	1.41	1.41	1.33	0.69	0.65	1.24	1.35	0.75	0.69	1.37	1.30
Ca	0.51	0.48	0.47	0.55	0.49	0.50	0.52	0.53	0.50	0.59	0.52	0.52
Na	0.00	0.00	0.01	0.00	0.01	0.00	0.00	0.00	0.02	0.01	0.00	0.00
K	0.00	0.00	0.00	0.00	0.00	0.00	0.00	0.00	0.00	0.00	0.00	0.00
Sum	8.00	8.00	8.00	7.99	7.99	7.95	8.00	8.00	7.98	7.99	8.00	8.00
Oxygen	12	12.00	12.00	12.00	12.00	12.00	12.00	12.00	12.00	12.00	12.00	12.00
Alm	0.36	0.35	0.34	0.36	0.59	0.59	0.39	0.36	0.56	0.55	0.35	0.38
Prp	0.44	0.47	0.47	0.45	0.23	0.23	0.41	0.45	0.26	0.23	0.46	0.43
Grs	0.17	0.16	0.16	0.19	0.17	0.18	0.17	0.17	0.17	0.20	0.17	0.17
Sps	0.01	0.01	0.01	0.01	0.01	0.01	0.01	0.01	0.01	0.02	0.01	0.01
Adr	0.02	0.02	0.03	-	-	-	0.02	0.002	-	-	0.01	-
XMg	0.55	0.57	0.58	0.56	0.29	0.28	0.51	0.55	0.32	0.30	0.57	0.53
XFe^{3+}	0.06	0.06	0.07	-	-	-	0.05	0.01	-	-	0.02	-

XMg = Mg/(Mg + Fe^{2+}); XFe^{3+} = Fe^{3+}/(Total Fe).

Abbreviations: Adr, andradite; Alm, almandine; Grs, grossular; Grt, garnet; Incl, inclusion; Prp, pyrope; Sps, spessartine; Zrn, zircon.

Table 3. Representative compositions of clinopyroxene for D'Entrecasteaux Islands eclogites

Sample	B20	B20	4329	4329	PNG08-010F	PNG08-010F	PNG12-95a	PNG12-95a	PNG12-95a	PNG09-041c	PNG09-041c	PNG09-041c	PNG10-035a	PNG10-035a	PNG12-82a	PNG12-82a
Mineral	Omp	Omp	Omp	Omp	Omp	Omp	Omp	Di	Di	Omp	Omp	Omp	Di	Di	Di	Di
Analysis	2_6	6_5	2_3	10	6_1	zrn_cpx12	7_6	1_4	2_2	4_2	2_2	1_2	2_5	5_1	3_2	6_3
type	Matrix	Incl	Matrix	Incl	Matrix	Incl	Matrix	Symp	Symp	Matrix	Incl	Symp	Matrix	Incl	Incl	Matrix
Assoc. min/loc.		Ky		Ky		Zrn		Omp	Matrix		Grt	Omp		Grt	Grt	
SiO_2	55.46	57.02	56.66	56.52	56.85	55.47	54.88	53.78	54.77	55.52	55.61	52.51	52.27	53.88	53.38	54.05
TiO_2	0.06	0.05	0.07	0.04	0.11	0.12	0.12	0.07	0.03	0.20	0.23	0.21	0.23	0.41	0.36	0.03
Al_2O_3	7.59	7.25	7.88	7.55	13.96	13.39	6.74	1.96	0.94	12.88	12.79	4.54	6.35	7.62	5.06	0.39
Cr_2O_3	0.07	0.11	0.14	0.10	0.01	0.01	0.00	0.03	0.00	0.01	0.03	0.03	0.04	0.02	0.00	0.01
Fe_2O_3	1.19	0.79	0.12	0.00	2.82	5.55	1.45	2.87	1.21	2.14	4.17	2.84	1.97	0.37	2.10	0.29
FeO	1.95	2.02	2.05	1.94	2.39	0.26	2.55	1.64	3.76	2.73	2.23	4.00	4.13	4.77	3.69	5.83
MnO	0.00	0.01	0.01	0.01	0.00	0.02	0.04	0.05	0.06	0.00	0.03	0.00	0.10	0.12	0.13	0.14
MgO	12.37	12.98	12.67	12.93	5.93	6.29	12.11	15.52	15.18	6.82	6.88	11.61	12.86	12.80	13.94	14.97
CaO	17.84	17.83	18.24	18.73	8.65	8.93	17.78	23.39	23.24	11.17	11.11	19.85	19.72	19.58	20.35	24.33
Na_2O	4.21	4.36	4.27	3.95	9.49	9.52	4.05	1.09	1.05	8.05	8.17	2.75	2.22	2.59	2.03	0.18
K_2O	0.00	0.00	0.00	0.00	0.01	0.01	0.00	0.00	0.00	0.02	0.02	0.03	0.00	0.00	0.00	0.00
Total	100.74	102.42	102.11	101.77	100.22	99.58	99.71	100.40	100.24	99.53	101.27	98.38	99.89	102.16	101.04	100.22
Si	1.97	1.99	1.98	1.98	1.99	1.96	1.98	1.96	2.00	1.97	1.95	1.95	1.91	1.91	1.93	1.99
Ti	0.00	0.00	0.00	0.00	0.00	0.00	0.00	0.00	0.00	0.01	0.01	0.01	0.01	0.01	0.01	0.00
Al	0.32	0.30	0.32	0.31	0.58	0.56	0.29	0.08	0.04	0.54	0.53	0.20	0.27	0.32	0.22	0.02
Cr	0.00	0.00	0.00	0.00	0.00	0.00	0.00	0.00	0.00	0.00	0.00	0.00	0.00	0.00	0.00	0.00
Fe^{3+}	0.03	0.02	0.003	0.00	0.08	0.15	0.04	0.08	0.03	0.06	0.11	0.08	0.05	0.01	0.06	0.01
Fe^{2+}	0.06	0.06	0.06	0.06	0.07	0.01	0.08	0.05	0.12	0.08	0.07	0.13	0.13	0.14	0.11	0.18
Mn	0.00	0.00	0.00	0.00	0.00	0.00	0.00	0.00	0.00	0.00	0.00	0.00	0.00	0.00	0.00	0.00
Mg	0.65	0.67	0.66	0.68	0.31	0.33	0.65	0.84	0.83	0.36	0.36	0.64	0.70	0.68	0.75	0.82
Ca	0.68	0.67	0.68	0.70	0.33	0.34	0.69	0.91	0.91	0.43	0.42	0.79	0.77	0.75	0.79	0.96
Na	0.29	0.29	0.29	0.27	0.65	0.65	0.28	0.08	0.07	0.56	0.56	0.20	0.16	0.18	0.14	0.01
K	0.00	0.00	0.00	0.00	0.00	0.00	0.00	0.00	0.00	0.00	0.00	0.00	0.00	0.00	0.00	0.00
Sum	4.00	4.00	4.00	4.00	4.00	4.01	4.00	4.00	4.00	4.00	4.00	4.00	4.00	4.00	4.00	4.00
Oxygen	6.00	6.00	6.00	6.00	6.00	6.00	6.00	6.00	6.00	6.00	6.00	6.00	6.00	6.00	6.00	6.00
Al(iv)	0.03	0.01	0.02	0.02	0.01	0.04	0.02	0.04	0.00	0.03	0.05	0.05	0.09	0.09	0.08	0.01
Al(vi)	0.29	0.28	0.30	0.29	0.57	0.52	0.26	0.04	0.04	0.51	0.48	0.15	0.18	0.23	0.14	0.01
XMg	0.92	0.92	0.92	0.92	0.82	0.98	0.89	0.94	0.88	0.82	0.85	0.84	0.85	0.83	0.87	0.82
Jd	0.30	0.31	0.30	0.28	0.66	0.66	0.29	0.08	0.08	0.57	0.57	0.20	0.17	0.19	0.15	0.01
XFe^{3+}	0.36	0.26	0.05	-	0.52	0.95	0.34	0.61	0.22	0.41	0.63	0.39	0.30	0.07	0.34	0.04

XMg = Mg/(Mg + Fe^{2+}); Jd = Na/(Na + Ca); XFe^{3+} = Fe^{3+}/(Total Fe).

Abbreviations: Di, diospide; Grt, garnet; Jd, jadeite; Ky, kyanite; Omp, omphacite; Zrn, zircon.

Table 4. Representative compositions of mica, plagioclase, and carbonate for D'Entrecasteaux Islands eclogites

Sample	B20	PNG08-010F	PNG08-010F	PNG10-035a	PNG12-82a	B20	4329	PNG08-010F	PNG12-95a	PNG12-95a	PNG09-041c	PNG10-035a	PNG12-82a	PNG12-82a	PNG09-041c	PNG09-041c
Mineral	Ph	Ph	Ph	Bt	Bt	Pl	Pl	Pl	Pl	Pl	Pl	Pl	Pl	Pl	Cal	Dol
Analysis	2_3	1_3	2_9	2_4	20	4_3	1_3	15	4_8	1_2	27	2_3	6_1	4_1	6	8
Type	Matrix	Incl	Matrix	Matrix	Matrix	Matrix	Matrix	Symp	Symp	Symp	Symp	Matrix	Matrix	Symp	Matrix	Matrix
Assoc. min/loc.		Grt				Ky	Ky		Matrix	Omp	Omp			Grt		
SiO_2	52.59	51.02	50.92	38.43	37.82	48.78	54.85	67.12	64.47	67.36	65.80	62.17	63.97	47.56	0.00	0.00
TiO_2	0.37	0.63	0.74	3.34	3.44	0.00	0.01	0.00	0.00	0.00	0.00	0.00	0.00	0.00	0.00	0.00
Al_2O_3	26.57	26.33	25.53	16.12	15.67	33.31	29.39	19.98	22.40	19.94	21.39	23.96	23.13	34.52	0.00	0.00
Cr_2O_3	0.15	0.00	0.00	0.06	0.01	0.00	0.00	0.00	0.00	0.00	0.00	0.00	0.00	0.00	0.00	0.00
Fe_2O_3	0.00	0.18	0.00	1.75	2.24	0.44	0.33	0.19	0.17	0.14	0.21	0.03	0.14	0.59	0.00	0.00
FeO	1.34	2.13	2.12	8.92	11.41	0.00	0.00	0.00	0.00	0.00	0.00	0.00	0.00	0.00	0.59	7.35
MnO	0.00	0.00	0.00	0.03	0.14	0.00	0.00	0.00	0.00	0.00	0.00	0.00	0.00	0.01	0.28	0.14
MgO	4.49	3.95	4.11	18.21	16.90	0.00	0.00	0.00	0.00	0.03	0.01	0.00	0.00	0.00	0.32	16.38
CaO	0.01	0.00	0.00	0.01	0.00	15.83	11.20	0.44	3.22	0.78	2.24	5.17	4.08	17.03	56.83	30.04
Na_2O	0.37	1.02	0.60	0.85	0.51	2.49	5.18	11.69	9.78	11.82	10.74	8.74	9.53	1.81	0.00	0.00
K_2O	10.57	9.17	9.91	7.73	6.87	0.04	0.00	0.03	0.04	0.03	0.03	0.08	0.00	0.00	0.00	0.00
Total	96.46	94.44	93.93	95.46	95.00	100.89	100.96	99.45	100.08	100.10	100.41	100.15	100.85	101.52	58.02	53.91
Si	3.45	3.42	3.44	2.77	2.76	2.21	2.45	2.96	2.84	2.95	2.88	2.75	2.80	2.15	0.00	0.00
Ti	0.02	0.03	0.04	0.18	0.19	0.00	0.00	0.00	0.00	0.00	0.00	0.00	0.00	0.00	0.00	0.00
Al	2.05	2.08	2.03	1.37	1.35	1.78	1.55	1.04	1.16	1.03	1.11	1.25	1.20	1.84	0.00	0.00
Cr	0.01	0.00	0.00	0.00	0.00	0.00	0.00	0.00	0.00	0.00	0.00	0.00	0.00	0.00	0.00	0.00
Fe^{3+}	0.00	0.01	0.00	0.10	0.12	0.02	0.01	0.01	0.01	0.01	0.01	0.00	0.01	0.02	0.00	0.00
Fe^{2+}	0.07	0.12	0.12	0.54	0.70	0.00	0.00	0.00	0.00	0.00	0.00	0.00	0.00	0.00	0.02	0.20
Mn	0.00	0.00	0.00	0.00	0.01	0.00	0.00	0.00	0.00	0.00	0.00	0.00	0.00	0.00	0.01	0.00
Mg	0.44	0.39	0.41	1.95	1.84	0.00	0.00	0.00	0.00	0.00	0.00	0.00	0.00	0.00	0.02	0.78
Ca	0.00	0.00	0.00	0.00	0.00	0.77	0.54	0.02	0.15	0.04	0.11	0.25	0.19	0.83	1.96	1.02
Na	0.05	0.13	0.08	0.12	0.07	0.22	0.45	1.00	0.84	1.01	0.91	0.75	0.81	0.16	0.00	0.00
K	0.88	0.78	0.85	0.71	0.64	0.00	0.00	0.00	0.00	0.00	0.00	0.01	0.00	0.00	0.00	0.00
Sum	6.97	6.97	6.98	7.74	7.67	5.00	5.00	5.02	5.00	5.03	5.02	5.00	5.00	5.00	2.00	2.00
Oxygen	11.00	11.00	11.00	11.00	11.00	8.00	8.00	8.00	8.00	8.00	8.00	8.00	8.00	8.00	6.00	0.00
Al(iv)	0.55	0.58	0.56	0.23	0.24											
Al(vi)	1.50	1.50	1.47	1.13	1.11											
XMg	0.86	0.77	0.78	0.78	0.73											
XCa						0.78	0.54							0.84		
XNa								0.98	0.84	0.96	0.90	0.75	0.81			

XMg = Mg/(Mg + Fe^{2+}); XCa = Ca/(Ca + Na + K); XNa = Na/(Ca + Na + K)

Abbreviations: Ab, albite; An, anorthite; Bt, biotite; Cal, calcite; Dol, dolomite; Grt, garnet; Incl, inclusion; Ky, kyanite; Omp, omphacite; Ph, phengite; Ps, pistacite; Pl, plagioclase; Symp, symplectite.

Table 5. Representative compositions of amphibole for D'Entrecasteaux Islands eclogites

Sample	B20	4329	PNG08-010F	PNG08-010F	PNG08-010F	PNG08-010F	PNG12-95a	PNG12-95a	PNG12-95a	PNG09-041c	PNG09-041c	PNG09-041c	PNG09-041c	PNG10-035a	PNG10-035a	PNG12-82a	PNG12-82a
Mineral	Mhb	Mhb	Trm	ferro-Trm	Trm	Ktp	Mhb	Sdg	Act	Trm	Sdg	Trm	Prg	Mhb	Ts	Mhb	ferri-Sdg
Analysis	7_3	60	46	35	39	2	120	6_4	5_2	16	19	27	32	2_2	4_1	2_3	2
Type	Matrix	Matrix	Matrix	Incl 1	Incl 2	Symp	Matrix	Matrix	Symp	Incl 1	Incl 2	Matrix	Matrix	Matrix	Incl	Matrix	Symp
Assoc min/loc*				Grt	Grt			Grt rim		Grt	Grt	Grt, Zrn, Cal–Dol	Grt rim		Grt		
SiO_2	52.21	54.21	45.01	42.77	39.86	46.51	53.97	39.76	54.23	41.48	39.27	40.96	43.22	45.99	44.35	43.98	38.65
TiO_2	0.17	0.14	0.53	0.07	0.00	0.28	0.18	0.42	0.27	0.62	0.93	0.60	0.87	1.18	0.37	1.52	0.45
Al_2O_3	9.32	6.68	15.99	15.03	18.51	11.69	7.07	18.77	3.64	18.10	19.68	18.06	13.83	12.64	17.77	12.43	17.79
Cr_2O_3	0.10	0.13	0.00	0.07	0.00	0.04	0.00	0.04	0.00	0.00	0.02	0.05	0.02	0.02	0.00	0.03	0.00
Fe_2O_3	2.33	2.22	1.87	6.21	7.99	3.10	2.80	5.78	1.02	3.16	3.66	4.61	3.72	4.58	4.41	4.55	8.84
FeO	2.84	2.34	10.35	16.68	9.95	10.07	2.80	6.79	5.54	11.22	12.46	11.12	11.76	4.63	4.05	6.84	5.76
MnO	0.01	0.03	0.03	0.22	0.24	0.05	0.03	0.27	0.04	0.19	0.06	0.11	0.15	0.08	0.04	0.10	0.36
MgO	19.47	20.99	10.77	7.18	8.70	13.00	19.24	12.10	19.33	9.64	9.18	9.52	11.26	16.11	15.36	14.17	12.17
CaO	10.25	11.03	6.92	4.90	7.99	8.51	10.21	11.24	12.73	8.43	8.62	8.42	9.14	10.98	10.47	11.76	10.99
Na_2O	1.24	0.95	5.73	5.88	5.69	4.60	2.01	2.89	0.54	4.73	4.41	4.71	4.21	1.70	2.13	1.64	2.49
K_2O	0.31	0.12	0.51	0.18	0.22	0.34	0.39	0.00	0.00	0.43	0.10	0.65	0.47	0.71	0.00	0.00	0.00
Total	98.24	98.84	97.72	99.19	99.15	98.19	98.70	98.06	97.33	98.00	98.38	98.80	98.64	98.62	98.95	97.02	97.50
Si	7.16	7.37	6.50	6.34	5.83	6.72	7.39	5.76	7.60	6.07	5.77	5.98	6.32	6.49	6.17	6.38	5.67
Ti	0.02	0.01	0.06	0.01	0.00	0.03	0.02	0.05	0.03	0.07	0.10	0.07	0.10	0.13	0.04	0.17	0.05
Al	1.51	1.07	2.72	2.63	3.19	1.99	1.14	3.21	0.60	3.12	3.41	3.11	2.38	2.10	2.92	2.13	3.08
Cr	0.01	0.01	0.00	0.01	0.00	0.00	0.00	0.01	0.00	0.00	0.00	0.01	0.00	0.00	0.00	0.00	0.00
Fe^{3+}	0.24	0.23	0.20	0.69	0.88	0.34	0.29	0.63	0.11	0.35	0.40	0.51	0.41	0.49	0.46	0.50	0.98
Fe^{2+}	0.33	0.27	1.25	2.07	1.22	1.22	0.32	0.82	0.65	1.37	1.53	1.36	1.44	0.55	0.47	0.83	0.71
Mn	0.00	0.00	0.00	0.03	0.03	0.01	0.00	0.03	0.01	0.02	0.01	0.01	0.02	0.01	0.01	0.01	0.05
Mg	3.98	4.25	2.32	1.59	1.90	2.80	3.92	2.61	4.04	2.10	2.01	2.07	2.45	3.39	3.19	3.06	2.66
Ca	1.51	1.61	1.07	0.78	1.25	1.32	1.50	1.75	1.91	1.32	1.36	1.32	1.43	1.66	1.56	1.83	1.73
Na	0.33	0.25	1.61	1.69	1.61	1.29	0.53	0.81	0.15	1.34	1.26	1.33	1.19	0.47	0.58	0.46	0.71
K	0.05	0.02	0.09	0.03	0.04	0.06	0.07	0.00	0.00	0.08	0.02	0.12	0.09	0.13	0.00	0.00	0.00
Sum	15.13	15.10	15.83	15.85	15.96	15.76	15.18	15.68	15.09	15.84	15.86	15.87	23.00	23.00	15.39	15.37	15.61
Oxygen	23.00	23.00	23.00	23.00	23.00	23.00	23.00	23.00	23.00	23.00	23.00	23.00	15.83	15.39	23.00	23.00	23.00
XMg	0.92	0.94	0.65	0.43	0.61	0.70	0.92	0.76	0.86	0.61	0.57	0.60	0.63	0.86	0.87	0.79	0.79

XMg = $Mg/(Mg + Fe^{2+})$.

Abbreviations: Act, actinolite; Cal, calcite; Dol, dolomite; Grt, garnet; Incl, inclusion; Ktp, katophorite; Mhb, magnesiohornblende; Prg, pargasite; Sdg, sadanagaite; Symp, symplectite Trm, taramite; Ts, tschermakite; Zrn, zircon.

* Associated mineral(s) and/or textural location

Table 5. Whole-rock analyses of (U)HP eclogites from the D'Enrecasteaux Islands

Weight %	B-20	8152-4329	PNG08-010F	PNG09-041C	PNG12-95A	PNG12-82A	PNG10-035A
SiO2	46.37	44.96	49.11	43.58	46.64	43.40	46.80
Al2O3	14.91	19.77	15.73	13.97	11.61	14.41	15.36
CaO	9.27	9.27	7.74	12.46	13.33	11.61	10.14
MgO	13.69	11.81	5.33	6.05	12.59	10.86	10.82
FeO (titr)	9.50	9.50	10.20	9.60	6.60	9.20	11.50
Fe2O3	0.52	0.76	2.72	2.37	2.54	2.23	-0.26
MnO	0.18	0.23	0.19	0.17	0.22	0.29	0.27
K2O	0.61	0.08	0.28	0.10	0.10	0.84	0.23
Na2O	1.30	0.99	4.21	3.66	1.91	1.23	1.23
TiO2	0.97	1.09	2.50	3.27	0.43	0.82	0.38
P205	0.13	0.14	0.77	2.44	0.11	0.18	0.04
LOI	0.93	0.14	-0.66	0.94	4.01	4.00	0.92
Total	99.44	99.81	99.27	99.67	100.83	100.10	98.72

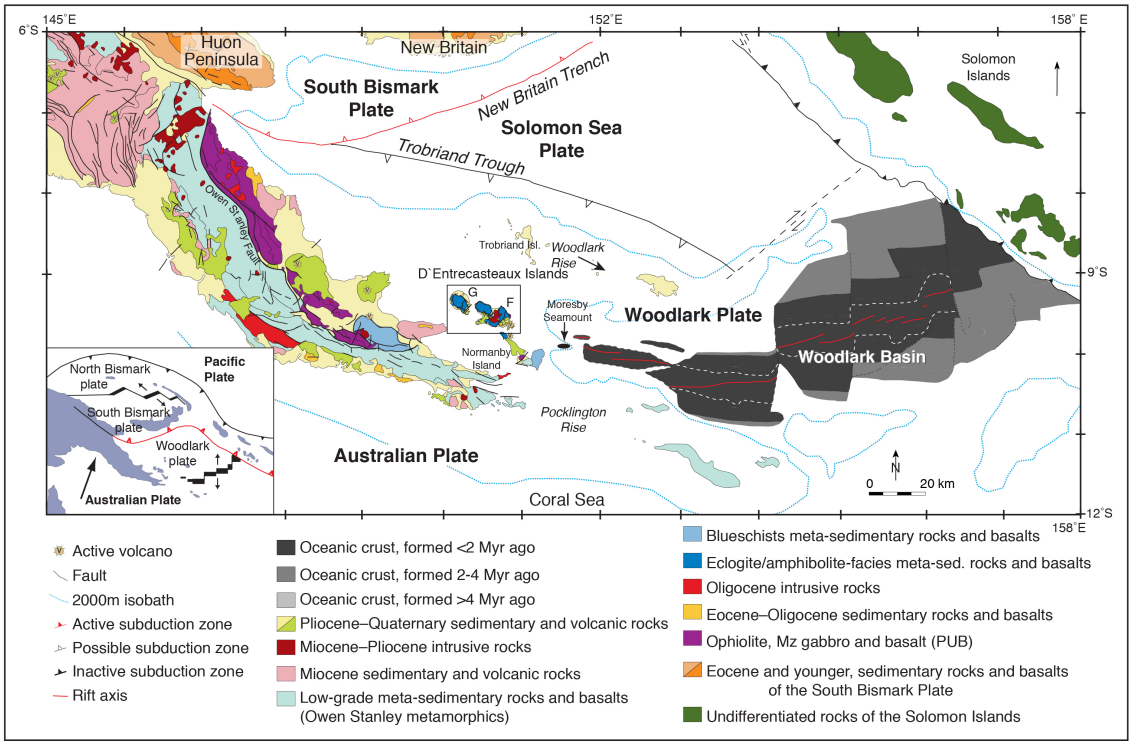

Figure 3.1: Simplified geological map of Eastern Papua New Guinea and the Woodlark Basin showing distribution of major structures and lithologies (after Baldwin et al., 2004). Box and outlined area indicate the location of the D'Entrecasteaux Islands (Figure 2) west of the Woodlark Rift. Lower left inset shows plate-tectonic setting of the region (after Wallace et al., 2004).

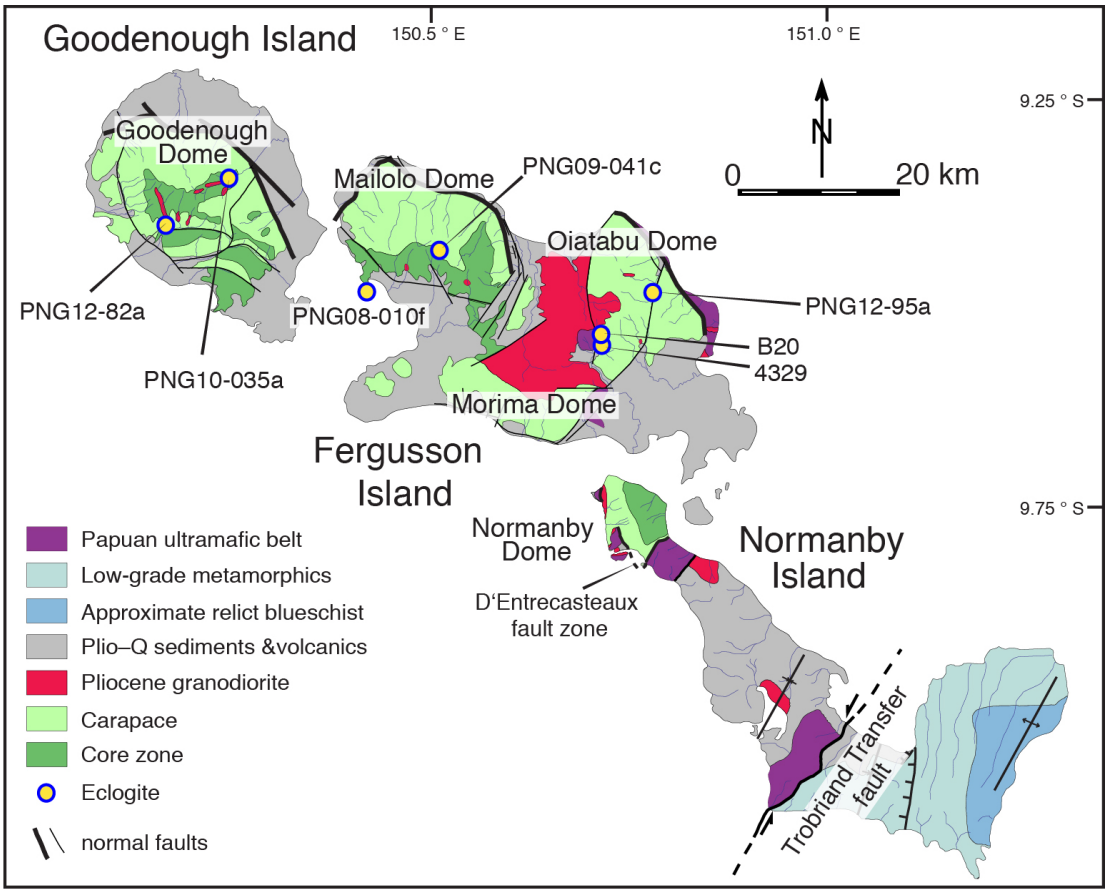

Figure 3.2: Simplified geological map of the D'Entrecasteuax Island gneiss domes showing various lithologies, the core and carapace zones, and the dome-bounding faults, including the D'Entrecasteaux fault zone (after Davies, 1973; Hill, 1994; Little et al., 2007, 2011). Colored circles mark eclogite sample locations for this study.

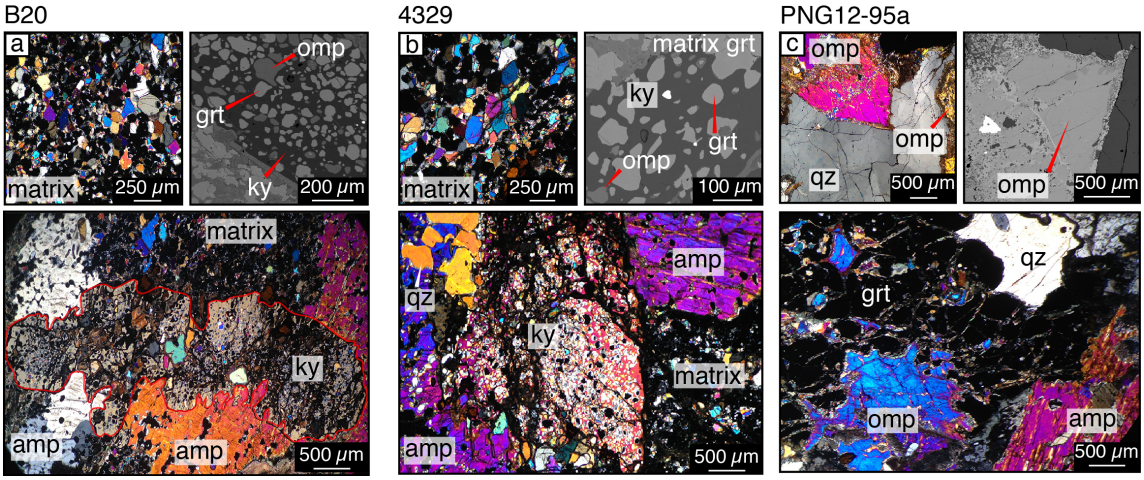

Figure 3.3: Photomicrographs of cross-polarized light and backscattered electron (BSE) images showing the textural relationships in Oiatabu Dome (U)HP eclogites. (a) Kyanite-phengite eclogite B20, top-left: fine-grained matrix of garnet, omphacite, and rutile; top-right: BSE image of kyanite poikoloblast that contains garnet and omphacite inclusions; and bottom: amphibole porphyroblasts overprinting peak kyanite poikiloblast and fine-grained matrix. (b) kyanite eclogite 4329, top-left: fine-grained matrix of garnet, omphacite, and rutile; top-right: BSE image of kyanite poikiloblast that contains garnet and omphacite inclusions, note matrix garnet being enveloped by kyanite poikiloblast in upper right; and bottom: amphibole porphyroblasts with quartz inclusions overprinting peak kyanite poikiliblast and fine-grained matrix. (c) eclogite PNG12-95a, top-left: photomicrograph of peak omphacite and quartz; top-right: BSE image of same omphacite grain with symplectite of diopside and plagioclase forming along the rims; and bottom: matrix garnet, omphacite, and quartz, with amphibole replacing garnet. Mineral abbreviations are after Whitney and Evans (2010).

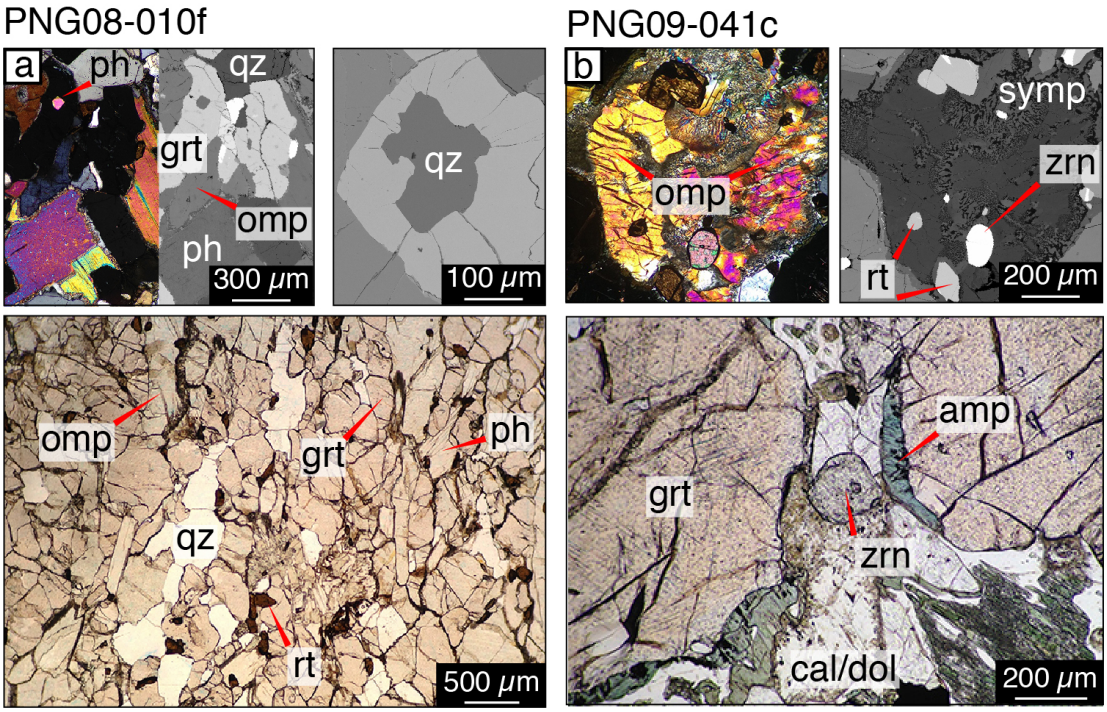

Figure 3.4: Photomicrographs of cross-polarized light and backscattered electron (BSE) images showing the textural relationships in Mailolo Dome (U)HP eclogites. (a) phengite eclogite PNG08-010f, top-left: photomicrograph and BSE images of peak garnet, omphacite, phengite, and quartz textures; top-right: radial fractures around quartz inclusion in host garnet and surrounding omphacite; and bottom: fresh matrix assemblage of garnet, omphacite, phengite, quartz, and rutile. (b) eclogite PNG09-041c, top-left–right: photomicrograph and BSE image of peak omphacite breaking down to symplectite of less-Na omphacite and plagioclase between garnet grains; and bottom: amphibole rimming garnet adjacent to coarse zircon associated with matrix calcite-dolomite. Mineral abbreviations are after Whitney and Evans (2010).

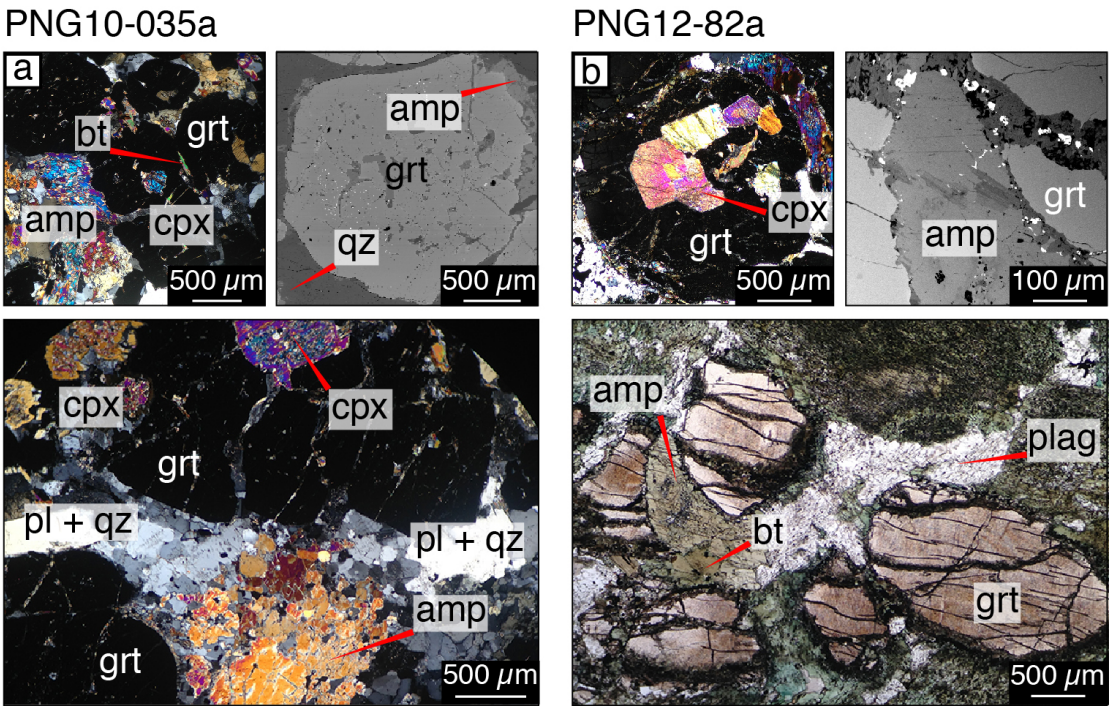

Figure 3.5: Photomicrographs of cross-polarized light and backscattered electron (BSE) images showing the textural relationships in Goodenough Dome (U)HP eclogites. (a) eclogite PNG10-035a, top-left: inclusion of diopsidic clinopyroxene within garnet, biotite and amphibole rim the garnet; top-right: garnet rimmed by amphibole and adjacent quartz; and bottom: diopsidic clinopyroxene included in garnet in a matrix of amphibole, plagioclase, and quartz. (b) eclogite PNG12-82a, top-left: diopsidic clinopyroxene inclusions within garnet; top-right: BSE image of amphibole growth along garnet margins; and bottom: matrix garnet, minor biotite, amphibole and plagioclase. Mineral abbreviations are after Whitney and Evans (2010).

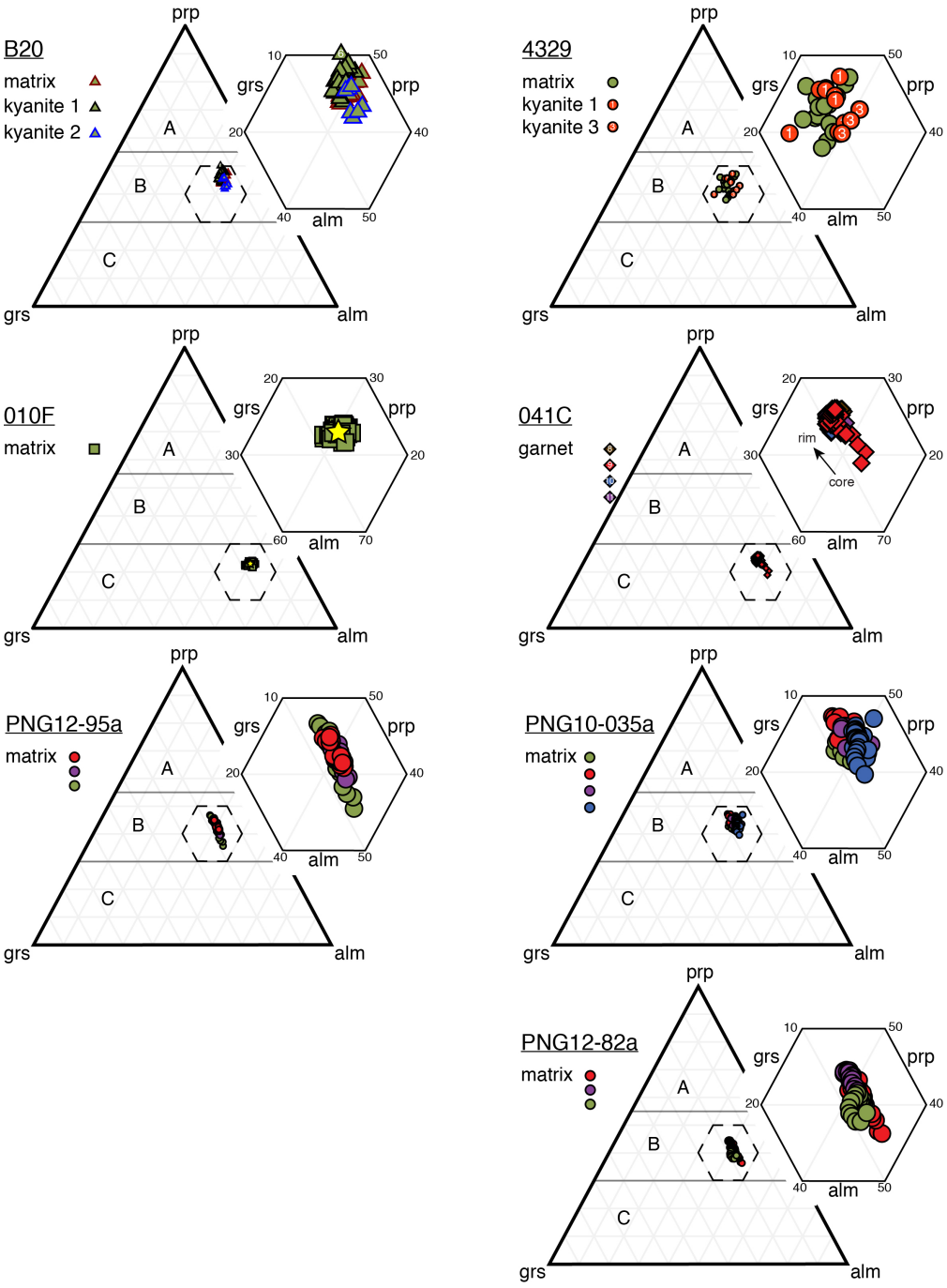

Figure 3.6: Garnet compositional plots for eclogites from Oiatabu, Mailolo, and Goodenough Domes shown within the classification scheme of Coleman et al. (1965), including section A: garnet in eclogite associated with blueschist, section B: garnet in eclogite associated with gneiss, and section C: eclogite associated with mantle and kimberlite xenoliths. Various colors represent analyses of different matrix grains and numbers distinguish between inclusions measured from various poikiloblastic kyanites from Oiatabu Dome eclogites.

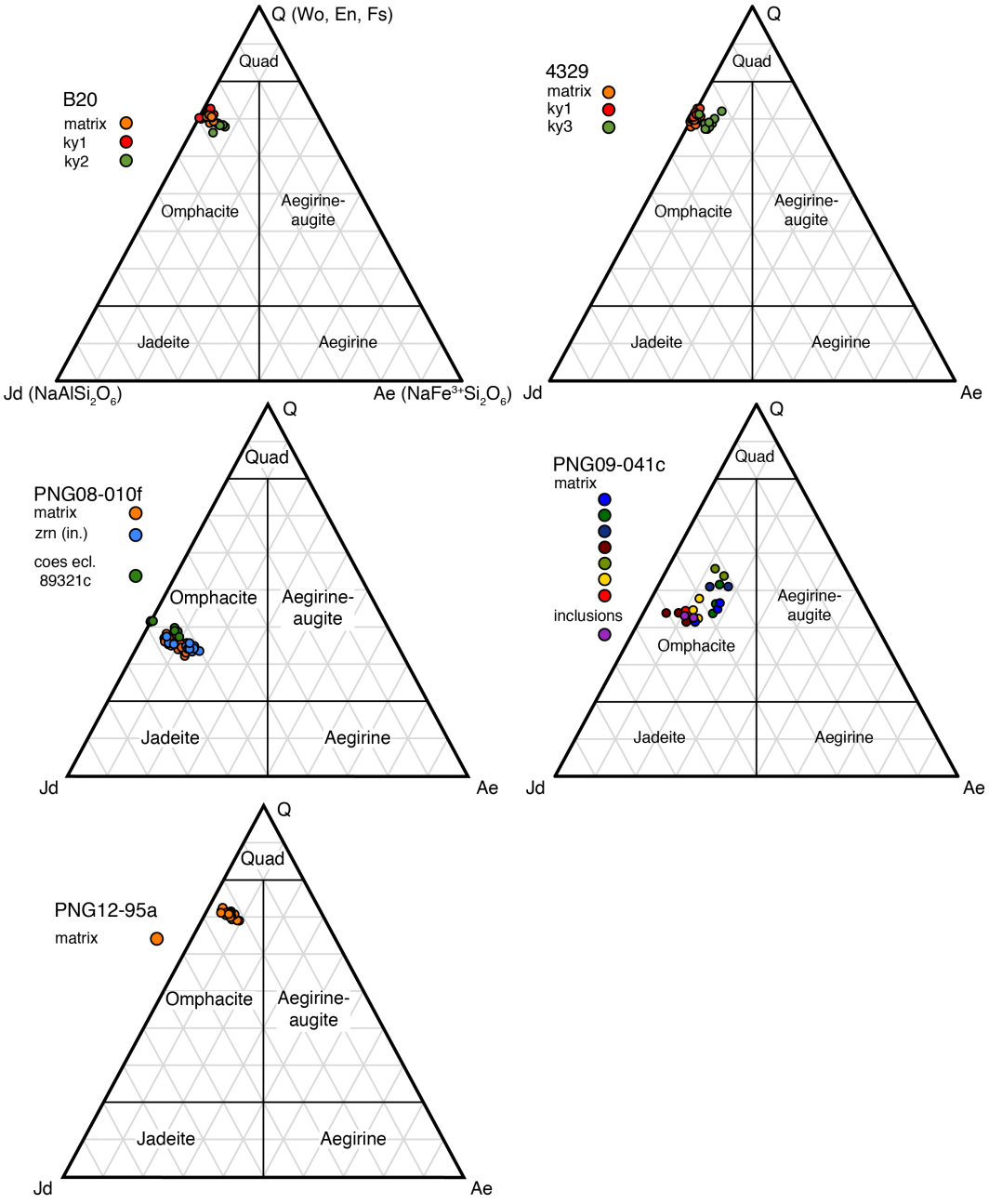

Figure 3.7: Omphacite compositional plots for eclogites from Oiatabu and Mailolo Domes in the classification scheme of Morimoto et al. (1988). Various colors represent analyses of different matrix grains.

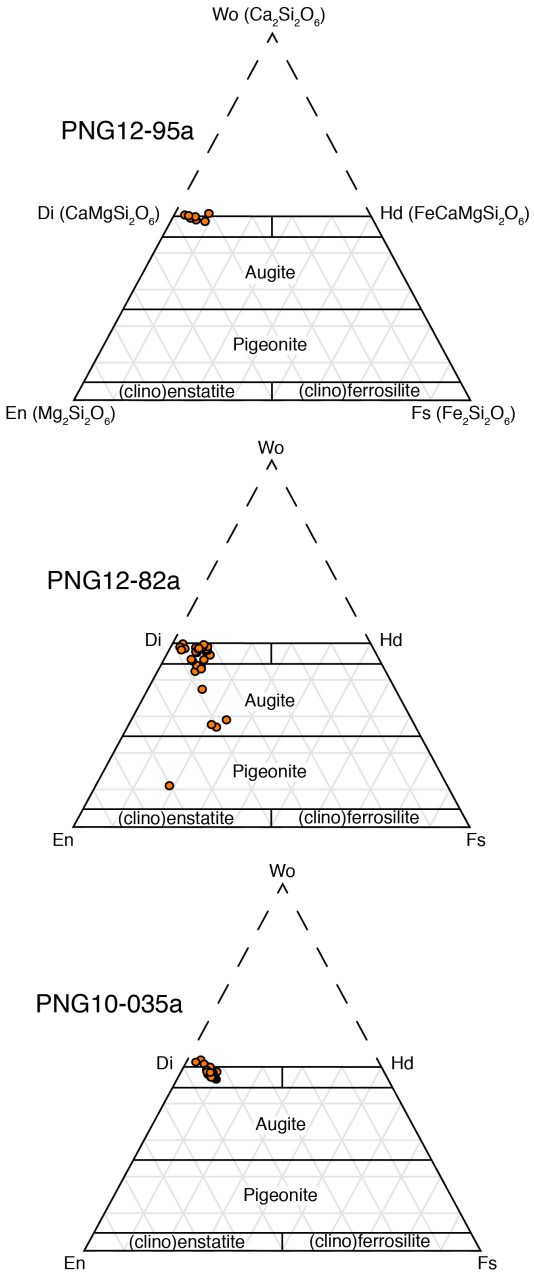

Figure 3.8: Clinopyroxene compositional plots for eclogites from Oiatabu and Goodenough Domes in the classification scheme of Morimoto et al. (1988).

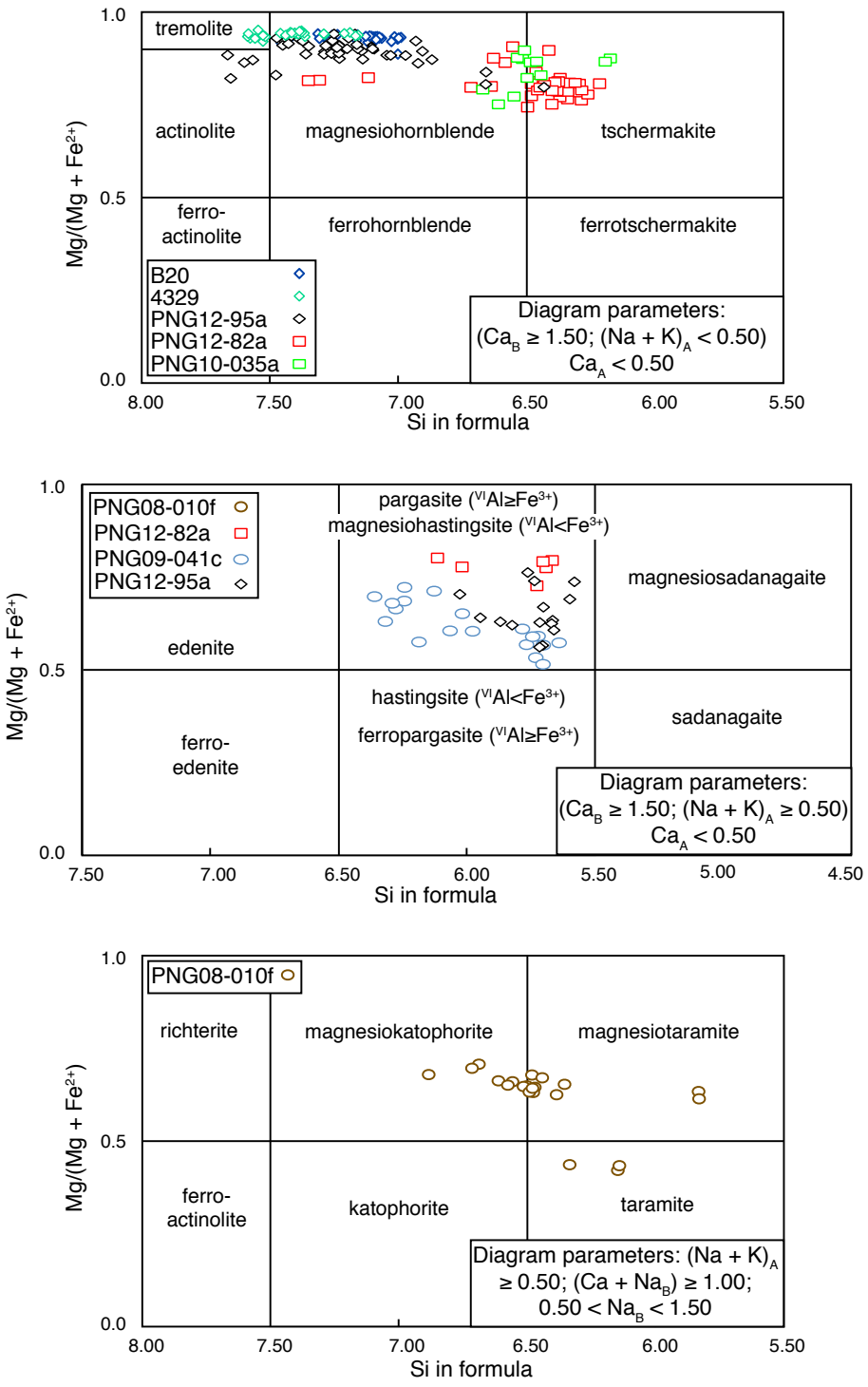

Figure 3.9: Amphibole compositional plots for eclogites from Oiatabu, Mailolo, and Goodenough Domes in the classification scheme of Leake et al. (1997) for calcic and sodic-calcic amphiboles.

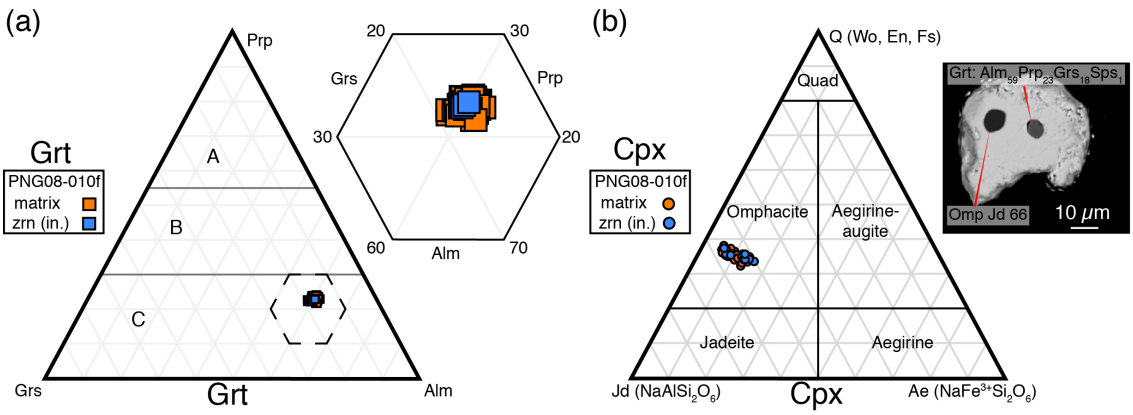

Figure 3.10: (a) Garnet and (b) omphacite compositional data for garnet and omphacite inclusions found within zircon compared to matrix compositional data from phengite eclogite PNG08-010f. BSE image of these inclusions within zircon.

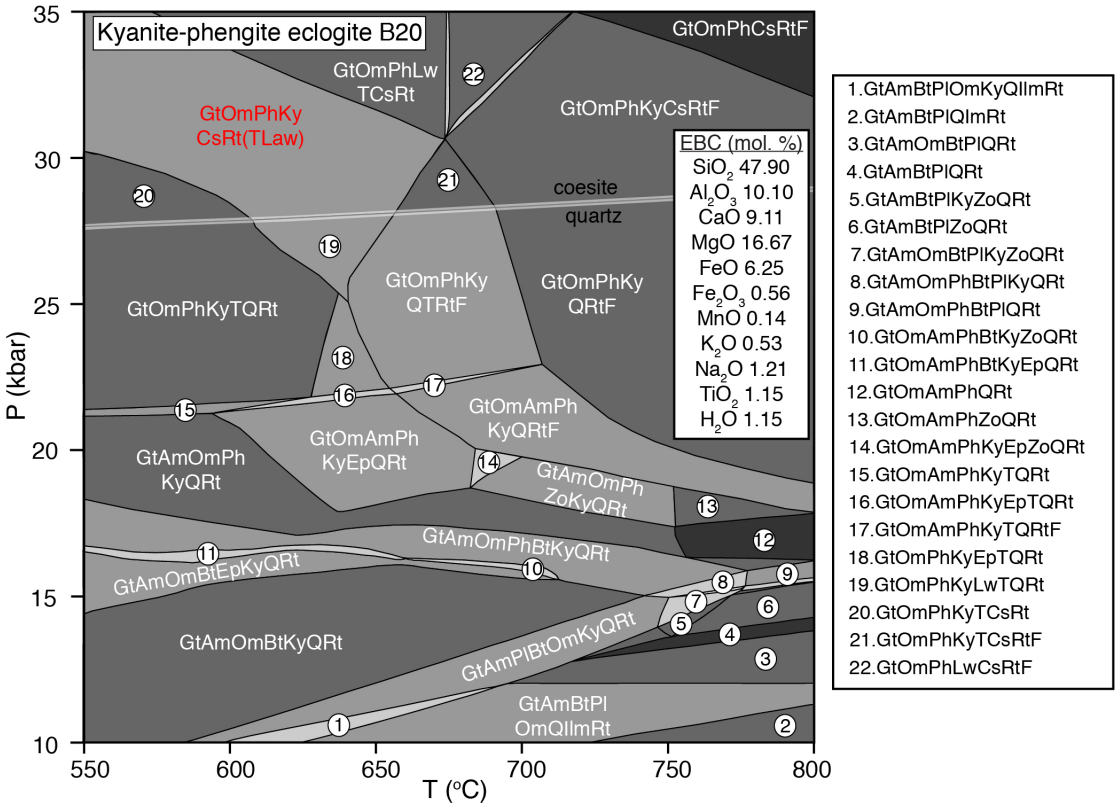

Figure 3.11: P-T pseudosection of kyanite-phengite eclogite B20 calculated for the peak metamorphic assemblage Grt-Omp-Ph-Ky-Qz/Cs-Rt (indicated in red text) based on an effective bulk composition shown in the inset. Mineral abbreviations: Am: amphibole, Bt: biotite, Ep: epidote, F: H2O, Gt: garnet, Im: ilmenite, Ky: kyanite, Lsw: lawsonite, Om: omphacite, Ph: phengite, Pl: plagioclase, Q: Quartz, Rt: rutile, T: talc, Zo: zoisite.

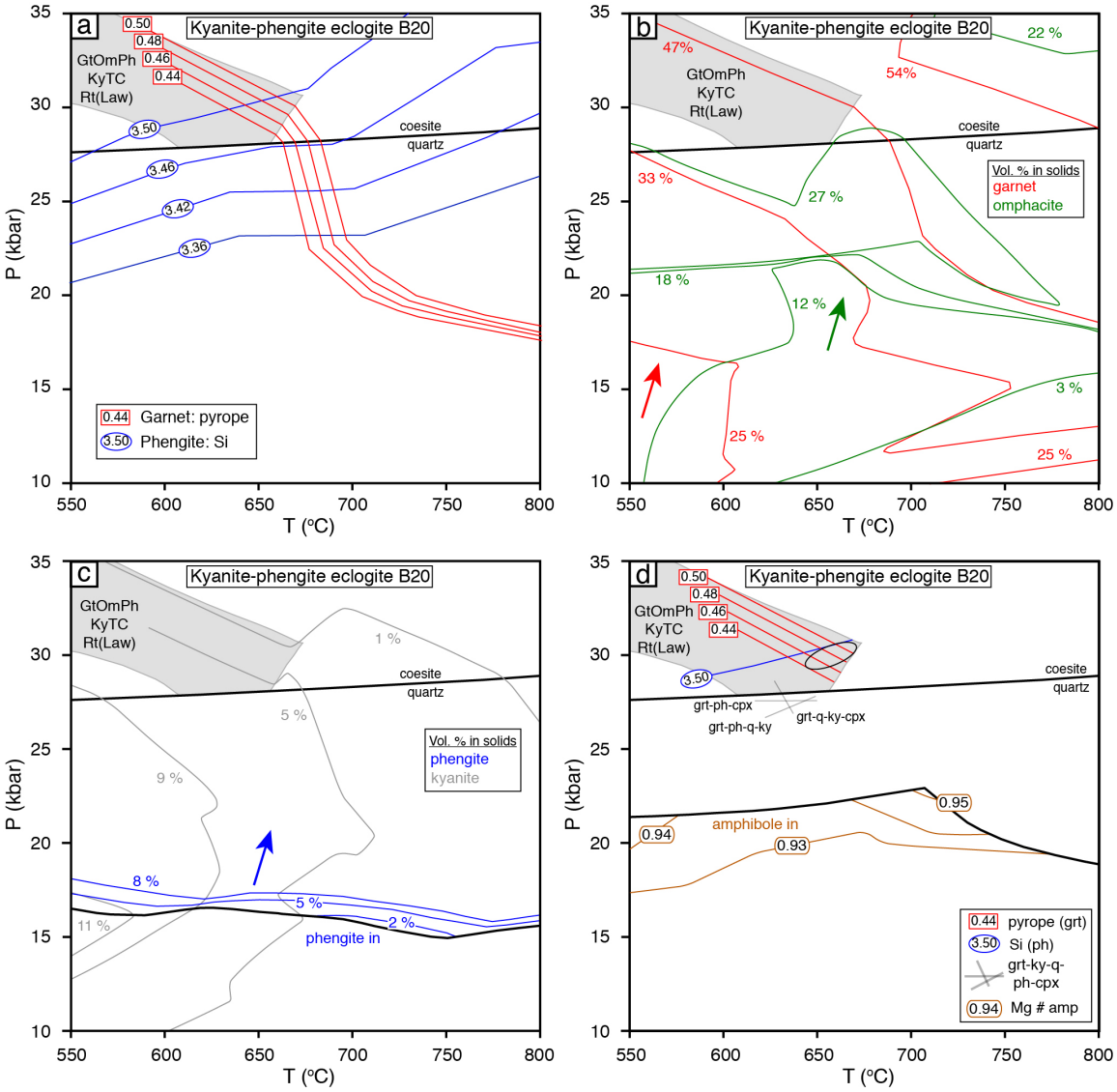

Figure 3.12: P-T pseudosection results contoured for isopleths and mineral proportions: (a) pyrope (in red) and Si in phengite (in blue) contents, (b) volume percent of omphacite (in green) and garnet (in red) and (c) kyanite (in grey) and phengite (in blue), and (d) intersections of isopleths, estimated thermobarometry P-T conditions from net-transfer reactions shown in grey, and amphibole stability from P-T pseudosection in Figure 11. All figures also show the peak mineral-stability field (grey outline) from Figure 11.

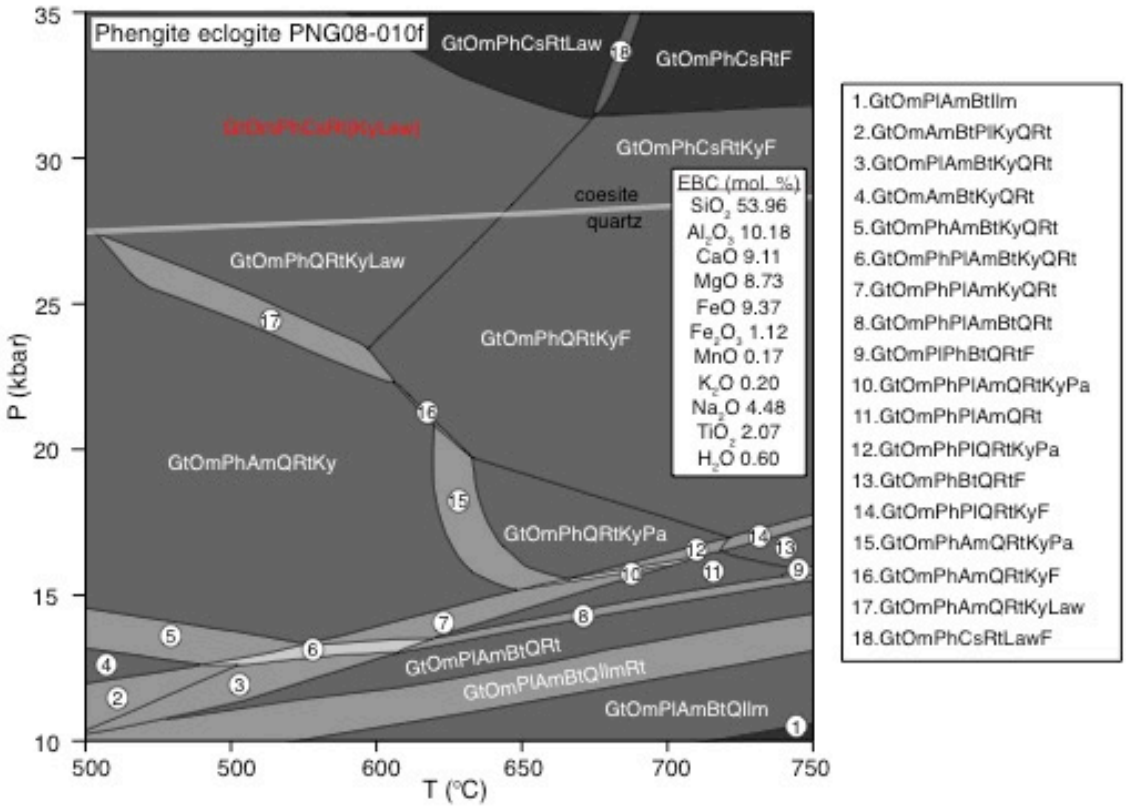

Figure 3.13: P-T pseudosection of phengite eclogite PNG08-010f calculated for the peak metamorphic assemblage Grt-Omp-Ph-Qz/Cs-Rt (indicated in red text) based on an effective bulk composition shown in the inset. Mineral abbreviations: Am: amphibole, Bt: biotite, Cs: coesite, F: H2O, Gt: garnet, Ilm: ilmenite, Ky: kyanite, Law: lawsonite, Om: omphacite, Pa: paragonite, Ph: phengite, Pl: plagioclase, Q: Quartz, Rt: rutile, T: talc.

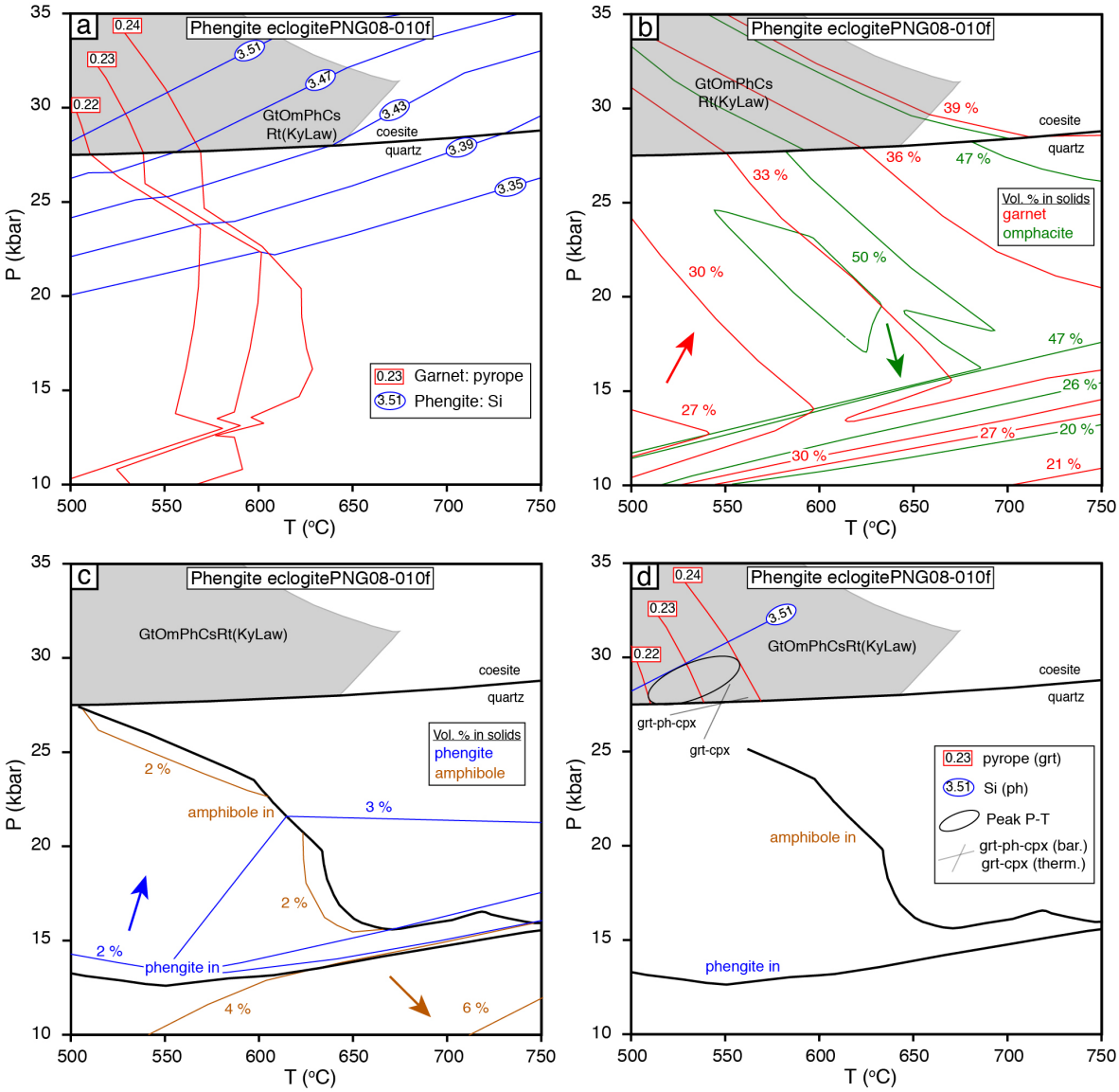

Figure 3.14: P-T pseudosection results contoured for isopleths and mineral proportions: (a) pyrope (in red) and Si in phengite (in blue) contents, (b) volume percent of omphacite (in green) and garnet (in red) and (c) phengite (in blue) and amphibole (in brown), and (d) intersections of isopleths, estimated thermobarometry P-T conditions shown in grey, and amphibole and phengite stability from P-T pseudosection in Figure 13. All figures also show the peak mineral-stability field (grey outline) from Figure 13.

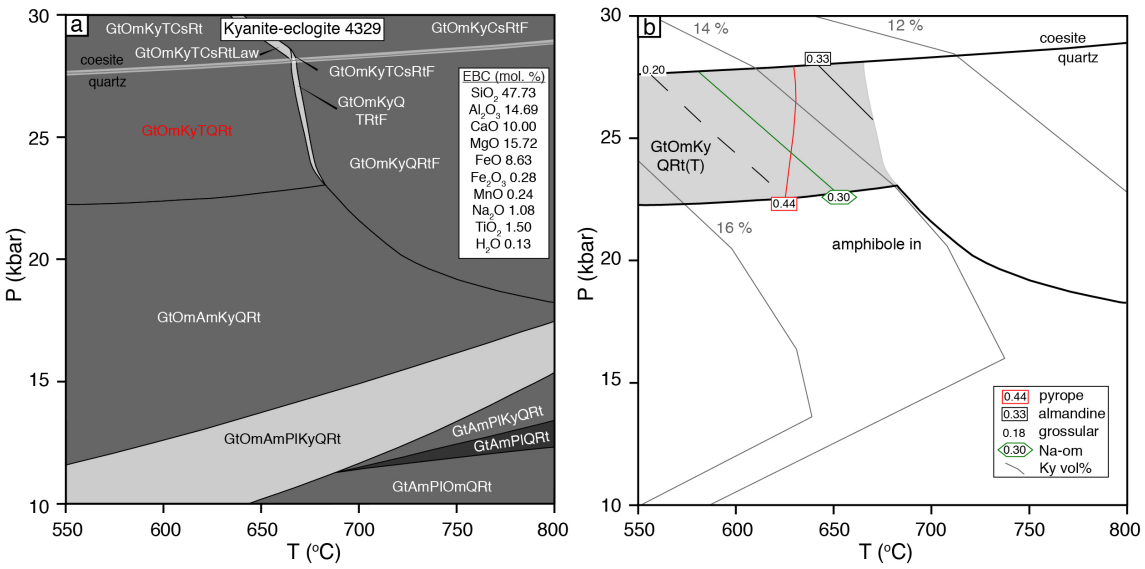

Figure 3.15: P-T pseudosection of (a) kyanite eclogite 4329 calculated for the peak metamorphic assemblage Grt-Omp-Ky-Qz/Cs-Rt (indicated in red text), (b) contoured isopleths of pyrope (in red), grossular (in dashed black), and almandine (in solid black) in garnet and jadeite in omphacite (in green) and mineral proportions of kyanite (volume percent, in grey). Peak mineral-stability field (grey outline) from Figure 13a. Mineral abbreviations: Am: amphibole, Cs: coesite, F: H2O, Gt: garnet, Ky: kyanite, Om: omphacite, Pl: plagioclase, Q: Quartz, Rt: rutile, T: talc.

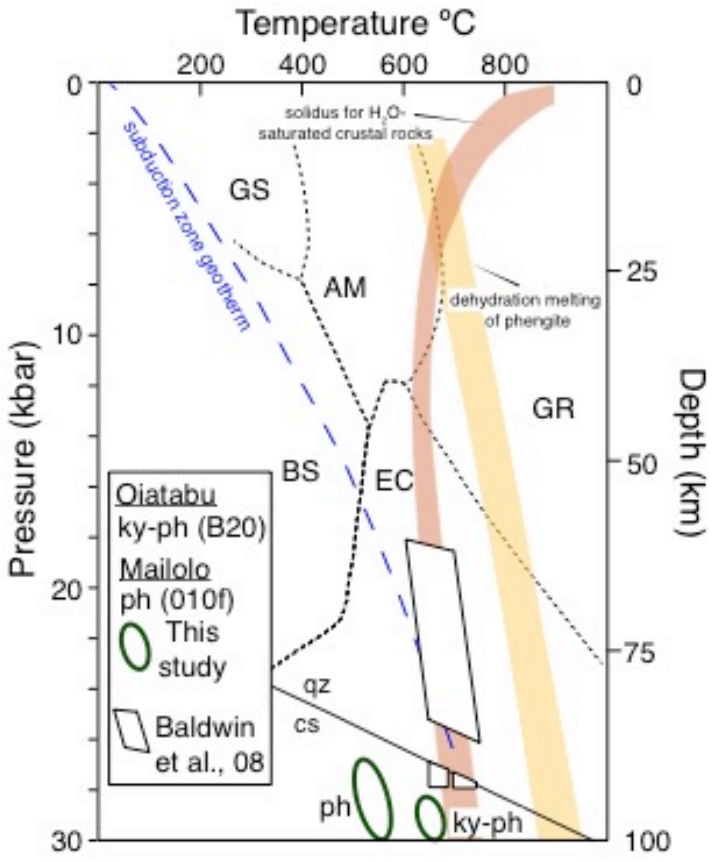

Figure 3.16: Peak pressure-temperature results for Mailolo and Oiatabu Dome kyanite-phengite eclogites from this study and the coesite eclogite (Baldwin et al., 2008). Abbreviations for metamorphic facies are blueschist (BS), greenschist (GS), amphibolite (AM), eclogite (EC), and granulite (GR); Mineral abbreviations are after Whitney and Evans (2010). Subduction zone geotherm and solidus for water-saturated crustal rocks (Hacker, 2006) and dehydration melting of phengite (Schmidt et al., 2004) are shown. Figure after Baldwin and Das (2015).

Chapter 4: Mantle to crustal depths at plate-tectonic rates: High-precision U-Pb and trace-element zircon results from the Pliocene Papua New Guinea (U)HP terrane

Joel W. DesOrmeau[*], Stacia M. Gordon[*], Timothy A. Little [**], Blair Schoene[***], Kyle M. Samperton[***], Nilanjan Chatterjee[****]

[*]Department of Geological Sciences, University of Nevada Reno, Nevada, USA
[**] School of Geography, Environment and Earth Sciences, Victoria University of Wellington, Wellington, New Zealand
[***]Department of Geosciences, Princeton University, Princeton, New Jersey, USA
[****]Department of Earth, Atmospheric, and Planetary Sciences, Massachusetts Institute of Technology, Cambridge, Massachusetts, USA

This chapter will be submitted to the *Science Advances* in the near future.

Abstract

The D'Entrecasteaux Islands of eastern Papua New Guinea host the youngest known ultrahigh-pressure (UHP) terrane and represent one of the only locations on Earth where UHP rocks are exhumed with an active rift. The UHP rocks, consisting of Pliocene eclogites and migmatitic gneisses, are exposed within five domal structures across the Islands. Uranium-Pb and trace-element compositions measured in zircon extracted from a suite of eclogite, host gneiss, dikes and pegmatite from three of the domes reveal the exhumation history of the PNG (U)HP terrane. Select eclogite zircon were first analyzed by high-spatial resolution laser ablation split-stream inductively coupled plasma mass spectrometry (LASS-ICP-MS), and the results suggest no chemical zoning within single crystals. Subsequently, the age and trace elements from the zircons, including those analyzed by LASS-ICP-MS and additional zircon from all samples, were measured using high-precision U-Pb chemical abrasion isotope dilution–thermal ionization mass spectrometry and solution ICP-MS trace-element analysis (TIMS-TEA). The TIMS-TEA results record discrete tectonic events across the three domes at a sub-million year timescale: 1) (U)HP metamorphism at ca. 6.0–5.2 Ma within the central Mailolo Dome, as evidenced by inclusions of the peak HP mineral assemblage (i.e., omphacite, garnet, rutile, phengite) within the zircon separates; 2) metamorphism of the host gneiss within Oiatabu Dome from ca. 5.7–4.5 Ma; 3) initial retrogression of eclogite-facies assemblages within the eastern and central Domes, Oiatabu and Mailolo, at ca. 4.6–4.3 Ma; 4) melt crystallization of weakly deformed dikes at ca. 3.0–2.9 Ma; and 5) more extensive, amphibolite-facies retrogression in the western Dome, Goodenough Dome, at ca. 2.8–2.6 Ma. The *in situ* and solution trace-element results for all of the eclogite zircon

reveal flat HREE slopes and absent negative Eu anomalies (Eu/Eu*), suggesting (re)crystallization during eclogite-facies metamorphism. This interpretation is at odds with textural evidence showing that most zircons are associated with retrograde phases. High-precision U-Pb zircon dates the youngest evidence for (U)HP metamorphism and provide compelling documentation of a rapid (≥1.5 cm/yr), near-vertical exhumation of the Pliocene PNG (U)HP terrane by tracking the timing of UHP metamorphism at ca. 6.0–5.2 Ma, followed by initial eclogite retrogression at ca. 4.6–4.3 Ma, and continued exhumation until final emplacement within the upper crust by ca. 1.8 Ma.

Introduction

The subduction of low density continental lithosphere to mantle depths and subsequent exhumation is widely recognized across Phanerozoic orogens through the preservation of accessory phases, such as coesite and diamond, within mainly eclogites and less commonly the host orthogneiss (i.e., Chopin, 1984; Smith, 1984; Sobolev and Shatsky, 1990; Ernst et al., 2001; O'Brien, 2001; Liou et al., 2004; Hacker, 2007; Liu et al., 2007; Gilotti, 2013). Multiple geochronometric techniques have been applied to eclogite and host gneiss exposed within UHP terranes to determine the timing of peak UHP metamorphism (U-Pb zircon, monazite, and allanite; Lu–Hf and Sm–Nd garnet) and retrogressive overprinting at amphibolite-facies conditions (U-Pb titanite and zircon, Sm-Nd garnet, Rb-Sr multimineral isochron), constraining the temporal evolution of the subducted continental lithosphere from the mantle to the upper crust (e.g., Gebauer et al., 1997; Amato et al., 1999; Lapen et al., 2003; Hacker et al., 2003, 2006; Parrish et al., 2006; Kylander-Clark et al., 2007, 2009; Korchinski et al., 2014). These studies reveal variable exhumation rates among UHP terranes, and this variability has been attributed to the size and duration of subduction and exhumation (e.g., large, thick, and slow: 10–30 Myr vs. small, thin, and fast: <10 Myr, Kylander-Clark et al., 2012).

Rapid exhumation from UHP depths to the lower crust at plate-tectonic rates (>1cm/year) has been reported for Paleozoic (Erzgebirge and Kokchetav, Hermann et al., 2001; Hacker et al., 2003; Massonne et al., 2007) and Cenozoic terranes (Tso Morari, de Sigoyer et al., 2000; Dora Maira, Rubatto and Hermann, 2001; Kaghan Valley, Kaneko et al., 2003; Parrish et al., 2006; and Papua New Guinea, Monteleone et al., 2007; Baldwin et al., 2008). The initial fast exhumation rates have been attributed to buoyancy forces

(i.e., large density contrast between the mantle and subducted mainly felsic crust) overcoming boundary tractions (Warren et al., 2008). For most UHP terranes, this portion of the exhumation to crustal levels is characterized by near-isothermal decompression (e.g., Rubatto and Hermann, 2001; Parrish et al, 2006; Monteleone et al., 2007) accompanied by partial melting. The presence of melt will weaken the exhuming body and further enhance buoyancy (e.g., Hill et al., 1995; Wallis et al., 2005; Lang and Gilotti, 2007; Gerya et al., 2008; Faccenda et al., 2009; Ragozin et al., 2009; Ellis et al., 2011; Labrousse et al., 2011; Li et al., 2011; Little et al., 2011; Gordon et al., 2012; Sizova et al., 2012).

Within eastern Papuan New Guinea (PNG), multiple domal structures expose Pliocene ultrahigh- to high-pressure ((U)HP) rocks (e.g., Davies and Warren, 1988, 1992; Hill and Baldwin, 1993; Baldwin et al., 2008; Little et al., 2011). Previous studies of this (U)HP terrane argue for a rapid (>1 cm/yr), near-isothermal decompression path, with the crustal rocks undergoing UHP metamorphism at ca. 8–7 Ma and exhumation to the near surface by ca. 1.8–0.3 Ma (Davies and Warren, 1988; Hill and Baldwin, 1993; Monteleone et al., 2007; Baldwin et al., 2008; Fitzgerald et al., 2008; Little et al., 2011; Zirakparvar et al., 2011). Throughout the gneiss domes, there is abundant evidence of melting, including layer-parallel leucosomes, dikes, and plutons (Hill et al., 1995, Gordon et al., 2012; DesOrmeau et al., 2014). Based on these characteristics, PNG represents an ideal locality to investigate the rapid exhumation and influence of buoyancy-driven, melt-assisted exhumation within UHP terranes. Zircon U-Pb and trace-element compositions were obtained by single-grain, chemical abrasion–isotope dilution–thermal ionization mass spectrometry (CA-ID-TIMS) and solution inductively coupled plasma mass

spectrometry (ICP-MS) (TIMS-TEA of Schoene et al., 2010) from a fresh eclogite, a suite of variably retrogressed eclogites, host gneisses, and weakly deformed dikes and pegmatite to more precisely document events during the rapid exhumation of the PNG (U)HP terrane from mantle depths. In addition, transects across zircons were analyzed by high-spatial resolution laser ablation-ICP-MS prior to analysis by high-precision TIMS-TEA to identify if the zircons contain multiple growth zones. The new results reveal that peak metamorphism lasted until ca. 6.0–5.2 Ma. The eclogites subsequently underwent initial retrogression at ca. 4.6–4.3 Ma, and were nearly completely retrogressed at lower-crustal conditions at ca. 2.8–2.6 Ma. Furthermore, zircon dates from the easternmost dome suggest the host gneiss was metamorphosed from ca. 5.7–4.6 Ma, overlapping with the timing of peak metamorphism and initial retrogression of the eclogite, and late melt (dikes) crystallizated at ca. 3.0–2.9 Ma, coeval with the latest amphibolite-facies retrogression. In combination with previous studies of the PNG (U)HP terrane, these results better define the fast exhumation (≥1.5 cm/yr) of this young UHP terrane and track the exhumation of the continental lithosphere exposed within the individual domes from mantle depths to their position in the brittle upper crust.

Geologic Setting

Woodlark Basin

The ongoing convergence of the Pacific and Australian plates at a rate of ~10–11 cm/yr across eastern Papua New Guinea has resulted in microplate formation and rotation since the Eocene (Tregoning et al., 1998; Wallace et al., 2004, 2014). During the Paleogene, this convergence caused the Papuan Orogen collisional event, which resulted in

subduction to the northeast of the northern Australian rifted margin beneath an island-arc terrane (Davies and Jacques, 1984; Cloos et al., 2005; Little et al., 2011). Subsequently, obduction of the island-arc basement, termed the Papuan Ultramafic Belt (PUB), occurred along the Owen Stanley Fault on the mainland Papuan Peninsula at 58.3 ± 0.4 Ma ($^{40}Ar/^{39}Ar$ amphibole; Lus et al., 2004). The PUB now sits structurally above deformed and metamorphosed Australian-derived sedimentary and basaltic rocks of the Owen Stanley metamorphics, including blueschist, pumpellyite-actinolite, and lower greenschist-facies rocks (Fig. 1) (Davies and Jacques, 1984; Davies and Warren, 1988). K-Ar and $^{40}Ar/^{39}Ar$ amphibole dates from the Owen Stanley metamorphics range from ca. 45 to 22 Ma, whereas white mica dates show cooling through ~400 °C by ca. 24–22 Ma (Davies and Williamson, 1988). These results suggest northward subduction of the Australian continent ended by the early Miocene (Davies and Jacques, 1984; Rogerson et al., 1987; Davies, 1990; Van Ufford and Cloos, 2005, Davies, 2012). Australian plate material deeply subducted during this collisional event from ca. 58 to 22 Ma is interpreted to be the protolith for the ultrahigh-pressure (UHP) terrane in the D'Entrecasteaux Islands, situated ~20 km offshore to the east of the mainland peninsula (Fig. 1).

Complex plate reorganization within eastern PNG associated with the cessation of subduction and continued oblique convergence between the Pacific and Australian plates caused the initiation of northward subduction of the Solomon Sea microplate at the New Britain Trench (Weissel et al., 1982; Wallace et al., 2004; Westaway, 2007). Slab pull associated with this subduction has driven northward, counterclockwise, rotation of the Woodlark and Solomon Sea microplates relative to Australia since the late Miocene

(Wallace et al., 2004). Since 6 Ma, this rotation has been accommodated through seafloor spreading within the Woodlark Basin (Fig. 1) (Taylor et al, 1999; Kington and Goodliffe, 2008). Seafloor spreading and high extension rates in the eastern Woodlark Basin (e.g., Taylor et al., 1999; Taylor and Huchon, 2002) give way to lower (<10–20 mm/yr) extension rates in the Woodlark Rift, the western continental portion of the rift-seafloor spreading system (Tregoning et al., 1998; Wallace et al., 2004). The D'Entrecasteaux Islands lay directly within this rift zone and extension associated with rifting has resulted in a thin crust (~20 km) directly beneath the Islands and the formation of a series of 2–2.5-km high gneiss domes spread across the Islands (Fig. 1; Abers et al., 2002). The combined geophysics, geodetic, and structural results suggest significant extension at all levels of the lithosphere, from the mantle to the crust (Tregoning, 1998; Taylor et al., 1999; Abers 2001; Abers et al., 2002; Wallace et al., 2004, 2014; Little et al., 2011, 2013; Eilon et al., 2014, 2015).

D'Entrecasteaux Islands

The D'Entrecasteaux Islands host five gneiss domes: Normanby (northwest Normanby Island), Morima (southern Fergusson Island), Oiatabu (eastern Fergusson Island), Mailolo (western Fergusson Island), and Goodenough (Goodenough Island) (Figs. 1 and 2). The domes consist mainly of migmatitic quartzofeldspathic orthogneiss, with lesser amounts of mafic eclogite and amphibolite, marble, paragneiss, and quartzite. Active normal faults flank the northern margins of Oiatabu, Mailolo, and Goodneough Domes, and the southwestern margin of the Morima Dome (Fig. 2). Little et al. (2011) show that these faults cut an older, more gently dipping structural boundary, the D'Entrecasteaux

fault zone (Fig. 2). The D'Entrecasteaux fault zone is interpreted to be correlative to the Owen Stanley Fault (Fig. 1), upon which obduction of the PUB occurred during the Paleogene Papuan Orogen. Minor remnants of the PUB and its nonmetamorphosed Neogene sedimentary cover are exposed in the upper plate of the domes (Fig. 2) (Davies and Warren, 1988). In contrast, the lower plate of the domes are characterized by the (U)HP rocks (Fig. 2; Davies and Warren, 1988, 1992; Hill et al., 1992; Baldwin et al., 2004, 2008; Monteleone et al., 2007; Little et al, 2011, 2013).

The lower plates of the domes can be structurally divided into an uppermost carapace zone (up to 1.5 km thick) that shows a strong, planar LS tectonite fabric, and an inner, structurally deeper, core zone with chaotic fabrics (Fig. 2) (Hill, 1994). Eclogite-facies mafic rocks and layer-parallel leucosomes, dikes, and plutons are evident throughout all structural levels of the domes; however, the amount of leucosome increases from ~15 vol. % in the carapace to upwards of 70 vol. % exposed in the dome cores (Gordon et al., 2012). Microstructural evidence based on quartz microstructures, melt-filled strain shadows, and shape-preferred orientations of magmatic feldspar support melt-present deformation within the dome cores (Little et al., 2011, 2013).

Previous thermobarometry studies of (U)HP eclogites from the D'Entrecasteaux Islands

Eclogites are exposed within all of the domes, but only the eclogites from the Oiatabu, Mailolo, and Goodenough Domes have been targeted in P-T investigations. The previous results give a considerable range in pressure and temperature results, which is likely related to the various degrees of retrogression present in the eclogites and to imprecision associated with the unknown content of Fe^{3+} in clinopyroxene used with the garnet-

clinopyroxene thermometer (Proyer et al., 2004). Only one coesite-bearing eclogite has been identified thus far across the domes (Baldwin et al., 2008). This eclogite yields a wide range in pressures and temperatures including: 1) grt–cpx–ph thermobarometry results of 18–27 kbar and 600–760 °C, and 2) Zr-in-rutile and Ti-in-zircon temperatures of 695–743 °C (assuming P=28 kbar) and 650–675 °C, respectively (Baldwin et al., 2008). Other eclogites from the three domes yield pressures and temperatures from 12–24 kbar and 530–840 °C (Davies and Warren, 1992) and 20–24 kbar and 730–930 °C (Hill and Baldwin, 1993; Baldwin et al., 2004).

Previous geochronological studies of the D'Entrecasteaux Islands

Efforts to determine the timing of UHP metamorphism have utilized multiple isotopic systems, including Lu-Hf garnet–whole rock isochrons, U-Pb zircon, $^{40}Ar/^{39}Ar$ phengite, and Rb-Sr whole rock–omphacite–phengite isochrons, and have only focused on eclogites from the Mailolo and Goodenough domes. The coesite-eclogite from Mailolo Dome gives various results: 1) a Lu–Hf garnet–whole rock date of 7.1 ± 0.7 Ma (2σ, MSWD = 1.1) (Zirakparvar et al., 2011); 2) *in situ* secondary ion mass spectrometry (SIMS) yielding a $^{206}Pb/^{238}U$–$^{207}Pb/^{206}Pb$ Terra Wasserburg intercept date of 7.9 ± 1.9 Ma (2σ, MSWD = 9.2) (Monteleone et al., 2007); 3) ID-TIMS single-grain $^{206}Pb/^{238}U$ (Th-corrected) dates of 5.60 ± 0.22 Ma to 4.61 ± 0.18 Ma (2σ, Gordon et al., 2012); and 4) apparent ages of ~84% of ^{39}Ar released gives an $^{40}Ar/^{39}Ar$ weighted mean date for phengite of 7.93 ± 0.10 Ma (1σ) (Baldwin and Das, 2015). Additional zircon SIMS analyses from eclogite resulted in $^{206}Pb/^{238}U$–$^{207}Pb/^{206}Pb$ Terra Wasserburg intercept dates ranging from 4.3 ± 0.4 Ma (MSWD = 3.3) in Mailolo Dome (Baldwin et al., 2004)

to 2.9 ± 0.4 (MSWD = 1.02) to 2.1 ± 0.5 (MSWD = 4.2) in Goodenough Dome (Monteleone et al., 2007). In addition, an Rb-Sr whole-rock–omphacite–phengite isochron date of 5.6 ± 1.6 Ma (MSWD = 1.0) for an eclogite from Mailolo Dome (Korchinski et al., 2014). In addition to eclogite, ID-TIMS zircon results from strongly deformed host gneiss in the easternmost dome, Normanby dome, likely also record HP metamorphism from 5.66 ± 0.02 to 5.04 ± 0.07 Ma (DesOrmeau et al., 2014).

Throughout all of the domes, ID-TIMS geochronology of host gneiss and variably deformed crystallized melt (leucosomes, sills, dikes, and plutons) brackets the timing of the (U)HP rock exhumation from the lower crust to the surface and the formation of the domes. ID-TIMS zircon dates from a variety of strongly deformed sills and layer-parallel leucosomes suggest that the (U)HP rocks were exhumed to likely lower-crustal levels by ca. 4.1 Ma in the eastern Normanby Dome (DesOrmeau et al., 2014), by ca. 3.5–3.0 Ma to the west in Mailolo Dome (Gordon et al., 2012), and in the far west in Goodenough dome, by ca. 3.9–2.8 Ma (DesOrmeau et al., 2014). Weakly deformed dikes record likely ponding and ductile deformation during amphibolite-facies retrogression of the domes at ca. 2.4 Ma within Mailolo Dome (Gordon et al., 2012) and ca. 2.3 Ma in Goodenough Dome (DesOrmeau et al., 2014). The end of ductile deformation and final emplacement of the dome is recorded by crystallization ages of nondeformed dikes and plutons that cut the dome-defining foliation throughout all of the D'Entrecasteaux domes by ca. 1.8 Ma (Baldwin et al., 1993; Gordon et al., 2012; DesOrmeau et al., 2014).

In comparison, $^{40}Ar/^{39}Ar$ dates of ca. 3.5–2.6 Ma from gneisses and pegmatite preserves the exhumation history related to temperatures below 500 °C within Mailolo Dome, whereas Goodenough Dome gneisses give a range in hornblende, white mica, and

biotite dates from ca. 3.0–1.5 Ma (Baldwin et al., 1993; Waggoner et al., 2008). Final emplacement within the shallow crust in both domes is recorded by low-temperature (< 80 °C) apatite (U-Th)/He and fission-track ages at ca. 1.8–0.3 Ma (Fitzgerald et al., 2008).

(U)HP eclogites, gneisses, and dikes sampled across the D'Entrecasteaux Islands

Given the rapid evolution of the PNG UHP terrane, the focus of this study is to use high-precision ID-TIMS zircon geochronology on a suite of (U)HP eclogites from numerous domes to refine the temporal history of peak metamorphism through exhumation and associated amphibolite-facies retrogression. In addition, samples of host gneiss and dikes were also obtained to better understand the timing of host-rock metamorphism and the final stages of melt crystallization and deformation during emplacement within the upper crust for the less extensively-studied Oiatabu Dome. Finally, a pegmatite intimately associated with one of the studied eclogites collected within the Goodneough Dome was also analyzed. Most of the samples were collected *in situ*; however, of the six eclogites, three were collected as cobbles within creek beds. As the topography is extremely steep, the drainages from which the float samples were collected provide a very limited source region; thus, we are confident that the samples did not travel far and are likely representative of the structural levels from which they were collected. If anything, the samples may have been sourced from structurally deeper within the domes (Fig. 2).

Oiatabu Dome (Fergusson Island)

One eclogite, three host gneiss and two dike samples were collected within the carapace of eastern Oiatabu Dome. An eclogite cobble (PNG12-95a) was collected ~2 km from the eastern dome-bounding fault along the Basuenoia River and is the first eclogite to be dated from Oiatabu Dome (Fig. 2). The eclogite has undergone extensive retrogression, resulting in anhedral garnet rimmed by dark green amphibole all within a matrix of coarser amphibole and pervasive symplectite growth of less Na-rich clinopyroxene and plagioclase after sparsely preserved peak omphacite (Fig. 3a). The original (U)HP assemblage was likely garnet + omphacite + quartz + rutile. Fresh (garnet + omphacite + kyanite ± phengite) eclogite samples were also collected from the southwest corner of Oiatabu Dome, but neither sample yielded zircon.

Nearby, five samples of strongly deformed host gneiss and deformed dikes were collected. The migmatitic muscovite-bearing host paragneiss (PNG12-85a) was collected structurally highest within the dome and closest to the eastern dome-bounding fault (Fig. 2). The remaining samples were collected structurally deeper and ~1 km farther west into the dome and are strongly and weakly deformed pairs from the same outcrops with the goal of using these pairs to track the different stages of the deformation history. Host orthogneiss PNG12-87a contains quartz, feldspar, and biotite, whereas mafic orthogneiss PNG12-92a contains abundant biotite with minor quartz and plagioclase. Samples of weakly deformed quartzofeldspathic dikes (PNG12-87b and PNG12-92b) that cut the host gneiss were also collected.

Mailolo Dome (Fergusson Island)

Two eclogite samples were collected from the core zone of Mailolo Dome along the Fagululu River drainage within western Fergusson Island and one sample from the coesite locality exposed on the adjacent Tumagabuna Island, also interpreted as part of the Mailolo Dome (Fig. 2). Eclogite PNG09-041c was collected *in situ* and is a medium- to coarse-grained eclogite consisting of garnet and omphacite within a matrix of amphibole, calcite–dolomite, and coarse symplectite of clinopyroxene and plagioclase. Zircon occurs associated with retrogression textures, including along garnets that have been broken down and are rimmed by amphibole (Fig. 3b), in contact with peak omphacite and symplectite, and as inclusions within interstitial calcite–dolomite. Zircon is also commonly texturally associated with rutile, quartz, and apatite, and minor zircon are found as garnet rim inclusions. Nearby within the core zone, eclogite PNG09-039b was collected as a cobble and consists of large (up to 1.0 cm across) garnet and omphacite set in a similar matrix of dolomite, phengite, and fine-grained symplectite associated with garnet, omphacite, and phengite (Vry and Gazley, in review). Similar to eclogite PNG09-041c, coarse (~200 μm) zircon, rutile, apatite, and quartz are found along the garnet and omphacite margins and associated with symplectite (Fig. 3c), although the eclogite does not reveal kelyphitic amphibole rims, and zircon is not preserved as inclusions within peak minerals as is observed in PNG09-041c.

Eclogite PNG08-010F collected from the UHP locality does not show significant retrogression as is observed in the other Mailolo eclogites. The peak assemblage consists of garnet and omphacite stringers that define a weak foliation, with interstitial quartz and phengite and apatite, rutile, clinozoisite, and zircon as accessory phases (Fig. 4d). Inclusions of quartz within garnet are associated with radial cracks, which is typical for

Mailolo Dome eclogites. Extensive retrogression is restricted to the outer rinds of the eclogite. Gordon et al. (2012) previously analyzed this eclogite by U-Pb zircon ID-TIMS, but further investigation of zircon separates from this important eclogite has led to the identification of an inclusion suite consisting of the peak metamorphic assemblage, including garnet, omphacite, rutile, and phengite (Figs. 4e and S3), within individual zircon crystals. Thus, further analysis of these crucial zircons, extracted from only the fresh portions of the eclogite, is necessary.

Goodenough Dome (Goodenough Island)

Two eclogites were collected from the core zone along the Galuwata and Fakwaoia Rivers on the northern and southern flanks of Goodenough Dome, respectively (Fig. 2). An outcrop along the Galuwata River exposes discordant granitic pegmatite (PNG10-035b) that locally intrudes into a large eclogite body, isolating numerous eclogite pieces within the pegmatite. Eclogite PNG10-035a is a piece of this eclogite body (Fig. 2). In comparison, eclogite sample PNG12-82a was collected as a cobble ~10 km to the southwest (Fig. 2). Both eclogites are extensively retrogressed and are characterized by inclusions of Na-poor clinopyroxene within peak garnet, kelyphitic amphibole growth along garnet rims (Fig. 3e), and amphibole, plagioclase, and biotite as matrix phases. Eclogite PNG12-82a also preserves symplectite of diopside and plagioclase and zircon growth within matrix amphibole (Fig. 3f).

Retrogression of PNG (U)HP eclogites

Eclogites, both fresh and variably retrogressed, occur across all domes; however, the preservation of peak eclogite-facies assemblages is different among individual domes. Mailolo Dome fresh eclogites achieved (U)HP, based on: 1) the presence of coesite (Baldwin et al., 2008); 2) Jd-rich omphacite (>Jd_{60}); and 3) high silica content of phengite (up to Si=3.5 atoms/per formula unit (a/fu); Davies and Warren, 1992; Hill and Baldwin, 1993; Baldwin et al., 2004, 2008; Chapter 3 in this dissertation). Approximately ~10 km to the east, Oiatabu Dome also preserves (U)HP phenigte-bearing (up to S=3.5 a/fu) eclogites, and here also containing kyanite, although coesite is not preserved and omphacite is characterized by lower Jd contents ($Jd_{28–32}$). Eclogite from Oiatabu Dome that reveals a higher degree of retrogression still preserves omphacite (Jd_{29}) that is overprinted by symplectite of amphibole and plagioclase. In the west, Goodenough Dome contains the most extensively retrogressed assemblages with diopsidic clinopyroxene ($Jd_{0–12}$) and a typical matrix of garnet, abundant amphibole, plagioclase, and biotite (Davies and Warren, 1992; Monteleone et al., 2007; Chapter 3 in this dissertation).

Methods

As discussed above, the least-retrogressed samples of eclogite were collected across the three domes; however, the samples do follow general trends described above for the Domes, with the most fresh samples from Mailolo and Oiatabu Domes and the more retrogressed from Goodenough Dome. In addition, representative host-gneiss and non-deformed dikes were collected from Oiatabu Dome and a pegmatite from Goodenough Dome. Zircons were extracted from the rocks via standard mineral-separation techniques. A combination of single grains, microsampled fragments of grains, and multiple

fragments of the same grain were analyzed by high-precision U-Pb zircon chemical-abrasion isotope-dilution thermal ionization mass spectrometry and solution ICP-MS, trace-element analysis (TIMS-TEA; Mattinson, 2005; Schoene et al., 2010). Chemical abrasion removes high-U zones of the zircon susceptible to Pb loss, thereby minimizing or wholly eliminating Pb-loss correction (Mattinson, 2005). The TIMS-TEA method allows for the same zircon, or fragment of zircon, dated by U-Pb ID-TIMS to be analyzed for trace-element composition (e.g., Schoene et al., 2010).

For TIMS-TEA analysis, all grains were annealed at 900 °C for 60 hours and chemically abraded at 220 °C for 12 hours (Mattinson et al., 2005). An unavoidable analytical challenge in dating these Pliocene zircons arises from the overall low abundance of radiogenic Pb (<0.5 pg) in many samples, and in all samples, the low abundance of ^{207}Pb. Based on this, ID-TIMS analyses of Pliocene zircons range in uncertainties for Th-corrected ^{206}Pb/^{238}U dates, which are inversely proportional to the radiogenic/common Pb ratio (Pb*/Pbc); therefore, samples with considerably low amounts of radiogenic Pb* have much higher uncertainties on individual analyses, ranging from 1–8%, whereas those with high amounts of radiogenic Pb* have uncertainties ranging from 0.08–0.75% (Table 1). Reported ID-TIMS weighted mean dates were calculated using the program ET_Redux (Bowring et al., 2011; McLean et al., 2011) and analyses that do not define a single population are given as individual Th-corrected ^{206}Pb/^{238}U dates. Reported uncertainties throughout the text, tables, and figures are at the 2-sigma or 95% confidence level. The online supporting information provides a more detailed description of the methodology for U-Pb TIMS-TEA zircon analyses.

Zircons from most of the samples reveal a distinct TIMS age population, suggesting that the whole grain or fragments of grains do not contain inherited cores and/or represent mixing ages. However, to identify intragrain heterogeneity within single crystals, representative zircons were mounted from four of the six eclogites, polished halfway through the grain, and imaged by cathodoluminescence (CL) (Fig. 4). These four eclogite samples contain the most radiogenic (Pb*) zircons; thus, preparing a grain mount and polishing away half of the grain does not drastically affect the later ID-TIMS analyses. Zircons from the other two eclogites, two of the three host gneiss samples, deformed dikes, and non-deformed pegmatite from Oiatabu and Goodenough Domes were not imaged due to their low levels of Pb*. The radiogenic grains were then analyzed by laser-ablation split-stream (LASS)–inductively coupled plasma-mass spectrometry, allowing for the simultaneous collection of U-Th-Pb data and trace-element data from an individual spot analysis (e.g., Kylander-Clark et al., 2013). The LASS analyses consisted of transects across the grains to try to analyze all potential chemical/growth "zones" within the individual grains. The LASS $^{206}Pb/^{238}U$ dates have typical uncertainties ranging from 2–14% for single-spot analyses, including both analytical and propagated uncertainties (Table 2). The large uncertainties for the LASS dates are a result of the difficulty in measuring such low amounts of radiogenic Pb, given the small volume of ablated material. Moreover, the two standards used, GJ1 (Jackson et al., 2004) and 91500 (Wiedenbeck et al., 1995), are significantly older and likely have different compositions; thus, they may not be the best matrix match for the Pliocene PNG grains. See online supporting information for a detailed description of the methodology for U-Pb TIMS-TEA and LASS zircon analyses.

We first report zircon U-Pb and trace-element data from grains that were analyzed by both LASS and TIMS-TEA. These results are then compared to zircons analyzed by TIMS-TEA only (Figs. 3, 4, and 5; Tables 1, 2, and 3). Zircon trace-element results for eclogites from Oiatabu, Mailolo, and Goodenough domes analyzed by solution ICP-MS and LASS are presented in Figs. 6 and S1 and in Tables 4 and 5. Host gneiss and dike zircons were only analyzed by solution ICP-MS, and the trace-element data are shown in Fig. S2 and Table 6.

Results

U-Pb zircon ID-TIMS geochronology

Zircons extracted from eclogites sampled from all domes are mainly anhedral to rounded (50–300 μm), with the exception of the Oiatabu Dome eclogite, which contains large (~200–450 μm) euhedral prismatic grains (Fig. 4a). Cathodoluminescence images for the eclogite zircons reveal patchy- and polygonal-sector zones with some thin rims displaying oscillatory zoning (Fig. 4). In comparison, zircon from host gneiss and dike samples are euhedral prismatic grains (~50–100 μm; Fig. 5).

Oitabu Dome eclogite, host-gneiss, and dikes

Eclogite sample PNG12-95a is from the carapace of eastern Oiatabu Dome (Fig. 2). Attempts to petrographically find the textual locations of the very coarse (up to 450 μm in length; Fig. 4a) prismatic zircons have proved unsuccessful. Transects across nine zircons by LASS give similar single-spot $^{206}Pb/^{238}U$ dates ranging from ca. 4.8 to 4.4 Ma (Fig. 4a; Table 2), suggesting no significant zoning within the grains. In addition, to test

for dispersion of ID-TIMS dates within a single grain, a ~300 μm zircon was microsampled, and the three fractions yield indistinguishable $^{206}Pb/^{238}U$ dates of 4.61 ± 0.03 Ma, 4.62 ± 0.02 Ma, and 4.62 ± 0.01 Ma (z16 in Fig. 4a; Table 1). All remaining ID-TIMS whole-grain analyses fall within a narrow range from 4.63 ± 0.03 Ma to 4.58 ± 0.01 Ma, including two of the same grains that were analyzed by LASS (n = 16; Fig. 4a; Table 1).

Zircons from the host paragneisses sampled from the carapace of Oiatabu Dome (PNG12-85a) are prismatic grains that display a core and rim texture with convolute rim zoning (Fig. 5; Corfu et al., 2003). These zircons occur mainly within quartz and plagioclase ribbons and as inclusions within muscovite. Whole-grain ID-TIMS analyses yield $^{206}Pb/^{238}U$ dates from 27.20 ± 0.06 Ma to 5.52 ± 0.04 Ma (n = 14; Table 1). Analysis of the microsampled zircon rim overgrowths only gives ID-TIMS $^{206}Pb/^{238}U$ dates of 5.66 ± 0.05 Ma to 4.49 ± 0.04 Ma (n = 5; Fig. 5; Table 1). Structurally deeper within the dome compared to PNG12-85a, another host gneiss, orthogneiss PNG12-87a, only yield inherited whole-grain results from ca. 84 to 53 Ma (Table 1), whereas seven zircons from a cross-cutting weakly deformed quartzofeldspathic dike (PNG12-87b) within the same outcrop give ID-TIMS $^{206}Pb/^{238}U$ dates of 3.02 ± 0.06 Ma to 2.93 ± 0.01 Ma (Fig. 5; Table 1). At similar structural levels and ~0.5 km to the south within the dome, a biotite-rich quartzofeldspathic orthogneiss (PNG12-92a) also only yield inherited whole grain results from ca. 90 to 56 Ma (Table 1). At the same outcrop, a weakly deformed cross-cutting pegmatitic quartzofeldspathic dike (PNG12-92b) yields seven

zircons with $^{206}Pb/^{238}U$ dates that range from 5.56 ± 0.23 Ma to 2.97 ± 0.08 Ma (Fig. 5), whereas a single analysis gave an older date of 88.91 ± 1.13 Ma (Table 1).

Mailolo Dome eclogites

Large, ~100–300 μm, rounded zircons from eclogite PNG09-041c typically have sector zoning and occur texturally associated with retrogression-reaction assemblages (Fig. 3b). Thirty-one zircons analyzed by LASS give single-spot $^{206}Pb/^{238}U$ dates ranging from ca. 5.8 to 4.3 Ma (Fig. 3b), with a single analysis yielding an older discordant date of ca. 36 Ma (Table 2). Analysis of these zircons by ID-TIMS yield $^{206}Pb/^{238}U$ dates of 4.65 ± 0.06 Ma to 4.51 ± 0.35 Ma (n = 12; Fig. 3b), which result in a weighted mean $^{206}Pb/^{238}U$ date of 4.63 ± 0.01 (MSWD = 0.70; n = 12). A single discordant analysis gives an older date of 5.41 ± 0.11 Ma (Table 1).

Eclogite PNG09-039b also contains coarse (100–300 μm), rounded zircons with sector zoning that are restricted to sites where garnet and omphacite are breaking down (Fig. 3c). Analysis of twenty-nine zircons with LASS yields single-spot $^{206}Pb/^{238}U$ dates ranging from ca. 4.8 to 4.1 Ma (n = 49; Fig. 4c; Table 2), with most of the older analyses (ca. 5.8–5.0 Ma) being discordant. Subsequent ID-TIMS analysis of seven of the same whole grains, or fragments of grains, give $^{206}Pb/^{238}U$ dates ranging from 4.38 ± 0.04 Ma to 4.33 ± 0.02 Ma (n = 10; Fig. 4c, Table 1). Additional whole grain analyses by ID-TIMS yield $^{206}Pb/^{238}U$ dates that cluster between 4.38 ± 0.07 Ma to 4.30 ± 0.01 Ma (n=8; Fig. 3b; Table 1).

Fresh eclogite PNG08-010f contains homogenous, rounded (~40–70 μm) zircons that are included within fresh garnet and omphacite and along their grain boundaries. Moreover, the zircons are not zoned and typically contain mineral inclusions representative of the peak (U)HP assemblage (e.g., omphacite, rutile, garnet, and phengite; Fig. 4e). The grains have very low amounts of radiogenic Pb* (0.06–0.17 pg); therefore, any attempt to date these zircons by low-precision *in situ* techniques (LASS or SIMS) will result in inaccurate and imprecise dates due to such large associated uncertainties (c.f., Gordon et al., 2012). Analysis of twelve zircons by ID-TIMS yields $^{206}Pb/^{238}U$ dates of 5.98 ± 0.17 Ma to 5.20 ± 0.33 Ma (Fig. 4e; Table 1).

Goodenough Dome eclogites

For eclogite PNG10-035a, the textural locations of the zircons could not be identified. The zircons are large (100–200 μm) subhedral grains with polygonal-sector zones and rims displaying oscillatory zoning (Fig. 4d). Transects across three zircons by LASS give single spot $^{206}Pb/^{238}U$ dates of ca. 3.5 to 2.8 Ma (n=6; Fig. 4d; Table 2), whereas ID-TIMS analyses of the same fragments of grains yield Th-corrected $^{206}Pb/^{238}U$ dates of 2.89 ± 0.03 Ma to 2.83 ± 0.23 Ma (n = 4; Fig. 4d; Table 1). Remaining ID-TIMS analyses of whole grains give $^{206}Pb/^{238}U$ dates of 2.87 ± 0.08 Ma to 2.65 ± 0.03 Ma (n = 9; Fig. 4d; Table 1). The pegmatite that intruded the eclogite (PNG10-035b) gives single-grain ID-TIMS $^{206}Pb/^{238}U$ dates of 2.64 ± 0.09 Ma to 2.48 ± 0.02 Ma (n = 10; Fig. 5; Table 1).

Zircons identified within the matrix amphibole of the highly retrogressed eclogite PNG12-82a show patchy- and polygonal-sector zones with some oscillatory zoning near the rims (Fig. 4f). The low amounts of radiogenic Pb* (0.13–0.80 pg) led to analysis only

by ID-TIMS. The results from ten zircons give $^{206}Pb/^{238}U$ dates of 2.78 ± 0.03 Ma to 2.62 ± 0.06 Ma (Fig. 4f; Table 1).

Zircon trace-element data

For all samples, the trace-element results from the solution ICP-MS TIMS-TEA and the LASS analyses are described together, as they typically give similar results.

Oiatabu Dome eclogite

Zircon REE patterns for Oiatabu Dome eclogite PNG12-95a reveal depleted HREE patterns ($Lu_N/Gd_N < 2$), except for a single LASS analysis of ~5 (Figs. 6 and S1), and flat-to-positive Eu anomalies ($Eu/Eu^* = Eu_N/(Sm_N \times Gd_N)^{0.5} > 0.75$) (Figs. 6 and S1; Table 5). The Th/U ratios range from 0.01–1.0, with most analyses yielding high ratios between 0.39–1.0 (Fig. 6; Table 5). Both techniques do not reveal any temporal trends with zircon composition (Fig. 6), although some LASS analyses do show overall lower REE abundances compared to solution-ICP-MS (Fig. S1).

Mailolo Dome eclogites

Mailolo Dome eclogite PNG09-041c zircons give consistent depleted HREE values ($Lu_N/Gd_N \leq 1$), flat-to-positive Eu anomalies ($Eu/Eu^* > 0.77$), and Th/U ratios of 0.27–0.80 (Figs. 6 and S1; Table 5). An inherited analysis shows a steep HREE pattern (Lu_N/Gd_N ~54; Fig. S1). Nearby, eclogite PNG09-039b shows mostly flat to negative HREE slopes ($Lu_N/Gd_N < 2$), with some LASS analyses giving steep HREE slopes (Lu_N/Gd_N up to 16) (Figs. 6 and S1; Table 5). The HREE variability in the LASS

analyses does not correlate with age. The zircons yield dominantly absent negative Eu anomalies (Eu/Eu* = 0.75–1.62; Table 5), whereas some negative Eu anomalies (Eu/Eu* = 0.69–0.74) were obtained by LASS analysis (Figs. 6 and S1). The Th/U ratios yield results from 0.21 to 0.77, with more scatter revealed in LASS analyses (Fig. 6).

Goodenough Dome eclogites

Zircons from eclogite PNG10-035a from Goodenough Dome yield consistent depleted HREE patterns ($Lu_N/Gd_N < 3$) and negative to positive Eu anomalies (Eu/Eu* = 0.71–1.05). The Th/U ratios are more variable, with low ratios from LASS (0.07–0.19) and higher ratios from TIMS-TEA (0.05–0.59) (Figs. 6 and S1; Table 5). Zircon REE patterns from PNG12-82a were only analyzed by TIMS-TEA and show very consistent results that are similar to PNG10-035a with mostly flat HREE slopes ($Lu_N/Gd_N < 3$), negative to slightly positive Eu anomalies (Eu/Eu* = 0.72–0.79), and higher Th/U ratios from 0.27–0.50 (Figs. 6 and S1; Table 6). The Th/U ratios measured by TIMS-TEA for PNG10-035a increase with younger (re)crystallization dates (Fig. 6).

Oiatabu host gneiss and dikes

Analysis by TIMS-TEA of host gneiss samples (PNG12-85a, 87a, 92a) show zircon REE patterns enriched in HREE (Lu_N/Gd_N = 8–166), dominantly negative Eu anomalies (Eu/Eu* = 0.23–0.72, except for a single positive anomaly of 0.83), and Th/U ratios ranging from 0.21 to 0.84 with a single low ratio of 0.02 (Fig. S2; Table 6). As discussed above, all three host gneiss samples from Oiatabu Dome show considerable inheritance

from ca. 90 Ma to 7 Ma, whereas metamorphic zircon (re)crystallization in host gneiss PNG12-85a is as young as ca. 4.5 Ma (i.e., microsampled zircon tip, Fig. 5).

Zircon trace-element results from weakly deformed dike PNG12-87b have variable HREE slopes (Lu_N/Gd_N = 3–578), mostly positive Eu anomalies (Eu/Eu* = 0.7–2.4), and low Th/U ratios from 0.01–0.25 (Fig. S2; Table 6). The other weakly deformed dike, PNG12-92b, yields zircon REE patterns that show moderate to steep HREE slopes (Lu_N/Gd_N = 5–60), negative to positive Eu anomalies (Eu/Eu* = 0.3–0.9), and variable Th/U ratios from 0.06 to 0.89 (Fig. S2; Table 6). For most of the gneiss and crystallized melt samples, the LREE were below detection limits.

Discussion

Eastern PNG is unique in that the world's youngest known (U)HP eclogites are currently exhuming within an active rift system, the Woodlark Rift (Baldwin et al., 2004, 2008; Wallace et al., 2004, 2014; Monteleone et al., 2007; Little et al., 2011, 2013; Zirakparvar et al., 2011; Gordon et al., 2012; DesOrmeau et al., 2014; Korchinski et al., 2014). The Pliocene (U)HP terrane has undergone an extremely rapid tectonic history that requires high-precision geochronometric results to capture events that occur on the sub-million year scale. The TIMS-TEA results from this study more clearly define the timing and extent of peak metamorphism and subsequent retrogression of eclogites, providing a more complete record of exhumation. Below we discuss the similarities and differences in the metamorphic and exhumation history across the gneiss domes of the D'Entrecasteaux Islands in light of our results.

Temporal evolution of the PNG (U)HP terrane

UHP metamorphism

Of all of the domes, Mailolo is the only one known to preserve coesite eclogite (Baldwin et al., 2008), and in general, many of the eclogites are fresh and show evidence that they were once likely at UHP conditions (i.e., radial cracks in host garnet around quartz; highest jadeite content in omphacite); therefore, this dome, and in particular, the coesite eclogite, provide the best opportunity to date peak metamorphism. Three studies of the coesite eclogite interpret peak metamorphism from ca. 8–7 Ma (SIMS U-Pb zircon, Monteleone et al., 2007; Lu-Hf whole rock–garnet date, Zirakparvar et al., 2011; $^{40}Ar/^{39}Ar$ phengite, Baldwin and Das, 2015). The SIMS $^{206}Pb/^{238}U$–$^{207}Pb/^{206}Pb$ Terra Wasserburg intercept date of 7.9 ± 1.9 Ma (MSWD = 9.2) relies upon results from nine analyses on four zircon inclusions in garnet that show considerable scatter in $^{206}Pb/^{238}U$ dates from 11.5 ± 1.7 Ma to 5.9 ± 0.8 Ma (Monteleone et al., 2007). The high MSWD is a reflection of real dispersion and/or inaccuracy in the data that is likely a result of variability among single-spot dates and/or that much older standards with different compositions than the Pliocene PNG zircons (i.e., not matrix matched) were used; therefore, the date is statistically unreliable (e.g., Williams, 1998; Black et al., 2004). For the Lu-Hf eclogite study, trace elements measured across four garnets of unknown dimensions were homogenous; however, the analyses were spaced quite far, with only 25 analyses in total for 4 grains. Moreover, Mg and Ca zoning was observed within a 0.5 mm garnet. The ca. 7 Ma Lu-Hf isochron date was determined from six garnet fractions and two whole-rock analyses. Given the few Lu analyses over the grains, potential Lu zoning in the six different 200–250 mg garnet fractions may exist. Thus, the Lu-Hf

isochron date of ca. 7 Ma could be the result of diffusion of Lu from garnet cores to rims causing isochron rotation to a steeper slope, resulting in an older age (e.g., Kohn, 2009; Bloch et al., 2013).

More recently, Baldwin and Das (2015) report an $^{40}Ar/^{39}Ar$ weighted mean age of 7.93 ± 0.10 Ma based on ~84% of ^{39}Ar released during a step-heating experiment. This is interpreted to date the timing of phengite crystallization within the coesite eclogite at UHP conditions (Baldwin and Das, 2015). Recent studies have stressed the importance of determining the spatial distribution of Ar within phengite to determine whether Ar has diffused during the grain's history and to provide additional information on possible inheritance and (re)crystallization during the retrograde path (e.g., Sherlock and Kelley, 2002; Mulch et al., 2005; Warren et al., 2011, 2012a, 2012b). These studies require detailed profiles or maps of intra-grain core to rim Ar concentration by UV laser-ablation techniques (e.g., Boundy et al., 1997; Sherlock and Arnaud, 1999; Warren et al., 2012b) to provide insight into the diffusion of Ar in a particular grain, which can then be compared with mineral chemistry, microstructural information, and numerical-diffusion modeling to assess age variation dependence on grain size (e.g., Warren et al., 2012a). Numerous studies of UHP terranes have stressed the overwhelming problem of excess argon in phengite, which results in geologically meaningless older dates (e.g., Li et al., 1994; Hacker et al., 1995, 2000, 2009; Boundy et al., 1997; Giorgis et al., 2000; Chen et al., 2007). Moreover, Warren et al. (2012a) suggest that multigrain step heating masks the variability in how Ar is distributed throughout the grain and thus resulting in an average age. As Baldwin and Das (2015) do not report the mineral chemistry, grain size, or evidence for homogenous distribution of Ar within grains, it is difficult to access if the

7.9 Ma age records UHP metamorphism or is product of excess argon or averaging multiple zones within a grain (e.g., Warren et al., 2012a).

Finally, a U-Pb zircon ID-TIMS study of eclogite PNG08-010f from the coesite locality suggests younger peak metamorphism at ca. 5.6–4.6 Ma (Gordon et al., 2012), but these analyzed zircons were separated from the bulk rock and were not further investigated; therefore, it is difficult to interpret when the zircons grew. A reassessment of additional zircon separates from eclogite PNG08-010f reveals the grains are not zoned and that many contain mineral inclusions consisting of the peak metamorphic assemblage, including omphacite, rutile, garnet, and phengite. As described above, the sample preserves quartz inclusions within garnet associated with radial fractures. In addition, phase-diagram calculations using the fresh matrix-mineral compositions of garnet, omphacite, and phengite, which are identical to the inclusions within the zircon, predict UHP conditions of ~2.8 GPa and 550–600 °C (Chapter 3 in this Dissertation). Based on all of these characteristics, we interpret the 6.0 to 5.2 Ma dates from this study to best represent the timing of peak metamorphism for the rocks exposed within the Mailolo Dome (Fig. 4; Table 1), and these results suggest a minimum duration of 770 ± 330 ka for peak UHP metamorphism. Moreover, if the previous geochronometric data are recording UHP metamorphism, than these new results suggest that the crustal rocks recrystallized at mantle depths for ~3 Myr.

Retrogression of eclogites across the D'Entrecasteaux Islands

Overprinting of peak mineral assemblages is prevalent in (U)HP terranes, as retrogression under amphibolite-facies conditions within the lower-to-middle crust drives the

breakdown of omphacite and garnet to amphibole and plagioclase, producing coarse- to fine-grained symplectites and in some cases, transforming the eclogites entirely into amphibolite-facies mineral assemblages. Eclogites from Oiatabu, Mailolo, and Goodenough Domes show evidence for distinct levels of retrogression, and in many cases the zircon is intimately associated with these textures (Fig. 3). Moreover, some zircons have textures indicative of fluid-assisted recrystallization (further described below). Based on the textural locations, we interpret that the zircons record important temporal evidence for the retrogression and thus exhumation history within the different domes (Fig. 3).

The oldest zircons associated with retrogression textures come from the Oiatabu eclogite, with single crystal ID-TIMS analyses showing a narrow range in dates from 4.63 ± 0.03 Ma to 4.58 ± 0.02 Ma (Fig. 4). The zircons within this sample are large (~300–500 μm) and prismatic compared to the more rounded grains found in other eclogites. Two types of amphibole are present in the retrogression textures: 1) abundant coarse, euhedral amphibole grains, and 2) fine-grained amphibole associated with symplectite overgrowths that overprint the peak mineral assemblage (grt + omph + qtz + rutile). The rapid (~40,000 yrs) zircon (re)crystallization associated with the Oiatabu eclogite and the growth of these large euhedral zircon and amphibole grains are attributed to retrogression related to fluid infiltration during exhumation.

To the west, the two eclogites analyzed in Mailolo Dome show similar breakdown of the peak garnet and omphacite assemblage, with amphibole growth along garnet rims and within symplecite overgrowths; however, these eclogites, do not contain the second coarse-grained amphibole observed in the Oiatabu eclogite. As described above, zircon is

texturally associated with the retrogression assemblage in both samples (Fig. 3b, c). Zircon from eclogite PNG09-041c gives an ID-TIMS weighted mean $^{206}Pb/^{238}U$ age that is similar to Oiatabu of 4.63 ± 0.01 Ma (Fig. 4), whereas zircon from eclogite PNG09-039b yield slightly younger ID-TIMS results of 4.38 ± 0.065 Ma to 4.30 ± 0.014 Ma (Fig. 4). The *in situ* ca. 4.6 Ma eclogite and the ca. 4.3 Ma eclogite collected as a river cobble may be recording similar retrogression upon exhumation to lower pressures, with the age discrepancy explained by the ca. 4.3 Ma eclogite cobble originally being sourced from deeper within the core zone of Mailolo Dome resulting in younger retrogression ages compared to the *in situ* ca. 4.6 Ma eclogite that may have resided in higher structural levels.

In the far west, Goodenough Dome eclogites are nearly amphibolites, with extensive evidence of retrogression. Diopsidic clinopyroxene ($Jd_{0–20}$) occurs as inclusions within garnet and in the matrix, and the primary assemblage consists of garnet, diopside, amphibole, plagioclase, and biotite. The two analyzed eclogites, PNG10-035a and PNG12-82a, give the youngest ID-TIMS zircon results that overlap from 2.89 ± 0.03 Ma to 2.62 ± 0.06 Ma (Fig. 4). This study and previous work of Goodenough eclogites document lower-pressure mineral assemblages within the eclogites in comparison to the other domes (Davies and Warren, 1992; Monteleone et al., 2007).

Zircon trace-element data

Numerous studies have used zircon REE composition, with flat HREE slopes and flat-to-positive Eu anomalies, to suggest growth under eclogite-facies conditions (Rubatto, 2002; Rubatto and Hermann, 2003; Bingen et al., 2004; Baldwin et al., 2004; Monteleone et al.,

2007; Mattinson et al., 2006; Rubatto and Hermann, 2007a, 2007b; Gilotti et al., 2013; DesOrmeau et al., 2015). As only Mailolo eclogite PNG08-010f provides irrefutable evidence for zircon growth at or near peak conditions, the REE patterns from zircons associated with retrogression breakdown textures in the other analyzed eclogites should be expected to vary from the Mailolo zircon that (re)crystallized during (U)HP eclogite-facies metamorphism. In this study, solution ICP-MS and LASS analyses of zircons from all PNG (U)HP eclogites yield similar REE patterns that suggest the zircons crystallized under eclogite-facies conditions (Fig. 6). There are no obvious differences among samples despite the fact that in the Goodenough eclogites, the zircons are clearly associated with retrogression textures (i.e., abundant plagioclase and amphibole and no omphacite). Moreover, strongly deformed leucosomes and sills from Goodenough Dome reveal melt-crystallization ages that are older and or coeval with the zircon ages obtained from the two Goodenough eclogites (ca. 3.9–2.8 Ma vs. 2.9–2.6 Ma, respectively) (DesOrmeau et al., 2014).

There are multiple possibilities for the similar flat HREE slope and flat-to-positive Eu anomalies revealed from the variably retrogressed eclogites, including: 1) zircon (re)crystallization in all eclogites took place at eclogite-facies conditions; 2) the REE composition obtained at (U)HP conditions was preserved, whereas the U-Pb system was reset during retrogression at lower pressures; or 3) there are other factors controlling the HREE and Eu uptake by zircon other than garnet and plagioclase stability. Not including the coesite-eclogite locality, the first scenario of all zircons forming at peak (U)HP conditions is unlikely considering that the zircons in the five other eclogites are associated with retrogression assemblages and textures, in particular the Goodenough

eclogites where diopside is the primary clinopyroxene phase (Fig. 3). It is possible that the U-Pb system was reset while the REE composition was preserved given that REE diffusion rates are slower than Pb by at least one order of magnitude under most temperatures of geologic interest (Cherniak and Watson, 2001). However, the fact that in general, zircon commonly preserves core and rim or multiple growth zones within a single crystal suggests similar slow diffusion rates of both REE and Pb in crystalline zircon (Cherniak and Watson, 2001). It should be noted that zoning is not observed in many of these grains from this study. For the diffusion of Pb to be substantial, the eclogites would had to have sustained high temperatures (~750 °C) for times greater than the age of the Earth or the zircon would have to show evidence for a radiation-damaged structure (Cherniak et al., 1997a, 1997b; Lee et al., 1997; Cherniak and Watson, 2001, 2003; Horie et al., 2006; Utsunomiya et al., 2007), neither of which are documented for the (U)HP eclogites in this study. Finally, during garnet breakdown, HREE should become available for uptake by zircon, which has a high affinity for HREE (e.g., Hinton and Upton, 1991); however, zircons from the Mailolo eclogites PNG09-041c and PNG09-039b are intimately associated with garnet breakdown textures, but still record low HREE compositions. There is also no indication of crystallization of other minerals that would compete for HREE (i.e., monazite). In addition for the Eu anomaly, it is possible that the flat-to-positive Eu anomalies are not related to zircon (re)crystallization in the presence of plagioclase, but rather are related to the availability of Eu (Eu^{3+}/Eu^{2+}) in the melt or fluid from which zircon (re)crystallizes. Zircon preferentially incorporates Eu^{3+}, whereas plagioclase takes up Eu^{2+}; therefore, a flat to positive Eu anomaly could record either that the fluid contained Eu^{3+} and/or that plagioclase incorporated Eu^{2+}. As

Eu^{2+} is incompatible in zircon, the plagioclase could be present without affecting the Eu in the zircon. Based on these characteristics, it is difficult to interpret a Eu anomaly without knowledge of the Eu content, specifically how much Eu^{2+} versus Eu^{3+} was in the fluid or melt from which the zircon (re)crystallized (Burnham and Berry, 2012). Overall, it is not clear as to what allowed the eclogite-facies REE patterns to persist in the variably retrogressed eclogites, but these results do suggest that metamorphic zircon REE compositions should be interpreted with caution. For the PNG eclogites, the (U)HP inclusions within the zircons and textural position of the zircon provide a more robust record of where along the *P-T* path the zircon likely (re)crystallized.

Exhumation within an active rift

Based on a variety of petrologic, structural, geophysical, and geochronologic constraints, Little et al. (2011) argue that the onset of Pliocene seafloor spreading within the Woodlark basin introduced hot asthenosphere ahead of the westward-propagating rift causing previously subducted Australian-margin crustal material to (re)crystallize under (U)HP conditions and detach from the remnant slab. The inherited ages of ca. 90 to 53 Ma from two orthogneisses in the Oiatabu Dome carapace (PNG12-87a, PNG12-92a) further support the suggestion that Cretaceous–Paleogene Australian plate material is the protolith for the lower plate gneisses and eclogites (Davies, 1980; Davies and Jacques, 1984; Davies and Warren, 1988; Hill and Baldwin, 1993; Baldwin and Ireland, 1995; Gordon et al., 2012; Zirakparvar et al., 2013; DesOrmeau et al., 2014). The then partially-molten eclogite-bearing material buoyantly rose at plate-tectonic rates (~1.7 cm/yr) (Davies and Warren, 1988; Hill and Baldwin, 1993; Baldwin et al., 2004), following a

near-isothermal decompression path, accompanied by partial melting, to the base of the crust (Ellis et al., 2011; Little et al., 2011). Further exhumation through the lower-to-middle crust was facilitated by ductile thinning that accompanied the mostly E–W oriented (parallel to the rift margins), gravity-driven flow of the stalled material (Little et al., 2011). Final emplacement of the domes within the upper crust was assisted by melt-induced buoyancy (Ellis et al., 2011; Gordon et al., 2012; DesOrmeau et al., 2014) and rapid concurrent tectonic extension in the upper crust (Tregoning et al., 1998; Taylor et al, 1999; Abers 2001; Abers et al., 2002; Taylor and Huchon, 2002; Wallace et al., 2004, 2014; Kington and Goodliffe, 2008; Eilon et al., 2014, 2015). The different phases of exhumation and deformation history for the (U)HP rocks as recorded by the variably retrogressed eclogites and a variety of host gneisses, sills, leucosomes, and dikes are discussed below.

Easternmost Dome: Oiatabu Dome

The Oiatabu Dome has received far less study in previous investigations of the D'Entrecasteaux Islands. In the SW carapace of the Oiatabu Dome, kyanite ± phengite eclogites that contain late amphibole porphyroblasts equilibrated at near (U)HP conditions of ~30–31 kbar and 635–660 °C (Davies and Warren, 1992; DesOrmeau et al., in prep.). Multiple attempts at extracting zircons from these near-UHP eclogites failed. The ca. 4.6 Ma retrogression ages from the carapace eclogite in Oiatabu Dome reveals the oldest record of the initial breakdown of peak metamorphic assemblages across the domes. Furthermore, host gneiss PNG12-85a from the highest structural levels within Oiatabu Dome reveals slightly older to coeval metamorphism from ca. 5.7 Ma to ca. 4.5

Ma, the range in ages from microsampled zircon rim overgrowths (Fig. 5). These zircons show enrichment in HREE and variable Eu anomalies and Th/U ratios that do not correlate with age, indicating the structurally higher paragneiss is most likely recording retrogression-related metamorphism; however, the ages do overlap with the near-peak metamorphism recorded in the Mailolo Dome.

Two crosscutting, weakly deformed dikes from similar structural levels of the carapace represent continued deformation and melt crystallization at ca. 3.0–2.9 Ma (Fig. 5). Trace-element compositions of the very radiogenic zircons record variable HREE enrichment and a wide range in Eu anomalies and Th/U ratios. The large variation in zircon REE contents in the weakly deformed dikes is attributed to fluid-assisted zircon (re)crystallization. These dikes record one of the latest melt-crystallization events likely related to the final stages of amphibolite-facies retrogression at middle-to-upper crustal levels.

In comparison, ~20 km to the south in Normanby Dome and also farthest east, maximum ages for retrogression-related metamorphism of carapace host gneisses are slightly older from ca. 5.6–5.0 Ma, deformed sills record melt crystallization at ca. 4.1 Ma, and ductile deformation ended at ca. 2.9 Ma (DesOrmeau et al., 2014). No eclogite has been dated from Normanby Dome; therefore, the carapace orthogneisses record a similar metamorphic history (ca. 5.6–5.0 Ma) compared to Oiatabu Dome (ca. 5.6–4.5 Ma).

Mailolo Dome

High-precision dating of peak metamorphism within Mailolo Dome eclogites at ca. 6.0–5.2 Ma and the onset of retrogression at ca. 4.6–4.3 Ma suggests initial exhumation from mantle depths was rapid, occurring in ~1.5–1.0 Myr. Strongly deformed leucosomes that show the same amphibolite-facies fabric as the host gneiss record melt crystallization near the base of the crust ~1.0 Myr later, from ca. 3.5–3.0 Ma (Gordon et al., 2012). This melt crystallization is likely related to E–W ductile thinning, cooling, and the achievement of neutral buoyancy after the (U)HP body traveled through the mantle (Little et al., 2011). Dikes within Mailolo Dome record an end to ductile deformation at ca. 2.4 Ma (Gordon et al., 2012).

Goodenough Dome

The westernmost exposed eclogites from Goodenough Dome are extensively retrogressed and thus there is no record of the near peak metamorphism for the Goodenough Dome. The oldest dates are from strongly-deformed leucosomes that crystallized at ca. 3.9–2.8 Ma, likely as the (U)HP body reached the lower crust (DesOrmeau et al., 2014). Retrogression of the eclogites likely occurred at this time, as indicated by the youngest and most protracted zircon (re)crystallization of all of the studied eclogites at ca. 2.8–2.6 Ma. Moreover, Baldwin and Ireland (1995) report host gneiss metamorphic SIMS zircon weighted-mean $^{206}Pb/^{238}U$ dates of 2.6 ± 0.2 Ma and 2.7 ± 0.3 Ma. Results from these leucosomes and host gneisses and the textural location of the zircons suggest that the ca. 2.8–2.6 Ma eclogites from Monteleone et al. (2007) and this study represent pervasive retrogression under amphibolite-facies conditions.

The degree of retrogression (i.e., abundant diopsidic clinopyroxene and plagioclase) and the ~2.0–1.5 Myr younger zircon ages found in the Goodenough Dome eclogites compared to those studied from Mailolo and Oiatabu Domes suggest the Goodenough eclogites: 1) may have resided in the lower–to–middle crust for a longer period of time and underwent more complete retrogression of peak phases; 2) did not reach the same peak P–T conditions as the other higher-pressure assemblages (i.e., coesite, kyanite, phengite); 3) being the farthest west, they may have resided longer at depth and been more thoroughly altered by the heat and/or fluids associated with rifting-related asthenospheric flow; or 4) the low Na and Si bulk-rock compositions result in the lack of omphacite (i.e., Davies and Warren, 1992). The previous thermobarometry argues that the rocks did not achieve as high of pressures (23–25 kbar) as the Mailolo Dome (Davies and Warren, 1992); however, temperatures are estimated to have reached >800 °C (Davies and Warren, 1992). These high temperatures suggest that the Goodenough Dome rocks may have interacted or been affected by rifting more extensively than the other domes. The combination of the influences of rifting and the bulk-rock composition is likely responsible for the lower pressure assemblages and youngest zircon ages within Goodenough compared to the other Domes.

The exhumation of the Goodenough HP rocks continued with the crystallization of the pegmatite that intruded eclogite PNG10-035a at ca. 2.6–2.4 Ma. Similar to Mailolo Dome, ductile deformation ended by ca. 2.3 Ma. Emplacement of all domes across the D'Entrecasteaux Islands within the brittle upper crust is recorded by nondeformed pluton and dike crystallization by 1.8 Ma (Baldwin et al., 1993; DesOrmeau et al., 2014).

Conclusion

High-precision U-Pb zircon ages track the exhumation history of eclogites and the host migmatitic rocks exposed within gneiss domes across the eastern PNG (U)HP terrane. The central Mailolo Dome attained the highest *P-T* conditions of all of the domes at ca. 6.0 to 5.2 Ma, as constrained by zircon containing (U)HP mineral phase inclusions. Retrogression associated with initial exhumation and the breakdown of peak mineral assemblages occurred at ca. 4.6 Ma within Mailolo Dome and in the Oiatabu Dome to the east, whereas an additional eclogite from Mailolo Dome, possibly from deeper structural levels, records early retrogression at ca. 4.3 Ma. The host gneiss within the Oiatabu Dome also underwent metamorphism at this time, from ca. 5.7 to 4.5 Ma. Late melt crystallization associated with ductile deformation within the Oiatabu Dome occurred at ca. 3.0–2.9 Ma. To the west, Goodenough Dome eclogites preserve lower-pressure mineral assemblages and much later retrogression at ca. 2.8–2.6 Ma, which is likely the result of more prolonged interaction with heat and fluids related to rifting. All domes record final non-deformed melt crystallization at ca. 1.8 Ma, marking the end of the ~3 Myr exhumation path taken from mantle depths to the upper crust.

References

Abers, G.A. (2001), Evidence for seismogenic normal faults at shallow depths in continental rifts. In: Wilson, R.C.L., R.B. Whitmarsh, B. Taylor, N. Froitzham, (Eds.), Non-volcanic Rifting of Continental Margins, pp. 305–318, *The Geological Society of London, Special Publications*, **187**, London.

Abers, G.A., A. Ferris, M. Craig, H. Davies, A.L. Lerner-Lam, J.C. Mutter, and B. Taylor (2002), Mantle compensation of active metamorphic core complexes at Woodlark rift in Papua New Guinea, *Nature*, **418**, 862–865, doi:10.1038/nature00990.

Amato, J.M., C. Johnson, L. Baumgartner, and B. Beard (1999), Sm–Nd geochronology indicates rapid exhumation of Alpine eclogites. *Earth Planet. Sci. Lett.*, **171**, 425–438.

Baldwin, S.L., and T.R. Ireland (1995), A tale of two eras: Pliocene-Pleistocene unroofing of Cenozoic and late Archean zircons from active metamorphic core complexes, Solomon Sea, Papua New Guinea, *Geology*, **23**, 1023–1026, doi: 10.1130/0091-7613(1995)023<1023:ATOTEP>2.3.CO;2.

Baldwin, S.L., and J.P. Das (2015), Atmospheric Ar and Ne returned from mantle depths to the Earth's surface by forearc recycling, *PNAS*, doi:10.1073/pnas.1424122112.

Baldwin, S.L., G.S. Lister, E.J. Hill, D.A. Foster, and I. McDougall (1993), Thermochronologic constraints on the tectonic evolution of active metamorphic core complexes, D'Entrecasteaux Islands, Papua New Guinea, *Tectonics*, **12**, 611–628, doi: 10.1029/93TC00235.

Baldwin, S.L., B. Monteleone, L.E. Webb, P.G. Fitzgerald, M. Grove, and E.J. Hill (2004), Pliocene eclogite exhumation at plate tectonic rates in eastern Papua New Guinea, *Nature*, **431**, 263–267, doi:10.1038/nature02846.

Baldwin, S.L., L.E. Webb, and B.D. Monteleone (2008), Late Miocene coesite-eclogite exhumed in the Woodlark Rift, *Geology*, **36**, 735–738, doi: 10.1130/G25144A.1.

Bingen, B., H. Austrheim, M.J. Whitehouse, and W.J. Davis (2004), Trace element signature and U–Pb geochronology of eclogite-facies zircon, Bergen Arcs, Caledonides of W Norway. *Contrib. Mineral. Petrol.*, **147**, 671–683, http://dx.doi.org/10.1007/s00410-004-0585-z.

Black L.P., et al. (2004), Improved 206Pb/238U microprobe geochronology by the monitoring of a trace-element-related matrix effect; SHRIMP, ID-TIMS, ELA-ICP-MS and oxygen isotope documentation for a series of zircon standards. *Chem. Geol.*, **205**, 115–140.

Bloch, E. (2013), Diffusion kinetics of lutetium and hafnium in garnet and clino-pyroxene: Experimental determination and consequences for ^{176}Lu-^{176}Hf geo-chronometry. Department of Geosciences, 197. University of Arizona, Tucson.

Bowring, J.F., N.M. McLean, and S.A. Bowring (2011), Engineering cyber infrastructure for U–Pb geochronology: Tripoli and U–Pb redux. *Geochem., Geophys., Geosyst.*, **12**, Q0AA19, http://dx.doi.org/10.1029/2010GC003479.

Burnham, A. D., and A.J. Berry (2012), An experimental study of trace element partitioning between zircon and melt as a function of oxygen fugacity. *Geochimica et Cosmochimica Acta*, **95**, 196-212.

Cherniak, D.J., and E.B. Watson (2001), Pb Diffusion in zircon, *Chem. Geol.*, **172**, 5-24.

Cherniak, D.J., and E.B. Watson (2003), Diffusion in zircon. *Reviews in Mineralogy and Geochemistry*, **53(1)**, 113-143.

Cherniak, D.J., J.M. Hanchar, and E.B. Watson (1997a), Rare-Earth diffusion in zircon, *Chem. Geol.*, **134**, 289-301.

Cherniak, D.J., J.M. Hanchar, and E.B. Watson (1997b) Diffusion of tetravalent cations in zircon, *Contrib. Mineral. Petrol.*, **127**, 383-390.

Chopin, C. (1984), Coesite and pure pyrope in high-grade blueschists of the western Alps: a first record and some consequence, *Contrib. Mineral. Petrol.*, **86**, 107–118, doi: 10.1007/BF00381838.

Cloos, M., B. Sapiie, Q.A. vanUfford, R.J. Weiland, P.Q. Warren, and T.P. McMahon (2005), Collisional delamination in New Guinea: the geotectonics of slab break-off, *Geological Society of America Special Paper* 400, **51**, doi: 10.1130/2005.2400.

Corfu, F., J.M. Hanchar, P.W.O Hoskin, and P. Kinny (2003), Atlas of zircon textures. In: Hanchar, J.M. and Hoskin P.W.O. (eds.), Zircon. *Reviews in Mineralogy and Geochemistry*, **53**, 468–500. Washington, DC: Mineralogical Society of America.

Davies, H. L. (1973), The Geology of Fergusson Island, *map with explanatory notes*, Australia Bureau of Mineral Resources.

Davies, H.L. (1980), Crustal structure and emplacement of ophiolite in southeastern Papua New Guinea, *Colloques Internationaux du C.N.R.S*, **272**, 17–33.

Davies, H.L. (1990), Structure and evolution of the border region of New Guinea. In: Carman, G.J., Z. Carman, (Eds.), Petroleum Exploration in Papua New Guinea: *Proceedings of the First PNG Petroleum Convention, Port Morseby, February 12–14, 1990*, 249–269.

Davies H.L. (2012), The geology of New Guinea: the cordilleran margin of the Australian continent, *Episodes*, **35**, 87–102.

Davies, H.L., and A.L. Jaques (1984), Emplacement of ophiolite in Papua New Guinea, *Geological Society of London Special Publication 13*, 341–350, doi: 10.1144/GSL.SP.1984.013.01.27.

Davies, H.L., and R.G Warren (1988), Origin of eclogite-bearing, domed, layered metamorphic complexes (core complexes) in the D'Entrecasteaux Islands, Papua New Guinea, *Tectonics,* **7**, 1–21, doi: 10.1029/TC007i001p00001.

Davies, H.L., and R.G. Warren (1992), Eclogites of the D'Entrecasteaux Islands, *Contrib. Mineral. Petrol.*, **112**, 463–474, doi: 10.1007/BF00310778.

Davies, H.L., and A.N. Williamson (1998), Buna, Papua New Guinea, 1:250,000 Geological Series, *Geological Survey of Papua New Guinea Explanatory Notes SC/55-3.*, Port Moresby, Papua New Guinea.

de Sigoyer, J., et al. (2000), Dating the Indian continental subduction and collisional thickening in the Northwest Himalaya: multichronology of the Tso Morari eclogites. Geology (Boulder) **28**, 487–490.

DesOrmeau, J. W., S. M. Gordon, T. A. Little, and S. A. Bowring (2014), Tracking the exhumation of a Pliocene (U)HP terrane: U-Pb and trace-element constraints from zircon, D'Entrecasteaux Islands, Papua New Guinea, *Geochem. Geophys. Geosyst.*, **15**, doi:10.1002/2014GC005396.

DesOrmeau, J.W., et al. (2015), Insights into (U)HP metamorphism of the Western Gneiss Region, Norway: A high-spatial resolution and high-precision zircon study, *Chem. Geol.*, **414**, 138–155, http://dx.doi.org/10.1016/j.chemgeo.2015.08.004.

Eilon, Z., G. A. Abers, G. Jin, and J. B. Gaherty (2014), Anisotropy beneath a highly extended continental rift, *Geochem. Geophys. Geosyst.*, **15**, 545–564, doi:10.1002/2013GC005092.

Eilon, Z., G. A. Abers, J. B. Gaherty, and G. Jin (2015), Imaging continental breakup using teleseismic body waves: The Woodlark Rift, Papua New Guinea, *Geochem. Geophys. Geosyst.*, **16**, doi:10.1002/2015GC005835.

Ellis, S.M., T.A Little, L.M. Wallace, B.R. Backer, and S.J.H Buiter (2011), Feedback between rifting and diapirism can exhume ultrahigh-pressure rocks, *Earth Planet. Sci. Lett.*, **311**, 427–438, doi: 10.1016/j.epsl.2011.09.031.

Ernst, W.G. (2001), Subduction, ultrahigh-pressure metamorphism, and regurgitation of buoyant crustal slices – implications for arcs and continental growth. In: Rubie, D., R.

van der Hilst, (Eds.), *Processes and Consequences of Deep Subduction*, 253–275, doi : 10.1016/S0031-9201(01)00231-X.

Faccenda, M., G. Minelli, and T.V. Gerya (2009), Coupled and decoupled regimes of continental collision: Numerical modeling, *Earth Planet. Sci. Lett.*, **278**, 337–349, doi:10.1016/j.epsl.2008.12.021.

Fitzgerald, P.G., S.L. Baldwin, S.L. Miller, S.E. Perry, L.E. Webb, and T.A. Little (2008), Low temperature constraints on the evolution of metamorphic core complexes of the Woodlark rift system, *Annual Meeting of the American Geophysical Union. AGU, EOS Transactions*, San Francisco, CA.

Gebauer, D., H.P. Schertl, M. Brix, and W. Schreyer (1997), 35 Ma old ultrahigh-pressure metamorphism and evidence for very rapid exhumation in the Dora Maira massif, Western Alps, *Lithos*, **41**, 5–24, doi: 10.1016/S0024-4937(97)82002-6.

Gerya, T.V., L.L. Perchuk, and J.P. Burg (2008), Transient hot channels: perpetrating and regurgitating ultrahigh-pressure, high temperature crust-mantle associations in collision belts. *Lithos*, **103**, 236-256.

Gilotti, J.A. (2013), The realm of ultrahigh-pressure metamorphism, *Elements*, **vol. 9**, 255–260.

Gordon, S.M., T.A. Little, B.R. Hacker, S.A. Bowring, S.L. Baldwin, and A.R.C. Kylander-Clark, (2012), Multi-stage exhumation of young UHP–HP rocks: timescales of melt crystallization in the D'Entrecasteaux Islands, southeastern Papua New Guinea, *Earth Planet. Sci. Lett.*, **351–352**, 237–246, doi: 10.1016/j.epsl.2012.07.014.

Hacker, B.R., A.T. Calvert, R.Y. Zhang, W.G. Ernst, and J.G. Liou (2003) Ultrarapid exhumation of ultrahigh pressure diamond-bearing metasedimentary and meta-igneous rocks of the Kokchetav Massif. Lithos, 70, 61–75.

Hacker, B.R., Wallis, S.R., Ratschbacher, L., Grove, M., Gehrels, G., 2006. High-temperature geochronology constraints on the tectonic history and architecture of the ultrahighpressure Dabie–Sulu orogen. Tectonics 25, TC5006. doi:10.1029/2005TC001937.

Hacker, B.R. (2007), Ascent of the ultrahigh-pressure Western Gneiss Region, Norway. In: Cloos, M., W.D. Carlson, M.C. Gilbert, J.G. Liou, and S.S. Sorenson (Eds.), Convergent Margin Terranes and Associated Regions, A Tribute to W.G. Ernst, *Geological Society of America Special Paper*, **419,** Geological Society of America, Boulder, CO, 171–184, doi: 10.1130/2006.2419(09).

Hermann, J., D. Rubatto, A. Korsakov, and V.S. Shatsky (2001), Multiple zircon growth during fast exhumation of diamondiferous, deeply subducted continental crust

(Kokchetav Massif, Kazakhstan), *Contrib. Mineral. Petrol.*, **141**, 66–82, doi: 10.1007/s004100000218.

Hill, E.J. (1994), Geometry and kinematics of shear zones formed during continental extension in eastern Papua New Guinea, *J. Struct. Geol.*, **16**, 1093–1105, doi: 10.1016/0191-8141(94)90054-X.

Hill, E.J., S.L. Baldwin, and G.S. Lister (1992), Unroofing of active metamorphic core complexes in the D'Entrecasteaux Islands, Papua New Guinea, Geology, **20**, 907–910, doi: 10.1130/0091-7613(1992) 020<0907:UOAMCC> 2.3.CO;2.

Hill, E.J., and Baldwin, S.L. (1993), Exhumation of high-pressure metamorphic rocks during crustal extension in the D'Entrecasteaux region: Papua New Guinea, *J. Metamorph. Geol.*, **11**, 261–277, doi: 10.1111/j.1525-1314.1993.tb00146.x.

Hill, J., S.L. Baldwin, and G.S Lister (1995), Magmatism as an essential driving force for formation of active metamorphic core complexes in eastern Papua New Guinea, *J. Geophys. Res.*, **100**, 10441–10451, doi: 10.1029/94JB03329.

Hinton, R., Upton, B. (1991), The chemistry of zircon: variations within and between large crystals from syenite and alkali basalt xenoliths. *Geochim. et Cosmochim. Acta.*, **55**, 3287–3302, http://dx.doi.org/10.1016/0016-7037(91)90489-R.

Horie, K., Hidaka, H., & Gauthier-Lafaye, F. (2006). Elemental distribution in zircon: Alteration and radiation-damage effects. *Physics and Chemistry of the Earth, Parts A/B/C*, *31*(10), 587-592.

Jackson, S.E., Pearson, N.J., Griffin, W.L., Belousova, E.A. (2004), The application of laser ablation-inductively coupled plasma-mass spectrometry to in situ U/Pb zircon geochronology. *Chem. Geol*., **211 (1–2)**, 47–69, http://dx.doi.org/10.1016/j.chemgeo.-2004.06.017.

Kaneko, Y., et al., 2003. Timing of Himalayan ultrahigh-pressure metamorphism: sinking rate and subduction angle of the Indian continental crust beneath Asia. J. Metamorph. Geol. 21, 589–599.

Kington, J. D., and A. M. Goodliffe (2008), Plate motions and continental extension at the rifting to spreading transition in Woodlark Basin, Papua New Guinea: Can oceanic plate kinematics be extended into continental rifts?, Tectonophysics, 458, 82–95.

Kohn, M. J. (2009). Models of garnet differential geochronology. *Geochimica et Cosmochimica Acta*, *73*(1), 170-182.

Korchinski, M., et al. (2014), Timing of UHP exhumation and rock fabric development in gneiss domes containing the world's youngest eclogite-facies rocks, Woodlark Rift, southeastern Papua New Guinea, *J. Metamorph. Geol*., **32**, 1019–1039, http://dx.doi.org/10.1111/jmg.12105.

Kylander-Clark, A.R.C., Hacker, B.R., Johnson, C.M., Beard, B.L., Mahlen, N.J., Lapen, T.J. (2007), Coupled Lu–Hf and Sm–Nd geochronology constrains prograde and exhumation histories of high- and ultrahigh-pressure eclogites from western Norway. *Chem. Geol.*, **242(1–2)**, 137–154, http://dx.doi.org/10.1016/j.chemgeo.2007.03.006.

Kylander-Clark, A.R.C., Hacker, B.R., Johnson, C.M., Beard, B.L., Mahlen, N.J. (2009), Slow subduction and rapid exhumation of a thick ultrahigh-pressure terrane. *Tectonics*, **28(2)**, TC2003, http://dx.doi.org/10.1029/2007TC002251.

Kylander-Clark, A. R. C., B.R. Hacker, C.G. Mattinson (2012), Size and exhumation rate of ultrahigh-pressure terranes linked to orogenic stage, *Earth Planet. Sci. Lett.*, **321–322**, 115–120, http://dx.doi.org/10.1016/j.epsl.2011.12.036.

Kylander-Clark, A.R.C., Hacker, B.R., Cottle, J.M., (2013), Laser-ablation split-stream ICP petrochronology. *Chem. Geol.*, **345**, 99–112, http://dx.doi.org/10.1016/j.chemgeo.-2013.02.019.

Labrousse, L., G. Prouteau, and A.C. Ganzhorn (2011), Continental exhumation triggered by partial melting at ultrahigh pressure, Geology, **39**, 1171–1174, doi: 10.1130/G32316.1.

Lang, H.J., and J.A. Gilotti (2007), Partial melting of metapelites at ultrahigh-pressure conditions, Greenland Caledonides, *J. Metamorph. Geol.*, **25**, 129–147, doi: 10.1111/j.1525-1314.2006.00687.x.

Lapen, T.J., Johnson, C.M., Baumgartner, L.P., Mahlen, N.J., Beard, B.L., Amato, J.M., 2003. Burial rates during prograde metamorphism of an ultra-high-pressure terrane: an example from Lago di Cignana, western Alps, Italy. Earth and Planetary Science Letters 215, 57–72.

Lee JKW, Williams IS, Ellis DJ (1997) Pb, U and Th diffusion in natural zircon. Nature 390:159-162.

Li, Z. H., Xu, Z. Q., and Gerya, T. V., 2011. Flat versus steep subduction: Contrasting modes for the formation and exhumation of high to ultrahigh-pressure rocks in continental collision zones, Earth Planet. Sci. Lett., 301, 65–77, doi:10.1016/j.epsl.2010.10.014.

Liou, J.G., Tsujimori, T., Zhang, R.Y., Katayama, I., Maruyama, S., 2004. Global UHP metamorphism and continent subduction/collision. The Himalayan model. International Geology Review 46, 1–27.

Liu F, Xu Z, Liou JG, Dong H, Xue H (2007) Ultrahigh-pressure mineral assemblages in zircons from surface to 5158 m depth in cores of the main drill hole, Chinese Continental Scientific Drilling Project, southwestern Sulu belt, China. International Geological Review, 49: 454-478.

Little, T. A., S. L. Baldwin, P. G. Fitzgerald, and B. Monteleone (2007), Continental rifting and metamorphic core complex formation ahead of the Woodlark Spreading Ridge, D'Entrecasteaux Islands, Papua New Guinea, Tectonics, 26, TC1002, doi:10.1029/2005TC001911.

Little, T.A., B.R. Hacker, S.M. Gordon, S.L. Baldwin, P.G. Fitzgerald, S. Ellis, and M. Korchinski (2011), Diapiric exhumation of Earth's youngest (UHP) eclogites in the gneiss domes of the D'Entrecasteaux Islands, Papua New Guinea, *Tectonophysics*, **510**, 39–68, doi: 10.1016/j.tecto.2011.06.006.

Little, T.A., B.R. Hacker, S.J. Brownlee, and G. Seward (2013), Microstructures and quartz lattice-preferred orientations in the eclogite-bearing migmatitic gneisses of the D'Entrecasteaux Islands, Papua New Guinea, *Geochem., Geophys., Geosyst.*, ***14*** **(6)**, 2030–2062, doi: 10.1002/ggge.20132.

Lus, W.Y., I. McDougall, and H.L. Davies (2004), Age of metamorphic sole of the Papuan Ultramafic Belt ophiolite, Papua New Guinea, *Tectonophysics, 392*, 85–101, doi: 10.1016/j.tecto.2004.04.009.

Massonne, H.J., Kennedy, A., Nasdala, L., Theye, T., 2007. Dating of zircon and monazite from diamondiferous quartzofeldspathic rocks of the Saxonian Erzgebirge-hints at burial and exhumation velocities. Mineralogical Magazine 71, 407–425.

Mattinson, J.M. (2005), Zircon U-Pb chemical abrasion ("CA-TIMS") method: combined annealing and multi-step partial dissolution analysis for improved precision and accuracy of zircon ages, *Chem. Geol.*, **220**, 47–66, doi: 10.1016/j.chemgeo.2005.03.011.

Mattinson, C.G., Wooden, J.L., Liou, J.G., Bird, D.K., Wu, C.L. (2006), Age and duration of eclogite-facies metamorphism, North Qaidam HP/UHP terrane, Western China. *Amer. J. Science*, **306**, 683–711, http://dx.doi.org/10.2475/09.2006.01.

Monteleone, B.D., S.L. Baldwin, L.E. Webb, P.G. Fitzgerald, M. Grove, and A.K. Schmitt (2007), Late Miocene–Pliocene eclogite facies metamorphism, D'Entrecasteaux Islands, SE Papua New Guinea, *J. Metamorph. Geol.*, **25**, 245–265, doi: 10.1111/j.1525-1314.2006.00685.x.

O'Brien, P.J., 2001. Subduction followed by collision: Alpine and Himalayan examples. Physics of the Earth and Planetary Interiors 127, 277–291.

Parrish, R.R., Gough, S.J., Searle, M.P., Waters, D.J., 2006. Plate velocity exhumation of ultrahigh-pressure eclogites in the Pakistan Himalaya. Geology 34, 989–992.

Proyer, A., Dachs, E. & McCammon, C., 2004. Pitfalls in geothermobarometry of eclogites: Fe3+ and changes in the mineral chemistry of omphacite at ultrahigh pressures. Contributions to Mineralogy and Petrology, 147, 305–318.

Ragozin, A. L., J. G. Liou, V.S. Shatsky, and N.V. Sobolev (2009), The timing of the retrograde partial melting in the Kumdy-Kol region (Kokchetav Massif, Northern Kazakhstan), *Lithos*, **109**, 274–284, doi:10.1016/j.lithos.2008.06.017.

Rogerson, R., D.B. Hilyard, E.J. Finlayson, D.J. Holland, S.T.S. Nion, R.M. Sumarang, J. Dugaman, and C.D.C. Loxton (1987), The geology and mineral resources of the Sepik headwaters region, Papua New Guinea, *Papua New Guinea Geological Surveys Memoir, 12*.

Rubatto, D. (2002), Zircon trace element geochemistry: distribution coefficients and the link between U-Pb ages and metamorphism, *Chem. Geol.*, **184**, 123–138, doi: 10.1016/S0009-2541(01)00355-2.

Rubatto, D., and J. Hermann (2001), Exhumation as fast as subduction?, *Geology*, **29***,* 3–6, doi: 10.1130/0091-7613(2001) 029<0003:EAFAS> 2.0.CO;2.

Rubatto, D., Hermann, J. (2003), Zircon formation during fluid circulation in eclogites (Monviso, Western Alps): implications for Zr and Hf budget in subduction zones. *Geochim. et Cosmochim. Acta.*, **67**, 2173–2187, http://dx.doi.org/10.1016/S0016-7037(02)01321-2.

Rubatto, D., Hermann, J. (2007a), Zircon behaviour in deeply subducted rocks, *Elements*, **3**, 31–35, http://dx.doi.org/10.2113/gselements.3.1.31.

Rubatto, D., Hermann, J. (2007b), Experimental zircon/melt and zircon/garnet trace element partitioning and implications for the geochronology of crustal rocks. *Chem. Geol.*, **241**, 38-61, http://dx.doi.org/10.1016/j.chemgeo.2007.01.027.

Schoene, B., C. Latkoczy, U. Schaltegegger, and D. Günther (2010), A new method integrating high-precision U–Pb geochronology with zircon trace-element analysis (U–Pb TIMS-TEA), *Geochim, et Cosmochim. Acta.*, **74**, 7144–7159, doi: 10.1016/j.gca.2010.09.016.

Sizova, E., Gerya, T., and Brown, M., 2012. Exhumation mechanism of ultrahigh pressure crustal rocks during collision of spontaneously moving plates, J. Metamorph. Geol., 30, 927–955, doi:10.1111/j.1525-1314.2012.01004.x.

Smith, D.C. (1984), Coesite in clinopyroxene in the Caledonides and its implications for geodynamics, *Nature*, **310**, 641–644, doi:10.1038/310641a0.

Sobolev, N.V., and V.S. Shatsky (1990), Diamond inclusions in garnets from metamorphic rocks; a new environment of diamond formation, *Nature*, **343**, 742–746, doi:10.1038/343742a0.

Sun S. S., and W.F. McDonough (1989), Chemical and isotopic systematics of oceanic basalts: implications for mantle composition and processes, *Geological Society of London Special Publications*, **42**, 313–345, doi: 10.1144/GSL.SP.1989.042.01.19.

Taylor, B., A.M. Goodliffe, F. Martinez (1999), How Continents break-up: insights from Papua New Guinea, *J. Geophys. Res.*, **104**, 7497–7512, doi: 10.1029/1998JB900115.

Taylor, B., and P. Huchon (2002), Active continental extension in the western Woodlark Basin: a synthesis of Leg 180 results, in Proceedings of the Ocean Drilling Program, Scientific Results [CD ROM], vol. 180, edited by P. Huchon, B. Taylor, and A. Klaus, pp. 1–36, Ocean Drill. Prog., Texas A&M Univ., College Station, Tex.

Tregoning, P., K. Lambeck, A. Stoltz, P. Morgan, S. C. McClusky, P. van der Beek, H. McQueen, R. J. Jackson, R. P. Little, A. Laing, and B. Murphy (1998), Estimation of current plate motions in Papua New Guinea from Global Positioning System observations, *J. Geophys. Res.*, **103**, 12,181– 12,203, doi: 10.1029/97JB03676.

Utsunomiya, S., Valley, J. W., Cavosie, A. J., Wilde, S. A., & Ewing, R. C. (2007). Radiation damage and alteration of zircon from a 3.3 Ga porphyritic granite from the Jack Hills, Western Australia. *Chemical Geology*, *236*(1), 92-111.

Van Ufford, Q.A., and M. Cloos (2005), Cenozoic tectonics of New Guinea, *Am. Assoc. Pet. Geol. Bull.*, **89**, 119–140, doi:10.1306/08300403073.

Vry, J., and M. Gazley (submitted manuscript), Zr-in-rutile: A thermobarometer for eclogites, *J. Metamorph. Geol.* (2015).

Waggoner, A., S.L. Baldwin, L.A Webb, T.A. Little, and P.G. Fitzgerald (2008), Temporal constraints on continental rifting and the exhumation of the youngest known HP metamorphic rocks, SE Papua New Guinea, *Eos Trans. AGU, 89(53)*, Fall Meet. Suppl., Abstract T41B-1961.

Wallace, L.M., C. Stevens, E. Silver, R. McCaffrey, W. Loratung, S. Hasiata, R. Stanaway, R. Curley, R. Rosa, and J. Taugaloidi (2004), GPS and seismological

constraints on active tectonics and arc-continent collision in Papua New Guinea: implications for mechanics of microplate rotations in a plate boundary zone, *J. Geophys. Res.*, **109**, doi:10.1029/2003JB002481.

Wallace, L. M., S. Ellis, T. Little, P. Tregoning, N. Palmer, R. Rosa, R. Stanaway, J. Oa, E. Nidkombu, and J. Kwazi (2014), Continental breakup and UHP rock exhumation in action: GPS results from the Woodlark Rift, Papua New Guinea, Geochem. Geophys. Geosyst., 15, 4267–4290, doi:10.1002/2014GC005458.

Warren, C.J., Beaumont, C. and Jamieson, R.A., 2008. Modelling tectonic styles and ultra-high pressure (UHP) rock exhumation during the transition from oceanic subduction to continental collision. Earth and Planetary Science Letters, 267(1-2): 129-145.

Wallis, S., Tsuboi, M., Suzuki, K., Fanning, M., Jiang, L., and Tanaka, T., 2005, Role of partial melting in the evolution of the Sulu (eastern China) ultrahigh-pressure terrane: Geology, v. 33, p. 129–132.

Weissel, J.K., B. Taylor, and G.D Karner (1982), The opening of the Woodlark Basin, subduction of the Woodlark spreading system, and the evolution of northern Melanesia since mid-Pliocene time, *Tectonophysics*, **87**, 253–277, doi: 10.1016/0040-1951(82)90229-3.

Westaway, R. (2007), Correction to "Active low angle normal-faulting in the Woodlark extensional province, Papua New Guinea: a physical model, *Tectonics*, **26**, TC1003.

Wiedenbeck, M., et al., (1995), Three natural zircon standards for U–Th–Pb, Lu–Hf, trace element and REE analyses. *Geostandards Newsletter*, **19 (1)**, 1–23, http://dx.doi.org/-10.1111/j.1751-908X.1995.tb00147.x.

Williams IS (1998) U–Th–Pb geochronology by ion microprobe. In: McKibben MA, Shanks WC III, and Ridley WI (eds.) Applications of Microanalytical Techniques to Understanding Mineralizing Porcesses. Reviews in Economic Geology, vol. 7, pp. 1–35. Littleton, CO: Society of Economic Geologists.

Zirakparvar, N.A., S.L. Baldwin, and J.D. Vervoort (2011), Lu–Hf garnet geochronology applied to plate boundary zones: insights from the (U)HP terrane exhumed within the Woodlark Rift, *Earth Planet. Sci. Lett.*, **309**, 56–66, doi: 10.1016/j.epsl.2011.06.016.

Zirakparvar, N.A., S.L. Baldwin, and J.D. Vervoort (2013), The origin and geochemical evolution of the Woodlark Rift of Papua New Guinea, *Earth Planet. Sci. Lett.*, **23**, 931–943, doi: 10.1016/j.gr.2012.06.013.

Table 1

Zircon U-Pb ID-TIMS isotopic data for (U)HP eclogites from the D'Entrecasteaux Islands

				Isotopic Ratios							Dates (Ma)					
Sample	location[a]	mineral assemblage[b]	Fraction	$^{206}Pb/^{204}Pb$ [i]	$^{206}Pb/^{238}U$ <Th> [j,c]	±2σ %	$^{207}Pb/^{235}U$ [j]	±2σ %	$^{207}Pb/^{206}Pb$ <Th> [j,c]	±2σ %	$^{206}Pb/^{238}U$ date <Th> [c]	±2σ abs	$^{207}Pb/^{235}U$ date [d]	±2σ abs	$^{207}Pb/^{206}Pb$ date <Th> [c]	±2σ abs
Fergusson Island: Oitabu Dome	E259565	Grt, Omp, Qz, Rt	z1	190.43	0.00072	0.62	0.0048	7.02	0.049	6.87	4.63	0.029	4.87	0.34	125.88	161.76
PNG12-95a, eclogite cobble	N8951010	(Amp, Di, Pl, Bt, Zrn)	z2	556.06	0.00072	0.35	0.0046	2.46	0.047	2.42	4.62	0.016	4.68	0.11	34.69	57.87
			z3	762.15	0.00072	0.39	0.0046	1.71	0.047	1.72	4.61	0.018	4.69	0.080	47.54	40.99
			z4	625.33	0.00071	0.34	0.0046	2.38	0.046	2.34	4.60	0.016	4.63	0.11	20.37	56.20
			z5	905.69	0.00072	0.26	0.0047	1.50	0.047	1.48	4.61	0.012	4.72	0.071	61.70	35.36
			z6	969.91	0.00071	0.30	0.0045	1.41	0.046	1.40	4.60	0.014	4.60	0.065	4.98	33.62
			z7	491.86	0.00072	0.41	0.0047	2.62	0.048	2.58	4.63	0.019	4.78	0.12	82.28	61.20
			z8	940.26	0.00071	0.42	0.0046	1.37	0.047	1.40	4.59	0.019	4.71	0.064	67.25	33.24
			z9	2481.04	0.00072	0.39	0.0047	0.58	0.047	0.67	4.62	0.018	4.73	0.027	60.95	15.98
			z10	5584.29	0.00072	0.28	0.0049	0.27	0.049	0.35	4.61	0.013	4.92	0.013	157.00	8.32
			z11	1061.15	0.00071	0.28	0.0048	1.18	0.049	1.18	4.59	0.013	4.84	0.057	130.10	27.79
			z12	1091.27	0.00071	0.26	0.0046	1.18	0.047	1.17	4.58	0.012	4.67	0.055	51.43	27.96
			z13	981.53	0.00072	0.44	0.0047	1.40	0.048	1.43	4.62	0.020	4.75	0.066	73.54	34.00
			z14-1-2	527.09	0.00072	0.31	0.0047	2.49	0.048	2.44	4.62	0.014	4.78	0.12	86.57	57.85
			z14-3	227.00	0.00072	0.53	0.0048	5.88	0.048	5.76	4.62	0.024	4.84	0.28	117.56	135.70
			z15-4	763.44	0.00072	0.38	0.0047	1.70	0.048	1.70	4.63	0.018	4.78	0.081	85.18	40.30
			z16-17	149.44	0.00071	0.74	0.0048	9.18	0.049	8.97	4.61	0.034	4.91	0.45	155.78	210.02
			z16-18	1059.66	0.00072	0.30	0.0048	1.27	0.049	1.26	4.62	0.014	4.86	0.061	125.85	29.60
			z16-frag	770.95	0.00072	0.30	0.0047	1.92	0.048	1.84	4.62	0.014	4.76	0.091	77.17	43.65
Fergusson Island: Mailolo Dome	E229905	Grt, Omp, Qz, Rt	z1-3	54.57	0.00071	2.6	0.0044	37.55	0.045	36.70	4.57	0.12	4.48	1.68	-44.20	892.05
PNG09-041c, eclogite	N8954470	(Amp, Cal–Dol, Pl,	z2-4	179.57	0.00072	0.60	0.0048	7.68	0.048	7.50	4.64	0.028	4.86	0.37	117.26	176.91
		Di, Zrn, Ap)	z2-5	56.46	0.00070	2.5	0.0045	34.47	0.046	33.64	4.54	0.11	4.54	1.56	2.53	810.39
			z3-6	240.27	0.00072	0.46	0.0047	5.88	0.047	5.74	4.62	0.021	4.72	0.28	54.80	136.82
			z3-7	49.13	0.00072	3.1	0.0047	42.96	0.047	41.89	4.62	0.14	4.72	2.02	53.60	999.57
			z4-8	81.45	0.00072	1.5	0.0050	19.14	0.051	18.60	4.61	0.070	5.08	0.97	235.62	429.06
			z5-9	215.69	0.00072	0.52	0.0047	6.46	0.047	6.31	4.61	0.024	4.73	0.31	66.45	150.26
			z6-17	44.51	0.00072	3.5	0.0050	44.26	0.050	43.29	4.65	0.16	5.05	2.23	201.64	1005.07
			z7-23	30.17	0.00070	7.7	0.0046	102.49	0.048	100.21	4.51	0.35	4.71	4.81	107.38	2367.29
			z8-26	63.77	0.00084	2.0	0.0066	22.85	0.057	22.27	5.41	0.11	6.67	1.52	489.22	491.24
			z9-28	170.39	0.00072	0.64	0.0048	8.13	0.048	7.94	4.64	0.030	4.86	0.39	113.28	187.47
			z10-42	93.43	0.00072	1.2	0.0049	15.86	0.050	15.50	4.65	0.057	5.01	0.79	178.12	361.47
			z11-44-45	87.35	0.00072	1.3	0.0046	18.25	0.047	17.86	4.62	0.062	4.68	0.85	34.60	427.76
PNG09-039b iv, eclogite cobble	E229901	Grt, Omp, Ph, Qz	z2	88.05	0.00067	1.5	0.0040	20.16	0.043	19.72	4.33	0.065	4.033	0.81	-170.07	491.27
	N8954173	(Ap, Rt, Zrn,	z4	268.36	0.00067	0.4	0.0044	5.04	0.048	4.93	4.30	0.017	4.43	0.22	78.12	117.09
		Cal–Dol, Pl)	z5	199.92	0.00067	0.6	0.0042	8.07	0.046	7.83	4.33	0.025	4.28	0.34	-24.62	189.61
			z6	245.48	0.00067	0.5	0.0044	5.90	0.048	5.74	4.33	0.020	4.47	0.26	77.36	136.28
			z9	240.68	0.00067	0.5	0.0041	6.86	0.044	6.67	4.32	0.021	4.12	0.28	-116.29	164.31
			z11	66.92	0.00068	1.9	0.0047	24.11	0.051	23.55	4.36	0.082	4.79	1.15	223.10	544.61
			z14	68.88	0.00067	1.8	0.0041	26.57	0.045	26.00	4.31	0.079	4.17	1.11	-77.98	636.18
			z15	76.66	0.00067	1.6	0.0042	22.68	0.046	22.16	4.33	0.070	4.28	0.97	-24.06	536.57
			z16-3-4	84.10	0.00067	1.4	0.0042	19.80	0.046	19.38	4.34	0.061	4.29	0.85	-23.60	469.24
			z16-5	42.82	0.00067	3.8	0.0039	57.22	0.043	56.04	4.30	0.161	3.97	2.27	-195.18	1402.87
			z17-8	90.62	0.00068	1.3	0.0046	16.63	0.049	16.25	4.36	0.056	4.62	0.77	142.11	381.47
			z17-9	156.93	0.00068	0.7	0.0045	8.90	0.049	8.70	4.35	0.030	4.58	0.41	125.85	204.81
			z18-12	164.08	0.00067	0.6	0.0045	8.33	0.048	8.15	4.35	0.028	4.56	0.38	116.34	192.13
			z19-17	55.64	0.00067	2.5	0.0043	34.77	0.046	34.01	4.34	0.107	4.31	1.50	-9.24	821.32
			z19-18	239.00	0.00068	0.4	0.0044	5.67	0.047	5.55	4.35	0.019	4.47	0.25	66.37	132.02
			z20-24	208.80	0.00067	0.5	0.0043	6.91	0.046	6.75	4.33	0.022	4.33	0.30	5.81	162.58
			z21-26	169.15	0.00067	0.6	0.0043	8.58	0.047	8.38	4.34	0.028	4.40	0.38	33.79	200.66
			z22-28-29	156.21	0.00067	0.7	0.0042	9.51	0.046	9.31	4.33	0.029	4.28	0.41	-19.85	225.35

PNG08-010F, eclogite	E221381	Grt, Omp, Qz, Ph,	z1	40.67	0.00083	4.2	0.0054	58.84	0.047	57.42	5.34	0.22	5.45	3.20	58.05	1369.04
	N8950186	Zrn, Rt	z3	37.89	0.00086	4.7	0.0053	67.07	0.045	65.70	5.55	0.26	5.36	3.59	-77.73	1607.46
		(Amp, Pl, Di, Ms)	z4	59.55	0.00083	2.4	0.0053	33.22	0.046	32.35	5.36	0.13	5.33	1.77	-5.24	780.65
			z5	33.36	0.00081	6.4	0.0038	125.47	0.034	122.90	5.20	0.33	3.86	4.83	-774.91	3467.99
			z6	29.43	0.00091	8.2	0.0064	104.27	0.051	101.78	5.85	0.48	6.44	6.70	232.76	2349.63
			z8	39.81	0.00083	4.3	0.0058	54.55	0.051	53.22	5.34	0.23	5.91	3.21	246.05	1225.51
			z9	35.39	0.00084	5.4	0.0049	83.24	0.042	81.49	5.42	0.29	4.97	4.12	-211.57	2046.43
			z10	34.86	0.00086	5.6	0.0057	75.09	0.048	73.40	5.57	0.31	5.74	4.30	80.72	1742.62
			z11	51.88	0.00093	2.8	0.0063	36.20	0.049	35.33	5.98	0.17	6.38	2.30	161.87	826.19
			z12	29.68	0.00086	8.1	0.0062	100.88	0.052	98.33	5.53	0.45	6.23	6.27	286.40	2248.14
			z13	33.85	0.00086	5.9	0.0059	76.05	0.050	74.30	5.52	0.32	5.95	4.52	185.80	1729.99
			z14	40.78	0.00092	4.1	0.0074	45.40	0.059	44.15	5.94	0.24	7.51	3.40	547.60	964.32
Goodenough Island: Goodenough Dome	E200566	Grt, Di–Aug, Bt,	z1	332.73	0.00045	0.33	0.0028	4.59	0.046	4.47	2.87	0.0094	2.87	0.13	-0.32	107.76
PNG10-035a, eclogite	N8968671	Qz, Rt	z2	222.77	0.00044	0.51	0.0020	12.16	0.033	11.98	2.84	0.014	2.01	0.24	-913.63	348.42
		(Amp, Pl, Zrn)	z4	105.46	0.00041	1.12	0.0027	14.73	0.048	14.36	2.65	0.030	2.76	0.41	96.89	339.87
			z5	65.28	0.00044	1.92	0.0031	24.62	0.050	24.08	2.86	0.055	3.13	0.77	212.08	557.98
			z6	193.10	0.00044	0.53	0.0028	7.47	0.047	7.29	2.85	0.015	2.88	0.21	22.68	175.03
			z7	65.11	0.00044	1.92	0.0029	26.10	0.048	25.54	2.86	0.055	2.97	0.77	92.96	605.02
			z8	52.43	0.00045	2.65	0.0031	34.88	0.050	34.07	2.87	0.076	3.10	1.08	183.59	793.55
			z9	882.73	0.00044	0.24	0.0028	1.70	0.046	1.68	2.86	0.0070	2.86	0.049	0.0072	40.47
			z10	1648.73	0.00044	0.12	0.0029	0.80	0.047	0.79	2.86	0.0034	2.90	0.023	38.86	18.92
			z11-1	29.48	0.00044	8.10	0.0030	115.11	0.049	112.26	2.83	0.23	3.03	3.49	167.63	2622.41
			z11-2	54.35	0.00044	2.53	0.0028	37.77	0.046	36.89	2.85	0.072	2.83	1.07	-14.08	891.62
			z12-3	41.58	0.00045	3.86	0.0032	48.32	0.052	47.19	2.87	0.11	3.23	1.56	279.91	1080.12
			z12-4	116.38	0.00045	0.92	0.0030	12.37	0.05	12.10	2.89	0.027	3.04	0.38	120.16	285.12
PNG12-82a, eclogite cobble	E191019	Grt, Di–Aug, Bt,	z2	133.99	0.00042	0.91	0.0025	12.47	0.044	12.18	2.73	0.025	2.58	0.32	-139.18	301.50
	N8960735	Qz, Rt	z4	61.40	0.00041	2.1	0.0022	36.14	0.039	35.42	2.66	0.057	2.27	0.82	-397.86	923.42
		(Amp, Pl, Zrn)	z5	63.76	0.00041	2.2	0.0023	36.10	0.041	35.16	2.62	0.057	2.36	0.85	-263.88	892.14
			z9	38.87	0.00043	4.3	0.0028	60.48	0.047	59.26	2.77	0.12	2.80	1.69	24.30	1421.85
			z10	50.34	0.00043	2.8	0.0032	32.75	0.055	32.00	2.75	0.076	3.27	1.07	410.43	715.63
			z11	42.03	0.00042	3.8	0.0029	49.08	0.051	47.95	2.70	0.10	2.98	1.46	240.01	1105.40
			z12	39.93	0.00042	4.2	0.0029	54.41	0.050	53.19	2.72	0.11	2.98	1.62	213.08	1232.35
			z13	119.78	0.00042	0.95	0.0028	12.31	0.048	12.023	2.74	0.026	2.84	0.35	88.07	285.05
			z14	90.23	0.00043	1.3	0.0028	17.61	0.047	17.24	2.78	0.036	2.85	0.50	63.38	410.58
			z15	30.97	0.00043	7.0	0.0032	83.11	0.055	81.18	2.76	0.19	3.28	2.72	406.76	1816.88

[a] All grid references (in meters) refer to Transverse Mercator Projection, Australian Geodetic Datum 1966, UTM zone 56L.

[b] inferred peak mineral assemblage with retrograde assemblage in parenthesis: Aug = augite, Amp = amphibole, Ap = apatite, Bt = biotite, Cal = calcite, Dol = dolomite, Grt = garnet, Ms = muscovite, Omp = omphacite, Ph = phengite, Pl = plagioclase, Qz = quartz, Rt = rutile, Zrn = zircon. Abbreviations after

[c] Corrected for initial Th/U disequilibrium using radiogenic 208Pb and Th/U[magma] = 2.8

[d] Isotopic dates calculated using the decay constants λ238 = 1.55125E-10 and λ235 = 9.8485E-10 (Jaffey et al. 1971).

[e] Th contents calculated from radiogenic 208Pb and the 207Pb/206Pb date of the sample, assuming concordance between U-Th and Pb systems.

[f] Total mass of radiogenic Pb.

[g] Total mass of common Pb.

[h] Ratio of radiogenic Pb (including 208Pb) to common Pb.

[i] Measured ratio corrected for fractionation and spike contribution only.

[j] Measured ratios corrected for fractionation, tracer and blank.

Correlation Coefficient	Composition			
$^{206}Pb/^{238}U$<Th>-$^{207}Pb/^{235}U$ corr. coeff.[j]	Pb*/Pbc [h]	Pb* (pg) [f]	Pbc (pg) [g]	Th/U [e]
0.34	2.93	3.29	1.12	0.53
0.36	9.04	3.17	0.35	0.49
0.31	12.85	4.45	0.35	0.59
0.36	10.12	2.36	0.23	0.46
0.34	14.49	3.94	0.27	0.38
0.37	15.79	3.98	0.25	0.45
0.35	8.17	5.43	0.66	0.59
0.34	16.22	5.01	0.31	0.66
0.41	42.96	9.51	0.22	0.63
0.52	92.42	20.00	0.22	0.44
0.32	17.18	9.00	0.52	0.41
0.34	17.56	6.79	0.39	0.39
0.34	17.13	4.33	0.25	0.70
0.38	8.37	4.05	0.48	0.41
0.35	3.50	2.10	0.60	0.47
0.34	12.86	3.83	0.30	0.58
0.34	2.12	1.37	0.65	0.34
0.40	17.37	4.78	0.28	0.46
0.53	12.23	3.72	0.30	0.37
0.38	0.60	0.21	0.35	0.41
0.35	2.70	0.70	0.26	0.47
0.38	0.61	0.16	0.25	0.32
0.38	3.73	0.77	0.21	0.48
0.39	0.51	0.26	0.51	0.43
0.41	1.07	0.44	0.41	0.49
0.36	3.32	1.92	0.58	0.49
0.33	0.45	0.35	0.76	0.57
0.35	0.20	0.08	0.38	0.50
0.34	0.77	0.46	0.61	0.46
0.36	2.58	0.69	0.27	0.52
0.34	1.25	0.57	0.46	0.43
0.34	1.16	0.50	0.43	0.48
0.34	1.10	0.45	0.41	0.27
0.35	4.04	3.70	0.92	0.34
0.46	2.98	0.71	0.24	0.41
0.41	3.62	1.84	0.51	0.30
0.45	3.54	0.94	0.26	0.30
0.35	0.80	1.18	1.49	0.37
0.36	0.79	1.11	1.40	0.24
0.37	0.95	0.95	1.00	0.37
0.35	1.03	0.34	0.33	0.25
0.36	0.37	0.12	0.31	0.14
0.34	1.17	0.42	0.36	0.34
0.35	2.23	0.63	0.28	0.32
0.34	2.36	0.85	0.36	0.35
0.35	0.62	0.30	0.48	0.41
0.35	3.60	1.14	0.32	0.37
0.36	3.20	0.81	0.25	0.49
0.37	2.51	0.62	0.25	0.46
0.34	2.19	0.63	0.29	0.28

0.38	0.33	0.14	0.43	0.06
0.34	0.30	0.17	0.56	0.10
0.41	0.61	0.16	0.26	0.04
0.43	0.21	0.06	0.30	-0.08
0.35	0.18	0.06	0.33	0.24
0.36	0.33	0.08	0.24	0.18
0.37	0.26	0.09	0.33	0.12
0.35	0.25	0.06	0.23	0.14
0.36	0.52	0.12	0.23	0.18
0.36	0.18	0.06	0.31	0.18
0.35	0.24	0.06	0.24	0.20
0.36	0.35	0.06	0.18	0.14
0.41	4.71	1.33	0.28	0.09
0.41	2.89	1.26	0.44	-0.06
0.41	1.51	0.54	0.36	0.59
0.34	0.79	0.23	0.29	0.46
0.38	2.59	1.04	0.40	0.05
0.35	0.75	0.32	0.42	0.29
0.37	0.54	0.24	0.45	0.26
0.19	12.89	5.17	0.40	0.08
0.26	25.11	7.86	0.31	0.18
0.41	0.17	0.05	0.31	0.08
0.40	0.54	0.45	0.84	0.06
0.35	0.37	0.09	0.25	0.28
0.35	1.50	0.39	0.26	0.15
0.41	2.08	0.33	0.16	0.74
0.39	0.68	0.16	0.24	0.27
0.48	0.66	0.13	0.19	-0.01
0.34	0.35	0.16	0.44	0.50
0.34	0.54	0.26	0.48	0.48
0.36	0.38	0.27	0.70	0.29
0.36	0.37	0.16	0.43	0.49
0.37	1.67	0.80	0.48	0.39
0.35	1.16	0.48	0.41	0.33
0.34	0.24	0.22	0.91	0.82

Whitney and Evans, 2010

Table 2

Zircon U-Th-Pb LA-ICP-MS isotopic data for (U)HP eclogites from the D'Entrecasteaux Islands

	Isotopic Ratios										
	$^{207}Pb/^{235}U$	±2σ abs	$^{206}Pb/^{238}U$	±2σ abs	Error Correlation	$^{238}U/^{206}Pb$	±2σ abs	$^{207}Pb/^{206}Pb$	±2σ abs	Error Correlation	$^{208}Pb/^{232}Th$
LA-ICP-MS results for Fergusson and Goodenough Islands eclogite dated by ID-TIMS											
Sample, Laser spot number, ID–TIMS zircon fraction											
Fergusson Island: Oitabu Dome, PNG12-95a, eclogite float											
PNG12-95a_1_z14	0.0053	0.00044	0.00071	0.000018	-0.16	1402.53	34.66	0.055	0.0052	0.348	0.00026
PNG12-95a_2_z14	0.0055	0.00037	0.00069	0.000017	-0.04	1449.28	36.57	0.057	0.0038	0.328	0.00026
PNG12-95a_3_z14	0.0052	0.00053	0.00070	0.000017	0.07	1432.67	34.26	0.053	0.0056	0.124	0.00025
PNG12-95a_4_z15	0.0048	0.00021	0.00071	0.000013	0.22	1409.84	25.65	0.050	0.0020	-0.025	0.00023
PNG12-95a_17_z16	0.0054	0.00032	0.00070	0.000012	-0.07	1421.87	25.05	0.056	0.0034	0.227	0.00023
PNG12-95a_18_z16	0.0048	0.00028	0.00069	0.000013	-0.06	1442.38	27.68	0.050	0.0029	0.317	0.00022
Fergusson Island: Mailolo Dome, PNG09-039b iv, eclogite float											
PNG09-039b_3_z16	0.013	0.0019	0.00074	0.000028	0.60	1358.70	53.85	0.13	0.019	-0.197	0.00076
PNG09-039b_4_z16	0.0040	0.00069	0.00066	0.000022	0.05	1519.76	53.59	0.044	0.0075	0.097	0.00025
PNG09-039b_5_z16	0.0055	0.00094	0.00066	0.000023	0.07	1522.07	55.85	0.063	0.011	0.254	0.00026
PNG09-039b_8_z17	0.0049	0.00092	0.00067	0.000020	0.00	1503.76	48.53	0.051	0.010	0.137	0.00023
PNG09-039b_9_z17	0.0045	0.00082	0.00067	0.000018	0.31	1497.01	44.22	0.050	0.0089	-0.066	0.00032
PNG09-039b_12_z18	0.0042	0.00049	0.00067	0.000013	-0.16	1497.01	33.35	0.046	0.0055	0.301	0.00023
PNG09-039b_17_z19	0.0067	0.00083	0.00067	0.000018	0.05	1503.76	44.57	0.071	0.0089	0.130	0.00026
PNG09-039b_18_z19	0.0045	0.00077	0.00066	0.000016	0.15	1519.76	41.47	0.048	0.0081	-0.047	0.00022
PNG09-039b_24_z20	0.0046	0.0012	0.00065	0.000027	0.16	1536.10	65.53	0.053	0.014	-0.059	0.00026
PNG09-039b_26_z21	0.0047	0.00045	0.00066	0.000014	-0.09	1510.57	35.54	0.053	0.0056	0.341	0.00022
PNG09-039b_28_z22	0.0059	0.00089	0.00068	0.000032	-0.01	1481.48	71.58	0.064	0.010	0.325	0.00028
PNG09-039b_29_z22	0.0060	0.00078	0.00067	0.000025	0.04	1501.50	58.61	0.062	0.0088	0.186	0.00027
Fergusson Island: Mailolo Dome, PNG09-041c, eclogite											
PNG09-041c_3_z1	0.0058	0.0031	0.00073	0.000034	-0.08	1369.86	65.25	0.059	0.032	0.100	0.00033
PNG09-041c_4_z2	0.012	0.0056	0.00078	0.000066	0.06	1278.77	109.62	0.119	0.055	0.331	0.00064
PNG09-041c_5_z2	0.0045	0.0020	0.00071	0.000030	-0.09	1402.53	60.80	0.043	0.020	0.150	0.00036
PNG09-041c_6_z3	0.0059	0.0053	0.00083	0.000068	0.33	1209.19	99.63	0.053	0.044	0.139	0.00054
PNG09-041c_7_z3	0.0023	0.0034	0.00067	0.000058	-0.15	1488.10	130.36	0.023	0.033	0.480	0.00030
PNG09-041c_8_z4	0.0058	0.0032	0.00075	0.000063	0.34	1328.02	112.88	0.063	0.035	-0.386	0.00038
PNG09-041c_9_z5	0.0053	0.0014	0.00072	0.000030	0.11	1386.96	59.54	0.051	0.015	0.124	0.00027
PNG09-041c_17_z6	0.011	0.0040	0.00082	0.000063	0.35	1223.99	94.68	0.11	0.040	-0.194	0.00061
PNG09-041c_23_z7	0.0053	0.0016	0.00075	0.000027	-0.24	1329.79	48.50	0.053	0.016	0.373	0.00031
PNG09-041c_26_z8	0.0052	0.0029	0.00077	0.000038	-0.05	1305.48	64.40	0.054	0.029	0.172	0.00035
PNG09-041c_28_z9	0.0055	0.0007	0.00073	0.000017	-0.09	1375.52	32.10	0.055	0.0072	0.268	0.00025
PNG09-041c_42_z10	0.0061	0.0020	0.00071	0.000040	-0.04	1412.43	80.64	0.059	0.022	0.087	0.00027
PNG09-041c_44_z11	0.0078	0.0014	0.00073	0.000029	-0.20	1375.52	55.09	0.078	0.015	0.453	0.00031
PNG09-041c_45_z11	0.0090	0.010	0.00080	0.000085	0.29	1251.56	132.91	0.10	0.11	-0.096	-0.00038
Goodenough Island: Goodenough Dome, PNG10-035a, eclogite											
PNG10-035a_1_z11	0.0060	0.0008	0.00048	0.000013	0.69	2070.39	56.46	0.088	0.010	-0.496	0.00066
PNG10-035a_2_z11	0.0035	0.0004	0.00044	0.000013	0.03	2293.58	67.32	0.058	0.0069	0.142	0.00021
PNG10-035a_3_z12	0.0106	0.0034	0.00054	0.000052	0.23	1862.20	179.05	0.14	0.051	0.175	0.0011

PNG10-035a_4_z12	0.0140	0.0019	0.00049	0.000021	0.32	2061.86	90.48	0.20	0.025	0.102	0.0013
LA-ICP-MS results for Fergusson and Goodenough Islands eclogite not dated by ID-TIMS											
Fergusson Island: Mailolo Dome, PNG09-039b iv, eclogite float											
Sample,z, LA-ICP-MS fraction, Laser spot number											
PNG09-039b_1_1	0.0057	0.0010	0.00066	0.000020	-0.14	1510.57	48.92	0.063	0.011	0.33	0.00028
PNG09-039b_1_2	0.0051	0.00085	0.00067	0.000023	0.18	1485.88	53.44	0.055	0.0090	-0.02	0.00033
PNG09-039b_2_6	0.0076	0.0017	0.00072	0.000026	-0.17	1383.13	52.13	0.076	0.018	0.42	0.00042
PNG09-039b_2_7	0.0075	0.0019	0.00068	0.000030	-0.05	1470.59	66.48	0.081	0.021	0.40	0.00031
PNG09-039b_4_10	0.0052	0.0019	0.00065	0.000042	0.01	1550.39	103.60	0.058	0.023	0.17	0.00022
PNG09-039b_4_11	0.014	0.0018	0.00075	0.000029	0.64	1336.90	53.91	0.13	0.013	-0.35	0.00073
PNG09-039b_5_13	0.0078	0.0014	0.00067	0.000031	0.11	1488.10	70.08	0.085	0.014	0.01	0.00025
PNG09-039b_6_14	0.013	0.0023	0.00074	0.000026	-0.04	1351.35	49.95	0.12	0.022	0.26	0.00084
PNG09_039b_7_15	0.0080	0.0016	0.00071	0.000033	0.12	1402.53	66.37	0.078	0.015	0.04	0.00038
PNG09-039b_7_16	0.0049	0.00042	0.00065	0.000018	0.07	1543.21	46.64	0.056	0.0050	0.16	0.00026
PNG09_039b_9_19	0.0040	0.0010	0.00065	0.000022	0.05	1536.10	54.65	0.044	0.011	0.15	0.00028
PNG09-039b_9_20	0.0052	0.00053	0.00067	0.000019	0.21	1501.50	46.41	0.056	0.0059	0.06	0.00024
PNG09-039b_10_21	0.0070	0.0014	0.00067	0.000036	-0.01	1494.77	81.35	0.078	0.0170	0.24	0.00025
PNG09-039b_10_22	0.0051	0.00040	0.00066	0.000017	0.05	1517.45	43.31	0.055	0.0043	0.24	0.00022
PNG09-039b_11_23	0.0050	0.00078	0.00068	0.000021	-0.19	1468.43	48.43	0.055	0.0090	0.36	0.00024
PNG09-039b_12_25	0.0052	0.0016	0.00065	0.000032	0.00	1536.10	76.69	0.062	0.018	0.12	0.00031
PNG09-039b_13_27	0.0053	0.00087	0.00066	0.000021	-0.08	1515.15	51.23	0.061	0.010	0.25	0.00027
PNG09-039b_15_30	0.0088	0.0025	0.00068	0.000034	0.14	1468.43	74.49	0.094	0.027	0.04	0.00028
PNG09-039b_16_31	0.0099	0.0024	0.00072	0.000032	-0.12	1386.96	63.16	0.097	0.025	0.30	0.00029
PNG09-039b_16_32	0.0043	0.0012	0.00064	0.000027	0.31	1562.50	67.67	0.044	0.011	-0.13	0.00028
PNG09-039b_17_33	0.0019	0.0012	0.00067	0.000028	-0.11	1494.77	64.36	0.021	0.013	0.13	0.00027
PNG09-039b_17_34	0.0069	0.00092	0.00067	0.000023	0.09	1485.88	53.44	0.074	0.010	0.11	0.00031
PNG09-039b_18_35	0.011	0.0014	0.00074	0.000027	0.50	1344.09	51.12	0.099	0.012	-0.18	0.00044
PNG09-039b_18_36	0.0052	0.0029	0.00069	0.000043	-0.07	1451.38	91.11	0.063	0.033	0.36	0.00056
PNG09-039b_19_37	0.0048	0.0015	0.00066	0.000031	-0.06	1524.39	73.37	0.052	0.016	0.19	0.00022
PNG09-039b_19_38	0.0042	0.00062	0.00063	0.000023	-0.05	1577.29	59.63	0.050	0.0077	0.28	0.00020
PNG09-039b_20_39	0.0072	0.0016	0.00066	0.000024	-0.04	1508.30	57.01	0.078	0.019	0.28	0.00034
PNG09-039b_20_40	0.0046	0.00085	0.00067	0.000018	0.10	1497.01	44.22	0.050	0.0094	0.07	0.00022
PNG09-039b_21_41	0.0060	0.0021	0.00068	0.000030	0.07	1474.93	66.85	0.066	0.025	0.06	0.00029
PNG09-039b_21_42	0.0044	0.0013	0.00069	0.000036	0.04	1440.92	75.82	0.047	0.015	0.11	0.00025
PNG09-039b_22_43	0.0046	0.0013	0.00067	0.000027	0.12	1490.31	61.92	0.053	0.015	-0.03	0.00040
PNG09-039b_23_44	0.0048	0.00051	0.00067	0.000018	0.25	1485.88	43.65	0.053	0.0059	0.01	0.00022
PNG09-039b_23_45	0.0062	0.0011	0.00066	0.000028	-0.09	1508.30	65.46	0.069	0.013	0.31	0.00026
PNG09-039b_24_46	0.0084	0.0010	0.00070	0.000019	0.22	1434.72	42.85	0.087	0.011	0.00	0.00040
PNG09-039b_24_47	0.0082	0.0022	0.00071	0.000036	0.16	1402.53	71.99	0.081	0.022	0.05	0.00063
PNG09-039b_25_48	0.0053	0.0011	0.00071	0.000023	0.18	1416.43	48.99	0.054	0.011	-0.06	0.00034
PNG09-039b_25_49	0.0056	0.00043	0.00066	0.000019	0.36	1515.15	47.16	0.062	0.0049	-0.09	0.00022
Fergusson Island: Mailolo Dome, PNG09-041c, eclogite											
PNG09-041c_1_1	0.0092	0.0036	0.00076	0.000059	-0.01	1317.52	104.31	0.10	0.034	0.17	0.00040
PNG09-041c_1_2	0.0038	0.0032	0.00067	0.000046	-0.06	1488.10	104.28	0.052	0.036	0.15	0.00031
PNG09-041c_2_10	0.054	0.0035	0.0057	0.00015	0.66	176.68	5.11	0.069	0.004	-0.34	0.0031
PNG09-041c_2_11	0.012	0.0032	0.00070	0.000065	0.14	1428.57	134.37	0.12	0.035	0.34	0.00042

PNG09-041c_3_12	0.0054	0.0032	0.00080	0.000044	-0.09	1253.13	70.09	0.066	0.032	0.11	0.00037
PNG09-041c_3_13	0.014	0.0051	0.00086	0.000052	-0.01	1164.14	71.29	0.13	0.043	0.12	0.0013
PNG09-041c_4_14	0.0053	0.0012	0.00075	0.000026	0.00	1340.48	49.22	0.051	0.012	0.10	0.00029
PNG09-041c_4_15	0.0054	0.0012	0.00073	0.000031	-0.10	1379.31	60.71	0.054	0.012	0.29	0.00030
PNG09-041c_5_16	0.0079	0.0023	0.00077	0.000050	-0.34	1300.39	85.13	0.065	0.023	0.63	0.00035
PNG09-041c_6_18	0.0094	0.0025	0.00078	0.000044	-0.03	1285.35	72.02	0.088	0.021	0.27	0.00039
PNG09-041c_7_19	0.0081	0.0013	0.00074	0.000026	-0.05	1356.85	48.65	0.081	0.014	0.24	0.00033
PNG09-041c_7_20	0.0059	0.0030	0.00074	0.000034	0.20	1360.54	62.65	0.057	0.028	-0.01	0.00043
PNG09-041c_8_21	0.011	0.0030	0.00073	0.000040	0.14	1367.99	74.01	0.10	0.029	0.01	0.00040
PNG09-041c_8_22	0.017	0.011	0.00073	0.00010	0.24	1369.86	188.77	0.15	0.13	-0.04	-0.00026
PNG09-041c_9_24	0.0053	0.0024	0.00075	0.000041	-0.04	1329.79	71.79	0.058	0.026	-0.03	0.00045
PNG09-041c_9_25	0.017	0.0062	0.00076	0.000069	0.22	1317.52	119.68	0.14	0.055	0.05	0.00078
PNG09041c_10_27	0.0064	0.0016	0.00071	0.000028	0.04	1410.44	55.88	0.064	0.016	0.10	0.00025
PNG09-041c_11_29	0.0065	0.0016	0.00073	0.000027	-0.14	1369.86	51.22	0.066	0.017	0.28	0.00025
PNG09-041c_12_30	0.0066	0.0014	0.00072	0.000025	-0.06	1390.82	49.14	0.071	0.015	0.23	0.00026
PNG09-041c_12_31	0.0076	0.0012	0.00075	0.000020	0.03	1326.26	34.46	0.074	0.012	0.15	0.00034
PNG09-041c_13_32	0.011	0.0037	0.00072	0.000046	0.17	1385.04	88.79	0.11	0.040	-0.05	0.00042
PNG09-041c_14_33	0.0086	0.0030	0.00077	0.000042	0.00	1297.02	70.05	0.083	0.029	0.15	0.00031
PNG09-041c_15_34	0.0083	0.0018	0.00074	0.000021	-0.19	1349.53	38.53	0.080	0.018	0.30	0.00040
PNG09-041c_15_35	0.012	0.0016	0.00078	0.000020	0.36	1290.32	32.93	0.11	0.013	-0.20	0.00045
PNG09-041c_16_36	0.0048	0.00055	0.00071	0.000018	0.02	1410.44	36.58	0.048	0.0056	0.16	0.00024
PNG09-041c_16_37	0.026	0.0048	0.00091	0.000046	0.04	1103.75	56.10	0.22	0.044	0.24	0.00089
PNG09-041c_17_38	0.020	0.0060	0.00085	0.000067	0.44	1175.09	92.82	0.16	0.049	-0.16	0.0017
PNG09-041c_17_39	0.020	0.0029	0.00081	0.000043	0.07	1228.50	64.56	0.17	0.026	0.39	0.00095
PNG09-041c_18_40	0.0042	0.0035	0.00077	0.000076	-0.32	1297.02	127.66	0.037	0.039	0.25	0.00071
PNG09-041c_19_41	0.015	0.0048	0.00072	0.000052	-0.16	1383.13	99.75	0.14	0.059	0.75	0.00031
PNG09-041c_20_43	0.012	0.0040	0.00078	0.000056	-0.13	1282.05	92.42	0.12	0.040	0.38	0.00039
Goodenough Island: Goodenough Dome, PNG10-035a, eclogite											
PNG10-035a_1_5	0.0038	0.00061	0.00044	0.000014	0.24	2262.44	70.18	0.062	0.010	-0.05	0.00023
PNG10-035a_1_6	0.0045	0.00043	0.00044	0.000011	0.08	2295.68	59.90	0.077	0.0077	0.10	0.00055
Fergusson Island: Oitabu Dome, PNG12-95a, eclogite float											
PNG12-95a_1_5	0.0045	0.00038	0.00070	0.000014	0.17	1423.69	27.44	0.046	0.0038	-0.01	0.00041
PNG12-95a_1_7	0.0049	0.00036	0.00071	0.000014	0.08	1408.65	28.58	0.050	0.0037	0.08	0.00090
PNG12-95a_2_8	0.0052	0.00022	0.00070	0.000013	-0.20	1421.67	25.48	0.053	0.0025	0.40	0.00026
PNG12-95a_2_9	0.0045	0.00020	0.00069	0.000012	0.00	1447.18	25.73	0.047	0.0021	0.21	0.00023
PNG12-95a_2_10	0.0048	0.00025	0.00071	0.000012	-0.12	1412.83	23.96	0.049	0.0025	0.26	0.00023
PNG12-95a_2_11	0.0049	0.00029	0.00070	0.000016	0.25	1422.48	32.32	0.050	0.0029	0.00	0.00033
PNG12-95a_2_12	0.0048	0.00030	0.00070	0.000014	-0.04	1431.43	27.78	0.050	0.0032	0.23	0.00023
PNG12-95a_2_13	0.0052	0.00034	0.00073	0.000016	0.12	1371.74	29.19	0.050	0.0033	0.13	0.00025
PNG12-95a_2_14	0.0047	0.00030	0.00071	0.000014	-0.06	1415.83	27.61	0.048	0.0033	0.28	0.00025
PNG12-95a_3_15	0.0053	0.00054	0.00070	0.000016	-0.03	1432.67	32.69	0.055	0.0055	0.20	0.00045
PNG12-95a_3_16	0.0050	0.00025	0.00071	0.000012	-0.19	1419.04	24.88	0.051	0.0027	0.37	0.00023
PNG12-95a_4_19	0.0095	0.00094	0.00075	0.000016	0.73	1338.69	28.14	0.091	0.0083	-0.62	0.00040
PNG12-95a_4_20	0.0053	0.00022	0.00073	0.000012	0.34	1377.22	23.32	0.053	0.0021	-0.15	0.00024

Composition				Dates (Ma)						ID-TIMS Dates (Ma)		
±2σ abs	Approx. U (ppm)	Approx. Th (ppm)	Th/U	$^{206}Pb/^{238}U$ date (Ma)	±2σ abs	$^{207}Pb/^{235}U$ date (Ma)	±2σ abs	$^{207}Pb/^{206}Pb$ date (Ma)	±2σ abs	Fraction (Table 1)	$^{206}Pb/^{238}U$ date <Th>	±2σ abs
0.000060	326.00	110.00	0.34	4.59	0.11	5.32	0.43	410.00	181.00	z14-1-2	4.62	0.014
0.000061	303.00	98.90	0.33	4.44	0.11	5.52	0.37	440.00	142.00			
0.000057	338.70	120.20	0.35	4.50	0.11	5.29	0.52	330.00	201.00	z14-3	4.62	0.024
0.000053	1379.00	1279.00	0.93	4.57	0.080	4.87	0.22	170.00	79.00	z15-4	4.63	0.018
0.000054	814.00	321.40	0.39	4.53	0.080	5.51	0.31	420.00	132.00	z16-17	4.61	0.034
0.000052	621.00	344.90	0.56	4.47	0.090	4.87	0.27	190.00	120.00	z16-18	4.62	0.014
										z16-frag	4.62	0.014
0.00019	155.30	45.90	0.30	4.74	0.18	12.80	2.00	1930.00	300.10	z16-3-4	4.35	0.048
0.000054	223.10	63.60	0.29	4.24	0.15	4.05	0.70	-30.00	-270.00			
0.000066	146.30	37.40	0.26	4.23	0.15	5.58	0.95	730.00	301.42	z16-5	4.34	0.13
0.000049	190.10	66.70	0.35	4.28	0.13	4.92	0.92	220.00	320.12	z17-8	4.38	0.044
0.000077	179.90	43.20	0.24	4.31	0.12	4.54	0.82	180.00	330.08	z17-9	4.36	0.024
0.000048	381.40	143.50	0.38	4.31	0.080	4.28	0.50	10.00	210.00	z18-12	4.36	0.022
0.000053	193.10	102.10	0.53	4.29	0.12	6.72	0.84	890.00	262.43	z19-17	4.36	0.085
0.000047	291.40	127.20	0.44	4.24	0.11	4.60	0.77	150.00	300.06	z19-18	4.36	0.016
0.000066	114.10	41.00	0.36	4.19	0.18	4.70	1.20	280.00	420.15	z20-24	4.34	0.019
0.000044	552.70	378.60	0.69	4.26	0.090	4.76	0.45	280.00	210.30	z21-26	4.35	0.023
0.000061	134.00	49.70	0.37	4.35	0.20	5.95	0.90	580.00	330.81	z22-28-29	4.33	0.023
0.000069	111.60	27.80	0.25	4.29	0.17	6.02	0.78	720.00	281.48			
0.00010	45.50	18.60	0.41	4.70	0.22	5.90	3.20	-200.00	-840.04	z1-3	4.57	0.12
0.00037	21.00	8.50	0.41	5.04	0.43	12.40	5.60	1100.00	1000.97	z2-4	4.64	0.028
0.000082	76.80	35.60	0.46	4.60	0.19	4.60	2.00	-60.00	-640.00	z2-5	4.54	0.11
0.00018	25.70	11.10	0.43	5.33	0.43	5.90	5.30	-500.00	-1300.15	z3-6	4.62	0.021
0.000081	34.10	23.10	0.68	4.33	0.37	2.30	3.40	-900.00	-1100.59	z3-7	4.62	0.14
0.00013	32.90	15.50	0.47	4.85	0.40	5.80	3.20	120.00	920.01	z4-8	4.61	0.070
0.000065	84.60	46.00	0.54	4.65	0.20	5.30	1.50	100.00	500.02	z5-9	4.61	0.024
0.00018	30.60	11.30	0.37	5.27	0.40	11.20	4.00	730.00	760.56	z6-17	4.65	0.16
0.000081	60.30	28.50	0.47	4.84	0.18	5.40	1.60	180.00	530.00	z7-23	4.51	0.35
0.00010	37.80	16.40	0.43	4.94	0.24	5.30	2.90	50.00	780.00	z8-26	5.41	0.11
0.000059	202.20	148.20	0.73	4.69	0.11	5.56	0.69	310.00	250.00	z9-28	4.64	0.030
0.000088	44.80	17.30	0.39	4.56	0.26	6.20	2.10	340.00	660.00	z10-42	4.65	0.057
0.000078	87.60	40.80	0.47	4.68	0.18	7.90	1.50	890.00	393.00	z11-44-45	4.62	0.062
-0.00065	18.00	4.80	0.27	5.15	0.55	9.00	10.00	-1200.00	-2301.00			
0.00019	373.10	36.60	0.10	3.12	0.080	6.08	0.75	1360.00	230.00	z11-1	2.83	0.23
0.000058	329.00	40.40	0.12	2.81	0.080	3.52	0.41	460.00	231.00	z11-2	2.85	0.072
0.00065	29.60	5.60	0.19	3.46	0.33	10.70	3.40	1630.00	834.00	z12-3	2.87	0.11

0.00037	83.00	14.20	0.17	3.13	0.14	14.10	1.91	2650.00	310.00	z12-4	2.89	0.027
0.000064	145.10	33.30	0.23	4.27	0.13	5.70	1.00	520.00	350.62			
0.000077	165.90	39.20	0.24	4.33	0.15	5.18	0.86	290.00	290.23			
0.00010	114.40	39.20	0.34	4.66	0.17	7.60	1.70	850.00	441.31			
0.00011	68.00	14.30	0.21	4.38	0.19	7.60	1.90	1110.00	482.05			
0.000070	63.20	21.20	0.34	4.16	0.27	5.20	1.90	180.00	640.04			
0.00016	200.00	69.60	0.35	4.82	0.19	14.30	1.81	2200.00	191.43			
0.000067	88.80	28.70	0.32	4.33	0.20	7.90	1.40	1030.00	392.17			
0.00020	118.40	31.30	0.26	4.77	0.17	13.30	2.30	1950.00	339.09			
0.00011	89.40	18.60	0.21	4.60	0.21	8.10	1.60	1060.00	382.36			
0.000053	330.90	104.50	0.32	4.18	0.12	4.95	0.42	390.00	180.67			
0.000061	125.90	48.00	0.38	4.19	0.15	4.10	1.00	-90.00	-400.02			
0.000049	340.90	186.40	0.55	4.29	0.12	5.22	0.53	380.00	210.55			
0.000060	90.30	44.80	0.50	4.31	0.23	7.00	1.50	930.00	431.61			
0.000045	407.40	294.90	0.72	4.25	0.11	5.13	0.40	410.00	170.79			
0.000050	194.50	106.70	0.55	4.39	0.14	5.02	0.79	310.00	310.25			
0.000092	64.50	21.70	0.34	4.19	0.20	5.30	1.60	800.00	481.07			
0.000065	141.80	33.10	0.23	4.26	0.14	5.37	0.88	480.00	320.58			
0.000092	62.20	20.50	0.33	4.39	0.22	8.90	2.50	880.00	591.05			
0.000088	61.80	23.20	0.38	4.64	0.21	9.90	2.50	1330.00	522.71			
0.000066	97.00	38.70	0.40	4.12	0.17	4.40	1.20	120.00	420.03			
0.000065	96.40	38.00	0.39	4.31	0.18	1.90	1.20	-840.00	-501.13			
0.000068	137.80	59.30	0.43	4.34	0.15	6.93	0.93	970.00	272.77			
0.00011	144.50	61.90	0.43	4.79	0.18	10.60	1.40	1570.00	277.21			
0.00026	47.10	9.20	0.20	4.44	0.27	5.20	2.90	-220.00	-840.05			
0.000067	96.30	26.80	0.28	4.23	0.19	4.90	1.50	410.00	480.28			
0.000042	239.20	122.90	0.51	4.09	0.15	4.28	0.62	160.00	270.08			
0.000086	92.40	24.80	0.27	4.27	0.16	7.30	1.60	750.00	500.90			
0.000050	198.20	67.00	0.34	4.31	0.12	4.62	0.86	180.00	310.08			
0.000077	58.00	23.60	0.41	4.37	0.19	6.10	2.10	620.00	590.52			
0.000067	77.40	30.30	0.39	4.47	0.23	4.50	1.30	-40.00	-460.00			
0.000094	96.30	23.10	0.24	4.32	0.18	4.60	1.30	50.00	480.00			
0.000044	391.20	301.60	0.77	4.33	0.12	4.82	0.51	260.00	210.26			
0.000063	121.70	42.70	0.35	4.27	0.18	6.30	1.10	700.00	391.00			
0.000088	153.10	54.00	0.35	4.49	0.13	8.50	1.00	1350.00	226.53			
0.00016	59.00	17.50	0.30	4.60	0.22	8.20	2.30	840.00	561.01			
0.000082	141.60	43.80	0.31	4.55	0.15	5.40	1.10	380.00	340.34			
0.000044	396.30	293.50	0.74	4.25	0.13	5.67	0.44	680.00	162.30			
0.00012	39.80	12.90	0.32	4.89	0.38	9.30	3.70	960.00	760.97			
0.00011	44.80	19.20	0.43	4.33	0.30	3.80	3.20	-10.00	-920.00			
0.00066	222.60	73.70	0.33	36.40	1.00	53.00	3.34	880.00	115.49			
0.00013	36.20	21.50	0.59	4.51	0.42	12.00	3.20	1690.00	613.73			

0.00013	39.80	14.20	0.36	5.14	0.28	6.20	3.40	380.00	810.14
0.00049	27.60	8.80	0.32	5.54	0.33	14.30	5.00	750.00	860.52
0.00007	107.50	50.40	0.47	4.81	0.17	5.40	1.20	240.00	400.12
0.00007	93.10	42.80	0.46	4.67	0.21	5.50	1.20	310.00	410.19
0.00010	46.10	20.20	0.44	4.95	0.31	8.00	2.40	560.00	620.40
0.00011	36.40	15.00	0.41	5.01	0.28	9.50	2.50	970.00	532.00
0.00008	63.20	29.50	0.47	4.75	0.17	8.20	1.40	1050.00	364.00
0.00013	30.00	11.50	0.38	4.74	0.21	5.90	3.00	230.00	760.00
0.00016	31.50	9.90	0.31	4.71	0.25	11.10	3.00	1440.00	555.00
-0.00063	11.50	3.90	0.34	4.69	0.64	17.00	11.00	1600.00	1702.00
0.00014	29.70	13.40	0.45	4.85	0.26	5.30	2.40	10.00	680.00
0.00037	14.70	6.30	0.43	4.89	0.45	16.50	6.20	1420.00	963.00
0.00007	59.00	26.40	0.45	4.57	0.18	6.50	1.70	440.00	481.00
0.00007	80.00	32.80	0.41	4.71	0.17	6.50	1.70	530.00	481.00
0.00006	80.80	42.60	0.53	4.63	0.16	6.70	1.40	600.00	431.00
0.00008	126.60	75.80	0.60	4.86	0.12	7.70	1.20	940.00	304.00
0.00013	30.20	13.40	0.44	4.65	0.30	11.40	3.70	900.00	851.00
0.00011	36.70	15.20	0.41	4.97	0.27	8.70	3.00	990.00	602.00
0.00010	67.10	30.90	0.46	4.78	0.14	8.40	1.90	880.00	482.00
0.00011	115.10	68.40	0.59	4.99	0.13	12.20	1.60	1770.00	246.00
0.00006	224.90	180.30	0.80	4.57	0.12	4.83	0.55	170.00	210.00
0.00024	28.20	14.60	0.52	5.84	0.29	25.80	4.71	2720.00	413.00
0.00051	22.30	7.80	0.35	5.48	0.43	19.60	6.00	1920.00	756.00
0.00026	36.90	14.00	0.38	5.25	0.27	20.10	2.91	2590.00	290.00
0.00059	20.50	6.20	0.30	4.97	0.49	4.20	3.60	-800.00	-1101.00
0.00010	24.30	13.70	0.56	4.66	0.34	15.20	4.80	1630.00	963.00
0.00014	27.90	11.50	0.41	5.03	0.36	11.60	4.00	810.00	801.00
0.000062	261.40	42.10	0.16	2.85	0.09	3.86	0.62	600.00	311.00
0.00017	207.10	15.10	0.07	2.81	0.07	4.60	0.43	990.00	206.00
0.00011	492.50	24.40	0.05	4.53	0.09	4.57	0.37	30.00	150.00
0.00084	438.30	2.50	0.01	4.57	0.09	5.03	0.37	200.00	150.00
0.000060	1319.00	202.20	0.15	4.53	0.08	5.22	0.23	313.00	100.00
0.000054	1290.00	676.00	0.52	4.45	0.08	4.59	0.20	78.00	84.00
0.000053	1232.00	998.00	0.81	4.56	0.08	4.83	0.25	150.00	100.00
0.000085	610.00	27.10	0.04	4.53	0.10	4.95	0.28	200.00	120.00
0.000053	810.00	447.40	0.55	4.50	0.09	4.87	0.30	190.00	130.00
0.000059	481.40	238.50	0.50	4.70	0.10	5.28	0.34	250.00	131.00
0.000057	747.00	382.00	0.51	4.55	0.09	4.75	0.29	120.00	130.00
0.00048	284.80	0.70	0.00	4.50	0.10	5.32	0.54	360.00	191.00
0.000053	737.10	300.00	0.41	4.54	0.08	5.03	0.25	250.00	111.00
0.00010	530.70	273.30	0.51	4.81	0.10	9.60	0.93	1350.00	183.00
0.000055	1414.00	1397.00	0.99	4.68	0.08	5.36	0.21	300.00	81.00

Table 3

Zircon U-Pb ID-TIMS isotopic data for host gneiss and crystallized melt from Oiatabu Dome

				Isotopic Ratios							Dates (Ma)
Sample	location[a]	mineral assemblage[b]	Fraction	$^{206}Pb/^{204}Pb$ [i]	$^{206}Pb/^{238}U$ <Th> [j,c]	±2σ %	$^{207}Pb/^{235}U$ [j]	±2σ %	$^{207}Pb/^{206}Pb$ <Th> [j,c]	±2σ %	$^{206}Pb/^{238}U$ date <Th> [c]
Fergusson Island: Oiatabu Dome	E260115	Qz, Pl, Ms, Bt, Zrn	z1	247.20	0.0013	0.43	0.0084	5.51	0.048	5.36	8.11
PNG12-85a, host orthogneiss	N8951078		z2	210.04	0.0016	0.51	0.010	6.59	0.047	6.43	10.30
			z3	152.41	0.00086	0.69	0.0057	9.14	0.048	8.93	5.52
			z4	119.22	0.0015	0.93	0.010	11.26	0.052	11.00	9.47
			z5	414.87	0.0012	0.25	0.0078	3.20	0.048	3.12	7.61
			z6	448.61	0.00090	0.23	0.0060	3.10	0.048	3.04	5.77
			z8	478.93	0.0017	0.25	0.011	2.87	0.046	2.79	10.72
			z9	376.48	0.0015	0.28	0.010	3.51	0.049	3.42	9.55
			z10	461.19	0.0011	0.23	0.0071	3.05	0.046	2.98	7.20
			z11	10068.24	0.0028	0.07	0.020	0.16	0.052	0.14	18.15
			z12	485.22	0.0042	0.22	0.029	2.59	0.049	2.53	27.20
			z13	638.77	0.0019	0.19	0.013	2.12	0.048	2.07	12.45
			z14	800.28	0.0018	0.16	0.012	1.79	0.048	1.74	11.58
			z15	967.99	0.0013	0.13	0.0088	1.40	0.048	1.37	8.63
			z16	667.28	0.00242	0.17	0.016	2.10	0.047	2.03	15.60
			z17_rim	114.63	0.00080	0.97	0.0051	13.42	0.046	13.10	5.17
			z18_rim	129.81	0.00088	0.84	0.0058	11.34	0.048	11.07	5.66
			z19_rim	119.36	0.00086	0.93	0.0055	12.76	0.047	12.45	5.51
			z20_rim	101.40	0.00076	1.1	0.0048	15.65	0.046	15.30	4.87
			z21_rim	121.02	0.00070	0.93	0.0044	12.93	0.046	12.62	4.49
PNG12-87a, host orthogneiss	E259590	Qz, Pl, Bt, Ms, Zrn	z1	209.65	0.011	0.55	0.070	7.16	0.045	6.98	71.88
	N8951020		z2	166.61	0.013	0.69	0.088	9.53	0.049	9.25	83.58
			z3	100.98	0.012	1.2	0.092	14.14	0.054	13.73	79.64
			z4	92.97	0.012	1.4	0.089	16.01	0.052	15.58	79.21
			z5	55.62	0.013	2.6	0.068	42.59	0.038	41.77	83.26
			z6	234.30	0.010	0.51	0.078	5.63	0.055	5.45	66.34
			z7	181.33	0.011	1.2	0.061	15.95	0.039	15.35	72.84
			z8	49.31	0.008	3.3	0.041	58.52	0.036	57.26	53.00
PNG12-87b, granodiorite dike	E259590	Qz, Pl, Kfs, Ms, Zrn	z1	205.54	0.00046	0.48	0.0030	6.40	0.048	6.27	2.93
	N8951020		z2	204.32	0.00045	0.49	0.0036	5.51	0.057	5.37	2.93
			z3	2353.03	0.00046	0.08	0.0029	0.60	0.047	0.57	2.93
			z4	517.55	0.00046	0.19	0.0031	2.37	0.049	2.32	2.94
			z5	1002.48	0.00047	0.11	0.0033	1.19	0.051	1.16	3.01
			z6	40.38	0.00047	4.10	0.0040	43.06	0.061	41.85	3.01

			z7	64.24	0.00047	2.00	0.0035	24.24	0.054	23.59	3.02
PNG12-92a, mafic orthogneiss	E259570	Bt, Qz, Pl, Zrn	z1	574.09	0.014	0.20	0.094	2.44	0.048	2.37	89.94
	N8951010		z2	273.42	0.0088	0.41	0.058	5.24	0.048	5.09	56.41
			z3	325.01	0.012	0.34	0.081	4.12	0.049	4.01	77.25
			z4	131.38	0.012	0.86	0.091	10.08	0.054	9.82	79.00
			z7	88.45	0.012	1.5	0.073	21.53	0.043	20.99	78.51
PNG12-92b, granodiorite dike	E259570	Qz, Pl, Kfs, Ms, Zrn	z1	95.98	0.014	1.28	0.10	14.73	0.053	14.34	88.91
	N8951010		z2	82.53	0.00075	1.47	0.0048	19.89	0.047	19.44	4.81
			z3	85.50	0.00074	1.48	0.0049	20.60	0.048	20.01	4.79
			z4	44.34	0.00086	4.13	0.0058	67.09	0.049	64.84	5.56
			z5	447.85	0.00047	0.23	0.0030	3.04	0.046	2.98	3.02
			z6	978.16	0.00047	0.12	0.0030	1.57	0.046	1.53	3.04
			z8	58.45	0.00046	2.68	0.0029	41.39	0.045	39.99	2.97
			z9	1629.77	0.00047	0.080	0.0030	0.83	0.047	0.82	3.02
Goodenough Dome	E200566	Qz, Pl, Kfs, Ms, Zrn	z1	97.56	0.00041	1.22	0.0022	19.61	0.040	19.18	2.63
PNG10-035b, pegmatite	N8968671		z2	117.76	0.00038	0.99	0.0025	13.35	0.048	12.99	2.48
			z3	142.08	0.00040	0.82	0.0025	12.00	0.044	11.69	2.61
			z4	49.20	0.00040	2.89	0.0028	37.42	0.050	36.60	2.59
			z5	249.25	0.00039	0.42	0.0026	5.32	0.049	5.19	2.51
			z6	46.56	0.00041	3.21	0.0026	45.78	0.046	44.79	2.64
			z7	82.58	0.00041	1.40	0.0030	17.50	0.053	17.10	2.63
			z8	58.08	0.00040	2.24	0.0029	27.26	0.053	26.63	2.55
			z9	79.84	0.00041	1.52	0.0027	20.90	0.048	20.41	2.63
			z10	90.69	0.00041	1.27	0.0026	17.74	0.047	17.33	2.62

[a] outcrop locality (UTM)

[b] mineral assemblage: Aug = augite, Amp = amphibole, Ap = apatite, Bt = biotite, Cal = calcite, Dol = dolomite, Grt = garnet, Ms = muscovite, Omp = omphacite, Ph = phengite, Pl = plagioclase, Qz = quartz, Rt = rutile

[c] Corrected for initial Th/U disequilibrium using radiogenic 208Pb and Th/U[magma] = 3.5

[d] Isotopic dates calculated using the decay constants λ238 = 1.55125E-10 and λ235 = 9.8485E-10 (Jaffey et al. 1971).

[e] Th contents calculated from radiogenic 208Pb and the 207Pb/206Pb date of the sample, assuming concordance between U-Th and Pb systems.

[f] Total mass of radiogenic Pb.

[g] Total mass of common Pb.

[h] Ratio of radiogenic Pb (including 208Pb) to common Pb.

[i] Measured ratio corrected for fractionation and spike contribution only.

[j] Measured ratios corrected for fractionation, tracer and blank.

±2σ abs	$^{207}Pb/^{235}U$ date [d]	±2σ abs	$^{207}Pb/^{206}Pb$ date <Th> [c]	±2σ abs	Correlation Coefficient $^{206}Pb/^{238}U$<Th>-$^{207}Pb/^{235}U$ corr. coeff. [j]	Composition Pb*/Pbc [h]	Pb* (pg) [f]	Pbc (pg) [g]	Th/U [e]
0.035	8.47	0.46	110.34	126.56	0.38	3.61	1.52	0.42	0.26
0.052	10.53	0.69	62.62	153.28	0.34	3.03	1.59	0.52	0.27
0.038	5.78	0.53	112.47	210.83	0.34	1.97	0.91	0.46	0.01
0.088	10.54	1.18	263.74	252.56	0.33	1.63	3.41	2.09	0.33
0.019	7.89	0.25	92.72	73.95	0.36	6.13	1.58	0.26	0.19
0.014	6.02	0.19	106.67	71.82	0.29	6.45	0.96	0.15	0.09
0.027	10.75	0.31	17.80	67.11	0.33	7.31	1.34	0.18	0.29
0.027	10.18	0.36	161.86	80.06	0.34	5.78	0.82	0.14	0.34
0.016	7.21	0.22	12.79	71.61	0.38	6.85	0.96	0.14	0.20
0.013	20.38	0.03	291.62	3.35	0.52	170.64	28.57	0.17	0.52
0.059	28.80	0.74	163.95	59.18	0.34	8.57	5.22	0.61	0.84
0.023	12.81	0.27	79.83	49.12	0.33	9.93	1.55	0.16	0.32
0.019	11.94	0.21	84.86	41.19	0.43	12.62	1.64	0.13	0.35
0.011	8.90	0.12	80.72	32.49	0.35	14.98	2.62	0.17	0.26
0.027	15.79	0.33	45.16	48.61	0.40	11.04	3.90	0.35	0.54
0.050	5.21	0.70	22.08	314.54	0.36	1.41	0.31	0.22	0.02
0.048	5.85	0.66	87.84	262.57	0.36	1.64	0.35	0.22	0.02
0.051	5.57	0.71	31.47	298.38	0.37	1.46	0.29	0.20	-0.02
0.055	4.87	0.76	5.29	368.42	0.36	1.21	0.52	0.43	0.00
0.042	4.50	0.58	7.31	303.75	0.38	1.50	0.38	0.25	0.01
0.40	68.47	4.74	-49.04	169.72	0.37	3.29	0.89	0.27	0.59
0.57	85.39	7.81	136.38	217.43	0.43	2.67	0.53	0.20	0.76
0.97	89.72	12.14	366.74	309.48	0.37	1.50	0.29	0.19	0.77
1.11	86.49	13.27	292.27	355.87	0.35	1.26	0.25	0.20	0.49
2.17	67.02	27.62	-480.45	1107.47	0.34	0.67	0.20	0.29	0.77
0.34	76.42	4.15	404.39	122.11	0.39	3.63	0.48	0.13	0.48
0.90	60.01	9.29	-426.64	402.55	0.51	2.59	1.11	0.43	0.32
1.73	40.62	23.30	-641.91	1570.43	0.41	0.53	0.15	0.28	0.57
0.014	3.04	0.19	85.60	148.60	0.33	2.74	3.78	1.38	0.013
0.014	3.60	0.20	481.58	118.62	0.35	2.88	1.24	0.43	0.17
0.0023	2.99	0.018	48.65	13.54	0.45	34.00	15.54	0.46	-0.0024
0.0056	3.09	0.073	125.15	54.64	0.33	7.30	24.24	3.32	0.0064
0.0033	3.30	0.039	227.44	26.75	0.34	14.40	5.56	0.39	0.0010
0.12	4.00	1.72	652.05	898.27	0.36	0.34	0.15	0.42	0.16

0.060	3.54	0.86	371.87	531.09	0.38	0.67	0.09	0.14	-0.033
0.18	90.95	2.13	117.46	55.89	0.41	9.60	1.53	0.16	0.60
0.23	57.35	2.92	96.53	120.50	0.40	4.47	0.67	0.15	0.66
0.26	79.44	3.15	145.90	94.15	0.35	5.31	1.00	0.19	0.61
0.68	88.39	8.53	350.04	222.02	0.34	1.94	0.40	0.21	0.56
1.14	71.37	14.84	-161.81	522.02	0.40	1.14	0.19	0.17	0.40
1.13	97.62	13.71	316.06	326.21	0.34	1.37	0.25	0.18	0.66
0.071	4.89	0.97	44.18	464.73	0.35	1.19	0.23	0.19	0.87
0.071	4.95	1.02	82.74	474.89	0.44	1.14	0.19	0.17	0.53
0.23	5.84	3.91	124.12	1526.99	0.58	0.38	0.08	0.21	-0.042
0.0069	3.03	0.092	10.25	71.58	0.36	6.46	1.19	0.18	0.10
0.0037	3.04	0.048	1.48	36.84	0.43	14.33	2.52	0.18	0.08
0.080	2.92	1.21	-37.09	970.70	0.57	0.57	0.085	0.15	-0.077
0.0024	3.04	0.025	23.70	19.58	0.29	23.90	3.84	0.16	0.057
0.032	2.28	0.45	-359.60	496.24	0.41	1.28	0.44	0.34	0.35
0.024	2.57	0.34	86.45	308.13	0.42	1.48	0.53	0.36	0.05
0.021	2.52	0.30	-86.73	286.45	0.44	1.98	0.83	0.42	0.32
0.075	2.82	1.05	199.76	849.94	0.34	0.51	0.43	0.84	0.40
0.011	2.65	0.14	128.43	122.21	0.36	3.54	1.83	0.52	0.15
0.085	2.64	1.21	-3.69	1080.47	0.36	0.47	0.19	0.41	0.42
0.037	3.01	0.53	319.40	388.60	0.35	1.06	0.45	0.42	0.40
0.057	2.94	0.80	327.69	604.27	0.34	0.63	1.58	2.51	0.24
0.040	2.72	0.57	86.70	483.90	0.38	1.00	0.29	0.29	0.35
0.033	2.66	0.47	36.78	414.95	0.38	1.17	0.74	0.63	0.33

:, Zrn = zircon. Abbreviations after Whitney and Evans, 2010

Table 4
Zircon solution ICP-MS and LASS trace-element data for (U)HP eclogites from the D'Entrecasteaux Islands

Zircon trace-element data: LASS	Hf	±1σ	Y	±1σ	Nb	±1σ	La	±1σ	Ce	±1σ	Pr	±1σ	Nd	±1σ	Sm	±1σ	Eu	±1σ	Gd	±1σ	Tb	±1σ
Fergusson Island: Oitabu Dome																						
PNG12-95a, eclogite cobble																						
Sample, Laser spot number, ID–TIMS zircon fraction																						
PNG12-95a_1_z14	9310	450	750	82	0.58	0.23	0.0047	0.0043	26.4	3.2	0.097	0.035	4.17	0.79	11.3	1.9	6.26	0.63	50.7	6.3	13.7	1.4
PNG12-95a_2_z14	9500	510	723	52	0.53	0.14	0.0011	0.0022	22.9	1.4	0.114	0.036	3.32	0.64	9.53	0.98	6.32	0.81	47.7	3.2	13.3	1
PNG12-95a_3_z14	9540	190	798	32	0.51	0.14	0.0072	0.0047	29.4	1.7	0.157	0.028	3.88	0.59	11.9	1	7.2	0.85	52.1	2.7	14.1	0.86
PNG12-95a_4_z15	9680	510	890	48	2.48	0.19	0.0117	0.0052	142	9.2	0.89	0.14	20.8	2.6	41.5	3.1	21	1.1	130.6	8.3	26	2
PNG12-95a_17_z16	11900	640	582	24	1.94	0.26	0.0015	0.0024	35.1	2.6	0.103	0.036	4.14	0.51	12.9	2.4	7.65	0.66	54.7	2.7	11.6	0.99
PNG12-95a_18_z16	9100	680	867	42	1.15	0.18	0.0057	0.0041	51.5	4.5	0.288	0.053	8.33	0.85	21.1	1.9	11.6	1.3	84.5	5.7	18.03	0.4
Fergusson Island: Oitabu Dome																						
PNG09-041c, eclogite																						
PNG09-041c_3_z1	6930	450	200.7	8.8	0.47	0.11	-0.02	0.02	6.34	0.71	0.18	0.05	5.90	0.48	7.80	1.20	4.76	0.59	23.90	1.60	5.37	0.68
PNG09-041c_4_z2	8090	450	104.2	5.3	0.261	0.084	0.02	0.01	3.76	0.35	0.06	0.02	1.11	0.32	2.83	0.57	2.22	0.29	10.80	1.30	2.49	0.22
PNG09-041c_5_z2	7470	490	334	28	0.327	0.094	-0.08	0.09	10.61	0.85	0.20	0.08	7.04	0.77	10.10	1.30	6.57	0.83	38.20	2.80	8.51	0.68
PNG09-041c_6_z3	7970	330	115.4	5.9	0.35	0.13	0.04	0.26	5.80	0.63	0.08	0.02	1.72	0.72	3.15	0.52	1.78	0.25	12.30	1.70	2.80	0.32
PNG09-041c_7_z3	8131	87	98.7	6.3	0.39	0.23	0.03	0.03	6.50	1.00	0.12	0.04	2.45	0.27	3.30	1.40	1.71	0.40	8.90	2.20	2.41	0.43
PNG09-041c_8_z4	7120	260	136.6	5	0.34	0.12	0.01	0.01	5.57	0.55	0.14	0.04	3.80	0.40	7.34	0.90	3.69	0.38	17.80	2.10	4.49	0.37
PNG09-041c_9_z5	7660	310	204	16	0.67	0.1	0.01	0.01	14.00	1.50	0.17	0.04	4.70	1.50	10.00	1.70	4.98	0.63	28.50	2.20	6.30	0.33
PNG09-041c_17_z6	7920	400	136.9	5.5	0.347	0.052	0.00	0.00	5.87	0.35	0.07	0.03	1.84	0.26	4.81	0.49	2.71	0.48	13.20	1.40	3.32	0.26
PNG09-041c_23_z7	7670	520	238	15	0.398	0.091	0.054	0.028	9.78	0.65	0.194	0.048	5.08	0.35	10.29	0.69	6.06	0.59	35.2	3.5	6.47	0.53
PNG09-041c_26_z8	7860	680	80.9	4.3	0.44	0.1	0.0016	0.0037	6.54	0.73	0.033	0.019	1.44	0.36	3.04	0.71	1.76	0.3	9.1	1.4	2.11	0.2
PNG09-041c_28_z9	7310	180	347	20	1.07	0.17	0.02	0.01	29.8	1.9	0.273	0.019	11.3	1.3	21.3	1.9	9.77	0.65	59	7.3	10.25	0.62
PNG09-041c_42_z10	7150	270	186	14	0.358	0.078	0.004	0.0066	6.9	0.46	0.128	0.045	3.31	0.63	5.9	1.1	3.44	0.51	23.4	2	5.05	0.6
PNG09-041c_44_z11	7040	510	254	12	0.494	0.06	0.013	0.01	10.46	0.73	0.261	0.047	6.69	0.53	9.9	1.1	5.61	0.95	39.5	1.8	7.86	0.62
PNG09-041c_45_z11	8510	440	50.5	3	0.327	0.061	0.0037	0.0052	4.33	0.29	0.052	0.034	0.83	0.43	1.75	0.56	1.08	0.26	6.1	1.2	1.23	0.14
Fergusson Island: Oitabu Dome																						
PNG09-039b iv, eclogite cobble																						
PNG09-039b_3_z16	11270	770	380	32	0.56	0.11	0.01	0.00	6.36	0.31	0.04	0.01	1.65	0.54	2.48	0.92	2.33	0.31	12.60	1.90	4.19	0.50
PNG09-039b_4_z16	10890	820	636	72	0.6	0.18	0.00	0.00	9.58	0.72	0.02	0.03	1.57	0.43	6.35	0.62	3.97	0.55	22.10	3.70	6.88	0.92
PNG09-039b_5_z16	11150	440	114.5	5.3	0.442	0.099	0.00	0.00	5.58	0.46	0.03	0.02	0.39	0.16	1.24	0.28	0.99	0.18	5.62	0.70	1.86	0.21
PNG09-039b_8_z17	7960	110	599	22	0.525	0.071	0.01	0.01	12.50	1.40	0.15	0.03	4.89	0.35	13.00	1.50	7.70	1.20	40.30	4.20	11.40	1.10
PNG09-039b_9_z17	8830	220	602	26	0.66	0.11	0.00	0.00	17.20	1.30	0.13	0.04	3.97	0.68	10.10	1.30	5.80	0.72	43.80	1.10	11.20	1.10
PNG09-039b_12_z18	8210	260	633	59	0.84	0.22	0.01	0.01	17.15	0.88	0.44	0.04	11.83	0.98	19.60	2.10	11.10	1.10	64.50	5.60	15.46	0.35
PNG09-039b_17_z19	9620	130	276.1	4.4	0.88	0.18	-0.02	0.02	17.50	1.40	0.09	0.03	4.80	1.30	10.20	1.60	5.84	0.93	35.60	5.80	8.06	0.79
PNG09-039b_18_z19	7940	590	673	37	0.88	0.16	-0.03	0.02	17.30	1.10	0.37	0.06	9.93	0.85	15.40	1.40	10.58	0.48	65.10	5.90	13.39	0.95
PNG09-039b_24_z20	8630	460	421	27	0.4	0.1	-0.01	0.01	10.41	0.90	0.20	0.07	4.70	1.10	10.40	1.60	4.86	0.34	39.80	5.50	8.24	0.48
PNG09-039b_26_z21	7940	390	393	26	2.1	0.4	-0.01	0.01	38.90	3.20	0.42	0.11	15.60	2.20	22.50	2.70	12.90	1.90	65.80	4.50	11.80	1.40
PNG09-039b_28_z22	8050	360	501	18	0.415	0.059	0.01	0.01	14.30	1.30	0.20	0.03	6.60	0.97	13.60	1.60	6.85	0.64	39.00	4.00	10.44	0.75
PNG09-039b_29_z22	9260	390	160	14	0.49	0.13	0.01	0.01	8.54	0.57	0.04	0.02	1.67	0.57	3.91	0.84	2.43	0.33	15.10	1.60	3.76	0.38
Goodenough Island: Goodenough Dome																						
PNG10-035a, eclogite																						
PNG10_035a_1	12190	410	148.1	6.6	0.48	0.13	0.0098	0.0062	3.41	0.38	0.011	0.013	0.87	0.22	2.39	0.66	1.32	0.22	8.2	1.6	2.13	0.23
PNG10_035a_2	10480	440	116.3	4.7	0.448	0.055	0.0099	0.0069	5.55	0.67	0.0087	0.0086	1.08	0.31	2.5	0.62	1.54	0.19	8.1	1.3	1.92	0.26
PNG10_035a_3	9310	580	16.2	1.1	0.283	0.097	0.003	0.0033	1.58	0.28	0.01	0.014	0.157	0.093	0.39	0.25	0.177	0.069	2.48	0.82	0.36	0.14
PNG10_035a_4	8590	540	45.8	2.9	0.322	0.049	0.01	0.0081	3.1	0.22	0.0082	0.0085	0.55	0.22	1.22	0.44	0.57	0.11	4.9	1.1	0.874	0.064

Remaining zircon solution ICP-MS and LASS trace-element data for (U)HP eclogites from the D'Entrecasteaux Islands

Zircons analyzed by ID-TIMS-TEA alone	Zr	±1σ	Hf	±1σ	Sc	±1σ	Y	±1σ	Nb	±1σ	Ta	±1σ	La	±1σ	Ce	±1σ	Pr	±1σ	Nd	±1σ	Sm	±1σ
Fergusson Island: Oitabu Dome																						
PNG12-95a, eclogite cobble																						
PNG 12-95a z1	480953.89	4184.30	10021.63	36.08	857.47	16.12	4602.40	85.14	1.051	0.003	-0.08	-0.01	0.61	0.01	273.03	2.48	3.24	0.08	57.92	0.30	112.93	1.96
PNG 12-95a z2	480543.55	8313.40	9295.73	350.45	925.31	8.42	5481.57	32.89	1.91	0.04	-0.103	-0.005	0.22	0.01	253.38	0.10	2.82	0.13	52.87	0.60	111.95	1.21
PNG 12-95a z3	482439.30	9069.86	10853.85	316.93	695.25	14.32	2855.89	91.96	0.815	0.004	-0.028	-0.001	0.25	0.00	177.87	0.64	2.33	0.01	40.49	0.69	78.11	0.86
PNG 12-95a z4	482078.46	6411.64	10110.88	265.92	769.89	51.12	3676.30	15.07	0.528	0.005	bdl	bdl	0.15	0.01	156.90	3.12	1.78	0.02	34.10	0.14	72.22	0.46
PNG 12-95a z5	480689.92	1201.72	13288.58	207.30	631.49	33.53	2370.40	35.32	1.50	0.02	bdl	bdl	0.05	0.00	83.87	1.59	1.37	0.02	25.62	0.35	55.41	0.03
PNG 12-95a z6	481527.59	8185.97	10032.39	21.07	814.63	4.64	4125.85	408.87	0.78	0.01	-0.0076	-0.0002	0.18	0.00	173.21	2.39	2.00	0.10	37.75	1.35	82.38	0.05
PNG 12-95a z7	482948.56	1448.85	9820.05	232.74	735.34	34.27	3236.94	113.62	1.244	0.005	0.0343	0.0003	0.14	0.00	202.07	3.92	1.98	0.01	38.01	0.02	79.03	0.40
PNG 12-95a z8	484576.38	1162.98	9823.29	109.04	623.20	2.56	2099.46	24.35	1.08	0.01	0.118	0.001	0.18	0.00	208.87	3.95	2.34	0.05	42.09	0.32	75.29	0.32
PNG 12-95a z9	483700.17	2660.35	10191.17	46.88	602.53	9.40	2516.70	23.66	1.33	0.01	0.066	0.002	0.34	0.00	221.97	3.71	2.64	0.02	46.41	0.49	84.82	0.66
PNG 12-95a z10	482069.25	192.83	13203.92	89.79	549.78	21.17	1442.06	13.41	1.36	0.01	0.032	0.001	0.11	0.00	95.41	0.42	0.93	0.00	18.06	0.19	40.30	0.07
PNG 12-95a z11	483094.80	5314.04	12571.71	242.63	548.71	17.72	1121.78	18.85	0.87	0.01	0.034	0.001	0.18	0.00	80.11	0.74	0.67	0.01	13.08	0.06	27.96	0.41
PNG 12-95a z12	483202.30	2416.01	11837.72	53.27	573.53	34.93	1598.14	2.88	0.51	0.01	0.035	0.002	0.05	0.00	80.37	1.44	0.95	0.01	17.34	0.33	37.42	0.46
PNG 12-95a z13	480603.64	6776.51	11780.64	301.58	565.93	4.75	3757.38	24.80	8.68	0.03	0.58	0.01	0.31	0.00	288.49	0.17	3.33	0.03	56.44	0.25	104.53	2.15
Fergusson Island: Mailolo Dome																						
PNG09-039b, eclogite cobble																						
PNG09-039b z2	485455.62	7233.29	11303.24	42.95	542.58	2.60	278.20	0.17	0.293	0.003	bdl	bdl	bdl	bdl	15.90	0.18	0.12	0.01	3.01	0.02	6.16	0.03
PNG09-039b z4	484835.18	583305.21	11183.88	14473.06	1002.41	22.85	497.51	13.68	0.77	0.03	0.074	0.001	0.18	0.00	35.01	0.65	0.52	0.00	8.23	0.02	14.49	0.06
PNG09-039b z5	486588.50	7055.53	10055.59	56.31	535.53	34.92	378.06	1.10	0.70	0.01	0.054	0.003	0.18	0.00	20.79	0.08	0.38	0.02	5.74	0.07	10.37	0.13
PNG09-039b z6	484902.43	1503.20	11895.42	134.42	526.01	8.26	258.15	0.57	0.358	0.001	0.022	0.001	0.59	0.00	15.51	0.29	0.31	0.00	3.61	0.09	6.17	0.08
PNG09-039b z9	485810.35	48.58	11068.13	158.27	336.05	3.16	346.59	3.05	4.45	0.02	0.491	0.004	0.02	0.00	17.18	0.07	0.23	0.00	4.14	0.08	8.30	0.10
PNG09-039b z11	485237.09	7278.56	11540.44	159.26	480.68	15.29	309.54	1.70	0.43	0.01	0.11	0.01	0.06	0.00	17.76	0.06	0.20	0.01	3.61	0.05	7.51	0.15
PNG09-039b z15	484891.20	4800.42	11983.84	156.99	365.58	12.83	328.56	3.42	0.647	0.004	bdl	bdl	0.53	0.00	17.78	0.05	bdl	bdl	2.94	0.06	7.12	0.09
Goodenough Island: Goodenough Dome																						
PNG10-035a, eclogite																						
PNG10-035a z1	485622.70	6051.99	11207.57	165.47	320.15	2.96	350.36	1.75	bdl	bdl	bdl	bdl	bdl	bdl	14.80	0.05	bdl	bdl	bdl	bdl	8.20	0.03
PNG10-035a z2	485595.40	1019.75	11694.23	209.33	nr	nr	248.21	0.72	1.32	0.01	0.213	0.004	0.11	0.01	9.76	0.04	0.10	0.00	2.01	0.10	5.32	0.02
PNG10-035a z4	486591.00	12991.98	10780.50	7.55	nr	nr	146.35	11.53	1.14	0.03	0.12	0.01	0.17	0.01	6.58	0.13	0.29	0.04	5.16	0.24	14.34	1.02
PNG10-035a z5	486402.17	2772.49	10920.95	32.76	nr	nr	188.46	1.41	1.81	0.04	0.33	0.01	0.08	0.00	12.46	0.09	0.35	0.01	6.25	0.21	13.58	0.01
PNG10-035a z6	485580.58	2913.48	11815.22	7.09	nr	nr	175.07	10.61	0.78	0.01	0.118	0.001	0.04	0.00	4.26	0.25	0.04	0.00	1.02	0.02	3.44	0.07
PNG10-035a z7	485743.60	1214.36	11620.43	8.13	nr	nr	172.61	1.83	0.76	0.02	0.18	0.01	0.21	0.00	14.19	0.21	0.25	0.00	4.29	0.11	9.56	0.46
PNG10-035a z8	486291.90	2431.46	11095.97	99.86	nr	nr	174.90	0.56	0.656	0.005	0.070	0.002	0.11	0.00	8.10	0.18	0.13	0.01	2.25	0.08	5.62	0.20
PNG10-035a z9	488160.58	213765.52	9279.12	2876.53	nr	nr	154.08	81.23	2.22	0.98	0.53	0.15	0.00	0.00	3.52	1.61	0.03	0.01	0.65	0.24	1.92	0.76
Goodenough Island: Goodenough Dome																						
PNG12-82a, eclogite cobble																						

PNG12-82a z4	486877.69	1704.07	9976.17	49.88	360.80	19.81	336.93	1.58	8.87	0.02	1.95	0.01	0.06	0.00	19.27	0.16	0.19	0.00	3.89	0.05	8.39	0.01
PNG12-82a z5	486550.73	437.90	10365.44	17.62	363.41	25.51	284.80	3.30	18.15	0.09	2.92	0.02	0.26	0.00	18.12	0.01	0.17	0.01	3.07	0.09	6.74	0.09
PNG12-82a z9	486573.66	5449.62	10469.68	168.56	nr	nr	310.96	9.30	104.05	0.30	37.59	0.55	0.86	0.00	18.16	0.28	0.33	0.03	3.83	0.15	7.65	0.31
PNG12-82a z10	486597.69	2432.99	10631.99	249.85	nr	nr	284.08	5.99	2.07	0.02	0.40	0.00	0.04	0.00	12.30	0.27	0.09	0.00	1.84	0.13	4.42	0.12
PNG12-82a z11	486686.48	2190.09	10378.17	141.14	nr	nr	317.43	6.32	92.44	0.40	24.26	0.07	0.18	0.00	15.83	0.07	0.15	0.02	2.23	0.06	5.34	0.05
PNG12-82a z12	486480.90	2821.59	10698.66	55.63	nr	nr	307.53	5.47	6.69	0.10	0.90	0.01	1.56	0.01	22.35	0.13	0.47	0.04	3.93	0.16	6.55	0.32
PNG12-82a z13 (used to be 1)	486306.55	5495.26	10414.32	206.20	567.11	2.84	276.82	0.11	0.73	0.02	0.044	0.001	0.55	0.01	19.58	0.04	0.23	0.00	2.79	0.05	4.84	0.12
Zircon trace-element data analyzed by LASS alone	Hf	±1σ	Y	±1σ	Nb	±1σ	La	±1σ	Ce	±1σ	Pr	±1σ	Nd	±1σ	Sm	±1σ	Eu	±1σ	Gd	±1σ	Tb	±1σ
Fergusson Island: Oitabu Dome																						
PNG12-95a, eclogite cobble																						
PNG12-95a_1_5	13250	650	78.7	9.8	0.32	0.07	-0.0002	0.0013	4.28	0.75	0.053	0.027	0.89	0.33	2.09	0.46	1.29	0.34	9.4	2.2	2.32	0.53
PNG12-95a_1_7	13450	570	30.9	2.7	0.226	0.076	0.0077	0.0054	1.066	0.084	-0.003	0.011	0.2	0.13	0.92	0.32	0.454	0.085	3.13	0.94	0.69	0.13
PNG12-95a_2_8	12220	510	709	22	2.62	0.37	0.0065	0.005	21.03	0.89	0.146	0.059	2.3	0.63	11.7	1.6	7.62	0.69	57.5	6.6	15.61	0.61
PNG12-95a_2_9	10870	410	596	34	2.91	0.29	0.004	0.0034	76	5.4	0.362	0.06	11.5	1	28.8	2	16	1.5	97.8	8.1	19.8	1.3
PNG12-95a_2_10	9490	420	626	26	2.06	0.29	0.0042	0.0036	121.6	7.8	0.804	0.079	18.6	1.6	36.5	3.5	19.3	1.2	112.4	7.3	23.6	1.5
PNG12-95a_2_11	8140	400	273	20	0.546	0.092	0.0055	0.0044	4.19	0.86	0.016	0.018	0.62	0.24	1.34	0.44	0.96	0.28	7.3	1.1	2.41	0.31
PNG12-95a_2_12	8200	500	1720	110	1.1	0.19	0.0068	0.0053	80.2	3.2	0.675	0.088	15.5	1.6	43.2	2.8	26.5	2.8	190	13	44.3	3.1
PNG12-95a_2_13	8820	330	464	32	0.8	0.14	0.0088	0.0036	43.5	2.2	0.265	0.055	7.3	1	19.4	2.4	8.7	1	64.7	6.6	13.1	1.1
PNG12-95a_2_14	8230	630	1437	56	0.83	0.12	0.0112	0.0056	71.4	4.7	0.568	0.089	12	1.3	35.8	2.9	20	1.3	146.7	9.8	33.2	1.4
PNG12-95a_3_15	14260	480	24	1.5	0.31	0.12	0.0008	0.0021	0.88	0.19	0.023	0.019	0.16	0.11	0.65	0.28	0.35	0.13	2.33	0.69	0.56	0.13
PNG12-95a_3_16	9680	520	1579	81	1.08	0.19	0.0088	0.0068	45.2	2.8	0.259	0.07	8.2	1.1	23.2	3.1	15.53	0.69	113	14	28.2	2.4
PNG12-95a_4_19	7670	450	443	16	0.98	0.21	0.0086	0.0048	46.2	2.1	0.254	0.06	6.21	0.71	16.2	2.1	8.54	0.84	50	2.3	10.07	0.85
PNG12-95a_4_20	8820	490	916	35	2.67	0.36	0.0189	0.0052	151	11	0.675	0.07	16.1	1.6	39.6	3	18.7	1.3	118.1	6.7	20.6	1.3
PNG12-95a_1_z14	9310	450	750	82	0.58	0.23	0.0047	0.0043	26.4	3.2	0.097	0.035	4.17	0.79	11.3	1.9	6.26	0.63	50.7	6.3	13.7	1.4
PNG12-95a_2_z14	9500	510	723	52	0.53	0.14	0.0011	0.0022	22.9	1.4	0.114	0.036	3.32	0.64	9.53	0.98	6.32	0.81	47.7	3.2	13.3	1
PNG12-95a_3_z14	9540	190	798	32	0.51	0.14	0.0072	0.0047	29.4	1.7	0.157	0.028	3.88	0.59	11.9	1	7.2	0.85	52.1	2.7	14.1	0.86
PNG12-95a_4_z15	9680	510	890	48	2.48	0.19	0.0117	0.0052	142	9.2	0.89	0.14	20.8	2.6	41.5	3.1	21	1.1	130.6	8.3	26	2
PNG12-95a_17_z16	11900	640	582	24	1.94	0.26	0.0015	0.0024	35.1	2.6	0.103	0.036	4.14	0.51	12.9	2.4	7.65	0.66	54.7	2.7	11.6	0.99
PNG12-95a_18_z16	9100	680	867	42	1.15	0.18	0.0057	0.0041	51.5	4.5	0.288	0.053	8.33	0.85	21.1	1.9	11.6	1.3	84.5	5.7	18.03	0.4
Fergusson Island: Mailolo Dome																						
PNG09-041c, eclogite																						
PNG09-041c_1_1	7200	300	132	10	0.354	0.08	0.00	0.01	6.31	0.58	0.03	0.02	2.20	0.60	2.65	0.69	1.76	0.29	12.10	1.90	2.49	0.14
PNG09-041c_1_2	7510	280	149	16	0.37	0.1	-0.03	0.04	6.80	1.30	0.11	0.04	2.60	0.97	3.62	0.45	2.50	0.73	17.20	3.30	3.24	0.32
PNG09-041c_2_11	8180	640	182.9	9.6	0.384	0.083	0.00	0.00	6.44	0.60	0.17	0.06	4.66	0.73	7.70	1.40	4.72	0.42	24.20	2.40	4.88	0.39
PNG09-041c_3_12	7160	290	119.8	6	0.36	0.11	0.00	0.00	5.41	0.40	0.05	0.03	1.12	0.35	3.11	0.72	1.31	0.23	8.10	0.97	2.36	0.26
PNG09-041c_3_13	8360	640	135	14	0.3	0.24	0.01	0.02	3.70	1.40	0.03	0.04	1.35	0.74	2.50	1.80	2.11	0.45	8.50	1.20	3.00	0.52
PNG09-041c_4_14	7110	340	308	21	0.54	0.13	0.01	0.01	10.08	0.80	0.35	0.06	7.80	1.10	11.70	1.30	7.07	0.74	37.10	4.20	9.16	0.58
PNG09-041c_4_15	7480	410	258	12	0.47	0.15	0.00	0.01	10.20	1.30	0.33	0.04	6.90	1.60	11.70	1.60	6.06	0.32	34.40	3.00	7.87	0.65
PNG09-041c_5_16	7400	460	185	17	0.409	0.088	0.01	0.01	8.44	0.87	0.14	0.07	4.00	1.00	8.40	1.20	4.66	0.30	24.90	2.20	5.32	0.29
PNG09-041c_6_18	7560	360	193	11	0.35	0.079	-0.017	0.013	7.69	0.71	0.135	0.034	3.58	0.51	7.6	1.3	4.53	0.54	27.4	4	5.07	0.22
PNG09-041c_7_19	7820	310	400	26	0.396	0.085	-0.033	0.024	10.2	0.77	0.193	0.062	6.5	1.2	12	1.6	6.8	0.67	48.2	1	8.66	0.48
PNG09-041c_7_20	7670	470	136	13	0.34	0.11	-0.031	0.026	6.44	0.31	0.075	0.031	2.19	0.53	4.4	0.84	2.17	0.37	16.6	2.2	3.24	0.21
PNG09-041c_8_21	7480	330	141	10	0.379	0.092	-0.051	0.066	6.9	0.61	0.038	0.032	1.42	0.21	3.03	0.5	2.21	0.29	13.7	1.5	2.9	0.31
PNG09-041c_8_22	8360	570	46.6	2.6	0.252	0.068	0.064	0.05	3.71	0.64	0.018	0.015	0.52	0.16	1.47	0.34	0.73	0.14	5.78	0.69	0.94	0.18
PNG09-041c_9_24	7860	350	106.6	6.7	0.362	0.083	0.057	0.032	6.07	0.62	0.112	0.06	1.88	0.37	3.19	0.56	2.24	0.26	13.9	1.5	2.68	0.33
PNG09-041c_9_25	8250	630	91	12	0.217	0.063	0.0131	0.0092	3.64	0.26	0.049	0.027	1.09	0.4	2.93	0.58	1.69	0.46	10.4	1.8	2.22	0.37
PNG09041c_10_27	7930	230	342	18	0.394	0.086	0.0115	0.0068	9.44	0.6	0.111	0.019	5.63	0.88	10.5	0.96	7.02	0.51	41	4.3	8.34	0.62
PNG09-041c_11_29	7850	360	266	9.6	0.271	0.053	0.0027	0.0031	9.35	0.54	0.158	0.053	5.02	0.75	8.7	1	5.49	0.81	36.3	1.9	7.76	0.69
PNG09-041c_12_30	8170	350	232	17	0.463	0.069	0.0089	0.0044	14.2	1.1	0.159	0.025	4.99	0.6	8.38	0.98	5.32	0.41	36.7	3.3	7.17	0.39
PNG09-041c_12_31	8230	210	256	21	0.85	0.16	0.0072	0.0046	19.5	1.4	0.175	0.034	6.29	0.98	12.2	1.3	6.61	0.53	39.7	3	7.98	0.88
PNG09-041c_13_32	6790	290	135	13	0.36	0.17	0.026	0.02	6.84	0.82	0.108	0.037	3.35	0.92	5.7	1.5	2.81	0.67	17.8	3.4	4.36	0.6
PNG09-041c_14_33	8280	490	195	16	0.47	0.12	0.0025	0.0037	7.69	0.34	0.088	0.038	3.14	0.47	6.67	0.92	4.18	0.36	24.2	2.8	4.95	0.57
PNG09-041c_15_34	7670	400	387	14	0.333	0.044	0.041	0.011	10.85	0.42	0.179	0.03	5.74	0.91	11.6	1.8	6.33	0.55	47.2	2.4	10.14	0.83
PNG09-041c_15_35	8330	390	215	10	0.71	0.11	0.0071	0.0042	16.9	1.3	0.098	0.034	4.83	0.92	10.17	0.65	5.45	0.41	33.5	2.5	6.91	0.61
PNG09-041c_16_36	7810	400	338	19	1.09	0.26	0.0079	0.0041	31	2.8	0.383	0.049	12.3	1.6	22.4	2.5	10.21	0.84	60	5	12.87	0.58
PNG09-041c_16_37	7440	390	118.4	3.7	0.488	0.086	0.0091	0.0069	6.54	0.6	0.059	0.016	3.1	0.29	5.76	0.77	2.75	0.29	17.8	1.7	3.31	0.33
PNG09-041c_17_38	8410	170	88.4	5.1	0.269	0.081	0.006	0.0062	4.83	0.31	0.036	0.016	1.28	0.39	3.22	0.43	1.64	0.28	12	1.4	2.39	0.41
PNG09-041c_17_39	7830	240	178.3	7.1	0.525	0.093	0.0024	0.0038	8.01	0.52	0.031	0.012	1.78	0.47	4.23	0.86	2.58	0.38	17	1.8	4.17	0.42
PNG09-041c_18_40	7470	180	49	1.5	0.308	0.089	0.0043	0.0039	4.64	0.28	0.035	0.015	0.88	0.48	2.08	0.78	1.12	0.24	5.51	0.52	1.41	0.25
PNG09-041c_19_41	7760	390	93.9	5.7	0.3	0.11	0.0043	0.0043	5.99	0.49	0.092	0.026	1.78	0.27	3.24	0.92	1.74	0.24	11.2	1.3	2.26	0.22
PNG09-041c_20_43	7230	350	153	11	0.39	0.14	0.0035	0.0051	5.86	0.58	0.119	0.021	2.26	0.71	5.1	1.2	2.49	0.46	15.5	2.8	3.86	0.36
PNG09-041c_2_10	14480	880	1150	110	3.02	0.76	0.09	0.03	7.20	2.00	0.16	0.11	2.76	0.94	3.50	1.10	1.79	0.38	14.50	3.70	7.30	1.30
PNG09-041c_3_z1	6930	450	200.7	8.8	0.47	0.11	-0.02	0.02	6.34	0.71	0.18	0.05	5.90	0.48	7.80	1.20	4.76	0.59	23.90	1.60	5.37	0.68
PNG09-041c_4_z2	8090	450	104.2	5.3	0.261	0.084	0.02	0.01	3.76	0.35	0.06	0.02	1.11	0.32	2.83	0.57	2.22	0.29	10.80	1.30	2.49	0.22
PNG09-041c_5_z2	7470	490	334	28	0.327	0.094	-0.08	0.09	10.61	0.85	0.20	0.08	7.04	0.77	10.10	1.30	6.57	0.83	38.20	2.80	8.51	0.68
PNG09-041c_6_z3	7970	330	115.4	5.9	0.35	0.13	0.04	0.26	5.80	0.63	0.08	0.02	1.72	0.72	3.15	0.52	1.78	0.25	12.30	1.70	2.80	0.32
PNG09-041c_7_z3	8131	87	98.7	6.3	0.39	0.23	0.03	0.03	6.50	1.00	0.12	0.04	2.45	0.27	3.30	1.40	1.71	0.40	8.90	2.20	2.41	0.43
PNG09-041c_8_z4	7120	260	136.6	5	0.34	0.12	0.01	0.01	5.57	0.55	0.14	0.04	3.80	0.40	7.34	0.90	3.69	0.38	17.80	2.10	4.49	0.37
PNG09-041c_9_z5	7660	310	204	16	0.67	0.1	0.01	0.01	14.00	1.50	0.17	0.04	4.70	1.50	10.00	1.70	4.98	0.63	28.50	2.20	6.30	0.33
PNG09-041c_17_z6	7920	400	136.9	5.5	0.347	0.052	0.00	0.00	5.87	0.35	0.07	0.03	1.84	0.26	4.81	0.49	2.71	0.48	13.20	1.40	3.32	0.26
PNG09-041c_23_z7	7670	520	238	15	0.398	0.091	0.054	0.028	9.78	0.65	0.194	0.048	5.08	0.35	10.29	0.69	6.06	0.59	35.2	3.5	6.47	0.53
PNG09-041c_26_z8	7860	680	80.9	4.3	0.44	0.1	0.0016	0.0037	6.54	0.73	0.033	0.019	1.44	0.36	3.04	0.71	1.76	0.3	9.1	1.4	2.11	0.2
PNG09-041c_28_z9	7310	180	347	20	1.07	0.17	0.02	0.01	29.8	1.9	0.273	0.019	11.3	1.3	21.3	1.9	9.77	0.65	59	7.3	10.25	0.62
PNG09-041c_42_z10	7150	270	186	14	0.358	0.078	0.004	0.0066	6.9	0.46	0.128	0.045	3.31	0.63	5.9	1.1	3.44	0.51	23.4	2	5.05	0.6
PNG09-041c_44_z11	7040	510	254	12	0.494	0.06	0.013	0.01	10.46	0.73	0.261	0.047	6.69	0.53	9.9	1.1	5.61	0.95	39.5	1.8	7.86	0.62
PNG09-041c_45_z11	8510	440	50.5	3	0.327	0.061	0.0037	0.0052	4.33	0.29	0.052	0.034	0.83	0.43	1.75	0.56	1.08	0.26	6.1	1.2	1.23	0.14
Fergusson Island: Mailolo Dome																						
PNG09-039b, eclogite cobble																						
PNG09_039b_1	10730	840	158	12	0.46	0.13	0.00	0.00	5.80	0.50	0.02	0.03	0.65	0.29	1.78	0.52	1.33	0.28	7.90	1.50	2.27	0.31
PNG09_039b_2	11240	680	381	21	0.52	0.12	0.00	0.00	6.60	0.65	0.04	0.02	1.76	0.45	2.94	0.74	2.45	0.31	14.52	0.81	4.25	0.26
PNG09_039b_6	8770	360	403	22	0.41	0.14	0.00	0.00	9.92	0.85	0.12	0.03	5.10	0.79	11.59	0.88	6.24	0.65	35.60	2.60	8.54	0.55
PNG09_039b_7	9270	450	95	3.3	0.376	0.081	0.00	0.00	4.85	0.80	0.04	0.03	0.71	0.41	1.84	0.53	1.35	0.32	7.00	1.00	1.87	0.26
PNG09_039b_10	8660	190	286	13	0.47	0.17	0.00	0.00	5.89	0.20	0.10	0.04	3.37	0.71	8.30	1.40	4.57	0.32	30.40	2.70	6.93	0.35
PNG09_039b_11	10860	300	254	23	0.698	0.094	0.01	0.01	13.40	1.30	0.11	0.04	2.61	0.63	7.60	1.50	3.96	0.39	21.80	2.90	4.68	0.58
PNG09_039b_13	8330	460	280	12	0.389	0.078	0.00	0.00	7.42	0.52	0.08	0.03	2.90	0.49	6.60	1.40	3.87	0.43	23.60	1.00	6.06	0.64

PNG09_039b_14	10700	640	205	13	0.587	0.093	0.00	0.00	7.61	0.41	0.05	0.02	1.61	0.59	3.27	0.60	2.02	0.20	12.90	2.00	3.30	0.16
PNG09_039b_15	9220	440	115.7	5.1	0.425	0.078	0.00	0.01	7.23	0.69	0.05	0.03	0.74	0.32	1.78	0.50	2.17	0.43	9.50	2.00	2.29	0.25
PNG09_039b_16	9530	420	642	20	0.88	0.13	0.03	0.03	14.43	0.83	0.32	0.11	9.60	1.70	13.60	1.20	8.64	0.78	56.30	3.50	11.94	0.55
PNG09_039b_19	8060	380	358	24	0.48	0.14	0.01	0.00	9.31	0.55	0.12	0.06	4.70	1.30	9.47	0.33	5.92	0.73	33.10	3.30	7.04	0.75
PNG09_039b_20	8890	240	316	17	1.17	0.22	-0.01	0.02	24.60	1.90	0.28	0.04	5.62	0.84	13.60	1.20	7.26	0.25	46.30	4.50	8.06	0.55
PNG09_039b_21	8610	380	328	20	0.5	0.11	0.00	0.01	7.91	0.80	0.18	0.03	4.96	0.28	9.20	1.90	5.90	0.62	34.60	4.00	7.01	0.76
PNG09_039b_22	9370	570	406	18	1.81	0.28	0.00	0.01	40.80	2.20	0.51	0.11	13.70	2.20	24.20	1.80	13.80	1.60	74.60	7.90	14.20	1.10
PNG09_039b_23	9410	650	279	25	1.06	0.18	0.00	0.00	17.10	1.50	0.16	0.06	5.90	1.30	15.00	1.60	8.50	1.20	45.10	3.10	7.97	0.79
PNG09_039b_25	9520	780	311	25	0.25	0.14	-0.01	0.02	7.60	1.10	0.10	0.08	3.60	0.61	6.90	1.90	3.98	0.56	30.40	2.00	7.10	1.30
PNG09_039b_27	8860	420	338	20	0.73	0.099	0.00	0.00	8.91	0.42	0.11	0.03	3.80	0.69	6.39	0.65	3.44	0.22	23.80	1.80	6.24	0.30
PNG09_039b_30	9050	300	240	18	0.32	0.11	0.00	0.00	7.60	0.66	0.08	0.03	2.41	0.32	7.50	1.20	3.44	0.55	19.80	1.50	4.98	0.41
PNG09_039b_31	8910	400	279	26	0.31	0.12	0.00	0.00	6.25	0.56	0.12	0.05	3.26	0.43	9.10	1.80	4.82	0.51	27.40	2.20	6.75	0.62
PNG09_039b_32	9630	450	143.5	6.9	0.63	0.2	0.00	0.00	9.77	0.79	0.09	0.03	1.58	0.42	5.40	1.00	2.34	0.32	13.70	1.50	3.57	0.40
PNG09_039b_33	8770	350	326	20	0.39	0.13	0.05	0.02	9.87	0.57	0.26	0.04	5.60	1.10	11.10	1.10	4.84	0.41	30.20	3.70	7.52	0.69
PNG09_039b_34	8810	550	244.3	7.7	0.68	0.18	0.00	0.01	13.38	0.43	0.17	0.06	4.70	1.00	11.10	1.40	5.09	0.50	31.40	2.40	7.82	0.58
PNG09_039b_35	9830	590	443	42	0.61	0.13	0.01	0.02	12.30	1.20	0.23	0.09	7.28	0.41	16.40	1.40	6.74	0.68	41.40	3.80	9.26	0.92
PNG09_039b_36	9220	490	50.3	2.6	0.46	0.13	0.01	0.01	4.82	0.21	0.02	0.02	0.49	0.20	1.97	0.47	0.96	0.21	5.58	0.87	0.80	0.12
PNG09_039b_37	8040	560	272	16	0.384	0.087	0.00	0.01	8.17	0.80	0.09	0.05	3.27	0.68	10.90	1.40	4.25	0.46	29.40	2.50	7.03	0.62
PNG09_039b_38	8720	530	541	31	0.73	0.15	0.01	0.01	28.42	0.88	0.24	0.08	7.91	0.73	18.90	1.60	8.42	0.71	56.90	2.90	13.00	1.10
PNG09_039b_39	8210	360	264	17	0.399	0.072	-0.01	0.01	8.13	0.67	0.15	0.05	3.00	0.48	10.90	1.20	4.36	0.36	27.40	2.20	6.08	0.42
PNG09_039b_40	8270	290	184	13	0.59	0.16	0.01	0.01	13.50	1.10	0.13	0.04	2.79	0.74	7.70	1.00	3.55	0.49	23.49	0.96	4.82	0.26
PNG09_039b_41	8790	520	182	11	0.248	0.083	-0.01	0.01	6.85	0.62	0.14	0.07	3.17	0.64	6.90	1.20	3.16	0.40	20.70	2.30	4.44	0.48
PNG09_039b_42	7760	520	210	21	0.25	0.15	0.02	0.02	6.83	0.60	0.21	0.08	4.94	0.60	11.00	1.50	4.63	0.84	32.30	3.90	6.75	0.83
PNG09_039b_43	10640	500	293	15	0.33	0.11	0.00	0.01	6.28	0.46	0.06	0.03	1.11	0.47	4.82	0.96	2.21	0.32	16.40	1.30	4.05	0.39
PNG09_039b_44	8920	270	522	13	1.47	0.46	0.00	0.03	49.40	2.60	0.68	0.22	17.10	1.90	36.80	2.50	15.00	1.40	97.10	6.10	17.70	1.00
PNG09_039b_45	7460	300	264	19	0.41	0.12	0.01	0.02	8.94	0.71	0.30	0.10	5.73	0.86	13.80	2.30	5.35	0.27	41.20	3.70	7.37	0.85
PNG09_039b_46	7600	120	391	17	0.51	0.2	0.01	0.02	10.80	0.78	0.25	0.08	5.30	1.00	13.00	1.80	5.96	0.53	40.00	6.80	8.70	0.73
PNG09_039b_47	8850	330	234	13	0.44	0.11	0.01	0.02	6.41	0.43	0.19	0.07	3.47	0.84	8.40	1.50	3.71	0.37	27.70	3.00	6.21	0.39
PNG09_039b_48	8300	460	378	24	0.39	0.15	0.01	0.01	10.12	0.74	0.52	0.10	7.08	0.88	13.60	1.10	6.15	0.55	39.40	3.60	9.42	0.60
PNG09_039b_49	8570	470	500	30	1.79	0.2	0.02	0.01	59.00	2.20	0.94	0.13	16.80	1.90	34.60	1.90	14.14	0.98	98.00	5.60	18.90	1.10
PNG09-039b_3_z16	11270	770	380	32	0.56	0.11	0.01	0.00	6.36	0.31	0.04	0.01	1.65	0.54	2.48	0.92	2.33	0.31	12.60	1.90	4.19	0.50
PNG09-039b_4_z16	10890	820	636	72	0.6	0.18	0.00	0.00	9.58	0.72	0.02	0.03	1.57	0.43	6.35	0.62	3.97	0.55	22.10	3.70	6.88	0.92
PNG09-039b_5_z16	11150	440	114.5	5.3	0.442	0.099	0.00	0.00	5.58	0.46	0.03	0.02	0.39	0.16	1.24	0.28	0.99	0.18	5.62	0.70	1.86	0.21
PNG09-039b_8_z17	7960	110	599	22	0.525	0.071	0.01	0.01	12.50	1.40	0.15	0.03	4.89	0.35	13.00	1.50	7.70	1.20	40.30	4.20	11.40	1.10
PNG09-039b_9_z17	8830	220	602	26	0.66	0.11	0.00	0.00	17.20	1.30	0.13	0.04	3.97	0.68	10.10	1.30	5.80	0.72	43.80	1.10	11.20	1.10
PNG09-039b_12_z18	8210	260	633	59	0.84	0.22	0.01	0.01	17.15	0.88	0.44	0.04	11.83	0.98	19.60	2.10	11.10	1.10	64.50	5.60	15.46	0.35
PNG09-039b_17_z19	9620	130	276.1	4.4	0.88	0.18	-0.02	0.02	17.50	1.40	0.09	0.03	4.80	1.30	10.20	1.60	5.84	0.93	35.60	5.80	8.06	0.79
PNG09-039b_18_z19	7940	590	673	37	0.88	0.16	-0.03	0.02	17.30	1.10	0.37	0.06	9.93	0.85	15.40	1.40	10.58	0.48	65.10	5.90	13.39	0.95
PNG09-039b_24_z20	8630	460	421	27	0.4	0.1	-0.01	0.01	10.41	0.90	0.20	0.07	4.70	1.10	10.40	1.60	4.86	0.34	39.80	5.50	8.24	0.48
PNG09-039b_26_z21	7940	390	393	26	2.1	0.4	-0.01	0.01	38.90	3.20	0.42	0.11	15.60	2.20	22.50	2.70	12.90	1.90	65.80	4.50	11.80	1.40
PNG09-039b_28_z22	8050	360	501	18	0.415	0.059	0.01	0.01	14.30	1.30	0.20	0.03	6.60	0.97	13.60	1.60	6.85	0.64	39.00	4.00	10.44	0.75
PNG09-039b_29_z22	9260	390	160	14	0.49	0.13	0.01	0.01	8.54	0.57	0.04	0.02	1.67	0.57	3.91	0.84	2.43	0.33	15.10	1.60	3.76	0.38
Goodenough Island: Goodenough Dome																						
PNG10-035a, eclogite																						
PNG10_035a_5	10070	620	121.9	5.5	0.394	0.093	0.0231	0.0089	4.51	0.39	0.043	0.023	0.57	0.26	2.25	0.57	1.18	0.22	9.6	1.5	1.7	0.3
PNG10_035a_6	10410	800	36.1	2.9	0.26	0.096	0.0019	0.0029	2.45	0.18	0.0004	0.0063	0.41	0.14	0.59	0.38	0.394	0.076	2.74	0.55	0.59	0.13
PNG10_035a_1	12190	410	148.1	6.6	0.48	0.13	0.0098	0.0062	3.41	0.38	0.011	0.013	0.87	0.22	2.39	0.66	1.32	0.22	8.2	1.6	2.13	0.23
PNG10_035a_2	10480	440	116.3	4.7	0.448	0.055	0.0099	0.0069	5.55	0.67	0.0087	0.0086	1.08	0.31	2.5	0.62	1.54	0.19	8.1	1.3	1.92	0.26
PNG10_035a_3	9310	580	16.2	1.1	0.283	0.097	0.003	0.0033	1.58	0.28	0.01	0.014	0.157	0.093	0.39	0.25	0.177	0.069	2.48	0.82	0.36	0.14
PNG10_035a_4	8590	540	45.8	2.9	0.322	0.049	0.01	0.0081	3.1	0.22	0.0082	0.0085	0.55	0.22	1.22	0.44	0.57	0.11	4.9	1.1	0.874	0.064

$Pm^* = (Nd_N * Sm_N)^{0.5}$

$Eu/Eu^* = Eu_N / (Sm_N * Gd_N)^{0.5}$

Chondrite normalized																									
Dy	±1σ	Ho	±1σ	Er	±1σ	Tm	±1σ	Yb	±1σ	Lu	±1σ	La	Ce	Pr	Nd	Pm*	Sm	Eu	Gd	Tb	Dy	Ho	Er	Tm	Yb	Lu
101.5	9.2	25.2	2.5	66.7	6.3	10.9	1.3	77.3	8.1	10.87	0.95	0.02	43.07	1.04	9.12	26.39	76.35	111.79	254.77	380.56	412.60	458.18	416.88	436.00	480.12	434.80
106	7.1	25.2	1.6	71.9	3.9	10.3	0.61	76.3	4.8	10.88	0.66	0.00	37.36	1.23	7.26	21.63	64.39	112.86	239.70	369.44	430.89	458.18	449.38	412.00	473.91	435.20
117.5	6.6	29.4	2	83.2	6.1	12.42	0.56	88.2	4.4	11.3	1	0.03	47.96	1.69	8.49	26.13	80.41	128.57	261.81	391.67	477.64	534.55	520.00	496.80	547.83	452.00
166	10	31.2	2.8	66.5	4	8.65	0.72	51.9	3.2	4.97	0.56	0.05	231.65	9.57	45.51	112.97	280.41	375.00	656.28	722.22	674.80	567.27	415.63	346.00	322.36	198.80
90.2	4.1	19.82	0.69	50.7	2.9	8.51	0.68	55.3	3.5	6.77	0.51	0.01	57.26	1.11	9.06	28.10	87.16	136.61	274.87	322.22	366.67	360.36	316.88	340.40	343.48	270.80
130	11	30.2	2.4	75.1	4.2	9.87	0.49	72.4	5.8	8.56	0.77	0.02	84.01	3.10	18.23	50.98	142.57	207.14	424.62	500.83	528.46	549.09	469.38	394.80	449.69	342.40
37.30	2.30	6.70	0.42	15.20	1.50	1.81	0.31	9.95	0.51	1.26	0.16	-0.06	10.34	1.88	12.91	26.08	52.70	85.00	120.10	149.17	151.63	121.82	95.00	72.40	61.80	50.40
18.70	1.80	3.33	0.39	7.35	0.70	0.73	0.13	5.17	0.71	0.47	0.18	0.08	6.13	0.59	2.43	6.81	19.12	39.64	54.27	69.17	76.02	60.55	45.94	29.20	32.11	18.80
51.40	4.90	10.30	1.50	25.10	2.30	2.94	0.31	21.30	2.70	2.56	0.38	-0.32	17.31	2.17	15.40	32.42	68.24	117.32	191.96	236.39	208.94	187.27	156.88	117.60	132.30	102.40
19.30	1.90	3.83	0.24	8.80	1.30	1.00	0.13	7.60	1.50	0.99	0.13	0.17	9.46	0.82	3.76	8.95	21.28	31.79	61.81	77.78	78.46	69.64	55.00	40.00	47.20	39.60
17.40	4.20	2.83	0.74	6.70	2.10	0.82	0.16	4.30	1.60	0.53	0.09	0.13	10.60	1.24	5.36	10.93	22.30	30.54	44.72	66.94	70.73	51.45	41.88	32.80	26.71	21.16
25.60	3.00	4.11	0.23	8.90	1.40	1.00	0.13	5.24	0.81	0.75	0.21	0.05	9.09	1.51	8.32	20.31	49.59	65.89	89.45	124.72	104.07	74.73	55.63	40.00	32.55	30.00
36.10	4.20	6.35	0.58	13.08	0.69	1.50	0.17	8.80	1.20	0.93	0.28	0.03	22.84	1.78	10.28	26.36	67.57	88.93	143.22	175.00	146.75	115.45	81.75	60.00	54.66	37.20
22.70	1.50	4.28	0.39	10.30	1.20	1.24	0.17	6.95	0.92	0.97	0.12	-0.01	9.58	0.71	4.03	11.44	32.50	48.39	66.33	92.22	92.28	77.82	64.38	49.60	43.17	38.80
39.2	2.5	7.55	0.86	14.2	1.5	1.71	0.42	8.85	0.78	0.94	0.14	0.23	15.95	2.09	11.12	27.80	69.53	108.21	176.88	179.72	159.35	137.27	88.75	68.40	54.97	37.60
14.2	1.5	2.66	0.3	5.45	0.82	0.64	0.15	3.97	0.6	0.33	0.11	0.01	10.67	0.35	3.15	8.05	20.54	31.43	45.73	58.61	57.72	48.36	34.06	25.60	24.66	13.20
60.4	4.1	12.09	0.79	22.6	2.3	2.34	0.29	14.9	2	1.47	0.3	0.08	48.61	2.94	24.73	59.65	143.92	174.46	296.48	284.72	245.53	219.82	141.25	93.60	92.55	58.80
30.8	1.7	6.2	0.39	12.7	1	1.786	0.086	10.64	0.91	1.18	0.14	0.02	11.26	1.38	7.24	16.99	39.86	61.43	117.59	140.28	125.20	112.73	79.38	71.44	66.09	47.20
46.3	3.7	7.91	0.72	16.48	0.9	1.86	0.22	12.2	1.6	1.07	0.16	0.05	17.06	2.81	14.64	31.29	66.89	100.18	198.49	218.33	188.21	143.82	103.00	74.40	75.78	42.80
10.1	1.1	1.67	0.35	3.68	0.5	0.56	0.1	3.14	0.82	0.297	0.087	0.02	7.06	0.56	1.82	4.63	11.82	19.29	30.65	34.17	41.06	30.36	23.00	22.40	19.50	11.88
36.00	3.30	12.60	1.40	60.20	5.00	12.78	0.80	129.00	10.00	25.60	3.30	0.02	10.38	0.41	3.61	7.78	16.76	41.61	63.32	116.39	146.34	229.09	376.25	511.20	801.24	1024.00
66.80	8.10	20.90	2.50	91.00	12.00	20.90	3.10	212.00	19.00	39.80	4.80	0.01	15.63	0.26	3.44	12.14	42.91	70.89	111.06	191.11	271.54	380.00	568.75	836.00	1316.77	1592.00
11.91	0.86	3.44	0.20	13.67	0.68	2.76	0.27	25.20	2.80	4.55	0.59	0.00	9.10	0.27	0.85	2.67	8.38	17.68	28.24	51.67	48.41	62.55	85.44	110.40	156.52	182.00
76.60	6.30	15.50	1.40	41.40	2.10	5.27	0.56	33.50	1.90	4.84	0.82	0.02	20.39	1.61	10.70	30.66	87.84	137.50	202.51	316.67	311.38	281.82	258.75	210.80	208.07	193.60
75.80	4.80	16.80	1.60	52.10	3.10	8.48	0.66	65.60	5.50	10.20	0.91	0.00	28.06	1.43	8.69	24.35	68.24	103.57	220.10	311.11	308.13	305.45	325.63	339.20	407.45	408.00
94.90	4.60	18.10	1.40	48.60	3.00	7.52	0.45	40.00	1.70	5.37	0.50	0.03	27.98	4.74	25.89	58.55	132.43	198.21	324.12	429.44	385.77	329.09	303.75	300.80	248.45	214.80
48.40	3.40	7.92	0.25	19.50	1.50	2.48	0.29	16.40	1.50	1.86	0.33	-0.07	28.55	0.92	10.50	26.90	68.92	104.29	178.89	223.89	196.75	144.00	121.88	99.20	101.86	74.40
100.30	5.80	18.40	1.20	48.60	2.80	7.50	0.45	39.20	3.40	5.33	0.53	-0.11	28.22	3.98	21.73	47.55	104.05	188.93	327.14	371.94	407.72	334.55	303.75	300.00	243.48	213.20
55.30	4.90	10.80	1.30	29.80	2.50	3.34	0.22	21.80	1.70	2.88	0.48	-0.05	16.98	2.14	10.28	26.88	70.27	86.79	200.00	228.89	224.80	196.36	186.25	133.60	135.40	115.20
73.60	4.90	12.50	1.00	29.20	1.10	3.79	0.58	21.40	3.00	2.71	0.46	-0.04	63.46	4.52	34.14	72.04	152.03	230.36	330.65	327.78	299.19	227.27	182.50	151.60	132.92	108.40
77.90	4.00	16.90	1.80	47.30	2.30	6.71	0.71	59.00	6.20	10.04	0.87	0.04	23.33	2.10	14.44	36.43	91.89	122.32	195.98	290.00	316.67	307.27	295.63	268.40	366.46	401.60
24.10	1.20	5.02	0.38	11.90	1.30	1.51	0.23	9.60	1.10	1.27	0.04	0.02	13.93	0.39	3.65	9.83	26.42	43.39	75.88	104.44	97.97	91.27	74.38	60.40	59.63	50.96
20.8	1.4	4.8	0.3	17.02	0.94	2.13	0.23	16.34	0.66	2.92	0.35	0.04	5.56	0.12	1.90	5.54	16.15	23.57	41.21	59.17	84.55	87.27	106.38	85.20	101.49	116.80
15.55	0.72	4	0.53	11.3	1.5	1.46	0.15	10	1.4	1.61	0.27	0.04	9.05	0.09	2.36	6.32	16.89	27.50	40.70	53.33	63.21	72.73	70.63	58.40	62.11	64.40
2.54	0.56	0.484	0.092	1.61	0.27	0.257	0.068	1.09	0.34	0.191	0.071	0.01	2.58	0.11	0.34	0.95	2.64	3.16	12.46	10.00	10.33	8.80	10.06	10.28	6.77	7.64
6.43	0.85	1.53	0.22	4.1	0.6	0.61	0.14	4.15	0.47	0.397	0.089	0.04	5.06	0.09	1.20	3.15	8.24	10.18	24.62	24.28	26.14	27.82	25.63	24.40	25.78	15.88

Chondrite normalized																									
Eu	±1σ	Gd	±1σ	Tb	±1σ	Dy	±1σ	Ho	±1σ	Er	±1σ	Tm	±1σ	Yb	±1σ	Lu	±1σ	La	Ce	Pr	Nd	Pm*	Sm	Eu	Gd	Tb
58.43	0.14	395.51	3.36	75.42	0.11	506.49	2.03	102.94	0.22	302.19	0.30	37.06	0.08	249.70	10.01	32.10	0.04	2.57	446.13	34.06	124.03	302.57	738.09	1007.43	1924.64	2016.59
60.07	1.72	450.09	1.76	87.72	0.37	604.60	6.23	125.99	3.58	353.84	12.88	42.82	0.56	263.17	6.16	39.45	0.19	0.94	414.02	29.64	113.22	287.83	731.72	1035.64	2190.22	2345.57
40.64	0.34	269.50	0.35	50.13	1.01	326.33	5.06	68.54	1.10	199.41	3.91	26.80	0.42	172.75	3.63	24.41	0.14	1.04	290.63	24.50	86.71	210.40	510.53	700.60	1311.45	1340.50
40.66	0.60	292.30	0.73	57.99	1.71	402.19	5.35	83.44	0.75	255.55	6.52	34.69	0.74	228.61	3.04	31.80	0.04	0.65	256.37	18.75	73.03	185.66	472.04	701.06	1422.38	1550.67
30.79	0.48	192.50	1.16	35.95	1.19	248.29	5.24	53.55	2.40	174.96	6.70	23.01	0.48	163.59	0.08	23.47	0.34	0.22	137.04	14.43	54.86	140.95	362.14	530.80	936.76	961.12
45.57	1.43	330.33	3.60	64.20	2.51	446.88	4.74	94.51	2.18	289.03	6.33	40.15	0.51	270.02	9.72	38.02	0.01	0.76	283.02	21.02	80.84	208.62	538.40	785.62	1607.46	1716.51
42.46	0.15	288.52	0.06	54.87	0.09	365.11	7.08	76.53	0.55	228.36	5.00	30.68	0.23	201.75	1.33	28.06	0.54	0.58	330.17	20.84	81.38	205.03	516.55	732.11	1403.99	1467.18
38.08	0.29	250.52	2.48	42.84	0.83	258.07	1.45	48.24	0.69	121.37	0.35	13.57	0.34	81.99	0.39	10.38	0.09	0.75	341.28	24.64	90.12	210.59	492.07	656.48	1219.08	1145.33
43.80	0.05	295.84	4.47	51.06	0.57	314.83	0.76	58.32	0.48	146.77	1.50	17.03	0.03	98.37	1.59	12.70	0.16	1.44	362.69	27.79	99.38	234.72	554.38	755.20	1439.61	1365.27
22.86	0.35	148.53	2.58	27.10	0.50	171.62	0.65	33.41	0.43	89.20	1.75	11.71	0.07	75.00	0.75	10.66	0.05	0.45	155.90	9.81	38.67	100.93	263.39	394.13	722.76	724.64
15.53	0.40	106.68	1.72	19.88	0.25	130.09	0.60	26.16	0.52	75.30	1.38	9.99	0.38	67.53	0.03	9.82	0.16	0.74	130.90	7.08	28.01	71.54	182.73	267.80	519.11	531.59
21.20	0.11	151.29	0.64	29.06	0.08	191.84	1.52	38.06	0.24	104.54	0.95	13.46	0.01	85.83	0.39	12.33	0.10	0.22	131.32	9.96	37.13	95.31	244.60	365.56	736.21	776.94
55.48	0.00	380.02	1.25	67.17	0.91	443.39	1.86	87.55	0.60	226.81	3.67	25.94	0.03	156.24	2.67	18.49	0.15	1.30	471.39	35.03	120.85	287.34	683.23	956.47	1849.26	1796.09
3.37	0.00	23.02	0.51	4.55	0.08	30.48	0.20	6.01	0.07	15.83	0.01	1.43	0.04	12.61	0.26	1.17	0.03		25.98	1.26	6.45	16.11	40.25	58.14	112.01	121.53
7.77	0.05	48.52	0.05	9.26	0.06	58.31	0.07	11.23	0.10	29.23	0.48	3.63	0.04	24.52	0.47	3.26	0.03	0.77	57.20	5.47	17.63	40.87	94.73	134.05	236.11	247.66
5.48	0.01	35.50	0.05	6.58	0.16	42.57	0.57	8.28	0.12	20.44	0.19	2.17	0.05	14.86	0.15	1.60	0.00	0.76	33.96	4.01	12.29	28.86	67.78	94.56	172.74	175.97
3.38	0.07	22.34	0.02	4.30	0.08	28.47	0.63	5.62	0.05	14.97	0.32	1.86	0.02	13.42	0.29	1.79	0.02	2.49	25.34	3.28	7.72	17.65	40.34	58.36	108.71	115.00
4.51	0.03	30.21	0.05	5.78	0.00	38.32	0.61	7.61	0.01	19.81	0.10	2.63	0.00	16.87	0.03	2.66	0.05	0.08	28.07	2.38	8.88	21.95	54.26	77.77	147.00	154.47
4.07	0.05	26.81	0.35	5.22	0.03	35.09	0.05	6.93	0.02	18.37	0.14	2.12	0.01	15.94	0.03	2.07	0.01	0.25	29.02	2.12	7.74	19.48	49.06	70.25	130.44	139.52
3.88	0.01	27.84	0.17	5.18	0.02	35.55	0.91	7.12	0.02	18.13	0.00	bdl	bdl	16.19	0.73	bdl	bdl	2.24	29.05		6.30	17.13	46.55	66.98	135.48	138.50
3.98	0.04	28.21	0.05	5.28	0.02	35.16	0.04	5.53	0.10	21.12	0.16	2.77	0.04	17.54	0.54	2.63	0.00		24.14				55.38	71.09	141.78	146.75
2.65	0.05	18.36	0.06	3.62	0.12	24.26	0.14	5.50	0.04	16.36	0.07	2.21	0.00	14.13	0.25	2.25	0.01	0.46	15.92	1.08	4.41	12.58	35.92	47.37	92.25	100.64
6.93	0.43	43.82	3.02	5.87	0.28	24.21	0.42	3.46	0.21	7.81	0.10	1.04	0.01	6.20	0.15	1.01	0.04	0.72	10.73	3.11	11.29	33.07	96.90	123.81	220.20	163.03
5.83	0.14	39.51	0.21	5.41	0.03	24.70	0.38	4.04	0.02	9.83	0.38	1.30	0.01	7.60	0.11	1.32	0.03	0.35	20.33	3.80	13.68	35.43	91.77	104.03	198.57	150.21
2.02	0.07	13.35	0.60	2.67	0.00	18.42	0.83	4.05	0.06	12.02	0.27	1.61	0.00	9.68	0.26	1.61	0.03	0.19	6.96	0.43	2.22	7.19	23.26	36.06	67.06	74.17
4.35	0.15	27.78	0.32	3.91	0.10	19.65	0.10	3.69	0.13	9.72	0.38	1.38	0.01	7.96	0.12	1.48	0.09	0.87	23.15	2.65	9.39	24.63	64.57	77.60	139.61	108.73
2.66	0.09	17.14	0.17	2.82	0.01	17.46	0.11	3.77	0.04	10.42	0.48	1.43	0.02	9.11	0.23	1.49	0.03	0.48	13.21	1.41	4.92	13.67	38.00	47.49	86.11	78.30
1.12	0.38	7.78	3.17	1.68	0.67	11.96	4.61	2.68	0.99	8.18	3.26	1.19	0.44	7.52	3.03	1.26	0.49	0.01	5.74	0.28	1.42	4.29	12.95	20.02	39.07	46.75

3.95	0.06	29.64	0.40	5.42	0.12	35.21	0.24	7.45	0.14	22.70	0.05	3.63	0.01	25.41	0.56	4.07	0.01	0.27	31.49	2.03	8.32	21.36	54.83	68.03	144.22	144.95
3.07	0.03	24.16	0.27	4.58	0.00	29.38	1.04	6.49	0.09	19.87	0.61	2.95	0.01	22.16	0.22	3.82	0.00	1.11	29.61	1.79	6.57	17.02	44.08	52.97	117.59	122.58
3.54	0.13	25.98	0.83	4.69	0.09	29.58	0.83	6.47	0.05	19.35	0.72	3.39	0.10	21.90	0.66	4.34	0.09	3.63	29.62	3.53	8.37	20.80	51.67	63.20	130.57	130.31
1.97	0.09	15.71	0.89	3.40	0.20	25.30	1.41	6.34	0.41	22.73	1.78	3.91	0.41	26.53	1.31	5.19	0.38	0.15	20.07	0.93	4.02	10.95	29.85	35.16	78.94	94.52
2.65	0.12	19.99	0.25	4.18	0.13	28.88	0.43	7.11	0.01	23.54	0.72	3.94	0.08	27.71	0.57	5.49	0.06	0.78	25.82	1.63	4.88	13.27	36.05	47.31	100.46	116.05
3.12	0.07	22.23	0.22	4.30	0.09	28.64	0.46	6.41	0.11	20.53	0.18	3.45	0.11	23.35	0.33	4.41	0.01	6.57	36.47	5.03	8.59	19.50	44.23	55.78	111.73	119.52
2.18	0.07	17.76	0.03	3.47	0.02	25.02	0.04	6.14	0.04	20.91	0.20	3.13	0.06	26.65	0.23	4.36	0.11	2.32	31.99	2.40	5.97	13.75	31.66	37.59	86.44	92.83
													Chondrite normalized													
Dy	±1σ	Ho	±1σ	Er	±1σ	Tm	±1σ	Yb	±1σ	Lu	±1σ	La	Ce	Pr	Nd	Pm*	Sm	Eu	Gd	Tb	Dy	Ho	Er	Tm	Yb	Lu
16.7	2.4	3.41	0.46	8	2.1	1.18	0.31	6.24	0.93	0.82	0.29	0.00	6.98	0.57	1.95	5.24	14.12	23.04	47.24	64.44	67.89	62.00	50.00	47.20	38.76	32.80
4.67	0.5	0.86	0.17	2.29	0.47	0.346	0.097	1.94	0.6	0.251	0.094	0.03	1.74	-0.03	0.44	1.65	6.22	8.11	15.73	19.17	18.98	15.64	14.31	13.84	12.05	10.04
110.1	6.1	24.5	1.7	62.7	3	8.81	0.57	59.5	5.6	7.57	0.58	0.03	34.31	1.57	5.03	19.95	79.05	136.07	288.94	433.61	447.56	445.45	391.88	352.40	369.57	302.80
120	4.4	21.1	1.2	47.4	3.6	4.9	0.26	30.8	2.7	3.33	0.42	0.02	123.98	3.89	25.16	69.98	194.59	285.71	491.46	550.00	487.80	383.64	296.25	196.00	191.30	133.20
133.9	8	22.3	1.6	45.1	3.2	5.32	0.44	27.88	0.97	2.88	0.26	0.02	198.37	8.65	40.70	100.19	246.62	344.64	564.82	655.56	544.31	405.45	281.88	212.80	173.17	115.20
27.5	2.8	8.73	0.77	28.4	2.1	4.45	0.34	30.8	2.7	4.56	0.46	0.02	6.84	0.17	1.36	3.50	9.05	17.14	36.68	66.94	111.79	158.73	177.50	178.00	191.30	182.40
287	19	57.1	3.1	125.1	7.8	15.6	0.43	89.2	7.3	10.82	0.78	0.03	130.83	7.26	33.92	99.50	291.89	473.21	954.77	1230.56	1166.67	1038.18	781.88	624.00	554.04	432.80
88.6	8.3	15.91	0.99	34.7	2.4	4.42	0.35	22.7	2.6	2.51	0.41	0.04	70.96	2.85	15.97	45.76	131.08	155.36	325.13	363.89	360.16	289.27	216.88	176.80	140.99	100.40
249	14	49.8	3.4	106.2	9.1	13.43	0.92	79.7	6.2	8.83	0.35	0.05	116.48	6.11	26.26	79.70	241.89	357.14	737.19	922.22	1012.20	905.45	663.75	537.20	495.03	353.20
4.03	0.43	0.88	0.16	1.45	0.44	0.222	0.052	1.62	0.59	0.184	0.066	0.00	1.44	0.25	0.35	1.24	4.39	6.25	11.71	15.56	16.38	16.00	9.06	8.88	10.06	7.36
232	13	55.5	3.2	139.7	6.4	19.75	0.87	128	9.4	16.7	1.1	0.04	73.74	2.78	17.94	53.03	156.76	277.32	567.84	783.33	943.09	1009.09	873.13	790.00	795.03	668.00
73.6	4.5	14.5	1.2	30.1	2.4	3.68	0.47	19.7	1.4	1.93	0.29	0.04	75.37	2.73	13.59	38.57	109.46	152.50	251.26	279.72	299.19	263.64	188.13	147.20	122.36	77.20
155.4	8.1	31.9	1.5	70.8	3.9	8.5	1	51.3	4.9	5.66	0.47	0.08	246.33	7.26	35.23	97.09	267.57	333.93	593.47	572.22	631.71	580.00	442.50	340.00	318.63	226.40
101.5	9.2	25.2	2.5	66.7	6.3	10.9	1.3	77.3	8.1	10.87	0.95	0.02	43.07	1.04	9.12	26.39	76.35	111.79	254.77	380.56	412.60	458.18	416.88	436.00	480.12	434.80
106	7.1	25.2	1.6	71.9	3.9	10.3	0.61	76.3	4.8	10.88	0.66	0.00	37.36	1.23	7.26	21.63	64.39	112.86	239.70	369.44	430.89	458.18	449.38	412.00	473.91	435.20
117.5	6.6	29.4	2	83.2	6.1	12.42	0.56	88.2	4.4	11.3	1	0.03	47.96	1.69	8.49	26.13	80.41	128.57	261.81	391.67	477.64	534.55	520.00	496.80	547.83	452.00
166	10	31.2	2.8	66.5	4	8.65	0.72	51.9	3.2	4.97	0.56	0.05	231.65	9.57	45.51	112.97	280.41	375.00	656.28	722.22	674.80	567.27	415.63	346.00	322.36	198.80
90.2	4.1	19.82	0.69	50.7	2.9	8.51	0.68	55.3	3.5	6.77	0.51	0.01	57.26	1.11	9.06	28.10	87.16	136.61	274.87	322.22	366.67	360.36	316.88	340.40	343.48	270.80
130	11	30.2	2.4	75.1	4.2	9.87	0.49	72.4	5.8	8.56	0.77	0.02	84.01	3.10	18.23	50.98	142.57	207.14	424.62	500.83	528.46	549.09	469.38	394.80	449.69	342.40
20.20	1.50	3.92	0.43	9.40	1.10	1.27	0.23	7.10	1.20	1.11	0.20	-0.01	10.29	0.30	4.81	9.28	17.91	31.43	60.80	69.17	82.11	71.27	58.75	50.80	44.10	44.40
24.70	2.70	4.18	0.42	10.56	0.74	1.29	0.13	7.10	1.10	0.98	0.23	-0.13	11.09	1.13	5.69	11.80	24.46	44.64	86.43	90.00	100.41	76.00	66.00	51.60	44.10	39.20
33.30	1.20	6.04	0.73	14.40	1.60	1.64	0.20	8.20	1.30	1.20	0.15	0.01	10.51	1.78	10.20	23.03	52.03	84.29	121.61	135.56	135.37	109.82	90.00	65.60	50.93	48.00
16.90	1.30	4.24	0.59	10.98	0.65	1.01	0.12	6.58	0.58	0.83	0.11	-0.01	8.83	0.56	2.45	7.18	21.01	23.39	40.70	65.56	68.70	77.09	68.63	40.40	40.87	33.20
20.70	3.60	4.24	0.40	12.19	0.69	1.77	0.50	12.70	1.50	1.12	0.31	0.02	6.04	0.37	2.95	7.06	16.89	37.68	42.71	83.33	84.15	77.09	76.19	70.80	78.88	44.80
51.60	1.80	8.87	0.92	20.10	1.00	1.96	0.19	11.58	0.67	1.23	0.20	0.04	16.44	3.71	17.07	36.73	79.05	126.25	186.43	254.44	209.76	161.27	125.63	78.40	71.93	49.20
47.90	4.70	8.55	0.79	19.00	1.40	1.81	0.22	13.89	0.97	2.05	0.22	0.01	16.64	3.54	15.10	34.55	79.05	108.21	172.86	218.61	194.72	155.45	118.75	72.40	86.27	82.00
36.60	5.30	6.23	0.66	13.56	0.60	1.40	0.24	8.00	0.96	0.84	0.24	0.04	13.77	1.48	8.75	22.29	56.76	83.21	125.13	147.78	148.78	113.27	84.75	56.00	49.69	33.60
34.7	2.8	6.23	0.77	14.2	1.2	1.61	0.32	11	1.7	1.21	0.29	-0.07	12.54	1.45	7.83	20.06	51.35	80.89	137.69	140.83	141.06	113.27	88.75	64.40	68.32	48.40
60.7	3.8	12.15	0.67	28	2	3.91	0.36	24.8	2.9	3.22	0.46	-0.14	16.64	2.08	14.22	33.96	81.08	121.43	242.21	240.56	246.75	220.91	175.00	156.40	154.04	128.80
21	2.2	4.15	0.42	7.67	0.85	1.11	0.14	7.45	0.81	0.84	0.14	-0.13	10.51	0.81	4.79	11.94	29.73	38.75	83.42	90.00	85.37	75.45	47.94	44.40	46.27	33.60
22.7	1.2	4.3	0.61	9.24	0.7	1.07	0.16	7.5	1.3	0.81	0.22	-0.22	11.26	0.41	3.11	7.98	20.47	39.46	68.84	80.56	92.28	78.18	57.75	42.80	46.58	32.40
6.5	1.1	1.56	0.3	4.24	0.85	0.531	0.084	2.91	0.62	0.4	0.12	0.27	6.05	0.19	1.14	3.36	9.93	13.04	29.05	26.11	26.42	28.36	26.50	21.24	18.07	16.00
19	1.6	3.54	0.42	7.38	0.74	0.89	0.14	5.65	0.8	0.8	0.17	0.24	9.90	1.20	4.11	9.42	21.55	40.00	69.85	74.44	77.24	64.36	46.13	35.60	35.09	32.00
15.1	2.5	3.02	0.49	7.5	1.4	0.78	0.19	5.9	1.1	0.63	0.21	0.06	5.94	0.53	2.39	6.87	19.80	30.18	52.26	61.67	61.38	54.91	46.88	31.20	36.65	25.20
54.9	4	11.58	0.62	22.3	1.6	3.13	0.25	18.66	0.84	1.81	0.21	0.05	15.40	1.19	12.32	29.56	70.95	125.36	206.03	231.67	223.17	210.55	139.38	125.20	115.90	72.40
47.4	3	8.73	0.9	18.1	2.3	2.24	0.22	11.57	0.78	1.48	0.24	0.01	15.25	1.70	10.98	25.41	58.78	98.04	182.41	215.56	192.68	158.73	113.13	89.60	71.86	59.20
41.2	2	7.71	0.81	14.9	1.5	1.65	0.25	11.7	1.1	1.26	0.15	0.04	23.16	1.71	10.92	24.86	56.62	95.00	184.42	199.17	167.48	140.18	93.13	66.00	72.67	50.40
48.7	1.6	8.3	0.81	16.4	1.5	2.1	0.25	9.48	0.98	1.1	0.15	0.03	31.81	1.88	13.76	33.68	82.43	118.04	199.50	221.67	197.97	150.91	102.50	84.00	58.88	44.00
25.1	2.1	4.67	0.39	11.5	1.4	1.4	0.21	9.9	1.4	0.98	0.23	0.11	11.16	1.16	7.33	16.80	38.51	50.18	89.45	121.11	102.03	84.91	71.88	56.00	61.49	39.20
34.3	2	6.16	0.76	12.46	0.93	1.56	0.26	10.3	1	1.22	0.32	0.01	12.54	0.95	6.87	17.60	45.07	74.64	121.61	137.50	139.43	112.00	77.88	62.40	63.98	48.80
61	2.2	11.07	0.56	27.7	1.5	3.15	0.32	21.2	1.8	2.53	0.39	0.17	17.70	1.92	12.56	31.38	78.38	113.04	237.19	281.67	247.97	201.27	173.13	126.00	131.68	101.20
38.8	1.8	7.27	0.68	13.69	0.91	1.67	0.17	8.44	0.76	1.01	0.15	0.03	27.57	1.05	10.57	26.95	68.72	97.32	168.34	191.94	157.72	132.18	85.56	66.80	52.42	40.40
66.2	6	11.15	0.93	22.7	1.5	2.5	0.37	17.5	2	1.74	0.4	0.03	50.57	4.12	26.91	63.82	151.35	182.32	301.51	357.50	269.11	202.73	141.88	100.00	108.70	69.60
20	2.6	3.55	0.48	7.58	0.74	1.25	0.26	7.51	0.6	1	0.14	0.04	10.67	0.63	6.78	16.25	38.92	49.11	89.45	91.94	81.30	64.55	47.38	50.00	46.65	40.00
15.9	2.2	2.8	0.24	7	1.1	0.86	0.15	4.8	0.59	0.62	0.15	0.03	7.88	0.39	2.80	7.81	21.76	29.29	60.30	66.39	64.63	50.91	43.75	34.40	29.81	24.80
28.6	2.1	5.69	0.29	13.12	0.88	1.67	0.27	10.99	0.84	1.41	0.22	0.01	13.07	0.33	3.89	10.55	28.58	46.07	85.43	115.83	116.26	103.45	82.00	66.80	68.26	56.40
8.4	1.1	1.61	0.28	3.49	0.59	0.36	0.11	2.31	0.95	0.26	0.061	0.02	7.57	0.38	1.93	5.20	14.05	20.00	27.69	39.17	34.15	29.27	21.81	14.40	14.35	10.40
16.6	2.3	2.99	0.41	6.53	0.87	0.94	0.1	4.55	0.69	0.589	0.091	0.02	9.77	0.99	3.89	9.23	21.89	31.07	56.28	62.78	67.48	54.36	40.81	37.60	28.26	23.56
27.51	0.82	5.3	0.49	11.35	0.81	1.4	0.19	10.9	1.5	1.27	0.28	0.01	9.56	1.28	4.95	13.05	34.46	44.46	77.89	107.22	111.83	96.36	70.94	56.00	67.70	50.80
104.50	8.50	37.30	4.60	202.00	10.00	44.90	4.20	466.00	35.00	99.00	12.00	0.36	11.75	1.72	6.04	11.95	23.65	31.96	72.86	202.78	424.80	678.18	1262.50	1796.00	2894.41	3960.00
37.30	2.30	6.70	0.42	15.20	1.50	1.81	0.31	9.95	0.51	1.26	0.16	-0.06	10.34	1.88	12.91	26.08	52.70	85.00	120.10	149.17	151.63	121.82	95.00	72.40	61.80	50.40
18.70	1.80	3.33	0.39	7.35	0.70	0.73	0.13	5.17	0.71	0.47	0.18	0.08	6.13	0.59	2.43	6.81	19.12	39.64	54.27	69.17	76.02	60.55	45.94	29.20	32.11	18.80
51.40	4.90	10.30	1.50	25.10	2.30	2.94	0.31	21.30	2.70	2.56	0.38	-0.32	17.31	2.17	15.40	32.42	68.24	117.32	191.96	236.39	208.94	187.27	156.88	117.60	132.30	102.40
19.30	1.90	3.83	0.24	8.80	1.30	1.00	0.13	7.60	1.50	0.99	0.13	0.17	9.46	0.82	3.76	8.95	21.28	31.79	61.81	77.78	78.46	69.64	55.00	40.00	47.20	39.60
17.40	4.20	2.83	0.74	6.70	2.10	0.82	0.16	4.30	1.60	0.53	0.09	0.13	10.60	1.24	5.36	10.93	22.30	30.54	44.72	66.94	70.73	51.45	41.88	32.80	26.71	21.16
25.60	3.00	4.11	0.23	8.90	1.40	1.00	0.13	5.24	0.81	0.75	0.21	0.05	9.09	1.51	8.32	20.31	49.59	65.89	89.45	124.72	104.07	74.73	55.63	40.00	32.55	30.00
36.10	4.20	6.35	0.58	13.08	0.69	1.50	0.17	8.80	1.20	0.93	0.28	0.03	22.84	1.78	10.28	26.36	67.57	88.93	143.22	175.00	146.75	115.45	81.75	60.00	54.66	37.20
22.70	1.50	4.28	0.39	10.30	1.20	1.24	0.17	6.95	0.92	0.97	0.12	-0.01	9.58	0.71	4.03	11.44	32.50	48.39	66.33	92.22	92.28	77.82	64.38	49.60	43.17	38.80
39.2	2.5	7.55	0.86	14.2	1.5	1.71	0.42	8.85	0.78	0.94	0.14	0.23	15.95	2.09	11.12	27.80	69.53	108.21	176.88	179.72	159.35	137.27	88.75	68.40	54.97	37.60
14.2	1.5	2.66	0.3	5.45	0.82	0.64	0.15	3.97	0.6	0.33	0.11	0.01	10.67	0.35	3.15	8.05	20.54	31.43	45.73	58.61	57.72	48.36	34.06	25.60	24.66	13.20
60.4	4.1	12.09	0.79	22.6	2.3	2.34	0.29	14.9	2	1.47	0.3	0.08	48.61	2.94	24.73	59.65	143.92	174.46	296.48	284.72	245.53	219.82	141.25	93.60	92.55	58.80
30.8	1.7	6.2	0.39	12.7	1	1.786	0.086	10.64	0.91	1.18	0.14	0.02	11.26	1.38	7.24	16.99	39.86	61.43	117.59	140.28	125.20	112.73	79.38	71.44	66.09	47.20
46.3	3.7	7.91	0.72	16.48	0.9	1.86	0.22	12.2	1.6	1.07	0.16	0.05	17.06	2.81	14.64	31.29	66.89	100.18	198.49	218.33	188.21	143.82	103.00	74.40	75.78	42.80
10.1	1.1	1.67	0.35	3.68	0.5	0.56	0.1	3.14	0.82	0.297	0.087	0.02	7.06	0.56	1.82	4.63	11.82	19.29	30.65	34.17	41.06	30.36	23.00	22.40	19.50	11.88
17.30	1.40	4.88	0.64	20.10	2.30	3.96	0.39	42.10	3.90	8.01	0.53	-0.01	9.46	0.20	1.42	4.14	12.03	23.75	39.70	63.06	70.33	88.73	125.63	158.40	261.49	320.40
37.80	3.70	12.00	1.00	54.50	3.30	11.20	1.20	111.00	11.00	23.50	1.50	0.02	10.77	0.38	3.85	8.75	19.86	43.75	72.96	118.06	153.66	218.18	340.63	448.00	689.44	940.00
58.80	3.40	11.20	0.65	31.10	1.30	4.08	0.49	27.00	2.60	3.03	0.36	0.01	16.18	1.29	11.16	29.56	78.31	111.43	178.89	237.22	239.02	203.64	194.38	163.20	167.70	121.20
12.00	1.70	2.78	0.25	9.30	1.30	1.57	0.34	11.70	1.20	2.01	0.26	0.01	7.91	0.44	1.55	4.39	12.43	24.11	35.18	51.94	48.78	50.55	58.13	62.80	72.67	80.40
42.60	2.80	7.99	0.65	19.90	2.00	2.55	0.34	16.80	1.20	2.26	0.41	0.01	9.61	1.09	7.37	20.34	56.08	81.61	152.76	192.50	173.17	145.27	124.38	102.00	104.35	90.40
33.40	1.50	7.12	0.61	22.70	1.50	3.57	0.37	22.70	2.30	3.78	0.46	0.04	21.86	1.13	5.71	17.13	51.35	70.71	109.55	130.00	135.77	129.45	141.88	142.80	140.99	151.20
36.50	1.60	7.65	0.67	21.02	0.96	3.02	0.17	15.80	0.93	2.11	0.16	0.01	12.10	0.81	6.35	16.82	44.59	69.11	118.59	168.33	148.37	139.09	131.38	120.80	98.14	84.40

25.80	2.30	6.08	0.58	20.10	1.90	3.55	0.29	29.70	1.30	5.63	0.41	-0.01	12.41	0.54	3.52	8.82	22.09	36.07	64.82	91.67	104.88	110.55	125.63	142.00	184.47	225.20
15.03	0.66	2.97	0.22	7.94	0.75	1.28	0.18	7.22	0.89	0.88	0.21	-0.02	11.79	0.48	1.62	4.41	12.03	38.75	47.74	63.61	61.10	54.00	49.63	51.20	44.84	35.20
93.50	5.20	16.86	0.83	50.70	2.80	6.83	0.45	39.30	3.80	4.86	0.43	0.11	23.54	3.44	21.01	43.94	91.89	154.29	282.91	331.67	380.08	306.55	316.88	273.20	244.10	194.40
46.90	3.40	10.45	0.71	28.40	1.20	4.17	0.41	29.30	2.00	4.21	0.26	0.06	15.19	1.31	10.28	25.65	63.99	105.71	166.33	195.56	190.65	190.00	177.50	166.80	181.99	168.40
52.60	3.60	8.96	0.59	23.60	2.70	2.89	0.34	14.20	1.70	1.92	0.23	-0.05	40.13	2.98	12.30	33.62	91.89	129.64	232.66	223.89	213.82	162.91	147.50	115.60	88.20	76.80
45.80	5.00	9.52	0.36	21.40	1.40	3.08	0.19	17.58	0.51	2.42	0.36	0.01	12.90	1.92	10.85	25.97	62.16	105.36	173.87	194.72	186.18	173.09	133.75	123.20	109.19	96.80
78.50	5.40	12.97	0.65	25.70	3.40	2.77	0.50	16.00	2.50	2.04	0.38	-0.01	66.56	5.48	29.98	70.01	163.51	246.43	374.87	394.44	319.11	235.82	160.63	110.80	99.38	81.60
52.10	4.10	8.14	0.84	16.30	3.20	1.82	0.36	11.80	2.00	1.23	0.06	0.00	27.90	1.69	12.91	36.17	101.35	151.79	226.63	221.39	211.79	148.00	101.88	72.80	73.29	49.36
44.40	4.90	9.72	0.98	19.80	1.70	2.60	0.31	18.90	2.60	3.06	0.32	-0.02	12.40	1.09	7.88	19.16	46.62	71.07	152.76	197.22	180.49	176.73	123.75	104.00	117.39	122.40
48.70	4.40	10.80	1.00	27.60	1.70	3.32	0.29	22.90	1.30	2.94	0.27	-0.01	14.54	1.14	8.32	18.95	43.18	61.43	119.60	173.33	197.97	196.36	172.50	132.80	142.24	117.60
37.80	2.40	7.60	0.71	20.40	1.50	2.93	0.40	21.20	1.90	3.88	0.20	-0.01	12.40	0.88	5.27	16.35	50.68	61.43	99.50	138.33	153.66	138.18	127.50	117.20	131.68	155.20
46.70	3.90	9.60	1.10	23.60	2.80	2.36	0.26	16.40	1.70	1.84	0.28	0.00	10.20	1.27	7.13	20.94	61.49	86.07	137.69	187.50	189.84	174.55	147.50	94.40	101.86	73.60
27.50	1.70	4.70	0.37	14.40	2.10	1.94	0.17	15.10	1.90	2.56	0.18	-0.01	15.94	0.94	3.46	11.23	36.49	41.79	68.84	99.17	111.79	85.45	90.00	77.60	93.79	102.40
52.20	2.40	10.74	0.78	26.30	2.20	3.18	0.26	21.10	2.00	2.88	0.28	0.22	16.10	2.78	12.25	30.32	75.00	86.43	151.76	208.89	212.20	195.27	164.38	127.20	131.06	115.20
48.50	4.70	9.50	1.10	17.80	1.20	1.86	0.22	11.80	1.30	1.43	0.21	0.01	21.83	1.80	10.28	27.77	75.00	90.89	157.79	217.22	197.15	172.73	111.25	74.40	73.29	57.20
69.40	5.50	13.70	1.60	34.00	3.50	3.83	0.25	24.50	3.20	2.58	0.32	0.05	20.07	2.42	15.93	42.01	110.81	120.36	208.04	257.22	282.11	249.09	212.50	153.20	152.17	103.20
7.19	0.99	1.47	0.16	4.03	0.59	0.53	0.07	3.16	0.72	0.48	0.18	0.02	7.86	0.19	1.07	3.78	13.31	17.14	28.04	22.22	29.23	26.73	25.19	21.08	19.63	19.20
43.00	1.80	8.84	0.99	23.50	2.40	2.70	0.26	18.50	1.30	2.49	0.27	0.02	13.33	1.00	7.16	22.96	73.65	75.89	147.74	195.28	174.80	160.73	146.88	108.00	114.91	99.60
83.40	5.70	19.00	1.20	52.40	2.50	7.09	0.80	55.10	3.90	8.47	0.50	0.06	46.36	2.57	17.31	47.01	127.70	150.36	285.93	361.11	339.02	345.45	327.50	283.60	342.24	338.80
40.50	4.20	7.57	0.39	19.60	1.50	2.36	0.11	16.90	1.50	2.38	0.28	-0.04	13.26	1.57	6.56	21.99	73.65	77.86	137.69	168.89	164.63	137.64	122.50	94.40	104.97	95.20
33.70	1.70	5.68	0.50	14.20	1.40	1.68	0.17	10.90	1.40	1.17	0.22	0.03	22.02	1.44	6.11	17.82	52.03	63.39	118.04	133.89	136.99	103.27	88.75	67.20	67.70	46.80
29.90	3.00	5.83	0.57	15.60	2.00	2.08	0.21	15.20	1.90	2.10	0.21	-0.04	11.17	1.47	6.94	17.98	46.62	56.43	104.02	123.33	121.54	106.00	97.50	83.20	94.41	84.00
45.10	3.70	6.90	0.72	14.70	1.70	1.69	0.34	8.20	0.64	1.06	0.27	0.09	11.14	2.28	10.81	28.34	74.32	82.68	162.31	187.50	183.33	125.45	91.88	67.60	50.93	42.40
37.50	3.50	10.00	0.75	38.20	3.10	7.40	0.63	75.20	7.40	14.60	1.80	-0.02	10.24	0.62	2.43	8.89	32.57	39.46	82.41	112.50	152.44	181.82	238.75	296.00	467.08	584.00
94.00	11.00	16.30	1.00	35.00	2.00	3.83	0.46	27.60	2.00	3.64	0.50	-0.01	80.59	7.31	37.42	96.46	248.65	267.86	487.94	491.67	382.11	296.36	218.75	153.20	171.43	145.60
47.70	3.00	9.30	1.00	20.50	1.90	2.46	0.33	16.30	1.60	2.07	0.23	0.05	14.58	3.23	12.54	34.19	93.24	95.54	207.04	204.72	193.90	169.09	128.13	98.40	101.24	82.80
60.20	5.20	13.00	1.80	32.90	2.00	4.43	0.54	25.50	2.50	4.20	0.64	0.06	17.62	2.66	11.60	31.92	87.84	106.43	201.01	241.67	244.72	236.36	205.63	177.20	158.39	168.00
40.10	3.60	7.87	0.53	17.90	2.00	2.52	0.21	18.20	1.60	3.04	0.39	0.04	10.46	2.05	7.59	20.76	56.76	66.25	139.20	172.50	163.01	143.09	111.88	100.80	113.04	121.60
59.70	3.40	12.81	0.95	32.90	1.20	4.54	0.46	29.70	2.80	4.43	0.51	0.04	16.51	5.59	15.49	37.73	91.89	109.82	197.99	261.67	242.68	232.91	205.63	181.60	184.47	177.20
94.80	6.50	16.81	0.94	37.00	2.10	5.01	0.42	31.80	2.40	4.93	0.46	0.08	96.25	10.11	36.76	92.71	233.78	252.50	492.46	525.00	385.37	305.64	231.25	200.40	197.52	197.20
36.00	3.30	12.60	1.40	60.20	5.00	12.78	0.80	129.00	10.00	25.60	3.30	0.02	10.38	0.41	3.61	7.78	16.76	41.61	63.32	116.39	146.34	229.09	376.25	511.20	801.24	1024.00
66.80	8.10	20.90	2.50	91.00	12.00	20.90	3.10	212.00	19.00	39.80	4.80	0.01	15.63	0.26	3.44	12.14	42.91	70.89	111.06	191.11	271.54	380.00	568.75	836.00	1316.77	1592.00
11.91	0.86	3.44	0.20	13.67	0.68	2.76	0.27	25.20	2.80	4.55	0.59	0.00	9.10	0.27	0.85	2.67	8.38	17.68	28.24	51.67	48.41	62.55	85.44	110.40	156.52	182.00
76.60	6.30	15.50	1.40	41.40	2.10	5.27	0.56	33.50	1.90	4.84	0.82	0.02	20.39	1.61	10.70	30.66	87.84	137.50	202.51	316.67	311.38	281.82	258.75	210.80	208.07	193.60
75.80	4.80	16.80	1.60	52.10	3.10	8.48	0.66	65.60	5.50	10.20	0.91	0.00	28.06	1.43	8.69	24.35	68.24	103.57	220.10	311.11	308.13	305.45	325.63	339.20	407.45	408.00
94.90	4.60	18.10	1.40	48.60	3.00	7.52	0.45	40.00	1.70	5.37	0.50	0.03	27.98	4.74	25.89	58.55	132.43	198.21	324.12	429.44	385.77	329.09	303.75	300.80	248.45	214.80
48.40	3.40	7.92	0.25	19.50	1.50	2.48	0.29	16.40	1.50	1.86	0.33	-0.07	28.55	0.92	10.50	26.90	68.92	104.29	178.89	223.89	196.75	144.00	121.88	99.20	101.86	74.40
100.30	5.80	18.40	1.20	48.60	2.80	7.50	0.45	39.20	3.40	5.33	0.53	-0.11	28.22	3.98	21.73	47.55	104.05	188.93	327.14	371.94	407.72	334.55	303.75	300.00	243.48	213.20
55.30	4.90	10.80	1.30	29.80	2.50	3.34	0.22	21.80	1.70	2.88	0.48	-0.05	16.98	2.14	10.28	26.88	70.27	86.79	200.00	228.89	224.80	196.36	186.25	133.60	135.40	115.20
73.60	4.90	12.50	1.00	29.20	1.10	3.79	0.58	21.40	3.00	2.71	0.46	-0.04	63.46	4.52	34.14	72.04	152.03	230.36	330.65	327.78	299.19	227.27	182.50	151.60	132.92	108.40
77.90	4.00	16.90	1.80	47.30	2.30	6.71	0.71	59.00	6.20	10.04	0.87	0.04	23.33	2.10	14.44	36.43	91.89	122.32	195.98	290.00	316.67	307.27	295.63	268.40	366.46	401.60
24.10	1.20	5.02	0.38	11.90	1.30	1.51	0.23	9.60	1.10	1.27	0.04	0.02	13.93	0.39	3.65	9.83	26.42	43.39	75.88	104.44	97.97	91.27	74.38	60.40	59.63	50.96
15.2	1.4	3.69	0.3	10.5	1.1	1.65	0.29	10.29	0.83	1.55	0.27	0.10	7.36	0.46	1.25	4.35	15.20	21.07	48.24	47.22	61.79	67.09	65.63	66.00	63.91	62.00
4.79	0.37	1.15	0.19	3.32	0.67	0.468	0.062	2.5	0.52	0.5	0.11	0.01	4.00	0.00	0.90	1.89	3.99	7.04	13.77	16.39	19.47	20.91	20.75	18.72	15.53	20.00
20.8	1.4	4.8	0.3	17.02	0.94	2.13	0.23	16.34	0.66	2.92	0.35	0.04	5.56	0.12	1.90	5.54	16.15	23.57	41.21	59.17	84.55	87.27	106.38	85.20	101.49	116.80
15.55	0.72	4	0.53	11.3	1.5	1.46	0.15	10	1.4	1.61	0.27	0.04	9.05	0.09	2.36	6.32	16.89	27.50	40.70	53.33	63.21	72.73	70.63	58.40	62.11	64.40
2.54	0.56	0.484	0.092	1.61	0.27	0.257	0.068	1.09	0.34	0.191	0.071	0.01	2.58	0.11	0.34	0.95	2.64	3.16	12.46	10.00	10.33	8.80	10.06	10.28	6.77	7.64
6.43	0.85	1.53	0.22	4.1	0.6	0.61	0.14	4.15	0.47	0.397	0.089	0.04	5.06	0.09	1.20	3.15	8.24	10.18	24.62	24.28	26.14	27.82	25.63	24.40	25.78	15.88

Lu_N/Gd_N	Eu/Eu*	Zr/Hf	Lu/Hf	Y/Hf	sum MREE–HREE abs. (ppm)	Th/U	$^{206}Pb/^{238}U$ (Th) date (Ma)	±2σ	Ti	±1σ
1.71	0.80	0	0.0012	0.081	363.13	0.34	4.59	0.11	20.5	5.5
1.82	0.91	0	0.0011	0.076	367.90	0.33	4.44	0.11	15.1	3.7
1.73	0.89	0	0.0012	0.084	415.42	0.35	4.50	0.11	21.2	5
0.30	0.87	0	0.0005	0.092	506.82	0.93	4.57	0.08	104	11
0.99	0.88	0	0.0006	0.049	305.25	0.39	4.53	0.08	32.4	5.4
0.81	0.84	0	0.0009	0.095	440.26	0.56	4.47	0.09	38	4.6
0.42	1.07	0	0.0002	0.029	106.25	0.41	4.70	0.22	18	6.2
0.35	1.23	0	0.0001	0.013	51.26	0.41	5.04	0.43	16.3	5.9
0.53	1.03	0	0.0003	0.045	166.88	0.46	4.60	0.19	19.3	3.9
0.64	0.88	0	0.0001	0.014	58.40	0.43	5.33	0.43	11.2	2.4
0.47	0.97	0	0.0001	0.012	45.60	0.68	4.33	0.37	6.1	1.6
0.34	0.99	0	0.0001	0.019	71.58	0.47	4.85	0.40	12.8	3.8
0.26	0.90	0	0.0001	0.027	106.54	0.54	4.65	0.20	38.1	6.2
0.58	1.04	0	0.0001	0.017	65.67	0.37	5.27	0.40	19.3	3.7
0.21	0.98	0	0.0001	0.031	120.18	0.47	4.84	0.18	20.6	5.7
0.29	1.03	0	0.0000	0.010	40.22	0.43	4.94	0.24	28	4.6
0.20	0.84	0	0.0002	0.047	192.82	0.73	4.69	0.11	66	10
0.40	0.90	0	0.0002	0.026	95.20	0.39	4.56	0.26	20.4	4.5
0.22	0.87	0	0.0002	0.036	138.79	0.47	4.68	0.18	25.9	5.5
0.39	1.01	0	0.0000	0.006	27.86	0.27	5.15	0.55	13.9	5.2
16.17	1.28	0	0.0023	0.034	295.30	0.30	4.74	0.18	13.1	3.6
14.34	1.03	0	0.0037	0.058	484.35	0.29	4.24	0.15	9.8	1.8
6.44	1.15	0	0.0004	0.010	70.00	0.26	4.23	0.15	7.7	2.1
0.96	1.03	0	0.0006	0.075	236.51	0.35	4.28	0.13	30.1	6
1.85	0.85	0	0.0012	0.068	289.78	0.24	4.31	0.12	25.9	3.5
0.66	0.96	0	0.0007	0.077	305.55	0.38	4.31	0.08	20.1	3.1
0.42	0.94	0	0.0002	0.029	146.06	0.53	4.29	0.12	33.2	3.8
0.65	1.02	0	0.0007	0.085	308.40	0.44	4.24	0.11	23	5.4
0.58	0.73	0	0.0003	0.049	176.82	0.36	4.19	0.18	23.2	4.2
0.33	1.03	0	0.0003	0.049	233.70	0.69	4.26	0.09	67	9.5
2.05	0.91	0	0.0012	0.062	274.14	0.37	4.35	0.20	11.6	2.4
0.67	0.97	0	0.0001	0.017	74.69	0.25	4.29	0.17	11.5	3.6
2.83	0.91	0	0.0002	0.012	75.66	0.10	3.12	0.08	9.4	3.9
1.58	1.05	0	0.0002	0.011	55.48	0.12	2.81	0.08	9.1	2.6
0.61	0.55	0	0.0000	0.002	9.19	0.19	3.46	0.33	4.7	3.6
0.64	0.71	0	0.0000	0.005	23.56	0.17	3.13	0.14	9.3	3.4

Dy	Ho	Er	Tm	Yb	Lu	Lu_N/Gd_N	Eu/Eu*	Zr/Hf	Lu/Hf	Y/Hf	sum MREE–HREE abs. (ppm)	Th/U	$^{206}Pb/^{238}U$ (Th) date (Ma)	±2σ
1994.07	1818.70	1825.93	1453.39	1468.84	1263.96	0.66	0.85	47.99	0.0032	0.459	1759.86	0.53	4.63	0.029
2380.30	2226.03	2138.01	1679.16	1548.08	1553.01	0.71	0.82	51.70	0.0042	0.590	2027.75	0.49	4.62	0.016
1284.76	1210.89	1204.91	1050.98	1016.17	961.03	0.73	0.86	44.45	0.0022	0.263	1178.51	0.59	4.61	0.018
1583.42	1474.17	1544.12	1360.59	1344.78	1252.11	0.88	0.86	47.68	0.0031	0.364	1427.25	0.46	4.60	0.016
977.51	946.15	1057.17	902.28	962.30	924.21	0.99	0.91	36.17	0.0018	0.178	946.11	0.38	4.61	0.012
1759.36	1669.71	1746.38	1574.57	1588.32	1496.95	0.93	0.84	48.00	0.0038	0.411	1618.70	0.45	4.60	0.014
1437.44	1352.16	1379.82	1203.16	1186.76	1104.53	0.79	0.86	49.18	0.0029	0.330	1316.34	0.59	4.63	0.019
1016.04	852.36	733.33	532.17	482.31	408.83	0.34	0.85	49.33	0.0011	0.214	865.06	0.66	4.59	0.019
1239.47	1030.41	886.83	667.75	578.66	500.19	0.35	0.85	47.46	0.0012	0.247	1038.73	0.63	4.62	0.018
675.66	590.20	538.97	459.15	441.18	419.84	0.58	0.90	36.51	0.0008	0.109	590.08	0.44	4.61	0.013
512.18	462.13	454.99	391.60	397.26	386.47	0.74	0.87	38.43	0.0008	0.089	460.98	0.41	4.59	0.013
755.27	672.48	631.69	527.75	504.89	485.26	0.66	0.86	40.82	0.0010	0.135	647.61	0.39	4.58	0.012
1745.62	1546.86	1370.43	1017.11	919.03	728.02	0.39	0.85	40.80	0.0016	0.319	1461.08	0.70	4.62	0.020
120.01	106.21	95.68	55.93	74.17	46.18	0.41	0.87	42.95	0.0001	0.025	98.47	0.28	4.34	0.055
229.55	198.42	176.60	142.52	144.26	128.48	0.54	0.90	43.35	0.0003	0.044	195.74	0.34	4.30	0.014
167.59	146.22	123.51	84.96	87.40	62.81	0.36	0.87	48.39	0.0002	0.038	137.47	0.41	4.33	0.022
112.09	99.21	90.47	72.97	78.94	70.55	0.65	0.88	40.76	0.0002	0.022	96.16	0.30	4.34	0.017
150.88	134.48	119.69	103.31	99.26	104.70	0.71	0.87	43.89	0.0002	0.031	128.41	0.31	4.33	0.018
138.15	122.50	111.00	83.33	93.77	81.61	0.63	0.88	42.05	0.0002	0.027	116.63	0.39	4.38	0.065
139.97	125.83	109.54		95.22		0.70	0.84	40.46	-	0.027	113.90	0.38	4.34	0.057
142.91	100.50	132.02	110.78	108.96	105.26	0.74	0.80	43.33	0.0002	0.031	122.23	0.09	2.87	0.0094
98.61	99.93	102.24	88.46	87.75	89.86	0.97	0.82	41.52	0.0002	0.021	89.33	-0.06	2.84	0.014
98.41	62.88	48.83	41.78	38.49	40.48	0.18	0.85	45.14	0.0001	0.014	100.36	0.59	2.65	0.030
100.40	73.51	61.41	52.18	47.22	52.89	0.27	0.77	44.54	0.0001	0.017	99.55	0.46	2.86	0.055
74.88	73.60	75.15	64.37	60.11	64.27	0.96	0.91	41.10	0.0001	0.015	65.42	0.05	2.85	0.015
79.87	67.14	60.76	55.18	49.42	59.12	0.42	0.82	41.80	0.0001	0.015	79.92	0.29	2.86	0.055
70.99	68.57	65.12	57.11	56.56	59.44	0.69	0.83	43.83	0.0001	0.016	66.29	0.26	2.87	0.076
48.60	48.72	51.10	47.44	46.73	50.51	1.29	0.89	52.61	0.0001	0.017	43.36	0.08	2.86	0.007

138.60	131.69	137.16	142.53	149.47	160.07	1.11	0.77	48.80	0.0004	0.034	137.47	0.27	2.66	0.057
115.68	114.75	120.04	115.77	130.35	150.42	1.28	0.74	46.94	0.0004	0.027	116.50	-0.01	2.62	0.057
120.23	117.58	120.92	135.76	136.03	173.77	1.33	0.77	46.47	0.0004	0.030	119.24	0.50	2.77	0.12
102.85	115.31	142.06	156.49	164.79	207.51	2.63	0.72	45.77	0.0005	0.027	111.08	0.48	2.75	0.076
117.38	129.30	147.14	157.59	172.09	219.64	2.19	0.79	46.90	0.0005	0.031	123.49	0.29	2.70	0.10
116.42	116.50	128.33	138.16	145.04	176.50	1.58	0.79	45.47	0.0004	0.029	116.46	0.49	2.72	0.11
98.52	108.42	126.36	122.63	156.74	171.66	1.99	0.72	46.70	0.0004	0.027	109.62	0.39	2.74	0.026

Lu_N/Gd_N	Eu/Eu*	Zr/Hf	Lu/Hf	Y/Hf	sum MREE–HREE abs. (ppm)	Th/U	$^{206}Pb/^{238}U$ (Th) date (Ma)	±2σ	Ti	±2σ
0.69	0.89	0	0.0001	0.006	49.36	0.05	4.53	0.09	4.3	1.2
0.64	0.82	0	0.0000	0.002	14.63	0.01	4.57	0.09	2.3	3.3
1.05	0.90	0	0.0006	0.058	353.91	0.15	4.53	0.08	37.9	4.6
0.27	0.92	0	0.0003	0.055	361.13	0.52	4.45	0.08	71.6	4.9
0.20	0.92	0	0.0003	0.066	392.68	0.81	4.56	0.08	88.8	6.8
4.97	0.94	0	0.0006	0.034	115.11	0.04	4.53	0.10	6.1	1.8
0.45	0.90	0	0.0013	0.210	845.62	0.55	4.50	0.09	67.5	3.2
0.31	0.75	0	0.0003	0.053	255.34	0.50	4.70	0.10	32.8	6.5
0.48	0.85	0	0.0011	0.175	706.86	0.51	4.55	0.09	57.1	6.3
0.63	0.87	0	0.0000	0.002	11.63	0.00	4.50	0.10	2.7	2.2
1.18	0.93	0	0.0017	0.163	748.38	0.41	4.54	0.08	40.6	6.3
0.31	0.92	0	0.0003	0.058	212.12	0.51	4.81	0.10	41.7	8.4
0.38	0.84	0	0.0006	0.104	480.96	0.99	4.68	0.08	108	15
1.71	0.80	0	0.0012	0.081	363.13	0.34	4.59	0.11	20.5	5.5
1.82	0.91	0	0.0011	0.076	367.90	0.33	4.44	0.11	15.1	3.7
1.73	0.89	0	0.0012	0.084	415.42	0.35	4.50	0.11	21.2	5
0.30	0.87	0	0.0005	0.092	506.82	0.93	4.57	0.08	104	11
0.99	0.88	0	0.0006	0.049	305.25	0.39	4.53	0.08	32.4	5.4
0.81	0.84	0	0.0009	0.095	440.26	0.56	4.47	0.09	38	4.6
0.73	0.95	0	0.0002	0.018	59.35	0.32	4.89	0.38	14.4	4.5
0.45	0.97	0	0.0001	0.020	71.75	0.43	4.33	0.30	9.9	3.5
0.39	1.06	0	0.0001	0.022	98.58	0.59	4.51	0.42	17.2	3.6
0.82	0.80	0	0.0001	0.017	52.31	0.36	5.14	0.28	21.3	5
1.05	1.40	0	0.0001	0.016	66.33	0.32	5.54	0.33	13.2	3.9
0.26	1.04	0	0.0002	0.043	148.67	0.47	4.81	0.17	16.4	2.3
0.47	0.93	0	0.0003	0.034	141.53	0.46	4.67	0.21	16.9	3.6
0.27	0.99	0	0.0001	0.025	101.51	0.44	4.95	0.31	23.2	3.1
0.35	0.96	0	0.0002	0.026	105.95	0.41	5.01	0.28	28.1	4.9
0.53	0.87	0	0.0004	0.051	196.44	0.47	4.75	0.17	22.8	6
0.40	0.78	0	0.0001	0.018	64.23	0.38	4.74	0.21	16	3.2
0.47	1.05	0	0.0001	0.019	64.43	0.31	4.71	0.25	20.1	4.5
0.55	0.77	0	0.0000	0.006	23.591	0.34	4.69	0.64	10.9	5.4
0.46	1.03	0	0.0001	0.014	56.08	0.45	4.85	0.26	15.7	5.2
0.48	0.94	0	0.0001	0.011	47.24	0.43	4.89	0.45	15.1	2.8
0.35	1.04	0	0.0002	0.043	168.74	0.45	4.57	0.18	26.4	5.2
0.32	0.95	0	0.0002	0.034	139.07	0.41	4.71	0.17	31.2	5.4
0.27	0.93	0	0.0002	0.028	127.61	0.53	4.63	0.16	18.8	5.3
0.22	0.92	0	0.0001	0.031	140.37	0.60	4.86	0.12	31.5	6.8
0.44	0.85	0	0.0001	0.020	78.52	0.44	4.65	0.30	13.4	5
0.40	1.01	0	0.0001	0.024	99.33	0.41	4.97	0.27	19.6	4.5
0.43	0.83	0	0.0003	0.050	190.32	0.46	4.78	0.14	23.7	4.3
0.24	0.90	0	0.0001	0.026	116.74	0.59	4.99	0.13	33.2	6.5
0.23	0.85	0	0.0002	0.043	204.87	0.80	4.57	0.12	73.8	6.8
0.45	0.83	0	0.0001	0.016	64.75	0.52	5.84	0.29	24.4	3.6
0.41	0.81	0	0.0001	0.011	48.01	0.35	5.48	0.43	16	4.7
0.66	0.93	0	0.0002	0.023	85.23	0.38	5.25	0.27	24.7	4.8
0.38	1.01	0	0.0000	0.007	24.47	0.30	4.97	0.49	11.2	2.5
0.42	0.89	0	0.0001	0.012	47.40	0.56	4.66	0.34	10.7	3.1
0.65	0.86	0	0.0002	0.021	79.58	0.41	5.03	0.36	18.2	3.6
54.35	0.77	0	0.0068	0.079	977.29	0.33	36.40	1.00	3.2	3.2
0.42	1.07	0	0.0002	0.029	106.25	0.41	4.70	0.22	18	6.2
0.35	1.23	0	0.0001	0.013	51.26	0.41	5.04	0.43	16.3	5.9
0.53	1.03	0	0.0003	0.045	166.88	0.46	4.60	0.19	19.3	3.9
0.64	0.88	0	0.0001	0.014	58.40	0.43	5.33	0.43	11.2	2.4
0.47	0.97	0	0.0001	0.012	45.60	0.68	4.33	0.37	6.1	1.6
0.34	0.99	0	0.0001	0.019	71.58	0.47	4.85	0.40	12.8	3.8
0.26	0.90	0	0.0001	0.027	106.54	0.54	4.65	0.20	38.1	6.2
0.58	1.04	0	0.0001	0.017	65.67	0.37	5.27	0.40	19.3	3.7
0.21	0.98	0	0.0001	0.031	120.18	0.47	4.84	0.18	20.6	5.7
0.29	1.03	0	0.0000	0.010	40.22	0.43	4.94	0.24	28	4.6
0.20	0.84	0	0.0002	0.047	192.82	0.73	4.69	0.11	66	10
0.40	0.90	0	0.0002	0.026	95.20	0.39	4.56	0.26	20.4	4.5
0.22	0.87	0	0.0002	0.036	138.79	0.47	4.68	0.18	25.9	5.5
0.39	1.01	0	0.0000	0.006	27.86	0.27	5.15	0.55	13.9	5.2
8.07	1.09	0	0.0007	0.015	107.85	0.23	4.27	0.13	11.4	2.9
12.88	1.15	0	0.0021	0.034	271.22	0.24	4.33	0.15	14.2	3.6
0.68	0.94	0	0.0003	0.046	185.59	0.34	4.66	0.17	24.3	2.9
2.29	1.15	0	0.0002	0.010	49.58	0.21	4.38	0.19	7.8	2.8
0.59	0.88	0	0.0003	0.033	134.00	0.34	4.16	0.27	20.9	4
1.38	0.94	0	0.0003	0.023	123.71	0.35	4.82	0.19	21.3	4.4
0.71	0.95	0	0.0003	0.034	119.63	0.32	4.33	0.20	11.4	2.5

3.47	0.95	0	0.0005	0.019	109.08	0.26	4.77	0.17	11.4	2.8
0.74	1.62	0	0.0001	0.013	49.28	0.21	4.60	0.21	9.5	3.7
0.69	0.96	0	0.0005	0.067	288.93	0.32	4.18	0.12	22.9	3.7
1.01	1.02	0	0.0005	0.044	169.49	0.38	4.19	0.15	26	3.7
0.33	0.89	0	0.0002	0.036	165.79	0.55	4.29	0.12	39.3	4.7
0.56	1.01	0	0.0003	0.038	147.31	0.50	4.31	0.23	23	7.7
0.22	1.00	0	0.0002	0.043	240.58	0.72	4.25	0.11	79	18
0.22	1.00	0	0.0001	0.030	152.96	0.55	4.39	0.14	33.7	5.1
0.80	0.84	0	0.0003	0.033	139.96	0.34	4.19	0.20	22.5	8
0.98	0.85	0	0.0003	0.038	149.74	0.23	4.26	0.14	20	2.4
1.56	0.87	0	0.0004	0.027	122.03	0.33	4.39	0.22	12.9	2.8
0.53	0.94	0	0.0002	0.031	139.47	0.38	4.64	0.21	12.5	3
1.49	0.83	0	0.0003	0.015	85.81	0.40	4.12	0.17	14.4	3.1
0.76	0.81	0	0.0003	0.037	158.96	0.39	4.31	0.18	13	3.2
0.36	0.84	0	0.0002	0.028	135.20	0.43	4.34	0.15	20.4	3.8
0.50	0.79	0	0.0003	0.045	205.41	0.43	4.79	0.18	19.7	5.1
0.68	0.89	0	0.0001	0.005	24.20	0.20	4.44	0.27	7.6	3.2
0.67	0.73	0	0.0003	0.034	139.71	0.28	4.23	0.19	20.3	3.3
1.18	0.79	0	0.0010	0.062	303.78	0.51	4.09	0.15	25.7	5.6
0.69	0.77	0	0.0003	0.032	127.15	0.27	4.27	0.16	12.4	2.3
0.40	0.81	0	0.0001	0.022	99.19	0.34	4.31	0.12	12.7	4.5
0.81	0.81	0	0.0002	0.021	99.01	0.41	4.37	0.19	11.1	2.7
0.26	0.75	0	0.0001	0.027	121.33	0.39	4.47	0.23	12.2	4.2
7.09	0.76	0	0.0014	0.028	205.56	0.24	4.32	0.18	12	1.9
0.30	0.77	0	0.0004	0.059	310.17	0.77	4.33	0.12	66.6	5.9
0.40	0.69	0	0.0003	0.035	152.25	0.35	4.27	0.18	10.2	3.3
0.84	0.80	0	0.0006	0.051	194.89	0.35	4.49	0.13	23.6	4.2
0.87	0.75	0	0.0003	0.026	127.25	0.30	4.60	0.22	13.5	2.5
0.89	0.81	0	0.0005	0.046	199.05	0.31	4.55	0.15	11.3	2.6
0.40	0.74	0	0.0006	0.058	321.39	0.74	4.25	0.13	57.6	6.2
16.17	1.28	0	0.0023	0.034	295.30	0.30	4.74	0.18	13.1	3.6
14.34	1.03	0	0.0037	0.058	484.35	0.29	4.24	0.15	9.8	1.8
6.44	1.15	0	0.0004	0.010	70.00	0.26	4.23	0.15	7.7	2.1
0.96	1.03	0	0.0006	0.075	236.51	0.35	4.28	0.13	30.1	6
1.85	0.85	0	0.0012	0.068	289.78	0.24	4.31	0.12	25.9	3.5
0.66	0.96	0	0.0007	0.077	305.55	0.38	4.31	0.08	20.1	3.1
0.42	0.94	0	0.0002	0.029	146.06	0.53	4.29	0.12	33.2	3.8
0.65	1.02	0	0.0007	0.085	308.40	0.44	4.24	0.11	23	5.4
0.58	0.73	0	0.0003	0.049	176.82	0.36	4.19	0.18	23.2	4.2
0.33	1.03	0	0.0003	0.049	233.70	0.69	4.26	0.09	67	9.5
2.05	0.91	0	0.0012	0.062	274.14	0.37	4.35	0.20	11.6	2.4
0.67	0.97	0	0.0001	0.017	74.69	0.25	4.29	0.17	11.5	3.6
1.29	0.78	0	0.0002	0.012	55.36	0.16	2.85	0.09	8.3	2.9
1.45	0.95	0	0.0000	0.003	16.45	0.07	2.81	0.07	6.2	3.2
2.83	0.91	0	0.0002	0.012	75.66	0.10	3.12	0.08	9.4	3.9
1.58	1.05	0	0.0002	0.011	55.48	0.12	2.81	0.08	9.1	2.6
0.61	0.55	0	0.0000	0.002	9.19	0.19	3.46	0.33	4.7	3.6
0.64	0.71	0	0.0000	0.005	23.56	0.17	3.13	0.14	9.3	3.4

Table 5

Zircon solution ICP-MS trace-element data for host gneiss and crystallized melt from Oiatabu Dome, Fergusson Island

Zircons analyzed by ID-TIMS-TEA	Zr	±1σ	Hf	±1σ	Sc	±1σ	Y	±1σ	Nb	±1σ	Ta	±1σ	La	±1σ	Ce	±1σ
Fergusson Island: Oitabu Dome, PNG12-85a, host orthogneiss																
PNG12-85a z1	475227	9219	14891	171	nr	nr	4489	41	41.8	0.5	79.8	1.8	3.8	0.2	29.2	1.8
PNG12-85a z2	477974	6548	14347	63	nr	nr	3106	37	45.8	1.4	101.8	0.6	1.5	0.0	23.5	0.4
PNG12-85a z3	480229	624	13740	137	nr	nr	2218	43	63.2	1.7	12.0	0.2	15.1	0.1	46.1	1.8
PNG12-85a z4	476073	6665	15272	43	nr	nr	3710	93	28.6	0.5	68.3	0.6	3.2	0.0	20.6	0.0
PNG12-85a z5	474797	3751	14814	27	nr	nr	4848	15	24.5	0.0	108.6	0.2	0.2	0.0	16.0	0.3
PNG12-85a z6	474744	10065	16294	119	nr	nr	3892	6	17.2	0.4	62.1	0.4	bdl	bdl	10.0	0.8
PNG12-85a z8	473946	758	14491	123	nr	nr	5728	36	36.0	0.3	76.1	1.3	bdl	bdl	28.7	1.5
PNG12-85a z9	475072	4228	14313	16	nr	nr	5109	100	30.1	0.1	81.4	0.5	0.1	0.1	19.0	0.0
PNG12-85a z10	475865	3712	16268	111	nr	nr	3191	42	54.9	0.7	50.0	0.2	bdl	bdl	16.6	0.1
PNG12-85a z11	478933	9339	15314	270	nr	nr	2352	190	2.99	0.02	0.94	0.01	1.1	0.0	21.1	1.1
PNG12-85a z12	474620	2705	12377	114	nr	nr	7151	105	16.97	0.01	70.7	0.2	0.1	0.0	30.9	0.5
PNG12-85a z13	480915	1683	12703	191	nr	nr	2469	34	11.5	0.1	31.9	0.4	0.0	0.0	7.7	0.0
PNG12-85a z14	478473	10239	12839	365	nr	nr	4002	89	16.1	0.5	56.9	1.0	0.7	0.0	22.6	0.6
PNG12-85a z15	477965	191	14463	42	nr	nr	3233	43	12.26	0.04	50.9	0.4	1.9	0.1	17.7	0.2
Fergusson Island: Oitabu Dome, PNG12-87a, host orthogneiss																
PNG-12-87a z1	482456	661	12115	28	379.80	6.92	1851	20	bdl	bdl	bdl	bdl	bdl	bdl	31.7	0.1
PNG-12-87a z2	479120	4305	12510	59	552.05	21.15	3795	2	bdl	bdl	bdl	bdl	5.1	0.0	96.3	3.4
Fergusson Island: Oitabu Dome, PNG12-87b, granodiorite dike																
PNG12-87b z1	473153	9463	20984	212	nr	nr	2558	32	10.4	0.2	2.9	0.04	0.4	0.01	2.1	0.1
PNG12-87b z2	474061	95	20013	78	nr	nr	2036	15	520.2	2.2	156.7	4.4	1.0	0.003	25.1	0.0
PNG12-87b z3	474254	10860	22391	710	nr	nr	648	31	4.4	0.1	0.6	0.03	0.5	0.01	1.7	0.1
PNG12-87b z4	472805	9172	22833	23	nr	nr	1422	89	14.8	0.6	4.5	0.04	0.3	0.02	0.8	0.0
PNG12-87b z5	444683	1680	47446	259	718.98	10.96	3063	46	97.2	0.5	75.7	0.3	1.1	0.03	13.9	0.0
PNG12-87b z6	482445	9745	14099	147	nr	nr	752	13	1.5	0.1	0.7	0.002	1.2	0.03	13.6	0.1
PNG12-87b z7	469680	1456	22306	62	nr	nr	3354	60	380.9	4.0	146.8	1.4	1.6	0.1	8.5	1.8
Fergusson Island: Oitabu Dome, PNG12-92a, host orthogneiss																
PNG12-92a z1	481902	2313	12643	29	nr	nr	2139	9	4.3	0.2	0.6	0.04	0.2	0.02	33.8	0.5
PNG12-92a z2	483379	2659	12182	121	nr	nr	1433	15	4.6	0.1	0.8	0.004	0.5	0.1	27.6	0.1
PNG12-92a z3	483176	4204	12437	78	nr	nr	1383	2	5.0	0.1	0.7	0.1	0.1	0.005	27.3	0.7
PNG12-92a z4	482044	11617	12737	203	nr	nr	1997	27	13.1	0.7	1.6	0.02	bdl	bdl	24.0	2.9
Fergusson Island: Oitabu Dome, PNG12-92b, granodiorite dike																
PNG12-92b z1	482379	4004	10172	12	nr	nr	3487	7	2.9	0.3	1.1	0.1	5.1	0.2	37.6	4.0
PNG12-92b z2	474243	4410	9754	29	nr	nr	9571	618	7.1	0.3	1.4	0.004	2.3	0.1	124.6	12.7
PNG12-92b z3	479820	30565	10098	713	nr	nr	5382	264	4.9	0.6	1.0	0.01	3.2	0.1	47.3	1.5
PNG12-92b z4	482309	707	13410	124	593.19	71.79	867	26	bdl	bdl	bdl	bdl	70.8	0.03	174.6	1.1
PNG12-92b z5	461085	8346	14713	508	nr	nr	16161	1002	17.8	1.4	7.6	0.02	3.5	0.4	24.3	1.0
PNG12-92b z6	462897	28052	17971	643	nr	nr	12528	1042	18.6	0.1	10.4	0.7	1.8	0.3	21.4	1.9
PNG12-92b z8	472831	1040	16788	42	nr	nr	5269	48	312.3	3.3	57.9	2.6	24.0	1.0	44.5	2.9
PNG12-92b z9	455217	1821	20945	31	nr	nr	16080	24	25.9	0.3	7.7	0.01	0.04	0.1	10.8	0.0

Pr	±1σ	Nd	±1σ	Sm	±1σ	Eu	±1σ	Gd	±1σ	Tb	±1σ	Dy	±1σ	Ho	±1σ	Er	±1σ
0.4	0.1	2.5	0.7	5.3	0.0	0.9	0.2	29.8	1.7	12.9	0.3	195.0	12.8	92.5	0.3	543.2	15.8
0.1	0.0	bdl	bdl	3.7	0.6	0.7	0.1	19.6	1.6	8.7	0.8	132.6	7.0	58.1	2.9	354.8	6.3
1.9	0.2	bdl	bdl	5.8	0.9	2.3	0.7	12.7	3.2	5.3	0.8	94.0	14.6	37.4	4.0	255.6	0.2
0.2	0.0	bdl	bdl	1.8	0.1	1.0	0.1	14.2	0.7	9.6	0.7	155.3	0.9	77.1	1.1	463.9	4.3
bdl	bdl	bdl	bdl	4.4	0.7	1.1	0.1	38.4	1.3	16.6	0.1	250.0	0.1	105.7	0.0	590.9	5.6
bdl	bdl	bdl	bdl	2.2	0.7	0.9	0.1	18.6	1.5	10.1	0.0	172.7	5.7	81.6	0.7	491.9	14.5
bdl	bdl	bdl	bdl	6.1	2.0	1.4	0.0	44.2	0.8	18.1	0.0	264.8	7.5	119.7	0.8	667.2	8.7
bdl	bdl	bdl	bdl	5.5	0.1	1.5	0.4	45.0	1.4	17.1	0.3	237.2	2.3	105.4	2.5	597.4	5.7
bdl	bdl	bdl	bdl	2.2	0.8	1.0	0.0	19.9	2.6	8.7	1.0	135.6	5.0	66.1	0.3	403.3	7.3
0.7	0.1	5.9	0.5	12.8	0.4	6.5	0.2	60.6	2.4	17.0	0.4	163.9	4.6	52.2	1.4	225.7	1.7
0.3	0.1	7.4	1.2	20.1	1.0	3.7	0.1	126.3	2.5	40.1	0.4	453.8	4.0	165.6	1.6	766.2	8.6
bdl	bdl	0.5	0.1	4.1	0.3	0.7	0.1	28.6	1.5	10.1	0.4	138.6	3.4	55.6	1.1	295.5	2.6
bdl	bdl	bdl	bdl	6.5	0.3	1.2	0.0	42.2	1.2	15.0	0.4	208.2	11.0	84.9	0.4	467.8	7.4
0.4	0.0	2.5	0.4	5.5	0.4	1.6	0.2	35.0	1.6	12.4	0.2	166.7	1.4	69.3	1.3	382.5	2.1
bdl	bdl	bdl	bdl	9.4	0.4	3.8	0.2	47.0	1.1	12.6	0.3	125.3	0.6	24.8	0.1	181.1	3.2
bdl	bdl	bdl	bdl	17.9	0.3	5.6	0.3	94.9	0.5	25.7	0.1	253.4	1.2	bdl	bdl	379.3	15.8
bdl	bdl	0.1	0.0	1.1	0.0	0.8	0.1	12.9	0.1	7.7	0.0	117.9	1.0	46.8	0.1	223.9	0.9
0.5	0.0	7.9	0.1	23.6	0.2	12.4	0.2	100.7	5.7	23.5	0.7	172.4	1.2	40.6	0.4	141.1	3.3
0.1	0.0	0.2	0.1	0.2	0.1	0.2	0.0	0.5	0.1	0.6	0.1	15.8	1.4	10.3	0.1	68.6	3.7
bdl	bdl	bdl	bdl	0.1	0.0	0.3	0.0	1.4	0.1	1.5	0.1	39.6	2.9	22.1	1.2	134.3	8.2
bdl	bdl	bdl	bdl	81.0	0.1	67.9	0.1	144.8	1.0	24.6	0.9	163.1	2.7	bdl	bdl	218.6	2.2
0.2	0.1	4.2	0.0	14.3	0.4	7.1	0.3	50.3	0.8	9.3	0.4	62.5	4.7	14.5	0.5	51.2	1.1
bdl	bdl	bdl	bdl	4.1	0.1	3.7	0.0	5.8	1.2	2.3	0.3	56.5	2.3	56.5	2.0	346.2	11.3
bdl	bdl	1.1	0.3	7.4	0.5	2.5	0.3	41.5	1.4	12.7	0.2	130.8	0.0	44.7	1.6	203.4	0.9
bdl	bdl	0.9	0.0	5.9	0.6	2.2	0.4	29.7	0.3	8.4	0.1	85.8	1.3	28.7	0.3	132.8	4.5
bdl	bdl	bdl	bdl	5.5	0.5	1.7	0.1	25.7	2.0	7.8	0.2	80.1	0.0	28.5	1.4	131.8	2.1
bdl	bdl	bdl	bdl	6.5	0.7	2.8	0.5	33.2	1.3	10.3	0.8	113.4	9.9	40.3	0.2	179.8	11.0
bdl	bdl	bdl	bdl	12.4	0.3	2.3	0.1	55.2	0.3	17.1	1.6	194.7	1.4	78.3	8.9	341.3	0.6
1.1	0.1	25.8	1.8	63.9	6.2	31.4	0.1	311.1	14.3	83.4	6.0	755.9	58.1	229.8	16.9	891.8	57.8
0.6	0.0	8.8	2.0	26.9	2.0	13.8	0.7	137.5	1.4	38.5	1.4	380.5	34.9	127.9	6.2	532.0	27.6
bdl	bdl	bdl	bdl	8.2	2.0	2.5	0.5	13.4	5.8	7.6	0.0	62.5	3.2	bdl	bdl	51.8	1.0
bdl	bdl	bdl	bdl	50.9	4.9	41.7	1.4	376.0	8.2	134.6	5.4	1342.5	25.9	372.4	22.9	1339.4	82.0
bdl	bdl	1.2	0.4	36.3	3.7	31.6	1.2	299.4	20.7	101.3	9.0	1013.9	72.0	277.4	19.7	982.5	65.6
2.3	0.8	bdl	bdl	13.2	1.5	3.8	0.9	25.2	2.8	13.2	0.8	194.9	22.6	105.2	4.1	557.4	3.9
bdl	bdl	bdl	bdl	30.5	2.1	29.1	0.7	323.7	1.9	127.1	1.6	1303.2	25.5	364.7	4.8	1296.2	10.1

Tm	±1σ	Yb	±1σ	Lu	±1σ
140.5	0.2	1524.2	30.3	337.8	4.7
99.2	0.1	1118.8	20.4	250.1	4.1
69.4	0.8	667.5	16.4	171.0	3.0
123.3	2.1	1327.4	7.0	296.7	7.7
148.8	2.6	1559.2	22.8	323.8	1.9
132.7	2.3	1414.0	4.4	301.8	2.6
163.2	3.0	1688.8	27.9	366.5	2.7
150.1	6.8	1518.5	17.3	343.0	2.9
110.1	2.1	1193.3	27.3	260.9	2.1
43.8	1.0	364.9	7.8	66.4	1.3
155.4	0.3	1371.4	8.6	269.5	3.4
71.7	0.3	746.2	5.4	155.5	2.2
109.0	3.2	1079.2	22.9	222.8	4.6
92.0	0.9	937.9	0.5	197.4	1.0
35.0	0.2	309.5	4.3	63.3	0.1
71.2	2.3	601.4	3.9	115.4	2.0
46.7	0.3	407.6	0.8	69.1	0.1
27.7	1.3	236.3	5.1	46.4	0.8
18.1	0.7	193.1	8.5	37.9	1.5
31.1	1.4	285.4	16.1	50.1	2.6
60.5	1.1	650.5	5.7	107.8	0.8
10.6	0.0	89.9	2.4	18.5	1.7
105.0	3.1	976.0	57.3	212.2	3.5
41.8	0.0	362.0	3.4	76.1	0.6
28.4	0.9	243.1	1.7	53.0	0.0
28.7	0.5	254.0	1.5	53.1	0.9
40.8	1.9	327.5	12.8	75.5	1.0
76.9	6.5	645.7	20.3	138.0	1.4
156.7	10.8	1181.7	74.4	209.1	15.2
97.7	3.5	781.2	26.1	144.3	5.8
8.6	0.3	55.1	1.2	11.2	0.7
218.1	6.6	1528.9	46.8	229.3	15.6
164.5	15.7	1119.6	101.9	170.5	10.4
126.3	2.3	1085.3	69.2	192.2	3.0
211.1	2.4	1468.3	40.2	206.3	0.8

Chondrite normalized

La	Ce	Pr	Nd	Pm*	Sm	Eu	Gd	Tb	Dy	Ho	Er	Tm	Yb	Lu	Lu_N/Gd_N	Eu/Eu*	Zr/Hf
15.84	47.61	4.81	5.46	13.94	35.60	16.67	149.52	358.27	792.80	1681.50	3394.78	5620.52	9467.10	13512.05	90.37	0.23	31.91
6.30	38.37	0.77	bdl	-	25.02	11.94	98.26	241.15	538.97	1056.57	2217.40	3966.39	6949.24	10005.41	101.83	0.24	33.32
63.65	75.27	19.93	bdl	-	39.32	41.36	63.70	147.74	381.93	680.27	1597.29	2775.26	4145.73	6841.04	107.40	0.83	34.95
13.31	33.62	2.25	bdl	-	12.37	18.50	71.33	267.40	631.17	1401.68	2899.57	4931.65	8244.58	11866.08	166.36	0.62	31.17
0.76	26.17	bdl	bdl	-	29.90	20.24	192.98	460.56	1016.15	1922.39	3692.97	5952.10	9684.62	12951.45	67.11	0.27	32.05
bdl	16.26	bdl	bdl	-	15.00	15.33	93.49	281.61	702.22	1484.26	3074.59	5308.52	8782.60	12070.59	129.11	0.41	29.14
bdl	46.80	bdl	bdl	-	41.35	24.84	222.05	502.59	1076.43	2176.36	4169.96	6527.05	10489.63	14659.83	66.02	0.26	32.71
0.34	30.93	bdl	bdl	-	37.48	26.16	226.32	475.56	964.04	1916.72	3733.95	6002.12	9431.79	13719.16	60.62	0.28	33.19
bdl	27.06	bdl	bdl	-	15.04	17.44	100.09	241.74	551.35	1202.71	2520.77	4403.15	7411.73	10434.42	104.25	0.45	29.25
4.66	34.39	7.93	12.99	33.57	86.77	116.76	304.39	471.01	666.19	949.22	1410.69	1750.86	2266.53	2657.87	8.73	0.72	31.27
0.62	50.49	3.53	16.27	47.04	135.99	65.33	634.46	1113.98	1844.91	3011.09	4788.68	6214.98	8517.90	10779.97	16.99	0.22	38.35
0.16	12.62	bdl	1.16	5.69	27.81	11.76	143.78	279.89	563.58	1010.66	1847.13	2867.14	4634.54	6220.14	43.26	0.19	37.86
2.94	36.82	bdl	bdl	-	44.15	20.69	211.92	415.77	846.26	1543.99	2923.74	4360.02	6703.36	8913.24	42.06	0.21	37.27
8.08	28.79	4.00	5.41	14.18	37.20	27.92	175.86	344.72	677.57	1259.74	2390.89	3679.61	5825.37	7894.01	44.89	0.35	33.05
bdl	51.72	bdl	bdl	-	63.55	67.90	236.03	349.86	509.43	451.69	1132.00	1398.77	1922.56	2531.24	10.72	0.55	39.82
21.73	157.02	bdl	bdl	-	120.71	99.79	476.64	714.83	1030.23	bdl	2370.93	2849.57	3735.67	4617.43	9.69	0.42	38.30
1.59	3.36	bdl	0.21	1.22	7.28	15.13	64.62	213.46	479.14	850.32	1399.58	1867.27	2531.90	2762.14	42.75	0.70	22.55
4.17	40.94	5.27	17.37	52.66	159.69	220.98	505.96	652.26	700.71	738.16	881.95	1107.76	1467.84	1856.50	3.67	0.78	23.69
1.91	2.73	0.82	0.46	0.74	1.17	3.78	2.63	15.35	64.25	187.96	428.65	725.13	1199.16	1517.33	577.83	2.15	21.18
1.15	1.25	bdl	bdl	-	0.84	4.50	7.09	42.70	160.94	401.97	839.09	1245.90	1772.62	2005.41	282.85	1.84	20.71
4.66	22.73	bdl	bdl	-	547.17	1213.34	727.89	684.20	663.17	bdl	1366.02	2419.63	4040.63	4312.00	5.92	1.92	9.37
5.23	22.16	2.32	9.16	29.70	96.37	126.02	252.98	258.48	253.99	263.83	319.74	423.49	558.55	740.05	2.93	0.81	34.22
6.91	13.87	bdl	bdl	-	27.41	66.08	28.97	65.24	229.85	1028.05	2163.94	4198.89	6062.06	8487.44	293.00	2.35	21.06
0.79	55.19	bdl	2.47	11.11	50.04	43.83	208.51	351.41	531.75	811.99	1271.47	1670.09	2248.48	3044.22	14.60	0.43	38.12
1.93	45.10	bdl	1.89	8.67	39.81	39.89	149.35	233.58	348.62	522.18	829.76	1137.91	1509.99	2120.53	14.20	0.52	39.68
0.34	44.53	bdl	bdl	-	37.25	30.05	129.33	217.54	325.81	518.94	823.81	1146.16	1577.36	2123.43	16.42	0.43	38.85
bdl	39.23	bdl	bdl	-	44.00	49.51	167.00	285.03	461.09	731.88	1123.98	1632.40	2034.37	3021.10	18.09	0.58	37.85
21.42	61.30	bdl	bdl	-	83.85	40.91	277.18	475.17	791.38	1424.47	2133.03	3077.81	4010.38	5518.83	19.91	0.27	47.42
9.58	203.21	11.91	56.43	156.15	432.07	561.52	1563.49	2316.44	3072.80	4177.53	5573.67	6268.35	7340.02	8364.84	5.35	0.68	48.62
13.56	77.13	6.03	19.31	59.29	182.06	245.97	691.03	1070.60	1546.55	2324.76	3325.11	3908.09	4852.44	5770.09	8.35	0.69	47.52
298.59	284.85	bdl	bdl	-	55.48	45.43	67.46	211.81	253.88	bdl	323.51	345.59	342.39	446.43	6.62	0.74	35.97
14.83	39.64	bdl	bdl	-	343.60	745.48	1889.39	3738.75	5457.20	6770.66	8371.48	8723.56	9496.13	9170.85	4.85	0.93	31.34
7.59	34.89	bdl	2.57	25.13	245.28	563.78	1504.54	2813.45	4121.42	5043.05	6140.55	6580.41	6953.80	6820.66	4.53	0.93	25.76
101.35	72.66	24.47	bdl	-	89.12	68.48	126.85	367.57	792.12	1912.45	3483.76	5050.20	6740.76	7686.56	60.60	0.64	28.16
0.16	17.69	bdl	bdl	-	205.89	520.28	1626.74	3531.35	5297.39	6630.44	8101.20	8442.27	9120.10	8251.37	5.07	0.90	21.73

Lu/Hf	Y/Hf	sum MREE–HREE abs. (ppm)	Th/U	$^{206}Pb/^{238}U$ (Th) date (Ma)	±2σ
0.0227	0.301	2876.78	0.26	8.11	0.035
0.0174	0.217	2042.51	0.28	10.30	0.052
0.0124	0.161	1315.12	0.16	5.52	0.038
0.0194	0.243	2468.47	0.02	9.47	0.088
0.0219	0.327	3034.51	0.34	7.61	0.019
0.0185	0.239	2624.39	0.19	5.77	0.014
0.0253	0.395	3333.87	0.30	10.72	0.027
0.0240	0.357	3015.18	0.34	9.55	0.027
0.0160	0.196	2198.93	0.21	7.20	0.016
0.0043	0.154	1001.00	0.52	18.15	0.013
0.0218	0.578	3351.92	0.84	27.20	0.059
0.0122	0.194	1502.46	0.32	12.45	0.023
0.0174	0.312	2230.27	0.35	11.58	0.019
0.0136	0.224	1894.70	0.27	8.63	0.011
0.0052	0.153	802.43	0.59	71.88	0.40
0.0092	0.303	1547.08	0.77	83.58	0.57
0.0033	0.122	933.33	0.03	2.93	0.014
0.0023	0.102	801.06	0.18	2.93	0.014
0.0017	0.029	345.14	0.00	2.93	0.0023
0.0022	0.062	565.83	0.01	2.94	0.0056
0.0023	0.065	1437.96	0.00	3.01	0.0033
0.0013	0.053	313.87	0.25	3.01	0.12
0.0095	0.150	1764.28	0.07	3.02	0.060
0.0060	0.169	915.37	0.60	89.94	0.18
0.0044	0.118	612.17	0.66	56.41	0.23
0.0043	0.111	611.45	0.61	77.25	0.26
0.0059	0.157	823.66	0.57	79.00	0.68
0.0136	0.343	1549.45	0.70	88.91	1.13
0.0214	0.981	3851.00	0.89	4.81	0.071
0.0143	0.533	2253.36	0.53	4.79	0.071
0.0008	0.065	212.73	-0.17	5.56	0.23
0.0156	1.098	5582.86	0.11	3.02	0.0069
0.0095	0.697	4160.57	0.09	3.04	0.0037
0.0114	0.314	2303.44	-0.25	2.97	0.080
0.0098	0.768	5329.69	0.06	3.02	0.0024

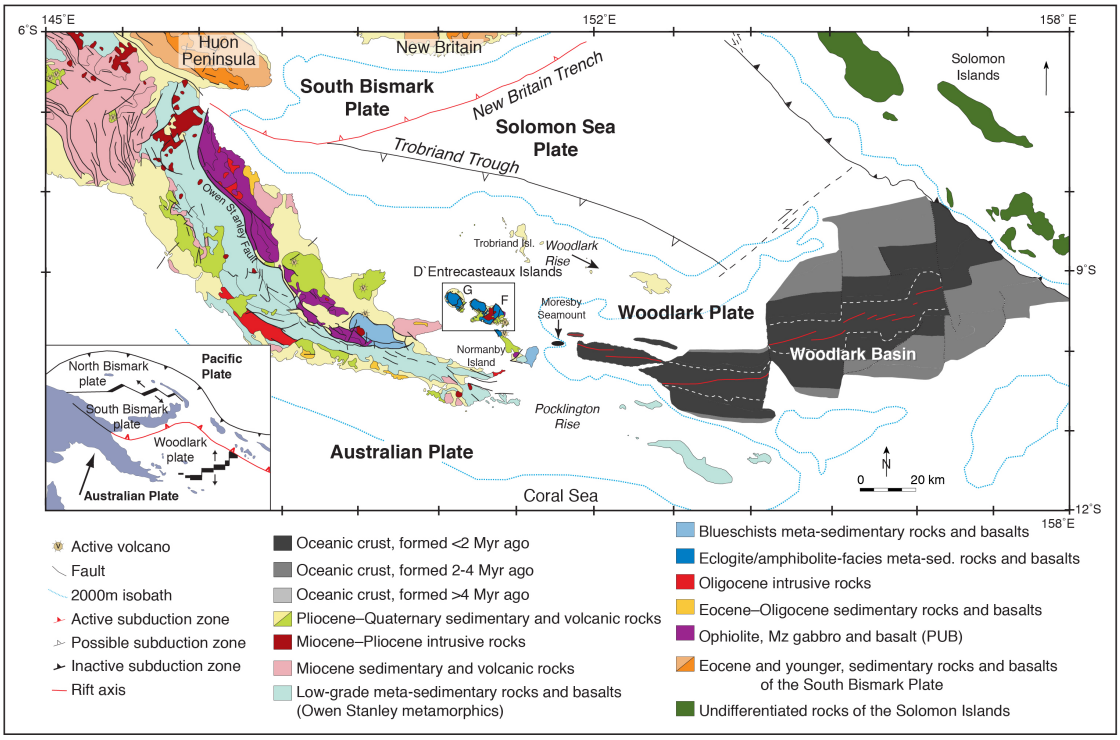

Figure 4.1: Simplified geological map of Eastern Papua New Guinea and the Woodlark Basin showing distribution of major structures and lithologies (after Baldwin et al., 2004). Box and outlined area indicate the location of the D'Entrecasteaux Islands (Figure 2) west of the Woodlark Rift. Lower left inset shows plate-tectonic setting of the region (after Wallace et al., 2004).

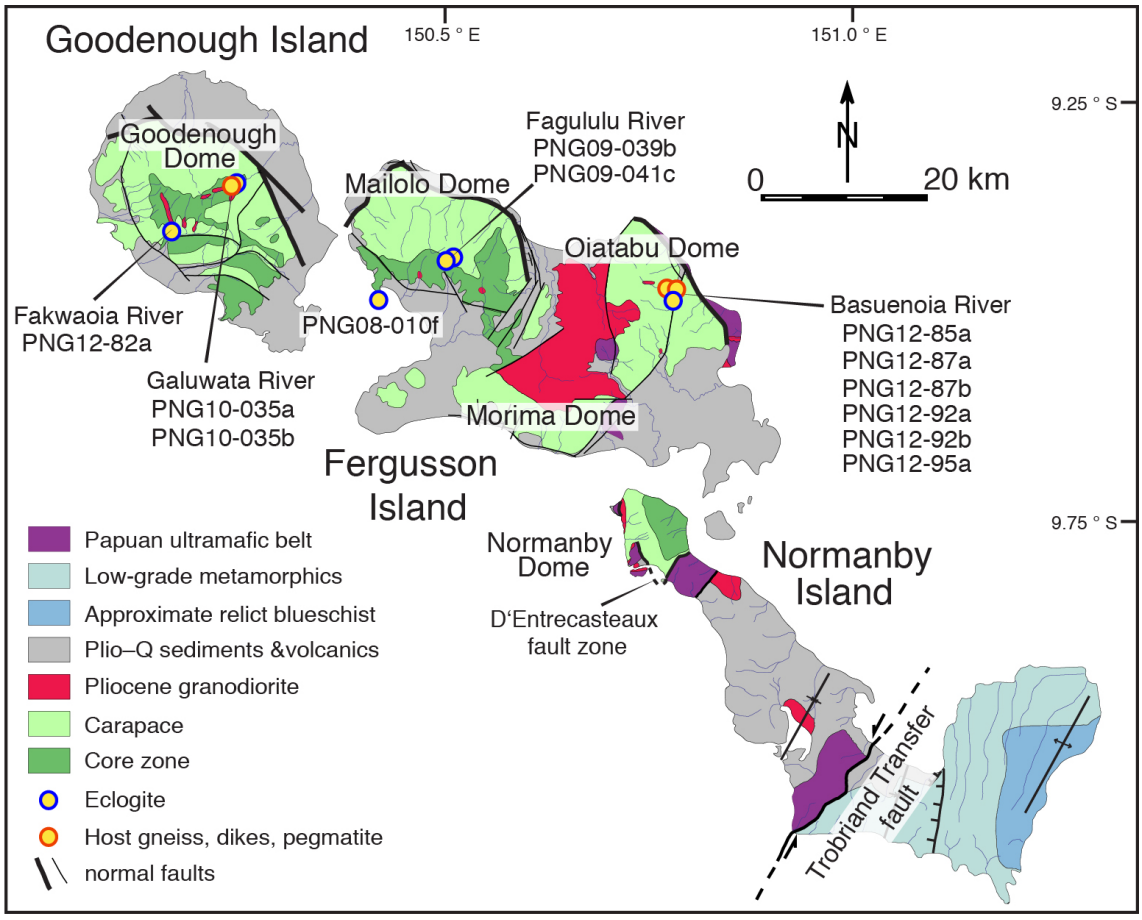

Figure 4.2: Simplified geological map of the D'Entrecasteuax Island gneiss domes showing various lithologies, the core and carapace zones, and the dome-bounding faults, including the D'Entrecasteaux fault zone (after Davies, 1973; Hill, 1994; Little et al., 2007, 2011). Colored circles mark sample locations for this study, with the blue outlined circles representing eclogite samples and the red, the analyzed gneiss, dikes, and pegmatite.

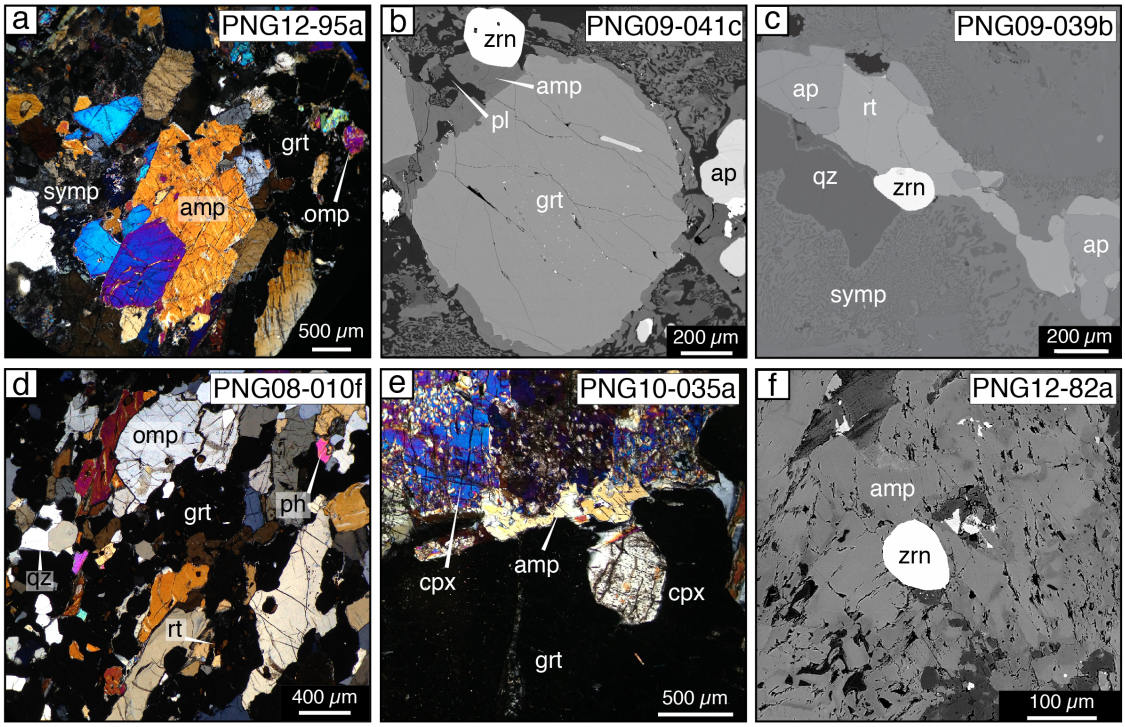

Figure 4.3: Photomicrographs of cross-polarized light and backscattered electron (BSE) images showing the textural relationships in the PNG (U)HP eclogites. (a) Amphibole, garnet, omphacite, and symplectite within the retrogressed Oiatabu Dome eclogite PNG12-95a; note the two generations of amphibole: the coarse grains and the fine-grained amphibole associated with symplectite; (b) BSE image showing the breakdown of garnet and omphacite to form coarse zircon, amphibole, symplectite (consisting of plagioclase and amphibole), and apatite within the Mailolo Dome eclogite PNG09-041c; (c) BSE image showing coarse zircon occurring with the retrogressed assemblage of quartz, apatite, rutile, and symplecite (consisting of plagioclase and amphibole) adjacent to garnet within Mailolo Dome eclogite PNG09-039b; (d) (U)HP fresh eclogite-facies assemblage of garnet, omphacite, quartz, phengite, and rutile within the Mailolo Dome eclogite PNG08-010f; (e) Diopsidic clinopyroxene inclusion within garnet, which is rimmed by amphibole and in contact with matrix diopsidic clinopyroxene within the heavily retrogressed Goodenough Dome eclogite PNG10-035a; (f) zircon associated with matrix amphibole in an additional heavily retrogressed Goodenough eclogite PNG12-82a. Mineral abbreviations are after Whitney and Evans (2010).

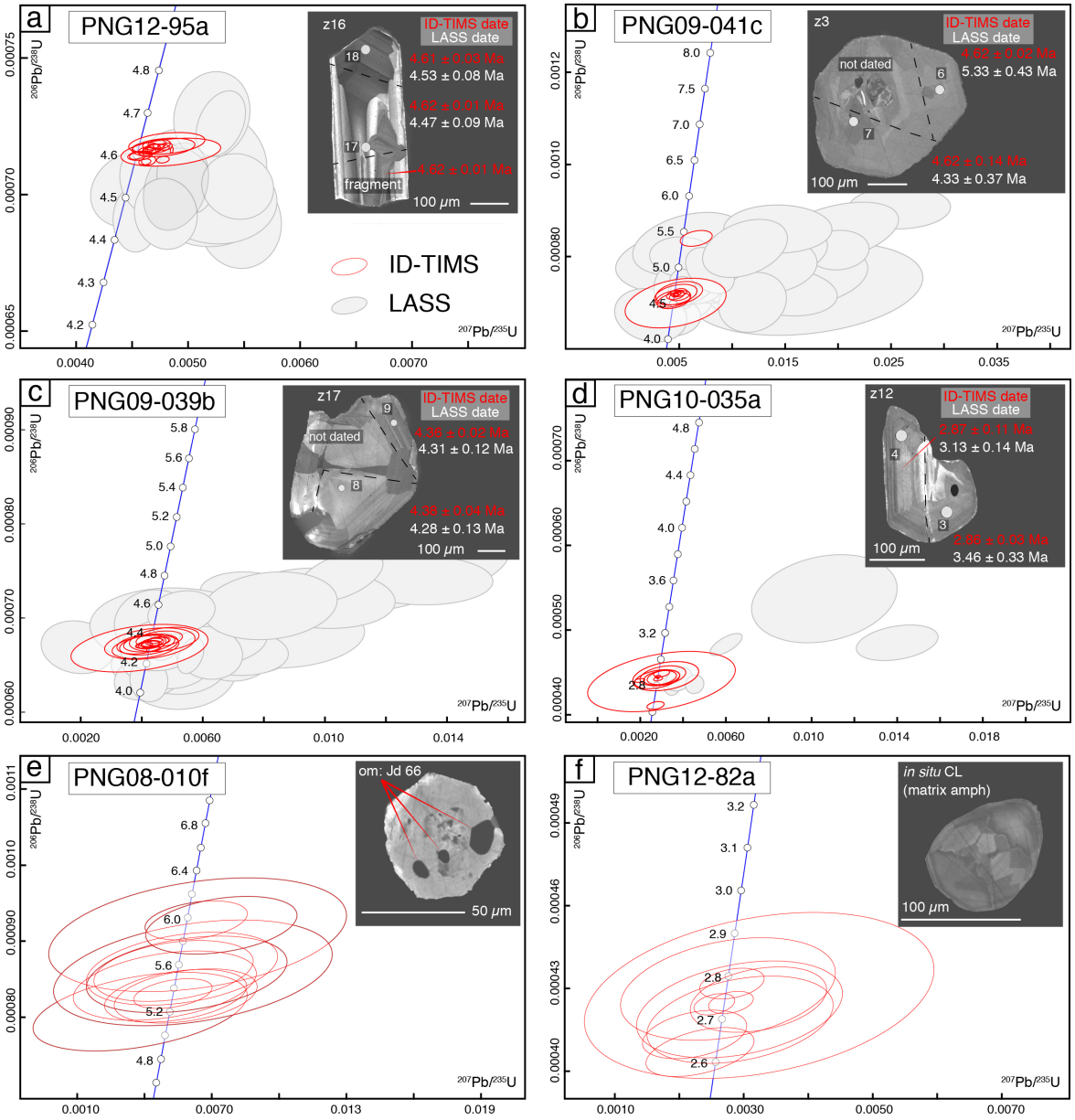

Figure 4.4: Concordia diagrams of the eclogite U-Pb zircon analyses showing all individual LASS (grey ellipses) and/or ID-TIMS (red ellipses, Th-corrected) results for Pliocene PNG (U)HP eclogites. Insets show cathodoluminescence images with representative zircons analyzed by both ID-TIMS (red) and LASS (white) with their respective ID-TIMS and LASS dates for 4a–d: (a) Oiatabu Dome PNG12-95a, bottom fragment of z16 was only dated by ID-TIMS, (b) Mailolo Dome PNG09-041c, (c) Mailolo Dome, PNG09-039b, and (d) Goodenough Dome PNG10-035a. For the ID-TIMS analyses, the grains shown were all microsampled, and the black dashed lines denote the individual microsampled fragments. The remaining eclogites were too low in radiogenic Pb and thus only ID-TIMS analyses were performed for samples e) Mailolo Dome PNG08-010f, and (f) Goodneough Dome PNG12-82a. Representative CL images

are shown; however, these grains were not analyzed. Each ellipse represents a single zircon analysis (whole grain, fragment, or single spot) and the 2-sigma uncertainties. Dates listed on concordia are given in Ma.

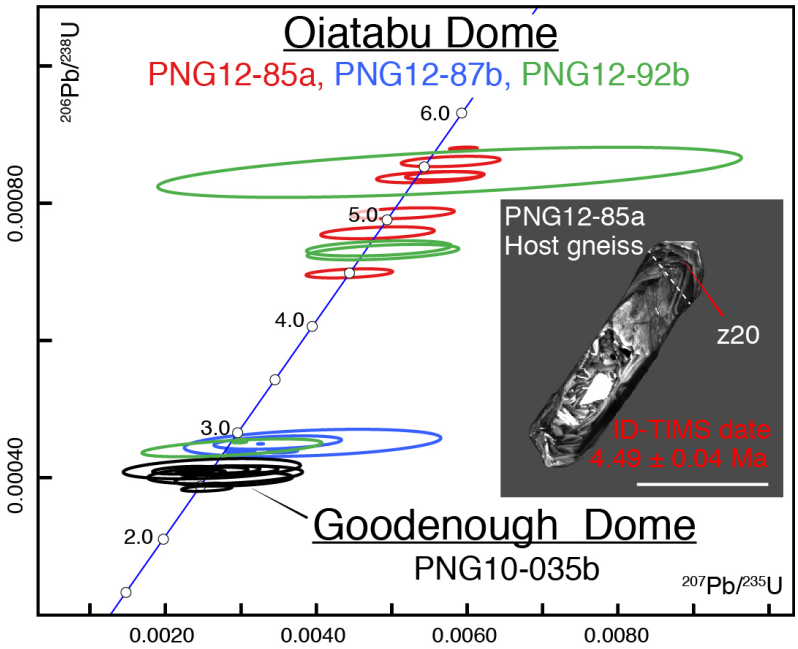

Figure 4.5: Concordia diagrams showing the U-Pb zircon results for Oiatabu Dome host gneiss PNG12-85a, the discordant weakly deformed dikes PNG12-87b and PNG12-92b and the Goodenough Dome pegmatite PNG10-035b. Inset shows host gneiss PNG12-85a microsampled zircon tip z20 and corresponding ID-TIMS date. Scale bar is 100 µm. Each ellipse represents a single zircon analysis and the 2-sigma uncertainties. The dates listed on concordia are in Ma.

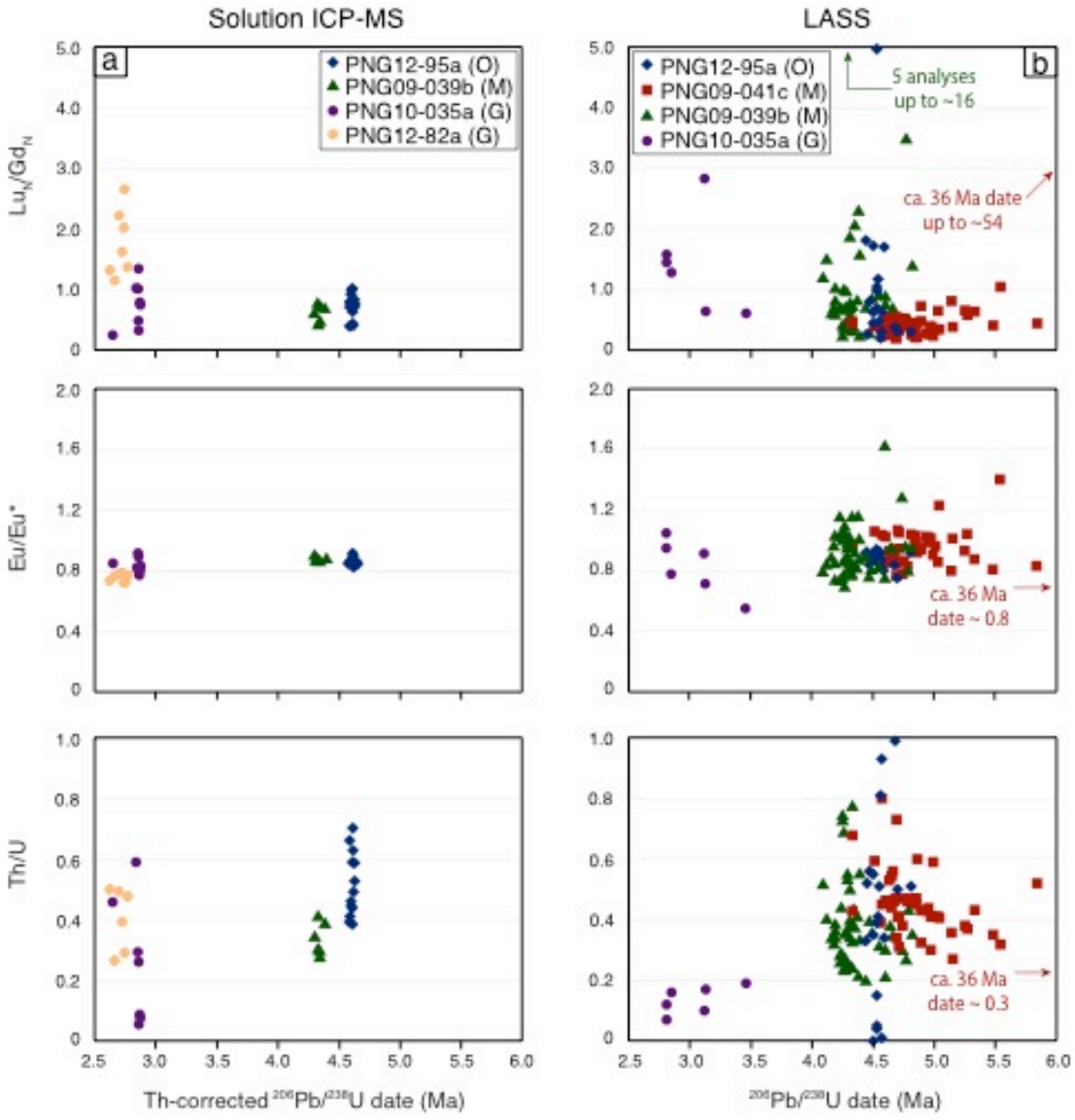

Figure 4.6: Selective Pliocene eclogite zircon trace elements measured by (a) solution ICP-MS and (b) LASS plotted as a function of time (Th-corrected ID-TIMS $^{206}Pb/^{238}U$ date and LASS $^{206}Pb/^{238}U$ date, respectively). The Lu_N/Gd_N, Eu/Eu*, and Th/U ratios are shown for both techniques. Analyses used for Lu_N/Gd_N and Eu/Eu* are normalized to chondrite values of Sun and McDonough (1989). O: Oiatabu Dome, M: Mailolo Dome, G: Goodenough Dome.

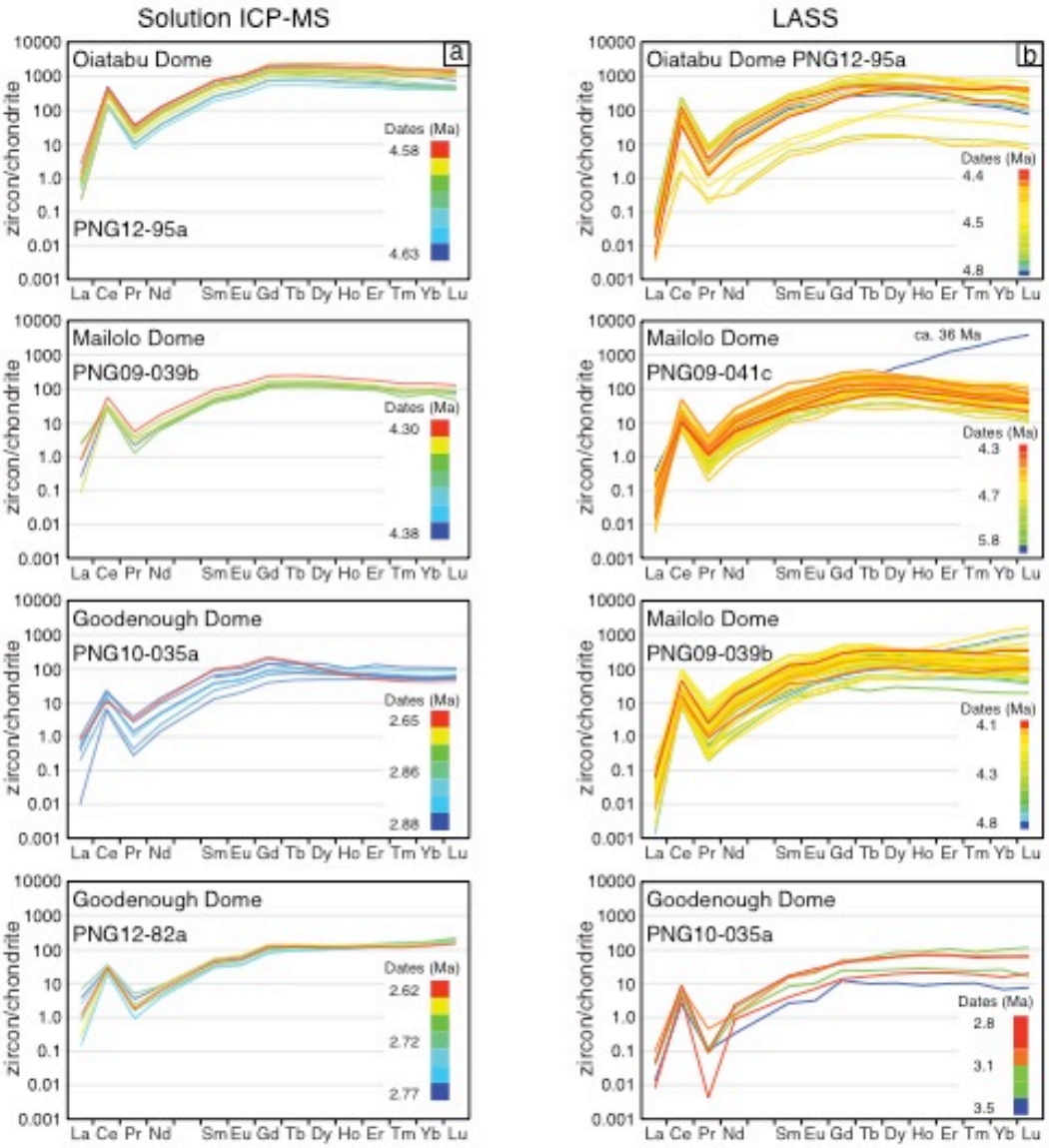

Figure 4.S1: Chondrite-normalized zircon trace-element data collected by (a) solution ICP-MS and (b) LASS for eclogites: PNG12-95a, PNG09-041c, PNG09-039b, PNG10-035a, and PNG12-82a (the latter two were only analyzed by solution ICP-MS). Individual REE patterns are color-coded by the corresponding ID-TIMS (Th-corrected $^{206}Pb/^{238}U$) and LASS ($^{206}Pb/^{238}U$) dates.

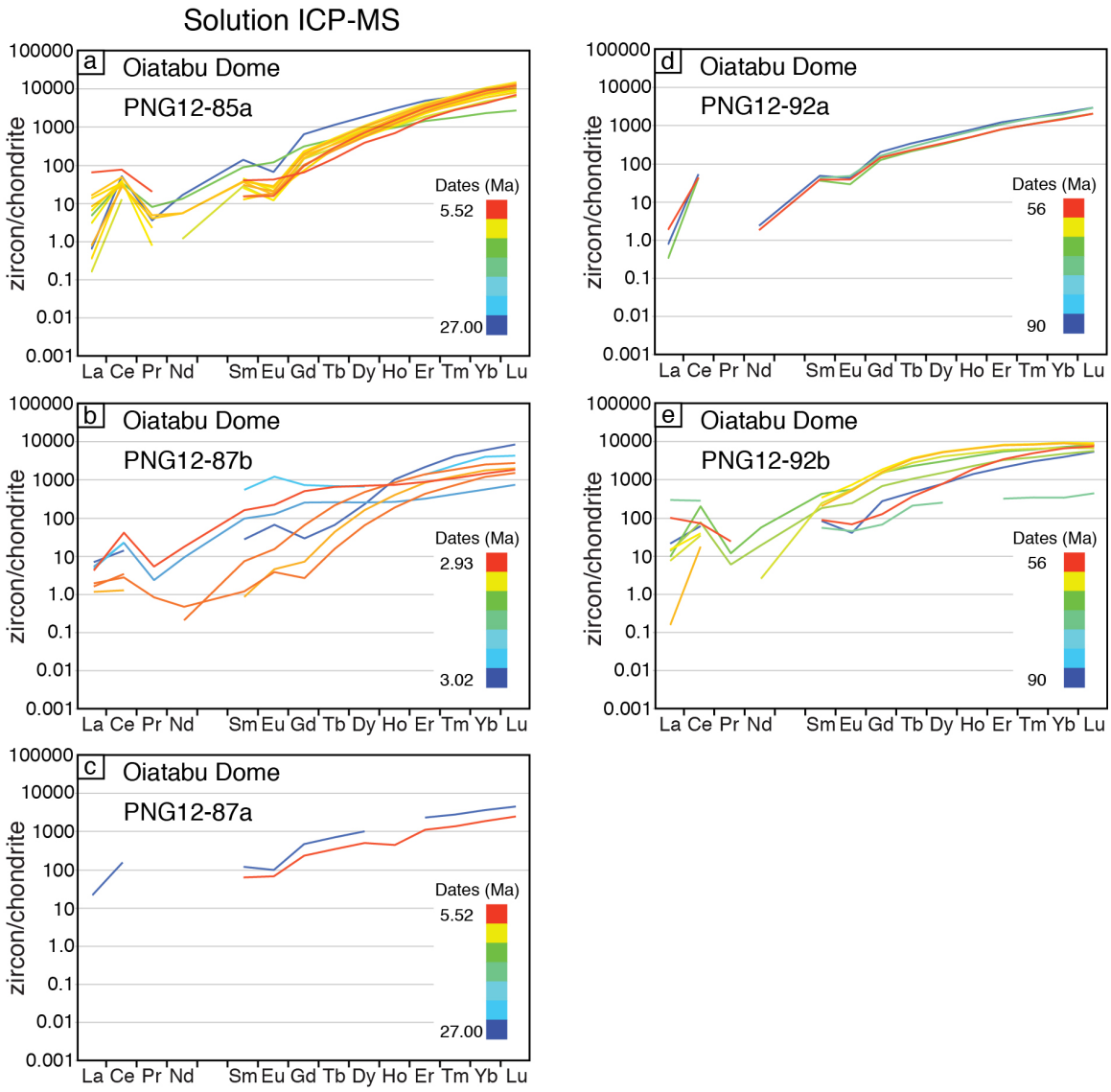

Figure 4.S2: Chondrite-normalized zircon trace-element data collected by solution ICP-MS for Oiatabu Dome host gneiss (PNG12-85a, PNG12-87a, PNG12-92a) and weakly deformed dikes (PNG12-87b and PNG12-92b). Individual REE patterns are color-coded by the corresponding ID-TIMS Th-corrected $^{206}Pb/^{238}U$ dates.

Chapter 5: Tracking the Exhumation of a Pliocene (U)HP terrane: U-Pb and Trace-element Constraints from Zircon, D'Entrecasteaux Islands, Papua New Guinea

Joel W. DesOrmeau[*], Stacia M. Gordon[*], Timothy A. Little [**], Samuel A. Bowring[***]

[*]Department of Geological Sciences, University of Nevada Reno, Nevada, USA
[**] School of Geography, Environment and Earth Sciences, Victoria University of Wellington, Wellington, New Zealand
[***]Department of Earth, Atmospheric, and Planetary Sciences, Massachusetts Institute of Technology, Cambridge, Massachusetts, USA

Abstract

Domal structures within the D'Entrecasteaux Islands of eastern Papua New Guinea expose ultrahigh-pressure (UHP) Pliocene (5.6–4.6 Ma) eclogites and evidence for partial melting. To better interpret the (U)HP exhumation history, U-Pb geochronology and trace-element abundances were determined in zircon from variably deformed host gneiss and crystallized melt (leucosomes, sills, dikes, and plutons) from the Goodenough and Normanby Domes by ID-TIMS (isotope-dilution thermal ionization mass spectrometry) and ICP-MS (inductively coupled plasma mass spectrometry), respectively, to constrain the timing of melt crystallization and deformation relative to UHP metamorphism. Zircons extracted from orthogneiss and deformed granodiorite sills of Normanby Dome, located ~40 km southeast of the UHP eclogite, record HP metamorphism from 5.66 ± 0.02 Ma to 5.04 ± 0.07 Ma and melt crystallization at ca. 4.1 Ma. Strongly deformed, layer-parallel leucosomes from Goodenough Dome, ~20 km northwest of the UHP eclogite, began to crystallize by 3.85 ± 0.02 Ma. These dates indicate that melt crystallization began in the Goodenough and Normanby Domes within ~0.75 m.y. of (U)HP metamorphism. The ID-TIMS dates from the orthogneiss and crystallized melt show that exhumation and cooling of the (U)HP rocks in the PNG terrane began first in the east, within Normanby Dome, then to the west, in the Goodenough Dome ~ 1 m.y. later, and finally the middle dome rocks, exposed within the Mailolo Dome, cooled ~ 2 m.y. after exhumation of Normanby Dome. All domes reveal synchronous crystallization of late, non-deformed melts and final extension-driven exhumation by 1.82 ± 0.03 Ma.

Introduction

The subduction of continental crust to mantle depths and subsequent exhumation is deduced from the rare preservation of ultrahigh-pressure (UHP) terranes at Earth's surface [e.g., Ernst et al., 2001; Hacker, 2007]. The recognition of coesite [*Chopin*, 1984; *Smith* 1984] and microdiamond [*Sobolev and Shatsky*, 1990; *Xu et al.*, 1992] inclusions in minerals from metamorphic rocks of supracrustal origin initiated the study of UHP metamorphism as well as the study of the mechanisms driving the subduction of crustal material to depths in excess of 100 km and its subsequent exhumation to the surface. Investigations over the last ~35 years have revealed major differences among UHP terranes (e.g., size, exhumation rate, and amount of crystallized melt associated with exhumation; e.g., *Kylander-Clark et al.*, [2012]), and thus a variety of numerical and field-based models have been proposed that describe the contrasting driving forces for subduction and exhumation among these terranes [e.g., *Hacker and Gerya*, 2013; *Warren*, 2013]. Phase equilibria modeling suggests that the initial exhumation of UHP material to the base of the crust is due to the positively buoyant nature of the mainly quartzofeldspathic continental material relative to the mantle at temperatures ≤ 800–900 °C and pressures up to 4 GPa [*Massonne*, 2007]. Along with buoyancy, other controls such as forces acting on the overriding and subducting plates (i.e., seismic coupling-decoupling and pressure gradients between the plates) and crustal and mantle rheology, must also play an important role in the exhumation of UHP terranes from mantle depths [*Scholz and Campos*, 1995; *Chemenda et al.*, 1996; *Heuret and Lallemand*, 2005; Beaumont et al., 2009*; Hacker and Gerya*, 2013]. Moreover, in many UHP terranes, final emplacement at mid- to upper-crustal levels may be the result of upper-crustal extension,

a process that might in part be driven by crustal overthickening associated with stalling of the partially exhumed UHP terranes at the base of the crust [*Walsh and Hacker*, 2004]. In contrast, geodynamic modeling of early collisional exhumation of UHP terranes demonstrates that the characteristic upper-crustal extensional structures seen in some UHP terranes result from, rather than cause, the exhumation of UHP material [*Beaumont et al.*, 2009].

Most UHP terranes contain some evidence for partial melting during their evolution. The presence of melt can substantially reduce the effective viscosity of the UHP material and cause weakening of the subducted crustal rocks [*Rosenberg and Handy*, 2005]. Partial melting may also allow the subducted crustal material to decouple from the subducted lithospheric slab, thus triggering exhumation of the UHP terrane, while also contributing to its buoyancy [*Labrousse et al.*, 2011].

Ultrahigh-pressure metamorphism commonly occurs at temperatures of 600–800 °C and pressures between ~2.6 GPa (quartz–coesite boundary) and 4 GPa [*Hacker*, 2006], although rare crustal material was subjected to extreme temperatures (>1000 °C) and pressures (up to 6 GPa; Erzgebirge and Kokchetav Massif) and later exhumed [*Shatsky et al.*, 1995; *Zhang et al.*, 1997; *Massonne*, 1999]. At these extreme pressures and temperatures, partial melting of the rocks would be expected to take place prior to (and during) ascent of the rocks from depths of >140 km [e.g., *Massonne*, 2003; *Schertl and Sobolev*, 2013]. Partial melting at lower temperatures (<900 °C) has been argued for other UHP terranes [e.g., *Warren*, 2013]. For example, the Norwegian Western Gneiss Region UHP terrane is thought to have undergone partial melting at ~800–850 °C and >2.5 GPa, based on melting experiments of the bulk host rock and leucosomes, the

pressure-temperature paths of the eclogites, direct evidence for melting and dehydration reactions in the host gneiss, and overlap in the timing of UHP metamorphism and partial melting [*Labrousse et al.*, 2011; *Gordon et al.*, 2013]. Moreover, a leucocratic metapelite in the northeast Greenland UHP terrane underwent partial melting at UHP conditions, based on preservation of products and reactants of the dehydration melting reaction, Phe + Qtz = Ky + Kfs + Rt + melt, as polyphase inclusions in garnet, and on unusual crown- and moat-like textures in garnet around polycrystalline quartz inclusions [*Lang and Gilotti*, 2007]. Thus, there is increasing evidence that partial melting may play a role in the initial exhumation of these deeply subducted rocks [*Labrousse et al.*, 2011].

Eastern Papua New Guinea (PNG) exposes Pliocene (U)HP eclogites within one of the most rapidly extending (>20 mm/yr) active continental rifts on Earth, the Woodlark Rift (Figure 1) [*Taylor et al.*, 1999; *Abers*, 2001; *Wallace*, 2004]. These eclogites are hosted in migmatitic gneisses of quartzofeldspathic composition (Figures 1 and 2) within gneiss domes found on the D'Entrecasteaux Islands, including from west to east, Goodenough, Fergusson, and Normanby Islands. The PNG (U)HP rocks underwent extensive partial melting, as is evidenced by abundant leucosomes (~10–20% of most outcrops, and up to 40% of the outcrop in the core of the domes), numerous dm- to m-thick crosscutting dikes (5–70%), and granodioritic to leucogranitic plutons that are tens of km in diameter [*Davies and Warren,* 1988; *Gordon et al.*, 2012]. The field and structural relationships among the migmatites, mafic eclogites, and crosscutting dikes in the PNG (U)HP terrane provide an opportunity to determine the timing of melt crystallization relative to (U)HP metamorphism and to evaluate the role of partial melting in the rapid exhumation of crustal rocks from mantle depths. Moreover, the multiple and

cross-cutting melt generations, and the variable degree to which they have been deformed, provide a record of incremental deformation and exhumation histories across the series of domes. Finally, because the subduction tectonics in this part of eastern PNG ceased by the early Miocene [*Davies and Jacques*; 1984; *Rogerson et al.*, 1987; *Davies*, 1990; *Van Ufford and Cloos*, 2005], the Pliocene (U)HP terrane has not been deformed since that time and thus preserves its structures related to the entire exhumation history.

This study reports new U-Pb zircon isotope-dilution thermal ionization mass spectrometry and trace-element analysis (ID-TIMS-TEA) results constraining the timing of melt crystallization and deformation during the ascent of this rapidly exhumed (U)HP terrane. Prior investigations of PNG (U)HP eclogites suggested a westward younging trend in eclogite-facies metamorphism across the domes, which was interpreted to be the result of an increased geothermal gradient associated with the westward propagation of the Woodlark Rift [*Monteleone et al.*, 2007]. Our data from the westernmost exposures within the Goodenough Dome indicates that a layer-parallel leucosome is as old as ca. 3.9 Ma, whereas to the east, the oldest layer-parallel leucosomes are ca. 3.5 Ma within the Mailolo Dome [*Gordon et al.*, 2012]. Moreover, metamorphism of the easternmost (U)HP exposures within the Normanby Dome occurred at ca. 5.6–5.0 Ma followed by the crystallization of a granodiorite sill at ca. 4.1 Ma. Thus our data argues against a westward progression in partial melting related to oceanic spreading center propagation. Moreover, our data reveal that throughout the D'Entrecasteaux Islands, crystallization of the strongly deformed leucosomes and sills from both domes occurred within ~0.75 m.y. of the termination of (U)HP metamorphism. These observations indicate that rapid exhumation is required to exhume this (U)HP material from > 90 km depths to the base

of the crust (~40 km), where we propose the first abundant and strongly deformed leucosomes formed. Crystallization ages for later, less deformed dikes and a non-deformed pluton suggest that subsequent melt segregations may have further increased the buoyancy of the already melt-rich (U)HP material, aiding in the rapid exhumation of the PNG (U)HP terrane to shallow crustal levels.

Geological Setting

Eastern Papua New Guinea has experienced considerable tectonic reorganization since the Cenozoic due to the ~110 mm/yr convergence between the Australian and Pacific plates as well as the development of multiple microplates [*Tregoning et al.*, 1998; *Wallace et al.*, 2004]. During the Paleogene, the Papuan Orogen, now exposed on the Papuan mainland, formed after the northern, rifted continental margin of the Australian plate collided with an island arc terrane to the northeast [*Davies and Jacques*, 1984; *Cloos et al.*, 2005; *Little et al.*, 2011]. This collision caused southwestward obduction of the arc basement, now called the Papuan Ultramafic Belt (PUB), above a deformed wedge of the Australian plate along the Owen Stanley Fault (Figure 1). The Australian sedimentary and basaltic rocks that were buried as part of this orogenic event are referred to as the Owen Stanley metamorphics and are structurally beneath the PUB on the mainland Papuan Peninsula (Figure 1) [*Davies and Jacques*, 1984; *Davies and Warren*, 1988]. $^{40}Ar/^{39}Ar$ amphibole dates on the metamorphic sole of the ophiolite constrain initial obduction along the Owen Stanley Fault to have taken place at 58.3 ± 0.4 Ma [*Lus et al.*, 2004]. Moreover, the blueschist, pumpellyite-actinolite, and lower greenschist-facies Owen Stanley metamorphic rocks have yielded K/Ar and $^{40}Ar/^{39}Ar$ amphibole

dates of ca. 45–22 Ma and white mica dates of ca. 24–22 Ma [*Davies and Williamson*, 1998], indicating that the orogen had cooled to ~400 °C, and the arc-continent collision had ceased by the early Miocene [*Davies and Jacques*; 1984; *Rogerson et al.*, 1987; *Davies*, 1990; *Van Ufford and Cloos*, 2005]. The more deeply subducted Australian plate is interpreted to be the protolith of the PNG (U)HP terrane within the D'Entrecasteaux Islands, which are 20 km offshore and to the north of the southern tip of the Papuan Peninsula (Figure 1). The PNG (U)HP terrane consists of felsic migmatitic gneisses and mafic eclogites, and the rocks are exposed in the up to ~2.5 km-high gneiss domes of the D'Entrecasteaux Islands [*Davies*, 1980; *Davies and Jacques*, 1984; *Davies and Warren*, 1988; *Hill and Baldwin*, 1993; *Baldwin and Ireland*, 1995; *Little et al.*, 2011; *Gordon et al.*, 2012].

Subsequent to the Papuan orogen, the multiple microplates, including the North and South Bismarck Plates, the Solomon Sea Plate, and the Woodlark Plate, formed in eastern PNG due to continued rapid convergence between the Australian and Pacific plates. Slab pull and counterclockwise rotation associated with northward subduction of the Solomon Sea Plate at the New Britain Trench caused seafloor spreading to begin at ca. 6 Ma in the Woodlark Basin; the Woodlark Rift separates the Woodlark microplate from the Australian Plate (Figure 1) [*Weissel et al.*, 1982; *Taylor et al.*, 1999; *Wallace et al.*, 2004; *Westaway*, 2007]. At the western end of the basin, seafloor spreading transitions westward into continental rifting [e.g., *Ferris et al.*, 2006]. Rift-related extension has resulted in thin crust (~20 km-thick) beneath the D'Entrecasteaux Islands. In contrast, the mountainous (>3 km-high) Papuan Peninsula to the south of the islands has a crustal thickness of ~30–35 km [*Abers et al.*, 2002]. Seismic velocity measurements from the

D'Entrecasteaux Islands reveal anomalously low-density mantle supporting the thinned crust, a relationship that suggests that extension has taken place in both the crust and lithospheric mantle within the Woodlark Rift [*Abers et al.*, 2002]. In addition, crustal extension is expressed by active normal faults within the Woodlark basin [*Abers*, 2001] and by the exposure of the east-west series of gneiss domes in the D'Entrecasteaux Islands [*Hill et al.*, 1992; *Little et al.*, 2011, 2013].

D'Entrecasteaux Islands

The D'Entrecasteaux Islands (Goodenough, Fergusson, and Normanby Islands) are situated along strike of the westward-propagating Woodlark Basin oceanic spreading center. The domal structures consist of quartzofeldspathic gneiss, with lesser amounts of mafic rocks (eclogite and amphibolite), and minor marbles, quartzites, and paragneiss (Figure 2) [*Davies and Warren*, 1988; *Little et al.*, 2011]. Active normal faults flank the north sides of the Goodenough Dome (on Goodenough Island) and the Mailolo and Oitabu Domes (on Fergusson Island) (Figure 2). These normal faults dip 30–40° to the north with convex-up scarps, and they crosscut an older, more gently dipping fault that preserves fragments of the ophiolitic upper plate rocks in its hanging wall [*Little et al.*, 2011]. This older structure, the D'Entrescasteaux fault zone, represents the boundary between the lower and upper plate rocks across the Islands and is interpreted to be correlative to the Owen Stanley fault zone along which obduction of the PUB occurred in the Paleogene (Figure 1) [*Little et al.*, 2011]. The upper plates of the gneiss domes consist of erosional remnants of the regionally extensive sheet of PUB and its unmetamorphosed Neogene sedimentary cover [*Davies and Warren*, 1988], whereas the lower plate of the

domes contain the above-mentioned suite of high-grade rocks that have experienced Miocene–Pliocene (U)HP metamorphism.

Structurally, the lower plate of the domal structures consists of an outer carapace zone and an inner core zone (Figure 2) [*Hill*, 1994]. A strong and planar LS tectonite fabric typifies the carapace and gives way to a more chaotic fabric in the core zone. Evidence for melting occurs in both zones and is ubiquitous throughout all structural levels of the domes; however, the percentage of leucosomes and dikes increases towards the dome centers from ~15% in the carapace to as much as ~70% in the structurally deepest exposures of the core zone [*Gordon et al.*, 2012]. In most cases, partial melting, and intrusion of granitoid dikes are interpreted to have been coeval with ductile deformation in the core of the domes [*Little et al.*, 2011, 2013]. Microstructures include prism-[c] slip lattice-preferred orientations, chessboard subgrain structure in quartz, melt-filled strain shadows, and shape-preferred orientations of euhedral, magmatic feldspars. All of these microstructures suggest high-temperature deformation in the presence of intergranular melt [*Little et al.*, 2011, 2013].

Throughout the domes, deformed amphibolite, retrogressed eclogite, and minor well-preserved eclogite are enclosed within the more abundant quartzofeldspathic gneiss. Temperature and pressure estimates for the only known coesite-bearing eclogite, located in the Mailolo Dome (Figure 2), are ~700 °C and ~27 kbar, respectively [*Monteleone et al.*, 2007, *Baldwin et al.*, 2008]. Other variably retrogressed eclogites have yielded temperatures and pressures of 530–840° C and 12–24 kbar [*Davies and Warren*, 1992] and 730–930° C and 20–24 kbar [*Hill and Baldwin*, 1993; *Baldwin et al.*, 2004]. A variety of dating techniques have been applied to the coesite-bearing eclogite, with

variable results: 1) a Lu-Hf garnet–whole rock date of 7.1 ± 0.7 Ma (MSWD=1.1) [*Zirakparvar et al.*, 2011]; 2) *in situ* dating of zircons by secondary ion mass spectrometry (SIMS), yielding a $^{206}Pb/^{238}U$–$^{207}Pb/^{206}Pb$ Terra Wasserburg intercept date of 7.9 ± 1.9 Ma (MSWD=9.2) [*Monteleone et al.*, 2007]; and 3) ID-TIMS zircon single-grain $^{206}Pb/^{238}U$ dates of 5.60 ± 0.22 Ma to 4.61 ± 0.18 Ma [*Gordon et al.*, 2012]. Finally, for other HP eclogites (lacking preserved coesite) in the D'Entrecasteaux Islands, SIMS analysis of zircon yield $^{206}Pb/^{238}U$–$^{207}Pb/^{206}Pb$ Terra Wasserburg intercept dates of 4.3 ± 0.4 Ma (MSWD=3.3) for a sample in the Mailolo Dome [*Baldwin et al.*, 2004] and 2.9 ± 0.4 Ma (MSWD=1.02), 2.8 ± 0.3 Ma (MSWD= 2.6), and 2.1 ± 0.5 Ma (MSWD=4.2) for samples in the Goodenough Dome [*Monteleone et al.*, 2007]. A non-coesite bearing sample from Mailolo dome has yielded a Rb-Sr whole-rock–omphacite–phengite isochron date of 5.6 ± 1.6 Ma (MSWD=1.0) [*Korchinski et al.*, in press].

Exhumation of the U(HP) eclogites from conditions of at least 21 kbar and 730–900° C was accompanied by near-isothermal decompression and amphibolite-facies retrogression at lower crustal conditions of 7–14 kbar and 570–730° C (*Hill and Baldwin*, 1993). Based on thermobarometry of the host rocks in Mailolo Dome, *Korchinski et al.* [in press] inferred retrogression of the eclogites took place at 12–14 kbar. Pervasive synexhumational deformation of the (U)HP terrane at amphibolite-facies conditions has overprinted most fabrics related to the initial ascent of the eclogites from mantle depths, and is characterized by a gently dipping foliation that was later folded to form the structural domes [*Davies and Warren*, 1988; *Davies and Warren*, 1992; *Hill and Baldwin*, 1993; *Baldwin et al.*, 2004; *Little et al.*, 2011, 2013].

ID-TIMS dating of strongly deformed foliation-parallel leucosomes, which represent an early stage of melting of the (U)HP host rocks within the lower crust, and weakly deformed cross cutting dikes constrains the timing of this exhumation history for the Mailolo Dome of Fergusson Island [*Gordon et al.*, 2012]: subsequent to the UHP event (at ca. 5.6–4.6 Ma), the crystallization of the strongly deformed leucosomes occurred at ca. 3.5 to 3.0 Ma, while weakly deformed granitoid dikes formed at ca. 2.4 Ma. On the basis of ID-TIMS zircon data, crystallization of the strongly deformed leucosomes in Mailolo Dome occurred ~1 m.y. after (U)HP metamorphism [*Gordon et al.*, 2012]. In a study of the Goodenough Dome core-zone gneisses, SIMS analysis of zircon yielded weighted-mean $^{206}Pb/^{238}U$ dates for two gneisses at 2.63 ± 0.16 Ma (n=12, MSWD=1.4) and 2.72 ± 0.26 Ma (n=6, MSWD=1.5); these dates were interpreted as recording zircon growth during decompression-related amphibolite-facies metamorphism [*Baldwin and Ireland*, 1995].

The final stages of exhumation at temperatures below 500 °C have been dated at ca. 3.5–2.6 Ma using $^{40}Ar/^{39}Ar$ thermochronology from gneisses and pegmatite within Mailolo Dome. In comparison, on Goodenough Dome, gneisses have $^{40}Ar/^{39}Ar$ hornblende, white mica, and biotite dates that range from approximately 3.0–1.5 Ma (no uncertainties reported for these dates) [*Baldwin et al.*, 1993, *Waggoner et al.*, 2008]. Rocks throughout both domes were exhumed to shallow crustal levels (< 80 °C) by ca. 1.8–0.3 Ma (no uncertainties reported), as recorded by apatite (U-Th)/He and fission-track ages [*Fitzgerald et al.*, 2008].

Whereas much of the previous work in the D'Entrecasteaux Islands terrane has focused on the Mailolo Dome of Fergusson Island, this study is focused on the timing of

melt crystallization relative to (U)HP metamorphism and the exhumation of rocks in the Goodenough Dome of Goodenough Island and Normanby Dome of northwest Normanby Island (Figure 2). We report crystallization dates for host quartzofeldspathic gneiss, granodioritic orthogneiss, leucosomes, sills, dikes, and non-deformed plutonic rocks from all structural levels of Goodenough and Normanby Domes. In this study, we use "leucosome" to refer to foliation-parallel quartzofeldspathic layers, whereas "dike" indicates bodies that are discordant to the foliation. In all cases, we interpret the leucosomes to have melted and crystallized approximately *in-situ* following the criteria of *Little et al.* [2011] and *Gordon et al.* [2012]: (1) occurrence of coarse-grained euhedral plagioclase (most with fine oscillatory zoning) and/or non-deformed hornblende; (2) parallel grain long axes of grains towards the centers of shear zones, indicative of rotated grains; (3) melanocratic margins composed of coarse-grained hornblende or garnet; and (4) diffuse margins.

Methods

For the U-Pb zircon analysis, we collected seventeen samples (seven from Goodenough Dome and ten from Normanby Dome) from a variety of gneisses and melt segregations from across the exposed structural levels in the two domes (Figure 2). Zircon was extracted from the samples using standard rock-crushing and mineral-separation procedures.

In an effort to resolve the multiple melt crystallization events that occurred on geologically short timescales (the eclogites were exhumed from mantle to surface in ca. 4–5 m.y.) [*Baldwin et al.*, 2004; *Gordon et al.*, 2012], we analyzed zircon using U-Pb

isotope dilution thermal ionization mass spectrometry (ID-TIMS), following the chemical-abrasion procedures modified after *Mattinson* [2005]. Analytical uncertainties associated with U-Pb ID-TIMS are typically an order of magnitude lower than *in situ* dating techniques, such as SIMS and laser ablation inductively coupled plasma mass spectrometry (LA-ICP-MS). Regardless of the method chosen, an unavoidable analytical challenge arises from the low abundance of ^{207}Pb within young zircons. This results in a significantly larger uncertainty in the ^{207}Pb/^{235}U date compared to the ^{206}Pb/^{238}U date. Moreover, these zircons have very low levels of radiogenic Pb—0.06–1.00 pg—for individual grains of Miocene–Pliocene age, thus requiring low laboratory blanks; in this study most blanks were 0.25–0.45 picograms. Typical calculated uncertainties on Pliocene ^{206}Pb/^{238}U dates are 0.003–0.250 Ma, which are proportional to the radiogenic/common Pb ratio (Table 1). In order to obtain the most precise analysis possible with ID-TIMS from scarce, low Pb zircons, we did not make polished grain mounts for cathodoluminescence (CL) imaging prior to analysis that requires polishing away about half of the zircon crystal. Each ID-TIMS result presented represents a single grain that has undergone a customized chemical abrasion method of a 9–12 hour leach at 220 °C designed to ensure that enough zircon remained to analyze.

A new approach in ID-TIMS zircon studies is the combination of high precision U-Pb dating with trace-element analyses measured by ICP-MS on the same zircon aliquot or "wash" solution (TIMS-TEA) [*Schoene et al.*, 2010]. The solution contains all of the trace elements in the zircon aliquot except for the U and Pb, which have been separated via ion-exchange columns for the ID-TIMS analyses. The advantage of this technique is that in some cases, the trace-element data can be used to link the U-Pb date to the *P–T*

path. For example, zircon formed at high-pressure conditions in mafic rocks is predicted to have: 1) a flat heavy rare earth element (HREE) pattern (Lu/Gd < 3) due to preferential partitioning of HREE in garnet; and 2) a lack of a negative Eu anomaly ($Eu/Eu^{*} > 0.75$) due to the absence of plagioclase at HP (~>16 kbar) conditions [e.g., *Rubatto*, 2002; *Rubatto and Hermann*, 2007]. For this study, only zircons from felsic rocks have been analyzed for trace elements and the lack of garnet in the studied samples limits the ability to link zircon trace-element data to pressure conditions. However, the trace-element data does provide a tool for tracking zircon composition with crystallization age within a sample (i.e., amount of HREE enrichment and presence of a Eu anomaly).

In this study, the dates are interpreted mainly by comparison with the previous geochronometric work on the (U)HP eclogites and the $^{40}Ar/^{39}Ar$ cooling ages from across the domes, and the trace-element profiles are used to support these interpretations. In addition, the different segregations of melt (i.e., *in situ* leucosomes, dikes, sills, and plutons), and also, the intrusive orthogneiss bodies contain some inherited grains. Our approach is to use the youngest date or dates as a maximum age of crystallization.

The TIMS-TEA method described above was applied to zircons from eight of the seventeen samples collected from Goodenough and Normanby Domes. From the eight samples, some analyses of zircon solutions yielded concentrations of trace elements near total procedural blank solution values and were not interpreted. Here, we only report trace-element results for analyses that were at least an order of magnitude greater than the blank solution analyses. It should be noted that our observations are preliminary due to the small number of analyses for most of the samples analyzed by TIMS-TEA. A more detailed methodology and data tables for the U-Pb ID-TIMS zircon analyses and ICP-MS

trace-element solutions are provided in the supporting information (Tables 1 and 2, respectively). Table 1 lists the zircon fractions from youngest to oldest. All reported uncertainties within the text, data tables, and figures are at the 2-sigma or 95% confidence level.

Results

Goodenough Dome: Leucosomes and Dikes

Seven samples of variably deformed felsic leucosomes and dikes were collected at the core–carapace transition along the Gulawata River and from within the core of the Goodenough dome (Figure 2) for ID-TIMS-TEA analyses. For most sites we analyzed a pair of samples from the same outcrop that record different stages of the deformation history, from strongly deformed to non-deformed.

Sample PNG10-029B, a vertical ~5 cm thick, non-deformed aplitic dike, was analyzed from the carapace zone. This dike crosscuts the main amphibolite-facies gneissic foliation of the carapace. Three zircons yielded $^{206}Pb/^{238}U$ dates from 2.60 ± 0.19 Ma to 2.30 ± 0.06 Ma (Figure 4b). Eighteen zircons revealed older $^{206}Pb/^{238}U$ dates from 71.47 ± 0.04 Ma to 21.55 ± 0.58 Ma and are thought to be derived from rocks melted to produce the dike (Table 1).

At the core–carapace transition of the dome, a strongly foliated granodioritic leucosome layer (PNG10-031A) that is concordant with the main amphibolite-facies foliation and a mafic amphibolite body, was sampled. Nine out of fourteen of the analyzed zircons gave $^{206}Pb/^{238}U$ dates ranging from 4.737 ± 0.005 Ma to 4.417 ± 0.009 Ma (Figure 4a). One zircon yielded a younger $^{206}Pb/^{238}U$ date of 3.85 ± 0.02 Ma, and

three additional zircons yielded dates of 22.71 ± 0.03 Ma, 10.03 ± 0.01 Ma, and 8.27 ± 0.01 Ma (Table 1). Sample PNG10-031B is a weakly foliated granodioritic dike that cross cuts PNG10-031A and the mafic amphibolite. Three zircons recorded $^{206}Pb/^{238}U$ dates of 3.52 ± 0.14 Ma, 2.77 ± 0.06 Ma, and 2.68 ± 0.11 Ma (Figure 4b), all younger than the youngest zircon in PNG10-031A, consistent with field relationships. Four zircons yielded $^{206}Pb/^{238}U$ dates, ranging from 88.35 ± 0.08 Ma to 18.68 ± 0.19 Ma (Table 1) and are assumed to be inherited.

From the core zone, a granodioritic, layer-parallel leucosome, PNG10-039A, was collected from within a dominantly quartzofeldspathic gneiss outcrop (Figure 3a). Eight zircons from the leucosome yielded $^{206}Pb/^{238}U$ dates from 4.568 ± 0.004 Ma to 2.78 ± 0.02 Ma (Figure 4a). Two zircons gave older $^{206}Pb/^{238}U$ dates of 31.20 ± 0.03 Ma and 15.31 ± 0.03 Ma (Table 1). From the same outcrop, a ~5 cm thick tabular, weakly deformed granodioritic dike (PNG10-039B) crosscuts the host gneiss and the layer-parallel leucosome PNG10-039A. Six zircons from this dike yielded $^{206}Pb/^{238}U$ dates from 2.98 ± 0.03 Ma to 2.27 ± 0.03 Ma (Figure 4b). In addition, seven older zircons had $^{206}Pb/^{238}U$ dates from 71.64 ± 0.53 Ma to 11.30 ± 0.03 Ma, and two additional zircons had $^{206}Pb/^{238}U$ dates of 6.49 ± 0.02 Ma and 3.81 ± 0.03 Ma (Table 1).

A late pegmatitic granodiorite, PNG12-78C, collected from the structurally deepest part of the Goodenough Dome core, crystallized within the strain shadow of a fractured retrogressed eclogite (now amphibolite) block (Figure 3c). Eight zircons have $^{206}Pb/^{238}U$ dates ranging from 3.63 ± 0.01 Ma to 2.09 ± 0.02 Ma (Figure 4b). One older zircon yielded a date of 8.10 ± 0.02 Ma (Table 1).

Late, non-deformed granodiorite plutons intruded and crystallized within all of the domes (Figure 2) [*Baldwin et al.*, 1993; *Baldwin & Ireland*, 1995]. A sample from one such pluton, PNG06-041B, was collected from within the core zone of Goodenough Dome. Four zircons yielded $^{206}Pb/^{238}U$ dates from 1.97 ± 0.06 Ma to 1.82 ± 0.03 Ma (Figure 4b). Two zircons revealed older $^{206}Pb/^{238}U$ dates of 49.90 ± 0.21 Ma and 34.33 ± 0.06 Ma (Table 1).

Normanby Dome

Ten samples from Normanby Dome were collected along a transect from structurally high levels in the carapace beneath the D'Entrecasteaux fault zone (near sea level, exposed in the west), to deeper levels in the core of the dome, exposed farther to the east.

Normanby Dome: Orthogneiss and associated amphibolite

The dominant lithology throughout the domes consists of strongly deformed, biotite-bearing quartzofeldspathic gneiss (Figure 3a), some of which is inferred to be part of a widespread felsic orthogneiss body. Three samples of the felsic orthogneiss body were collected at different structural levels of the dome to evaluate spatial variation in the timing of metamorphism. In addition, one amphibolite (inferred to be part of the host rock to the orthogneiss body) was analyzed.

From the western carapace zone of the dome, a 15-cm thick strongly deformed granodioritic orthogneiss (PNG10-016C) intrudes a garnet-bearing paragneiss unit. This orthogneiss yielded fifteen zircons with $^{206}Pb/^{238}U$ dates from 6.01 ± 0.01 Ma to 5.04 ± 0.07 Ma (Figure 4c) and two older $^{206}Pb/^{238}U$ dates of 30.29 ± 0.02 Ma and 9.38 ± 0.04

Ma. One km farther to the south within the carapace, a similar granodioritic orthogneiss, but in this case with a mylonitic fabric, PNG10-002D, yielded eight zircons with $^{206}Pb/^{238}U$ dates from 6.82 ± 0.02 Ma to 5.66 ± 0.02 Ma (Figure 4c). Eleven other zircons are older with $^{206}Pb/^{238}U$ dates from 461.24 ± 0.41 Ma to 24.30 ± 0.05 Ma (Table 1).

From the core of Normanby Dome farther to the east, a sample of host quartzofeldspathic gneiss (PNG09-065A) yielded six zircon $^{206}Pb/^{238}U$ dates ranging from 115.93 ± 0.10 Ma to 78.98 ± 0.12 Ma, with no evidence of Pliocene recrystallization (Table 1). The host sample amphibolite (PNG09-067A) just to the north yielded three zircon grains with $^{206}Pb/^{238}U$ dates of 925.60 ± 0.65 Ma, 915.96 ± 1.13 Ma, and 911.77 ± 0.60 Ma (Table 1), again with no evidence of Pliocene recrystallization.

Normanby Dome: Sills and Dikes

Six variably deformed sills and dikes were collected from the carapace and core zone of Normanby Dome. Two granodioritic sills were sampled from the carapace zone along the northwestern coast of Normanby Island near the village of Io'yo (Figure 2) and are within the D'Entrecasteaux fault zone. A sample of the granodioritic sill was collected away from the fault (PNG10-021A) and near the contact with the fault (PNG12-94C). Sample PNG10-021A contains relict large (~1 cm in diameter) igneous feldspars that are preserved as porphyroclasts. Seven $^{206}Pb/^{238}U$ zircon dates from this sill have a narrow range from 4.14 ± 0.05 Ma to 4.10 ± 0.01 Ma (Figure 4c). Near the fault, sample PNG12-94C was collected where the granodioritic sill develops a protomylonitic fabric within ~5 m of the contact with the hanging-wall rocks [*Little et al.*, 2011]. Eight zircons from this

part of the sill yielded a weighted mean $^{206}Pb/^{238}U$ date of 4.11 ± 0.01 Ma (MSWD=1.1; Figure 4c), identical to the less deformed phase. From the same outcrop, a non-deformed andesitic dike (PNG12-94B) intrudes the PNG10-021A sill (Figure 3b). Five zircons gave $^{206}Pb/^{238}U$ dates ranging from 4.08 ± 0.02 Ma to 1.98 ± 0.01 Ma (Figure 4d), and thirteen much older zircons yielded $^{206}Pb/^{238}U$ dates that range from 114.37 ± 0.13 Ma to 59.81 ± 0.11 Ma (Table 1).

From the core zone on the east side of the dome (Figure 2), a weakly foliated pegmatitic dike, PNG09-062C crosscuts host orthogneiss similar to dated orthogneiss samples described above. This sample yielded four $^{206}Pb/^{238}U$ zircon dates from 5.24 ± 0.12 Ma to 4.38 ± 0.13 Ma (Figure 4d). Twenty-three older zircons span from 140.64 ± 0.64 Ma to 9.92 ± 0.14 Ma (Table 1). From the drainage to the northwest, a non-deformed andesitic dike occurs as part of a densely intruded, lit-par-lit swarm of steeply dipping, meter-thick dikes that are discordant to the main gneissic foliation that they crosscut [*Little et al.*, 2011]. A ~0.75 kg sample of this dike, PNG12-39D, yielded only one zircon. The zircon has a $^{206}Pb/^{238}U$ date of 2.946 ± 0.003 Ma. Nearby, another non-deformed, more felsic dike, PNG09-075A, yielded seven zircon $^{206}Pb/^{238}U$ dates that range from 1.89 ± 0.03 Ma to 1.99 ± 0.04 Ma (Figure 4d), and one zircon with a $^{206}Pb/^{238}U$ date of 3.60 ± 0.03 Ma (Table 1).

TIMS-TEA Zircon Analysis

Following ID-TIMS analyses, the trace elements from single zircons from eight of the variably deformed orthogneiss, leucosome, granodioritic sills, and intermediate and felsic

dikes of Goodenough and Normanby Dome were analyzed. The zircon trace-element data was obtained for the youngest zircons in each sample, and these are shown in the form of rare earth element (REE) diagrams with their corresponding date in Figure 5 and Table 2. All data are normalized to chondrite values of *Sun and McDonough* [1989].

Goodenough Dome: Leucosomes and Dikes

From the core–carapace transition, the layer-parallel leucosome (PNG10-031A) yielded an individual zircon chondrite-normalized REE pattern (z15) with a strong enrichment of HREE relative to MREE ($Lu_N/Gd_N = 31.0$) and no negative Eu anomaly ($Eu/Eu^* = Eu_N/(Sm_N * Gd_N)^{0.5} = 1.00$) (Figure 5b; Table 2).

Zircons from a weakly deformed pegmatitic dike, PNG10-039B, from the core zone, yielded individual zircon REE patterns (z14, z17) with mostly positive and steep HREE slopes ($Lu_N/Gd_N = 3.9–21.5$) and negative to absent Eu anomalies ($Eu/Eu_* = 0.65–0.78$) (Figure 5b; Table 2).

Normanby Dome: Orthogneiss, Sills, and Dikes

Zircons from strongly deformed granodioritic orthogneiss in the carapace of the dome, PNG10-016C, show consistent REE patterns for all zircons analyzed (z2, z3, z4) with depletion of HREE ($Lu_N/Gd_N = 2.14–3.15$), although the slightly older z3 has a greater depletion in HREE, and all three zircons show an absence of negative Eu anomalies ($Eu/Eu_* = 0.83–0.97$) (Figure 5a, Table 2). Also from the carapace, zircons from the weakly foliated granodioritic sill, PNG10-021A, yielded relatively consistent REE patterns for all four zircons (z8, z9, z10, z11) with slight enrichment of HREE relative to

MREE (Lu/Gd = 3.48–7.10) and no negative Eu anomalies (Eu/Eu^* = 0.80–0.90; Table 2). Farther west and at structurally higher levels near the contact of the D'Entrecasteaux fault zone, the protomylonitic granodioritic sill, PNG12-94C, yielded a single zircon REE pattern (z9) showing similar enrichment of HREE (Lu_N/Gd_N = 6.74) to the less deformed portion of the sill and a slightly negative Eu anomaly (Eu/Eu^* = 0.72) (Figure 5a; Table 2). Sample PNG12-94B, the non-deformed andesitic dike that crosscuts PNG10-021A, yielded zircons (z17, z13, z22) with positive HREE slopes (Lu_N/Gd_N = 4.70–9.25) and negative Eu values (Eu/Eu^* = 0.52–0.70). The youngest zircon (z22) is much more enriched in most of the REEs relative to the older z17 and z13. One analysis (z13) showed a less prominent negative Eu anomaly (Eu/Eu^* = 0.82) (Figure 5b; Table 2).

The non-deformed andesitic dike PNG12-39D from the dike swarm that crosscuts the core-zone gneisses yielded only one zircon. This has a REE pattern (z3) showing strong enrichment of HREE (Lu_N/Gd_N = 62.2) and a prominent negative Eu anomaly (Eu/Eu^* = 0.22). Finally, for the nearby granodioritic-composition dike (PNG09-075A) in the same swarm we report a single zircon trace-element pattern (z21) with a moderately steep HREE slope (Lu_N/Gd_N = 10.2) and a negative Eu anomaly (Eu/Eu^* = 0.49) (Figure 5b; Table 2).

Discussion

Throughout the PNG (U)HP terrane, outcrops of host gneiss contain abundant (10–60% of outcrop) granodioritic to leucogranitic leucosomes, sills, dikes, and plutons [*Hill et al.*, 1995; *Gordon et al.*, 2012]. These variably deformed leucosomes and bodies, such as the sills, dikes, and plutons, reflect local melting and intrusive events that record the

deformation history associated with exhumation. The focus of this study is to use U-Pb geochronology to determine the relative timing of melt crystallization in relation to Pliocene (U)HP metamorphism. We interpret the crystallization ages of late non-deformed dikes, both felsic and andesitic, and a pluton to provide constraints on the final emplacement of the domes within the upper crust. Hereafter, besides a core zone gneiss and an amphibolite from the core zone of Normanby Dome, dates are only discussed that are interpreted to record melt crystallization or metamorphism, which in all samples, as stated above, is the youngest population of zircons. In general, we interpret our older dates as inheritance of either whole grains or possible mixing of small cores and younger overgrowths. The presence of older zircon (i.e., cores or whole grains) is consistent with zircon entrainment during melting and/or assimilation of older rocks by the mostly Pliocene age melts.

We use our new higher precision geochronological constraints and the zircon trace-element data to build on and modify the interpretations based on previous thermo- and geochronology of the (U)HP eclogites and associated gneisses and melt-related fractions (i.e., *Baldwin et al.*, 1993; *Baldwin and Ireland*, 1995; *Baldwin et al.*, 2004; *Monteleone et al.*, 2007; *Gordon et al.*, 2012). The new zircon trace-element data from the host orthogneiss and a variety of texturally distinct melt-related fractions are used to help strengthen the interpretations of the more convincing ID-TIMS analyses.

Goodenough Dome

Previous geochronometric studies of Goodenough Dome have focused on the timing of metamorphism and exhumation of the rocks to the shallow crust ($T < \sim 300$ °C). For

example, previous *in situ* U-Pb SIMS analyses of zircon from variably retrogressed HP eclogites collected at the core–carapace transition and in the core zone of Goodenough Dome were interpreted as recording the timing of HP metamorphism at 2.9 ± 0.4 to 2.1 ± 0.5 Ma ($^{206}Pb/^{238}U$–$^{207}Pb/^{206}Pb$ Terra Wasserburg intercept dates) [*Monteleone et al.*, 2007]. Moreover, two core zone quartzofeldspathic host gneisses also dated by SIMS yielded zircon weighted-mean $^{206}Pb/^{238}U$ dates within error of each other at 2.63 ± 0.16 Ma and 2.72 ± 0.26 Ma [*Baldwin and Ireland*, 1995]. Argon–Argon thermochronology from these two host gneiss samples yielded dates within error of the U-Pb zircon ages: ca. 2.6 Ma for ~60% of the hornblende $^{40}Ar/^{39}Ar$ apparent age and 2.71 Ma for a hornblende $^{40}Ar/^{39}Ar$ plateau age, respectively [*Baldwin et al*., 1993]. *Baldwin and Ireland* [1995] argued that the similarity in the U-Pb and Ar-Ar dates indicates that the zircons from the gneiss record the timing of decompression-related amphibolite-facies metamorphism. The multiple melt generations that have been dated in this study when combined with previous geochronology, as well as the overall deformational evolution of the Goodenough Dome, allow some new insights into the evolution of the region.

Based on field relationships, the strongly deformed granodioritic leucosomes are the oldest generation and share the same amphibolite-facies fabric as the host gneiss dated as part of the *Baldwin and Ireland* [1995] study. From the core–carapace transition, leucosome PNG10-031A contained zircons ranging from 4.737 ± 0.005 Ma to 3.85 ± 0.02 Ma. The youngest age, 3.85 ± 0.02 Ma, is interpreted to be the maximum crystallization age for the layer-parallel leucosome. Structurally deeper within the core of the dome, leucosome PNG10-039A records a younger maximum crystallization age of

2.78 ± 0.02 Ma (Figure 6b). Overall, these crystallization ages for the strongly deformed, layer-parallel leucosomes indicate that this phase of melting may have lasted ~1 m.y. across the dome, with the youngest crystallization ages overlapping the weighted mean dates of 2.63 ± 0.16 Ma and 2.72 ± 0.26 Ma for the core-zone gneisses reported by *Baldwin and Ireland* [1995]. The REE pattern of the individual zircon from the core–carapace leucosome contains a strong, negative Eu anomaly and a moderate to steep HREE slope (Figure 5b; Table 2). The timing of the end of strongly deformed leucosome crystallization (~2 m.y. after (U)HP metamorphism ended) throughout the dome and the magmatic zircon REE pattern (Figure 5b; PNG10-031A, z15) suggest crystallization of the leucosomes took place at crustal conditions.

Crosscutting, weakly deformed dikes, non-deformed aplitic and pegmatitic dikes, and plutonic rocks provide evidence for the continued intrusion of melt throughout all exposed levels of the dome. Zircons from weakly deformed core-zone dike PNG10-039B range from 2.98 ± 0.03 Ma to 2.27 ± 0.03 Ma. In addition, two zircons were dated from a weakly deformed core–carapace dike PNG10-031B at 2.77 ± 0.06 and 2.68 ± 0.11. This sample also contained five older grains, with the youngest being a 3.52 ± 0.14 Ma date; this date, which overlaps with dates from the layer-parallel leucosomes, may indicate re-melting or assimilation of these older leucosomes or host gneiss. However, the youngest grains (2.27 Ma and 2.68 Ma) with zircons that reveal a negative Eu anomaly from the two weakly deformed dikes of the core and carapace are interpreted to record the maximum age for melt crystallization toward the end of ductile deformation in the Goodenough Dome (Figure 5b, 6b).

The non-deformed carapace dike PNG10-029B and non-deformed core-zone pegmatite PNG12-78C that intrude a retrogressed eclogite, records continued melt crystallization between 2.30 ± 0.06 Ma and 2.09 ± 0.02 Ma, respectively. Finally, zircons from the non-deformed pluton, PNG06-041B in the dome core, record the youngest crystallization ages from 1.97 ± 0.06 Ma to 1.82 ± 0.03 Ma (Figure 6b). The crystallization of the ca. 1.9 Ma non-deformed pluton that cuts the dome-defining foliation represents the final stages of the dome-forming event within Goodenough Island.

In summary, a strongly deformed leucosome from the core–carapace transition records the earliest melt crystallization within Goodenough Dome at ca. 3.9 Ma, the oldest igneous date from leucosomes and sills recorded thus far from the Goodenough Dome. In addition, the structurally deeper core-zone leucosome records a younger crystallization history of ca. 2.8 Ma (Figure 6b). The timing of melt crystallization for these strongly deformed leucosomes and of the previously dated host gneiss are seemingly at odds with the interpretation of the ca. 2.9–2.1 Ma eclogite zircon dates from Goodenough Dome reported by *Monteleone et al*. [2007]. If leucosome crystallization occurred in the dome from ca. 3.9–2.8 Ma, the enclosed eclogite should have formed at HP eclogite-facies conditions prior to leucosome crystallization. Therefore, we infer that the reported HP eclogite zircon dates most likely represent recrystallization during amphibolite-facies retrogression, which the host gneiss also experienced [*Baldwin and Ireland*, 1995]. Weakly deformed dikes represent continued magmatism during the final stages of ductile deformation until ca. 2.3 Ma. The crystallization of the ca. 2.0 Ma non-

deformed pegmatite and ca. 1.9 Ma pluton mark the final stages of melt crystallization (Figure 6b).

Normanby Dome

The mafic rocks, lower plate gneisses, granodioritic intrusions, and dikes of Normanby Dome have received far less attention in previous studies of the D'Entrecasteaux Islands. Normanby Dome is unusual in that it exposes a section of the D'Entreacasteaux Fault Zone that preserves upper plate PUB rocks atop a near-complete section of carapace rocks [*Little et al.*, 2011]. Within the fault zone, a granodiorite sill, from which the samples PNG10-021A and PNG12-94C were collected, forms the structural uppermost unit of the lower plate carapace and is in fault contact with the upper plate PUB rocks (Figure 2 and 6a).

A few samples collected and dated from the core of the Normanby Dome do not contain any Pliocene zircons: 1) the volumetrically dominant felsic host gneiss (PNG09-065A) yielded dates from ca. 116 to 79 Ma; and 2) a host amphibolite (PNG09-067A) yielded dates of ca. 926 to 912 Ma (Table 1). Inherited Cretaceous zircons are common throughout the D'Entrecasteaux igneous and metamorphic rocks and are consistent with the suggestion that Australian plate material is the protolith for the lower plate gneisses and eclogites [*Davies*, 1980; *Davies and Jacques*, 1984; *Davies and Warren*, 1988; *Hill and Baldwin*, 1993; *Baldwin and Ireland*, 1995; *Gordon et al.*, 2012; *Zirakparvar et al.*, 2013]. The ca. 920 Ma amphibolite age, however, is one of the first discoveries of a Neoproterozoic mafic protolith within the lower plate rocks of the D'Entrecasteaux Islands. The basement rocks of southern and central Papua New Guinea are thought to be

Paleozoic and Precambrian extensions of the Australian craton [*Davies*, 2012] and may be the protolith for the amphibolite.

The remaining dated samples from Normanby do reveal evidence for metamorphic zircon growth and melt crystallization during the Pliocene. The granodioritic orthogneiss from the carapace (PNG10-016C) yielded zircons with $^{206}Pb/^{238}U$ dates of 6.01 ± 0.01 Ma to 5.04 ± 0.07 Ma. The zircon REE patterns show flat HREE slopes, although z2 and z4 are more enriched in HREE relative to the slightly older z3 (Figure 5a). This could be the result of garnet breakdown in the rock or possibly the breakdown of another HREE-liberating phase (e.g., monazite, although it was never identified). The absence of negative Eu anomalies is consistent throughout the zircon fractions.

Nearby to the south, a mylonitic orthogneiss (PNG10-002D) records slightly older metamorphism from 6.82 ± 0.02 Ma to 5.66 ± 0.02 Ma. The range of ~1–1.5 m.y. within the different orthogneiss samples indicate that these dates may represent mixing of metamorphic core and/or rim overgrowths; therefore, the youngest dates of 5.04 ± 0.07 Ma and 5.66 ± 0.02 Ma are interpreted to be maximum ages for constraining metamorphism within Normanby Dome.

The timing of metamorphism within Normanby Dome directly coincides with the ca. 5.6–4.6 Ma UHP metamorphism within Mailolo Dome [*Gordon et al.*, 2012]. Given the overlap in dates, as well as the REE patterns, it is likely that the orthogneiss samples from Normanby Dome were metamorphosed under HP conditions. However, the Normanby orthogneiss samples lack the mineral assemblage required for thermobarometry estimates to be determined. No eclogite has been dated from Normanby Dome, and thus these ca.

5.0 and ca. 5.6 Ma orthogneisses are the first constraints on the timing of the postulated HP metamorphism of the rocks within Normanby Dome.

The samples collected from the contact between the upper and lower plate of the domes represent important markers for understanding the relationship between melt intrusion within the lower plate and the ophiolitic cover during exhumation of the dome. As mentioned above, there are few localities throughout the D'Entrecasteaux Islands where the contact between the PUB and lower-plate gneiss is preserved. In northwest Normanby, this location is especially critical because the fault zone, the overlying upper plate PUB rocks, and the underlying carapace gneisses are exposed on the inverted limb of a mushroom-shaped fold on the outer flank of the dome (Figure 6a) [*Little et al.*, 2011]. Such folds are commonly seen in diapirs [e.g., *Jackson and Talbot*, 1989] and reflect the outward flow of rocks from the rising central stem of the diapir, together with an inward return flow from the margins. The variably deformed granodioritic sill samples (PNG10-021A and PNG12-94C) collected from the uppermost rocks of the carapace zone yielded zircons that record melt crystallization from 4.18 ± 0.11 Ma to 4.09 ± 0.02 Ma and provide a maximum age constraint at ca. 4.1 Ma for melt crystallization within the carapace of Normanby Dome (Figure 6a). The intrusion of the granodiorite sills ~1–1.5 m.y. after metamorphism of the older carapace rocks and the minor enrichment of HREE and the presence of slightly negative Eu anomalies within these igneous zircons (z8, z9, z10, z11) are interpreted to indicate growth at crustal conditions (Figure 5a; Table 2).

The weakly foliated granodioritic dike (PNG09-062C) zircons from the core zone range from 5.24 ± 0.12 Ma to 4.38 ± 0.13 Ma. We interpret the 4.38 ± 0.13 Ma date to represent the maximum age for melt crystallization within the core of Normanby Dome.

Finally, the youngest zircons from the late, non-deformed carapace andesitic dike PNG12-94B and the non-deformed core-zone andesitic dike PNG12-39D constrain their intrusion at 1.98 ± 0.01 Ma and 2.947 ± 0.003 Ma, respectively. Sample PNG12-94B contained older zircons at 3.33 ± 0.01 Ma and 4.08 ± 0.02 Ma and much older grains ranging from 114.37 ± 0.13 Ma to 59.81 ± 0.11 Ma, again alluding to a potential Cretaceous protolith. The zircon REE patterns of the older zircons (z13 and z17) of PNG12-94B are depleted in HREE relative to the youngest zircon (z22), which also has a distinctive negative Eu anomaly relative to z13 and z17 (Figure 5a). The difference in age and REE composition between z13 and z17 relative to z22 suggest multiple sources provided young (< ca. 3.3 Ma) zircon to this dike. Moreover, the steep HREE slope and prominent negative Eu anomaly of the zircon (z3; Figure 5b) of PNG12-39D are indicative of igneous zircons. The field and age relationships, along with the zircon REE compositions, indicate the dikes crystallized at crustal conditions.

In comparison to the andesitic dike, the non-deformed core-zone granodioritic dike PNG09-075A yielded zircons that record slightly younger dates from 1.99 ± 0.04 Ma to 1.89 ± 0.03 Ma (Figure 6b) and a few inherited grains with the youngest at 3.60 ± 0.03 Ma. The $^{206}Pb/^{238}U$ date of 3.60 Ma is interpreted as inheritance from an older leucosome or gneiss. The REE signature for the ca. 1.9 Ma non-deformed dike zircon (z21) shows a steep HREE slope and a strong negative Eu signature (Figure 5b; Table 2).

The 2.947 ± 0.003 Ma to 1.89 ± 0.03 Ma melt-crystallization ages for all the non-deformed dikes from the core and carapace zones and the REE signatures suggest that this was the last pulse of melt crystallization that occurred during the end of deformation within Normanby Dome as the dome was most likely emplaced in the upper crust. Moreover, the youngest, ca. 1.9 Ma, crystallization ages for the andesitic and granodioritic dikes are in agreement with the timing of crystallization for late granodiorite intrusions and plutons, including the Goodenough Island sample (PNG06-041B), throughout the D'Entrecasteaux Islands (i.e., *Baldwin et al.*, 1993).

In summary, the metamorphism of the carapace orthogneiss bodies in the Normanby Dome took place from ca. 5.6–5.0 Ma at likely HP conditions (Figure 6b). The granodiorite body in contact with the D'Entrecasteaux fault zone indicates melt crystallization may have ended ~1 m.y after orthogneiss metamorphism. Deformation within Normanby Dome may have come to an end ~ 1 m.y later, as recorded by the crystallization of the ca. 2.94 Ma non-deformed intermediate dike. However, the last phase of melt crystallization of non-deformed dikes of the core and carapace zones at ca. 1.8–1.9 Ma is the most reliable record of the end of ductile deformation throughout all structural levels of the dome. The U-Pb crystallization ages of the dikes are within error of cooling dates reported from Normanby Dome, including: 1) K-feldspar $^{40}Ar/^{39}Ar$ thermochronology of a deformed schist and granodiorite near the same fault zone described above that yielded dates of 2.00 ± 0.02 Ma and 2.01 ± 0.02 Ma, respectively; and 2) a K/Ar whole rock age of 1.78 ± 0.03 Ma from a non-deformed dolerite dike also from the fault zone [*Baldwin et al.*, 1993].

Pressure-Temperature-Deformation-time (P–T–d–t) history for the PNG (U)HP Terrane

The variety of gneisses and multiple generations of leucosome, dike, and granitoid fractions found within the D'Entrecasteaux Islands capture different phases of dome exhumation and associated deformation. A comparison will now be made between our data and the diapiric exhumation model for the PNG (U)HP terrane described in *Little et al.* [2011]. During the Papuan arc-continent collision (ca. 58–22 Ma), a large nappe of Australian-derived continental crust was most likely subducted to mantle depths, where the material is inferred to have undergone a Paleogene phase of eclogite-facies metamorphism [*Davies and Warren*, 1988; *Zirakparvar et al.*, 2011]. At present there are no data for the evolution of the PNG (U)HP terrane after the end of the Papuan Orogen. It is thought that the subducted nappe resided in the (now inactive) paleosubduction channel until asthenospheric flow associated with the westward-propagation of the Woodlark Rift provided fluids for reheating of the subducted material, causing widespread recrystallization of the crustal nappe at (U)HP conditions. This is interpreted to have occurred in the early Pliocene at ca. 5.6–4.3 Ma within Mailolo Dome [*Baldwin et al.*, 2004; *Gordon et al.*, 2012]. Based on the timing of metamorphism within Normanby Dome (ca. 5.6–5.0; Figure 6b) and the zircon trace-element data, the orthogneiss samples (PNG10-002D and PNG10-016C) likely were also metamorphosed under HP conditions at this time.

Following (U)HP metamorphism, the partially-molten, eclogite-bearing material began to rise buoyantly to the base of the crust as diapiric bodies at rates of ~1.7 cm/yr, which are constrained by previous geochronology and thermobarometry [*Davies and*

Warren, 1988; *Hill and Baldwin*, 1993; *Baldwin et al.*, 2004; *Little et al.*, 2011]. Two- and three-dimensional thermomechanical modeling of the exhumation of the D'Entrecasteaux Islands UHP terrane, including its melting, shows that large-scale partial melting would be a likely effect to accompany its near-isothermal decompression path [*Hill and Baldwin et al.,* 1993; *Baldwin et al.,* 1993], as it ascended near vertically from mantle depths [*Ellis et al.*, 2011]. This partial melting would cause both a reduction in density and effective viscosity of the exhuming rocks relative to the surrounding mantle [*Clemens and Droop*, 1998], further enhancing buoyancy of the UHP terrane. The ca. 4.1 Ma deformed granodiorite sill (PNG10-021A and PNG12-94C) is evidence for melt crystallization in Normanby Dome within lower crustal levels, although the particular source of the granodiorite is unkown.

Upon reaching the base of the crust, the density contrast between the rising (U)HP diapir and the mantle would have been greatly reduced [e.g., *Walsh and Hacker*, 2004; *Ellis et al.*, 2011], allowing the partially-molten body to spread laterally along the base of the crust [e.g., *Walsh and Hacker*, 2004; *Hacker et al.*, 2011]. *Little et al.* [2011] suggests that the ductile thinning that accompanied the mostly E-W oriented (parallel to the rift margins), gravity-driven flow of the stalled material may have accommodated ~ 25 km of vertical exhumation of the terrane. During this lateral flow, *in situ* melt coalesced to form foliation-parallel leucosomes, and intruded sill-like bodies began crystallizing upon cooling and were subsequently deformed throughout the domes. Within Goodenough Dome, this deformational event and melt crystallization was recorded at ca. 3.9 Ma within the structurally higher levels of the dome and continued to ca. 2.7 Ma in the core of the dome, based on the layer-parallel leucosomes. In comparison, similar leucosomes

within Mailolo Dome, to the east, record melt crystallization from ca. 3.0–3.5 Ma (Figure 6b) [*Gordon et al.*, 2012], whereas strongly-deformed leucosomes of these ages have yet to be observed in Normanby Dome. At this time, the dominant sub-horizontal foliation observed throughout the domes developed during amphibolite-facies overprinting [*Little et al.*, 2011]. During this overprinting, the terrane continued to undergo anatexis [*Little et al.*, 2011]. Further melting may have reduced the bulk rock density of the body to such an extent that it resumed its buoyantly driven upward path, probably accompanied by upper-crustal extension, leading to final emplacement of the terrane as gneiss domes at upper crustal levels.

As the (U)HP body was exhumed into the upper crust, numerical modeling predicts the fraction of melt may have reached a maximum of ~40 vol.% [*Ellis et al.*, 2011], comparable to estimates of leucosomes, sills, dikes, and plutons observed in the D'Entrecasteaux Islands [*Little et al.*, 2011; *Gordon et al.*, 2012]. We correlate this predicted episode of melting and granitoid dike intrusion to the weakly deformed dikes (PNG10-031B and PNG10-039B) that are preserved within Goodenough Dome at ca. 2.3 Ma and in Mailolo Dome at ca. 2.4 Ma [*Gordon et al.*, 2012] during the final stages of amphibolite-facies metamorphism. In comparison, an age for similar dikes from the core zone of Normanby Dome (PNG09-062C) is much older at 4.38 ± 0.13 Ma (Figure 6b).

Towards the end of its ascent, the (U)HP body was juxtaposed against the ophiolitic upper plate along the D'Entrecasteaux fault zone, creating the domal structures across the D'Entrecasteaux Islands. The dome-forming event in Normanby and Goodenough Domes was complete by ca. 1.82 ± 0.03 to 1.99 ± 0.04 Ma (Figure 6b), which represent the crystallization of the non-deformed dikes and plutons (PNG09-075A, PNG12-94B, and

PNG06-041B) that cut the dome-defining foliation throughout all structural levels (Figure 6a). These dates are consistent with a ca. 1.9 Ma biotite $^{40}Ar/^{39}Ar$ cooling age within Mailolo Dome [*Baldwin et al.*, 1993]. Melt-induced buoyancy and rapid concurrent tectonic extension in the upper crust both assisted in the final emplacement of the domes within the shallow crust by ca. 1.8 Ma [*Fitzgerald et al.*, 2008].

Papua New Guinea: a small UHP terrane

UHP terranes have been categorized into two main groups depending on a variety of characteristics, including their size, timing of metamorphism, and subsequent exhumation to crustal levels: 1) large terranes that have evolved slowly over 10–30 m.y. (both subduction and exhumation are relatively slow); and 2) small terranes that were rapidly (< 10 m.y.) subducted and exhumed [*Kylander-Clark et al.*, 2012]. The eastern PNG terrane falls into the "small" end member category, and notably, these types of UHP terranes also tend to occur in tectonically active orogens, such as the D'Entrecasteaux Island terrane, exposed in the active Woodlark rift [*Kylander-Clark et al.*, 2012].

The Dora Maira Massif is one of the most studied of the "small" UHP terranes. It is part of three internal crystalline massifs exposed in the Western Alps and contains coesite-bearing crustal rocks that experienced UHP metamorphism at ca. 35 Ma [*Chopin*, 1984; *Gebauer*, 1997; *Rubatto and Hermann*, 2001]. This UHP terrane has undergone rapid exhumation at rates of 1.6–3.4 cm/yr [*Rubatto and Hermann*, 2001]; rates similar to that inferred for PNG (~1.7 cm/yr) [*Baldwin et al.*, 2004]. In comparison to PNG, however, Dora Maira differs in that it has experienced slightly greater pressures (>3.2 GPa) [*Schertl et al.*, 1991; *Compagnoni et al.*, 1995], does not appear to have undergone

partial melting, and structurally lies within two nappe units that have experienced low-temperature eclogite facies and epidote–blueschist conditions, respectively (*Chopin et al.*, 1991). Both Dora Maira and PNG provide an opportunity to understand the switch from continental subduction and concurrent UHP metamorphism to very rapid (~2 cm/yr) exhumation of crustal material; however, these two "small" UHP terranes preserve evidence that there are multiple mechanisms by which the very fast exhumation rates can be achieved (i.e., via tectonic stacking/thrusting [e.g., *Chopin*, 1987] versus a near-vertically ascending diapir).

The idea of partial melting driving exhumation is not unique to either "large" or "small" UHP terranes. For example, the Kokchetav and Erzgebirge UHP terranes have achieved very high temperatures (> 1000 °C) and pressures (> 40 kbar) and preserve evidence for UHP silicate and carbonate melts within garnet and clinopyroxene, indicating partial melt was present at UHP conditions [*Shatsky et al.*, 1995; *Zhang et al.*, 1997; *Massonne*, 1999; *Stöckhert et al.*, 2001; *Korsakov and Hermann*, 2006]. For both terranes, deeply subducted metasedimentary rocks are thought to have undergone anatexis with melts (or crystal mashes) rapidly ascending from depths > 140 km, producing diamondiferous quartz-rich rocks [*Massonne*, 2003]. In Kokchetav, the rapid ascent (~1.8 cm/yr) [*Hermann et al.*, 2001] is thought to have occurred as a migmatitic, diapir-like body ascending from mantle depths to the base of the crust, which is also interpreted for the PNG terrane, although the latter was derived from much shallower depths of ~90 km.

Even though the Kokchetav UHP terrane is thought to have been rapidly exhumed in the presence of melt [*Hermann and Green*, 2001; *Hermann et al.*, 2006], geochronology

suggests that melting took place 5–10 m.y. after peak UHP metamorphism during an exhumation-related granulite-facies overprinting event [*Ragozin et al.*, 2009]. The timescales for decompression melting subsequent to UHP metamorphism in PNG are much faster than for Kokchetav, with melt crystallization taking place within the PNG UHP terrane as early as 1 m.y. after peak conditions [*Gordon et al.*, 2012; *this study*]. PNG represents a terrane that shares a rapid exhumation and partial-melt driven history with other UHP terranes, but is unique in that it has been exhumed as near-vertically ascending diapirs over extremely short timescales within an active rift setting.

Conclusions

This study documents the near-continuous exhumation of the youngest (ca. 4.6–5.6 Ma) known (U)HP terrane on Earth and provides constraints on the evolution of a small (~4000 km^2), melt-rich crustal terrane. Within PNG, (U)HP metamorphism is recorded by coesite-bearing eclogite at ca. 5.6–4.6 Ma in the Mailolo Dome, which is coincident with likely HP metamorphism at ca. 5.6–5.0 Ma of orthogneiss bodies within Normanby Dome. Even though the (U)HP terrane is small, there are robust differences in the timing of exhumation among the different domes exposed across the three D'Entrecasteaux Islands (Figure 6b). The youngest UHP metamorphic dates (ca. 4.6 Ma) are slightly older than the ca. 4.1 Ma deformed granodiorite sill in Normanby Dome and the crystallization of layer-parallel leucosomes within Goodenough Dome from ca. 3.9–2.8 Ma, which based on their field and age relationships and trace-element results crystallized at crustal conditions. Moreover, the leucosomes are strongly deformed by the main exhumation-related foliation. In Mailolo Dome on Fergusson Island, the crystallization of layer-

parallel leucosomes are similar to the dates recorded in Goodenough from the same textural samples, although crystallization appears to have occurred within a shorter time interval from ca. 3.0–3.5 Ma.

Subsequent melt intrusion and crystallization during the final phases of ductile deformation record continued exhumation of Goodenough Dome from ca. 2.3–2.7 Ma and of Mailolo Dome at ca. 2.4 Ma. However, a texturally similar less deformed dike from the core of the Normanby Dome records a much older date of ca. 4.4 Ma. The final intrusion of late non-deformed dikes and plutons across all the D'Entrecasteaux domes marks the end of the ductile-doming event by ca. 1.8 Ma. High-precision dating of orthogneiss and the multiple crystallization events has documented the rapid exhumation (over a ~3 m.y. period) of all of the D'Entrecasteaux Islands Domes from mantle depths to their permanent residence in the brittle upper crust.

Acknowledgements

Data supporting Figures 4 and 5 is available in Supporting Information Tables 1 and 2, respectively.

This work was supported by NSF Grant EAR-1019709 (Gordon) and a Marsden Fund Grant 08-VUW-020 (Little). High-precision mass spectrometry at MIT is possible because of an Instrumentation and Facilities grant (EAR-0931839 to S.A.B) and the collective sharing of knowledge by the EARTHTIME community. This manuscript was greatly improved by helpful reviews from Clare Warren, Loïc Labrousse, and two anonymous reviewers. We would like to thank Jahan Ramezani for his assistance in the

MIT Isotope Laboratory. We would also like to thank Blair Schoene and Mélanie Barboni for performing the TIMS-TEA analyses at Princeton.

References

Abers, G.A. (2001), Evidence for seismogenic normal faults at shallow depths in continental rifts. In: Wilson, R.C.L., R.B. Whitmarsh, B. Taylor, N. Froitzham, (Eds.), Non-volcanic Rifting of Continental Margins, pp. 305–318, *The Geological Society of London, Special Publications*, **187**, London.

Abers, G.A., A. Ferris, M. Craig, H. Davies, A.L. Lerner-Lam, J.C. Mutter, and B. Taylor (2002), Mantle compensation of active metamorphic core complexes at Woodlark rift in Papua New Guinea, *Nature*, **418**, 862–865, doi:10.1038/nature00990.

Baldwin, S.L., and T.R. Ireland (1995), A tale of two eras: Pliocene-Pleistocene unroofing of Cenozoic and late Archean zircons from active metamorphic core complexes, Solomon Sea, Papua New Guinea, *Geology*, **23**, 1023–1026, doi: 10.1130/0091-7613(1995)023<1023:ATOTEP>2.3.CO;2.

Baldwin, S.L., G.S. Lister, E.J. Hill, D.A. Foster, and I. McDougall (1993), Thermochronologic constraints on the tectonic evolution of active metamorphic core complexes, D'Entrecasteaux Islands, Papua New Guinea, *Tectonics*, **12**, 611–628, doi: 10.1029/93TC00235.

Baldwin, S.L., B. Monteleone, L.E. Webb, P.G. Fitzgerald, M. Grove, and E.J. Hill (2004), Pliocene eclogite exhumation at plate tectonic rates in eastern Papua New Guinea, *Nature*, **431**, 263–267, doi:10.1038/nature02846.

Baldwin, S.L., L.E. Webb, and B.D. Monteleone (2008), Late Miocene coesite-eclogite exhumed in the Woodlark Rift, *Geology*, **36**, 735–738, doi: 10.1130/G25144A.1.

Beaumont, C., R.A. Jamieson, J.P. Butler, and C.J. Warren (2009), Crustal structure: A key constraint on the mechanism of ultra-high-pressure rock exhumation, *Earth Planet. Sci. Lett.*, **287**, 116–129, doi:10.1016/j.epsl.2009.08.001.

Chemenda, A.I., M. Mattauer, J. Malavieille, and A.N. Bokun (1995), A mechanism for syncollisional rock exhumation and associated normal faulting: results from physical modeling, *Earth Planet. Sci. Lett.*, **132**, 225–232, doi: 10.1016/0012-821X(95)00042-B.

Chemenda, A.I., M. Mattauer, and A.N. Bokun (1996), Continental subduction and a mechanism for exhumation of high-pressure metamorphic rocks: new modeling and field data from Oman, *Earth Planet. Sci. Lett.*, **143**, 173–182, doi: 10.1016/0012-821X(96)00123-9.

Chopin, C. (1984), Coesite and pure pyrope in high-grade blueschists of the western Alps: a first record and some consequence, *Contrib. Mineral. Petrol.*, **86**, 107–118, doi: 10.1007/BF00381838.

Chopin, C. (1987), Very-high-pressure metamorphism in the western Alps: implications for subduction of continental crust [and discussion], *Phil. Trans. R. Soc. Lond. A*, **321**, 183–197, doi:10.1098/rsta.1987.0010.

Chopin, C., C. Henry, and A. Michard (1991), Geology and petrology of the coesite-bearing terrain, Dora Maira Massif, Western Alps, *Eur. .I. Mineral.* **3**, 263-291, doi:10.1127/ejm/3/2/0263.

Clemens, J.D., and G.T.R. Droop (1998), Fluids, P-T paths and the fate of anatectic melts in the Earth's crust, *Lithos*, **44**, 21–36, doi: 10.1016/S0024-4937(98)00020-6.

Compagnoni, R., T. Hirajima, and C. Chopin (1995), Ultra-high-pressure metamorphic rocks in the Western Alps, in Coleman, R.G., and X. Wang, (Eds.), Ultrahigh pressure metamorphism, pp. 206–243, *Cambridge University Press*, Cambridge, UK.

Cloos, M., B. Sapiie, Q.A. vanUfford, R.J. Weiland, P.Q. Warren, and T.P. McMahon (2005), Collisional delamination in New Guinea: the geotectonics of slab break-off, *Geological Society of America Special Paper* 400, 51, doi: 10.1130/2005.2400.

Davies, H. L. (1973), The Geology of Fergusson Island, *map with explanatory notes*, Australia Bureau of Mineral Resources.

Davies, H.L. (1980), Crustal structure and emplacement of ophiolite in southeastern Papua New Guinea, *Colloques Internationaux du C.N.R.S*, **272**, 17–33.

Davies, H.L. (1990), Structure and evolution of the border region of New Guinea. In: Carman, G.J., Z. Carman, (Eds.), Petroleum Exploration in Papua New Guinea: *Proceedings of the First PNG Petroleum Convention, Port Morseby, February 12–14, 1990*, 249–269.

Davies H.L. (2012), The geology of New Guinea: the cordilleran margin of the Australian continent, *Episodes*, **35**, 87–102.

Davies, H.L., and A.L. Jaques (1984), Emplacement of ophiolite in Papua New Guinea, *Geological Society of London Special Publication 13*, 341–350, doi: 10.1144/GSL.SP.1984.013.01.27.

Davies, H.L., and R.G Warren (1988), Origin of eclogite-bearing, domed, layered metamorphic complexes (core complexes) in the D'Entrecasteaux Islands, Papua New Guinea, *Tectonics,* **7**, 1–21, doi: 10.1029/TC007i001p00001.

Davies, H.L., and R.G. Warren (1992), Eclogites of the D'Entrecasteaux Islands, *Contrib. Mineral. Petrol.*, **112**, 463–474, doi: 10.1007/BF00310778.

Davies, H.L., and A.N. Williamson (1998), Buna, Papua New Guinea, 1:250,000 Geological Series, *Geological Survey of Papua New Guinea Explanatory Notes SC/55-3.*, Port Moresby, Papua New Guinea.

Ellis, S.M., T.A Little, L.M.Wallace, B.R. Backer, and S.J.H Buiter (2011), Feedback between rifting and diapirism can exhume ultrahigh-pressure rocks, *Earth Planet. Sci. Lett.*, **311**, 427–438, doi: 10.1016/j.epsl.2011.09.031.

Ernst, W.G. (2001), Subduction, ultrahigh-pressure metamorphism, and regurgitation of buoyant crustal slices – implications for arcs and continental growth. In: Rubie, D., R. van der Hilst, (Eds.), *Processes and Consequences of Deep Subduction*, 253–275, doi : 10.1016/S0031-9201(01)00231-X.

Ferris, A., G.A. Abers, B. Zelt, B. Taylor, and S. Roecker (2006), Crustal structure across the transition from rifting to spreading: the Woodlark rift system of Papua New Guinea, *Geophysical Journal International*, **166**, p. 622–634, doi: 10.1111/j.1365-246X.2006.02970.x.

Fitzgerald, P.G., S.L. Baldwin, S.L. Miller, S.E. Perry, L.E. Webb, T.A. Little (2008), Low temperature constraints on the evolution of metamorphic core complexes of the Woodlark rift system, *Annual Meeting of the American Geophysical Union. AGU, EOS Transactions*, San Francisco, CA.

Gebauer, D., H.-P Schertl, M. Brix, and W. Schreyer (1997), 35 Ma old ultrahigh-pressure metamorphism and evidence for very rapid exhumation in the Dora Maira massif, Western Alps, *Lithos*, **41**, 5–24, doi: 10.1016/S0024-4937(97)82002-6.

Gordon, S.M., T.A. Little, B.R. Hacker, S.A. Bowring, S.L. Baldwin, and A.R.C. Kylander-Clark, (2012), Multi-stage exhumation of young UHP–HP rocks: timescales of melt crystallization in the D'Entrecasteaux Islands, southeastern Papua New Guinea, *Earth Planet. Sci. Lett.*, **351–352**, 237–246, doi: 10.1016/j.epsl.2012.07.014.

Gordon, S.M., D.L. Whitney, C. Teyssier, and H. Fossen (2013), U-Pb dates and trace-element geochemistry of zircon from migmatite, Western Gneiss Region, Norway: Significance for history of partial melting in continental subduction, *Lithos*, **170–171**, 35–53, doi: 10.1016/j.lithos.2013.02.003.

Hacker, B.R. (2006), Pressures and temperatures of ultrahigh-pressure metamorphism: Implications for UHP tectonics and H2O in subducting slabs, *International Geology Review*, **48**, 1053–1066, doi: 10.2747/0020-6814.48.12.1053.

Hacker, B.R. (2007), Ascent of the ultrahigh-pressure Western Gneiss Region, Norway. In: Cloos, M., W.D. Carlson, M.C. Gilbert, J.G. Liou, and S.S. Sorenson (Eds.), Convergent Margin Terranes and Associated Regions, A Tribute to W.G. Ernst,

Geological Society of America Special Paper, **419,** Geological Society of America, Boulder, CO, 171–184, doi: 10.1130/2006.2419(09).

Hacker, B.R., P.B. Kelemen, and M.D. Behn (2011), Differentiation of the continental crust by relamination, *Earth Planet. Sci. Lett.*, **307**, 501–516, doi: 10.1016/j.epsl.2011.05.024.

Hacker, B.R., and T.V. Gerya (2013), Paradigms, new and old, for ultrahigh-pressure tectonism, *Tectonophysics*, **603**, 79–88, doi: 10.1016/j.tecto.2013.05.026.

Hermann, J., and D.H. Green (2001), Experimental constraints on high pressure melting in subducted crust, *Earth Planet. Sci. Lett.*, **188**, 149–168, doi: 10.1016/S0012-821X(01)00321-1.

Hermann, J., D. Rubatto, A. Korsakov, and V.S. Shatsky (2001), Multiple zircon growth during fast exhumation of diamondiferous, deeply subducted continental crust (Kokchetav Massif, Kazakhstan), *Contrib. Mineral. Petrol.*, **141**, 66–82, doi: 10.1007/s004100000218.

Hermann, J., C. Spandler, Alistair Hack, and A. Korsakov (2006), Aqueous fluids and hydrous melts in high-pressure and ultra-high pressure rocks: Implications for element transfer in subduction zones, *Lithos*, **92**, 399–417, doi: /10.1016/j.lithos.2006.03.055.

Heuret, A., and S. Lallemand (2005), Plate motions, slab dynamics and back-arc deformation, *Phy. Earth Planet. Int.*, **149**, 31–51, doi: 10.1016/j.pepi.2004.08.022.

Hill, E.J. (1994), Geometry and kinematics of shear zones formed during continental extension in eastern Papua New Guinea, *J. Struct. Geol.*, **16**, 1093–1105, doi: 10.1016/0191-8141(94)90054-X.

Hill, E.J., S.L. Baldwin, and G.S. Lister (1992), Unroofing of active metamorphic core complexes in the D'Entrecasteaux Islands, Papua New Guinea, *Geology*, **20**, 907–910, doi: 10.1130/0091-7613(1992) 020<0907:UOAMCC> 2.3.CO;2.

Hill, E.J., and Baldwin, S.L. (1993), Exhumation of high-pressure metamorphic rocks during crustal extension in the D'Entrecasteaux region: Papua New Guinea, *J. Metamorph. Geol.*, **11**, 261–277, doi: 10.1111/j.1525-1314.1993.tb00146.x.

Hill, J., S.L. Baldwin, and G.S Lister (1995), Magmatism as an essential driving force for formation of active metamorphic core complexes in eastern Papua New Guinea, *J. Geophys. Res.*, **100**, 10441–10451, doi: 10.1029/94JB03329.

Jackson, M.P.A., and C.J. Talbot (1989), Anatomy of mushroom-shaped diapirs, *J. Struct. Geol.*, **11**, 211–230, doi: 10.1016/0191-8141(89)90044-8.

Korchinski, M., et al. (in review), Timing of UHP exhumation and rock fabric development in gneiss domes containing the world's youngest eclogite-facies rocks, Woodlark Rift, southeastern Papua New Guinea, *J. Metamorph. Geol*.

Korsakov, A.V., and J. Hermann (2006), Silicate and carbonate melt inclusions associated with diamonds in deeply subducted carbonate rocks, *Earth Planet. Sci. Lett.*, **241**, 104–118, doi: 10.1016/j.epsl.2005.10.037.

Kylander-Clark, A. R. C., B.R. Hacker, and C.G. Mattinson (2012), Size and exhumation rate of ultrahigh-pressure terranes linked to orogenic stage, *Earth Planet. Sci. Lett.*, **321–322**, 115–120, doi: 10.1016/j.epsl.2011.12.036.

Labrousse, L., G. Prouteau, and A.C. Ganzhorn (2011), Continental exhumation triggered by partial melting at ultrahigh pressure, Geology, **39**, 1171–1174, doi: 10.1130/G32316.1.

Lang, H.J., and J.A. Gilotti (2007), Partial melting of metapelites at ultrahigh-pressure conditions, Greenland Caledonides, *J. Metamorph. Geol.*, **25**, 129–147, doi: 10.1111/j.1525-1314.2006.00687.x.

Little, T.A., B.R. Hacker, S.M. Gordon, S.L. Baldwin, P.G. Fitzgerald, S. Ellis, and M. Korchinski (2011), Diapiric exhumation of Earth's youngest (UHP) eclogites in the gneiss domes of the D'Entrecasteaux Islands, Papua New Guinea, *Tectonophysics*, **510**, 39–68, doi: 10.1016/j.tecto.2011.06.006.

Little, T.A., B.R. Hacker, S.J. Brownlee, and G. Seward (2013), Microstructures and quartz lattice-preferred orientations in the eclogite-bearing migmatitic gneisses of the D'Entrecasteaux Islands, Papua New Guinea, *Geochem., Geophys., Geosyst.*, ***14*** **(6)**, 2030–2062, doi: 10.1002/ggge.20132.

Lus, W.Y., I. McDougall, and H.L. Davies (2004), Age of metamorphic sole of the Papuan Ultramafic Belt ophiolite, Papua New Guinea, *Tectonophysics, 392*, 85–101, doi: 10.1016/j.tecto.2004.04.009.

Mattinson, J.M. (2005), Zircon U-Pb chemical abrasion ("CA-TIMS") method: combined annealing and multi-step partial dissolution analysis for improved precision and accuracy of zircon ages, *Chem. Geol.*, **220**, 47–66, doi: 10.1016/j.chemgeo.2005.03.011.

Massonne, H.J. (1999), A new occurrence of microdiamonds in quartzofeldspatic rocks of the Saxonian Erzgebirge Germany and their metamorphic evolution, In: Gurney, J.J., L.G. Gurney, M.D. Pascoe, and S.H. Richardson (Eds.), *Proceedings of the 7th International Kimberlite Conference, vol. 2. Cape Town, South Africa*, 533–539.

Massonne, H.J. (2003), A composition of the evolution of diamondiferous quartz-rich rocks from the Saxonian Erzgebirge and the Kokchetav Massif: are so-called diamondiferous gneisses magmatic rocks?, *Earth Planet. Sci. Lett.*, **216**, 347–364, doi: 10.1016/S0012-821X(03)00512-0.

Massonne, H.J., A.P. Willner, and T.V. Gerya (2007), Densities of metapelitic rocks at high to ultrahigh pressure conditions: what are the geodynamic consequences?, *Earth Planet. Sci. Lett.*, **256**, 12–27, doi: 10.1016/j.epsl.2007.01.013.

Monteleone, B.D., S.L. Baldwin, L.E. Webb, P.G. Fitzgerald, M. Grove, and A.K. Schmitt (2007), Late Miocene–Pliocene eclogite facies metamorphism, D'Entrecasteaux Islands, SE Papua New Guinea, *J. Metamorph. Geol.*, **25**, 245–265, doi: 10.1111/j.1525-1314.2006.00685.x.

Rey, P.F., C. Teyssier, and D.L. Whitney (2009), Extension rates, crustal melting, and core complex dynamics, *Geology*, **37**, 391–394, doi: 10.1130/G25460A.1.

Ragozin, A. L., J. G. Liou, V.S. Shatsky, and N.V. Sobolev (2009), The timing of the retrograde partial melting in the Kumdy-Kol region (Kokchetav Massif, Northern Kazakhstan), *Lithos*, **109**, 274–284, doi:10.1016/j.lithos.2008.06.017.

Rosenberg, C.L., and M.R. Handy (2005), Experimental deformation of partially melted granite revisited: Implications for the continental crust, *J. Metamorph. Geol.*, **23**, 19–28, doi: 10.1111/j.1525-1314.2005.00555.x.

Rogerson, R., D.B. Hilyard, E.J. Finlayson, D.J. Holland, S.T.S. Nion, R.M. Sumarang, J. Dugaman, and C.D.C. Loxton (1987), The geology and mineral resources of the Sepik headwaters region, Papua New Guinea, *Papua New Guinea Geological Surveys Memoir, 12*.

Rubatto, D. (2002), Zircon trace element geochemistry: distribution coefficients and the link between U-Pb ages and metamorphism, *Chem. Geol.*, **184**, 123–138, doi: 10.1016/S0009-2541(01)00355-2.

Rubatto, D., and J. Hermann (2001), Exhumation as fast as subduction?, *Geology*, **29**, 3–6, doi: 10.1130/0091-7613(2001) 029<0003:EAFAS> 2.0.CO;2.

Rubatto, D., and J. Hermann (2007), Zircon behaviour in deeply subducted rocks, *Elements*, **3**, 31–35, doi: 10.2113/gselements.3.1.31.

Schoene, B., C. Latkoczy, U. Schaltegegger, and D. Günther (2010), A new method integrating high-precision U–Pb geochronology with zircon trace-element analysis (U–Pb TIMS-TEA), *Geochim, et Cosmochim. Acta.*, **74**, 7144–7159, doi: 10.1016/j.gca.2010.09.016.

Scholz, C.H., and J. Campos (1995), On the mechanism of seismic decoupling and back arc spreading at subduction zones, *J. Geophys. Res.*, **100**, 22103–22115, doi: 10.1029/95JB01869.

Schertl, H.-P., W. Schreyer, and C. Chopin (1991), The pyrope–coesite rocks and their country rocks at Parigi, Dora-Maira Massif, Western Alps: detailed petrography, mineral chemistry and PT-path, *Contrib. Mineral. Petrol.*, **108**, 1–21, doi: 10.1007/BF00307322.

Schertl, H.-P., and N.V. Sobolev (2013), The Kokchetav Massif, Kazakhstan: **"**Type locality**"** of diamond-bearing UHP metamorphic rocks, *J. Asian Earth Sci.*, **63**, 5–38, doi: 10.1016/j.jseaes.2012.10.032.

Shatsky, V.S., N.V. Sobolev, and M.A. Vavilov (1995), Diamond-bearing metamorphic rocks of the Kokchetav Massif (northern Kazakhstan), In: Coleman, R.G., X. Wang (Eds.), Ultrahigh Pressure Metamorphism, *Cambridge University Press*, 427–455.

Smith, D.C. (1984), Coesite in clinopyroxene in the Caledonides and its implications for geodynamics, *Nature*, **310**, 641–644, doi:10.1038/310641a0.

Sobolev, N.V., and V.S. Shatsky (1990), Diamond inclusions in garnets from metamorphic rocks; a new environment of diamond formation, *Nature*, **343**, 742–746, doi:10.1038/343742a0.

Stöckhert, B., J. Duyster, C. Trepmann, and H.J. Massone (2001), Microdiamond daughter crystals precipitated from supercritical COH + silicate fluids included in garnet, Erzgebirge, Germany, *Geology*, **29**, 391–394, doi: 10.1130/0091-7613(2001) 029<0391:MDCPFS> 2.0.CO;2.

Sun S. S., and W.F. McDonough (1989), Chemical and isotopic systematics of oceanic basalts: implications for mantle composition and processes, *Geological Society of London Special Publications*, **42**, 313–345, doi: 10.1144/GSL.SP.1989.042.01.19.

Taylor, B., A.M. Goodliffe, F. Martinez (1999), How Continents break-up: insights from Papua New Guinea, *J. Geophys. Res.*, **104**, 7497–7512, doi: 10.1029/1998JB900115.

Tregoning, P., K. Lambeck, A. Stoltz, P. Morgan, S. C. McClusky, P. van der Beek, H. McQueen, R. J. Jackson, R. P. Little, A. Laing, and B. Murphy (1998), Estimation of current plate motions in Papua New Guinea from Global Positioning System observations, *J. Geophys. Res.*, **103**, 12,181– 12,203, doi: 10.1029/97JB03676.

Van Ufford, Q.A., and M. Cloos (2005), Cenozoic tectonics of New Guinea, *Am. Assoc. Pet. Geol. Bull.*, **89**, 119–140, doi:10.1306/08300403073.

Waggoner, A., S.L. Baldwin, L.A Webb, T.A. Little, and P.G. Fitzgerald (2008), Temporal constraints on continental rifting and the exhumation of the youngest known HP metamorphic rocks, SE Papua New Guinea, *Eos Trans. AGU, 89(53)*, Fall Meet. Suppl., Abstract T41B-1961.

Wallace, L.M., C. Stevens, E. Silver, R. McCaffrey, W. Loratung, S. Hasiata, R. Stanaway, R. Curley, R. Rosa, and J. Taugaloidi (2004), GPS and seismological constraints on active tectonics and arc-continent collision in Papua New Guinea: implications for mechanics of microplate rotations in a plate boundary zone, *J. Geophys. Res.*, **109**, doi:10.1029/2003JB002481.

Walsh, E.O., and B.R. Hacker (2004), The Fate of Subducted Continental Margins: Two-Stage Exhumation of the High-Pressure to Ultrahigh-Pressure Western Gneiss Region, Norway, *J. Metamorph. Geol.*, **22**, 671–689, doi: 10.1111/j.1525-1314.2004.00541.x.

Warren, C. (2013), Exhumation of (ultra-)high-pressure terranes: concepts and mechanisms, *Solid Earth*, ***4***, 75–92, doi: 10.5194/se-4-75-2013.

Weinberg, R.F., and Yu Podladchikov (1994), Diapiric ascent of magmas through power–law crust and mantle, *J. Geophys. Res.*, **99**, 9543–9559, doi: 10.1029/93JB03461.

Weissel, J.K., B. Taylor, and G.D Karner (1982), The opening of the Woodlark Basin, subduction of the Woodlark spreading system, and the evolution of northern Melanesia since mid-Pliocene time, *Tectonophysics*, **87**, 253–277, doi: 10.1016/0040-1951(82)90229-3.

Westaway, R. (2007), Correction to "Active low angle normal-faulting in the Woodlark extensional province, Papua New Guinea: a physical model, *Tectonics*, **26**, TC1003.

Xu, S.T., A.I. Okay, S.Y. Ji, A.M.C. Sengor, W. Su, Y.C. Liu, L.L. Jiang (1992), Diamond from the Dabie Shan metamorphic rocks and its implication for tectonic setting, *Science*, **256**, 80–82.

Zhang, R.Y., J.G. Liou, W.G. Ernst, R.G. Coleman, N.V Sobolev, and V.S. Shatsky (1997), Metamorphic evolution of diamond-bearing rocks from the Kokchetav Massif, northern Kazakhstan, *J. Metamorph. Geol.*, **15**, 479–496, doi: 10.1111/j.1525-1314.1997.00035.x.

Zirakparvar, N.A., S.L. Baldwin, and J.D. Vervoort (2011), Lu–Hf garnet geochronology applied to plate boundary zones: insights from the (U)HP terrane exhumed within the Woodlark Rift, *Earth Planet. Sci. Lett.*, **309**, 56–66, doi: 10.1016/j.epsl.2011.06.016.

Zirakparvar, N.A., S.L. Baldwin, and J.D. Vervoort (2013), The origin and geochemical evolution of the Woodlark Rift of Papua New Guinea, *Earth Planet. Sci. Lett.*, **23**, 931–943, doi: 10.1016/j.gr.2012.06.013.

Table 1. Zircon U-Pb ID-TIMS Isotopic Data

				Dates (Ma)							Correlation Coefficient	Composition				Isotopic Ratios							
	location[a]	mineral assemblage[b]	Fraction	206Pb/238U date <Th> [h]	±2σ abs	207Pb/235U date [i]	±2σ abs	207Pb/206Pb date <Th> [h]	±2σ abs		206Pb/238U<Th>-207Pb/235U corr. coeff.[j]	Pb*/ Pbc [c]	Pbc (pg) [d]	Th/ U [e]	206Pb/ 204Pb [f]	206Pb/238U <Th> [g,h]	±2σ %	207Pb/ 235U [g]	±2σ %		207Pb/206Pb <Th> [g,h]	±2σ %
PNG10-029B	E 202051	Pl, Kfs, Qtz, Bt	z12	2.30	0.06	2.66	1.0	341	822	PNG10-029B	0.25	0.37	0.20	0.25	42	0.0004	2.79	0.0026	PNG10-029B	36.9	0.0533	36.3
	N 8969220	Zrn	z6	2.39	0.04	1.93	0.5	-536	745		0.34	0.57	0.48	-0.30	63	0.0004	1.63	0.0019		28.3	0.0373	27.8
			z2	2.60	0.19	3.34	2.7	572	1714		0.22	0.15	1.62	0.39	28	0.0004	7.12	0.0033		80.1	0.0592	78.8
			z8	21.55	0.58	18.56	7.5	-354	1040		0.26	0.50	1.08	0.69	47	0.0033	2.68	0.0184		40.9	0.0400	40.3
			z5	22.04	0.46	23.26	6.2	152	605		0.48	0.79	0.94	0.50	66	0.0034	2.11	0.0232		26.8	0.0491	25.8
			z23	22.14	0.05	23.29	0.7	144	66		0.41	6.55	0.37	0.68	394	0.0034	0.24	0.0232		2.9	0.0489	2.8
			z19	23.26	0.94	32.73	12.8	798	816		0.23	0.32	2.12	0.83	36	0.0036	4.03	0.0328		39.6	0.0658	38.9
			z13	24.42	0.09	25.95	1.2	170	109		0.27	3.54	0.20	0.45	233	0.0038	0.36	0.0259		4.8	0.0495	4.7
			z10	28.33	0.11	29.79	1.5	149	115		0.30	3.31	0.42	0.49	218	0.0044	0.39	0.0298		5.0	0.0490	4.9
			z11	31.44	0.22	32.90	1.8	141	128		0.33	3.45	0.30	0.62	219	0.0049	0.69	0.0329		5.7	0.0489	5.5
			z4	31.51	0.17	30.23	2.3	-71	186		0.35	2.57	0.47	0.62	169	0.0049	0.54	0.0302		7.8	0.0447	7.6
			z18	34.91	0.25	36.45	3.5	139	227		0.29	1.77	0.36	0.65	120	0.0054	0.73	0.0365		9.9	0.0488	9.7
			z9	38.38	0.94	44.62	11.8	394	591		0.29	0.61	0.78	0.86	52	0.0060	2.47	0.0449		27.0	0.0546	26.4
			z3	39.31	1.20	50.81	16.2	633	693		0.23	0.38	2.88	0.49	41	0.0061	3.05	0.0513		32.8	0.0609	32.2
			z21	39.60	0.13	41.69	1.7	164	98		0.25	3.79	0.56	0.63	238	0.0062	0.33	0.0419		4.3	0.0494	4.2
			z16	45.04	0.48	52.26	6.4	397	276		0.31	1.31	0.31	0.88	89	0.0070	1.08	0.0528		12.6	0.0547	12.3
			z14	45.87	0.08	47.42	0.9	126	46		0.39	10.3	0.36	0.61	616	0.0071	0.17	0.0478		2.0	0.0486	1.9
			z17	48.78	0.11	50.96	1.2	155	54		0.30	7.42	0.48	0.57	455	0.0076	0.22	0.0515		2.4	0.0492	2.3
			z20	52.76	0.08	54.38	1.0	127	43		0.25	8.76	0.75	0.58	533	0.0082	0.15	0.0550		1.8	0.0486	1.8
			z24	55.72	0.03	57.14	0.3	117	11		0.15	39.2	0.37	0.95	2119	0.0087	0.06	0.0579		0.5	0.0484	0.5
			z22	71.47	0.04	72.95	0.2	122	6.1		0.39	64.8	0.45	0.56	3849	0.0111	0.06	0.0745		0.3	0.0485	0.3
PNG10-031A	E 201780	Pl, Kfs, Qtz, Bt, Ms	z8	3.85	0.02	4.12	0.1813	162	100	PNG10-031A	0.43	3.58	1.22	0.13	256	0.0006	0.39	0.0041	PNG10-031A	4.4	0.0493	4.3
	N 8969055	Zrn	z3	4.42	0.01	4.49	0.0878	46.5	44		0.57	9.28	0.40	0.02	657	0.0007	0.21	0.0044		2.0	0.0470	1.8
			z18	4.46	0.01	4.67	0.1646	113	82		0.28	4.05	0.33	0.03	296	0.0007	0.27	0.0046		3.5	0.0483	3.5
			z9	4.573	0.004	4.92	0.0234	177	11		0.36	33.3	0.21	0.03	2294	0.0007	0.10	0.0049		0.5	0.0496	0.4
			z15	4.60	0.02	5.05	0.2305	227	104		0.26	2.88	0.34	-0.01	218	0.0007	0.36	0.0050		4.6	0.0507	4.5
			z5	4.61	0.01	4.68	0.1208	40.6	60		0.40	6.62	0.80	0.01	477	0.0007	0.21	0.0046		2.6	0.0469	2.5
			z17	4.63	0.01	4.82	0.1819	100	87		0.45	4.47	0.34	0.02	326	0.0007	0.29	0.0048		3.8	0.0480	3.7
			z4	4.67	0.01	4.72	0.2135	29.2	107		0.32	3.42	1.12	0.03	253	0.0007	0.32	0.0047		4.5	0.0466	4.4
			z1	4.692	0.009	4.73	0.1040	24.6	51		0.42	8.57	0.30	0.37	551	0.0007	0.19	0.0047		2.2	0.0465	2.1
			z10	4.737	0.005	5.05	0.0431	159	19		0.45	20.1	0.27	0.02	1399	0.0007	0.10	0.0050		0.9	0.0492	0.8
			z14	8.27	0.01	10.2	0.1533	492	33		0.23	8.79	0.86	0.41	554	0.0013	0.17	0.0101		1.5	0.0570	1.5
			z2	10.03	0.01	10.4	0.0631	98.7	13		0.44	33.4	0.32	0.29	2147	0.0016	0.11	0.0103		0.6	0.0480	0.6
			z12	22.71	0.03	23.5	0.0955	102	8		0.52	74.2	0.39	0.22	4826	0.0035	0.14	0.0234		0.4	0.0481	0.4
PNG10-031B	E 201780	Pl, Kfs, Qtz, Bt	z3	2.68	0.112	1.7	1.73	-1242	3149	PNG10-031B	0.27	0.25	0.44	0.27	35	0.000	4.2	0.002	PNG10-031B	102	0.0292	101
	N 8969055	Zrn	z2	2.77	0.063	2.9	0.94	124	748		0.26	0.49	0.62	0.40	48	0.000	2.3	0.003		32	0.0485	32
			z8	3.52	0.140	2.9	2.07	-447	1819		0.38	0.27	0.22	0.03	37	0.001	4.0	0.003		70	0.0386	69
			z1	18.7	0.188	18.9	2.77	41	347		0.34	1.26	0.36	0.51	94	0.003	1.0	0.019		15	0.0469	14
			z4	38.7	0.042	48.2	0.45	548	20		0.29	13.5	1.22	0.26	877	0.006	0.1	0.049		0.95	0.0585	0.9
			z7	39.7	0.221	37.8	2.85	-79	184		0.33	2.37	0.81	0.37	166	0.006	0.6	0.038		7.7	0.0446	7.5
			z9	88.4	0.077	89.6	0.64	123	17		0.35	21.6	0.33	0.31	1386	0.014	0.1	0.092		0.75	0.0485	0.7
PNG10-039A	E 198221	Pl, Kfs, Qtz, Bt, Ms	z1	2.78	0.02	2.99	0.31	175	227	PNG10-039A	0.78	1.1	0.63	0.035	90	0.000431	0.637	0.0029	PNG10-039A	10.2	0.0496	9.74
	N 8967202	Zrn	z2	2.90	0.01	2.89	0.22	-8	171		0.80	1.6	0.40	0.044	130	0.000451	0.482	0.0029		7.5	0.0459	7.10
			z7	3.23	0.01	3.17	0.24	-42	173		0.74	2.0	0.58	0.016	158	0.000501	0.443	0.0031		7.4	0.0452	7.11
			z5	3.37	0.003	3.79	0.03	276	14		0.55	23.2	0.43	0.068	1577	0.000523	0.099	0.0037		0.7	0.0518	0.61
			z10	4.20	0.01	4.47	0.14	157	69		0.74	5.3	0.28	0.110	374	0.000651	0.254	0.0044		3.1	0.0492	2.96
			z9	4.25	0.01	4.48	0.18	127	90		0.74	3.5	0.34	0.112	250	0.000660	0.250	0.0044		4.0	0.0486	3.81
			z3	4.53	0.03	4.92	0.44	200	198		0.80	1.1	0.98	0.031	96	0.000703	0.635	0.0049		9.0	0.0501	8.54
			z6	4.568	0.004	4.68	0.05	64	26		0.15	13.8	0.56	0.016	969	0.000709	0.092	0.0046		1.1	0.0473	1.08
			z4	15.3	0.03	15.5	0.54	43	80		0.78	4.3	0.63	0.050	313	0.002378	0.200	0.0154		3.5	0.0469	3.34
			z8	31.20	0.03	32.3	0.22	112	15		0.39	21.2	0.87	0.505	1285	0.004852	0.082	0.0323		0.7	0.0483	0.66
PNG10-039B	E 198221	Pl, Kfs, Qtz, Bt, Ms	z3	2.27	0.03	2.23	0.44	-39.19	474.00	PNG10-039B	0.26	0.8	0.46	0.230	70	0.000352	1.32	0.00220	PNG10-039B	19.82	0.04533	19.52
	N 8967202	Zrn	z14	2.31	0.02	2.75	0.37	409.91	292.68		0.30	1.1	0.60	0.43	85	0.00036	1.07	0.0027		13.37	0.0550	13.09
			z11	2.31	0.22	3.99	3.20	1185.89	1555.11		0.24	0.1	1.01	0.408	26	0.000359	9.32	0.00394		80.45	0.07959	78.72
			z8	2.35	0.25	2.89	3.67	471.87	2769.79		0.24	0.1	1.77	0.404	25	0.000365	10.53	0.00285		127.23	0.05652	125.17
			z13	2.88	0.06	3.51	0.83	455.60	509.67		0.35	0.7	0.50	0.590	57	0.000448	1.91	0.00346		23.57	0.05611	22.97
			z17	2.98	0.03	3.70	0.40	501.7	236		0.23	1.1	0.55	0.12	89.7	0.00046	0.94	0.00365		10.9	0.0573	10.7
			z16	3.81	0.03	4.42	0.38	348.70	189.76		0.29	1.5	0.36	0.030	122	0.000592	0.68	0.00436		8.56	0.05349	8.39
			z12	6.49	0.02	6.59	0.16	45.94	57.96		0.26	7.1	0.35	0.556	439	0.001007	0.27	0.00651		2.48	0.04696	2.43
			z4	11.30	0.03	11.83	0.38	120.56	74.65		0.29	5.2	0.94	0.584	322	0.001755	0.27	0.01172		3.23	0.04846	3.17
			z9	15.19	0.12	16.38	1.69	193.85	236.64		0.31	1.4	1.46	0.087	111	0.002360	0.79	0.01626		10.39	0.05000	10.18
			z5	16.61	0.32	11.40	4.68	-989.09	1194.76		0.48	0.7	0.40	0.296	63	0.002580	1.94	0.01129		41.29	0.03175	40.40
			z15	26.89	0.03	28.22	0.34	142.81	27.45		0.40	15.0	0.21	0.325	961	0.004180	0.12	0.02818		1.21	0.04892	1.17
			z1	52.45	0.07	53.83	0.80	115.92	35.25		0.28	10.1	2.09	0.266	666	0.008169	0.14	0.05445		1.53	0.04836	1.49
			z6	64.72	0.06	65.19	0.46	82.40	16.54		0.48	24.3	0.42	0.316	1553	0.010091	0.09	0.06631		0.74	0.04768	0.70
			z7	71.64	0.53	74.60	6.82	170.20	217.41		0.27	1.8	4.37	0.646	120	0.011176	0.74	0.07623		9.49	0.04949	9.31
PNG12-78C	E194531	Pl, Qtz, Kfs, Bt	z2	2.09	0.02	2.30	0.31	231.37	300.90	PNG12-78C	0.49	1.4	0.38	-0.038	119	0.000324	0.78	0.00227	PNG12-78C	13.39	0.05081	13.03
	N 8961464	Zrn	z6	2.48	0.02	2.85	0.29	330.26	222.07		0.33	1.4	0.56	-0.008	112	0.000385	0.78	0.00282		10.01	0.05306	9.79

			z5	2.49	0.01	2.87	0.15	333.31	118.91		0.40	2.7	0.49	-0.021	204	0.000387	0.41	0.00283		5.39	0.05313	5.24
			z1	2.49	0.00	2.92	0.03	368.57	22.64		0.31	13.9	0.84	0.011	974	0.000387	0.10	0.00288		1.03	0.05396	1.00
			z9	2.50	0.01	2.91	0.09	356.99	66.98		0.40	4.5	0.54	0.007	330	0.000387	0.31	0.00287		3.07	0.05369	2.97
			z3	3.04	0.01	3.05	0.11	8.46	81.97		0.38	5.1	0.41	0.032	368	0.000472	0.24	0.00301		3.49	0.04623	3.41
			z13	3.21	0.02	3.64	0.31	296.99	187.87		0.40	1.8	0.52	0.054	140	0.000499	0.63	0.00359		8.47	0.05229	8.23
			z4	3.63	0.01	3.83	0.13	132.92	74.70		0.57	5.5	0.45	0.080	391	0.000564	0.30	0.00378		3.34	0.04871	3.18
			z11	8.10	0.02	8.74	0.19	189.36	50.81		0.28	7.1	0.42	0.391	456	0.001258	0.19	0.00865		2.23	0.04990	2.18
PNG06-041B	E 198221	Pl, Qtz, Kfs, Ms, Bt	z7	1.82	0.03	1.07	0.53	-1480.62	1618.01	PNG06-041B	0.30	0.5	0.55	0.053	55	0.000282	1.85	0.00105	PNG06-041B	49.41	0.02712	48.89
	N 8967202	Zrn	z11	1.83	0.09	1.99	1.28	202.79	1480.68		0.21	0.2	2.31	0.271	32	0.000283	4.76	0.00196		64.64	0.05017	63.79
			z4	1.85	0.04	1.63	0.63	-312.46	967.83		0.35	0.5	0.35	0.315	50	0.000287	2.22	0.00161		38.49	0.04060	37.77
			z8	1.97	0.06	1.53	0.97	-647.78	1720.23		0.25	0.3	0.79	0.238	39	0.000305	3.29	0.00151		63.39	0.03578	62.64
			z9	34.33	0.06	36.54	0.35	184.00	18.83		0.99	15.9	0.35	0.327	1017	0.005340	0.18	0.03664		0.99	0.04976	0.81
			z10	49.90	0.21	51.87	2.56	144.11	115.14		0.39	3.7	0.58	0.693	230	0.007771	0.42	0.05242		5.06	0.04892	4.91
PNG10-002D	E 253335	Qz, Pl, Bt, Ms, Grt	z9	5.66	0.02	6.22	0.31	229	110	PNG10-002D	0.33	3.0	0.18	0.76	213	0.000879	0.41	0.00615	PNG10-002D	5	0.050758	4.9
	N 8921798	Zrn, Rt, Ttn	z5	5.68	0.03	6.28	0.38	240	140		0.26	3.0	0.31	0.79	169	0.000882	0.49	0.0062		6.1	0.050999	6
			z2	5.92	0.10	5.1	1.4	-386	730		0.28	1.0	0.45	1.33	61	0.000918	1.7	0.005		28	0.039476	28
			z24	5.96	0.07	7.12	0.99	420	300		0.39	0.42	0.15	-1.89	90	0.000925	1.1	0.00704		14	0.055217	14
			z18	6.01	0.02	7.17	0.22	419	66		0.22	5.0	0.19	0.8	316	0.000932	0.3	0.00709		3	0.055204	3
			z28	6.05	0.12	6.4	1.8	128	660		0.34	1.0	0.14	1.3	56	0.000938	2	0.0063		28	0.048606	28
			z22	6.10	0.04	6.17	0.58	33	220		0.35	2.0	0.17	1.08	135	0.000947	0.68	0.0061		9.5	0.046703	9.2
			z17	6.82	0.02	7.2	0.4	137	130		-0.08	4.0	0.25	1.25	204	0.001058	0.32	0.00711		5.6	0.048795	5.6
			z19	24.30	0.05	26.48	0.61	229	53		0.31	7.0	0.38	0.69	435	0.003777	0.2	0.02642		2.3	0.050763	2.3
			z25	50.48	0.18	47.8	2.4	-82	120		0.44	4.0	0.2	0.71	262	0.007861	0.36	0.0482		5.1	0.044534	5
			z16	79.88	0.35	80.5	4.7	100	140		0.29	3.0	0.23	0.58	188	0.012468	0.45	0.0825		6	0.048029	5.9
			z27	80.70	0.55	83.7	6.7	171	190		0.35	2.0	0.27	0.71	146	0.012597	0.69	0.086		8.3	0.049514	8.1
			z21	91.28	0.17	93.5	1.5	151	35		0.68	11.0	0.41	0.85	614	0.014261	0.19	0.0965		1.6	0.049083	1.5
			z3	110.44	0.24	114.6	2.8	201	58		0.33	7.0	0.31	0.60	409	0.017279	0.22	0.1194		2.6	0.050152	2.5
			z13	124.94	0.15	127.8	1.4	181	26		0.34	15.0	0.34	0.58	881	0.019571	0.12	0.1341		1.2	0.04972	1.1
			z6	128.11	0.31	130.9	3.5	182	66		0.19	6.0	0.37	0.66	359	0.020072	0.24	0.1376		2.9	0.049749	2.8
			z12	131.77	0.35	135.6	4.1	203	74		0.27	5.0	0.3	0.76	310	0.020652	0.27	0.1428		3.2	0.050187	3.2
			z11	150.21	0.47	152.8	5.7	193	92		0.26	4.0	0.32	0.69	254	0.023574	0.31	0.1624		4	0.049986	4
			z15	461.24	0.41	473.5	2.7	533	15		0.31	19.0	0.42	0.28	1229	0.074172	0.091	0.5941		0.7	0.05812	0.68
PNG10-016c	E 253335	Qz, Pl, Ms, Bt, Grt	Z9	5.04	0.07	4.42	0.97	-319	560	PNG10-016c	0.34	1.0	0.16	0.55	75	0.000781	1.30	0.00436	PNG10-016c	22	0.040518	22
	N 8921798	Zrn, Rt	Z15	5.04	0.09	3.6	1.3	-852	1000		0.28	0.6	0.15	0.1	60	0.000782	1.70	0.0036		35	0.033278	35
			z18	5.15	0.06	3.08	0.82	-1427	860		0.34	1.1	0.26	0.44	88	0.0008	1.10	0.00304		27	0.027576	26
			Z10	5.16	0.02	4.95	0.29	-93	140		0.31	3.6	0.17	0.73	219	0.0008	0.41	0.00489		5.9	0.044331	5.7
			Z8	5.18	0.02	4.83	0.29	-164	150		0.40	3.5	0.17	0.61	224	0.000804	0.40	0.00477		6.1	0.043077	5.9
			z4	5.21	0.03	5.26	0.46	26	210		0.33	2.2	0.25	0.83	139	0.000809	0.64	0.00519		8.8	0.046563	8.6
			z2	5.25	0.01	5.3	0.1	30	45		0.24	10.7	0.34	0.82	610	0.000815	0.22	0.00524		1.9	0.046637	1.9
			Z14	5.26	0.02	5.46	0.2	93	85		0.27	5.4	0.2	1.03	300	0.000817	0.33	0.00539		3.7	0.047901	3.6
			Z13	5.29	0.02	5.42	0.19	64	80		0.62	4.8	0.16	-0.37	393	0.000821	0.31	0.00535		3.5	0.047306	3.3
			z7	5.31	0.06	6.81	0.92	579	290		0.32	1.0	0.21	0.32	81	0.000823	1.10	0.00673		14	0.059344	13
			Z17	5.362	0.009	5.55	0.1	87	43		0.33	9.7	0.23	0.36	622	0.000832	0.17	0.00548		1.9	0.047778	1.8
			z23	5.47	0.08	6.9	1.1	534	350		0.33	1.0	0.32	0.91	70	0.000849	1.50	0.0068		16	0.058134	16
			z3	5.47	0.02	5.76	0.32	129	130		0.31	3.3	0.29	0.72	202	0.000849	0.42	0.00569		5.6	0.048629	5.5
			z22	5.74	0.03	6.09	0.37	148	140		0.42	2.5	0.17	0.03	192	0.000891	0.48	0.00602		6.1	0.049027	5.9
			z24	6.01	0.01	6.3	0.17	117	60		0.49	6.4	0.17	0.05	457	0.000933	0.21	0.00622		2.6	0.048392	2.5
			z21	9.38	0.04	9.79	0.65	114	150		0.47	2.9	0.21	0.44	197	0.001456	0.46	0.00969		6.6	0.048319	6.4
			z20	30.29	0.02	31.46	0.24	122	18		0.25	21.4	0.19	0.56	1283	0.004709	0.079	0.03147		0.78	0.048492	0.76
PNG09-065A	E 259332	Qz, Pl, Bt, Amp, Kfs	z8	78.98	0.12	80.04	1.17	112	33.41	PNG09-065A	0.70	8.4	0.70	0.743	496	0.012328	0.15	0.08201	PNG09-065A	1.51	0.04827	1.41
	N 8919002	Zrn, Rt, Py	z9	96.50	0.07	97.89	0.48	132	11.24		0.63	22.7	0.69	0.518	1381	0.015082	0.07	0.10121		0.52	0.04869	0.48
			z3	109.90	0.07	109.54	0.53	102	12.53		-0.16	28.6	0.50	0.785	1619	0.017195	0.07	0.11392		0.52	0.04805	0.53
			z1	113.93	0.10	114.39	0.59	124	12.09		0.49	27.6	0.27	0.804	1556	0.017830	0.09	0.11925		0.55	0.04851	0.51
			z5	114.26	0.07	113.82	0.36	105	7.72		0.21	52.2	0.28	0.734	2982	0.017882	0.06	0.11862		0.33	0.04811	0.33
			z6	115.93	0.10	115.44	0.86	105	17.70		0.44	24.0	0.33	0.792	1358	0.018146	0.09	0.12041		0.78	0.04812	0.75
PNG09-067A	E 259332	Pl, Amph, Bt, Qtz	z4	911.77	0.60	917.93	1.65	933	5.22	PNG09-067A	0.38	43.0	0.36	0.115	2843	0.151930	0.07	1.46953	PNG09-067A	0.27	0.07018	0.25
	N 8919002	Zrn, Py	z3	915.96	1.13	919.62	1.87	928	5.50		0.51	42.3	0.47	0.306	2655	0.152678	0.13	1.47364		0.31	0.07003	0.27
			z2	925.60	0.65	929.12	1.24	937	3.36		0.66	115.0	0.24	0.229	7343	0.154403	0.08	1.49687		0.20	0.07034	0.16
PNG10-021A	E 253335	Pl, Kfs, Qtz, Ms, Bt	z8	4.10	0.07	4.62	0.93	284	450.13	PNG10-021A	0.40	0.8	0.76	0.586	67	0.000636	1.65	0.00456	PNG10-021A	20.28	0.05200	19.68
	N 8921798	Zrn	z11	4.10	0.01	4.25	0.09	90.1	47.46		0.29	9.4	0.21	0.726	550	0.000637	0.23	0.00420		2.06	0.04784	2.00
			z10	4.11	0.02	4.14	0.22	19.4	126.36		0.33	3.3	0.22	0.406	222	0.000638	0.41	0.00409		5.38	0.04644	5.26
			z9	4.12	0.01	4.22	0.12	59.4	67.19		0.25	6.5	0.26	0.707	387	0.000639	0.27	0.00416		2.88	0.04722	2.82
			z1	4.13	0.03	4.35	0.47	131	245.27		0.40	1.8	0.28	0.709	120	0.000640	0.81	0.00429		10.73	0.04866	10.43
			z4	4.13	0.03	4.15	0.40	14.3	230.38		0.30	1.9	0.33	0.607	128	0.000641	0.68	0.00409		9.76	0.04632	9.58
			z2	4.14	0.05	4.48	0.67	195	340.55		0.26	1.4	0.28	1.738	83	0.000642	1.18	0.00442		14.91	0.04999	14.65
PNG12-94C	E 253335	Pl, Kfs, Qtz, Bt, Ms	z7	4.09	0.02	4.10	0.28	61.4	157.88	PNG12-94C	0.34	3.1	0.28	0.766	193	0.000635	0.48	0.00405	PNG12-94C	6.79	0.04628	6.64
	N 8921798	Zrn	z11	4.10	0.04	4.41	0.52	227	266.76		0.41	1.7	0.25	0.684	112	0.000637	0.87	0.00436		11.90	0.04962	11.57
			z2	4.11	0.02	4.12	0.28	64.6	155.15		0.36	2.9	0.37	0.646	183	0.000637	0.49	0.00407		6.69	0.04630	6.53
			z9	4.11	0.06	4.74	0.85	393	390.11		0.36	0.9	0.31	0.330	72	0.000638	1.40	0.00468		17.89	0.05325	17.43
			z5	4.12	0.03	4.27	0.33	125	175.64		0.30	3.0	0.27	1.538	160	0.000640	0.63	0.00422		7.65	0.04782	7.48

			z4	4.12	0.06	4.62	0.81	319	390.09		0.28	0.9	0.36	0.700	71	0.000640	1.36	0.00456		17.52	0.05168	17.20
			z3	4.15	0.08	4.92	1.16	448	512.30		0.30	0.7	0.38	0.739	55	0.000644	2.00	0.00486		23.62	0.05475	23.10
			z6	4.18	0.11	5.28	1.62	592	649.43		0.29	0.5	0.43	0.561	45	0.000648	2.64	0.00522		30.67	0.05839	30.02
PNG09-062C	E 260279	Pl, Kfs, Qtz, Bt	Z8	4.38	0.13	18.15	1.85	2764	153.6	PNG09-062C	0.45	0.4	0.29	-0.095	46	0.000680	2.86	0.01804	PNG09-062C	10.31	0.19262	9.36
	N 8918662	Zrn	z7	4.41	0.24	10.90	3.66	1867	585.84		0.31	0.2	0.26	-0.272	31	0.000685	5.47	0.01079		33.77	0.11426	32.47
			z6	4.62	0.06	6.69	0.82	833	245.70		0.41	1.0	0.25	0.089	83	0.000717	1.22	0.00661		12.24	0.06687	11.79
			Z9	5.24	0.12	6.23	1.76	410	616.1		0.39	0.5	0.23	0.092	53	0.000813	2.21	0.00616		28.32	0.05496	27.54
			z31	9.92	0.14	12.56	1.96	552	336.3		0.28	0.8	0.40	0.125	70	0.001540	1.38	0.01244		15.73	0.05862	15.41
			z27	13.53	0.12	12.85	1.76	-113	334.7		0.29	1.1	0.44	-0.038	99	0.002101	0.90	0.01274		13.82	0.04399	13.59
			z28	15.07	0.04	16.71	0.55	259	74.12		0.40	4.6	0.39	0.083	328	0.002341	0.27	0.01659		3.32	0.05143	3.23
			z30	15.21	0.18	16.00	2.68	136	380.0		0.60	3.3	0.42	0.533	215	0.002363	1.20	0.01588		16.86	0.04877	16.17
			Z20	15.25	0.16	45.42	2.27	2229	84.61		0.31	1.2	0.57	0.194	89	0.002368	1.05	0.04575		5.11	0.14020	4.89
			z3	20.32	0.07	23.68	0.93	379	87.02		0.35	4.1	0.30	0.589	258	0.003157	0.34	0.02360		3.97	0.05423	3.87
			Z10	26.82	0.09	53.41	1.10	1507	38.18		0.39	4.2	0.47	0.168	286	0.004169	0.32	0.05400		2.12	0.09399	2.02
			z25	34.24	0.13	37.38	1.87	244	114.2		0.36	3.6	0.72	0.714	221	0.005326	0.40	0.03750		5.09	0.05109	4.96
			Z14	34.84	0.07	57.74	0.69	1155	23.65		0.24	7.4	1.63	0.095	501	0.005419	0.19	0.05851		1.22	0.07835	1.19
			z2	34.93	0.22	36.99	3.02	172	189.65		0.33	2.0	0.42	0.572	138	0.005434	0.64	0.03710		8.31	0.04954	8.12
			Z11	37.99	0.12	40.90	1.26	215	68.20		0.64	8.2	0.39	0.588	501	0.005910	0.31	0.04110		3.13	0.05046	2.95
			Z12	42.10	0.10	66.09	1.36	1054	42.36		0.16	5.1	0.95	0.149	345	0.006552	0.24	0.06725		2.13	0.07448	2.10
			Z13	46.35	0.12	47.80	1.61	121	79.93		0.28	4.6	0.63	0.135	325	0.007217	0.26	0.04820		3.46	0.04846	3.39
			Z21	46.82	0.09	48.74	1.04	144	50.08		0.32	8.0	0.71	0.645	482	0.007289	0.18	0.04918		2.19	0.04895	2.13
			Z23	47.14	0.09	47.96	0.80	89.1	37.45		0.72	11.5	0.60	0.173	777	0.007339	0.19	0.04836		1.71	0.04782	1.58
			Z18	47.22	0.04	49.38	0.44	155	20.32		0.46	25.0	0.46	0.707	1438	0.007352	0.10	0.04984		0.91	0.04918	0.87
			Z22	47.75	0.30	56.83	4.02	458	158.1		0.28	1.8	0.88	0.144	135	0.007434	0.64	0.05756		7.28	0.05618	7.13
			Z15	52.32	0.07	52.75	0.70	72.2	30.13		0.65	13.3	0.61	0.085	919	0.008150	0.14	0.05333		1.36	0.04748	1.27
			Z16	53.09	0.04	57.34	0.35	239	13.78		0.37	32.8	0.36	0.770	1851	0.008269	0.08	0.05810		0.62	0.05098	0.60
			Z19	53.48	0.05	56.19	0.56	174	23.29		0.39	16.2	0.54	0.114	1101	0.008330	0.10	0.05690		1.03	0.04956	1.00
			z29	53.76	0.04	56.05	0.42	155	17.49		0.31	23.0	0.31	0.658	1342	0.008374	0.07	0.05676		0.77	0.04918	0.75
			Z17	63.07	0.07	66.57	0.89	194	31.32		0.39	12.8	0.71	0.752	739	0.009832	0.12	0.06776		1.39	0.05000	1.35
			z1	140.64	0.64	155.57	5.75	389	86.68		0.32	4.1	0.28	0.596	258	0.022057	0.46	0.16558		3.98	0.05447	3.86
PNG12-39D	E 259846	Cpx, Pl, Amp	z3	2.947	0.003	2.98	0.01	28.8	6.75	PNG12-39D	0.38	69.2	0.34	0.022	4779	0.000457	0.09	0.00294	PNG12-39D	0.30	0.04662	0.28
	N 8919345	Zrn, Py																				
PNG12-94B	E 25335	Cpx, Pl, Amp	z22	1.98	0.01	1.99	0.10	6.64	114.5	PNG12-94B	0.17	4.5	0.36	1.363	236	0.000307	0.71	0.00196	PNG12-94B	4.80	0.04619	4.76
	N 8921798	Zrn, Py	z10	3.33	0.01	3.67	0.20	233	121.8		0.25	2.6	0.92	0.147	187	0.000517	0.42	0.00363		5.37	0.05085	5.28
			z13	3.34	0.04	3.21	0.62	-92.1	464.8		0.35	0.9	0.24	-0.007	78	0.000518	1.22	0.00316		19.34	0.04435	18.95
			z17	3.34	0.01	3.29	0.17	-31.5	121.4		0.4	3.4	0.20	0.036	251	0.000518	0.35	0.00325		5.14	0.04547	5.01
			z9	4.08	0.02	4.02	0.30	-32.6	179.0		0.42	3.3	0.64	0.569	212	0.000633	0.42	0.00397		7.55	0.04545	7.38
			z19	59.81	0.11	64.58	1.21	245	43.10		0.37	8.2	0.38	0.393	522	0.009321	0.18	0.06566		1.93	0.05112	1.87
			z7	72.09	0.05	73.81	0.54	130	18.19		-0.23	23.1	0.49	0.691	1340	0.011246	0.07	0.07540		0.75	0.04865	0.77
			z8	90.02	0.18	86.59	2.14	-7.00	60.73		0.35	7.3	1.05	0.597	446	0.014062	0.20	0.08902		2.58	0.04593	2.52
			z18	96.21	0.09	98.42	0.92	152	22.03		0.43	19.6	0.24	0.581	1169	0.015037	0.09	0.10178		0.98	0.04912	0.94
			z6	96.28	0.19	97.36	2.10	124	51.71		0.38	7.3	0.71	0.397	472	0.015047	0.19	0.10064		2.26	0.04853	2.19
			z14	97.46	0.28	99.38	3.50	146	85.14		0.28	4.4	0.66	0.562	279	0.015233	0.29	0.10283		3.70	0.04898	3.63
			z12	98.05	0.09	99.40	0.89	132	21.64		0.31	17.3	1.83	0.511	1056	0.015326	0.09	0.10284		0.94	0.04869	0.92
			z2	98.72	0.22	99.48	2.54	118	61.46		0.35	6.6	0.74	0.609	404	0.015432	0.22	0.10293		2.68	0.04840	2.61
			z4	103.85	0.17	106.57	1.66	168	35.99		0.63	13.2	0.65	0.555	797	0.016240	0.17	0.11066		1.64	0.04944	1.54
			z11	103.95	0.19	105.66	1.40	144	31.57		0.36	12.2	1.20	0.478	758	0.016256	0.18	0.10967		1.40	0.04895	1.35
			z5	109.67	0.17	109.77	1.60	112	34.82		0.42	11.6	0.64	0.625	696	0.017158	0.16	0.11417		1.53	0.04828	1.47
			z16	109.76	0.25	112.78	2.39	177	49.92		0.48	8.5	0.24	0.533	525	0.017173	0.23	0.11747		2.24	0.04964	2.14
			z3	114.37	0.13	114.15	1.27	110	26.51		0.49	17.7	0.61	0.803	1002	0.017900	0.11	0.11898		1.17	0.04823	1.12
PNG09-075A	E 259332	Pl, Kfs, Qtz, Bt, Ms	z3	1.89	0.03	2.67	0.44	770.7	337	PNG09-075A	0.45	1.2	0.41	1.517	72	0.000294	1.71	0.00263	PNG09-075A	16.69	0.06492	16.00
	N 8919002	Zrn	z16	1.91	0.02	1.82	0.33	-114.5	436		0.33	1.3	0.61	1.261	85	0.000297	1.28	0.00180		18.08	0.04395	17.70
			z17	1.92	0.02	1.93	0.28	9.35	344		0.32	1.6	0.25	1.230	97	0.000298	1.15	0.00190		14.60	0.04625	14.28
			z2	1.92	0.08	2.17	1.17	280.6	1219		0.26	0.3	0.52	1.316	35	0.000298	4.16	0.00214		54.21	0.05192	53.27
			z20	1.94	0.12	2.06	1.78	150.5	1990		0.31	0.2	0.25	0.976	30	0.000300	6.05	0.00203		86.59	0.04908	84.93
			z21	1.97	0.08	2.72	1.22	722.9	923		0.41	0.4	0.20	1.139	38	0.000306	3.90	0.00268		44.96	0.06346	43.51
			z25	1.99	0.04	2.68	0.52	676.5	404		0.26	1.0	0.18	1.974	59	0.000309	1.97	0.00264		19.29	0.06210	18.88
			z15	3.60	0.03	3.20	0.43	-291.3	332		0.71	2.2	0.32	0.223	165	0.000559	0.84	0.00316		13.57	0.04096	12.99

[a] All grid references (in meters) refer to Transverse Mercator Projection, Australian Geodetic Datum 1966, UTM zone 56L.

[b] Mineral abbreviations: Amph = amphibole, Bt = biotite, Grt = garnet, Ilm = ilmenite, Kfs = potassium feldspar, Ms = muscovite, Omp = omphacite, Ph = phenite, Pl = plagioclase, Qz = quartz, and Rt = rutile.

[c] Ratio of radiogenic Pb (including 208Pb) to common Pb.

[d] Total mass of common Pb.

[e] Th contents calculated from radiogenic 208Pb and the 207Pb/206Pb date of the sample, assuming concordance between U-Th and Pb systems.

[f] Measured ratio corrected for fractionation and spike contribution only.

[g] Measured ratios corrected for fractionation, tracer and blank.

[h] Corrected for initial Th/U disequilibrium using radiogenic 208Pb and Th/U[magma] = 3.5.

[i] Isotopic dates calculated using the decay constants λ238 = 1.55125E-10 and λ235 = 9.8485E-10 (Jaffey et al. 1971).

[j] Correlation coefficient.

Table 2. Normalized zircon trace-element data measured by the TIMS-TEA technique

Fraction	Dates (Ma) ± 2σ	La	Ce	Pr	Nd	Sm	Eu	Gd	Tb	Dy	Ho	Er	Tm	Yb	Lu	Lu/Gd	Eu/Eu*
Normanby Dome gneiss and sills																	
PNG10-016C z2	5.25 ± 0.01	3.00	202	16.6	56.8	375	509	994	1348	1608	1843	2169	2411	2786	2772	2.79	0.83
PNG10-016C z3	5.47 ± 0.02	7.00	172	36.0	81.3	258	294	412	472	493	551	622	732	869	880	2.14	0.90
PNG10-016C z4	5.21 ± 0.03	67.8	296	76.1	48.2	289	457	774	1182	1354	1718	1977	3026	2548	2437	3.15	0.97
PNG10-021A z8	4.10 ± 0.07	13.5	125	15.1	20.9	126	182	393	517	636	807	1061	1359	1498	1798	4.57	0.82
PNG10-021A z9	4.12 ± 0.01	23.0	244	27.4	41.5	196	271	577	765	945	1263	1667	2059	2422	2815	4.87	0.81
PNG10-021A z10	4.11 ± 0.02	41.0	172	21.9	24.8	150	220	508	749	951	1350	1923	2469	2966	3609	7.10	0.80
PNG10-021A z11	4.10 ± 0.01	12.0	175	19.3	33.5	191	295	558	700	832	1013	1253	1489	1746	1941	3.48	0.90
PNG12-94C z9	4.11 ± 0.06	95.7	189	51.1	45.1	155	205	520	794	1214	1679	2511	2964	3877	3507	6.74	0.72
Normanby Dome dikes																	
PNG12-39D z3	2.947 ± 0.003	2.92	11.8	2.12	2.92	36.9	21.2	257	834	1811	3386	6296	10222	15221	15983	62.2	0.22
PNG12-94B z13	3.34 ± 0.04	47.0	35.5	25.1	15.9	38.2	50.3	99.4	234	252	361	529	884	858	919	9.25	0.82
PNG12-94B z17	3.34 ± 0.01	2.46	13.3	bdl	0.83	32.5	49.1	149	228	339	415	533	495	933	700	4.70	0.70
PNG12-94B z22	1.98 ± 0.01	1.04	207	24.7	80.8	353	295	924	1181	1720	2479	3598	4544	7200	7700	8.33	0.52
PNG09-075A z21	1.97 ± 0.08	191	190	143	134	182	137	435	637	945	1474	2124	2860	3586	4457	10.2	0.49
Goodenough Dome leucosome and dikes																	
PNG10-031A z15	4.60 ± 0.02	1.12	1.97	0.0193	0.341	4.83	10.7	23.4	61.6	102	173	289	400	542	726	31.0	1.00
PNG10-039B z14	2.31 ± 0.02	2.09	56.0	8.54	24.9	124	153	308	326	356	422	583	681	916	1209	3.9	0.78
PNG10-039B z17	2.98 ± 0.03	1.31	12.0	2.07	3.30	12.9	18.4	55.8	88.8	157	251	429	541	854	1201	21.5	0.69

Normalization after Sun and McDonough (1989)

[a] Eu/Eu* = Eu/sqrt(Sm*Gd)

bdl = below detection limit

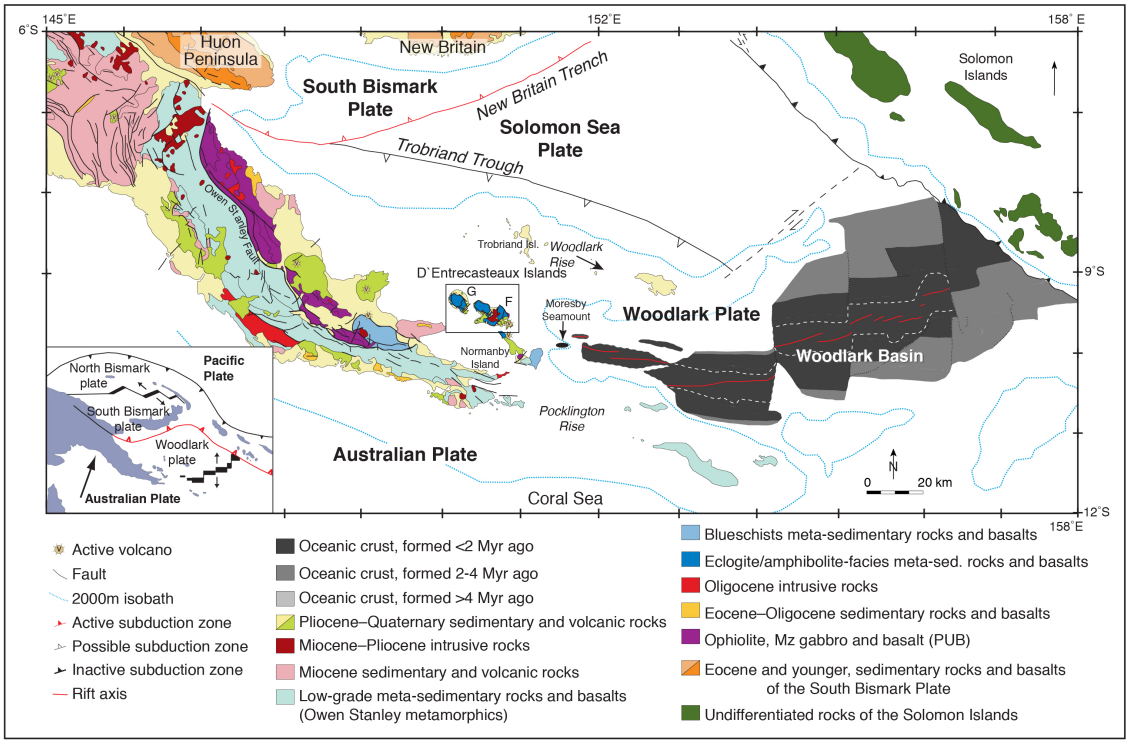

Figure 5.1: Simplified geologic map of eastern Papua New Guinea showing the major structures and rock types (after *Baldwin et al.*, [2004]). The area outlined indicates the location of the D'Entrecasteaux Islands (represented in Figure 2) west of the Woodlark Rift. The lower left inset (after *Wallace et al.*, [2004]) shows the plate-tectonic setting of the region.

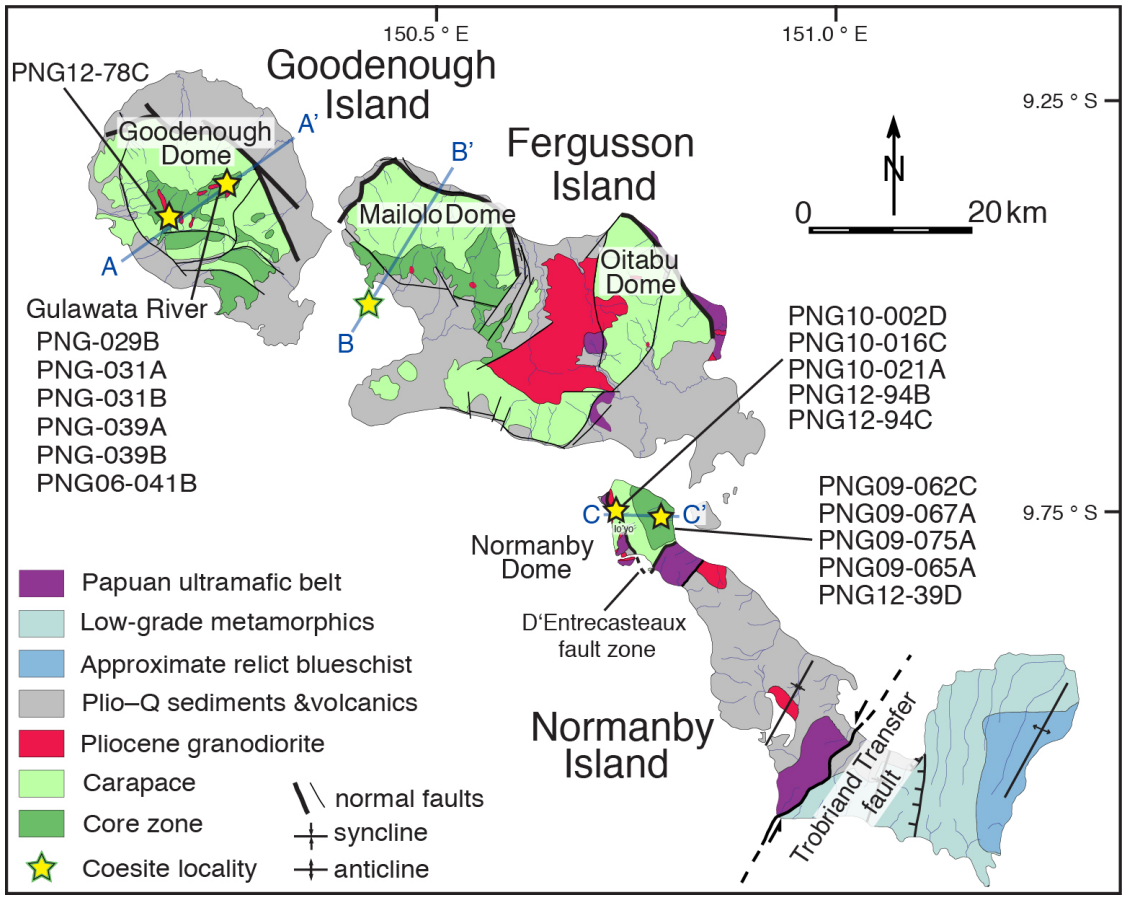

Figure 5.2: Simplified geological map of the D'Entrecasteuax Island gneiss domes (after *Davies*, 1973; *Hill*, 1994; *Little et al.*, 2007). Stars mark sample locations for this study and lines A–A', B–B', and C–C' show locations of cross-sections in Figure 6a.

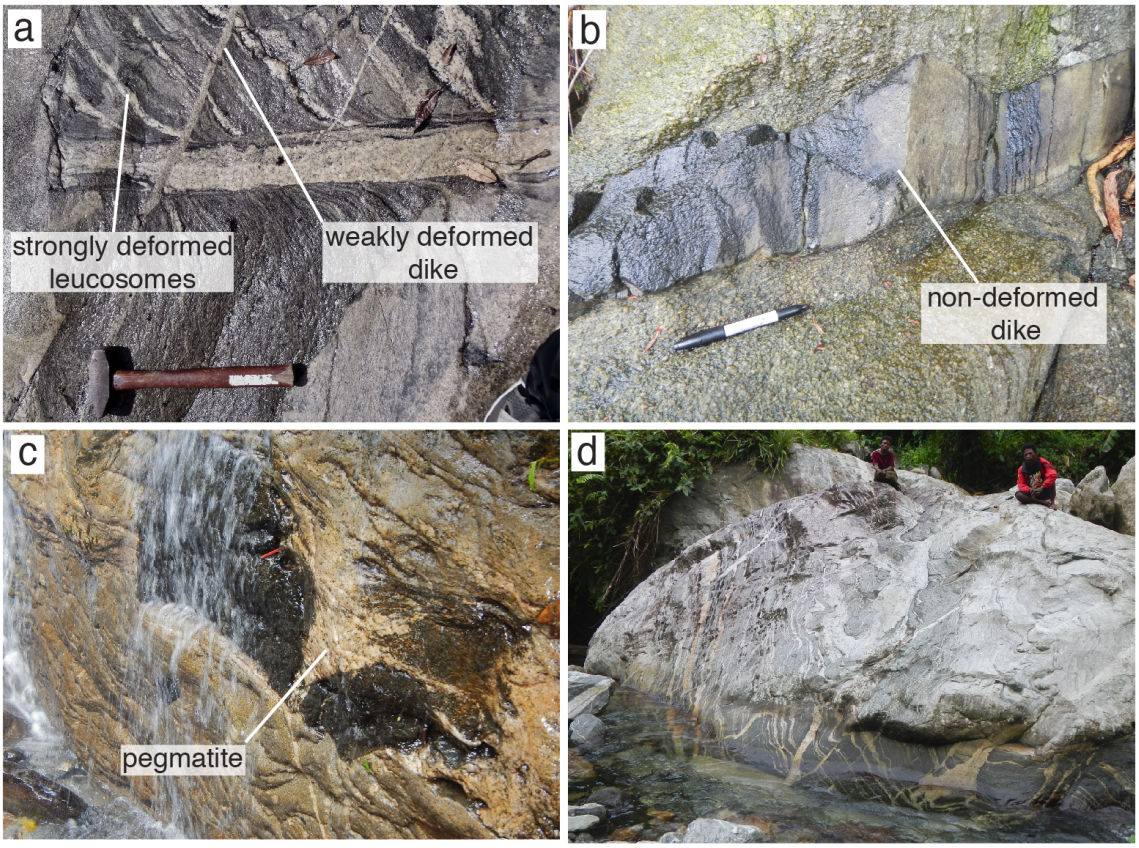

Figure 5.3: Field photos of various melt fractions found throughout the gneiss domes: (a) Layer-parallel leucosomes (PNG10-039A) within the dominant quartzofeldspathic host gneiss that are cut by weakly deformed deformed dike (PNG10-039B) in the core zone of Goodenough Dome; (b) Non-deformed andesitic dike (PNG12-94B) crosscutting deformed granodiorite sill (PNG10-021A) in the carapace zone of Normanby Dome; (c) Fractured, retrogressed eclogite with non-deformed pegmatite infill within the core zone of Goodenough Dome, note red chisel for scale; (d) Outcrop of multiple generations of layer-parallel and discordant melt within host gneiss in the core zone of Goodenough Dome.

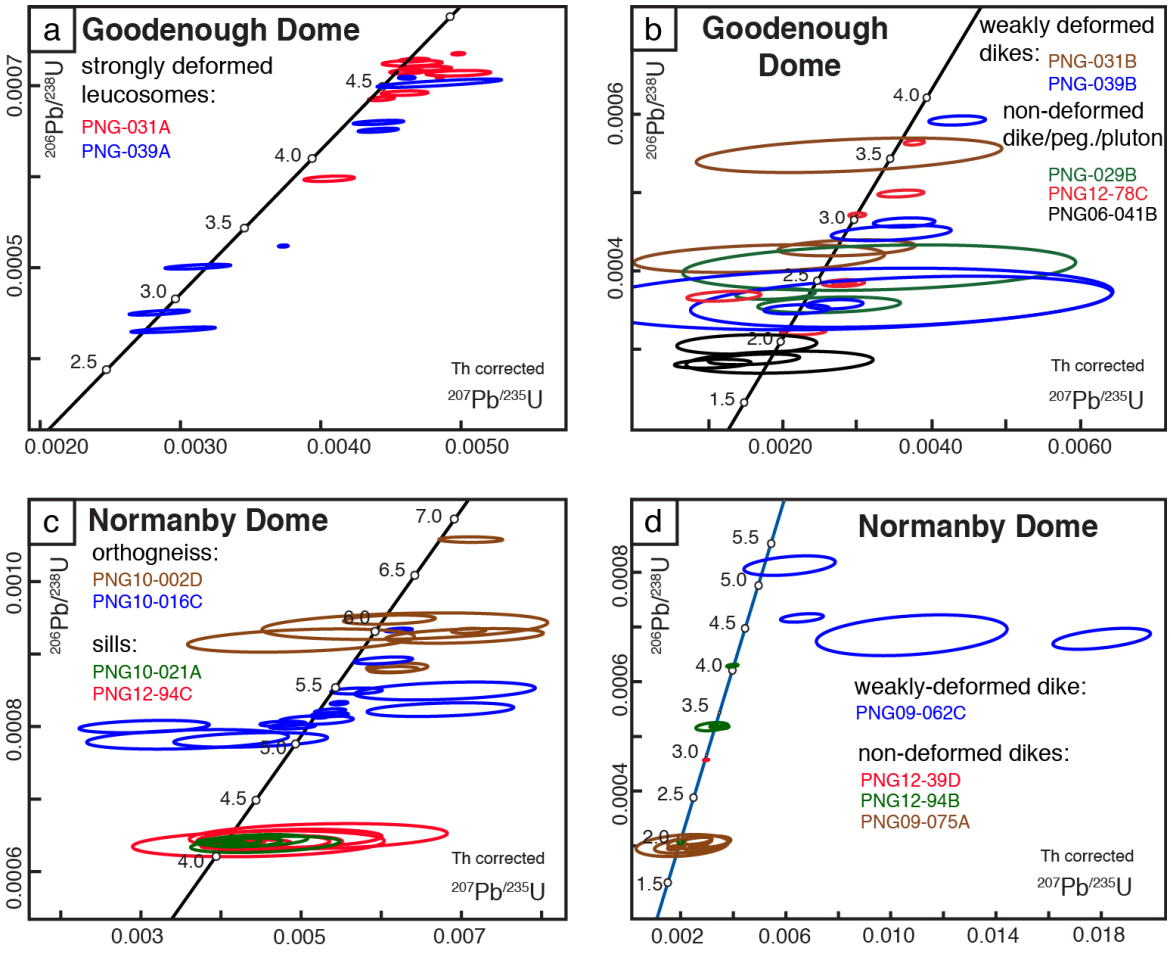

Figure 5.4: Concordia diagrams showing the U-Pb zircon results from PNG samples: Goodenough Dome (a) strongly deformed leucosomes; (b) weakly deformed dikes, non-deformed dikes, pegmatite, and pluton; Normanby Dome (c) gneisses and deformed granodiorite sills; (d) weakly deformed dike and non-deformed dikes. Each ellipse represents a single zircon analysis and the 2-sigma uncertainties. The dates listed on concordia are in Ma.

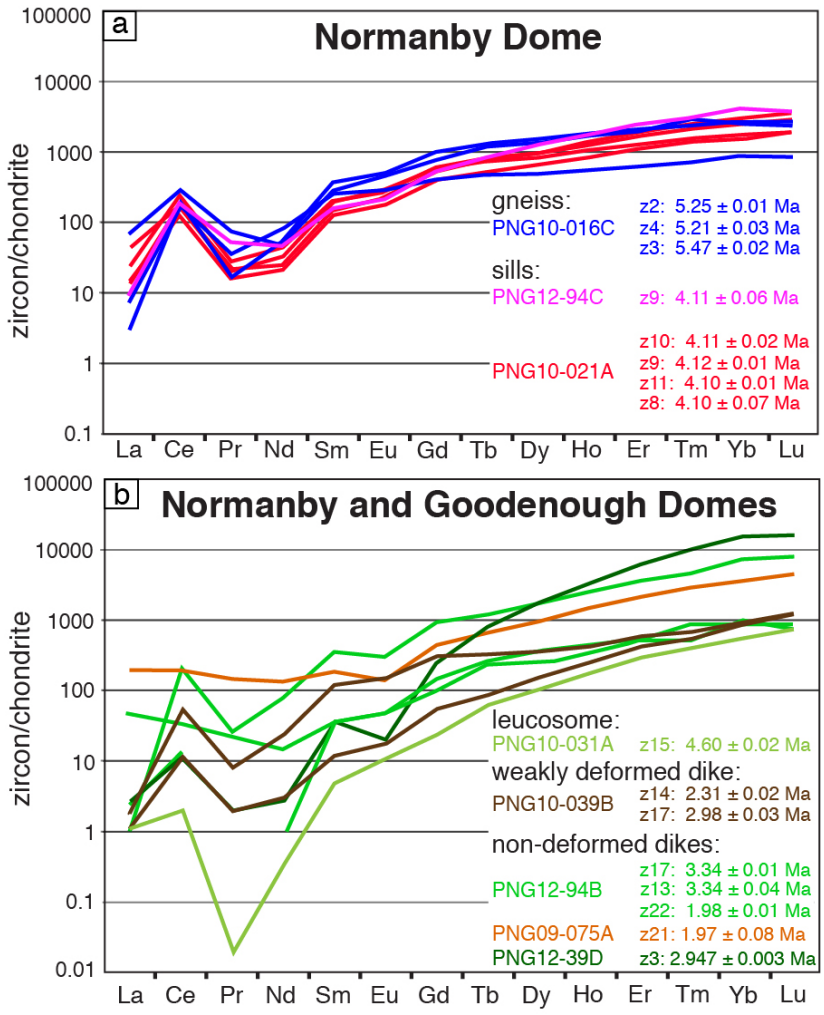

Figure 5.5: Trace-element patterns for individual zircon grains measured by TIMS-TEA for (a) Normanby Dome orthogneiss and sills; (b) Normanby and Goodenough Domes layer-parallel leucosome and weakly and non-deformed dikes. Zircon fraction labels and corresponding date are in order of decreasing Lu concentrations (i.e., PNG10-016C z2 has the highest concentration of Lu). All analyses are normalized to chrondrite values of *Sun and McDonough*, [1989].

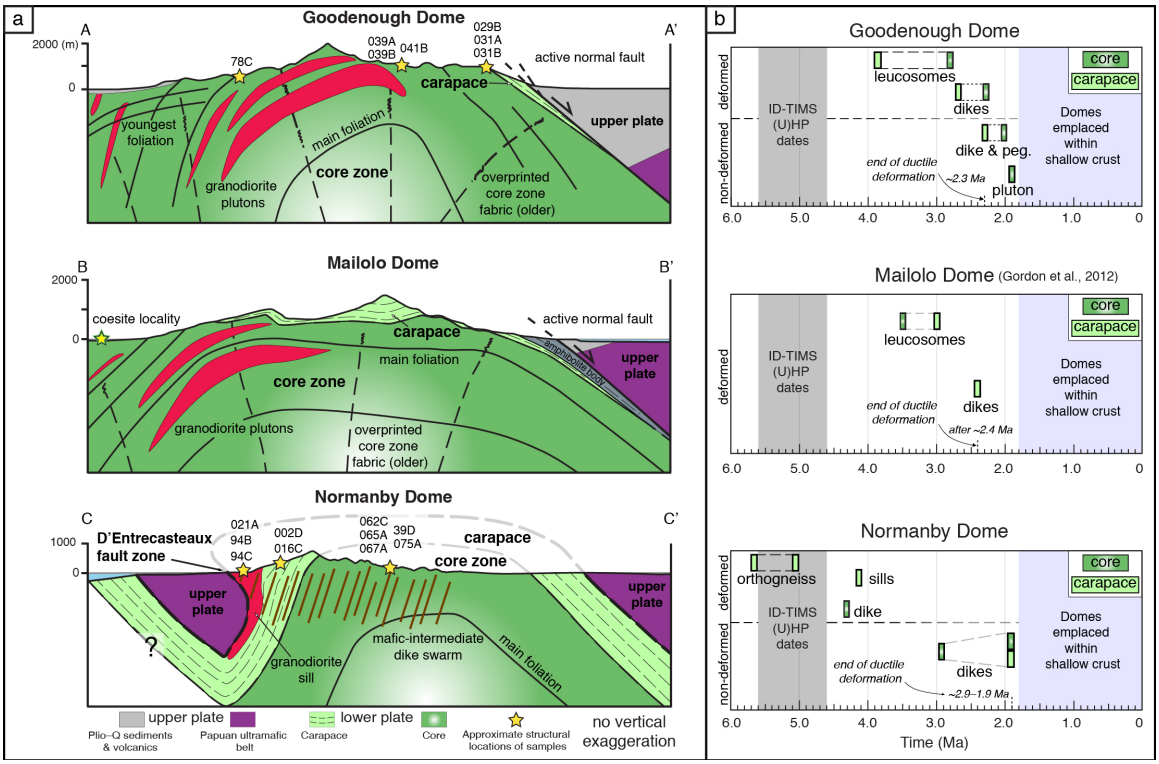

Figure 5.6: Simplified cross-sections of D'Entrecasteaux Islands gneiss domes (Goodenough, Fergusson (Mailolo), Normanby) showing the fabrics preserved within the carapace and core zones (after *Little et al.*, [2011]). (a) A–A', NE–SW structural cross-section of Goodenough Dome, B–B', NE–SW structural cross-section of Mailolo Dome, and C–C', W–E structural cross-section of Normanby Dome (see figure 2 for location of cross-sections A–A', B–B', and C–C'). Stars represent approximate structural location of samples; (b) Zircon U-Pb ID-TIMS age summary for the D'Entrecasteaux Islands gneiss domes. Timing of ultrahigh-pressure metamorphism within Mailolo Dome is based on zircon ID-TIMS dates from *Gordon et al.* [2012]. Emplacement of the gneiss domes within the upper crust at ca. 1.8 Ma is based on apatite (U-Th)/He and fission track data for the D'Entrecasteaux Islands from *Fitzgerald et al.* [2008].

Chapter 6: Conclusion to the Thesis

Timing of ultrahigh-pressure metamorphism

Ultrahigh-pressure (UHP) metamorphism results from subduction and thus consumption of oceanic crust followed by an island arc, microcontinent, or nappe of crustal material to depths of ~90–130 km (within the coesite- and diamond-stability fields) along the subducting slab (Ernst, 2006). Evidence for the subduction of this continental material to mantle depths and its subsequent exhumation to the surface is well documented within ~20 UHP terranes worldwide. Ultrahigh-pressure terranes have been grouped into 2 end members: 1) large (30,000 km^2) coherent terranes that subducted and were exhumed slowly (>20 Myr); and 2) small (~4,000 km^2) terranes that subducted and were exhumed rapidly (<10 Myr) (Kylander-Clark et al., 2012). Knowledge of the distribution, timing, and duration of peak pressures and temperatures attained during subduction, and the timing and extent of retrogression during exhumation are crucial for determining why these two end-member terranes behave so differently despite having experienced similar upper-mantle conditions.

The Western Gneiss Region (WGR), Norway, is one of the largest, best-exposed, and well-studied UHP terranes on Earth (e.g., Krogh et al., 1974, 2011; Krogh, 1977, 1982; Lappin and Smith, 1978; Griffin and Brueckner, 1980, 1985; Smith, 1984; Austrheim, 1987; Tucker et al., 1990; Andersen et al., 1991, 1998; Wain, 1997; Cuthbert et al., 2000; Wain et al., 2000; Terry et al., 2000a, 2000b; Root et al., 2005; Hacker, 2007; Kylander-Clark et al., 2009; Hacker et al., 2010: Gordon et al., 2013; Kylander-Clark and Hacker, 2014; Chapter 2 of this dissertation). Geochronological studies argue for an extensive subduction/eclogite-facies history of ca. 425–400 Ma (Terry et al., 2000a; Bingen et al., 2004; Root et al., 2004, 2005; Kylander-Clark et al., 2007, 2009; Spengler et al., 2009;

Krogh et al., 2011), followed by ~15 Myr of near-isothermal decompression and exhumation of the UHP terrane to shallow depths (Tucker et al., 1990, 2004; Schärer and Labrousse, 2003; Walsh and Hacker, 2004; Root et al., 2005; Hacker, 2007; Kylander-Clark et al., 2008; Krogh et al., 2011; Gordon et al., 2013; Spencer et al., 2013; Kylander-Clark and Hacker, 2014). In comparison, the small UHP terrane exposed in the D'Entrecasteaux Islands of eastern Papua New Guinea experienced peak metamorphism and subsequent exhumation from upper mantle depths in ~3 Myr (Davies and Warren, 1992; Hill and Baldwin, 1993; Baldwin et al., 1993, 2004, 2008; Little et al., 2011; Gordon et al., 2012; Chapters 3, 4, and 5 of this Dissertation).

Within all UHP terranes, estimates for the timing and duration of peak metamorphism have relied on a variety of different geochronometric techniques, including: U-Pb zircon high-spatial resolution ion microprobe and laser-ablation ICPMS analyses; U-Pb ID-TIMS dating of multi-grain separates and single crystals of zircon, allanite, rutile, and titanite; Sm-Nd and Lu-Hf garnet-whole rock isochron ages; and Ar–Ar phengite dating. In many cases, these geochronometric techniques produce ages that are either inaccurate or imprecise. Problems encountered with these previous studies include: large uncertainties associated with small sample volume, multi-grain separates of zircon and rutile may result in inaccurate and/or mixed ages, and fractions of garnet may be averaging dates from multiple, distinct growth zones. In light of these issues, chapters 2 and 4 from this dissertation have combined high-spatial resolution and high-precision zircon geochronology of single crystals, or fragments of crystals, to resolve UHP metamorphism at sub-million-year-timescales that had not yet been previously attained.

Chapter 2 of this dissertation uses high-spatial resolution LASS zircon geochronology on two UHP eclogites from the giant WGR UHP terrane to find Scandian-aged zircon. Subsequently, the exact same Scandian zircon, or portion of zircon, was dated with high precision ID-TIMS-TEA. The zircon U-Pb and trace-element results record two distinct eclogite-facies (re)crystallization events at ca. 409–407 Ma and ca. 402 Ma from eclogites at two widely separated localities. These results reveal two eclogite-facies events within a ~7 Myr time window, which contrasts with previous interpretations that a large portion of the WGR resided for > 20 Myr at eclogite-facies depths (e.g., Kylander-Clark et al., 2007, 2009).

Chapter 4 of this dissertation attempts to better understand the timing of UHP metamorphism in the world's youngest known UHP terrane. Zircon within eclogite was carefully mapped throughout the thin section and inclusions within zircon were also noted. Subsequently, zircon were extracted from the rock and analyzed by ID-TIMS-TEA to decipher between peak metamorphism and retrogression-related metamorphism associated with exhumation to the surface. The results document tectonic events at a sub-million year timescale, with peak metamorphism occurring at ca. 6.0–5.2 Ma, followed by initial eclogite retrogression at 4.6–4.3 Ma and near-complete overprinting of eclogites at ca. 2.8–2.6 Ma.

The high-precision results from both terranes provide insight into discrete tectonic events during UHP metamorphism and exhumation from mantle depths that have not been resolved in the previous geochronometric studies of these UHP terranes (e.g., Kylander-Clark et al., 2007, 2009; Krogh et al., 2011; Monteleone et al., 2007, Zirakparvar et al., 2011). The similar eclogite-facies (re)crystallization events recorded in

two of the UHP domains across the giant WGR support the interpretation that the subducted crustal rocks were exhumed as a large, coherent body. In comparison, the timing of peak UHP metamorphism in the PNG terrane combined with timing estimates for emplacement of the terrane within the upper crust, indicate some of the most rapid exhumation rates (≥1.5 cm/yr) reported among UHP terranes.

Building upon previous studies from the WGR and the eastern PNG UHP terranes, this dissertation has investigated the pressures and temperatures at which UHP eclogites equilibrate, the timing of peak metamorphism and retrogression-reactions within eclogites taking place during initial exhumation, and the decompression-related melt crystallization events that occur as the UHP rocks were exhumed to the crust. Deciphering which rocks experienced UHP metamorphism within a terrane and then combining this distribution with structural data from the host gneiss and high-precision temporal results provides insight into the dynamics of subduction-zone processes, such as the amount of material, rates, and mechanisms responsible for the subduction–exhumation of continental rocks. New insight into the duration at which subducted crustal material remains within the mantle and the rates of exhumation, whether continuous or incremental, can now be implemented into high-resolution numerical models attempting to decipher UHP exhumation mechanisms and the cause of variations seen among different collisional orogens.

References

Andersen, T.B., Jamtveit, B., Dewey, J.F., Swensson, E. (1991), Subduction and eduction of continental crust: major mechanisms during continent-continent collision and orogenic extensional collapse, a model based on the south Norwegian Caledonides. *Terra Nova*, **3**, 303-310, http://dx.doi.org/10.1111/j.1365-3121.1991.tb00148.x.

Andersen, T.B., Berry, H.B. IV, Lux, D.R., and Andresen, A. (1998), The tectonic significance of pre-Scandian $^{40}Ar/^{39}Ar$ phengite cooling ages in the Caledonides of western Norway. *Geological Society [London] Journal*, **155**, 297–309, http://dx.doi.org/10.1144/-gsjgs.155.2.0297.

Austrheim, H. (1987), Eclogitization of lower crustal granulites by fluid migration through shear zones. *Earth Planet. Sci. Lett.*, **81**, 221–232, http://dx.doi.org/10.1016/0012-821X(87)90158-0.

Austrheim, H. (1998), The influence of fluid and deformation on metamorphism of the deep crust and consequences for the geodynamics of collision zones. In: Hacker, B., Liou, J.G. (Eds.), When Continents Collide: Geodynamics and Geochemistry of Ultrahigh Pressure Rocks, *Chapman & Hall*, 297–323, http://dx.doi.org/10.1007/978-94-015-9050-1_12.

Baldwin, S.L., G.S. Lister, E.J. Hill, D.A. Foster, and I. McDougall (1993), Thermochronologic constraints on the tectonic evolution of active metamorphic core complexes, D'Entrecasteaux Islands, Papua New Guinea, *Tectonics*, **12**, 611–628, doi: 10.1029/93TC00235.

Baldwin, S.L., B. Monteleone, L.E. Webb, P.G. Fitzgerald, M. Grove, and E.J. Hill (2004), Pliocene eclogite exhumation at plate tectonic rates in eastern Papua New Guinea, *Nature*, **431**, 263–267, doi:10.1038/nature02846.

Baldwin, S.L., L.E. Webb, and B.D. Monteleone (2008), Late Miocene coesite-eclogite exhumed in the Woodlark Rift, *Geology*, **36**, 735–738, doi: 10.1130/G25144A.1.

Bingen, B., Austrheim, H., Whitehouse, M.J., Davis, W.J. (2004), Trace element signature and U–Pb geochronology of eclogite-facies zircon, Bergen Arcs, Caledonides of W Norway. *Contrib. Mineral. Petrol.*, **147**, 671–683, http://dx.doi.org/10.1007/s00410-004-0585-z.

Cuthbert, S.J., Carswell, D.A., Krogh-Ravna, E.J., Wain, A. (2000), Eclogites and eclogites in the Western Gneiss Region, Norwegian Caledonides. *Lithos*, **52**, 165–195, http://dx.doi.org/10.1016/S0024-4937(99)00090-0.

Davies, H.L., and R.G. Warren (1992), Eclogites of the D'Entrecasteaux Islands, *Contrib. Mineral. Petrol.*, **112**, 463–474, doi: 10.1007/BF00310778.

Ernst, W. G. (2006). Preservation/exhumation of ultrahigh-pressure subduction complexes. *Lithos*, *92*(3), 321-335.

Griffin, W.L., H.K. Brueckner (1980), Caledonian Sm-Nd ages and a crustal origin for Norwegian eclogites, *Nature*, **285**, 319–321, http://dx.doi.org/10.1038/285319a0.

Griffin, W.L., Brueckner, H.K. (1985), REE, Rb-Sr and Sm-Nd studies of Norwegian eclogites. *Chem. Geol.*, **52**, 249–271, http://dx.doi.org/10.1016/0168-9622(85)90021-1.

Gordon, S.M., T.A. Little, B.R. Hacker, S.A. Bowring, S.L. Baldwin, and A.R.C. Kylander-Clark, (2012), Multi-stage exhumation of young UHP–HP rocks: timescales of melt crystallization in the D'Entrecasteaux Islands, southeastern Papua New Guinea, *Earth Planet. Sci. Lett.*, **351–352**, 237–246, doi: 10.1016/j.epsl.2012.07.014.

Gordon, S. M., Whitney, D. L., Teyssier, C. & Fossen, H. (2013), U–Pb dates and trace-element geochemistry of zircon from migmatite, Western Gneiss Region, Norway: significance for history of partial melting in continental subduction. *Lithos*, **170–171**, 35–53, http://dx.doi.-org/10.1016/j.lithos.2013.02.003.

Hacker, B.R. (2007), Ascent of the ultrahigh-pressure Western Gneiss Region, Norway. In: Cloos, M., W.D. Carlson, M.C. Gilbert, J.G. Liou, and S.S. Sorenson (Eds.), Convergent Margin Terranes and Associated Regions, A Tribute to W.G. Ernst, *Geological Society of America Special Paper*, **419,** 171–184, Geological Society of America, Boulder, CO, http://dx.doi.org/10.1130/2006.2419(09).

Hacker, B.R., Andersen, T.B., Johnston, S., Kylander-Clark, A.R.C., Peterman, E.M., Walsh, E.O., Young, D. (2010), High-temperature deformation during continental-margin subduction & exhumation: the ultrahigh-pressure Western Gneiss Region of Norway. *Tectonophysics*, **480(1–4)**, 149–171. doi:http://dx.doi.org/10.1016/j.tecto.2009.08.012.

Hill, E.J., and Baldwin, S.L. (1993), Exhumation of high-pressure metamorphic rocks during crustal extension in the D'Entrecasteaux region: Papua New Guinea, *J. Metamorph. Geol.*, **11**, 261–277, doi: 10.1111/j.1525-1314.1993.tb00146.x.

Jamtveit, B., Carswell, D.A, Mearns, E.W. (1991), Chronology of the high-pressure metamorphism of Norwegian garnet peridotites/pyroxenites, *J. Metamorph. Geol.*, **9**, 125–139, http://dx.doi.org/10.1111/j.1525-1314.1991.tb00509.x.

Krogh, E.J. (1977), Evidence for Precambrian continent-continent collision in western Norway. *Nature*, **267**, 17-19, http://dx.doi.org/10.1038/267017a0.

Krogh, E.J. (1982), Metamorphic evolution of Norwegian country-rock eclogites, as deduced from mineral inclusions and compositional zoning in garnets. *Lithos*, **15**, 305-321, http://dx.doi.org/10.1016/0024-4937(82)90021-4.

Krogh, T.E., Mysen, B.O., Davis, G.L. (1974), A Paleozoic age for the primary minerals of a Norwegian eclogite. Annual Report of the Geophysical Laboratory. *Carnegie Institution*, Washington, **73**, 575–576.

Krogh, T.E., Kamo, S.L., Robinson, P., Terry, M.P., Kwok, K. (2011), U–Pb zircon geochronology of eclogites from the Scandian Orogen, northern Western Gneiss Region, Norway: 14–20 million years between eclogite crystallization and return to amphibolite-facies conditions. *Can. J. Earth Sciences*, **48(2)**, 441–472, http://dx.doi.org/10.1139/E10-076.

Kylander-Clark, A.R.C., Hacker, B.R. (2014), Age and significance of felsic dikes from the UHP western gneiss region. *Tectonics*, http://dx.doi.org/10.1002/2014TC003582.

Kylander-Clark, A.R.C., Hacker, B.R., Johnson, C.M., Beard, B.L., Mahlen, N.J., Lapen, T.J. (2007), Coupled Lu–Hf and Sm–Nd geochronology constrains prograde and exhumation histories of high- and ultrahigh-pressure eclogites from western Norway. *Chem. Geol.*, **242(1–2)**, 137–154, http://dx.doi.org/10.1016/j.chemgeo.2007.03.006.

Kylander-Clark, A.R.C., Hacker, B.R., Mattinson, J.M. (2008), Slow exhumation of UHP terranes: titanite and rutile ages of the Western Gneiss Region, Norway. *Earth Planet. Sci. Lett.*, **272(3-4)**: 531–540, http://dx.doi.org/10.1016/j.epsl.2008.05.019.

Kylander-Clark, A.R.C., Hacker, B.R., Johnson, C.M., Beard, B.L., Mahlen, N.J. (2009), Slow subduction and rapid exhumation of a thick ultrahigh-pressure terrane. *Tectonics*, **28(2)**, TC2003, http://dx.doi.org/10.1029/2007TC002251.

Kylander-Clark, A. R. C., B.R. Hacker, C.G. Mattinson (2012), Size and exhumation rate of ultrahigh-pressure terranes linked to orogenic stage, *Earth Planet. Sci. Lett.*, **321–322**, 115–120, http://dx.doi.org/10.1016/j.epsl.2011.12.036.

Kylander-Clark, A.R.C., Hacker, B.R., Cottle, J.M., (2013), Laser-ablation split-stream ICP petrochronology. *Chem. Geol.*, **345**, 99–112, http://dx.doi.org/10.1016/j.chemgeo.-2013.02.019.

Lappin, M.A., Smith, D.C. (1978), Mantle-equilibrated orthopyroxene eclogite pods from the Basal Gneisses in the Selje District, western Norway. *J. Petrol.*, **19**, 530–584, http://dx.doi.org/10.1093/petrology/19.3.530.

Little, T.A., B.R. Hacker, S.M. Gordon, S.L. Baldwin, P.G. Fitzgerald, S. Ellis, and M. Korchinski (2011), Diapiric exhumation of Earth's youngest (UHP) eclogites in the

gneiss domes of the D'Entrecasteaux Islands, Papua New Guinea, *Tectonophysics*, **510**, 39–68, doi: 10.1016/j.tecto.2011.06.006.

Monteleone, B.D., Baldwin, S.L., Webb, L.E., Fitzgerald, P.G., Grove, M., Schmitt, A.K. (2007), Late Miocene–Pliocene eclogite facies metamorphism, D'Entrecasteaux Islands, SE Papua New Guinea, *J. Metamorph. Geol.*, **25**, 245–265, http://dx.doi.org/10.1111/j.1525-1314.2006.00685.x.

Root, D.B., Hacker, B.R., Mattinson, J.M., Wooden, J.L. (2004), Zircon geochronology and ca. 400 Ma exhumation of Norwegian ultrahigh-pressure rocks: an ion microprobe and chemical abrasion study. *Earth Planet. Sci. Lett.*, **228**, 325–341, http://dx.doi.org/10.1016/-j.epsl.2004.10.019.

Root, D.B., Hacker, B.R., Gans, P.B., Ducea, M.N., Eide, E.A., Mosenfelder, J.L. (2005), Discrete ultrahigh-pressure domains in the Western Gneiss Region, Norway: implications for formation and exhumation. *J. Metamorph. Geol.*, **23**, 45–61, http://dx.doi.org/10.1111/-j.1525-1314.2005.00561.x.

Schärer, U., Labrousse, L. (2003), Dating the exhumation of UHP rocks and associated crustal melting in the Norwegian Caledonides, *Contrib. Mineral. Petrol.*, **144**, 758–770, http://-dx.doi.org/10.1007/s00410-002-0428-8.

Schaltegger, U., Fanning, C.M., Günther, D., Maurin, J.C., Schulmann, K., Gebauer, D. (1999), Growth, annealing and recrystallization of zircon and preservation of monazite in high-grade metamorphism: conventional and in situ U–Pb isotope, cathodoluminescence and microchemical evidence. *Contrib. Mineral. Petrol.*, **134**, 186–201, http://dx.doi.org/10.1007/-s004100050478.

Smith, D.C. (1984), Coesite in clinopyroxene in the Caledonides and its implications for geodynamics. *Nature*, **310**, 641–644, http://dx.doi.org/10.1038/310641a0.

Spencer, K.J., Hacker, B.R., Kylander-Clark, A.R.C., Andersen, T.B., Cottle, J.M., Stearns, M.A., Poletti, J.E., Seward, G.G.E. (2013), Campaign style titanite U–Pb dating by laser-ablation ICP: implications for crustal flow, phase transformations and titanite closure. *Chem. Geol.*, **341**, 84–101, http://dx.doi.org/10.1016/j.chemgeo.2012.11.012.

Spengler, D., Brueckner, H.K., van Roermund, H.L.M., Drury, M.R., Mason, P.R.D. (2009), Long-lived, cold burial of Baltica towards 200 km depth. *Earth Planet. Sci. Lett.*, **281**, 27–35, http://dx.doi.org/10.1016/j.epsl.2009.02.001.

Terry, M.P., Robinson, P., Ravna, E.J.K. (2000a), Kyanite eclogite thermobarometry and evidence for thrusting of UHP over HP metamorphic rocks, Nordøyane, Western Gneiss Region, Norway. *Amer. Mineral.*, **85**, 1637–1650.

Terry, M.P., Robinson, P., Hamilton, M.A., Jercinovic, M.J. (2000b), Monazite geochronology of UHP and HP metamorphism, deformation, and exhumation, Nordøyane, Western Gneiss Region, Norway, *Amer. Mineral.*, **85**, 1651–1664.

Tucker, R.D., Robinson, P., Solli, A., Gee, D.G., Thorsnes, T., Krogh, T.E., Nordgulen, Ø., Bickford, M.E. (2004), Thrusting and extension in the Scandian hinterland, Norway: New U–Pb ages and tectonostratigraphic evidence. *Amer. J. Science*, **304(6)**, 477–532, http://-dx.doi.org/10.2475/ajs.304.6.477.

Tucker, R.D., Krogh, T.E., Råheim, A. (1990), Proterozoic evolution and age-province boundaries in the central part of the Western Gneiss Region, Norway. Results of U–Pb dating of accessory minerals from Trondheimsfjord to Geiranger. In Mid-Proterozoic Laurentia–Baltica. Edited by C.F. Gower, A.B. Ryan, and T. Rivers. *Geological Association of Canada, Special Paper*, **38**, 149–173.

Wain, A. (1997), New evidence for coesite in eclogite and gneisses: Defining an ultrahigh-pressure province in the Western Gneiss region of Norway. *Geology*, **25**, 927–930, http-://dx.doi.org/0.1130/0091-7613(1997) 025<0927:NEFCIE> 2.3.CO;2.

Wain, A., Waters, D., Jephcoat, A., Olijnyk, H. (2000), The high-pressure to ultrahigh-pressure transition in the Western Gneiss Region, Norway. *Eur. J. Mineral.*, **12**, 667–687, http://-dx.doi.org/10.1127/0935-1221/2000/0012-0667.

Wain, A., Waters, D., Austrheim, H. (2001), Metastability of granulites and processes of eclogitization in the UHP region of western Norway, *J. Metamorph. Geol.*, **19**, 609–625, http://dx.doi.org/10.1046/j.0263-4929.2001.00333.x.

Walsh, E.O., Hacker, B.R. (2004), The fate of subducted continental margins: two-stage exhumation of the high-pressure to ultrahigh-pressure Western Gneiss Region, Norway. *J. Metamorph. Geol.*, **22**, 671–687, http://dx.doi.org/10.1111/j.1525-1314.2004.00541.x.

Zirakparvar, N.A., S.L. Baldwin, and J.D. Vervoort (2011), Lu–Hf garnet geochronology applied to plate boundary zones: insights from the (U)HP terrane exhumed within the Woodlark Rift, *Earth Planet. Sci. Lett.*, **309**, 56–66, doi: 10.1016/j.epsl.2011.06.016.